Novel Methods for Chiral Molecules in the Gas Phase and Neoteric Solvents

Dissertation
zur
Erlangung des Doktorgrades (Dr. rer. nat.)
der
Mathematisch-Naturwissenschaftlichen Fakultät
der
Rheinischen Friedrich-Wilhelms-Universität Bonn

vorgelegt von

Jan Blasius

aus
Koblenz

Bonn 2023

Angefertigt mit Genehmigung der Mathematisch-Naturwissenschaftlichen Fakultät der
Rheinischen Friedrich-Wilhelms-Universität Bonn

Betreuerin/Erstgutachterin:	Prof. Dr. Barbara Kirchner
Zweitgutachter:	Prof. Dr. Thomas Bredow
Tag der Promotion:	19.01.2024
Erscheinungsjahr:	2024

Statement of Authorship

I, Jan Blasius, hereby declare that I am the sole author of this thesis. The ideas and work of others, whether published or unpublished, have been fully acknowledged and referenced in this thesis.

Bonn, August 2023

Publications

Parts of this thesis have already been published in peer-reviewed journals or are currently submitted for publication:

1. **J. Blasius**, P. Zaby, J. Dölz, B. Kirchner, "Uncertainty Quantification of Phase Transition Quantities from Cluster Weighting Calculations", *J. Chem. Phys.* **2022**, *157*, 014505, *doi:10.1063/5.0093057*.

2. **J. Blasius**, B. Kirchner, "Cluster-Weighting in Bulk Phase Vibrational Circular Dichroism", *J. Phys. Chem. B* **2020**, *124*, 7272–7283, *doi:10.1021/acs.jpcb.0c06313*.

3. B. Kirchner, **J. Blasius**, L. Esser, W. Reckien, "Predicting Vibrational Spectroscopy for Flexible Molecules and Molecules with Non-Idle Environments", *Adv. Theory Simul.* **2021**, *4*, 2000223, *doi:10.1002/adts.202000223*.

4. **J. Blasius**, K. Drysch, F. H. Pilz, T. Frömbgen, P. Kielb, B. Kirchner, "Efficient Prediction of Mole Fraction Related Vibrational Frequency Shifts", *submitted for publication in J. Phys. Chem. Lett.*

5. **J. Blasius**, R. Elfgen, O. Hollóczki, B. Kirchner, "Glucose in Dry and Moist Ionic Liquid: Vibrational Circular Dichroism, IR, and Possible Mechanisms", *Phys. Chem. Chem. Phys.* **2020**, *22*, 10726–10737, *doi:10.1039/c9cp06798a*.

6. **J. Blasius**, P. Zaby, O. Hollóczki, B. Kirchner, "Recognition in Chiral Ionic Liquids: The Achiral Cation Makes the Difference!", *J. Org. Chem.* **2022**, *87*, 1867–1873, *doi:10.1021/acs.joc.1c00939*.

7. B. Kirchner, **J. Blasius**, V. Alizadeh, A. Gansäuer, O. Hollóczki, "Chemistry Dissolved in Ionic Liquids. A Theoretical Perspective", *J. Phys. Chem. B* **2022**, *126*, 766–777, *doi:10.1021/acs.jpcb.1c09092*.

8. **J. Blasius**, B. Kirchner, "Selective Chirality Transfer to the Bis(trifluoromethylsulfonyl)-imide Anion of an Ionic Liquid", *Chem. Eur. J.* **2023**, e202301239, *doi:10.1002/chem.-202301239*.

Further publications which are not part of this thesis:

9. J. Ingenmey, **J. Blasius**, G. Marchelli, A. Riegel, B. Kirchner, "A Cluster Approach for Activity Coefficients: General Theory and Implementation", *J. Chem. Eng. Data* **2019**, *64*, 255–261, *doi:10.1021/acs.jced.8b00779*.

10. a) **J. Blasius**, E. Perlt, J. Ingenmey, M. von Domaros, O. Hollóczki, B. Kirchner, "Predicting Mole-Fraction-Dependent Dissociation for Weak Acids", *Angew. Chem. Int. Ed.* **2019**, *58*, 3212–3216, *doi:10.1002/anie.201811839*.
    b) **J. Blasius**, E. Perlt, J. Ingenmey, M. von Domaros, O. Hollóczki, B. Kirchner, "Dissoziation schwacher Säuren über den gesamten Molenbruchbereich", *Angew. Chem.* **2019**, *131*, 3245–3249, *doi:10.1002/ange.201811839*.

11. M. A. Grasser, T. Pietsch, **J. Blasius**, O. Hollóczki, E. Brunner, T. Doert, M. Ruck, "Coexistence of Tellurium Cations and Anions in Phosphonium-Based Ionic Liquids", *Chem. Eur. J.* **2022**, *28*, e202103770, *doi:10.1002/chem.202103770*.

12. S. Taherivardanjani, **J. Blasius**, M. Brehm, R. Dötzer, B. Kirchner, "Conformer Weighting and Differently Sized Cluster Weighting for Nicotine and Its Phosphorus Derivatives", *J. Phys. Chem. A* **2022**, *126*, 7070–7083, *doi:10.1021/acs.jpca.2c03133*.

13. H. Niemöller, **J. Blasius**, O. Hollóczki, B. Kirchner, "How do Alternative Amino Acids Behave in Water? A Comparative *Ab Initio* Molecular Dynamics Study of Solvated α-Amino Acids and α-Amino Amidines", *J. Mol. Liq.* **2022**, *367*, 120282, *doi:10.1016/j.molliq.2022.120282*.

14. T. Frömbgen, **J. Blasius**, V. Alizadeh, A. Chaumont, M. Brehm, B. Kirchner, "Cluster Analysis in Liquids: A Novel Tool in TRAVIS", *J. Chem. Inf. Model.* **2022**, *62*, 5634–5644, *doi:10.1021/acs.jcim.2c01244*.

15. T. Pietsch, **J. Blasius**, J. Richter, M. A. Grasser, O. Hollóczki, P. Wollmann, I. Weidinger, M. Ruck, E. Brunner, "Processing Gray Selenium in Phosphonium-Based Ionic Liquids", *Inorg. Chem.* **2023**, *62*, 1667–1678, *doi:10.1021/acs.inorgchem.2c04094*.

16. P. Zaby, **J. Blasius**, A. K. Müller, S. P. Nolan, O. Hollóczki, "Liquid Dynamics Determine Transition Metal-*N*-Heterocyclic Carbene Complex Formation", *Chem. Eur. J.* **2023**, *29*, e202203636, *doi:10.1002/chem.202203636*.

17. T. Frömbgen, **J. Blasius**, L. Dick, K. Drysch, V. Alizadeh, L. Wylie, B. Kirchner, "Reducing Uncertainties in and Analysis of Ionic Liquid Trajectories", *Reference Module in Chemistry, Molecular Sciences and Chemical Engineering* **2023**, tba, *doi:10.1016/B978-0-12-821978-2.00097-0*.

Presentations and posters on conferences and workshops:

1. Poster on "Calculating VCD Spectra from AIMD Simulations", *Lorentz Center Workshop – Chirality in Industry: Integrated Solutions for Vibrational Circular Dichroism*, **April 2019**, Leiden, Netherlands.

2. Poster on "New Approaches for Calculating VCD Spectra", *31th Symposium on Chirality – Chirality 2019*, **July 2019**, Bordeaux, France.

3. Poster on "A Cluster Approach for Population Weighted VCD Spectra", *55th Symposium on Theoretical Chemistry*, **September 2019**, Rostock, Germany.

4. Invited talk ("CIC Advancement Young Scientist Award For Computational Chemistry" award lecture) on "Cluster-Weighting in Vibrational Circular Dichroism Spectroscopy", *GCC 2020 and SAMPL Satellite Workshop*, **November 2020**, online conference.

5. Contributed talk on "Glucose in Dry and Moist Ionic Liquids", *Workshop on Ionic Liquids*, **January 2021**, online conference.

6. Poster on "Enantiomeric Recognition in Chiral Ionic Liquids: Spectroscopic and Structural Imprints", *3rd IMPRS RECHARGE Symposium*, **May 2021**, online conference.

7. Contributed talk on "Chirality Transfer and Molecular Recognition in Chiral Ionic Liquids: Spectroscopic Insights", *Webinar of the European Society of Ionic Matter: Spectroscopy of Ionic Liquids*, **February 2022**, online conference.

8. Poster on "Predicting Mole-Fraction-Dependent Acid Dissociation, pK_a, Ion Concentration and Conductivity", *RSCPoster Twitter Conference*, **March 2022**, online conference.

9. Invited talk on "Ionic Liquids and Deep Eutectic Solvents – Sustainable Media for CO_2 Absorption", *DPG Meeting of the Condensed Matter Section*, **September 2022**, Regensburg, Germany.

10. Invited talk on "Modeling Vibrational Spectroscopy and Chirality Transfer in Ionic Liquids", *Seminar of the Chemistry Department*, **November 2022**, Debrecen, Hungary.

11. Poster on "How to Obtain Liquid Phase Vibrational Spectra from Molecular Dynamics", *25th JCF Spring Symposium*, **March 2023**, Giessen, Germany.

12. Poster on "Chirality Transfer and Enantiomeric Recognition in Chiral Ionic Liquids", *9th International Congress on Ionic Liquids – COIL9*, **April 2023**, Lyon, France.

13. Poster on "How to Obtain Liquid Phase Vibrational Spectra from Molecular Dynamics", *9th International Congress on Ionic Liquids – COIL9*, **April 2023**, Lyon, France.

14. Invited talk on "Modeling Liquid Phase Vibrational Spectra: From Molecular to Ionic Liquids", *CiTQ Multidisciplinary Seminars*, **May 2023**, Tarragona, Spain.

Acknowledgements

The content of this thesis has been developed in the research group of Prof. Dr. Barbara Kirchner at the University of Bonn from November 2019 to August 2023. At this point, I would like to thank all the people who supported me during this time and made this thesis possible.

First of all, I would like to thank my supervisor, Prof. Dr. Barbara Kirchner, for giving me the opportunity to join her research group and for offering the scientific freedom to realize all the fascinating research projects we have been working on. Thank you for sharing your overwhelming scientific expertise and experience with me, and of course thank you for providing all the necessary infrastructure, computational resources, and financial support.

I would like to thank Prof. Dr. Thomas Bredow for being the second referee of this thesis, Prof. Dr. Patrycja Kielb for being the head of the committee, and PD Dr. Gregor Hagelüken for completing the committee.

Also, many thanks to Prof. Dr. Oldamur Hollóczki for giving me the opportunity and trust to participate in his research and for teaching me a lot about writing scientific articles.

Special thanks to all my former and current colleagues from the Kirchner research group who made the time at the Mulliken Center unforgettable. Thank you for all the fruitful discussions, scientific collaborations, barbecues in the garden, and enthusiastic Spikeball games.

I am very grateful to Leonard Dick, Tom Frömbgen, Sascha Leyendecker, Henrik Niemöller, Dr. Werner Reckien, and Paul Zaby for proofreading this thesis.

Concerning technical issues, I would like to thank Dr. Werner Reckien and Jens Mekelburger for maintaining the computers and HPC clusters.

Another special thanks to Prof. Dr. Patrycja Kielb and Frank Hendrik Pilz from the University of Bonn for providing experimental reference spectra.

Regarding financial support, I would like to thank the University of Bonn and the DFG, as well as the FWO and F.R.S.-FNRS under the Excellence of Science program.

Finally, I would like to thank all my friends from home, my parents Rainer & Susanne, my sister Julia, and my girlfriend Valerija for all the emotional support over the last years.

Abstract

This thesis deals with the development and application of computational methods for the calculation of infrared (IR) and vibrational circular dichroism (VCD) spectra in the gas and liquid phase. A key aspect involves the simulation of solvent and environmental effects, with particular emphasis on solvents that strongly interact with the molecules of interest. In this context, there are two main objectives to be addressed. First, the development of a new method for the calculation of liquid phase IR and VCD spectra that is capable of modeling the effects of intermolecular interactions and the concentration dependence of vibrational spectra at low computational costs, and second, the study of chirality transfer in ionic liquids (ILs) and its influence on enantiomeric recognition processes.

Chapter 1 introduces the topics of vibrational optical activity, ILs, and chirality transfer, and chapter 2 provides a comprehensive overview of the essential theoretical foundations required for the modeling of vibrational spectra with different approaches.

The first objective of the thesis is addressed in chapters 3 to 6 by introducing the cluster-weighting approach, which determines the vibrational spectra of a system as weighted average of a cluster ensemble. The cluster weights are determined by quantum cluster equilibrium (QCE) calculations, which require experimental input data. In chapter 3, a preliminary investigation is conducted to study how uncertainties in these experimental input data affect vaporization enthalpies, vaporization entropies, and cluster populations computed with QCE. Through a systematic variation of the input data and the application of two uncertainty propagation methods, namely the Monte Carlo method and the Gauss–Hermite quadrature, it is shown that typical measurement errors do not significantly affect the results of the QCE calculations.

In chapters 4 and 5, the cluster-weighting approach for vibrational spectra is introduced and applied to calculate gas and liquid phase IR and VCD spectra for (*R*)-butan-2-ol. For the gas phase spectra, excellent agreement with experimental reference data is observed when using a representative conformer ensemble of monomers. For the liquid phase, it is shown that the best agreement between experimental and calculated spectra is obtained for cluster sets composed only of global minimum structures and that clusters up to hexamers are generally sufficient to model the characteristics of the liquid phase IR and VCD spectra. As a result, it is not necessary to include a large number of clusters for the liquid phase, which reduces the overall computational effort of the cluster-weighting approach. A comparison of cluster-weighting with a well-established method based on *ab initio* molecular dynamics (AIMD) simulations and the correlation of dipole moments shows that this AIMD approach yields spectra of superior quality but at a significantly higher computational cost. During the application of the AIMD approach, the problem of insufficient conformer sampling is encountered and the conformer replica simulations

approach is proposed to solve this issue. Furthermore, since the AIMD approach suffers from the time-consuming calculation of magnetic dipole moments to obtain VCD spectra, a promising alternative approach based on atomic partial charges and classical definitions of dipole moments is proposed and applied to calculate gas phase IR and VCD spectra of (*R*)-butan-2-ol.

In chapter 6, the cluster-weighting approach is extended to binary systems and applied to calculate mole fraction dependent IR and VCD spectra for acetonitrile/(*R*)-butan-2-ol mixtures. The obtained IR spectra are in good agreement with experimental references and a mole fraction related vibrational frequency shift can be modeled with deviations of less than $1\,\mathrm{cm}^{-1}$ between experiment and calculation. Although the calculated VCD spectra cannot be fully validated due to missing experimental data, their mole fraction dependence is reasonable considering that acetonitrile is achiral and thus does not contribute to the VCD spectra of the mixtures.

The second objective of the thesis is addressed in chapters 7 to 10 by studying the dissolution of chiral molecules in ILs using AIMD simulations. In chapter 7, the dissolution of different D-glucose isomers in 1-ethyl-3-methylimidazolium acetate and its mixtures with water is investigated. In addition to investigating possible reactions for the anomeric conversion and decomposition of D-glucose, it is observed that the addition of water weakens the cation–anion interactions, causing peak shifts in the calculated IR spectra. Furthermore, the transiently chiral 1-ethyl-3-methylimidazolium shows a pronounced VCD activity, revealing that the chiral D-glucose units transfer chiral information to the cation.

Chapter 8 investigates the recognition of butan-2-ol enantiomers by the chiral IL 1-ethyl-3-methylimidazolium L-alaninate. The dissolution of (*R*)-butan-2-ol in the IL is energetically more favorable by $18.8\,\mathrm{kJ\,mol}^{-1}$ than the dissolution of (*S*)-butan-2-ol, in part due to discriminative interactions between the butan-2-ol enantiomers and the L-alaninate anion, but also due to chirality transfer from all involved chiral molecules to the 1-ethyl-3-methylimidazolium cation. In particular, (*R*)-butan-2-ol and L-alaninate induce the same conformation in the cation, while (*S*)-butan-2-ol induces a mirrored structure, causing an energetic destabilization as (*S*)-butan-2-ol competes with the anion to induce opposite conformations in the cation.

The occurrence of this chirality transfer is evidenced by calculated VCD spectra in chapter 9 and the importance of an accurate description of the intermolecular interactions for the study of chirality transfer phenomena is emphasized. In addition, chapter 9 provides an overview of the achievements and future challenges associated with modeling reactions, chirality, and radicals in ILs. For these three examples, extensive literature reviews are provided, and some of the challenges are illustrated using case studies.

In Chapter 10 the dissolution of (*R*)-1,2-propylene oxide in 1-ethyl-3-methylimidazolium bis(trifluoromethylsulfonyl)imide is investigated. In contrast to the systems studied before, the employed IL consists of two transiently chiral ions and it is observed that the chiral solute selectively transfers chiral information to the anion while the cation remains unaffected. This selective chirality transfer is manifested by an excess population of one of two mirrored *trans* conformers, and vibrational optical activity of the anion is observed in calculated VCD spectra.

In the end, chapter 11 summarizes the observations and achievements of the thesis and puts them into perspective for future research.

Contents

1. Introduction

Growing populations, changing climatic conditions, and shrinking arable land are undoubtedly some of the most important challenges facing societies and humanity as a whole. While these problems are obviously related to many social and political questions, they also pose serious challenges to the chemical industry, as the global market for chiral compounds is experiencing significant growth. This increasing demand for chiral chemicals is primarily driven by the growing global need for pharmaceuticals, agrochemicals, and food ingredients. For example, to address concerns about global food security, chiral agrochemicals such as herbicides, pesticides, plant growth regulators, or fungicides are widely used to achieve optimal agricultural productivity, and the growing population coupled with the expansion of healthcare infrastructure is leading to an increased need for chiral drug molecules.

These examples illustrate applications for chiral components, but much of the chiral chemicals market is also based on the technologies required to produce the chemical compounds. In many cases, chiral substances are used in their enantiomerically pure form, either to increase their efficacy or to avoid unwanted effects. An illustrative case of the consequences that can arise when drugs are not administered in their enantiomerically pure form is the tragic incident involving Contergan, the sleeping pill marketed as a racemic mixture of the barbiturate thalidomide.[18] While the (*R*)-enantiomer of thalidomide has a soothing effect, the (*S*)-enantiomer can cause limb deformities,[19] resulting in thousands of children worldwide being born with malformations in the 1950s and 1960s. This raised awareness of the importance of enantiopurity in the field of drug discovery, and in 1992, the Food and Drug Administration issued a policy statement concerning the development of stereoisomeric drugs,[20,21] which for the first time emphasized the importance of enantiopurity in the drug discovery and development process. In agricultural applications, chiral compounds are still mostly used as racemates, but it is known that enantiomerically pure compounds can result in higher yields and better crop protection.[22,23]

This need for enantiomerically pure products requires a critical and continuous evaluation of the manufacturing processes and underlying technologies, including the improvement of existing and the development of new methods for the synthesis, separation, and analysis of chiral chemicals. To give a brief overview, the synthesis of enantiopure compounds can for instance be achieved by asymmetric catalysis[24,25] or chiral pool synthesis.[26] Common methods for separating enantiomers include crystallization,[27] liquid–liquid extraction,[28,29] and chromatographic[27] or membrane-based separation.[30] Examples of methods for analyzing the absolute configuration and enantiomeric purity (or enantiomeric excess) of a chiral compound include X-ray crystallography,[31] nuclear magnetic resonance (NMR) spectroscopy,[32,33] or optical activity methods.[34–36]

Among these analytical techniques, vibrational optical activity (VOA) methods[34,36,37] such as

vibrational circular dichroism (VCD),[38–41] which is the chiral version of infrared (IR) spectroscopy, are particularly powerful for determining the three-dimensional structure and thus the absolute configuration of molecules. Although the measurement of such spectra is nowadays a routine task, the interpretation of the results requires reference data of known chirality or enantiomeric purity, usually derived from computational chemistry calculations. Accordingly, there is a great need for reliable theoretical methods to calculate VCD spectra. The fact that the first methods were presented in the early 1980s,[42,43] but the development of new methods continues to this day,[44,45] shows that there are still many unsolved problems to be addressed.

Therefore, the main purpose of this thesis is the development, evaluation, and application of computational methods for the calculation of IR and VCD spectra in the gas and liquid phase. Since these spectra are often measured in solution, special emphasis is placed on modeling solvent and environmental effects, with particular attention to non-idle solvents that strongly interact with the solute molecules of interest. These solute–solvent interactions can have significant effects on vibrational spectra, causing peak shifts, intensity perturbations, or even changes in peak signs,[2,3,5,8,46–50] and have to be taken into account in calculations. Examples of such solvents are alcohols and ionic liquids (ILs), which are in the focus of this thesis. In addition, some of the presented methods are used to study chirality transfer in ILs and the ability of ILs to recognize chiral molecules. The study and understanding of these phenomena can provide valuable insights for the development of novel extraction and separation processes using ILs.

1.1. Vibrational Optical Activity

In its most general definition, VOA is a spectroscopic measure of the different interaction of a chiral molecule with left and right circularly polarized radiation during a vibrational transition.[34,36,37] VOA consists of two phenomena, VCD, which is the difference in absorption of left minus right circularly polarized IR radiation for a vibrational transition in a fixed electronic state,[38–41] and vibrational Raman optical activity (ROA), which is the difference in Raman scattering intensity for right minus left circularly polarized incident and/or scattered radiation.[51,52] Considering a pair of enantiomers, for example (*R*)- and (*S*)-1,2-propylene oxide, the IR or Raman spectra of these molecules are indistinguishable, but their VCD or ROA spectra are mirror images of each other, which means they are equal in intensity but opposite in sign. To illustrate this, fig. 1.1 shows calculated IR and VCD spectra of (*R*)- and (*S*)-1,2-propylene oxide together with an experimental VCD spectrum of (*S*)-1,2-propylene oxide. This figure also illustrates the importance of calculated reference data, since the experimental VCD spectrum alone does not provide any information about the absolute configuration of the chiral molecule. Only a comparison with the calculated reference data of known chirality allows the conclusion that the measured VCD spectrum belongs to the (*S*)-enantiomer of 1,2-propylene oxide.

The first discovery of VOA dates back to the mid-1970s,[51,53–56] and since that time, VOA techniques have evolved into well-established and widely used methods. While most routine applications involve the elucidation of absolute configurations for small organic molecules,[34,57] VOA has also been successfully applied for the structural characterization of natural products,[58]

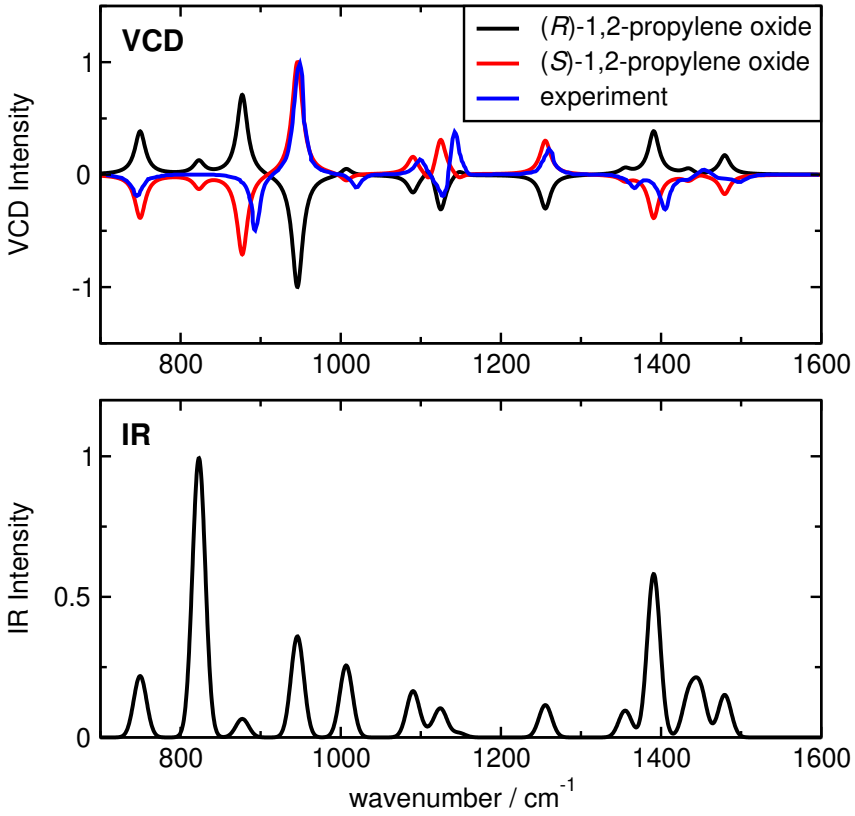

Figure 1.1. Theoretical VCD (top) and IR (bottom) spectra of (*R*)- and (*S*)-1,2-propylene oxide calculated at the BP86[68,69]/def2-TZVP[70] level of theory using the Turbomole 7.6 software package.[71–74] In addition, an experimental VCD spectrum of (*S*)-1,2-propylene oxide is shown.[75] Note that the IR spectra of the two enantiomers are the same.

peptides,[59–61] proteins,[59] carbohydrates,[62,63] or nucleic acids.[64] In addition, enantiomeric excess can be determined[65,66] and reaction progress can be followed when chiral molecules are involved.[67]

A special feature of VCD is its high structural sensitivity, not only to the absolute configuration but also to the conformation of a molecule. This leads to the fact that different conformers of the same molecule can show significant differences in their VCD spectra, as illustrated in fig. 1.2, where calculated VCD spectra for two conformers of (*R*)-butan-2-ol are shown. Although the structures of these conformers differ only in the orientation of the hydroxyl group, they show pronounced differences in their VCD spectra, especially around 1060 cm^{-1}, 1225 cm^{-1}, and in the range of 1310–1420 cm^{-1}, where the spectra are mirrored with respect to the wavenumber axis. This characteristic feature of VCD allows the study of conformer distributions[76] and conformational heterogeneity,[77] or the occurrence of predominant conformations.[46] However, it also poses severe challenges to VCD calculations, since reliable spectra can only be modeled by representative conformer ensembles. This requires a sufficient exploration of the conformational space and a weighting of all relevant conformers, which is not always trivial, for example, due to inaccuracies in calculated Boltzmann factors[76,77] or sampling problems in molecular simulations.[3] In addition, environmental or solvent effects can significantly alter the conformational preferences of molecules,[3,6,78,79] which has to be carefully considered when calculating VCD spectra.

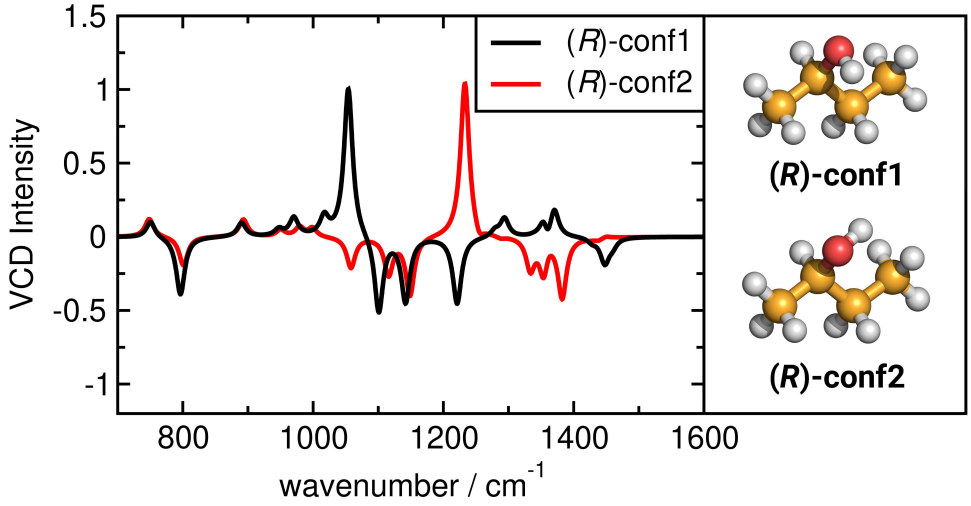

Figure 1.2. VCD spectra of two (*R*)-butan-2-ol conformers calculated at the BP86[68,69]/def2-TZVP[70] level of theory using the Turbomole 7.6 software package.[71–74]

Compared to other analytical techniques such as X-ray crystallography or NMR, VCD has several advantages. While X-ray crystallography remains one of the most reliable techniques for structure elucidation, it requires the growth of single crystals, which can be challenging.[31] Mosher's NMR method is used primarily for alcohols and amines, but requires derivatization prior to measurements,[32] and chiral liquid crystal NMR typically requires complex experimental setups and large sample sizes.[33] VCD, on the other hand, can be measured on samples in the liquid, solid, or gas phase and does not require single crystals or derivatization. However, depending on the molecule under investigation, VCD spectra can show quite complex peak patterns,[80] which complicates the comparison with calculated reference data. All of these techniques should therefore not necessarily be considered as independent tools, but rather as complementary methods.

1.2. Ionic Liquids

ILs are a class of substances that consist entirely of mobile ions and are liquid at moderate temperatures, typically with a melting point below 100 °C.[81–84] Thus, they can also be considered as molten salts, and in general, any salt that melts below 100 °C without decomposing or evaporating yields an IL. This unique property of ILs is due to their molecular composition, as they are typically composed of large, polyatomic, and charge-diffuse organic cations with low symmetry, and organic or inorganic anions with weak basicity.[85,86] Compared to conventional salts of monoatomic ions, such as sodium chloride, which has a melting point of 800.7 °C,[87] the hybrid organic-ionic nature of ILs and the resulting intermolecular interactions do not allow crystal formation at moderate temperatures. In addition, ILs generally have a negligibly low vapor pressure, high chemical, thermal, and electrochemical stability, and are liquid over a wide temperature range,[88] making them interesting solvents for industrial applications.[89]

An outstanding feature of ILs is the almost infinite tunability of their physicochemical properties. Some common IL anions and cations are shown in fig. 1.3, but in total there are millions of

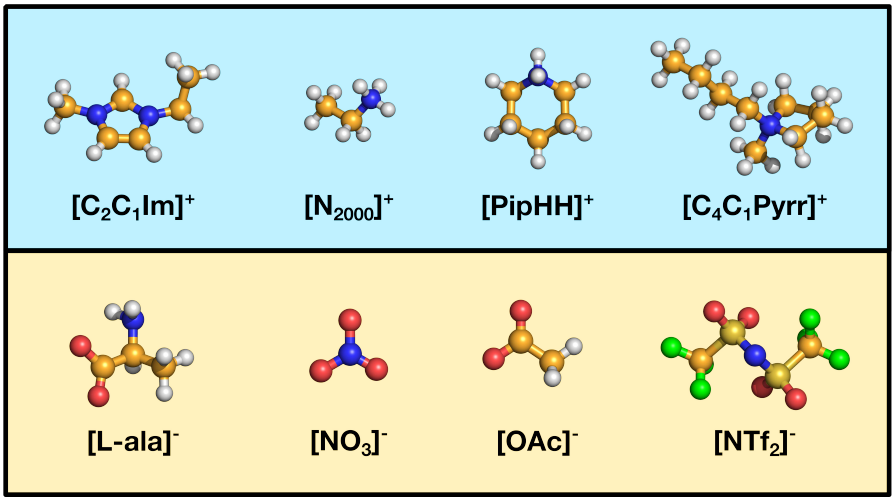

Figure 1.3. Ball-and-stick images of common IL anions and cations. Color code for the atoms is: white: H; orange: C; blue: N; red: O; green: F; yellow: S. Abbreviations for the ions are: $[C_2C_1Im]^+$: 1-ethyl-3-methylimidazolium; $[N_{2000}]^+$: ethylammonium; $[PipHH]^+$: piperidinium; $[C_4C_1Pyrr]^+$: 1-butyl-1-methyl-pyrrolidinium; $[L-ala]^-$: L-alaninate; $[NO_3]^-$: nitrate; $[OAc]^-$: acetate; $[NTf_2]^-$: bis(trifluoromethylsulfonyl)imide.

possible ILs that can be formed by combining different ions. The properties of ILs can therefore be tailored to specific applications by selecting the right combination of ions or by functionalizing the constituent ionic species.[90,91] To this end, and to enable efficient screening processes for suitable ILs, the study of structure–function relationships and IL–solute interactions is of paramount importance. Here, computational methods can serve as a powerful tool to study the properties of ILs prior to their synthesis.[92–97]

Common applications of ILs include the use as solvents, co-solvents, ligands, or catalysts in (asymmetric) synthesis,[98–104] as media in gas absorption processes,[105–107] or as electrolytes in fuel cells,[108] supercapacitors,[109–111] batteries,[109,112] and solar cells.[113–115] Furthermore, they are successfully applied in separation processes[116] such as liquid–liquid extraction, where ILs can act as additives[29] or selectors[28] to extract for example metals[117,118] or phenols[119] from liquid media. Among the various liquid–liquid extraction techniques, chiral separation methods based on ILs are of particular interest in the context of this thesis, as they can provide cheap, practical, and energy-efficient alternatives either for resolving racemic mixtures or for extracting chiral molecules from, for example, reaction media. The essential idea underlying chiral separation is the diastereomeric interaction between a chiral selector and the enantiomers in a racemic mixture,[120,121] resulting in the formation of distinct diastereomeric pairs that can be resolved.

Consequently, if an IL is to act as a chiral selector, it has to be chiral itself, which can be achieved by incorporating chiral ions such as amino acid anions.[122,123] This leads to the subgroup of chiral ILs (CILs),[121,124–126] which have already been successfully used for the separation or extraction of chiral molecules, especially for molecules with long chain or cross-linked residues.[125–129] The chiral species in CILs can be either the cation, the anion, or both.[125] While the chiral ions are required to achieve diastereomeric interactions between the IL and the enantiomers to be separated, the achiral counterions can also play an important role in chiral separation processes by interacting

with the chiral molecules through hydrogen bonding, dipole–dipole, or dispersion interactions. These interactions can cause chirality induction[120] in the achiral IL ions. Investigating the significance of this effect for the recognition and separation of chiral molecules will be the main subject of chapters 8 and 10, which is why a brief introduction to chirality induction in ILs will be given in the following section 1.3.

1.3. Chirality Induction

Many flexible molecules can adopt chiral structures in the form of enantiomeric pairs of local minima, that is, enantiomeric conformers that are mirror images of each other. An example of such a molecule is the 1-ethyl-3-methylimidazolium cation, whose conformational flexibility arises solely from the rotation of the ethyl group, resulting in the two enantiomeric conformers c'1 and c'2 shown in fig. 1.4. Since these conformers are mirror images of each other, they have opposite optical activities and consequently mirrored VCD spectra. If the energy barrier for the conversion between c'1 and c'2 is sufficiently low to allow for racemization, the abundance of both conformers is equal and their opposite optical activities cancel each other out. In this scenario, the 1-ethyl-3-methylimidazolium cation is not chiral and no optical activity can be detected. However, a neighboring chiral object or entity (e.g., a molecule[6,8,130] or metal nanoparticle[131]) interacting with the cation can break the symmetry between the enantiomeric conformers, resulting in an energetic preference and increased abundance of either c'1 or c'2.[6,130,132] This phenomenon is called chirality induction or chirality transfer and the cation is referred to as a transiently chiral molecule.[120] The resulting symmetry breaking of the conformational distribution causes the optical activities of the two conformers to no longer cancel out, which can be detected by optical activity methods such as VCD.[5,7,130,132] Other transiently chiral molecules for which such a symmetry breaking in the conformational distribution has been observed are for example ethanol,[133] 2-phenylethylthiol,[131] or the bis(trifluoromethylsulfonyl)imide anion.[8]

Possible mechanisms of chirality induction are manifold and always based on interactions between the chiral object and the molecule to which chirality is transferred. These interactions can be hydrogen bonding, π–π, dispersive, dipolar, or electrostatic interactions. The effectiveness of the chirality transfer is thereby often determined by the strength of the intermolecular interactions, that is, the stronger the intermolecular interactions, the more effective the chiral induction.[134,135] For example, it has been observed that enantioselective reactions in chiral amino ethers[136] or lactate-based ILs[137] produce only small enantiomeric excesses, probably due to the presence of charge-neutral transition states. For reactions in ILs with proposed ionic transition states, higher enantioselectivities are often observed, for example in the synthesis of functionalized chiral allylic amines by an aza-Baylis–Hillman reaction in CILs.[138] Furthermore, it has been shown that the dissolution of ILs in solvents with a high dielectric constant reduces the ability of chiral IL anions to recognize the enantiomers of chiral counter cations.[125] These examples clearly support the assumption that the transfer of chiral information between two species is strongly dependent on the strength of their interactions. For recognition and separation processes in ILs where chirality transfer plays a role, it is therefore advantageous if the interactions between the IL ions and the

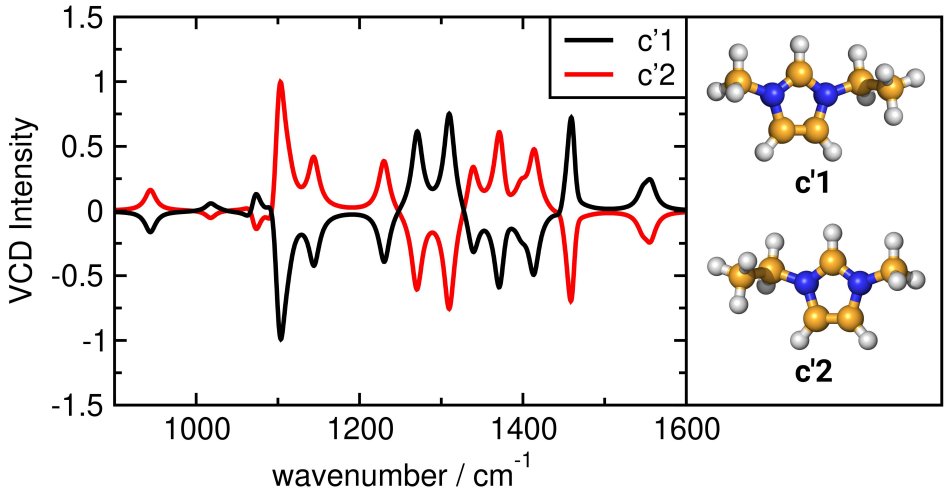

Figure 1.4. VCD spectra of the two enantiomeric 1-ethyl-3-methylimidazolium conformers calculated at the BP86[68,69]/def2-TZVP[70] level of theory using the Turbomole 7.6 software package.[71–74]

enantiomers to be separated are strong enough to compete with the intermolecular interactions of the IL moieties.

1.4. Scope of the Thesis

The scope of this thesis follows two main objectives, first, the development of a new method that allows a computationally efficient calculation of liquid phase IR and VCD spectra, and second, the study of chirality transfer in ILs and its effect on chiral recognition processes. Chapters 3 to 6 address the first goal by introducing and evaluating the cluster-weighting approach for calculating vibrational spectra of bulk phases. This approach is based on a weighted average of quantum chemically calculated clusters, whose populations (also termed as cluster weights) are determined by quantum cluster equilibrium calculations,[139–141] see section 2.2 for a methodological introduction. Since quantum cluster equilibrium calculations rely on experimental input data that are prone to measurement errors, the influence of these uncertainties on the results of the calculations is investigated in chapter 3. Therefore, two uncertainty propagation methods[142,143] are used and special emphasis is given to the calculated cluster populations.[1] In chapter 4, the cluster-weighting approach for vibrational spectra is introduced and applied for the calculation of bulk phase IR and VCD spectra of (*R*)-butan-2-ol.[2] Furthermore, the sensitivity of the cluster weights on the quantum chemical level of theory and the dependence of the calculated spectra on the employed cluster set are extensively tested. Chapter 5 compares the cluster-weighting approach with an established method for calculating bulk phase vibrational spectra which is based on *ab initio* molecular dynamics simulations.[3] Here, the influence of the quantum chemical level of theory on the quality of the vibrational spectra obtained from cluster-weighting is further tested. For the approach based on *ab initio* molecular dynamics simulations,[47,144] the importance of conformational sampling is emphasized and the conformer replica simulations approach is proposed to improve the sampling quality and the resulting vibrational spectra. In

chapter 6, the cluster-weighting approach is extended to binary systems and applied to mixtures of acetonitrile and (*R*)-butan-2-ol. This enables the computationally efficient calculation of mole fraction dependent IR and VCD spectra and the prediction of mole fraction related vibrational frequency shifts.

Chapters 7 to 10 deal with the second objective of the thesis by studying chirality transfer phenomena in ILs. All four chapters are based primarily on the performance and analysis of *ab initio* molecular dynamics simulations. In chapter 7, the dissolution of different D-glucose isomers in dry and moist 1-ethyl-3-methylimidazolium acetate is investigated with a focus on the influence of intermolecular interactions on possible reaction mechanisms and the vibrational spectra of the systems.[5] Chapter 8 deals with the molecular recognition of butan-2-ol enantiomers by the 1-ethyl-3-methylimidazolium L-alaninate CIL and examines the role of chirality transfer to the cation in this process. Due to the flexibility of butan-2-ol, the conformer replica simulations approach proposed in chapter 5 is applied for the molecular dynamics simulations. Chapter 9 is a perspective article that highlights some of the recent advances in the theoretical modeling of reactions, chirality transfer, and radicals in ILs.[7] The work provides an overview of methodological advances and discusses challenges that still need to be overcome for IL research to become predictive and follow the latest research trends. In chapter 10, the chirality transfer from the chiral (*R*)-1,2-propylene oxide to the ions of the 1-ethyl-3-methylimidazolium bis(trifluoromethylsulfonyl)imide IL is investigated.[8] In particular, this work explores the possibility of a selective chirality transfer from (*R*)-1,2-propylene oxide to the IL anion while leaving the cation unaffected. Finally, the impact of the thesis is summarized in chapter 11 and an outlook on future research is given.

2. Theoretical Background

2.1. Electronic Structure Methods

2.1.1. The Schrödinger Equation

Any theoretical description of a molecular system is ultimately based on the Schrödinger equation,[145] which requires the wave function Ψ of a quantum mechanical system to obtain the energy E. Its non-relativistic, time-independent form is the foundation of electronic structure theory and reads as

$$\hat{H}\Psi = E\Psi\,, \tag{2.1}$$

where $\hat{H}$ is the Hamiltonian operator. The Hamiltonian operator is commonly expressed as the sum of the kinetic energy operator $\hat{T}$ and the potential energy operator $\hat{V}$ which are composed of contributions from the electrons and nuclei:

$$\hat{H} = \hat{T}_\mathrm{e} + \hat{T}_\mathrm{n} + \hat{V}_\mathrm{ee} + \hat{V}_\mathrm{ne} + \hat{V}_\mathrm{nn}\,. \tag{2.2}$$

In eq. (2.2), $\hat{T}_\mathrm{e}$ and $\hat{T}_\mathrm{n}$ are the kinetic energy of the electrons and nuclei, respectively, $\hat{V}_\mathrm{ee}$ and $\hat{V}_\mathrm{nn}$ are the Coulomb repulsion between electrons and nuclei, respectively, and $\hat{V}_\mathrm{ne}$ is the Coulomb attraction between electrons and nuclei. Following that, the Hamiltonian for a system with N electrons and M nuclei can explicitly be expressed as

$$\hat{H} = -\sum_{i=1}^{N}\frac{\hbar^2}{2m_\mathrm{e}}\nabla_i^2 - \sum_{A=1}^{M}\frac{\hbar^2}{2M_A}\nabla_A^2 + \frac{e^2}{4\pi\varepsilon_0}\left(\sum_{i=1}^{N}\sum_{j=i+1}^{N}\frac{1}{r_{ij}} - \sum_{i=1}^{N}\sum_{A=1}^{M}\frac{Z_A}{r_{iA}} + \sum_{A=1}^{M}\sum_{B=A+1}^{M}\frac{Z_A Z_B}{r_{AB}}\right), \tag{2.3}$$

with m_e being the mass of an electron, M_A and Z_A are the mass and charge of nucleus A, e is the elementary charge, and ε_0 is the vacuum permittivity. The distances between two electrons i and j, between two nuclei A and B, and between an electron i and a nucleus A are given by r_{ij}, r_{AB} and r_{iA}, respectively. For the sake of simplicity, atomic units are used from here onwards.[146]

To simplify the Hamiltonian, the Born–Oppenheimer approximation[147] is commonly applied to decouple the electronic and nuclear motions. This approximation is justified by the much larger mass of the nuclei compared to the electrons.* Assuming fixed nuclear positions, the kinetic energy operator of the nuclei $\hat{T}_\mathrm{n}$ is omitted and the Coulomb interaction $\hat{V}_\mathrm{nn}$ between the nuclei

*The mass of a proton is 1.007 u whereas the mass of an electron is $5.485 \cdot 10^{-4}$ u.[148]

reduces to a constant. The resulting electronic Hamiltonian $\hat{H}_{\mathrm{el}}$ reads as

$$\hat{H}_{\mathrm{el}} = \hat{T}_{\mathrm{e}} + \hat{V}_{\mathrm{ne}} + \hat{V}_{\mathrm{ee}}\,, \tag{2.4}$$

where the operators can be grouped into one-electron and two-electron operators

$$\hat{H}_{\mathrm{el}} = \hat{h}_{\mathrm{e}} + \hat{V}_{\mathrm{ee}} \quad \text{with} \quad \hat{h}_{\mathrm{e}} = \hat{T}_{\mathrm{e}} + \hat{V}_{\mathrm{ne}}\,. \tag{2.5}$$

The resulting Schrödinger equation involving the electronic Hamiltonian can then be expressed as

$$\hat{H}_{\mathrm{el}}\Psi_{\mathrm{el}} = E_{\mathrm{el}}\Psi_{\mathrm{el}} \quad \text{with} \quad \Psi_{\mathrm{el}} = \Psi_{\mathrm{el}}\left(\{\mathbf{r}_i\};\{\mathbf{R}_A\}\right) \quad \text{and} \quad E_{\mathrm{el}} = E_{\mathrm{el}}\left(\{\mathbf{R}_A\}\right). \tag{2.6}$$

The electronic wave function Ψ_{el} thus depends explicitly on the full set of electronic coordinates $\{\mathbf{r}_i\}$ and parametrically on the set of nuclear coordinates $\{\mathbf{R}_A\}$ while the electronic energy E_{el} depends parametrically on the nuclear coordinates. To obtain the total energy E, the constant nuclear repulsion is added

$$E = E_{\mathrm{el}} + V_{\mathrm{nn}}\,. \tag{2.7}$$

The electronic Schrödinger equation derived in eq. (2.6) is only exactly solvable for $H_2{}^+$ or similar one-electron systems, as the electron–electron coupling prevents an analytical solution. For many-electron systems, the solution of the electronic Schrödinger equation has to rely on approximate methods that are often based on the variational principle, which states that the energy of any approximate wave function will be above or equal to the exact energy.[149] One such approximate method is wave function theory which is usually based on the Hartree–Fock (HF) self-consistent field (SCF) procedure.[150,151] Therein, the explicit treatment of electron–electron interactions is avoided and the motion of each individual electron is considered in a mean-field created by the other electrons. The exact N-body wave function of such a system with N electrons occupying N spin-orbitals $\phi_N(N)$ can be approximated by a single Slater determinant

$$\Psi_{\mathrm{SD}}(1,2,\ldots,N) = \frac{1}{\sqrt{N!}}\begin{vmatrix} \phi_1(1) & \phi_2(1) & \cdots & \phi_N(1) \\ \phi_1(2) & \phi_2(2) & \cdots & \phi_N(2) \\ \vdots & \vdots & \ddots & \vdots \\ \phi_1(N) & \phi_2(N) & \cdots & \phi_N(N) \end{vmatrix}; \langle\phi_i|\phi_j\rangle = \delta_{ij}\,, \tag{2.8}$$

an antisymmetric object which causes the system's wave function to change its sign if any two electrons are interchanged.[146] The representation of the system's wave function as Slater determinant ensures compliance with the Pauli principle,[152] and the determinant vanishes if one spin-orbital is occupied by more than one electron. By applying the variational principle, a set of N pseudo-eigenvalue equations can be derived for the N spin-orbitals. The solution of this set of HF equations is solved iteratively by an SCF procedure and yields the energy of the system.

One major inconvenience of the HF theory is the missing instantaneous Coulomb correlation

between the electrons, also termed dynamic correlation. This missing energy contribution is termed correlation energy E_c and corresponds to the energy difference between the HF energy and the exact solution of the non-relativistic Schrödinger equation:[153,154]

$$E_\mathrm{c} = E_\mathrm{exact} - E_\mathrm{HF}\,. \tag{2.9}$$

Post-HF methods like coupled cluster[155,156] or perturbation theory[157] are approaches to calculate or at least approximate this correlation energy by improving the HF wave function. However, such methods are not part of this thesis and will therefore not be the subject of further discussion here.

2.1.2. Kohn–Sham Density Functional Theory

Another approach to include electron correlation is density functional theory (DFT). DFT is based on the two Hohenberg–Kohn theorems[158,159] of which the first one states that the electron density uniquely determines the ground state properties of a many-electron system. It is therefore sufficient to calculate the electron density instead of the wave function. This reduces the high dimensional problem of an N-electron system with spin and spatial coordinates for all electrons to a three-dimensional problem of the electron density. In this framework, the electronic energy $E_\mathrm{el}[\rho(\mathbf{r})]$ is a functional of the electron density $\rho(\mathbf{r})$ and can be formulated in analogy to the electronic Hamiltonian defined in eq. (2.4):[160,161]

$$\begin{aligned} E_\mathrm{el}[\rho(\mathbf{r})] &= T_\mathrm{e}[\rho(\mathbf{r})] + V_\mathrm{ne}[\rho(\mathbf{r})] + V_\mathrm{ee}[\rho(\mathbf{r})] \\ &= T_\mathrm{e}[\rho(\mathbf{r})] + V_\mathrm{ne}[\rho(\mathbf{r})] + J[\rho(\mathbf{r})] + K[\rho(\mathbf{r})]\,. \end{aligned} \tag{2.10}$$

Therein, $T_\mathrm{e}[\rho(\mathbf{r})]$ is the kinetic energy of the electrons, $V_\mathrm{ne}[\rho(\mathbf{r})]$ is the nuclear–electron attraction, and the electron–electron interaction $V_\mathrm{ee}[\rho(\mathbf{r})]$ is divided into Coulomb $J[\rho(\mathbf{r})]$ and exchange $K[\rho(\mathbf{r})]$ parts. The functionals $V_\mathrm{ne}[\rho(\mathbf{r})]$ and $J[\rho(\mathbf{r})]$ can be formulated by classical expressions, but an exact formulation of the functional $T_\mathrm{e}[\rho(\mathbf{r})]$ remains unknown.

Therefore, Kohn–Sham-DFT (KS-DFT) introduces a fictitious reference system of non-interacting electrons that reproduces the ground-state electron density of the real system of interest.[159] In analogy to the HF theory, the wave function of these non-interacting electrons is given by a single Slater determinant. By introducing KS orbitals ϕ_i, the kinetic energy $T_\mathrm{s}[\rho(\mathbf{r})]$ of the non-interacting electrons is given as

$$T_\mathrm{s}[\rho(\mathbf{r})] = \sum_{i=1}^{N} \left\langle \phi_i \left| -\frac{1}{2}\nabla^2 \right| \phi_i \right\rangle, \tag{2.11}$$

and the electron density as

$$\rho(\mathbf{r}) = \sum_{i=1}^{N} |\phi_i|^2\,. \tag{2.12}$$

Since $T_\mathrm{s}[\rho(\mathbf{r})]$ is calculated for a fictitious system of non-interacting particles, there is an energy difference to the exact kinetic energy of the electrons. This energy difference as well as the electron correlation and exchange energy are included in the exchange-correlation functional

$$\begin{aligned} E_\mathrm{xc}[\rho(\mathbf{r})] &= (T_\mathrm{e}[\rho(\mathbf{r})] - T_\mathrm{s}[\rho(\mathbf{r})]) + (V_\mathrm{ee}[\rho(\mathbf{r})] - J[\rho(\mathbf{r})]) \\ &= E_\mathrm{x}[\rho(\mathbf{r})] + E_\mathrm{c}[\rho(\mathbf{r})]\,. \end{aligned} \tag{2.13}$$

Therein, $E_\mathrm{x}[\rho(\mathbf{r})]$ and $E_\mathrm{c}[\rho(\mathbf{r})]$ represent the exchange and correlation parts, respectively. By reformulating eq. (2.10), the energy expression in the framework of KS-DFT is thus given by

$$E_\mathrm{el}^\mathrm{KS}[\rho(\mathbf{r})] = T_\mathrm{s}[\rho(\mathbf{r})] + V_\mathrm{ne}[\rho(\mathbf{r})] + J[\rho(\mathbf{r})] + E_\mathrm{xc}[\rho(\mathbf{r})]\,. \tag{2.14}$$

In this equation, $E_\mathrm{xc}[\rho(\mathbf{r})]$ is the only functional for which an exact expression remains unknown. The various density functionals used in quantum chemistry approximate this unknown exchange-correlation functional by estimating the exchange-correlation contribution. These density functionals can be categorized according to the Jacob's ladder.[162] In local density approximation (LDA) functionals, the electron density $\rho(\mathbf{r})$ is treated as uniform electron gas.[163,164] This approximation of a completely homogeneous electron density distribution typically leads to an overestimation of the electron correlation and an underestimation of the exchange energy. To account for inhomogeneous electron density distributions, generalized gradient approximation (GGA) functionals like BP86[68,69] or BLYP[68,69] additionally include the gradient of the electron density $\nabla\rho(\mathbf{r})$. Meta-GGA functionals go one step beyond that and include higher order derivatives of the electron density $\nabla^2\rho(\mathbf{r})$ or the kinetic energy density. Popular examples for meta-GGA functionals are TPSS[165] or B95[166]. Hybrid functionals like B3LYP[68,69] additionally include contributions from the non-local HF exchange energy. The proportion of included HF exchange varies between different functionals and often depends on the property of interest. An improved description of the electron correlation can be achieved by double-hybrid functionals (e.g., B2PLYP[167]) which include virtual orbital information.

A shortcoming of the exchange-correlation functionals mentioned above is that they do not adequately describe dispersive interactions. To account for these interactions, the DFT-D method and its extensions are commonly used.[168–171] Therein, the energy contribution of dispersion interactions is calculated by the empirical correction term

$$E_\mathrm{disp} = -\sum_{A=1}^{M}\sum_{B=A+1}^{M}\sum_{n=6,8,10,\ldots} s_n \frac{C_n^{AB}}{r_{AB}^n} f_\mathrm{damp}\left(r_{AB}\right), \tag{2.15}$$

which is added to the energy of the system. Here, M is the number of atoms in the system, s_n is a global scaling factor adjusted to the exchange-correlation functional, and C_n^{AB} is the averaged nth-order dispersion coefficient for the atom pair AB separated by a distance r_{AB}. The damping function f_damp is used to avoid near-singularities at small r_{AB} and double-counting effects at intermediate distances.[171] In case of DFT-D3, the sum in eq. (2.15) is truncated after $n = 8$.[170] More specialized approaches to include dispersion interactions are, for example, dispersion-

corrected atom-centered potentials[172,173] or non-local van der Waals functionals.[174,175]

To finally solve the KS equations derived above, the unknown molecular orbitals ϕ_i used in the Slater determinant can be represented by a linear combination of n basis functions (atomic orbitals) χ_α and coefficients $c_{\alpha i}$

$$\phi_i = \sum_{\alpha}^{n} c_{\alpha i} \chi_\alpha \,. \tag{2.16}$$

Note that in eq. (2.16) the basis functions are known and the coefficients need to be determined. Inserting eq. (2.16) into the KS energy expression and variational energy minimization transforms the KS equations into an according matrix notation

$$\mathbf{KC} = \mathbf{SC}\epsilon \,. \tag{2.17}$$

In eq. (2.17), $\mathbf{K}$ is the KS matrix, $\mathbf{C}$ contains the molecular orbital coefficients, $\mathbf{S}$ is the atomic orbital overlap matrix, and ϵ is a diagonal matrix of the orbital energies ϵ_i. Since $\mathbf{K}$ depends on $\mathbf{C}$, the unknown coefficients have to be determined in an iterative procedure. Therefore, $\mathbf{K}$ is evaluated with an initial guess of $\mathbf{C}$ and new coefficients are calculated by solving the generalized eigenvalue problem given by eq. (2.17). Based on the new coefficients, $\mathbf{K}$ is calculated again and the procedure is repeated until the coefficients are self-consistent.

There are different types of basis functions that have been proposed. Slater-type orbitals (STOs) can correctly describe the atomic orbitals as they possess a cusp at $r = 0$ and an exponential decay at long range. However, since the two-electron integrals over STOs are difficult to calculate, it is very common in quantum chemistry to use contracted Gaussian-type orbitals (GTOs) instead. Although GTOs do not possess a cusp at $r = 0$ and show a too rapid decay at long range, the fact that the product of two Gaussians can be represented by another Gaussian (Gaussian product theorem) simplifies the integral calculations and decreases the computational effort.

In solid state physics and periodic molecular simulations, plane wave basis sets with basis functions of the general form

$$\phi = \frac{1}{\sqrt{\Omega}} \exp\left(\mathrm{i}\mathbf{G} \cdot \mathbf{r}\right) \tag{2.18}$$

are commonly used. Here, Ω is the volume of the periodic cell and $\mathbf{G}$ is the wave vector which has to comply with the periodic boundary conditions. The wave vectors to be included in the basis set expansion (eq. (2.16)) are determined by a cutoff. Although plane wave basis sets are usually employed for calculations of periodic condensed phase systems, gas phase calculations like the ones presented in chapter 5 are also possible. For this purpose, the size of the periodic cell has to be chosen large enough to avoid interactions between the periodic images. However, the drawback of this approach is that most parts of the cell are actually empty and that a large number of basis functions are used solely for the description of this empty space.

One major disadvantage of plane wave basis sets is their inefficiency in describing the rapid oscillations of the wave functions of the valence electrons near the nucleus. Here, a large number of

basis functions would be necessary to achieve an accurate description in an all-electron calculation. This issue can be overcome by introducing pseudopotentials that replace the core electrons and the Coulomb potential of the nucleus with a weaker pseudopotential that acts on pseudo wave functions rather than the true valence wave functions. By this, lower cutoffs and therefore fewer wave vectors are sufficient to achieve an accurate description of the electronic structure which reduces the computational effort.

A special implementation of DFT, the Gaussian and plane waves method, will be discussed in section 2.3.3 in the context of *ab initio* molecular dynamics simulations.

2.2. Quantum Cluster Equilibrium

The majority of chemically relevant processes take place in the condensed phase with a special focus on liquid media in this thesis. In such media, environmental and solvation effects play a significant role,[7] and taking these effects into account is of utmost importance when modeling, for example, liquid phase vibrational spectra, as shown in chapters 4 to 6. Consequently, there is great interest among scientists in developing theoretical methods that can accurately model these properties of the liquid phase at reasonable computational cost. One such method is the quantum cluster equilibrium (QCE) or cluster-weighting, which describes the liquid phase as a dynamic equilibrium of quantum chemically accessible clusters.[139–141] It can thus be seen as an extension of the classical Boltzmann weighting of clusters, but with the possibility to weight differently sized clusters at the same time.[2,13]

The underlying concepts of the QCE theory were first published by Frank Weinhold in 1998 where he defined clusters as distinctive configurations of molecules that are intermediate between monomeric species in low-density gases and the fully aggregated state of the condensed phase.[139] He argued that the continuity of gases and liquids in the critical phase implies that the cluster picture of a dense gas can be continuously extended to the liquid phase by adjusting the cluster distribution according to the pressure and temperature of the system. A more detailed description of the QCE theory was provided by Barbara Kirchner in 2005,[140] who implemented the underlying equations in Peacemaker,[176,177] a software package for performing QCE calculations. This major step enabled the use of QCE to calculate thermodynamic functions for a myriad of liquids, including water,[140,178–189] alcohols[9,181,190–196] (see also chapter 3), amides,[197–200] ammonia,[201] liquid sulfur,[202] organic acids,[10,11,203,204] and hydrogen halides.[205–207] Furthermore, it has also been shown that QCE can be used to predict vibrational spectra[2,3,198] of neat liquids and binary mixtures (see also chapters 4 to 6). Later on, the theory was extended to binary (bQCE)[141] and multi-component (mQCE)[208] systems by the Kirchner group. These extensions opened doors for a variety of new applications such as the investigation of ILs,[209] the calculation of activity coefficients,[9,196] or the description of mole fraction dependent acid dissociation.[10,11]

Parts of the work presented in this thesis are based on the QCE and bQCE theory. Therefore, an introduction to the underlying concepts and equations of QCE and its extension to bQCE will be given in the following.[140,141] An extensive derivation of the theory including all recently implemented modifications is provided in appendix A.

2.2.1. Statistical Thermodynamics

The QCE theory is derived in the canonical ensemble, that is, for a system characterized by the particle number N, the volume V, and the temperature T. For the sake of simplicity, the function variables are omitted in the following explanations and all thermodynamic functions are assumed to be functions of N, V, and T or a selection of these. In the canonical ensemble, the probability p_j for a system to be in the energy state E_j is determined by the Boltzmann factor

$$p_j \propto \exp\left(-\frac{E_j}{k_\mathrm{B}T}\right), \tag{2.19}$$

with k_B being the Boltzmann constant. To ensure that the sum of all probabilities p_j equals one, the normalization constant

$$Q = \sum_j \exp\left(-\frac{E_j}{k_\mathrm{B}T}\right) \tag{2.20}$$

is introduced to obtain the Boltzmann factor as

$$p_j = \frac{1}{Q}\exp\left(-\frac{E_j}{k_\mathrm{B}T}\right). \tag{2.21}$$

Here, Q is called the system partition function which enables the calculation of all thermodynamic state functions. If a system of N independent and indistinguishable particles obeys Boltzmann statistics, its partition function may be formulated as

$$Q = \frac{1}{N!}q^N. \tag{2.22}$$

Therein, q is a single particle partition function that can be written as the product of the individual particle partition functions for the translational, rotational, vibrational, and electronic degrees of freedom

$$q = q^\mathrm{trans}q^\mathrm{rot}q^\mathrm{vib}q^\mathrm{elec}. \tag{2.23}$$

Accordingly, the energy ε for a particle with such a partition function corresponds to the sum of the energy contributions of all degrees of freedom

$$\varepsilon = \varepsilon^\mathrm{trans} + \varepsilon^\mathrm{rot} + \varepsilon^\mathrm{vib} + \varepsilon^\mathrm{elec}. \tag{2.24}$$

The translational, rotational, and vibrational partition functions can be derived from standard models for the particle in a box, the rigid rotator and the harmonic oscillator[210,211], respectively:

$$q^\mathrm{trans} = \frac{V}{\Lambda^3} \qquad \text{with} \quad \Lambda = \sqrt{\frac{h^2}{2\pi m k_\mathrm{B}T}}, \tag{2.25}$$

$$q^\mathrm{rot} = \frac{\sqrt{\pi}}{\sigma}\sqrt{\frac{T^3}{\Theta_A^\mathrm{rot}\Theta_B^\mathrm{rot}\Theta_C^\mathrm{rot}}} \qquad \text{with} \quad \Theta_j^\mathrm{rot} = \frac{h^2}{8\pi^2 I_j k_\mathrm{B}}, \tag{2.26}$$

$$q^{\mathrm{vib}} = \prod_{i=1}^{3N-x} \frac{\exp\left(-\Theta_i^{\mathrm{vib}}/2T\right)}{1-\exp\left(-\Theta_i^{\mathrm{vib}}/T\right)} \qquad \text{with} \quad \Theta_i^{\mathrm{vib}} = \frac{h\nu_i}{k_{\mathrm{B}}}\,. \tag{2.27}$$

In eqs. (2.25) to (2.27), Λ is the thermal de Broglie wavelength, h the Planck constant, m the particle mass, σ the rotational-symmetry number, Θ_j^{rot} and Θ_j^{vib} are the rotational and vibrational temperatures, I_j is the moment of inertia, and ν_i the frequency of the respective vibrational mode i. The number of vibrational degrees of freedom corresponds to $3N - x$, with $x = 5$ for linear molecules and $x = 6$ for nonlinear molecules. Assuming that the electronic ground state is the only populated electronic energy level under the applied ambient conditions, the electronic partition function is governed by the electronic ground state energy $\varepsilon_1^{\mathrm{elec}}$ and the degeneracy g_1 of the ground state

$$q^{\mathrm{elec}} = g_1 \exp\left(-\frac{\varepsilon_1^{\mathrm{elec}}}{k_{\mathrm{B}}T}\right). \tag{2.28}$$

2.2.2. Quantum Cluster Equilibrium Theory

The central idea of the QCE theory is the description of the liquid phase as a dense gas of molecular clusters which are built up from monomers of one (neat system), two (binary system), or even more (multicomponent system) components. These clusters are assumed to be in thermodynamic equilibrium which allows for the formation and disaggregation of clusters. The corresponding chemical equation for this cluster equilibrium may be expressed in a general form as

$$i(\wp)\mathrm{C}_1 + j(\wp)\mathrm{C}_2 \rightleftharpoons \wp\,, \tag{2.29}$$

where a cluster $\wp$ is composed of $i(\wp)$ and $j(\wp)$ monomers of the components 1 and 2, respectively. This general formulation allows for the simultaneous presence of multiple clusters with the same composition and enables the consideration of different conformers and structural motifs, which can be of particular importance for the calculation of VCD spectra as presented in chapters 4 to 6. Following eq. (2.29), the primary aim of the QCE theory is to obtain the set of cluster populations $\{N_\wp\}$ that minimizes the free energy of the system

$$A = -k_{\mathrm{B}}T \ln Q^{\mathrm{tot}} \tag{2.30}$$

at a given temperature T, volume V, and total number of monomers $N^{\mathrm{tot}} = N_1^{\mathrm{tot}} + N_2^{\mathrm{tot}}$. For such a system of molecular clusters, the partition function $q_\wp^{\mathrm{tot}}$ of a cluster $\wp$ can be formulated analogously to eq. (2.23) as

$$q_\wp^{\mathrm{tot}} = q_\wp^{\mathrm{trans}} q_\wp^{\mathrm{rot}} q_\wp^{\mathrm{vib}} q_\wp^{\mathrm{elec}}\,, \tag{2.31}$$

and the total system partition function Q^{tot} is given as

$$Q^{\mathrm{tot}} = \prod_\wp \frac{1}{N_\wp!} \left(q_\wp^{\mathrm{tot}}\right)^{N_\wp}. \tag{2.32}$$

Therein, $N_\wp$ is the population of cluster $\wp$ and the product includes all clusters in the cluster set. The rotational and vibrational cluster partition functions are calculated according to eqs. (2.26) and (2.27) while the translational and electronic partition functions are obtained by extensions of eqs. (2.25) and (2.28) as follows.

The translational partition function given in eq. (2.25) is valid for a system of point-shaped particles that have no volume. However, on the basis of non-point-shaped molecular clusters, not all of the total volume is accessible to the particles and therefore needs to be corrected in the translational partition function. This is done by introducing an exclusion volume of the clusters as

$$V_{\mathrm{ex}} = b_{\mathrm{xv}} \sum_{\wp} N_\wp v_\wp = b_{\mathrm{xv}} \left(v_1 N_1^{\mathrm{tot}} + v_2 N_2^{\mathrm{tot}} \right), \tag{2.33}$$

which is subtracted from the total volume V. In eq. (2.33), $v_\wp$ is the volume of cluster $\wp$, v_1 and v_2 are the volumes of the monomers, and b_{xv} is a dimensionless empirical parameter that scales the inaccessible volume. This scaling is necessary as the cluster volumes are often sensitive to the choice of the atomic radii.[178] The translational partition function as used in QCE is therefore given by

$$q_\wp^{\mathrm{trans}} = \frac{V - V_{\mathrm{ex}}}{\Lambda^3} = \frac{V - b_{\mathrm{xv}} \left(v_1 N_1^{\mathrm{tot}} + v_2 N_2^{\mathrm{tot}} \right)}{\Lambda^3}. \tag{2.34}$$

The electronic partition function is calculated from the adiabatic binding energy

$$\Delta_{\mathrm{bind}} \varepsilon_\wp^{\mathrm{elec}} = \varepsilon_\wp^{\mathrm{elec}} - i(\wp)\varepsilon_1^{\mathrm{elec}} - j(\wp)\varepsilon_2^{\mathrm{elec}}, \tag{2.35}$$

where $\varepsilon_\wp^{\mathrm{elec}}$ is the electronic ground state energy of cluster $\wp$ and the corresponding electronic ground state energies of the monomers are given by $\varepsilon_1^{\mathrm{elec}}$ and $\varepsilon_2^{\mathrm{elec}}$. To account for inter-cluster interactions, a density and cluster size-dependent mean-field type energy term is introduced as

$$\varepsilon_\wp^{\mathrm{mf}} = -\frac{a_{\mathrm{mf}} \left(i(\wp) + j(\wp) \right)}{V}, \tag{2.36}$$

where a_{mf} is the empirical mean-field parameter with the dimension $\mathrm{J\,m^3\,mol^{-2}}$. Inserting eqs. (2.35) and (2.36) into eq. (2.28) yields the electronic partition function as used in the QCE theory:

$$q_\wp^{\mathrm{elec}} = \exp\left(-\frac{\Delta_{\mathrm{bind}} \varepsilon_\wp^{\mathrm{elec}} - \left(i(\wp) + j(\wp) \right) \frac{a_{\mathrm{mf}}}{V}}{k_{\mathrm{B}} T} \right). \tag{2.37}$$

The two empirical parameters a_{mf} and b_{xv} are usually optimized to minimize the deviation of the QCE results from experimental reference data. Further details of the optimization process are provided in section 2.2.3.

To determine thermodynamic data from the canonical partition function, the three independent quantities $(\{N_\wp\}, V, T)$ characterizing the ensemble, have to be determined. The conservation of

the particle number is ensured by introducing the following condition

$$\begin{aligned} N_1^{\mathrm{tot}} + N_2^{\mathrm{tot}} &= \sum_{\wp} \left(i(\wp) + j(\wp)\right) N_\wp \,, \\ 0 &= \sum_{\wp} \frac{\left(i(\wp) + j(\wp)\right) N_\wp}{N_1^{\mathrm{tot}} + N_2^{\mathrm{tot}}} - 1 = \sum_{\wp} I_\wp - 1 \,, \end{aligned} \tag{2.38}$$

where $I_\wp$ is the monomer-normalized cluster population. Under the condition of thermodynamic equilibrium, it is possible to express every cluster population $N_\wp$ with respect to the particle number of the monomers:

$$0 = \sum_{\wp} i(\wp) \left(\frac{\partial A}{\partial N_1}\right) d\lambda + \sum_{\wp} j(\wp) \left(\frac{\partial A}{\partial N_2}\right) d\lambda - \sum_{\wp} \left(\frac{\partial A}{\partial N_\wp}\right) d\lambda \,, \tag{2.39}$$

where $d\lambda$ denotes the reaction progress. Equation (2.39) states that the slope of the free energy with respect to the cluster populations is zero, or in other words, that an infinitesimal change in a cluster population must not affect the free energy. This means that any change in free energy due to cluster disaggregation must be compensated by an equal change in free energy due to increasing monomer populations. Since eq. (2.39) has to be fulfilled for any reaction progress and cluster independently, it can be simplified to

$$\left(\frac{\partial A}{\partial N_\wp}\right) = i(\wp) \left(\frac{\partial A}{\partial N_1}\right) + j(\wp) \left(\frac{\partial A}{\partial N_2}\right). \tag{2.40}$$

Considering the connection between the free energy and the total system partition function (*cf.* eqs. (2.30) and (2.32))

$$\begin{aligned} A &= -k_{\mathrm{B}} T \ln Q^{\mathrm{tot}} = -k_{\mathrm{B}} T \ln \left(\prod_{\wp} \frac{1}{N_\wp!} \left(q_\wp^{\mathrm{tot}}\right)^{N_\wp} \right) \\ &= -k_{\mathrm{B}} T \sum_{\wp} \left(N_\wp \ln q_\wp^{\mathrm{tot}} - \ln N_\wp! \right) , \end{aligned} \tag{2.41}$$

eq. (2.40) can be written as

$$\begin{aligned} \frac{\partial}{\partial N_\wp} \sum_{\wp} \left(N_\wp \ln q_\wp^{\mathrm{tot}} - \ln N_\wp! \right) = i(\wp) \left(\frac{\partial}{\partial N_1} \sum_{\wp} \left(N_\wp \ln q_\wp^{\mathrm{tot}} - \ln N_\wp! \right) \right) \\ + j(\wp) \left(\frac{\partial}{\partial N_2} \sum_{\wp} \left(N_\wp \ln q_\wp^{\mathrm{tot}} - \ln N_\wp! \right) \right) . \end{aligned} \tag{2.42}$$

Applying the Stirling approximation[†] to solve the differentials in eq. (2.42) and rearranging

[†] $\ln(n!) \approx n \cdot \ln(n) - n$

yields

$$N_\wp = q_\wp^{\mathrm{tot}} \left(\frac{N_1}{q_1^{\mathrm{tot}}}\right)^{i(\wp)} \left(\frac{N_2}{q_2^{\mathrm{tot}}}\right)^{j(\wp)}, \tag{2.43}$$

which is an expression that relates the cluster populations $N_\wp$ to the monomer populations N_1 and N_2. It is therefore sufficient to determine the monomer populations and from these the whole set of cluster populations $\{N_\wp\}$ according to eq. (2.43). However, since eq. (2.43) represents a system of polynomial equations that can only be solved exactly for fixed N_1 and N_2, two additional independent equations are needed. One of these equations is the so-called population polynomial which is obtained by inserting eq. (2.43) into eq. (2.38) and reads as

$$0 = \sum_\wp \frac{i(\wp) + j(\wp)}{N_1^{\mathrm{tot}} + N_2^{\mathrm{tot}}} \cdot q_\wp^{\mathrm{tot}} \left(\frac{N_1}{q_1^{\mathrm{tot}}}\right)^{i(\wp)} \left(\frac{N_2}{q_2^{\mathrm{tot}}}\right)^{j(\wp)} - 1\,. \tag{2.44}$$

For neat systems with $N_2^{\mathrm{tot}} = 0$ and $j(\wp) = 0$, the population polynomial is exactly solvable to obtain the monomer population N_1 and from that the set of cluster populations. For binary systems, however, a second polynomial is needed to determine the two unknown variables N_1 and N_2. Following the expression for the conservation of the particle number given in eq. (2.38), the conservation of mass can be introduced accordingly as

$$\begin{aligned} M_1 N_1^{\mathrm{tot}} + M_2 N_2^{\mathrm{tot}} &= \sum_\wp \left(i(\wp) M_1 + j(\wp) M_2\right) N_\wp\,, \\ 0 &= \sum_\wp \frac{i(\wp) M_1 + j(\wp) M_2}{M_1 N_1^{\mathrm{tot}} + M_2 N_2^{\mathrm{tot}}} N_\wp - 1\,, \end{aligned} \tag{2.45}$$

where M_1 and M_2 are the molecular masses of the components. From that, the so-called mass polynomial can be obtained by inserting eq. (2.43) into eq. (2.45):

$$0 = \sum_\wp \frac{i(\wp) M_1 + j(\wp) M_2}{M_1 N_1^{\mathrm{tot}} + M_2 N_2^{\mathrm{tot}}} \cdot q_\wp^{\mathrm{tot}} \left(\frac{N_1}{q_1^{\mathrm{tot}}}\right)^{i(\wp)} \left(\frac{N_2}{q_2^{\mathrm{tot}}}\right)^{j(\wp)} - 1\,. \tag{2.46}$$

The population and mass polynomials represent a system of two non-linear equations with two unknown variables that can be solved numerically to obtain the monomer and cluster populations of a binary system.

The equations derived so far allow the determination of the system partition function at any temperature for a given volume. In principle, any physically reasonable volume could be chosen, but it is desirable to obtain the volume as an intrinsic property depending on the cluster populations. To achieve this, the so-called volume polynomial is employed whose derivation starts with the definition of the pressure p as defined in statistical thermodynamics:

$$p = k_{\mathrm{B}} T \left(\frac{\partial \ln Q^{\mathrm{tot}}}{\partial V}\right), \tag{2.47}$$

$$0 = -p + k_\mathrm{B}T \left(\frac{\partial \ln Q^\mathrm{tot}}{\partial V} \right). \tag{2.48}$$

Inserting the system partition function as defined in eq. (2.32) into eq. (2.48) yields

$$0 = -p + k_\mathrm{B}T \sum_\wp N_\wp \left(\frac{\partial \ln q_\wp^\mathrm{tot}}{\partial V} \right). \tag{2.49}$$

The rotational and vibrational partition functions (*cf.* eqs. (2.26) and (2.27)) are not explicitly dependent on the volume and will therefore vanish if they are differentiated by the volume. The partial derivatives for the translational and electronic partition functions on the other hand read as

$$\frac{\partial \ln q_\wp^\mathrm{trans}}{\partial V} = \frac{1}{V - V_\mathrm{ex}}, \tag{2.50}$$

and

$$\frac{\partial \ln q_\wp^\mathrm{elec}}{\partial V} = -a_\mathrm{mf} \frac{(i(\wp) + j(\wp))}{k_\mathrm{B}TV^2}, \tag{2.51}$$

respectively. Insertion of eqs. (2.50) and (2.51) into eq. (2.49) yields the volume polynomial as

$$\begin{aligned} 0 = &- pV^3 + \left(\sum_\wp k_\mathrm{B}TN_\wp + pb_\mathrm{xv} \left(v_1 N_1^\mathrm{tot} + v_2 N_2^\mathrm{tot} \right) \right) V^2 \\ &- \left(\sum_\wp N_\wp \left(i(\wp) + j(\wp) \right) a_\mathrm{mf} \right) V \\ &+ \sum_\wp N_\wp \left(i(\wp) + j(\wp) \right) a_\mathrm{mf} \cdot b_\mathrm{xv} \left(v_1 N_1^\mathrm{tot} + v_2 N_2^\mathrm{tot} \right). \end{aligned} \tag{2.52}$$

The two eqs. (2.44) and (2.52) are solved in an iterative procedure since the cluster populations must be known to solve the volume polynomial and vice versa. In practice, the population polynomial is first solved for an initial guess of the volume to obtain the set of cluster populations $\{N_\wp\}$, which are then used to obtain a new volume by solving the volume polynomial. If there are multiple solutions for $(V, \{N_\wp\})$, the one with the lowest Gibbs energy

$$G = -k_\mathrm{B}T \ln Q^\mathrm{tot} + Vk_\mathrm{B}T \left(\frac{\partial \ln Q^\mathrm{tot}}{\partial V} \right) \tag{2.53}$$

is chosen and the difference in the Gibbs energy $|G|$ is chosen as convergence criterion ε_G for the iterative procedure. While the cluster populations are in the focus of this work to obtain vibrational spectra as presented in chapters 4 to 6, the calculation of other thermodynamic functions like the inner energy U, the enthalpy H, and the entropy S is of relevance for the work presented in chapter 3. The connections between these thermodynamic functions and the system

partition function Q^{tot} are given by

$$U = k_{\mathrm{B}}T^2 \left(\frac{\partial \ln Q^{\mathrm{tot}}}{\partial T} \right), \tag{2.54}$$

$$H = U + pV = k_{\mathrm{B}}T^2 \left(\frac{\partial \ln Q^{\mathrm{tot}}}{\partial T} \right) + V k_{\mathrm{B}}T \left(\frac{\partial \ln Q^{\mathrm{tot}}}{\partial V} \right), \quad \text{and} \tag{2.55}$$

$$S = \frac{U - A}{T} = k_{\mathrm{B}}T \left(\frac{\partial \ln Q^{\mathrm{tot}}}{\partial T} \right) + k_{\mathrm{B}} \ln Q^{\mathrm{tot}}. \tag{2.56}$$

2.2.3. Peacemaker

All QCE and bQCE calculations presented in this thesis have been performed with the Peacemaker 2 code, which is an open source program for QCE calculations that is actively developed by the Kirchner group. Historically, the original code for Peacemaker was developed by Barbara Kirchner in the early 2000s[140] and developments by the Kirchner group continued until 2011.[141,176,177,208,212,213] When the extension to bQCE was proposed in 2011, the underlying equations were first implemented in a new program called "Mixtures in Cluster Equilibrium" (Mice)[141] as a proof of concept. Later on, the original Peacemaker code and Mice were unified in the program package Peacemaker 2.[177,213] Peacemaker 2 is currently the only publicly available program for QCE calculations, it is freely available and licensed under the GNU General Public License. The procedure for performing QCE calculations with this program will be explained in the following.

Peacemaker 2 is a non-interactive program that reads two files: the input and the cluster set file. The cluster set file contains all relevant information about the clusters, including the geometries, adiabatic binding energies, vibrational frequencies, rotational symmetry numbers, and the volumes of the monomers. User-defined conditions like pressure, temperature range, and composition (in the case of bQCE calculations), as well as instructions for the calculation of a_{mf} and b_{xv} are summarized in the input file.

The QCE main iteration to solve the polynomial equations is the core of Peacemaker and consists of the following steps:

1. calculate an initial estimate V^0 for the phase volume V by the ideal gas law,
2. calculate all cluster partition functions $q_{\wp}^{\mathrm{tot}}$ at the current volume V and temperature T,
3. solve the population polynomial to obtain the set of cluster populations $\{N_{\wp}\}$,
4. calculate the new phase volume V by solving the volume polynomial with the cluster distribution $\{N_{\wp}\}$,
5. compare the relative change in the Gibbs energy ΔG to the last iteration. If $\Delta G < \varepsilon_G$, the iteration is converged, if $\Delta G > \varepsilon_G$ return to step 2,
6. if there are multiple solutions for $(V, \{N_{\wp}\})$, chose the one with the lowest Gibbs energy.

This procedure is performed for each temperature, but instead of performing step 1 for each instance, the volume obtained for the previous temperature is employed as an initial guess for the phase volume.

It has to be noted that the initial estimation of the volume is a critical step in the QCE main iteration, since the choice of the initial volume may determine whether stable or metastable solutions are found. If for instance a high-density volume is given, the QCE iteration may favorably converge to a liquid phase solution whereas a low-density volume may lead to a gas phase solution. To prevent this, the QCE main iteration is performed twice, once in a so-called gas phase loop and once in a liquid phase loop.[200] In the gas phase loop, the initial volume is set to that of an ideal gas V^{id} and the mean-field parameter a_{mf} is set to zero, thus neglecting all inter-cluster interactions. The liquid phase loop on the other hand uses a fraction of the ideal gas volume $V^0 = \lambda V^{\mathrm{id}}$ as the initial volume guess and does not modify a_{mf}. By default, λ is set to 0.01. If both loops converge, the solution with the lower Gibbs energy is selected for each investigated temperature. This procedure not only avoids metastable solutions but also allows to model first-order phase transitions as shown in chapter 3.

The two empirical parameters a_{mf} and b_{xv} can be set by the user or optimized to minimize the deviation of the QCE results from reference data, which are typically given by the experimental boiling point $T_{\mathrm{b}}^{\mathrm{exp}}$ and the density ρ^{exp} at a distinct temperature, an isobar of the molar volume, or a combination of the latter with the other two reference points. To determine the best pair of a_{mf} and b_{xv}, Peacemaker calculates the deviation of the QCE results from the reference data as

$$\mathrm{error} = w_\rho \left(\frac{\rho - \rho^{\mathrm{exp}}}{\rho^{\mathrm{exp}}} \right)^2 + w_T \left(\frac{T_{\mathrm{b}} - T_{\mathrm{b}}^{\mathrm{exp}}}{T_{\mathrm{b}}^{\mathrm{exp}}} \right)^2 + w_V \frac{1}{N} \sum_{i=1}^{N} \left(\frac{V_i - V_i^{\mathrm{exp}}}{V_i^{\mathrm{exp}}} \right)^2 , \tag{2.57}$$

where N is the number of volumes V_i contained in the isobar. The weighting parameters for the errors of density, boiling point, and isobar, w_ρ, w_T, and w_V, can be chosen by the user but are set to one by default. Note that this parameter sampling takes place in an outer loop that encloses the QCE main iteration, which means that a_{mf} and b_{xv} remain constant within the main iteration.

2.3. Molecular Simulations

While cluster approaches like QCE take environmental and solvation effects into account, they do neglect any effects arising from the motion of the molecules. However, the consideration of dynamic effects is often necessary to fully understand chemical processes at the molecular level, such as reaction or chirality transfer mechanisms. Molecular simulations aim to capture these effects by modeling the temporal evolution of the system of interest to predict dynamic and time-dependent properties. The basis for this is the Newtonian equation of motion, which is used to describe the movement of each particle i according to

$$\mathbf{F}_i = m_i \cdot \mathbf{a}_i \,, \tag{2.58}$$

where m_i and $\mathbf{a}_i$ are the mass and acceleration of the respective particle, and $\mathbf{F}_i$ is the force acting upon it. Considering that the force corresponds to the negative gradient of the potential energy and that the acceleration is the second time derivative of the position, eq. (2.58) can be rewritten as

$$\mathbf{F}_i = -\left(\frac{\partial U}{\partial \mathbf{R}_i}\right) = m_i \left(\frac{\partial^2 \mathbf{R}_i}{\partial t^2}\right). \tag{2.59}$$

The forces are thus derived from the potential energy surface (PES) which is a function of all nuclear coordinates, hence $U\left(\mathbf{R}^N\right) = U\left(\mathbf{R}_1, \mathbf{R}_2, \dots\right)$. Detailed explanations on the form and construction of a typical PES follow in sections 2.3.2 and 2.3.3.

2.3.1. Molecular Dynamics

The first molecular simulation of a liquid phase system was based on the Monte Carlo method as introduced by Metropolis and Ulam in 1949.[214,215] However, since classical Monte Carlo methods rely on a repeated random sampling of molecular configurations, they do not describe the explicit time evolution of a molecular system. Therefore, the technique of molecular dynamics (MD) was developed, which determines the time evolution of a molecular system by approximately solving Newton's equation of motion. The method was first introduced by Alder and Wainwright to describe hard-sphere particles moving at a constant velocity, treating each encounter between two particles as an elastic collision.[216,217] For such a simplified system, the dynamic problem is exactly solvable without any approximation. In reality, however, the potential between two particles is not constant but a function of their distance, which means that the forces acting on the particles change continuously as the particles move. Consequently, the Newtonian equation of motion must be solved in an iterative procedure as a set of differential equations involving a defined time increment δt.[218–221] By this time-discretization of eq. (2.59), the positions and velocities at time t can be predicted from functional values of preceding time steps. The positions and velocities are then stored in a trajectory from which time-dependent properties of the molecular system can be calculated.

To solve the time-dependent differential equations numerically, suitable numerical algorithms have to be applied. In general, the requirements for such algorithms are manifold, as they should

1. be applicable for both short and long time increments δt,
2. keep the number of force evaluations low to reduce the computational cost and memory requirements,
3. account for energy and momentum conservation,
4. be time-reversible,
5. be easy to implement.

Given the above requirements, the Störmer–Verlet family of algorithms[219,220] is best suited and consequently most commonly used to solve the Newtonian equation of motion. The classical

Verlet algorithm is based on a forward-backward third-order Taylor series expansion of the particle positions $\mathbf{R}_i(t)$:

$$\mathbf{R}_i(t+\delta t) = \mathbf{R}_i(t) + \delta t \frac{\mathrm{d}}{\mathrm{d}t}\mathbf{R}_i(t) + \frac{1}{2}\delta t^2 \frac{\mathrm{d}^2}{\mathrm{d}t^2}\mathbf{R}_i(t) + \frac{1}{6}\delta t^3 \frac{\mathrm{d}^3}{\mathrm{d}t^3}\mathbf{R}_i(t) + \mathcal{O}\left(\delta t^4\right), \tag{2.60}$$

$$\mathbf{R}_i(t-\delta t) = \mathbf{R}_i(t) - \delta t \frac{\mathrm{d}}{\mathrm{d}t}\mathbf{R}_i(t) + \frac{1}{2}\delta t^2 \frac{\mathrm{d}^2}{\mathrm{d}t^2}\mathbf{R}_i(t) - \frac{1}{6}\delta t^3 \frac{\mathrm{d}^3}{\mathrm{d}t^3}\mathbf{R}_i(t) + \mathcal{O}\left(\delta t^4\right). \tag{2.61}$$

Adding eqs. (2.60) and (2.61), and inserting eq. (2.59) results in the classical Verlet algorithm:

$$\mathbf{R}_i(t+\delta t) = 2\mathbf{R}_i(t) - \mathbf{R}_i(t-\delta t) + \delta t^2 \frac{\mathrm{d}^2}{\mathrm{d}t^2}\mathbf{R}_i(t) + \mathcal{O}\left(\delta t^4\right). \tag{2.62}$$

Unfortunately, the above derivation eliminates the velocities $\mathbf{v}_i(t)$ from eq. (2.62) but they are often necessary to calculate certain physical quantities, such as the kinetic energy at a given time t. An expression for the velocities can be obtained by subtracting eq. (2.61) from eq. (2.60):

$$\mathbf{v}_i(t) = \frac{\mathrm{d}}{\mathrm{d}t}\mathbf{R}_i(t) = \frac{\mathbf{R}_i(t+\delta t) - \mathbf{R}_i(t-\delta t)}{2\delta t} + \mathcal{O}\left(\delta t^2\right). \tag{2.63}$$

However, eq. (2.63) can cause technical difficulties in MD simulations, since the velocities at time t, and thus the kinetic energy and temperature, can only be calculated if the particle positions at time $t+\delta t$ are known. To avoid this problem, it is more convenient to use the velocity Verlet algorithm[222] instead, which reads as

$$\mathbf{R}_i(t+\delta t) = \mathbf{R}_i(t) + \delta t \frac{\mathrm{d}}{\mathrm{d}t}\mathbf{R}_i(t) + \frac{1}{2}\delta t^2 \frac{\mathrm{d}^2}{\mathrm{d}t^2}\mathbf{R}_i(t), \tag{2.64}$$

$$\mathbf{v}_i(t+\delta t) = \mathbf{v}_i(t) + \frac{1}{2}\delta t \left(\frac{\mathrm{d}^2}{\mathrm{d}t^2}\mathbf{R}_i(t) + \frac{\mathrm{d}^2}{\mathrm{d}t^2}\mathbf{R}_i(t+\delta t)\right). \tag{2.65}$$

A complete MD procedure based on the velocity Verlet algorithm therefore consists of the following steps:

1. start from initial particle positions $\mathbf{R}_i(t)$ and velocities $\mathbf{v}_i(t)$,
2. calculate the forces $\mathbf{F}_i(t)$ from the coordinates $\mathbf{R}_i(t)$,
3. calculate the particle positions $\mathbf{R}_i(t+\delta t)$ by eq. (2.64),
4. calculate the forces $\mathbf{F}_i(t+\delta t)$ from the new particle positions $\mathbf{R}_i(t+\delta t)$,
5. calculate the velocities $\mathbf{v}_i(t+\delta t)$ by eq. (2.65).

This procedure is repeated until the desired simulation time is obtained.

One important aspect to consider in an MD simulation is the ensemble, which refers to different conditions. The microcanonical or NVE ensemble conserves the particle number N, the volume V, and the total energy E. Therefore, it corresponds to an isolated system that does not exchange matter or heat with the environment. In practice, however, it is often desirable to perform MD

simulations that can be compared to experimental reference data which are usually measured under controlled temperature. For this purpose, the canonical or NVT ensemble can be employed, which conserves the particle number N, the volume V, and the temperature T. To control the temperature, a thermostat has to be applied, for example the Nosé–Hoover thermostat,[223–225] which introduces an additional degree of freedom as a heat bath. To deal with difficult cases, different heat baths can be linearly coupled to obtain a so-called Nosé–Hoover thermostat chain,[226] which can be coupled to a different number of degrees of freedom.

2.3.2. Classical Force Fields

As mentioned above, the interactions between the particles and the resulting forces are derived from the PES, which can have different forms depending on the type of MD simulation. A very popular approach to model the PES are classical force fields, which consider atoms as the smallest units and do not explicitly model the electrons. To describe the intra- and intermolecular interactions between atoms, a set of empirical parameters is defined for each atom type, describing the energy contributions of bond stretching, angle bending, dihedral rotations, dispersion forces, and electrostatic interactions. The functions describing the different energy contributions may vary between different force fields, which is why only the generalized Amber[227] and the OPLS-AA[228] force fields will be discussed here. Both force fields are largely based on the same expressions. The generalized Amber force field (GAFF) is employed for the cluster generation in chapters 3 to 6 and the OPLS-AA force field as well as its refined parameters for ILs[229–231] are used for the pre-equilibration of the simulation boxes analyzed in chapters 7 to 10.

In a system of N particles, the potential energy (or force field energy) $U\left(\mathbf{R}^N\right) = U\left(\mathbf{R}_1, \mathbf{R}_2, \dots\right)$ can be expressed as the sum of the individual energy contributions listed above:

$$U = U_{\mathrm{str}} + U_{\mathrm{bend}} + U_{\mathrm{dih}} + U_{\mathrm{vdW}} + U_{\mathrm{el}}\,, \tag{2.66}$$

where U_{str} is the bond stretching energy, U_{bend} the angle bending energy, U_{dih} the dihedral rotation energy, U_{vdW} the van der Waals energy, and U_{el} the electrostatic interaction energy. The contributions of U_{str}, U_{bend}, and U_{dih} can be categorized as bonded interactions, while U_{vdW} and U_{el} correspond to non-bonded interactions.

The description of bonded interactions is mostly based on geometric criteria and the corresponding potentials are calculated by harmonic expressions. The potential for the harmonic bond stretching is for instance given as

$$U_{\mathrm{str}} = K_{ij}^{r}\left(r_{ij} - r_0\right)^2. \tag{2.67}$$

Therein, K_{ij}^{r} is the force constant for the respective bond between the particles i and j, r_{ij} is the distance between the particles, and r_0 is the equilibrium bond length. The harmonic potential for the angle bending energy is defined accordingly and reads as

$$U_{\mathrm{bend}} = K_{ijk}^{\theta}\left(\theta_{ijk} - \theta_0\right)^2, \tag{2.68}$$

where K^{θ}_{ijk} is the force constant for the respective angle between the particles i, j, and k, θ_{ijk} is the angle between the three particles, and θ_0 is the equilibrium angle. Note that the prefactor of $\frac{1}{2}$, which is typical for harmonic potentials, is already included in K^{r}_{ij} and K^{θ}_{ijk}.

The dihedral rotation energy is given by periodic functions and differs between GAFF and OPLS-AA. In the GAFF description, the dihedral rotation energy $U^{\mathrm{GAFF}}_{\mathrm{dih}}$ is calculated as

$$U^{\mathrm{GAFF}}_{\mathrm{dih}} = \frac{V^{\phi}_{ijkl}}{2}\left(1 + \cos\left(n\phi_{ijkl} - \gamma_{ijkl}\right)\right), \tag{2.69}$$

where V^{ϕ}_{ijkl} is the force constant for the respective dihedral angle between the four particles i, j, k, and l, n corresponds to the phase, and γ_{ijkl} is a shift parameter for the cosine. The dihedral rotation energy $U^{\mathrm{OPLS}}_{\mathrm{dih}}$ in the OPLS-AA force field reads similar, but allows a summation of up to four dihedral profiles:

$$U^{\mathrm{OPLS}}_{\mathrm{dih}} = \sum_{n=1}^{4} \frac{V^{\phi,n}_{ijkl}}{2}\left(1 + \cos\left(n\phi_{ijkl}\right)\right), \tag{2.70}$$

where $V^{\phi,n}_{ijkl}$ corresponds to the force constant for the nth phase.

Van der Waals interactions are typically described by a 12–6 Lennard-Jones (LJ) potential[232] which includes dispersion and repulsion effects. It consists of an attractive $-C_6 r_{ij}^{-6}$ term and a repulsive $C_{12} r_{ij}^{-12}$ term, which are combined in the LJ potential as

$$U_{\mathrm{vdW}} = U_{\mathrm{LJ}} = 4\varepsilon_{ij}\left[\left(\frac{\sigma_{ij}}{r_{ij}}\right)^{12} - \left(\frac{\sigma_{ij}}{r_{ij}}\right)^{6}\right];\ \varepsilon_{ij}, \sigma_{ij} \geq 0\,. \tag{2.71}$$

In eq. (2.71), σ_{ij} is the distance at which the LJ potential is zero, and ε_{ij} is the depth of the potential energy well. For two particles i and j, these pair parameters are determined by combining the parameters ε_i, σ_i and ε_j, σ_j of the respective particles. In the case of GAFF, the Lorenz–Berthelot mixing rules[233,234] are applied for this, which determine ε_{ij} as geometric average and σ_{ij} as arithmetic average:

$$\varepsilon_{ij} = \sqrt{\varepsilon_i \varepsilon_j}\,, \tag{2.72}$$

$$\sigma_{ij} = \frac{1}{2}\left(\sigma_i + \sigma_j\right). \tag{2.73}$$

In the OPLS-AA force field, ε_{ij} and σ_{ij} are both determined as geometric average.[228] The LJ potential is frequently used in many different force fields and has been shown to be a good approximation of the real intermolecular interactions.[235] In addition, it does not require numerically demanding evaluations and is mathematically easy to handle, for example, r_{ij}^{-12} is easily accessible as the square of r_{ij}^{-6}. More complicated and computationally demanding potentials are, for example, the Morse potential[236] and the Buckingham potential.[237]

The contribution of the electrostatic potential is derived from the Coulomb potential as

$$U_{\mathrm{el}} = \frac{q_i q_j}{4\pi\varepsilon_0 r_{ij}}\,, \tag{2.74}$$

where q_i and q_j are the charges of two particles separated by a distance r_{ij}, and ε_0 is the vacuum permittivity. In contrast to the LJ potential, the electrostatic potential is proportional to r_{ij}^{-1} and thus a long-ranged interaction.

2.3.3. Ab Initio Molecular Dynamics Simulations

In *ab initio* molecular dynamics (AIMD) simulations, the PES and the forces acting on the nuclei are calculated by electronic structure calculations that are performed "on-the-fly" as the MD trajectory is generated. By this, the electronic variables are considered as active degrees of freedom. This allows the study of "chemically complex" systems, for example reactions, provided that a suitable approximation for the many-electron problem is used. The seminal work on AIMD simulations dates back to Car and Parinello in 1985.[238] Since then, many more techniques have been developed to incorporate the electronic structure in MD simulations, like for instance Ehrenfest or Born–Oppenheimer dynamics.[239] Throughout this thesis, AIMD simulations based on Born–Oppenheimer MD are used to simulate the systems analyzed in chapters 7 to 10, which is why a brief introduction on the underlying methodology will be given in the following.

In Born–Oppenheimer MD, the nuclear and electronic degrees of freedom are separated, which means that the static electronic structure problem is solved in each time step for a set of fixed nuclei. This reduces the electronic structure and force calculations to solving the time-independent Schrödinger equation, and the nuclei are propagated by classical MD. The underlying equation for the electronic ground state reads as

$$m_A \left(\frac{\partial^2 \mathbf{R}_A}{\partial t^2}\right) = -\nabla_A \min\left\{\left\langle \Psi_0 \middle| \hat{H}_{\mathrm{el}} \middle| \Psi_0 \right\rangle\right\}, \tag{2.75}$$

where the eigenvalue of the electronic Hamiltonian corresponds to the ground state energy (*cf.* eq. (2.1)). Accordingly, $\left\{\left\langle \Psi_0 \middle| \hat{H}_{\mathrm{el}} \middle| \Psi_0 \right\rangle\right\}$ has to be minimized for every time step of the simulation. In most routine applications and in chapters 7 to 10, DFT is used as electronic structure method. If the according KS operator $\hat{H}_{\mathrm{el}}^{\mathrm{KS}}$ is inserted in eq. (2.75), this results in

$$m_A \left(\frac{\partial^2 \mathbf{R}_A}{\partial t^2}\right) = -\nabla_A \min\left\{\left\langle \Psi_0 \middle| \hat{H}_{\mathrm{el}}^{\mathrm{KS}} \middle| \Psi_0 \right\rangle\right\} = -\nabla_A \min\left\{E^{\mathrm{KS}}\right\}, \tag{2.76}$$

which means that the minimum of the KS energy corresponds to the electronic ground state energy of a system with nuclei fixed at the positions $\mathbf{R}_A$.

The AIMD simulations presented in this thesis are performed using the CP2K[240,241] program package, which includes the Gaussian and plane waves (GPW) method[242,243] to solve the KS equations efficiently. Within the GPW method, the KS orbitals are expanded in terms of GTO basis functions, and an auxiliary basis of plane waves (PWs) is added to obtain a second

description of the electron density. A conversion between these two representations is achieved by mapping the electron density in the GTO basis onto a real-space grid, for which the spacing is determined by a given PW cutoff. The PW coefficients are obtained by a discrete Fourier transform. To reduce the required PW cutoff (*cf.* section 2.1.2), the Goedecker–Teter–Hutter (GTH) pseudopotentials[244–246] are employed, which allow for an analytical calculation of the corresponding matrix elements in the GTO basis set. The contribution of the kinetic energy to the KS matrix is evaluated in the GTO basis, but the exchange-correlation and the electrostatic potential can be calculated more efficiently in the PW basis. The contributions obtained from the PW representation are then transferred back to the Gaussian basis set representation to construct the KS matrix. Overall, this procedure results in a KS matrix construction scheme that scales linearly with system size, allowing an efficient computation of large systems with several hundreds or thousands of atoms.

Due to the application of GTH pseudopotentials, the electron density approaches zero close to the nuclei and vanishes at the nuclei positions. This can cause numerical issues and poor convergence in the calculation of the exchange-correlation near the nuclei, especially for gradient-corrected functionals which often contain terms with the electron density as denominator. The total energy is thus dependent on the nuclei positions relative to the real-space grid imposed by the PW basis. Instead of using very high cutoffs, this effect can be reduced by applying several smoothing procedures that have been developed and implemented in CP2K.[243]

For the equilibration of AIMD simulations, it is convenient to use massive thermostats, which couple an individual Nosé–Hoover thermostat chain to each degree of freedom. This reduces the equilibration time and excites stiff modes that are only loosely coupled to other vibrational modes. This is especially important when calculating vibrational spectra as it is done in chapters 7, 9 and 10. Here, the neglect of massive thermostats can lead to unexcited vibrational modes that would be missed in the calculated spectra.

2.4. Vibrational Circular Dichroism

Vibrational circular dichroism (VCD) spectroscopy measures the different absorption of left and right circularly polarized infrared (IR) radiation and can thus be seen as the extension of electronic circular dichroism (ECD) into the IR and near-IR region where vibrational transitions occur.[36,37,41,247] Compared to ECD, which requires chromophoric groups in the molecules under investigation, VCD has a richer structural content as any chemical bond serves as a probe. This makes VCD one of the most powerful techniques to determine the absolute configuration of chiral molecules.[34,247,248] Additionally, the high structural sensitivity of VCD allows the study of conformational distributions or even small structural changes, for example in antibiotics or natural products.[46,77]

The VCD signal can simply be expressed as

$$\Delta A = A_{\mathrm{L}} - A_{\mathrm{R}}\,, \tag{2.77}$$

where A_L and A_R are the absolute absorbance of the left and right circularly polarized radiation, respectively. Since circularly polarized light is itself chiral, any chiral molecule will interact differently with either the left or right circularly polarized radiation, causing measurable differences in A_L and A_R. However, although VCD is based on IR spectroscopy, VCD itself is an intrinsically weak phenomenon,[41] as the difference in the absorbance of left and right circularly polarized light is typically several orders of magnitude smaller than the conventional IR signals. Nevertheless, the first successful VCD measurements were already reported in 1973 by Hsu and Holtzwarth,[53] and in the following years Nafie and Diem developed the Fourier transform VCD spectrometer[249] for routine applications of VCD.

To better understand the phenomenon of VCD, it is worth taking a look at the Rosenfeld equation,[250] which is the fundamental equation for all kinds of circular dichroism:

$$R_{0n} = \mathrm{Im}\left\{\langle\Psi_0\left|\hat{\mu}\right|\Psi_n\rangle\,\langle\Psi_n\left|\hat{m}\right|\Psi_0\rangle\right\}. \tag{2.78}$$

In eq. (2.78), R_{0n} is the rotational strength describing a transition from the ground state 0 to an excited state n, with $\hat{\mu}$ and $\hat{m}$ being the electric and magnetic dipole operators, respectively. In the case of VCD, Ψ_0 and Ψ_n are vibrational wave functions, in the case of ECD they are wave functions of the electronic states.

With the Rosenfeld equation, some typical properties of VCD spectra can be explained. The electric dipole moment transforms as a translation, while the magnetic dipole moment transforms as a rotation. Hence, under reflection, the electric dipole moment changes its sign while the magnetic dipole moment does not, resulting in an overall change in the sign of the rotational strength. The opposite is true under inversion, where the magnetic dipole moment changes its sign and the electric dipole moment does not. This implies that the rotational strengths of enantiomers are of equal magnitude but opposite sign, resulting in VCD spectra that are mirrored with respect to the wavenumber axis. Achiral molecules, on the other hand, have a rotational strength of zero and are thus not VCD active. Based on this fundamental property, VCD spectroscopy can be used to distinguish between two enantiomers, as long as it is known which spectrum belongs to which enantiomer. Therefore, VCD measurements typically need to be supported by reference spectra, which are most often based on calculations. The possibilities to calculate VCD spectra are generally manifold, a brief overview of two methods used throughout this thesis is given in the following.

Although the first VCD spectra were already measured in the early 1970s, the calculation of such spectra remained a challenge for a long time. The first theory for the calculation of VCD spectra, proposed by Nafie and Freedman in 1983,[42,43] is based on the nuclear velocity perturbation (NVP) theory.[251–253] A few years later, Stephens derived an alternative approach based on the magnetic field perturbation (MFP) theory[254,255] which was later implemented in the Gaussian quantum chemistry (QC) program[256,257] by Cheeseman *et al.*[258] These advances made it possible to calculate VCD spectra at the computationally affordable DFT level of theory, and the comparison of calculated and experimental spectra became a common procedure in most VCD studies.

Nowadays, the calculation of VCD spectra by static QC methods is a routine task and the underlying equations are implemented in many software packages like Turbomole,[72] Gaussian,[258] or ADF.[259] These implementations are mostly based on the NVP and MFP theories mentioned above but can vary between different software packages. Therefore, the following explanation initially follows the definitions as implemented in Turbomole (based on MFP),[72] since this is the software package used to compute the VCD spectra presented in chapters 4 to 6.

According to eq. (2.78), the calculation of VCD requires knowledge about the electric dipole moment $\boldsymbol{\mu}$ and the magnetic dipole moment $\mathbf{m}$. Within the harmonic approximation, these are given by

$$(\boldsymbol{\mu}_n)_\beta = \sqrt{\frac{\hbar}{\omega_n}} \sum_{C\alpha} \mathbf{P}^C_{\alpha\beta} \mathbf{S}_{C\alpha,n} \tag{2.79}$$

and

$$(\mathbf{m}_n)_\beta = -\sqrt{2\hbar^3\omega_n} \sum_{C\alpha} \mathbf{M}^C_{\alpha\beta} \mathbf{S}_{C\alpha,n}\,, \tag{2.80}$$

where ω_n is the frequency of the nth normal mode, α and β are Cartesian coordinates, C counts the nuclei, and $\mathbf{S}_{C\alpha,n}$ is the transformation matrix from Cartesian to normal coordinates. The central quantities of eqs. (2.79) and (2.80) are the atomic polar tensor (APT) $\mathbf{P}^C_{\alpha\beta}$ and the atomic axial tensor (AAT) $\mathbf{M}^C_{\alpha\beta}$, which are both divided into electronic and nuclear contributions. For the APT, the nuclear contribution is given by a tensor containing the nuclear charges in all diagonal positions, and the electronic contribution is given by

$$\mathbf{E}^C_{\alpha\beta} = \left(\sum_{i=1}^{N_\mathrm{occ}} \frac{\partial \langle \phi_i | \mathbf{r}_\beta | \phi_i \rangle}{\partial \mathbf{R}_{C\alpha}} \right)_{\mathbf{R}^0}, \tag{2.81}$$

where $\mathbf{R}_C$ is the position of nucleus C, ϕ_i are occupied molecular orbitals, and the superscript 0 symbolizes the evaluation at equilibrium geometry. The nuclear and electronic contributions to the AAT are given by

$$\mathbf{J}^C_{\alpha\beta} = \frac{\mathrm{i}eZ_C}{4\hbar c} \sum_{C}^{N_\mathrm{atoms}} \varepsilon_{\alpha\beta\gamma} \mathbf{R}^0_{C\gamma} \tag{2.82}$$

and

$$\mathbf{I}^C_{\alpha\beta} = \sum_{i=1}^{N_\mathrm{occ}} \left\langle \left(\frac{\partial \phi_i}{\partial \mathbf{R}_{C\alpha}} \right)_{\mathbf{R}^0} \middle| \left(\frac{\partial \phi_i}{\partial \mathbf{B}_\beta} \right)_{\mathbf{B}=0} \right\rangle, \tag{2.83}$$

respectively. Therein, e is the elementary charge, Z_C is the charge of nucleus C, $\varepsilon_{\alpha\beta\gamma}$ is the Levi-Civita epsilon, and $\mathbf{B}$ is a magnetic field. The derivatives of the molecular orbitals with respect to the perturbation of the magnetic field can be calculated within the coupled perturbed HF formalism.[72] The VCD intensities I_n, which are proportional to the rotational strength, are

then obtained by the imaginary part of the scalar product between the electric and magnetic dipole moments

$$I_n \propto R_n = \mathrm{Im}\left(\boldsymbol{\mu}_n \cdot \mathbf{m}_n\right). \tag{2.84}$$

The methodology described above is a computationally efficient approach to calculate VCD spectra for static structures, most often for isolated monomers. However, although the technical application as implemented in Turbomole is rather straightforward, some important aspects have to be considered to obtain reliable VCD spectra. Due to the high structural sensitivity of VCD, the spectra of different conformers tend to differ significantly.[2,3,46,260] Consequently, a sufficient sampling of the conformational space has to be ensured, which is usually done by a weighted average of the VCD spectra of all relevant molecular conformers.[77] The weighting techniques that can be applied for this are generally manifold, for example, classical Boltzmann weighting,[76,77] cluster-weighting,[2–4] or the "wisdom of the crowd" approach[77] which simply calculates the arithmetic mean. Another aspect to consider is a non-idle environment, for example in self-aggregating liquids that interact through hydrogen bonding. Here, monomer structures are mostly not sufficient to model the features of liquid phase vibrational spectra, even when implicit solvation models are used.[2,3] It is therefore necessary to consider a weighted average of clusters (e.g., dimers, trimers, or tetramers) that explicitly account for intermolecular interactions.[2,3,261,262]

A second approach to calculate VCD spectra is based on AIMD simulations and used for the analysis of the trajectories presented in chapters 7 to 10. The foundation is the Green–Kubo or correlation function approach, which states that any vibrational spectrum can be expressed as the Fourier transform of a certain correlation function.[263,264] According to the Wiener–Khintchine theorem,[265,266] the auto-correlation function of any time-dependent function $f(t)$ is given as

$$\langle f(\tau)\, f(t+\tau)\rangle_\tau = \frac{1}{2\pi}\int \left|\int f(t)\exp\left(-\mathrm{i}\omega t\right)\mathrm{d}t\right|^2 \exp\left(\mathrm{i}\omega t\right)\mathrm{d}\omega\,, \tag{2.85}$$

with τ and ω being the delay time and frequency, respectively. In terms of correlation functions, a VCD spectrum is defined as the Fourier transform of the cross-correlation function of the time derivatives of the electric and magnetic dipole moments:[60,267,268]

$$\Delta A(\omega) \propto \int \left[\langle \dot{\boldsymbol{\mu}}(\tau)\, \dot{\mathbf{m}}(t+\tau)\rangle_\tau - \langle \dot{\mathbf{m}}(\tau)\, \dot{\boldsymbol{\mu}}(t+\tau)\rangle_\tau\right]\exp\left(-\mathrm{i}\omega t\right)\mathrm{d}t\,. \tag{2.86}$$

An IR spectrum is defined accordingly and based on the auto-correlation function of the electric dipole moment time derivatives.[269] Consequently, the electric and magnetic dipole moments need to be determined along the AIMD trajectory.

The electric dipole moments can be obtained with the help of a Voronoi tessellation, which divides the Euclidean space (i.e., the simulation box and the electron density) into a set of Voronoi cells.[144] This division is based on a set of n sites $\mathbf{s}_i$ which are typically the atoms contained in the simulation. In the traditional Voronoi tessellation,[270] a Voronoi cell consists of all points in space that are closer to a particular site than to any other site. To account for asymmetric electron density distributions, for instance in polar covalent bonds, the radical

Voronoi tessellation introduces additional radii r_i, defining a circle around each site:[144]

$$\mathbf{C}_i^r = \{\mathbf{x} \in \mathbb{R}^3 \,|(\mathbf{x}-\mathbf{s}_i)^2 - r_i^2 \leq (\mathbf{x}-\mathbf{s}_j)^2 - r_j^2 \,\forall\, j \neq i\};\; i,j \in \{1,\ldots,n\}\,. \tag{2.87}$$

If each atom serves as a site, eq. (2.87) divides the Euclidean space into atomic cells which can be merged to obtain N molecular Voronoi cells $\mathbf{M}_k$. Based on these molecular Voronoi cells, the molecular electric dipole moments can then be obtained by spatial integration of the electron density as

$$\boldsymbol{\mu}_k = \int_{\mathbf{M}_k} \mathbf{r}\rho(\mathbf{r})\mathrm{d}\mathbf{r};\; k \in \{1,\ldots,N\}\,. \tag{2.88}$$

The magnetic dipole moments can be obtained by the Thomas–Kirchner approach.[47] This approach is based on the classical expression of the magnetic dipole moment, which reads as the cross product between the electric current density $\mathbf{j}(\mathbf{r})$ and the spatial coordinates $\mathbf{r}$:

$$\mathbf{m} = \frac{1}{2}\int \mathbf{r} \times \mathbf{j}(\mathbf{r})\mathrm{d}\mathbf{r}\,. \tag{2.89}$$

The electric current density can be defined by the continuity equation

$$\frac{\partial\rho(\mathbf{r},t)}{\partial t} + \nabla\mathbf{j}(\mathbf{r},t) = 0\,, \tag{2.90}$$

which states that temporal changes in the electron density act as sources and sinks of an electric current. The time derivative of the electron density can be obtained by saving it in each simulation step and using the finite difference method afterward.[47] However, eq. (2.90) does not uniquely determine the electric current density, since arbitrary eddy currents do not appear as changes in the electron density. To circumvent this issue, a second condition is introduced, which states that the electric current density is a product of the electron density and a conservative velocity field $\mathbf{v}(\mathbf{r},t)$:

$$\mathbf{j}(\mathbf{r},t) = -\rho(\mathbf{r},t)\nabla\alpha(\mathbf{r},t) \quad \text{with} \quad \mathbf{v}(\mathbf{r},t) = -\alpha(\mathbf{r},t)\,. \tag{2.91}$$

Equation (2.91) ensures that the electric current flows only into regions with a finite electron density. Inserting eq. (2.91) into eq. (2.90) yields the following partial differential equation

$$\frac{\partial\rho(\mathbf{r},t)}{\partial t} = \nabla\rho(\mathbf{r},t)\nabla\alpha(\mathbf{r},t) + \rho(\mathbf{r},t)\Delta\alpha(\mathbf{r},t)\,. \tag{2.92}$$

Solving eq. (2.92) to find the scalar field $\alpha(\mathbf{r},t)$ allows to uniquely determine the electric current density from eq. (2.91) and the magnetic dipole moments from eq. (2.89). Since the electric and magnetic dipole moments are obtained as molecular quantities, it is possible to calculate VCD spectra for individual molecules. This makes it possible to determine the contributions of different species to the VCD spectrum of a system, which is of particular importance for the study of chirality transfer phenomena, as discussed in chapters 7 to 10.

2.5. Sampling Quality in Molecular Simulations

The ability of a molecular simulation to realistically describe the properties of a system of interest is often highly dependent on the sampling of the phase space. This is especially true for structurally sensitive properties such as VCD, where an insufficient sampling of the conformational landscape may result in non-converged spectra, but it is certainly also true for many structural and dynamic properties. Consequently, questions often arise regarding the best way to adequately sample the phase space and how to assess the sampling quality of molecular simulations. An excellent review and best practices article[271] on these questions has recently been published of which the most important aspects will be highlighted in the following.

One of the simplest reasons for poor sampling is the lack of proper equilibration, which means that if a system continues to relax from its initial configuration, statistical sampling has not even begun. Therefore, the first step should be to verify that proper equilibration has been achieved by checking the time convergence of scalar quantities, such as the potential energy or temperature. In addition, visual inspection of the trajectory may help to determine whether a simulation is systematically changing over time or not. Once sufficient equilibration is achieved, the "equilibration" or "burn-in" time t_{equil} should be discarded and only the remaining "production" trajectory should be used for the purpose of data analysis.

Although being important, a proper equilibration alone does not guarantee a sufficient conformational sampling and good statistics, since a well-equilibrated simulation may, for example, still get stuck near a local minimum without sampling other important regions of the conformational space.[3] The data series computed for such a simulation are usually highly correlated, which means that the numerical values of individual simulation steps tend to be similar to each other and do not provide fully "new" information about the quantity of interest. To estimate the correlation in a time series of data $x(t)$, the correlation time τ can be calculated, which corresponds to the longest separation time Δt over which $x(t)$ and $x(t+\Delta t)$ remain correlated. The correlation time can thus be seen as the time over which a system keeps memory of its previous states. Knowing τ, the number of uncorrelated samples generated by a simulation can be estimated by the quotient of the total simulation time and the correlation time.

Another possibility to determine the sampling quality of a simulation is based on configurational distance measures. However, since a system with N particles possesses $3N$ degrees of freedom, it is rather difficult to assess whether and to what extent a simulation has adequately explored the entire conformational space. Therefore, it is common to select only a few degrees of freedom, usually those that are expected to be most important in describing the quantity of interest. In the case of VCD, for example, this would be the molecular conformations, which can most often be monitored by combinations of certain dihedral angles.[3,6,8] Other configurational distance measures are, for example, specific distances or the root mean square deviation (RMSD) between two configurations:

$$\text{RMSD}(\mathbf{r},\mathbf{s}) = \sqrt{\frac{1}{N}\sum_{i=1}^{N}|\mathbf{r}_i - \mathbf{s}_i|^2}\,. \tag{2.93}$$

In eq. (2.93), $\mathbf{r}_i$ and $\mathbf{s}_i$ are the Cartesian coordinates of atom i in the two configurations $\mathbf{r}$ and $\mathbf{s}$. A very powerful RMSD-based convergence measure is the "all-to-all RMSD", which calculates the RMSD of each trajectory snapshot with respect to all other snapshots. This allows to identify very similar structures. Besides that, it may sometimes be beneficial to select only a subset of atoms for RMSD calculations in order to discard higher frequency fluctuations that may not be relevant in some cases, for example, when monitoring the backbone structure of a protein.

If the tests described above reveal that a single trajectory does not sufficiently sample the conformational space, one of the most straightforward approaches to improve the sampling quality is to perform additional independent simulations with different initial structures.[3,6,7] Ideally, the set of initial structures should be chosen to span the space to be sampled, but this is not always possible as it requires some prior knowledge of the phase space. Of course, with such an approach, it must be kept in mind that the individual simulations are not correlated. This means that properties derived from correlation functions (*cf.* eq. (2.85)) have to be calculated for each trajectory individually and the overall expectation value for the property of the system can then be obtained as (weighted) average.[3,6,7] This applies also to the calculation of vibrational spectra from molecular simulations (*cf.* eq. (2.86)), where it proved to be very successful to perform independent simulations starting from all relevant conformers of the molecule of interest (see chapters 5, 8 and 9). Throughout this thesis, this approach will therefore be referred to as conformer replica simulations.

3. Uncertainty Quantification of Phase Transition Quantities from Cluster Weighting Calculations

Jan Blasius,[*] Paul Zaby,[*] Jürgen Dölz,[†] and Barbara Kirchner[*]

Received: 25 March 2022, Published online: 05 July 2022.

Reprinted (adapted) in appendix A with permission[‡] from

J. Blasius, P. Zaby, J. Dölz, and B. Kirchner, *J. Chem. Phys.* **2022**, *157*, 014505.

doi:10.1063/5.0093057.

For this article a Supporting Information is available free of charge at:
https://aip.scitation.org/doi/suppl/10.1063/5.0093057.

Contributions to the manuscript

- Co-development of the concept
- Supervision and analysis of the calculations
- Interpretation of the results
- Writing of the manuscript

[*] Mulliken Center for Theoretical Chemistry, Clausius Institute for Physical and Theoretical Chemistry, University of Bonn, Beringstr. 4–6, 53115 Bonn, Germany
[†] Institute for Numerical Simulation, University of Bonn, Friedrich-Hirzebruch-Allee 7, 53115 Bonn, Germany
[‡] Permission requests to reuse material from this chapter should be directed to AIP Publishing.

In this initial work, the influence of uncertainties in experimental reference data on the results of QCE calculations is investigated by means of two uncertainty propagation methods, the Monte Carlo method[143] and the Gauss–Hermite quadrature.[142] As explained in section 2.2.2, the empirical QCE parameters a_{mf} and b_{xv} (*cf.* eqs. (2.33) and (2.36)) are usually optimized with respect to reference data, which are mostly experimentally determined and therefore susceptible to measurement errors. However, despite the long history of QCE, to date, there has been no systematic study of how such measurement errors can affect the outcome of QCE calculations. Therefore, the main objective of this study is to achieve a comprehensive understanding of the overall dependence of vaporization enthalpies, vaporization entropies, and cluster populations calculated from QCE on the experimental inputs, namely density and boiling temperature. Especially the influence of possible inaccuracies or measurement errors on the cluster populations is relevant in the context of this thesis since these are the basis for the methodological approach developed and presented in chapters 4 to 6. A full reprint of this work[1] can be found in appendix A.

The set of herein investigated substances includes seven organic molecules, five nonpolar and aprotic hydrocarbons (ethane, ethylene, propane, propylene, and butane) and two polar alcohols (methanol and (*R*)-butan-2-ol). First, two methods for the calculation of vaporization enthalpies and entropies are introduced and compared: the standard QCE approach[272] and the Clausius–Clapeyron approach.[1,210] For the investigated substances, both approaches are found to perform comparably well and the mean absolute deviations from experimental reference data are 2.86 kJ mol^{-1}/2.79 kJ mol^{-1} (12.57 %/12.84 %, standard QCE/Clausius–Clapeyron) for the vaporization enthalpies and 15.23 J mol^{-1} K^{-1}/15.01 J mol^{-1} K^{-1} (16.58 %/16.56 %) for the vaporization entropies.

For the purpose of uncertainty quantification, the standard QCE approach is followed, since the Clausius–Clapeyron approach is computationally more expensive and suffers from other drawbacks, such as that the vaporization enthalpy can only be calculated at the boiling point and is considered to be temperature independent. A prerequisite for the later application of the Gauss–Hermite quadrature is that the calculated quantities of interest show a smooth dependence with respect to changes in the input data.[142,210] By varying the experimental input quantities in ranges of ±20 % with increments of 1 %, it is ensured that the vaporization enthalpies and entropies show such a behavior and it is observed that an increase/decrease of density or boiling temperature consistently causes an increase/decrease of the vaporization quantity. In addition, it is shown that the vaporization enthalpies are much more sensitive to inaccuracies in the boiling temperature than in the density. In particular, a density variation of ±20 % leads to changes of 0.4–5.0 % in the vaporization enthalpies, whereas a variation of the boiling temperature by ±20 % results in changes of more than 20 % for all investigated systems. The vaporization entropies are generally less sensitive to deviations in the boiling temperature. A density variation of ±20 % induces changes of 0.7–4.9 % in the vaporization entropies and a variation of the boiling temperature by ±20 % causes changes of 1.4–4.3 %. It has to be noted that the variation of the input quantities by ±20 % is not connected to the actual measurement errors, which are typically below 1 K (<1 %) and 0.0001 g cm^{-3} (≪1 %). The reason for examining such a large range is mainly to ensure that there are no discontinuities in the thermodynamic functions anywhere

near the experimental input region and also to be able to discuss the observed trends with more comprehensible numbers.

The above observations concerning the thermodynamic functions can be explained by the changes in the cluster populations and empirical QCE parameters that are induced by variations in the input data. Increasing the density and boiling temperature both leads to increased populations of larger clusters. This results in larger values for the vaporization quantities since an increased amount of energy is required to break these clusters into monomers during a phase transition from the liquid to the gas phase. The opposite is true for decreased densities and boiling temperatures. Additionally, it is observed that a_{mf} is sensitive to changes in the boiling temperature while b_{xv} is mainly influenced by the density. This explains why the vaporization entropy is much less sensitive to changes in the boiling temperature since the entropy calculated in the QCE model (*cf.* eq. (2.56)) is not directly dependent on the electronic partition function and a_{mf} (*cf.* eq. (2.37)). The influence of the input data on the cluster populations is found to be minor, especially considering that the experimental uncertainties are significantly smaller than the $\pm 20\,\%$ used here.

Finally, the influence of measurement errors in the input data is quantified using the Monte Carlo method and the Gauss–Hermite quadrature. Using the vaporization enthalpy of (*R*)-butan-2-ol as an example, the slow convergence behavior of the Monte Carlo method compared to the Gauss–Hermite quadrature is shown, and the Gauss–Hermite quadrature is used to quantify the uncertainty in the calculated vaporization enthalpy of (*R*)-butan-2-ol as $30.95 \cdot 10^{-3}\,\mathrm{kJ\,mol^{-1}}$. Since chemical accuracy is usually considered to be around $4\,\mathrm{kJ\,mol^{-1}}$, this uncertainty is negligible in a chemical sense which means that vaporization enthalpies can be calculated with QCE without the need to consider measurement errors in detail. Although this statement is not necessarily transferable to all other quantities, the analyses performed throughout this work strongly suggest that at least the vaporization entropies and cluster populations are hardly affected by inaccuracies in the experimental input data. Consequently, the QCE model provides reliable and robust cluster populations that can be employed for the methodological approach presented in chapters 4 to 6.

4. Cluster-Weighting in Bulk Phase Vibrational Circular Dichroism

Jan Blasius* and Barbara Kirchner*

Received: 10 July 2020, Published online: 21 July 2020.

Reprinted (adapted) in appendix B with permission† from

J. Blasius and B. Kirchner, *J. Phys. Chem. B* **2020**, *124*, 7272–7283.

doi:10.1021/acs.jpcb.0c06313.

For this article a Supporting Information is available free of charge at:
https://pubs.acs.org/doi/10.1021/acs.jpcb.0c06313.

Contributions to the manuscript

- Development of the concept
- Performance of all calculations
- Interpretation of the results
- Writing of the manuscript

*Mulliken Center for Theoretical Chemistry, Clausius Institute for Physical and Theoretical Chemistry, University of Bonn, Beringstr. 4–6, 53115 Bonn, Germany
†Permission requests to reuse material from this chapter should be directed to the American Chemical Society.

This work introduces cluster-weighting as a new method for the calculation of bulk phase IR and VCD spectra. In this approach, the system under consideration is represented by an ensemble of quantum-chemically optimized clusters, to which weights are assigned by the cluster populations obtained from QCE calculations. Based on these cluster weights, the IR and VCD spectra of the ensemble can be obtained by weighting the individual spectra of all considered clusters. By this, environmental effects are explicitly taken into account, which is usually necessary to model peak shifts and intensity perturbations induced by intermolecular interactions such as hydrogen bonding.[45,47,49,262,273] Compared to classical Boltzmann weighting, the main advantage of cluster-weighting is that clusters of different sizes can be considered simultaneously, allowing the inclusion of various structural motifs.[13] Furthermore, the consideration of differently sized clusters improves conformational sampling, which can be of particular importance for the modeling of VCD spectra. After introducing methodological details, the approach is extensively tested at the example of (*R*)-butan-2-ol, which is known to self-aggregate due to hydrogen bonding interactions in the liquid phase. These intermolecular interactions cause significant peak shifts in the bulk phase IR and VCD spectra compared to the gas phase,[45–47] making (*R*)-butan-2-ol an ideal test case for the cluster-weighting approach. A full reprint of this work[2] can be found in appendix B.

As a first step, the dependence of cluster-weighting and classical Boltzmann weighting with respect to the underlying quantum chemical level of theory is investigated. Therefore, cluster weights and Boltzmann factors are calculated for nine monomer conformers of (*R*)-butan-2-ol using different combinations of the BP86 functional[68,69], the D3 dispersion correction[170,171], the implicit solvation model COSMO,[274] and the two basis sets def2-SVP[70] and def2-TZVP.[70] Further benchmark tests with other functionals are provided in the Supporting Information. From these tests, it is observed that the cluster weights of the monomers are less sensitive to the choice of the basis set compared to their Boltzmann weights. Using the obtained weights, gas phase IR and VCD spectra of (*R*)-butan-2-ol are calculated as a weighted average of the monomer spectra. Here, it is observed that Boltzmann and cluster-weighting yield gas phase spectra of similar quality which compare well with experimental reference data. In addition, it is shown that the vibrational spectra of the neat liquid phase can not be modeled on the basis of monomers alone, even when implicit solvation is used.

Since the focus and main motivation of this work is the calculation of bulk phase vibrational spectra with cluster-weighting, the proposed method is extensively tested in this regard using 16 different cluster sets which are composed of different numbers and types of monomers and oligomeric clusters. The compositions of all cluster sets are given in appendix B and an overview is provided in the Supporting Information. The main questions to be answered in this work are 1) how important is the inclusion of a variety of conformers for monomers and oligomers, 2) which structural motifs need to be considered, and 3) can low populated clusters be excluded to decrease the size of the cluster set and accelerate the calculations. To answer these questions, IR and VCD spectra of (*R*)-butan-2-ol are systematically calculated using all the constructed cluster sets and the results are compared to experimental liquid phase spectra. Note that a comparison between cluster-weighting and Boltzmann weighting is not possible here, since classical Boltzmann

weighting does not allow for the inclusion of differently sized clusters.

It is shown that the bulk phase IR and VCD spectra of (*R*)-butan-2-ol can be successfully modeled with some of the cluster sets, while other cluster sets fail to reproduce the liquid phase vibrational spectra. On the basis of these tests, the following conclusions are drawn in order to answer the questions listed above. The inclusion of a wide range of conformers does not appear to be essential for modeling the main features of the liquid phase vibrational spectra, and low populated clusters can be systematically excluded without significantly altering the results. Furthermore, the inclusion of isomeric structures (e.g., rings and chains) seems to become less important with increasing cluster size, and already at the size of trimers, ring-like structures are found to be the dominant structural motifs. The low populations of chain-like structures can be attributed to the number of hydrogen bonds that can form in a given cluster since there are fewer hydrogen bonds in chain-like structures than in ring-like structures. In addition, the best agreement with experimental reference spectra is observed for a cluster set containing only the global minimum structures of the monomer up to the decamer. This observation allows the design of a workflow that considers only global minimum structures, thus reducing the computational effort required for the cluster construction and associated quantum chemical calculations.

In summary, the new cluster-weighting approach was successfully applied to the calculation of bulk phase IR and VCD spectra of (*R*)-butan-2-ol, showing that peak shifts and intensity perturbations induced by intermolecular interactions can be accurately modeled. In addition, guidelines for applications to similar systems could be derived. However, further testing of the method is still necessary, for example, the dependence of the bulk phase vibrational spectra on the underlying quantum chemical level of theory or a comparison to other established methods. This is the scope of chapter 5.

5. Predicting Vibrational Spectroscopy for Flexible Molecules and Molecules with Non-Idle Environments

Barbara Kirchner,[*] Jan Blasius,[*] Lars Esser,[*] and Werner Reckien[*]

Received: 22 September 2020, Published online: 16 December 2020.

Reprinted (adapted) in appendix C with permission[†] from

B. Kirchner, J. Blasius, L. Esser, and W. Reckien, *Adv. Theory Simul.* **2021**, *4*, 2000223.

doi:10.1002/adts.202000223.

For this article a Supporting Information is available free of charge at:
https://onlinelibrary.wiley.com/doi/full/10.1002/adts.202000223.

Contributions to the manuscript

- Development of the concept
- Performance of all calculations except for the SCF convergence and DFT integration grid tests
- Interpretation of the results
- Co-writing of the manuscript

[*] Mulliken Center for Theoretical Chemistry, Clausius Institute for Physical and Theoretical Chemistry, University of Bonn, Beringstr. 4–6, 53115 Bonn, Germany
[†] Permission requests to reuse material from this chapter should be directed to Wiley-VCH GmbH.

In this methodological work, different methods for the prediction of vibrational spectra of flexible molecules and molecules in non-idle environments are compared and assessed. The first method is the cluster-weighting approach[2] that was presented in chapter 4 and is further tested here. The second method is based on AIMD simulations and the correlation of electric and magnetic dipole moments to obtain IR and VCD intensities, see section 2.4 for a methodological overview. Herein, two approaches are followed for the calculation of the dipole moments: 1) the electric dipole moments are obtained by a radical Voronoi tessellation and subsequent integration of the electron density[144] and the magnetic dipole moments are calculated with the Thomas–Kirchner approach,[47] and 2) the electric and magnetic dipole moments are approximated by classical definitions that rely on atomic partial charges.[275] All these methods are applied to calculate IR and VCD spectra of (*R*)-butan-2-ol in the gas and bulk phase in order to elaborate the advantages and disadvantages of each approach. A full reprint of this work[3] can be found in appendix C.

With the AIMD approach, excellent agreement between calculated and experimental gas and bulk phase spectra is obtained when the dipole moments are calculated using a radical Voronoi tessellation and the Thomas–Kirchner approach. For the bulk phase, a single AIMD simulation of 16 molecules proves sufficient for the calculation of vibrational spectra. Gas phase simulations of isolated molecules, on the other hand, are found to suffer from insufficient conformational sampling. In particular, conformational analyses reveal that the rotational barriers between some of the (*R*)-butan-2-ol conformers can not be overcome on the applied time scales of 30 ps. To solve this issue, the conformer replica simulations approach is proposed (*cf.* section 2.5), in which independent simulations with different starting structures are averaged to improve the conformational sampling. In addition, empirical scaling factors for vibrational spectra obtained from AIMD simulations are proposed to further improve the agreement between theory and experiment.

For the cluster-weighting approach, the influence of the applied quantum chemical level of theory on the quality of the calculated bulk phase vibrational spectra is tested. Therefore, the B3LYP, BLYP, and BP86 functionals[68,69] are combined with the def2-SVP and def2-TZVP basis sets.[70] All tested combinations of functionals and basis sets yield spectra that are in good agreement with the experiment and the best results are obtained for the BP86/def2-TZVP and B3LYP/def2-TZVP levels of theory. Although the cluster weights are found to depend on the underlying level of theory, the calculated vibrational spectra are not affected by this too much. Furthermore, a rough convergence trend of the vibrational spectra with increasing cluster size is observed, indicating that for hydrogen-bonded systems, clusters up to hexamers are generally sufficient to achieve a qualitative agreement of the calculated bulk phase IR and VCD spectra with the experiment. Again, empirical scaling factors for the vibrational frequencies are proposed to improve the agreement between experiment and theory.

A comparison of the AIMD approach and cluster-weighting shows that the AIMD approach, in combination with dipole moments calculated using a radical Voronoi tessellation and the Thomas–Kirchner approach, yields vibrational spectra that are superior to those obtained with cluster-weighting. However, this superiority comes with a significantly increased computational

effort, as the calculation of the magnetic dipole moments is especially time-consuming. The use of cluster-weighting can thus be recommended when qualitatively reasonable results at low computational cost are desired, while the AIMD approach with dipole moments based on a Voronoi tessellation and the Thomas–Kirchner approach is recommended for the calculation of high-quality vibrational spectra.

The last part of the work examines an alternative and computationally less expensive approach for the calculation of dipole moments from AIMD simulations. Therefore, the electric and magnetic dipole moments of a single (*R*)-butan-2-ol gas phase AIMD simulation are analyzed. The dipole moments are calculated using a radical Voronoi tessellation and the Thomas–Kirchner approach, as well as the classical definitions of dipole moments based on atomic partial charges obtained from Mulliken, Löwdin, and Blöchl population analyses. The classical approximation of the electric dipole moments in combination with the charges from the population analyses leads to an excellent agreement with the electric dipole moments obtained with a radical Voronoi tessellation, and the IR spectra calculated from both approaches agree very well in peak location. Although the magnetic dipole moments based on the population analyses do not fluctuate in phase with the ones obtained from the Thomas–Kirchner approach, similar dipole moment distributions are obtained. Interestingly, the VCD spectrum based on the Blöchl population analysis reproduces the main features of the VCD spectrum computed with the radical Voronoi tessellation and the Thomas–Kirchner approach, but at a much lower computational cost. This alternative approach for the calculation of the dipole moments may therefore be a promising method to reduce the computational cost for the calculation of vibrational spectra from AIMD simulations.

6. Efficient Prediction of Mole Fraction Related Vibrational Frequency Shifts

Jan Blasius,[*] Katrin Drysch,[*] Frank Hendrik Pilz,[†] Tom Frömbgen,[*] Patrycja Kielb,[†‡] and Barbara Kirchner[*]

Submitted for publication in J. Phys. Chem. Lett.

Printed in appendix D.

Contributions to the manuscript

- Development of the concept
- Supervision and performance of all calculations
- Interpretation of the results
- Writing of the manuscript

[*] Mulliken Center for Theoretical Chemistry, Clausius Institute for Physical and Theoretical Chemistry, University of Bonn, Beringstr. 4–6, 53115 Bonn, Germany
[†] Clausius Institute of Physical and Theoretical Chemistry, University of Bonn, Wegelerstraße 12, 53115 Bonn, Germany
[‡] Transdisciplinary Research Area "Building Blocks of Matter and Fundamental Interactions" (TRA Matter), University of Bonn, Bonn, Germany

In this work, the cluster-weighting approach is extended to binary systems and applied to calculate mole fraction dependent IR and VCD spectra for mixtures of acetonitrile and (*R*)-butan-2-ol. The calculation of mole fraction dependent vibrational spectra is of particular interest for the computational support of quantitative analytical measurements, as it enables the identification of connections between concentration dependent spectral features and the molecular structure of mixtures.[276,277] In addition, calculated mole fraction dependent spectra can be used as a reference for experimental measurements to determine the composition of unknown mixtures. Common methods for calculating vibrational spectra of mixtures are either MD simulations or Boltzmann weighting of cluster ensembles containing only clusters that represent the composition of interest. However, the need to run individual MD simulations[276] or to construct individual cluster sets for each composition of interest[278] severely limits these approaches if the calculation of mole fraction dependent spectra is desired. Here, cluster-weighting can serve as a powerful approach, since ideally, a single cluster set is sufficient to calculate any composition of interest.[9–11,177,196] A full print of this work[4] can be found in appendix D.

Before applying the cluster-weighting approach to the acetonitrile/(*R*)-butan-2-ol mixtures, it is applied to neat acetonitrile. Acetonitrile molecules are known to interact in the neat bulk phase by dipole–dipole and CH···N interactions, causing observable intensity perturbations in the bulk compared to the gas phase IR spectra, while the vibrational frequencies are almost unaffected by this self-aggregation.[279] The calculated bulk phase IR spectra of acetonitrile are found to be in excellent agreement with the experimental reference, demonstrating that cluster-weighting is capable of modeling not only peak shifts (*cf.* chapters 4 and 5) but also intensity perturbations induced by intermolecular interactions. In addition, the influence of functional and basis set on the bulk phase IR spectra of acetonitrile is tested, detailed information is provided in the Supporting Information in appendix D.

For the cluster-weighting calculations of the mixtures, the cluster sets of the neat substances are combined and extended by mixed acetonitrile/(*R*)-butan-2-ol clusters, representing all possible intermolecular interactions between the two components. Given the mole fraction of (*R*)-butan-2-ol x_b, IR and VCD spectra are calculated for mixtures with compositions of $x_b = 0.2$, 0.5 and 0.8 and compared with experimental IR spectra measured at the same mole fractions. With the exception of the region around 1400 cm^{-1}, the calculated IR spectra generally show good agreement with the experimental reference data. Furthermore, most of the mole fraction dependent changes in the spectra are accurately modeled, especially for the wavenumber regions where the IR spectra of neat acetonitrile and (*R*)-butan-2-ol overlap. Unfortunately, the calculated VCD spectra cannot be fully validated due to the lack of experimental reference data. However, considering that acetonitrile is achiral, the mole fraction dependence of the calculated VCD spectra seems reasonable as they resemble the calculated VCD spectrum of neat (*R*)-butan-2-ol, but with reduced intensities.

Special attention is given to mole fraction related peak shifts in the experimental IR spectra. Observations show that a peak associated with asymmetric CH_3 bending vibrations shifts from 1420 cm^{-1} in neat acetonitrile to 1440 cm^{-1} in neat (*R*)-butan-2-ol. Unfortunately, the cluster-weighted IR spectra fail to adequately describe this redshift due to the absence of intensity at

1400 cm^{-1}. Nevertheless, another significant redshift is found for a peak related to CH_3 rocking vibrations, shifting from 1040 cm^{-1} in neat acetonitrile to 1030 cm^{-1} in neat (*R*)-butan-2-ol. Remarkably, the calculated IR spectra model this shift almost perfectly, showing deviations of less than 1 cm^{-1} between the experimental and calculated peak maxima. The fact that this redshift can be almost perfectly modeled with a single cluster set and computationally fast QCE calculations exemplifies the efficiency of the cluster-weighting approach for modeling mole fraction related changes in vibrational spectra. In addition, the cluster weights obtained from the QCE calculations provide insights into the molecular structure of the mixtures which can be directly related to the vibrational spectra.

7. Glucose in Dry and Moist Ionic Liquid: Vibrational Circular Dichroism, IR, and Possible Mechanisms

Jan Blasius,[*] Roman Elfgen,[*] Oldamur Hollóczki,[†*] and Barbara Kirchner[*]

Received: 17 December 2019, Published online: 28 February 2020.

Reprinted (adapted) in appendix E with permission[‡] from

J. Blasius, R. Elfgen, O. Hollóczki, and B. Kirchner, *Phys. Chem. Chem. Phys.* **2020**, *22*, 10726–10737.

doi:10.1039/c9cp06798a.

For this article a Supporting Information is available free of charge at:
https://pubs.rsc.org/en/content/articlelanding/2020/cp/c9cp06798a.

Contributions to the manuscript

- Performance of the analyses
- Interpretation of the results
- Co-writing of the manuscript

[*] Mulliken Center for Theoretical Chemistry, Clausius Institute for Physical and Theoretical Chemistry, University of Bonn, Beringstr. 4–6, 53115 Bonn, Germany
[†] Department of Physical Chemistry, Faculty of Science and Technology, University of Debrecen, 4010 Debrecen, Hungary
[‡] Permission requests to reuse material from this chapter should be directed to the Royal Society of Chemistry.

In this work, the dissolution of different D-glucose isomers (α, β, and open-chain) in the dry and moist IL 1-ethyl-3-methylimidazolium acetate ($[C_2C_1Im][OAc]$) is studied by means of AIMD simulations. Such mixtures show remarkable features in cellulose processing,[280–282] and understanding the behavior of the cellulose carbohydrate units in these solvents is essential for the design of novel solvents and procedures for processing biopolymers. The aim of this study is to gain insight into the interactions between the IL and the different D-glucose isomers and their effects on the IR and VCD spectra of the systems. The vibrational spectra are calculated with the help of a radical Voronoi tessellation[144] and the Thomas–Kirchner[47] approach, see section 2.4 for methodological details. Furthermore, the occurrence of potential reaction mechanisms is investigated. These comprise onsets for 1) the crystallization of D-glucose in the moist IL, 2) a ring closure of the open-chain D-glucose, 3) a ring opening of α- and β-D-glucose, and 4) a carbene catalysis that can occur either at the carbonyl group of the open-chain form or at the ether bonds of α- and β-D-glucose. A full reprint of this work[5] can be found in appendix E.

A total of six AIMD simulations are investigated, in each of which one of the three D-glucose isomers is dissolved either in the dry or moist IL ($wt\%(\text{water}) = 20\,\%$). Investigations of the intermolecular interactions show that the solvation of the carbohydrates is affected by all species in the solutions, but the anion–D-glucose interactions are more pronounced than those between cations and D-glucose molecules. Interestingly, the addition of water results in shortened hydrogen bonds between open-chain or α-D-glucose molecules, indicating the onset of D-glucose crystallization due to water contamination. This agrees with experimental observations which show that cellulose precipitates from moist solutions.[282] The strength of anion–cation, anion–D-glucose, and cation–D-glucose interactions is in turn reduced by the addition of water, resulting in an elongation of the respective hydrogen bonds. The weakening of anion–cation interactions is also observed in the calculated IR spectra, where peaks associated with these interactions shift to lower wavenumbers upon the addition of water.[283]

Overall, the calculated IR and VCD spectra show good agreement with experimental reference data, further validating the application of the radical Voronoi tessellation and the Thomas–Kirchner approach for the calculation of vibrational spectra, even for complex systems such as ILs and their solutions. The calculated VCD spectra are dominated by the chiral D-glucose molecules but significant contributions from the IL are also observed. These contributions are mainly from the cation, which is a clear indication of chirality transfer from the chiral carbohydrates to the transiently chiral 1-ethyl-3-methylimidazolium cation, a phenomenon that will be further investigated in chapters 8 to 10.

Although it is known that the applied IL shows remarkable features in dissolving and processing cellulose, the exact role of the ionic compounds, especially the one of the cation is still under discussion. Regarding the isomerization of D-glucose units (i.e., the anomeric conversion), it is found that this reaction is energetically possible with a slightly higher probability in the moist IL, since a ring opening of α- and β-D-glucose seems to be energetically less demanding in the presence of water. The subsequent ring closure reaction of the open-chain form occurs by a nucleophilic attack of a hydroxyl group at the carbon atom of the carbonyl group. This reaction is therefore facilitated by curled structures of the open-chain form, where the two reacting atoms

are in close proximity to each other. While such curled structures are frequently observed in the dry IL, the addition of water results in mostly linear arrangements of the open-chain form. Thus, the selective addition of water can prevent ring closure reactions and maintain open-chain units of D-glucose at the terminal positions of a cellulose strand. Furthermore, it is observed that the ring closure is facilitated by a proton abstraction of the anion at the reacting hydroxyl group and by various interactions of the cation with the carbonyl group. These interactions increase the nucleophilicity of the attacking oxygen atom and the electrophilicity of the carbonyl group.

In addition, the onset of carbene-like reactions of the IL is observed in which the cation reacts either with the ether bond of α- and β-D-glucose or with the carbonyl group of the open-chain D-glucose. It is known that $[C_2C_1Im][OAc]$ can degrade cellulose by a reverse benzoin reaction that continuously cleaves individual H_2CO units from the end of the carbohydrate chain,[284] but the possibility of carbene-like reactions may facilitate cellulose degradation by cleaving the ether bonds that link the individual D-glucose units. Such a reaction could efficiently break down long cellulose chains into smaller units, which are then degraded by further reactions, for example by a reverse benzoin reaction at the terminal positions.

8. Recognition in Chiral Ionic Liquids: The Achiral Cation Makes the Difference!

Jan Blasius,[*] Paul Zaby,[*] Oldamur Hollóczki,[†*] and Barbara Kirchner[*]

Received: 22 April 2021, Published online: 28 July 2021.

Reprinted (adapted) in appendix F with permission[‡] from

J. Blasius, P. Zaby, O. Hollóczki, and B. Kirchner, *J. Org. Chem.* **2022**, *87*, 1867–1873.

doi: 10.1021/acs.joc.1c00939.

For this article a Supporting Information is available free of charge at:
https://pubs.acs.org/doi/10.1021/acs.joc.1c00939.

Contributions to the manuscript

- Development of the concept
- Performance of all calculations
- Interpretation of the results
- Writing of the manuscript

[*] Mulliken Center for Theoretical Chemistry, Clausius Institute for Physical and Theoretical Chemistry, University of Bonn, Beringstr. 4–6, 53115 Bonn, Germany
[†] Department of Physical Chemistry, Faculty of Science and Technology, University of Debrecen, 4010 Debrecen, Hungary
[‡] Permission requests to reuse material from this chapter should be directed to the American Chemical Society.

In this work, the ability of the 1-ethyl-3-methylimidazolium L-alaninate ($[C_2C_1Im][L-ala]$) CIL to recognize and discriminate the enantiomers of butan-2-ol is investigated. While there have been attempts to use CILs for enantiomeric recognition and separation processes,[125–127,129,285] the separation of small enantiomers such as those of butan-2-ol remains challenging and often requires the addition of functional groups prior to separation.[286] To avoid the cost and waste of these additional synthetic steps, the development of new IL-based selectors for small chiral molecules is highly desirable. Therefore, the systems investigated herein serve as model systems to understand the fundamental working principles of the chiral recognition mechanism of butan-2-ol in $[C_2C_1Im][L-ala]$. A full reprint of this work[6] can be found in appendix F.

For the purpose of this work, AIMD simulations are investigated in which either one molecule of (*R*)- or (*S*)-butan-2-ol is dissolved in ten ion pairs of the IL. To improve the conformational sampling and to adequately explore the potential energy surface, the conformer replica simulations approach (*cf.* section 2.5) proposed in chapter 5 is followed by employing independent simulations, starting from each of the nine conformers of butan-2-ol. In total this results in 18 AIMD simulations, nine for (*R*)-butan-2-ol (termed as heterochiral system **R**) and nine for (*S*)-butan-2-ol (termed as homochiral system **S**) dissolved in the CIL. In addition, the gas and neat bulk phase simulations of (*R*)-butan-2-ol from chapter 5 are used for comparison.

In the gas and neat bulk phase, all nine conformers of (*R*)-butan-2-ol are found to be significantly populated with a preference for structures that feature a stretched carbon chain (see also chapter 5 and the reprint in appendix C). Note that the same conformational distribution can be expected for (*S*)-butan-2-ol in the gas and neat bulk phase, but with mirrored conformers. In the CIL, the populations of conformers with stretched carbon chains are significantly reduced, implying that mainly curled butan-2-ol conformers are present. This is also reflected by the average exposed surface area of butan-2-ol, which is reduced from 174 Å^2 in the neat bulk phase to 164 Å^2 in the systems **R** and **S**. Comparing the populations of each conformer in system **R** and its mirror image in system **S**, a pronounced dominance of one distinct conformer is observed for (*R*)- but not for (*S*)-butan-2-ol. This particular conformer features a population of 39 % in system **R** while its mirrored counterpart is populated by only 23 % in system **S**. This is a first indication of an enantiomeric discrimination of the two butan-2-ol enantiomers by the CIL, which is further underlined by an overall energetic stabilization of the heterochiral system **R** by $\Delta E = 18.8\,\mathrm{kJ\,mol^{-1}}$ compared to the homochiral system **S**. Although this energetic stabilization could be attributed to interactions between the chiral L-alaninate anion and the two butan-2-ol enantiomers, the role of the cation may still be important.

Investigations of the intermolecular interactions show that the hydrogen bonds between the carboxylate group of the anions and the hydroxyl group of butan-2-ol barely alter between the two enantiomers. However, the amino group of the L-alaninate anion acts as donor for both butan-2-ol enantiomers, but on rare occasions also as acceptor for (*S*)-butan-2-ol. This is an indication of discriminative interactions and the ability of (*S*)-butan-2-ol to interact with the anion through two different hydrogen bonds results in a disordered arrangement of the anion around the (*S*)-enantiomer. In contrast, the anion is spatially confined to one side of the (*R*)-enantiomer, leaving room for the cations to adapt to the structure of the alcohol.

To understand the role of the cation in the chiral recognition of butan-2-ol, it is important to remember that 1-ethyl-3-methylimidazolium has two mirrored conformers whose symmetric conformational distribution can be distorted in a chiral environment, leading to an increased occurrence of one conformer (*cf.* section 1.3). This asymmetrization causes the cation to become chiral,[130,132] and consequently can have a significant influence on the chiral recognition of butan-2-ol. By investigating the conformational distribution of the cation around the anion and the two butan-2-ol enantiomers, it is observed that L-alaninate and (*R*)-butan-2-ol induce the same conformation in the cation while L-alaninate and (*S*)-butan-2-ol induce mirrored conformations. The anion of the CIL thus creates an environment in which (*R*)-butan-2-ol fits well, while (*S*)-butan-2-ol competes with the anion to induce opposite conformations in the cation. This chiral induction (or chirality transfer) effect causes an energetic stabilization of system **R** and illustrates the important role that achiral or transiently chiral compounds can play in enantiomeric recognition processes.

In conclusion, the chiral discrimination of butan-2-ol in the CIL 1-ethyl-3-methylimidazolium L-alaninate results not only from the interactions between the two chiral compounds (i.e., anion–alcohol interactions) but also from the interplay between the chiral alcohol and the cation. The knowledge gained about the preferred interactions of the butan-2-ol enantiomers with different conformations of the 1-ethyl-3-methylimidazolium cation opens doors for the design of new IL-based chiral selectors in which the cation is modified to resemble the structures imprinted by the respective solute molecules.

9. Chemistry Dissolved in Ionic Liquids. A Theoretical Perspective

Barbara Kirchner,[*] Jan Blasius,[*] Vahideh Alizadeh,[*] Andreas Gansäuer,[†] and Oldamur Hollóczki[‡*]

Received: 19 October 2021, Published online: 17 January 2022.

Reprinted (adapted) in appendix G with permission[§] from

B. Kirchner, J. Blasius, V. Alizadeh, A. Gansäuer, and O. Hollóczki, *J. Phys. Chem. B* **2022**, *126*, 766–777.

doi:10.1021/acs.jpcb.1c09092.

For this article a Supporting Information is available free of charge at:
https://pubs.acs.org/doi/abs/10.1021/acs.jpcb.1c09092.

Contributions to the manuscript

- Performance of all calculations presented in chapter "Chirality: Complications from Asymmetry"
- Interpretation of the results presented in chapter "Chirality: Complications from Asymmetry"
- Writing of chapter "Chirality: Complications from Asymmetry"
- Co-writing of the other chapters

[*] Mulliken Center for Theoretical Chemistry, Clausius Institute for Physical and Theoretical Chemistry, University of Bonn, Beringstr. 4–6, 53115 Bonn, Germany
[†] Kekulé-Institut für Organische Chemie und Biochemie, Gerhard-Domagk-Str. 1, University of Bonn, 53121 Bonn, Germany
[‡] Department of Physical Chemistry, Faculty of Science and Technology, University of Debrecen, 4010 Debrecen, Hungary
[§] Permission requests to reuse material from this chapter should be directed to the American Chemical Society.

This perspective highlights the recent methodological advances that have been achieved in the theoretical modeling of ILs and points out difficulties that still need to be overcome. For this purpose, three examples of advanced IL research are discussed, 1) reactions 2) chirality transfer, and 3) radicals in ILs. These topics are chosen as examples because they all require the simultaneous use of realistic models and accurate methods. "Realistic models" in this context means, for example, that the simulation time as well as the system size and complexity have to be carefully considered, while "accurate methods" are needed for the description of the electronic structure. Only a careful consideration of both aspects will allow IL research to be predictive and follow the latest research trends. This work reviews methodological advances for the selected examples and presents additional case studies that are the focus of this summary. A full reprint of this work[7] can be found in appendix G.

Starting with the first example, reactions in ILs, it is important to recall that the electronic structure usually has to be treated explicitly in order to get a proper description of bond breaking and formation. Consequently, when using MD simulations, classical simulations based on force fields are not suitable for the description of reactivity. On the other hand, reactions can only be observed in AIMD simulations if the reaction barrier is lower than about $k_\mathrm{B}T$. If this requirement is met, spontaneous reactions can occur in AIMD simulations; otherwise, free energy methods need to be used. The case studies presented herein deal with Grotthuss diffusion in ILs, which was first observed by AIMD simulations for mixtures of 1-ethyl-3-methylimidazolium chloride ($[C_2C_1Im][Cl]$) with aluminum trichloride.[92] In these mixtures, chloride anions can be transferred from anionic to neutral aluminum clusters, which explains the excellent performance of these mixtures in electrochemical applications.[92] A similar mechanism was observed for mixtures of 1-butyl-3-methylimidazolium chloride ($[C_4C_1Im][Cl]$) with phosphorus trichloride (PCl_3) by AIMD simulations.[287] While the presented case studies show that the investigation of Grotthuss diffusion in ILs is feasible with AIMD simulations, the obvious drawbacks of these simulations are the short simulation time and the small system size. This limits the sampling quality and often restricts the application to small molecules. Promising approaches to circumvent these issues are further reviewed in appendix G and include, for example, the use of tight-binding semiempirical methods to describe the electronic structure.

The main challenge for the second topic, chirality transfer in ILs, is the correct description of intermolecular interactions and their dynamics since this phenomenon is often associated with the formation of molecular complexes involving many particles. Therefore, the use of AIMD or polarizable force field[96,288] simulations is generally recommended, since classical force fields are usually fitted to macroscopic properties of known substances and do not necessarily provide a good description of the intermolecular interactions. The advantage of AIMD simulations is that the explicit treatment of the electronic structure allows the calculation of VCD spectra (*cf.* section 2.4), which can help to detect and understand chirality transfer in more detail. On the other hand, the limitation to small system sizes allows only the study of local phenomena. The case study presented herein is based on chapter 8, where it was shown that (*R*)-butan-2-ol and L-alaninate induce the same conformation in the 1-ethyl-3-methylimidazolium cation, while (*S*)-butan-2-ol induces a mirrored conformation.[6] This effect was observed by structural analyses

of AIMD simulations where (*R*)- or (*S*)-butan-2-ol was dissolved in 1-ethyl-3-methylimidazolium L-alaninate ($[C_2C_1Im][L-ala]$). To support the conclusions of chapter 8, VCD spectra of the respective systems are reported here, showing mirrored VCD spectra for the cation depending on whether (*R*)- or (*S*)-butan-2-ol is dissolved in the IL. This clearly demonstrates the occurrence of chirality transfer and the preference of the cation to adopt opposite conformations depending on the chirality of butan-2-ol.

Examples from the third topic, radicals in ILs, typically provide cases with a difficult electronic structure that must be treated accurately. Consequently, the choice of the underlying quantum chemical method is of paramount importance. However, if AIMD simulations are desired, the use of accurate but computationally expensive methods (e.g., hybrid functionals) is typically not feasible, but usually necessary. To demonstrate the difficulty of functional selection, reaction energies are calculated for four artificial gas phase exchange reactions of the chloride ligand of a titanocene complex[289,290] with the anion of an IL. For these benchmark tests, the PBE0,[291] PBE,[291] revPBE,[292] BLYP,[68,293] B3LYP,[68,293] and TPSS[165] functionals and the DZVP-[294] and TZVP-MOLOPT-SR-GTH[294,295] basis sets are chosen. Furthermore, the auxiliary density matrix method (ADMM)[296] is tested for the hybrid functionals. It is observed that the computational time increases by a factor of about 40 when going from GGA to hybrid functionals, a comparison between revPBE and PBE0 even yields a factor of 200. Although the use of the ADMM approximation reduces this to a factor of 5, the fact that this increased computational cost has to be paid in each step of an AIMD simulation drastically limits the use of hybrid functionals for this purpose. This shows that the theoretical treatment of radicals in ILs by MD simulations is still far from being straightforward and that further methodological development will be necessary in the future.

10. Selective Chirality Transfer to the Bis(trifluoromethylsulfonyl)imide Anion of an Ionic Liquid

Jan Blasius* and Barbara Kirchner*

Received: 19 April 2023, Published online: 21 June 2023.

Reprinted (adapted) in appendix H with permission† from

J. Blasius and B. Kirchner, *Chem. Eur. J.* **2023**, e202301239.

doi:10.1002/chem.202301239.

For this article a Supporting Information is available free of charge at:
https://chemistry-europe.onlinelibrary.wiley.com/doi/abs/10.1002/chem.202301239.

Contributions to the manuscript

- Development of the concept
- Performance of all calculations
- Interpretation of the results
- Writing of the manuscript

*Mulliken Center for Theoretical Chemistry, Clausius Institute for Physical and Theoretical Chemistry, University of Bonn, Beringstr. 4–6, 53115 Bonn, Germany

In chapters 7 to 9 it has been extensively shown that the transiently chiral 1-ethyl-3-methylimidazolium cation is prone to symmetry breaking in a chiral environment, which can have significant effects on chiral recognition mechanisms.[5–7] However, since anions usually have a much greater influence on the properties of ILs than cations,[105–107,297–299] chirality transfer to anions may have an even greater influence on such processes. Therefore, this work explores the possibility of chiral induction in IL anions by studying the dissolution of the chiral solute (*R*)-1,2-propylene oxide ((*R*)-PO) in the 1-ethyl-3-methylimidazolium bis(trifluoromethylsulfonyl)imide ($[C_2C_1Im][NTf_2]$) IL. The choice of this particular solute–solvent combination has mainly two reasons. First, due to its very restricted conformational space, (*R*)-PO does not suffer from the sampling problems encountered for (*R*)-butan-2-ol[3] (*cf.* chapter 5), and second, the conformational landscape of the $[NTf_2]^-$ anion allows for a symmetry breaking.[300] For the purpose of this study, three AIMD simulations with the following compositions are investigated: 1) 18 ion pairs of $[C_2C_1Im][NTf_2]$ (labeled as **IL**), 2) 1 (*R*)-PO molecule dissolved in 18 ion pairs of $[C_2C_1Im][NTf_2]$ (labeled as **(*R*)-PO@IL**), and 3) 1 isolated (*R*)-PO molecule (labeled as **(*R*)-PO$_{iso}$**). A full reprint of this work can be found in appendix H.

To determine whether chirality transfer to the IL takes place at all, VCD spectra are calculated for the simulations **(*R*)-PO@IL** and **(*R*)-PO$_{iso}$** using a radical Voronoi tessellation[144] and the Thomas–Kirchner[47] approach, see section 2.4 for methodological details. When comparing the spectra of the (*R*)-PO molecule in its isolated and dissolved states, certain notable peak shifts and changes in peak signs are observed, indicating the presence of strong solute–solvent interactions. Furthermore, the cation exhibits essentially negligible VCD activity, whereas the anion shows significant contributions to the global VCD spectrum of **(*R*)-PO@IL**. This is in contrast to the observations from chapters 7 to 9 and indicates that there is a selective chirality transfer from (*R*)-PO to $[NTf_2]^-$ while the cation remains unaffected.

The reason for this selective chirality transfer lies in the intermolecular interactions between the chiral solute and the ions of the IL. According to the literature, (*R*)-PO transfers its chiral information at the anti-side, precisely at the position of the H* atom, which is connected to the chiral carbon center C*.[301] While the anion approaches this particular H* atom with its oxygen and fluorine atoms to form hydrogen bond-like contacts, the cation approaches (*R*)-PO on the syn-side (i.e., the side of the methyl group), where no chirality can be transferred. Due to this particular molecular arrangement, chirality transfer occurs selectively to the anion, causing a symmetry breaking in its conformational distribution.

To understand how this symmetry breaking occurs, one must be aware of the conformational flexibility of $[NTf_2]^-$. While most of the literature simplifies the conformational landscape of the anion by referring only to *cis* and *trans* conformations, it is actually more complex. In particular, there are a total of four $[NTf_2]^-$ conformations, including two *cis* and two *trans* conformers that are mirror images of each other, which means they are enantiomeric conformers.[300,302] In the neat IL, the abundance of these enantiomeric conformers is equal, resulting in an overall achiral nature of the anion. However, when (*R*)-PO is dissolved in $[C_2C_1Im][NTf_2]$, it is observed that $[NTf_2]^-$ adopts a specific *trans* conformation **t1** in close proximity to (*R*)-PO. This leads to a decreased population of the mirrored *trans* conformer **t2** and the excess population of **t1** causes

optical activity of the anion.

In summary, it has been shown that (*R*)-PO can transfer its chiral information selectively to the anion of the $[C_2C_1Im][NTf_2]$ IL while leaving the cation unaffected. Combined with the results of the work presented in chapters 7 to 9, this shows that the type of IL must be carefully considered since ions that allow a symmetry breaking in their conformational distribution can have significant effects on chiral processes. Furthermore, the results show that a selective chirality transfer can be achieved by the right combination of IL ions and chiral inducer molecules, which opens doors for the design of new chiral selectors and molecular recognition processes.

11. Summary and Outlook

This thesis dealt with the theoretical calculation of IR and VCD spectra in the gas and liquid phase, with a particular emphasis on modeling environmental and solvent effects in the latter. To this end, two main objectives had to be addressed:

1. The development of a new method for the calculation of liquid phase IR and VCD spectra, that is capable of modeling effects of intermolecular interactions and the concentration dependence of vibrational spectra at low computational cost. Since most VCD measurements are performed on solvated systems and require reference calculations for comparison, such a method is highly desirable. Its implementation would greatly facilitate routine VCD applications and provide important support to researchers in this field.

2. The investigation of chirality transfer in ILs and its effects on molecular recognition mechanisms. Studying these effects can provide valuable insights into the design of new IL-based chiral separators, facilitating the development of efficient strategies for detecting and differentiating enantiomers in liquid–liquid extraction or separation processes.

While addressing these two main objectives, drawbacks and problems of other methods for calculating vibrational spectra were identified and, if appropriate, possible solutions and alternative approaches were proposed.

The first goal of the thesis was achieved by introducing the cluster-weighting approach in chapters 3 to 6, which determines liquid phase IR and VCD spectra as a property of an ensemble of quantum chemically calculated clusters. Using QCE calculations,[139–141] weights are assigned to these clusters, and the vibrational spectra of the ensemble are then determined as a weighted average of the individual cluster spectra. This approach explicitly considers intermolecular interactions and, in contrast to classical Boltzmann weighting, allows the simultaneous weighting of differently sized clusters.[2,13]

Since QCE calculations rely on experimental input data, typically density and boiling temperature, an initial study was conducted in chapter 3 to investigate how uncertainties in these data affect the outcome of QCE calculations. Therefore, vaporization enthalpies, vaporization entropies, and cluster populations were calculated for seven organic liquids, and the influence of changes in the input data on these quantities was studied. Considering that experimental measurements typically exhibit inaccuracies of $<1\,\mathrm{K}$ and $\leq 0.0001\,\mathrm{g\,cm^{-3}}$, it was demonstrated that these uncertainties do not significantly affect the calculated vaporization quantities or cluster populations. To quantify the uncertainty resulting from experimental inaccuracies, two uncertainty propagation methods were used, namely the Monte Carlo method and the Gauss–Hermite

quadrature. By analyzing the vaporization enthalpy of (*R*)-butan-2-ol as an example, the uncertainty introduced by experimental inaccuracies was determined to be $30.95 \cdot 10^{-3}\,\mathrm{kJ\,mol^{-1}}$, which is negligible from a chemical point of view.

After ensuring that the QCE method yields robust cluster populations, the cluster-weighting approach for vibrational spectra was introduced in chapter 4 and applied to calculate bulk phase IR and VCD spectra of (*R*)-butan-2-ol. In a first step, the sensitivity of Boltzmann and cluster weights with respect to the underlying quantum chemical level of theory was tested, and it was shown that cluster weights are less sensitive to the choice of the basis set. To clarify which types of clusters are necessary to model the liquid phase IR and VCD spectra of (*R*)-butan-2-ol, different cluster sets were systematically tested and the calculated spectra were compared with experimental reference data measured for liquid (*R*)-butan-2-ol. Based on these tests, it was shown that ring-like molecular arrangements are the dominant structural motifs and that it is not necessary to include a variety of conformers to model the main features of the liquid phase vibrational spectra. Furthermore, the systematic exclusion of low-populated clusters did not change the results, and the best agreement with the experiment was obtained for cluster sets consisting only of global minimum structures for any given cluster size. This allows the design of a workflow based only on global minimum structures, thereby reducing the overall computational effort of the cluster-weighting approach.

To benchmark the performance of cluster-weighting, additional tests were conducted in chapter 5 to further investigate the influence of the selected functional and basis set on the cluster weights and vibrational spectra. The results showed that the cluster weights can be highly sensitive to the chosen level of theory, but the influence of functional and basis set on the resulting vibrational spectra is less significant, and good agreement with the experiment was observed for almost all functional/basis set combinations tested. The best overlap with the experiment was achieved for combinations of the BP86 and B3LYP functionals with the def2-TZVP basis set, and to further improve the agreement, empirical scaling factors were proposed. Moreover, it was observed that cluster sizes up to hexamers are sufficient to adequately capture the characteristics of the bulk phase IR and VCD spectra of (*R*)-butan-2-ol.

As a next step, the cluster-weighting method was compared with the AIMD approach, where IR and VCD spectra are calculated from correlation functions of the electric and magnetic dipole moments computed along an AIMD simulation.[60,263,264,267,268] The dipole moments can be obtained by many approaches, but when they are calculated using a radical Voronoi tessellation[144] and the Thomas–Kirchner approach,[47] the resulting IR and VCD spectra were found to be superior to those obtained by cluster-weighting. However, this superiority is accompanied by a tremendous increase in computational cost, as the performance of AIMD simulations, and especially the subsequent calculation of the magnetic dipole moments, is computationally expensive. Therefore, the use of the AIMD approach in combination with dipole moments from a radical Voronoi tessellation and the Thomas–Kirchner approach is recommended when high-quality vibrational spectra are required, while the cluster-weighting approach provides a computationally efficient alternative to obtain qualitatively reasonable vibrational spectra.

During the application of the AIMD approach in chapter 5 to calculate IR and VCD spectra

for (*R*)-butan-2-ol, the potential problem of insufficient conformer sampling was encountered. In particular, it was observed that certain rotational barriers could not be overcome in gas phase simulations of isolated molecules, and as a result, the simulations tended to remain close to a local minimum structure. Accordingly, the calculated VCD spectra showed poor agreement with the experimental reference due to the insufficient sampling of the conformational space. To address this issue, the conformer replica simulation approach was proposed, which averages multiple independent simulations with different initial configurations to improve the sampling quality. The application of this approach to the calculation of gas phase IR and VCD spectra of (*R*)-butan-2-ol yielded excellent agreement with experimental reference spectra, validating its effectiveness.

In addition, an alternative approach for the calculation of dipole moments based on atomic partial charges and classical definitions was proposed and tested for the calculation of gas phase vibrational spectra. The atomic partial charges were calculated using the Mulliken, Löwdin, and Blöchl population analyses, and the resulting IR spectra were in good agreement with those obtained using a radical Voronoi tessellation of the electron density. For VCD, the agreement between the different approaches was found to be worse, although the VCD spectrum based on the Blöchl population analysis reproduced the main characteristics of the one calculated with a radical Voronoi tessellation and the Thomas–Kirchner approach. Here, there is clearly much room for further development and testing, especially for bulk phase simulations, but the presented approach may serve as a computationally efficient method for calculating dipoles and vibrational spectra from AIMD simulations.

In chapter 6, the cluster-weighting approach was extended to binary systems and applied for the calculation of mole fraction dependent IR and VCD spectra for mixtures of (*R*)-butan-2-ol and acetonitrile. The great advantage of cluster-weighting for this application is that every possible composition of a mixture can be calculated with the same cluster set, whereas in the case of the AIMD approach, individual simulations have to be performed for each desired composition. It was shown that the calculated IR spectra are in good agreement with experimentally measured data and that mole fraction dependent changes in the spectra, such as peak shifts, can be accurately modeled. Although the calculated VCD spectra could not be fully validated due to a lack of experimental data, their concentration dependence seems reasonable considering that acetonitrile is achiral and therefore should not contribute to the VCD activity of the mixtures.

The second goal of the thesis was addressed in chapters 7 to 10 by performing and analyzing AIMD simulations of chiral solutes dissolved in ILs. In chapter 7 the dissolution of different D-glucose isomers (α, β, and open-chain) in 1-ethyl-3-methylimidazolium acetate and the effects of water addition to these solutions were investigated. First, the microscopic structure of these mixtures and the influence of intermolecular interactions on the IR and VCD spectra of the systems were studied in detail. In particular, it was observed that the addition of water weakens the cation–anion interactions, resulting in observable peak shifts in the calculated IR spectra. In addition, the transiently chiral 1-ethyl-3-methylimidazolium cation was found to exhibit significant VCD activity, which is a clear indication of chirality transfer from the chiral D-glucose units to the cation. Studying the origin and detailed mechanism behind this chirality transfer

will be the subject of future research.

Furthermore, the onset of possible reactions was investigated, since IL/water mixtures show remarkable characteristics for the degradation of cellulose into glucose units. It was found that the anomeric conversion is energetically feasible and less demanding in the moist IL. However, the addition of water also resulted in predominantly linear arrangements of the open-chain form, thereby impeding a ring closure reaction by an intramolecular nucleophilic attack. The onset of a ring closure reaction in the dry IL was found to be facilitated by hydrogen bond abstraction of the anion and various interactions of the cation, increasing the nucleophilicity of the reacting oxygen atom and the electrophilicity of the carbonyl group. In addition, carbene-like reactions of the IL cation with the ether bonds of α- and β-D-glucose or with the carbonyl group of the open form were observed.

Chapter 8 dealt with the enantiomeric recognition of butan-2-ol by the CIL 1-ethyl-3-methylimidazolium L-alaninate and the importance of chirality transfer in this process. The dissolution of (*R*)-butan-2-ol in the CIL was found to be energetically more favorable by 18.8 kJ mol^{-1} than the dissolution of (*S*)-butan-2-ol, indicating chiral discrimination. In addition to discriminating hydrogen bond interactions between the chiral anion and both butan-2-ol enantiomers, chiral induction in the transiently chiral cation was found to be involved in the enantiomeric recognition mechanism. In particular, it was observed that L-alaninate and (*R*)-butan-2-ol induce the same conformation in the cation, whereas L-alaninate and (*S*)-butan-2-ol induce mirrored conformations (*cf.* also section 1.3). Accordingly, the CIL itself provides an environment in which the (*R*)-enantiomer of butan-2-ol fits well, while the (*S*)-enantiomer competes with the chiral anion to induce mirrored conformations in the cation.

In chapter 9, the challenges associated with modeling the electronic structure and intermolecular interactions in ILs were discussed, as well as the importance of using accurate methods and realistic models for this purpose. Therefore, extensive literature reviews and case studies based on AIMD simulations were presented for the three examples of reactions, chirality, and radicals in ILs. For reactions and radicals in ILs, the importance of an accurate description of the electronic structure and the drawbacks of short simulation times, small system sizes, and limitations in the choice of functional and basis sets were emphasized. For chirality in ILs, VCD spectra were presented for the systems studied in chapter 8 to further investigate the chirality transfer from L-alaninate and the butan-2-ol enantiomers to 1-ethyl-3-methylimidazolium. The calculated spectra were found to support the conclusions of chapter 8, showing mirrored VCD spectra for 1-ethyl-3-methylimidazolium depending on whether (*R*)- or (*S*)-butan-2-ol is dissolved in the CIL. Furthermore, the importance of an accurate description of the intermolecular interactions was emphasized for the observation of chirality transfer phenomena, which usually requires the use of either AIMD or polarizable force field simulations.

As a last step, the possibility of a selective chirality transfer from the chiral solute (*R*)-1,2-propylene oxide to the ions of the 1-ethyl-3-methylimidazolium bis(trifluoromethylsulfonyl)imide IL was investigated in chapter 10. In contrast to the systems investigated in chapter 8, where the IL was composed of a transiently chiral cation and a permanently chiral anion, 1-ethyl-3-methylimidazolium bis(trifluoromethylsulfonyl)imide is composed of two transiently chiral ions,

which are both prone to symmetry breaking. From conformational analysis and calculated VCD spectra, a symmetry breaking in the conformational distribution of the anion was observed, resulting in a pronounced VCD activity. This symmetry breaking was found to manifest as an excess population of one of two mirrored *trans* conformers. In contrast, the VCD spectrum and conformational distribution of the cation were found to be unaffected by the chiral solute, demonstrating the occurrence of a selective chirality transfer from (*R*)-1,2-propylene oxide to the anion of the IL.

In conclusion, both objectives of the thesis were successfully addressed through the research projects presented. Nevertheless, it is important to acknowledge that there is still a lot of room for future research and further development and refinement of the methods introduced in this thesis. First, it will be necessary to apply the cluster-weighting method for vibrational spectra to other neat substances and binary mixtures to validate the conclusions drawn and the workflows proposed in chapters 4 to 6. This is the subject of current research projects where cluster-weighting is used to calculate bulk phase IR and VCD spectra for neat nicotine and phenyl alcohols, and their mixtures with conventional solvents such as dimethyl sulfoxide and acetonitrile. In the context of binary cluster-weighting, it will be particularly interesting to investigate mixtures of two chiral compounds (e.g., (*R*)-1,2-propylene oxide with (*R*)-butan-2-ol) to further validate the approach for mole fraction dependent VCD spectra. This aspect is also an integral part of ongoing research.

The insights gained from chapters 7 to 10 can be rationalized to design new IL-based chiral selectors. To further elucidate the importance of the cation in the recognition of butan-2-ol, it will be interesting to use CILs with cations whose side chains are modified to resemble the structures imprinted by the butan-2-ol enantiomers. Moreover, other amino acid-based CILs and their ability to recognize butan-2-ol and other small molecules should be investigated. Here, there may be great potential to impose specific structures on 1-ethyl-3-methylimidazolium if different amino acids induce different conformational distributions in the cation. In such a case, the geometry of 1-ethyl-3-methylimidazolium could be adjusted for specific applications by choosing the appropriate amino acid anion.

Bibliography

[1] J. Blasius, P. Zaby, J. Dölz, B. Kirchner, *J. Chem. Phys.* **2022**, *157*, 014505.

[2] J. Blasius, B. Kirchner, *J. Phys. Chem. B* **2020**, *124*, 7272–7283.

[3] B. Kirchner, J. Blasius, L. Esser, W. Reckien, *Adv. Theory Simul.* **2021**, *4*, 2000223.

[4] J. Blasius, K. Drysch, F. H. Pilz, T. Frömbgen, P. Kielb, B. Kirchner, *submitted for publication.*

[5] J. Blasius, R. Elfgen, O. Hollóczki, B. Kirchner, *Phys. Chem. Chem. Phys.* **2020**, *22*, 10726–10737.

[6] J. Blasius, P. Zaby, O. Hollóczki, B. Kirchner, *J. Org. Chem.* **2021**, *87*, 1867–1873.

[7] B. Kirchner, J. Blasius, V. Alizadeh, A. Gansäuer, O. Hollóczki, *J. Phys. Chem. B* **2022**, *126*, 766–777.

[8] J. Blasius, B. Kirchner, *Chem. Eur. J* **2023**, e202301239.

[9] J. Ingenmey, J. Blasius, G. Marchelli, A. Riegel, B. Kirchner, *J. Chem. Eng. Data* **2019**, *64*, 255–261.

[10] J. Blasius, J. Ingenmey, E. Perlt, M. von Domaros, O. Hollóczki, B. Kirchner, *Angew. Chem. Int. Ed.* **2019**, *58*, 3212–3216.

[11] J. Blasius, J. Ingenmey, E. Perlt, M. von Domaros, O. Hollóczki, B. Kirchner, *Angew. Chem.* **2019**, *131*, 3245–3249.

[12] M. A. Grasser, T. Pietsch, J. Blasius, O. Hollóczki, E. Brunner, T. Doert, M. Ruck, *Chem. Eur. J.* **2022**, *28*, e202103770.

[13] S. Taherivardanjani, J. Blasius, M. Brehm, R. Dötzer, B. Kirchner, *J. Phys. Chem. A* **2022**, *126*, 7070–7083.

[14] H. Niemöller, J. Blasius, O. Hollóczki, B. Kirchner, *J. Mol. Liq.* **2022**, *367*, 120282.

[15] T. Frömbgen, J. Blasius, V. Alizadeh, A. Chaumont, M. Brehm, B. Kirchner, *J. Chem. Inf. Model.* **2022**, *62*, 5634–5644.

[16] T. Pietsch, J. Blasius, J. Richter, M. A. Grasser, O. Hollóczki, P. Wollmann, I. M. Weidinger, M. Ruck, E. Brunner, *Inorg. Chem.* **2023**, *62*, 1667–1678.

[17] P. Zaby, J. Blasius, A. K. Müller, S. P. Nolan, O. Hollóczki, *Chem. Eur. J* **2023**, *29*, e202300502.

[18] T. Stephens, R. Brynner, *Dark remedy: the impact of thalidomide and its revival as a vital medicine*, Basic Books, **2009**.

[19] G. Blaschke, H. Kraft, K. Fickentscher, F. Koehler, *Arzneim.-Forsch.* **1979**, *29*, 1640–1642.

[20] Announcement, *Chirality* **1992**, *4*, 338–340.

[21] *Development of New Stereoisomeric Drugs*, https://www.fda.gov/regulatory-information/search-fda-guidance-documents/development-new-stereoisomeric-drugs, Accessed: 2023-06-22.

[22] A. Williams, *Pestic. Sci.* **1996**, *46*, 3–9.

[23] P. Jeschke in *Agricultural Biocatalysis*, Jenny Stanford Publishing, **2022**, pp. 359–407.

[24] R. Noyori, *Angew. Chem. Int. Ed.* **2002**, *41*, 2008–2022.

[25] J. T. Mohr, M. R. Krout, B. M. Stoltz, *Nature* **2008**, *455*, 323–332.

[26] Z. G. Brill, M. L. Condakes, C. P. Ting, T. J. Maimone, *Chem. Rev.* **2017**, *117*, 11753–11795.

[27] H. Lorenz, A. Seidel-Morgenstern, *Angew. Chem. Int. Ed.* **2014**, *53*, 1218–1250.

[28] B. Schuur, B. J. Verkuijl, A. J. Minnaard, J. G. De Vries, H. J. Heeres, B. L. Feringa, *Org. Biomol. Chem.* **2011**, *9*, 36–51.

[29] X. Cui, Q. Ding, R.-N. Shan, C.-H. He, K.-J. Wu, *Chirality* **2019**, *31*, 457–467.

[30] C. A. Afonso, J. G. Crespo, *Angew. Chem. Int. Ed.* **2004**, *43*, 5293–5295.

[31] H. Flack, G. Bernardinelli, *Chirality* **2008**, *20*, 681–690.

[32] J. A. Dale, H. S. Mosher, *J. Am. Chem. Soc.* **1973**, *95*, 512–519.

[33] V. M. Marathias, G. J. Tawa, I. Goljer, A. C. Bach, *Chirality* **2007**, *19*, 741–750.

[34] Y. He, W. Bo, R. K. Dukor, L. A. Nafie, *Appl. Spectrosc.* **2011**, *65*, 699–723.

[35] S. Zhu, M. Sun, *Appl. Spectrosc. Rev.* **2021**, *56*, 553–587.

[36] L. A. Nafie, *Chirality* **2020**, *32*, 667–692.

[37] L. A. Nafie, *Annu. Rev. Phys. Chem.* **1997**, *48*, 357–386.

[38] L. A. Nafie, T. Keiderling, P. Stephens, *J. Am. Chem. Soc.* **1976**, *98*, 2715–2723.

[39] T. A. Keiderling, *Appl. Spectrosc. Rev.* **1981**, *17*, 189–226.

[40] P. Stephens, M. Lowe, *Annu. Rev. Phys. Chem.* **1985**, *36*, 213–241.

[41] G. Magyarfalvi, G. Tarczay, E. Vass, *Wiley Interdiscip. Rev. Comput. Mol. Sci.* **2011**, *1*, 403–425.

[42] L. A. Nafie, *J. Chem. Phys.* **1983**, *79*, 4950–4957.

[43] L. A. Nafie, T. B. Freedman, *J. Chem. Phys.* **1983**, *78*, 7108–7116.

[44] S. Jähnigen, A. Zehnacker, R. Vuilleumier, *J. Phys. Chem. Lett.* **2021**, *12*, 7213–7220.

[45] D. R. Galimberti, *J. Chem. Theory Comput.* **2022**, *18*, 6217–6230.

[46] F. Wang, P. L. Polavarapu, *J. Phys. Chem. A* **2000**, *104*, 10683–10687.

[47] M. Thomas, B. Kirchner, *J. Phys. Chem. Lett.* **2016**, *7*, 509–513.

[48] K. Le Barbu-Debus, A. Scherrer, A. Bouchet, D. Sebastiani, R. Vuilleumier, A. Zehnacker, *Physi. Chem. Chem. Phys.* **2018**, *20*, 14635–14646.

[49] L. Weirich, C. Merten, *Phys. Chem. Chem. Phys.* **2019**, *21*, 13494–13503.

[50] S. Jähnigen, D. Sebastiani, R. Vuilleumier, *Phys. Chem. Chem. Phys.* **2021**, *23*, 17232–17241.

[51] L. Barron, M. Bogaard, A. Buckingham, *J. Am. Chem. Soc.* **1973**, *95*, 603–605.

[52] L. D. Barron, J. Vrbancich, *Struct. Chem.* **2005**, 151–182.

[53] E. C. Hsu, G. Holzwarth, *J. Chem. Phys.* **1973**, *59*, 4678–4685.

[54] G. Holzwarth, E. C. Hsu, H. S. Mosher, T. R. Faulkner, A. Moscowitz, *J. Am. Chem. Soc.* **1974**, *96*, 251–252.

[55] W. Hug, S. Kint, G. F. Bailey, J. R. Scherer, *J. Am. Chem. Soc.* **1975**, *97*, 5589–5590.

[56] L. Nafie, J. Cheng, P. Stephens, *J. Am. Chem. Soc.* **1975**, *97*, 3842–3843.

[57] P. L. Polavarapu, S. T. Pickard, H. E. Smith, T. M. Black, L. D. Barron, L. Hecht, *Talanta* **1993**, *40*, 545–549.

[58] P. L. Polavarapu, E. Santoro, *Nat. Prod. Rep.* **2020**, *37*, 1661–1699.

[59] T. A. Keiderling, *Curr. Opin. Chem. Biol.* **2002**, *6*, 682–688.

[60] S. Yang, M. Cho, *J. Chem. Phys.* **2009**, *131*, 135102.

[61] M. A. Koenis, L. Visscher, W. J. Buma, V. P. Nicu, *J. Phys. Chem. B* **2020**, *124*, 1665–1677.

[62] P. K. Bose, P. L. Polavarapu, *Carbohydr. Res.* **1999**, *319*, 172–183.

[63] T. Taniguchi, I. Tone, K. Monde, *Chirality* **2008**, *20*, 446–453.

[64] L. Ashton, A. Hobro, G. L. Conn, M. Rouhi, E. W. Blanch, *J. Mol. Struct.* **2008**, *883*, 187–194.

[65] C. Guo, R. D. Shah, R. K. Dukor, X. Cao, T. B. Freedman, L. A. Nafie, *Anal. Chem.* **2004**, *76*, 6956–6966.

[66] C. Guo, R. D. Shah, R. K. Dukor, X. Cao, T. B. Freedman, L. A. Nafie, *Appl. Spectrosc.* **2005**, *59*, 1114–1124.

[67] C. Guo, R. D. Shah, J. Mills, R. K. Dukor, X. Cao, T. B. Freedman, L. A. Nafie, *Chirality* **2006**, *18*, 775–782.

[68] A. D. Becke, *Phys. Rev. A* **1988**, *38*, 3098–3100.

[69] J. P. Perdew, *Phys. Rev. B* **1986**, *33*, 8822–8824.

[70] F. Weigend, R. Ahlrichs, *Phys. Chem. Chem. Phys.* **2005**, *7*, 3297–3305.

[71] *TURBOMOLE V7.4 2017, a development of University of Karlsruhe and Forschungszentrum Karlsruhe GmbH, 1989-2007, TURBOMOLE GmbH, since 2007; available from http://www.turbomole.com.*

[72] K. Reiter, M. Kühn, F. Weigend, *J. Chem. Phys.* **2017**, *146*, 054102.

[73] R. Ahlrichs, M. Bär, M. Häser, H. Horn, C. Kölmel, *Chem. Phys. Lett.* **1989**, *162*, 165–169.

[74] S. G. Balasubramani, G. P. Chen, S. Coriani, M. Diedenhofen, M. S. Frank, Y. J. Franzke, F. Furche, R. Grotjahn, M. E. Harding, C. Hättig, et al., *J. Chem. Phys.* **2020**, *152*, 184107.

[75] R. W. Kawiecki, F. Devlin, P. Stephens, R. Amos, N. Handy, *Chem. Phys. Lett.* **1988**, *145*, 411–417.

[76] V. P. Nicu, S. R. Domingos, B. H. Strudwick, A. M. Brouwer, W. J. Buma, *Chem. Eur. J.* **2016**, *22*, 704–715.

[77] M. A. Koenis, Y. Xia, S. R. Domingos, L. Visscher, W. J. Buma, V. P. Nicu, *Chem. Sci.* **2019**, *10*, 7680–7689.

[78] S. Ma, S. Shen, H. Lee, N. Yee, C. Senanayake, L. A. Nafie, N. Grinberg, *Tetrahedron: Asymmetry* **2008**, *19*, 2111–2114.

[79] C. Merten, F. Li, K. Bravo-Rodriguez, E. Sanchez-Garcia, Y. Xu, W. Sander, *Phys. Chem. Chem. Phys.* **2014**, *16*, 5627–5633.

[80] C. Guo, R. D. Shah, R. K. Dukor, T. B. Freedman, X. Cao, L. A. Nafie, *Vib. Spectrosc.* **2006**, *42*, 254–272.

[81] K. R. Seddon, *J. Chem. Tech. Biotechnol.* **1997**, *68*, 351–356.

[82] T. Welton, *Chem. Rev.* **1999**, *99*, 2071–2083.

[83] J. D. Holbrey, K. Seddon, *Clean Prod. Proc.* **1999**, *1*, 223–236.

[84] T. Welton, *Biophys. Rev.* **2018**, *10*, 691–706.

[85] H. Weingärtner, *Angew. Chem. Int. Ed.* **2008**, *47*, 654–670.

[86] H. Weingärtner, *Angew. Chem.* **2008**, *120*, 664–682.

[87] W. M. Haynes, *CRC Handbook of Chemistry and Physics*, CRC press: Boca Raton, Florida, **2014**.

[88] P. Wasserscheid, T. Welton, *Ionic liquids in synthesis*, *Vol. 1*, Wiley Online Library, **2008**.

[89] N. V. Plechkova, K. R. Seddon, *Chem. Soc. Rev.* **2008**, *37*, 123–150.

[90] J. H. Davis, *Chem. Lett.* **2004**, *33*, 1072–1077.

[91] H. Li, T. Niemann, R. Ludwig, R. Atkin, *J. Phys. Chem. Lett.* **2020**, *11*, 3905–3910.

[92] B. Kirchner, A. P. Seitsonen, *Inorg. Chem.* **2007**, *46*, 2751–2754.

[93] E. J. Maginn, *J. Phys.: Condens. Matter* **2009**, *21*, 373101.

[94] B. Kirchner, *Ionic Liquids from Theoretical Investigations*, B. Kirchner (Ed.), Springer Berlin Heidelberg, Berlin, Heidelberg, **2010**, pp. 213–262.

[95] B. Kirchner, O. Hollóczki, J. N. Canongia Lopes, A. A. H. Pádua, *Wiley Interdiscip. Rev.: Comput. Mol. Sci.* **2015**, *5*, 202–214.

[96] D. Bedrov, J.-P. Piquemal, O. Borodin, A. D. MacKerell Jr, B. Roux, C. Schröder, *Chem. Rev.* **2019**, *119*, 7940–7995.

[97] S. Koutsoukos, F. Philippi, F. Malaret, T. Welton, *Chem. Sci.* **2021**, *12*, 6820–6843.

[98] M. Gruttadauria, S. Riela, C. Aprile, P. L. Meo, F. D'Anna, R. Noto, *Adv. Synth. Catal.* **2006**, *348*, 82–92.

[99] O. Acevedo, W. L. Jorgensen, J. D. Evanseck, *J. Chem. Theory Comput.* **2007**, *3*, 132–138.

[100] K. Bica, P. Gaertner, *Eur. J. Org. Chem.* **2008**, *2008*, 3235–3250.

[101] M. Vasiloiu, D. Rainer, P. Gaertner, C. Reichel, C. Schröder, K. Bica, *Catal. Today* **2013**, *200*, 80–86.

[102] M. Vasiloiu, P. Gaertner, R. Zirbs, K. Bica, *Eur. J. Org. Chem.* **2015**, *2015*, 2374–2381.

[103] A. Cognigni, P. Gaertner, R. Zirbs, H. Peterlik, K. Prochazka, C. Schröder, K. Bica, *Phys. Chem. Chem. Phys.* **2016**, *18*, 13375–13384.

[104] A. Gilbert, R. S. Haines, J. B. Harper, *Org. Biomol. Chem.* **2020**, *18*, 5442–5452.

[105] D. S. Firaha, O. Hollóczki, B. Kirchner, *Angew. Chem. Int. Ed.* **2015**, *54*, 7805–7809.

[106] J. F. Brennecke, B. E. Gurkan, *J. Phys. Chem. Lett.* **2010**, *1*, 3459–3464.

[107] W. Lin, M. Pan, Q. Xiao, H. Li, C. Wang, *J. Phys. Chem. Lett.* **2019**, *10*, 3346–3351.

[108] U. A. Rana, M. Forsyth, D. R. MacFarlane, J. M. Pringle, *Electrochim. Acta* **2012**, *84*, 213–222.

[109] D. R. MacFarlane, N. Tachikawa, M. Forsyth, J. M. Pringle, P. C. Howlett, G. D. Elliott, J. H. Davis, M. Watanabe, P. Simon, C. A. Angell, *Energy Environ. Sci.* **2014**, *7*, 232–250.

[110] M. Salanne, *Top. Curr. Chem.* **2017**, *375*, 63.

[111] L. Miao, Z. Song, D. Zhu, L. Li, L. Gan, M. Liu, *Energy Fuels* **2021**, *35*, 8443–8455.

[112] P. Ray, A. Balducci, B. Kirchner, *J. Phys. Chem. B* **2018**, *122*, 10535–10547.

[113] Y. Zhao, T. Bostrom, *Curr. Org. Chem.* **2015**, *19*, 556–566.

[114] H. Weber, T. Bredow, B. Kirchner, *J. Phys. Chem. C* **2015**, *119*, 15137–15149.

[115] S. Denizalti, A. K. Ali, Ç. Ela, M. Ekmekci, S. Erten-Ela, *Chem. Phys. Lett.* **2018**, *691*, 373–378.

[116] M. Vasiloiu, K. Bica, *Chiral Ionic Liquids in Separation Sciences*, H. Rodríguez (Ed.), Springer Berlin Heidelberg, **2016**, pp. 167–192.

[117] A. P. Abbott, G. Frisch, K. S. Ryder, *Annu. Rep. Prog. Chem., Sect. A* **2008**, *104*, 21–45.

[118] N. Papaiconomou, J.-M. Lee, J. Salminen, M. Von Stosch, J. M. Prausnitz, *Ind. Eng. Chem. Res.* **2008**, *47*, 5080–5086.

[119] O. G. Sas, I. Domínguez, B. González, Á. Domínguez, *J. Environ. Manage.* **2018**, *228*, 475–482.

[120] A. Zehnacker, M. A. Suhm, *Angew. Chem. Int. Ed.* **2008**, *47*, 6970–6992.

[121] M. Vasiloiu, I. Cervenka, P. Gaertner, M. Weil, C. Schröder, K. Bica, *Tetrahedron: Asymmetry* **2015**, *26*, 1069–1082.

[122] H. Ohno, K. Fukumoto, *Acc. Chem. Res.* **2007**, *40*, 1122–1129.

[123] X. Chen, X. Li, A. Hu, F. Wang, *Tetrahedron: Asymmetry* **2008**, *19*, 1–14.

[124] J. Ding, D. W. Armstrong, *Chirality* **2005**, *17*, 281–292.

[125] S. Yu, S. Lindeman, C. D. Tran, *J. Org. Chem.* **2008**, *73*, 2576–2591.

[126] T. Payagala, D. W. Armstrong, *Chirality* **2012**, *24*, 17–53.

[127] J. Ding, T. Welton, D. W. Armstrong, *Anal. Chem.* **2004**, *76*, 6819–6822.

[128] S. P. Ventura, F. A. e Silva, M. V. Quental, D. Mondal, M. G. Freire, J. A. Coutinho, *Chem. Rev.* **2017**, *117*, 6984–7052.

[129] T. E. Sintra, M. G. Gantman, S. P. Ventura, J. A. Coutinho, P. Wasserscheid, P. S. Schulz, *J. Mol. Liq.* **2019**, *283*, 410–416.

[130] P. Oulevey, S. Luber, B. Varnholt, T. Bürgi, *Angew. Chem. Int. Ed.* **2016**, *55*, 11787–11790.

[131] I. Dolamic, B. Varnholt, T. Bürgi, *Nat. Commun.* **2015**, *6*, 7117.

[132] P. Oulevey, S. Luber, B. Varnholt, T. Bürgi, *Angew. Chem.* **2016**, *128*, 11962–11966.

[133] J. P. I. Hearn, R. V. Cobley, B. J. Howard, *J. Chem. Phys.* **2005**, *123*.

[134] P. S. Schulz, N. Müller, A. Bösmann, P. Wasserscheid, *Angew. Chem. Int. Ed.* **2007**, *46*, 1293–1295.

[135] K. Schneiders, A. Bösmann, P. S. Schulz, P. Wasserscheid, *Adv. Synth. Catal.* **2009**, *351*, 432–440.

[136] H. J. r. Bestmann, D. Sandmeier, *Angew. Chem. Int. Ed.* **1975**, *14*, 634–634.

[137] M. J. Earle, P. B. McCormac, K. R. Seddon, *Green Chem.* **1999**, *1*, 23–25.

[138] R. Gausepohl, P. Buskens, J. Kleinen, A. Bruckmann, C. W. Lehmann, J. Klankermayer, W. Leitner, *Angew. Chem. Int. Ed.* **2006**, *45*, 3689–3692.

[139] F. Weinhold, *J. Chem. Phys.* **1998**, *109*, 367–372.

[140] B. Kirchner, *J. Chem. Phys.* **2005**, *123*, 204116.

[141] M. Brüssel, E. Perlt, S. B. Lehmann, M. von Domaros, B. Kirchner, *J. Chem. Phys.* **2011**, *135*, 194113.

[142] J. Stoer, R. Bulirsch, *Introduction to Numerical Analysis*, Springer, New York, **1993**.

[143] R. E. Caflisch, *Acta Numer.* **1998**, *7*, 1–49.

[144] M. Thomas, M. Brehm, B. Kirchner, *Phys. Chem. Chem. Phys.* **2015**, *17*, 3207–3213.

[145] E. Schrödinger, *Phys. Rev.* **1926**, *28*, 1049.

[146] A. Szabo, N. S. Ostlund, *Modern quantum chemistry: introduction to advanced electronic structure theory*, Courier Corporation, **2012**.

[147] M. Born, R. Oppenheimer, *Ann. Phys.* **1927**, *389*, 457–484.

[148] P. J. Mohr, B. N. Taylor, D. B. Newell, *J. Phys. Chem. Ref. Data* **2012**, *41*.

[149] I. Ekeland, *J. Math. Anal. and Appl.* **1974**, *47*, 324–353.

[150] D. R. Hartree, *Math. Proc. Cambridge* **1928**, *24*, 89–110.

[151] V. Fock, *Z. Physik* **1930**, *61*, 126–148.

[152] W. Pauli, *Phys. Rev.* **1940**, *58*, 716.

[153] E. Wigner, *Phys. Rev.* **1934**, *46*, 1002.

[154] P.-O. Löwdin, *Phys. Rev.* **1955**, *97*, 1509.

[155] R. J. Bartlett, *Annu. Rev. Phys. Chem.* **1981**, *32*, 359–401.

[156] R. J. Bartlett, M. Musiał, *Rev. Mod. Phys.* **2007**, *79*, 291.

[157] C. Møller, M. Plesset, *Phys. Rev.* **1934**, *46*, 618.

[158] P. Hohenberg, W. Kohn, *Phys. Rev.* **1964**, *136*, B864.

[159] W. Kohn, L. J. Sham, *Phys. Rev.* **1965**, *140*, A1133.

[160] W. Koch, M. C. Holthausen, *A Chemists Guide to Density Functional Theory*, Wiley, **2001**.

[161] E. Engel, R. Dreizler, *Density Functional Theory*, Springer, **2011**.

[162] J. P. Perdew, K. Schmidt, *AIP Conf. Proc.* **2001**, *577*, 1–20.

[163] P. Dirac, *Math. Proc. Camb.* **1930**, *26*, 376–385.

[164] J. C. Slater, *Phys. Rev.* **1951**, *81*, 385.

[165] J. Tao, J. P. Perdew, V. N. Staroverov, G. E. Scuseria, *Phys. Rev. Lett.* **2003**, *91*, 146401.

[166] A. D. Becke, *J. Chem. Phys.* **1996**, *104*, 1040–1046.

[167] S. Grimme, *J. Chem. Phys.* **2006**, *124*, 034108.

[168] S. Grimme, *J. Comput. Chem.* **2004**, *25*, 1463–1473.

[169] S. Grimme, *J. Comput. Chem.* **2006**, *27*, 1787–1799.

[170] S. Grimme, J. Antony, S. Ehrlich, H. Krieg, *J. Chem. Phys.* **2010**, *132*, 154104.

[171] S. Grimme, S. Ehrlich, L. Goerigk, *J. Comput. Chem.* **2011**, *32*, 1456–1465.

[172] O. A. Von Lilienfeld, I. Tavernelli, U. Rothlisberger, D. Sebastiani, *Phys. Rev. Lett.* **2004**, *93*, 153004.

[173] Y. Sun, Y.-H. Kim, K. Lee, S. Zhang, *J. Chem. Phys.* **2008**, *129*, 154102.

[174] D. C. Langreth, M. Dion, H. Rydberg, E. Schröder, P. Hyldgaard, B. I. Lundqvist, *Int. J. Quantum Chem.* **2005**, *101*, 599–610.

[175] T. Sato, T. Tsuneda, K. Hirao, *Mol. Phys.* **2005**, *103*, 1151–1164.

[176] B. Kirchner, C. Spickermann, S. B. Lehmann, E. Perlt, J. Langner, M. von Domaros, P. Reuther, F. Uhlig, M. Kohagen, M. Brüssel, *Comput. Phys. Commun.* **2011**, *182*, 1428–1446.

[177] M. von Domaros, E. Perlt, J. Ingenmey, G. Marchelli, B. Kirchner, *SoftwareX* **2018**, *7*, 356–359.

[178] F. Weinhold, *J. Chem. Phys.* **1998**, *109*, 373–384.

[179] R. Ludwig, F. Weinhold, *J. Chem. Phys.* **1999**, *110*, 508–515.

[180] R. Ludwig, F. Weinhold, *Phys. Chem. Chem. Phys.* **2000**, *2*, 1613–1619.

[181] P. Borowski, J. Jaroniec, T. Janowski, K. Woliński, *Mol. Phys.* **2003**, *101*, 1413–1421.

[182] R. Ludwig, *ChemPhysChem* **2007**, *8*, 938–943.

[183] C. Spickermann, S. B. Lehmann, B. Kirchner, *J. Chem. Phys.* **2008**, *128*, 244506.

[184] A. Lenz, L. Ojamäe, *J. Chem. Phys.* **2009**, *131*, 134302.

[185] S. Lehmann, C. Spickermann, B. Kirchner, *J. Chem. Theory Comput.* **2009**, *5*, 1640–1649.

[186] S. Lehmann, C. Spickermann, B. Kirchner, *J. Chem. Theory Comput.* **2009**, *5*, 1650–1656.

[187] F. Weinhold, *J. Phys. Chem. B* **2014**, *118*, 7792–7798.

[188] E. Perlt, M. von Domaros, B. Kirchner, R. Ludwig, F. Weinhold, *Sci. Rep.* **2017**, *7*, 10244.

[189] B. Kirchner, J. Ingenmey, M. von Domaros, E. Perlt, *Molecules* **2022**, *27*, 1286.

[190] R. Ludwig, F. Weinhold, T. Farrar, *Mol. Phys.* **1999**, *97*, 465–477.

[191] R. Ludwig, F. Weinhold, T. Farrar, *Mol. Phys.* **1999**, *97*, 479–486.

[192] M. Huelsekopf, R. Ludwig, *J. Mol. Liq.* **2000**, *85*, 105–125.

[193] M. Huelsekopf, R. Ludwig, *J. Mol. Liq.* **2002**, *98*, 163–171.

[194] R. Ludwig, *ChemPhysChem* **2005**, *6*, 1369–1375.

[195] R. Ludwig, *ChemPhysChem* **2005**, *6*, 1376–1380.

[196] G. Marchelli, J. Ingenmey, B. Kirchner, *ChemistryOpen* **2020**, *9*, 774–785.

[197] R. Ludwig, F. Weinhold, T. Farrar, *J. Phys. Chem. A* **1997**, *101*, 8861–8870.

[198] R. Ludwig, O. Reis, R. Winter, F. Weinhold, T. Farrar, *J. Phys. Chem. B* **1998**, *102*, 9312–9318.

[199] M. Huelsekopf, R. Ludwig, *Magn. Reson. Chem.* **2001**, *39*, S127–S134.

[200] M. von Domaros, S. Jähnigen, J. Friedrich, B. Kirchner, *J. Chem. Phys.* **2016**, *144*, 064305.

[201] R. Ludwig, F. Weinhold, T. Farrar, *Berich. Bunsen Gesell.* **1998**, *102*, 197–204.

[202] R. Ludwig, J. Behler, B. Klink, F. Weinhold, *Angew. Chem. Int. Ed.* **2002**, *41*, 3199–3202.

[203] M. A. Wendt, F. Weinhold, T. C. Farrar, *J. Chem. Phys.* **1998**, *109*, 5945–5947.

[204] M. Hansen, M. Wendt, F. Weinhold, *Mol. Phys.* **2003**, *101*, 1147–1153.

[205] E. Perlt, J. Friedrich, M. von Domaros, B. Kirchner, *ChemPhysChem* **2011**, *12*, 3474–3482.

[206] C. Spickermann, E. Perlt, M. von Domaros, M. Roatsch, J. Friedrich, B. Kirchner, *J. Chem. Theory Comput.* **2011**, *7*, 868–875.

[207] M. von Domaros, E. Perlt, *J. Chem. Phys.* **2017**, *146*, 124114.

[208] Johannes Carl Maria Ingenmey, Ph.D. thesis, Rheinische Friedrich-Wilhelms-Universität Bonn, **2021**. https://hdl.handle.net/20.500.11811/9298.

[209] J. Ingenmey, M. von Domaros, E. Perlt, S. P. Verevkin, B. Kirchner, *J. Chem. Phys.* **2018**, *148*, 193822.

[210] D. A. McQuarrie, J. D. Simon, *Physical chemistry: a molecular approach*, University Science Books: USA, **1997**.

[211] G. Wedler, H.-J. Freund, *Lehrbuch der physikalischen Chemie*, *Vol. 1*, John Wiley & Sons, **2012**.

[212] M. Brüssel, E. Perlt, M. von Domaros, M. Brehm, B. Kirchner, *J. Chem. Phys.* **2012**, *137*, 164107.

[213] Michael von Domaros, Ph.D. thesis, Rheinische Friedrich-Wilhelms-Universität Bonn, **2018**. https://hdl.handle.net/20.500.11811/7600.

[214] N. Metropolis, S. Ulam, *J. Am. Stat. Assoc.* **1949**, *44*, 335–341.

[215] N. Metropolis, A. W. Rosenbluth, M. N. Rosenbluth, A. H. Teller, E. Teller, *J. Chem. Phys.* **1953**, *21*, 1087–1092.

[216] B. J. Alder, T. E. Wainwright, *J. Phys. Chem.* **1957**, *27*, 1208–1209.

[217] B. J. Alder, T. E. Wainwright, *J. Chem. Phys.* **1959**, *31*, 459–466.

[218] A. Rahman, *Phys. Rev.* **1964**, *136*, 405.

[219] L. Verlet, *Phys. Rev.* **1967**, *159*, 98.

[220] L. Verlet, *Phys. Rev.* **1968**, *165*, 201.

[221] J. Nicolas, K. Gubbins, W. Streett, D. Tildesley, *Mol. Phys.* **1979**, *37*, 1429–1454.

[222] W. C. Swope, H. C. Andersen, P. H. Berens, K. R. Wilson, *J. Chem. Phys.* **1982**, *76*, 637–649.

[223] S. Nosé, *Mol. Phys.* **1984**, *52*, 255–268.

[224] S. Nosé, *J. Chem. Phys.* **1984**, *81*, 511–519.

[225] W. G. Hoover, *Phys. Rev. A* **1985**, *31*, 1695–1697.

[226] G. J. Martyna, M. L. Klein, M. Tuckerman, *J. Chem. Phys.* **1992**, *97*, 2635–2643.

[227] J. Wang, R. M. Wolf, J. W. Caldwell, P. A. Kollman, D. A. Case, *J. Comput. Chem.* **2004**, *25*, 1157–1174.

[228] W. L. Jorgensen, D. S. Maxwell, J. Tirado-Rives, *J. Am. Chem. Soc.* **1996**, *118*, 11225–11236.

[229] J. N. Canongia Lopes, J. Deschamps, A. A. Pádua, *J. Phys. Chem. B* **2004**, *108*, 2038–2047.

[230] J. N. Canongia Lopes, A. A. Pádua, *J. Phys. Chem. B* **2004**, *108*, 16893–16898.

[231] J. N. Canongia Lopes, A. A. Pádua, *J. Phys. Chem. B* **2006**, *110*, 19586–19592.

[232] J. E. Lennard-Jones, *Proc. Phys. Soc.* **1931**, *43*, 461–483.

[233] H. A. Lorentz, *Ann. Phys.* **1881**, *248*, 127–136.

[234] D. Berthelot, *Compt. Rendus* **1898**, *126*, 1703–1706.

[235] D. J. Tildesley, M. P. Allen, *Computer simulation of liquids*, Clarendon Oxford, **1987**.

[236] P. M. Morse, *Phys. Rev.* **1929**, *34*, 57.

[237] R. A. Buckingham, *Proc. R. Soc. Lond. A Math. Phys. Sci.* **1938**, *168*, 264–283.

[238] R. Car, M. Parrinello, *Phys. Rev. Lett.* **1985**, *55*, 2471.

[239] D. Marx, J. Hutter, *Ab initio molecular dynamics: basic theory and advanced methods*, Cambridge University Press, **2009**.

[240] J. Hutter, M. Iannuzzi, F. Schiffmann, J. VandeVondele, *Wiley Interdiscip. Rev. Comput. Mol. Sci.* **2014**, *4*, 15–25.

[241] CP2k developers group under the terms of the GNU General Public License; see http://www.cp2k.org.

[242] G. Lippert, J. Hutter, M. Parrinello, *Mol. Phys.* **1997**, *92*, 477–488.

[243] J. VandeVondele, M. Krack, F. Mohamed, M. Parrinello, T. Chassaing, J. Hutter, *Comput. Phys. Commun.* **2005**, *167*, 103–128.

[244] S. Goedecker, M. Teter, J. Hutter, *Phys. Rev. B* **1996**, *54*, 1703–1710.

[245] C. Hartwigsen, S. Gœdecker, J. Hutter, *Phys. Rev. B* **1998**, *58*, 3641–3662.

[246] M. Krack, *Theor. Chem. Acc.* **2005**, *114*, 145–152.

[247] C. Merten, T. P. Golub, N. M. Kreienborg, *J. Org. Chem.* **2019**, *84*, 8797–8814.

[248] T. B. Freedman, X. Cao, R. K. Dukor, L. A. Nafie, *Chirality* **2003**, *15*, 743–758.

[249] L. A. Nafie, M. Diem, *Appl. Spectrosc.* **1979**, *33*, 130–135.

[250] L. Rosenfeld, *Z. Phys.* **1929**, *52*, 161–174.

[251] A. Scherrer, R. Vuilleumier, D. Sebastiani, *J. Chem. Theory Comput.* **2013**, *9*, 5305–5312.

[252] A. Scherrer, F. Agostini, D. Sebastiani, E. Gross, R. Vuilleumier, *J. Chem. Phys.* **2015**, *143*, 074106.

[253] A. Scherrer, R. Vuilleumier, D. Sebastiani, *J. Chem. Phys.* **2016**, *145*, 084101.

[254] P. J. Stephens, *J. Phys. Chem.* **1985**, *89*, 748–752.

[255] P. Stephens, *J. Phys. Chem.* **1987**, *91*, 1712–1715.

[256] J. B. Foresman, A. Frisch, Gaussian, Inc.: Pittsburgh, PA, USA, 2015.

[257] M. J. Frisch, G. W. Trucks, H. B. Schlegel, G. E. Scuseria, M. A. Robb, J. R. Cheeseman, G. Scalmani, V. Barone, G. A. Petersson, H. Nakatsuji, et al., Gaussian, Inc.: Wallingford, CT, USA, 2016.

[258] J. Cheeseman, M. Frisch, F. Devlin, P. Stephens, *Chem. Phys. Lett.* **1996**, *252*, 211–220.

[259] V. P. Nicu, J. Neugebauer, S. K. Wolff, E. J. Baerends, *Theor. Chem. Acc.* **2008**, *119*, 245–263.

[260] M. A. Koenis, O. Visser, L. Visscher, W. J. Buma, V. P. Nicu, *J. Chem. Inf. Model.* **2019**, *60*, 259–267.

[261] M. R. Poopari, Z. Dezhahang, Y. Xu, *Phys. Chem. Chem. Phys.* **2013**, *15*, 1655–1665.

[262] A. S. Perera, J. Thomas, M. R. Poopari, Y. Xu, *Front. Chem.* **2016**, *4*, 9.

[263] M. S. Green, *J. Chem. Phys.* **1954**, *22*, 398–413.

[264] R. Kubo, *J. Phys. Soc. Jpn.* **1957**, *12*, 570–586.

[265] N. Wiener, *Acta Math.* **1930**, *55*, 117–258.

[266] A. Khintchine, *Math. Ann.* **1934**, *109*, 604–615.

[267] S. Abbate, G. Longhi, K. Kwon, A. Moscowitz, *J. Chem. Phys.* **1998**, *108*, 50–62.

[268] J. Horníček, P. Kaprálová, P. Bouř, *J. Chem. Phys.* **2007**, *127*, 084502.

[269] M. Thomas, M. Brehm, R. Fligg, P. Vöhringer, B. Kirchner, *Phys. Chem. Chem. Phys.* **2013**, *15*, 6608–6622.

[270] G. Voronoi, *J. Reine Angew. Math.* **1908**, *1908*, 198–287.

[271] A. Grossfield, P. N. Patrone, D. R. Roe, A. J. Schultz, D. W. Siderius, D. M. Zuckerman, *Living J. Comp. Mol. Sci.* **2018**, *1*, 5067.

[272] P. Zaby, J. Ingenmey, B. Kirchner, S. Grimme, S. Ehlert, *J. Chem. Phys.* **2021**, *155*, 104101.

[273] V. P. Nicu, J. Neugebauer, E. J. Baerends, *J. Phys. Chem. A* **2008**, *112*, 6978–6991.

[274] A. Klamt, G. Schüürmann, *J. Chem. Soc., Perkin Trans. 2* **1993**, 799–805.

[275] J.-H. Choi, M. Cho, *J. Chem. Theory Comput.* **2011**, *7*, 4097–4103.

[276] Z. Zhu, M. E. Tuckerman, *J. Phys. Chem. B* **2002**, *106*, 8009–8018.

[277] M. Urbanová, V. Setnicka, F. Devlin, P. Stephens, *J. Am. Chem. Soc.* **2005**, *127*, 6700–6711.

[278] A. S. Perera, J. Cheramy, C. Merten, J. Thomas, Y. Xu, *ChemPhysChem* **2018**, *19*, 2234–2242.

[279] D. Mathieu, M. Defranceschi, J. Delhalle, *Int. J. Quantum Chem.* **1993**, *45*, 735–746.

[280] F. Hermanutz, M. P. Vocht, N. Panzier, M. R. Buchmeiser, *Macromol. Mater. Eng.* **2019**, *304*, 1800450.

[281] A. R. R. Teles, T. B. Dinis, E. V. Capela, L. M. Santos, S. P. Pinho, M. G. Freire, J. A. Coutinho, *Phys. Chem. Chem. Phys.* **2016**, *18*, 19722–19730.

[282] H. Wang, G. Gurau, R. D. Rogers, *Chem. Soc. Rev.* **2012**, *41*, 1519–1537.

[283] K. Fumino, A. Wulf, R. Ludwig, *Angew. Chem. Int. Ed.* **2008**, *47*, 3830–3834.

[284] M. T. Clough, K. Geyer, P. A. Hunt, S. Son, U. Vagt, T. Welton, *Green Chem.* **2015**, *17*, 231–243.

[285] J. Radicke, E. Roos, D. Sebastiani, M. Brehm, J. Kressler, *J. Polym. Sci.* **2023**, *61*, 372–384.

[286] A. Berthod, *Anal. Chem.* **2006**, *78*, 2093–2099.

[287] O. Hollóczki, *ACS Sustain. Chem. Eng.* **2018**, *7*, 2626–2633.

[288] A. Szabadi, C. Schröder, *J. Comput. Biophys. Chem.* **2022**, *21*, 415–429.

[289] A. Gansäuer, D. von Laufenberg, C. Kube, T. Dahmen, A. Michelmann, M. Behlendorf, R. Sure, M. Seddiqzai, S. Grimme, D. V. Sadasivam, et al., *Eur. J. Chem.* **2015**, *21*, 280–289.

[290] P. Funk, R. B. Richrath, F. Bohle, S. Grimme, A. Gansäuer, *Angew. Chem. Int. Ed.* **2021**, *60*, 5482–5488.

[291] J. P. Perdew, K. Burke, M. Ernzerhof, *Phys. Rev. Lett.* **1996**, *77*, 3865.

[292] J. P. Perdew, A. Ruzsinszky, G. I. Csonka, O. A. Vydrov, G. E. Scuseria, L. A. Constantin, X. Zhou, K. Burke, *Phys. Rev. Lett.* **2008**, *100*, 136406.

[293] C. Lee, W. Yang, R. G. Parr, *Phys. Rev. B* **1988**, *37*, 785.

[294] J. VandeVondele, J. Hutter, *J. Chem. Phys.* **2007**, *127*, 114105.

[295] S. Ling, B. Slater, *Primary Basis Sets Optimised from Molecular Calculations*, https://fossies.org/linux/cp2k/data/BASIS_MOLOPT_UCL, Accessed: 2021-10-09.

[296] M. Guidon, J. Hutter, J. VandeVondele, *J. Chem. Theory Comput.* **2010**, *6*, 2348–2364.

[297] A. Balducci, *Ionic Liquids II* **2018**, 1–27.

[298] T. Rüther, A. I. Bhatt, A. S. Best, K. R. Harris, A. F. Hollenkamp, *Batter. Supercaps* **2020**, *3*, 793–827.

[299] F. Chen, M. Forsyth, *J. Phys. Chem. Lett.* **2019**, *10*, 7414–7420.

[300] J. N. Canongia Lopes, K. Shimizu, A. A. Pádua, Y. Umebayashi, S. Fukuda, K. Fujii, S.-i. Ishiguro, *J. Phys. Chem. B* **2008**, *112*, 1465–1472.

[301] M. Losada, P. Nguyen, Y. Xu, *J. Phys. Chem. A* **2008**, *112*, 5621–5627.

[302] F. Philippi, D. Pugh, D. Rauber, T. Welton, P. A. Hunt, *Chem. Sci.* **2020**, *11*, 6405–6422.

A. Uncertainty Quantification of Phase Transition Quantities from Cluster Weighting Calculations

Jan Blasius,[*] Paul Zaby,[*] Jürgen Dölz,[†] and Barbara Kirchner[*]

Received: 25 March 2022, Published online: 05 July 2022.

Reprinted (adapted) in appendix A with permission[‡] from

J. Blasius, P. Zaby, J. Dölz, and B. Kirchner, *J. Chem. Phys.* **2022**, *157*, 014505.

doi:10.1063/5.0093057.

For this article a Supporting Information is available free of charge at:
https://aip.scitation.org/doi/suppl/10.1063/5.0093057.

Contributions to the manuscript

- Co-development of the concept
- Supervision and analysis of the calculations
- Interpretation of the results
- Writing of the manuscript

[*] Mulliken Center for Theoretical Chemistry, Clausius Institute for Physical and Theoretical Chemistry, University of Bonn, Beringstr. 4–6, 53115 Bonn, Germany
[†] Institute for Numerical Simulation, University of Bonn, Friedrich-Hirzebruch-Allee 7, 53115 Bonn, Germany
[‡] Permission requests to reuse material from this chapter should be directed to AIP Publishing.

The Journal of Chemical Physics ARTICLE scitation.org/journal/jcp

Uncertainty quantification of phase transition quantities from cluster weighting calculations

Cite as: J. Chem. Phys. 157, 014505 (2022); doi: 10.1063/5.0093057
Submitted: 25 March 2022 • Accepted: 9 June 2022 •
Published Online: 5 July 2022

Jan Blasius,[1] Paul Zaby,[1] Jürgen Dölz,[2,a)] and Barbara Kirchner[1,b)]

AFFILIATIONS

[1] Mulliken Center for Theoretical Chemistry, Institute for Physical and Theoretical Chemistry, University of Bonn, Beringstr. 4+6, 53115 Bonn, Germany
[2] Institute for Numerical Simulation, University of Bonn, Friedrich-Hirzebruch-Allee 7, 53115 Bonn, Germany

[a)] E-mail: doelz@ins.uni-bonn.de
[b)] Author to whom correspondence should be addressed: kirchner@thch.uni-bonn.de

ABSTRACT

In this work, we investigate how uncertainties in experimental input data influence the results of quantum cluster equilibrium calculations. In particular, we focus on the calculation of vaporization enthalpies and entropies of seven organic liquids, compare two computational approaches for their calculation, and investigate how these properties are affected by changes in the experimental input data. It is observed that the vaporization enthalpies and entropies show a smooth dependence on changes in the reference density and boiling point. The reference density is found to have only a small influence on the vaporization thermodynamics, whereas the boiling point has a large influence on the vaporization enthalpy but only a small influence on the vaporization entropy. Furthermore, we employed the Gauss–Hermite estimator in order to quantify the uncertainty in thermodynamic functions that stems from inaccuracies in the experimental reference data for the example of the vaporization enthalpy of (*R*)-butan-2-ol. We quantify the uncertainty as $30.95 \cdot 10^{-3}$ kJ mol^{-1}. In addition, we compare the convergence behavior and computational effort of the Gauss–Hermite estimator with the Monte Carlo approach and show the superiority of the former. Using this study, we present how uncertainty quantification can be applied to examples from theoretical chemistry.

INTRODUCTION

Fast but approximate methods are needed in theoretical chemistry in order to reduce the computational costs while still providing results at acceptable accuracy for assessing complex and large chemical spaces,[1,2] i.e., on the order of Avogadro's number. Since these methods allow the treatment of larger and, thus, more realistic systems with reasonable computational effort,[3] they are a necessary step in terms of sustainable research as they can also help to save expensive computer time. Not only will larger and more complex systems be accessible via computations, but also the reduced computational effort will allow the usage of smaller work stations using less resources. In this respect, many pioneering works have been undertaken in computational chemistry, in particular electronic structure theory. Examples include developments and applications in the context of density functional theory, including low-cost but well-performing functionals and composite methods,[4] and wave function-based theories such as local coupled cluster methods, which have made major contributions to this field of research.[5] Similarly, the development of semiempirical tight-binding methods[6] or so-called embedding methods[7] is also a large step forward in allowing to calculate more realistic problems. In this regard, some simulation techniques of note include coarse-grained or enhanced sampling techniques[8,9] and other linear scaling methods.[10]

Despite these efforts, realistic applications from sustainable chemistry often require complex or involved models of the underlying chemistry and large computing time. Examples include the inclusion of liquids or solvents such as ionic liquids[11–14] and the appropriate description of interfaces[15,16] or systems from energy devices.[17–19]

When using such approximate methods, the assessment of the uncertainties involved is of great importance. In this article, we use the quantum cluster equilibrium (QCE) method[20,21] in order to explore the nature of liquids and calculate their properties. The QCE

method treats clusters quantum chemically in the mean field of a liquid and calculates the cluster populations at a given phase point. Since the QCE model samples a dynamic cluster ensemble, it provides an approximate method compared to, for example, *ab initio* molecular dynamics simulations if the same level of electronic structure is used.

As opposed to classical Boltzmann factors, which are limited to same-sized structures at a given time, the QCE approach allows the simultaneous inclusion of differently sized clusters.[22] While in its original form, the theory has been developed for neat substances,[20,21,23–25] it has been further extended to binary systems,[26–28] enabling the calculation of activity coefficients[29] or concentration-dependent acid dissociation.[30,31]

Within the QCE framework, molecular clusters including monomers and several oligomers are considered to be in chemical equilibrium. Interactions between the clusters are described by the mean field of the cluster ensemble. Nonetheless, within the clusters themselves, all interactions are treated explicitly. This allows the application of a variety of quantum chemical methods,[23] enabling the treatment of the condensed phase with low-cost methods[32] on par with highly accurate post-Hartree–Fock electronic structure methods such as the coupled cluster method.[33]

For a given ensemble of clusters, the connection between the thermodynamic quantities of the condensed phase and the set of structures is given by the system's partition function, for which an approximate but analytical expression is available. Based on this expression, any thermodynamic function of the cluster ensemble is accessible. While the treatment of the liquid phase as a thermodynamic equilibrium of clusters can circumvent sampling problems and thus the computational bottleneck of, e.g., *ab initio* molecular dynamics simulations, a combination of the explicit cluster approach with the mean field keeps the computational effort low. QCE is, thus, a promising method for calculating properties of liquids and their mixtures at low cost. Nevertheless, a quantification of the uncertainties due to the approximations made is desirable, especially because QCE computations require experimental input data, which are prone to measurement errors.

Therefore, the focus of this article is to gain a basic understanding of the influence of *measurement errors in physical quantities* on the results of QCE calculations. To this end, we follow *uncertainty quantification* approaches used in various scientific fields[34] and assume the experimental uncertainty to be a random quantity. As such, the physical quantities affected by these measurement errors and entering the QCE calculations are considered as random parameters. This propagates through the QCE calculations such that the QCE results themselves need to be considered as a random quantity. The aim of uncertainty quantification is then to quantify the statistical behavior of the calculation results, given some information on the statistical behavior of the measurement errors.

The most straightforward approach to achieve this aim is the Monte Carlo (MC) method.[35] Drawing random values from the probability distributions of the input parameters, the Monte Carlo method performs a QCE calculation for each of these random parameter sets to compute statistical quantities of interest for the outputs obtained, such as the empirical mean and the empirical standard deviation. Unfortunately, Monte Carlo simulations often require many samples and, thus, model evaluations to yield sufficiently accurate results and[36] are, therefore, computationally quite expensive, even when the underlying model can be evaluated at a relatively low cost.

Given a certain amount of *a priori* knowledge on how smoothly the outcome of the calculations changes with variations in the input parameters, various deterministic methods and acceleration techniques can be applied to speed up computations in uncertainty quantification. Most of them are based on the mathematical representations of mean, variance, etc. as integrals in one or several variables over the range of possible parameter values,[37,38] which are then approximated by a combination of one-dimensional numerical quadrature rules.[37,39] This usually works well for a small number of parameters, significantly less than ten. For a larger number of parameters, the curse of dimensionality makes this approach computationally prohibitive, and special quadrature rules need to be employed to increase the calculation speed, such as quasi-Monte Carlo methods,[35,40] sparse grids,[41] or other multilevel techniques.[42,43]

This article is structured as follows: First, we present two approaches for the calculation of vaporization enthalpies and entropies. Both approaches are based on QCE computations, and we apply them to seven organic liquids in order to compare the quality of the results and the computational effort. Afterward, we investigate the dependence of the calculated vaporization enthalpies and entropies as well as of the cluster populations with respect to variations in the experimental reference data that need to be provided for QCE calculations. This investigation is necessary because a smooth dependence of the vaporization enthalpies and entropies on the input quantities is required for the application of the statistical analyses in a later chapter, where we use an uncertainty quantification approach in order to assess the uncertainty in the vaporization enthalpy that originates from inaccuracies in the experimental input data. We compare the computational effort and convergence behavior of the used method with the well-known Monte Carlo method and finally provide a quantification of the uncertainty that is inherent in the vaporization enthalpy obtained from the QCE method.

THEORETICAL BACKGROUND

Quantum cluster equilibrium

In the following, the theory behind the QCE method will be explained in greater detail. For a shortened presentation, the reader is referred to Refs. 22, 32, and 44. Readers familiar with this approach may skip this section. The QCE method[20,23] describes the liquid and the gaseous phase of a system in terms of quantum chemically optimized clusters that are in thermodynamic equilibrium with each other. Clusters are an accumulation of multiple molecules (monomers), which arrange in optimal conformations and which are held together by attractive interactions, see also Fig. 1. The thermodynamic equilibrium of a set of clusters can be described as follows:

$$\mathrm{C}_1 \rightleftharpoons \frac{\mathrm{C}_2}{i_\mathrm{C}(\mathrm{C}_2)} \rightleftharpoons \frac{\mathrm{C}_3}{i_\mathrm{C}(\mathrm{C}_3)} \rightleftharpoons \cdots \rightleftharpoons \frac{\wp}{i_\mathrm{C}(\wp)}, \tag{1}$$

where $i_\mathrm{C}(\wp)$ describes the number of monomers of component C present in a cluster $\wp$.

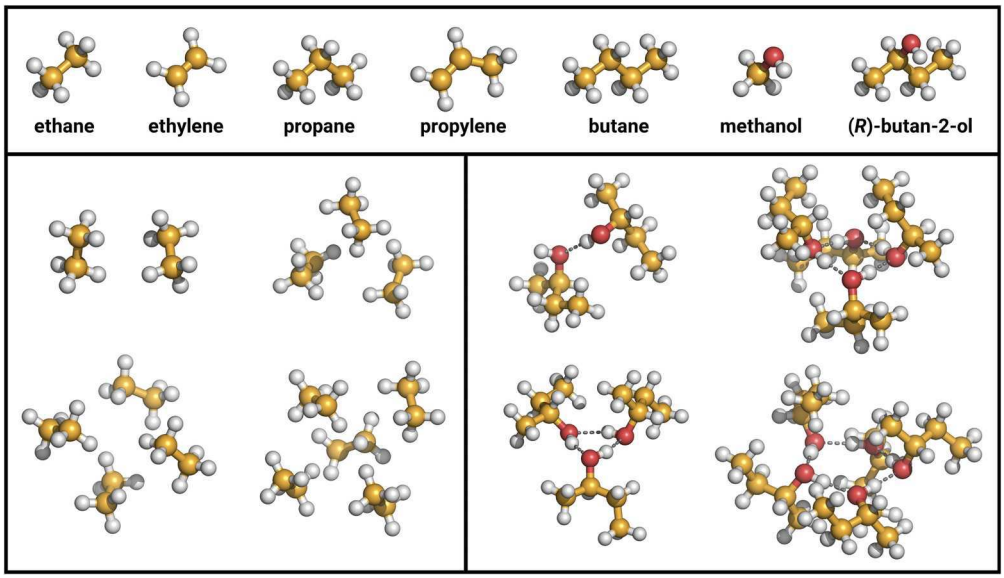

FIG. 1. Ball-and-stick images of the seven organic molecules investigated as well as some examples of different ethane and (*R*)-butan-2-ol clusters.

The aim of the QCE method is to find an equilibrium distribution $\{N_\wp\}$ of the cluster populations $N_\wp$, for which the free energy A at a given volume V and temperature T becomes minimal. Our starting point is the canonical partition function:

$$Q^{\mathrm{tot}}(\{N_\wp\},V,T)=\prod_{\wp=1}\frac{1}{N_\wp!}\left[q_\wp^{\mathrm{tot}}(V,T)\right]^{N_\wp}, \tag{2}$$

where $q_\wp^{\mathrm{tot}}$ denotes the partition function of a cluster $\wp$. The cluster partition function is a product of the partition functions of the different degrees of freedom:

$$q_\wp^{\mathrm{tot}}(V,T)=q_\wp^{\mathrm{trans}}(V,T)q_\wp^{\mathrm{rot}}(T)q_\wp^{\mathrm{vib}}(T)q_\wp^{\mathrm{elec}}(V,T). \tag{3}$$

The translational, rotational, and vibrational partition functions are calculated by using standard equations from textbooks that are derived from simple models such as the particle in a box, the rigid rotor, or the harmonic oscillator models,[37,45]

$$q^{\mathrm{trans}}(V,T)=\frac{V}{\Lambda^3(T)}\quad\text{with}\quad\Lambda(T)=\sqrt{\frac{h^2}{2\pi m k_{\mathrm{B}}T}}, \tag{4}$$

$$q^{\mathrm{rot}}(T)=\frac{\sqrt{\pi}}{\sigma}\sqrt{\frac{T^3}{\Theta_A^{\mathrm{rot}}\Theta_B^{\mathrm{rot}}\Theta_C^{\mathrm{rot}}}}\quad\text{with}\quad\Theta_j^{\mathrm{rot}}=\frac{h^2}{8\pi^2 I_j k_{\mathrm{B}}}, \tag{5}$$

$$q^{\mathrm{vib}}(T)=\prod_{i=1}^{3N-x}\frac{e^{-\Theta_i^{\mathrm{vib}}/2T}}{1-e^{-\Theta_i^{\mathrm{vib}}/T}}\quad\text{with}\quad\Theta_i^{\mathrm{vib}}=\frac{h\nu_i}{k_{\mathrm{B}}}. \tag{6}$$

Here, Λ is the thermal de Broglie wavelength, h the Planck constant, m the mass of the particle, k_{B} the Boltzmann constant, σ the symmetry-number, Θ_j^{rot} and Θ_j^{vib} the characteristic rotational and vibrational temperatures, respectively, I_j the moments of inertia, and ν_i the frequency of the respective vibrational modes. The variable x in the sum of the vibrational partition function is equal to 5 for linear molecules and 6 for nonlinear molecules. A detailed discussion can be found in physical chemistry textbooks.[37]

With the electronic ground state energy $\epsilon_0^{\mathrm{elec}}$ and the degeneracy of the ground state g_0, the electronic partition function can be expressed by the following equation:

$$q^{\mathrm{elec}}(T)=g_0 e^{-\frac{\epsilon_0^{\mathrm{elec}}}{k_{\mathrm{B}}T}}. \tag{7}$$

All input data for those partition functions can be obtained from the quantum chemical calculations of the clusters.

The translational partition function as presented above is problematic since it describes an ideal gas where the molecules do not have a volume themselves. To counteract this, a correction inspired by the van der Waals equation is introduced. The new parameter b_{xv} scales the volume that is not available for translation since it is occupied by the clusters. This exclusion volume V_{ex} is given by

$$V_{\mathrm{ex}}=b_{\mathrm{xv}}\sum_{\wp=1}^{N}N_\wp v_\wp. \tag{8}$$

Usually, b_{xv} is considered as being temperature independent; however, a recent extension of the QCE theory introduces a linear temperature dependence of b_{xv},

$$b_{\mathrm{xv}}(T)=T\cdot\beta_{\mathrm{xv}}+b_{\mathrm{xv}}^0, \tag{9}$$

with β_{xv} being the exclusion volume expansion coefficient and b_{xv}^0 the base of the intercept.[46]

The resulting translational partition function is now given as follows:

$$q^{\mathrm{trans}}(V,T) = \frac{V - V_{\mathrm{ex}}}{\Lambda^3(T)}. \tag{10}$$

The second parameter a_{mf} is introduced in order to scale the mean field binding energies of the clusters, which is expressed by a density-dependent term as follows:

$$\epsilon^{\mathrm{mf}}(V) = -\frac{a_{\mathrm{mf}} \sum_{\mathrm{C}} i_{\mathrm{C}}(\wp)}{V}. \tag{11}$$

Together with the adiabatic binding energy,

$$\Delta_{\mathrm{bind}}\epsilon_{\wp}^{\mathrm{elec}} = \epsilon_{\wp}^{\mathrm{elec}} - \sum_{\mathrm{C}} i_{\mathrm{C}}(\wp)\epsilon_{\mathrm{C}_1}^{\mathrm{elec}}, \tag{12}$$

the electronic partition function changes to the following expression:

$$q^{\mathrm{elec}}(V,T) = e^{-\frac{\Delta_{\mathrm{bind}}\epsilon^{\mathrm{elec}} + \epsilon^{\mathrm{mf}}(V)}{k_{\mathrm{B}}T}}. \tag{13}$$

The two parameters introduced in the QCE theory, namely b_{xv} and a_{mf}, are optimized with respect to experimental inputs. In particular, the difference between the calculated results and the reference data is minimized.

Knowledge of the three independent variables $(\{N_{\wp}\}, V, T)$ in equilibrium allows us to obtain thermodynamic data from the canonical partition function solely. The following condition is introduced to ensure the conservation of the mass/particle number:

$$\begin{aligned} \sum_{\mathrm{C}} N_{\mathrm{C}}^{\mathrm{tot}} &= \sum_{\wp=1}^{N} \sum_{\mathrm{C}} i_{\mathrm{C}}(\wp) N_{\wp}, \\ 0 = \sum_{\wp=1}^{N} \sum_{\mathrm{C}} \frac{i_{\mathrm{C}}(\wp)}{N_{\mathrm{C}}^{\mathrm{tot}}} \cdot N_{\wp} - 1 &= \sum_{\wp=1}^{N} I_{\wp} - 1, \end{aligned} \tag{14}$$

where $I_{\wp}$ is the monomer-normalized population of a cluster $\wp$. As long as the system is in equilibrium and all thermodynamic variables stay constant, the slope of the free energy A dependent on the cluster populations is zero,

$$\begin{aligned} 0 = \sum_{\mathrm{C}} \sum_{\wp=1}^{N} i_{\mathrm{C}}(\wp) \left(\frac{\partial A}{\partial N_{\mathrm{C}1}} \right)_{\{N_{\mathrm{m}}(m\neq 1)\},V,T} d\lambda \\ - \sum_{\wp=1}^{N} \left(\frac{\partial A}{\partial N_{\wp}} \right)_{\{N_{\mathrm{m}}(m\neq 1)\},V,T} d\lambda. \end{aligned} \tag{15}$$

Here, $d\lambda$ describes how the reaction progresses. Since this equation is independent of the reaction progress and has to hold for every cluster, it can be rearranged as follows:

$$\left(\frac{\partial A}{\partial N_{\wp}} \right) = \sum_{\mathrm{C}} i_{\mathrm{C}}(\wp) \left(\frac{\partial A}{\partial N_{\mathrm{C}_1}} \right). \tag{16}$$

The mathematical expression relating the free energy A and the canonical partition function is given by

$$A = -k_{\mathrm{B}}T \ln Q^{\mathrm{tot}}(\{N_{\wp}\}, V, T), \tag{17}$$

which in combination with Eqs. (2) and (15) leads to the following expression:

$$\begin{aligned} &\frac{\partial}{\partial N_{\wp}} \sum_{\wp=1}^{N} \left(N_{\wp} \ln q_{\wp}^{\mathrm{tot}} - \ln N_{\wp}! \right) \\ &\quad = \sum_{\mathrm{C}} i_{\mathrm{C}}(\wp) \left(\frac{\partial}{\partial N_{\mathrm{C}_1}} \sum_{\wp=1}^{N} \left(N_{\wp} \ln q_{\wp}^{\mathrm{tot}} - \ln N_{\wp}! \right) \right). \end{aligned} \tag{18}$$

By using the Stirling equation and rearranging, one obtains the following equation for $N_{\wp}$:

$$N_{\wp} = \prod_{\mathrm{C}} q_{\wp}^{\mathrm{tot}} \left(\frac{N_{\mathrm{C}_1}}{q_{\mathrm{C}_1}^{\mathrm{tot}}} \right)^{i_{\mathrm{C}}(\wp)}. \tag{19}$$

Inserting this equation in Eq. (14) gives the generalized population polynomial, which is one of the central equations of the QCE theory,

$$0 = \sum_{\wp=1}^{N} \sum_{\mathrm{C}} \frac{i_{\mathrm{C}}(\wp)}{N_{\mathrm{C}}^{\mathrm{tot}}} \cdot \prod_{\mathrm{C}} q_{\wp}^{\mathrm{tot}} \left(\frac{N_{\mathrm{C}_1}}{q_{\mathrm{C}_1}^{\mathrm{tot}}} \right)^{i_{\mathrm{C}}(\wp)} - 1. \tag{20}$$

For neat liquids, this equation is exactly solvable.

The second central equation is the so-called volume polynomial. In order to derive this, the pressure of the system is defined as in statistical thermodynamics as the negative volume derivative of the free energy at constant temperature,

$$p = -\left(\frac{\partial A}{\partial V} \right)_{T,\{N_{\wp}\}}. \tag{21}$$

By inserting the expression of the free energy A in terms of the canonical partition function, one obtains the following equation:

$$0 = -p + k_{\mathrm{B}}T \left(\frac{\partial \ln Q^{\mathrm{tot}}}{\partial V} \right)_{T,\{N_{\wp}\}}. \tag{22}$$

Since the vibrational and the rotational partition functions do not depend on the volume, only the translational and electronic parts of the partition function have to be taken into account here. By inserting Eqs. (2), (3), (8), (10), (11), and (13), the volume polynomial is obtained as follows:

$$\begin{aligned} 0 = -pV^3 &+ \left(pb_{\mathrm{xv}} \sum_{\wp=1}^{N} N_{\wp} v_{\wp} + k_{\mathrm{B}}T \sum_{\wp=1}^{N} N_{\wp} \right) V^2 \\ &- \left(\sum_{\wp=1}^{N} \sum_{\mathrm{C}} N_{\wp} i_{\mathrm{C}}(\wp) a_{\mathrm{mf}} \right) V \\ &+ \left(\sum_{\wp=1}^{N} \sum_{\mathrm{C}} N_{\wp} i_{\mathrm{C}}(\wp) a_{\mathrm{mf}} \right) \cdot \left(b_{\mathrm{xv}} \sum_{\wp=1}^{N} N_{\wp} v_{\wp} \right). \end{aligned} \tag{23}$$

While solving the population and the volume polynomial, the volume, the cluster populations, and the partition function are independent, meaning those equations have to be solved iteratively. If multiple combinations of the volume and the populations exist,

which solve both polynomials, the solution with the lowest Gibbs energy G is taken with,

$$G = -k_B T \ln Q^{tot} + V k_B T \left(\frac{\partial \ln Q^{tot}}{\partial V} \right)_{T,\{N_\varphi\}}. \quad (24)$$

After the best solution is determined, the absolute enthalpy at a given temperature can be obtained using the following expression:

$$H = k_B T^2 \left(\frac{\partial \ln Q^{tot}}{\partial V} \right)_{T,\{N_\varphi\}}. \quad (25)$$

In order to calculate enthalpies of vaporization $\Delta_{vap}H$, absolute gas phase enthalpies are needed. These are obtained by performing another QCE calculation, called QCE^0, where the parameter b_{xv} is artificially set to 1 and the parameter a_{mf} is set to 0, which enforces a nearly ideal gas phase behavior. The absolute enthalpies of the two calculations can then be subtracted, yielding an enthalpy required to vaporize the liquid at a given temperature. The same procedure can be applied for the calculation of vaporization entropies $\Delta_{vap}S$, with the absolute entropy given as

$$S = k_B T \left(\frac{\partial \ln Q^{tot}}{\partial T} \right)_{V,\{N_\varphi\}} + k_B \ln Q^{tot}. \quad (26)$$

Finally, low vibrational frequencies can (optionally) be treated as hindered rotations since the vibrational partition function diverges for $\nu_i \longrightarrow 0$.[47] Within this modified rigid rotor–harmonic oscillator (mRRHO) approach, a modified vibrational partition function is introduced as follows:

$$q_i^{vib} = \prod_{\nu_i}^{N_i^{vib}} \left(q_{HO}^{vib}(\nu_i) \right)^{f(\nu_i)} \cdot \left(q_{HR}^{vib}(\nu_i) \right)^{1-f(\nu_i)}, \quad (27)$$

where q_{HO}^{vib} is the vibrational partition function derived from the harmonic oscillator discussed above [Eq. (6)] and q_{HR}^{vib} is the vibrational partition function of the hindered rotor,

$$q_{HR}^{vib}(\nu_i) = \sqrt{\frac{2\,\mu'(\nu_i)}{\pi \hbar^2 \beta}}$$

with

$$\mu'(\nu_i) = \frac{\mu(\nu_i)\bar{I}}{\mu(\nu_i) + \bar{I}}$$

and

$$\mu(\nu_i) = \frac{\hbar}{4\pi\nu_i}, \quad (28)$$

where $\bar{I}$ is the average moment of the molecule, μ is the moment corresponding to the normal mode, and $\hbar$ is the reduced Planck constant. As switching function $f(\nu_i)$ between the two partition functions, the Chai–Head-Gordon damping function[48] is used,

$$f(\nu_i) = \left(1 + \left(\frac{\nu_0}{\nu_i} \right)^4 \right)^{-1}, \quad (29)$$

with ν_0 being the user-defined rotor cutoff, which is usually assigned a value of 50 or 100 cm^{-1}.

Uncertainty quantification

The QCE computations depend on physical input quantities, for example, one input density ρ_{in} and the boiling point T_b, whose exact values are unknown and cannot be determined due to unavoidable measurement errors. As these measurement errors can be assumed to be random and normally distributed, it is reasonable to model ρ_{in} and T_b as normally distributed random variables. To that end, experimental data from the literature are considered as the means μ_ρ and μ_T of ρ_{in} and T_b and the estimated uncertainties are considered as the standard deviations σ_ρ and σ_T for the distribution. The probability of ρ_{in} and T_b having a certain value s is then given by the following probability distributions:

$$p_\rho(s) = \frac{1}{\sqrt{2\pi}\sigma_\rho} e^{-\frac{(s-\mu_\rho)^2}{2\sigma_\rho^2}}, \qquad p_T(s) = \frac{1}{\sqrt{2\pi}\sigma_T} e^{-\frac{(s-\mu_T)^2}{2\sigma_T^2}}. \quad (30)$$

An immediate consequence of considering ρ_{in} and T_b as uncertain variables is that all quantities calculated with the QCE method must also be regarded as uncertain variables and are, thus, subject to an *a priori* unknown uncertainty, which needs to be quantified. For this purpose, the mean of the vaporization enthalpy is given by

$$\mathbb{E}[\Delta_{vap}H] = \frac{1}{2\pi\sigma_\rho\sigma_T} \int_{\mathbb{R}} \int_{\mathbb{R}} \Delta_{vap}H(\rho_{in}, T_b) \times p_\rho(\rho_{in}) p_T(T_b) \mathrm{d}\rho_{in} \mathrm{d}T_b, \quad (31)$$

and its standard deviation is given by

$$\sigma[\Delta_{vap}H] = \sqrt{\mathbb{V}[\Delta_{vap}H]} = \sqrt{\mathbb{E}[\Delta_{vap}H^2] - \mathbb{E}[\Delta_{vap}H]^2}. \quad (32)$$

Since the integral Eq. (31) cannot be analytically determined, it must be numerically approximated. To that end, it should be noted that most deterministic numerical approximation methods for integrals require some kind of "smooth" dependence of the integrand on the integration variable for reliable results.[37,39] However, the behavior of $\Delta_{vap}H(\rho_{in}, T_b)$ in dependence of ρ_{in} and T_b in QCE is quite complicated and, to the best of our knowledge, has not yet been analyzed. A robust alternative to deterministic methods that does not assume a smooth dependence of the integrand is the Monte Carlo method.[35] According to this method, given N random sample densities $\rho_{in}^{(i)}$ and boiling temperatures $T_b^{(i)}$, $i = 1, \ldots, N$, drawn from the probability distributions in Eq. (30), the Monte Carlo estimator reads as follows:

$$\mathbb{E}[\Delta_{vap}H] \approx \frac{1}{N} \sum_{i=1}^{N} \Delta_{vap}H\left(\rho_{in}^{(i)}, T_b^{(i)} \right). \quad (33)$$

The estimator is an established tool in computational uncertainty quantification if the smoothness behavior of the integrand is unknown and the standard benchmark for other methods.

Despite its popularity, the Monte Carlo estimator has a few disadvantages, the obvious one being that its value strongly depends

on the randomly drawn samples for ρ_{in} and T_b. Approximation estimates for the estimator can, therefore, only be made in the statistical sense that the root mean square error of all possible Monte Carlo simulations will converge to the exact value of the integral for an increasing number of samples. Moreover, the error behaves like $\mathcal{O}(N^{-1/2})$ with the number of samples,[35] resulting in roughly $\mathcal{O}(10^6)$ samples to achieve an accuracy of $\mathcal{O}(10^{-3})$, for example. Since each evaluation of $\Delta_{\text{vap}}H\left(\rho_{\text{in}}^{(i)}, T_b^{(i)}\right)$ requires a QCE computation, it should be clear that the Monte Carlo method is computationally somewhat intensive and time-consuming.

To investigate the potential for more efficient deterministic approximation methods, we, therefore, performed a numerical study on the behavior of $\Delta_{\text{vap}}H(\rho_{\text{in}}, T_b)$ in dependence of ρ_{in} and T_b. Its detailed results are discussed below, but they suggest that $\Delta_{\text{vap}}H(\rho_{\text{in}}, T_b)$ presumably changes indeed smoothly with varying ρ_{in} and T_b, which paves the way for more efficient approximation methods for Eq. (31). Thus, in a second step, we replaced the Monte Carlo estimator by a Gauss–Hermite quadrature, which is a special case of Gauss quadrature on the real line. The general idea is that we replace the mean of randomly chosen samples as in the Monte Carlo estimator by a more sophisticated weighted average of specific samples. These samples are determined from specific quadrature nodes.[39] That is, for a smooth function f depending on a single variable, a number of samples N, and generic mean μ and variance σ^2, we replace the approximation

$$\frac{1}{\sqrt{2\pi}\sigma}\int_{\mathbb{R}} f(x)e^{-\frac{(x-\mu)^2}{2\sigma^2}}\,\mathrm{d}x \approx \frac{1}{N}\sum_{i=1}^{N} f(x_i), \tag{34}$$

with randomly chosen x_i, $i = 1, \ldots, N$, by

$$\frac{1}{\sqrt{2\pi}\sigma}\int_{\mathbb{R}} f(x)e^{-\frac{(x-\mu)^2}{2\sigma^2}}\,\mathrm{d}x \approx \frac{1}{\sqrt{\pi}}\sum_{i=1}^{N} \omega_i f\left(\sqrt{2}\sigma x_i + \mu\right), \tag{35}$$

where (ω_i, x_i), $i = 1, \ldots, N$, are the quadrature weights and nodes of the Gauss–Hermite quadrature, see also Eq. (25.4.46) and Table 25.10 in Abramowitz and Stegun[38] or Table S5 in the supplementary material for their specific values. The deterministic estimator for Eq. (31) then reads

$$\mathbb{E}[\Delta_{\text{vap}}H] \approx \frac{1}{\pi}\sum_{i,j=1}^{N} \omega_i\omega_j\Delta_{\text{vap}}H\left(\sqrt{2}\sigma_\rho x_i + \mu_\rho, \sqrt{2}\sigma_T x_j + \mu_T\right). \tag{36}$$

Given the presumed sufficient smooth dependence of $\Delta_{\text{vap}}H$ on ρ_{in} and T_b, the error of the Gauss–Hermite quadrature decays exponentially, i.e., like $\mathcal{O}(e^{-cN})$ for some $c > 0$, with the number of quadrature nodes N. Thus, the approximation of the integral Eq. (31) can be achieved with only a few QCE calculations on a standard laptop.

COMPUTATIONAL DETAILS

The quantum chemical calculations dealing with the investigated apolar liquids liquids have been carried out in a previous study, which provides more details about the computational protocol.[32] The clusters were built with the OGOLEM program package[49,50] in combination with the generalized AMBER force field.[51] The clusters contain up to ten monomers, and several distinct minima of the potential energy surface were selected. The geometry optimizations as well as frequency calculations were carried out with GFN2-xTB[6] using the `xtb` 6.2.1 program package.[52]

If not specified otherwise, all QCE computations were carried out at a fixed pressure of 101.325 kPa employing PEACEMAKER 2, our publicly available software package for neat and binary QCE calculations.[23,26,44] The cluster volumes were assumed to be van der Waals volumes with radii from Bondi's compilation.[53] The empirical parameters a_{mf} and b_{xv} were optimized in order to reproduce the boiling point and density at the given temperature (see Table I) as accurately as possible. Throughout this study, b_{xv} is treated as being temperature independent. In the QCE^0-calculations, the empirical parameters were set to $a_{\text{mf}} = 0.0$ and $b_{\text{xv}} = 1.0$, which results in the neglection of intercluster interactions and the unscaled van der Waals volume as the exclusion volume. For all calculations, the mRRHO correction with a rotor cutoff value of 100 cm^{-1} was used.

TABLE I. Experimental boiling points T_{b} in K with combined expanded uncertainties as well as reference densities $\rho_{T\text{ref}}$ in g cm^{-3} at reference temperatures T_{ref} in K. If not stated otherwise, the experimental data are taken from Ref. 54. The uncertainty of the experimental densities is estimated to be 0.0001 g cm^{-3}.

Substance	T_{b}	$\rho_{T\text{ref}}$	T_{ref}
Ethane	184.55 ± 0.40	0.5446	184.15
Ethylene	169.35 ± 0.30	0.5678	169.15
Propane	231.04 ± 0.09	0.5935[55]	220.00
Propylene	225.55 ± 0.10	0.6158[55]	220.00
Butane	272.65 ± 0.50	0.6041[55]	270.00
(*R*)-butan-2-ol	372.55 ± 0.20	0.8663	293.15
Methanol	337.65 ± 0.70	0.7914	293.15

SYSTEMS INVESTIGATED

In this study, we investigate seven organic substances: ethane, ethylene, propane, propylene, butane, methanol, and the chiral (*R*)-butan-2-ol. Ball-and-stick images of the respective molecules as well as some exemplary clusters of ethane and (*R*)-butan-2-ol are shown in Fig. 1. The first five substances represent nonpolar and aprotic hydrocarbons whose intermolecular interactions are mainly dominated by van der Waals interactions. In contrast, methanol and (*R*)-butan-2-ol are polar alcohols, which are able to form hydrogen bonds (see dotted lines in Fig. 1). Table I summarizes the experimental boiling points for all seven substances as well as the experimental densities at the respective reference temperatures.

RESULTS AND DISCUSSION

Calculating thermodynamic functions of vaporization

As already shown in previous studies,[32,56] the vaporization enthalpy of neat liquids at a specific temperature can be calculated by taking the difference between the absolute QCE^0-enthalpy and the absolute enthalpy obtained from a QCE calculation in which the empirical parameters were optimized, at the respective temperature. Similarly, the vaporization entropy can be obtained by subtracting

the absolute QCE entropy from the absolute QCE^0-entropy. Throughout this work, we will label this procedure for the calculation of thermodynamic vaporization functions as *standard QCE approach*.

However, another approach for the calculation of vaporization enthalpies makes use of the well-known Clausius–Clapeyron relation,[37]

$$\frac{dp}{dT} = \frac{\Delta H}{T \cdot \Delta V}, \tag{37}$$

which gives the slope of the tangents (dp/dT) on a coexistence curve in a pressure–temperature $(P–T)$ diagram. Here, ΔH is the enthalpy change and ΔV is the specific volume change for the phase transition. If only transitions from a condensed phase to the gas phase are considered and for temperatures far below the critical temperature, the specific volume change corresponds approximately to the gas phase volume. By using the ideal gas law, the relation shown above can be rewritten to obtain the Clausius–Clapeyron equation,

$$\frac{dp}{dT} = \frac{p \cdot \Delta_{\mathrm{vap}} H}{T^2 \cdot R}, \tag{38}$$

where R is the ideal gas constant. In practice, $\Delta_{\mathrm{vap}}H$ is a function of the temperature; however, for most systems, it only varies slightly with the temperature and is, thus, considered as constant. Applying this approximation allows the integration of the Clausius–Clapeyron equation, which yields the following expression:

$$\ln(p) = -\frac{\Delta_{\mathrm{vap}} H}{R} \cdot \frac{1}{T} + c. \tag{39}$$

Using Eq. (39), the enthalpy of vaporization can be calculated by plotting the natural logarithm of the pressure against the inverse of the boiling temperature (or in the case of a solid–gas transition, the sublimation temperature) under the respective pressure.

In order to obtain several data points on the liquid–gas coexistence curve, the boiling points of the respective substance have to be determined at different pressures. Using PEACEMAKER,[23,26,44] this can be done by first optimizing the two QCE parameters a_{mf} and b_{xv} at a pressure of one atmosphere based on the experimental boiling point and an experimental density. After that, QCE calculations can be performed at different pressures (in this case, ranging from 20 to 500 kPa in increments of 20 kPa) by using the optimized parameters a_{mf} and b_{xv} as fixed input parameters. Based on this procedure, the boiling point at a respective pressure corresponds to the temperature point at which the thermodynamic functions of the system experience the steepest slope. In order to identify this steepest slope, many thermodynamic functions can be used, such as the absolute enthalpy H, the absolute entropy S, the molar volume V, or the heat capacity c_{v}. However, note that this artificial phase transition is not always recognizable and does not necessarily correspond to the actual boiling point at the respective pressure. Throughout this work, we will label this procedure for the calculation of thermodynamic vaporization functions as the *Clausius–Clapeyron approach*.

In order to assess the quality of the standard QCE and the Clausius–Clapeyron approach, we calculated vaporization enthalpies for the seven investigated organic liquids. The results are summarized in Table II together with the experimental references. The absolute and relative deviations of the calculated enthalpies with respect to the experimental references are summarized in Table S1.

For the five aprotic systems, the vaporization enthalpies based on the standard QCE approach were already calculated in a previous study.[32] The obtained vaporization enthalpies of these systems were found to be in good agreement with the experimental references, showing deviations within a range of 0.44 (3.2%) to 5.21 kJ mol^{-1} (23.3%). Astonishingly, employing the Clausius–Clapeyron approach generally results in vaporization enthalpies that are only 0.13–0.29 kJ mol^{-1} smaller compared to the ones obtained with the standard QCE approach. Even though this results in a somewhat worse agreement with the experimental references, the largest difference between both approaches is observed for butane, with a deviation of 0.29 kJ mol^{-1} (<2%) between the two calculated values, thus being almost negligible. Consequently, the deviations of the vaporization enthalpies obtained with the Clausius–Clapeyron approach with respect to the experiment are similar compared to the standard QCE approach, between 0.67 (4.9%) and 5.50 kJ mol^{-1} (24.5%).

In addition to the investigation of the five aprotic systems, both approaches were applied to two protic substances as well, namely methanol and (*R*)-butan-2-ol, the last one being simply termed butanol. In the case of butanol, both approaches result in theoretical vaporization enthalpies that differ from each other by only 0.96 kJ mol^{-1} and agree almost perfectly with the experiment. The deviation from the experimental reference equals 0.48 kJ mol^{-1}, respectively, with the standard QCE approach underestimating the experimental value and the Clausius–Clapeyron approach overestimating it. Thus, we see that butanol is the only system investigated for which the Clausius–Clapeyron approach yields a larger vaporization enthalpy than the standard QCE approach. For methanol, the standard QCE approach yields a vaporization enthalpy of 43.13 kJ mol^{-1} while the Clausius–Clapeyron approach results in a smaller value of only 41.60 kJ mol^{-1}. This system shows the largest difference between both theoretical methods, which equals to 1.53 kJ mol^{-1}. The deviations to the experimental reference are 5.73 kJ mol^{-1} (15.3%) for the standard QCE approach and 4.20 kJ mol^{-1} (11.2%) for the Clausius–Clapeyron approach. Methanol is, therefore, the only system investigated for which both approaches overestimate the

TABLE II. Calculated enthalpies of vaporization using the standard QCE approach, $\Delta_{\mathrm{vap}}^{\mathrm{calc}}H$ [see Eq. (25)], and the Clausius–Clapeyron approach, $\Delta_{\mathrm{vap}}^{\mathrm{clau}}H$ [see Eq. (39)], as well as experimental vaporization enthalpies, $\Delta_{\mathrm{vap}}^{\mathrm{exp}}H$, in kJ mol^{-1} averaged from various references and measured at the according transition temperatures T in K.

Substance	$\Delta_{\mathrm{vap}}^{\mathrm{calc}}H$	$\Delta_{\mathrm{vap}}^{\mathrm{clau}}H$	$\Delta_{\mathrm{vap}}^{\mathrm{exp}}H$	T
Ethane	13.50[32]	13.37	14.7[54,57]	184
Ethylene	13.21[32]	12.98	13.6[54,58,59]	169
Propane	15.15[32]	14.97	18.9[54,60]	231
Propylene	15.55[32]	15.32	18.8[54,59,61]	225
Butane	17.20[32]	16.91	22.4[54,62]	272
(*R*)-butan-2-ol	49.22	50.18	49.7[54]	298
Methanol	43.13	41.60	37.4[54]	298

experimental vaporization enthalpy. Such an overestimation of the vaporization enthalpy has already been observed before[46] and might be due to the reason that methanol molecules aggregate to small clusters in the gas phase,[63] which is not properly sampled by the QCE^0-calculations.

To summarize, the deviations from the experimental vaporization enthalpies are found to lie within a range of 0.44–5.73 kJ mol^{-1} for the standard QCE approach and within a range of 0.48 –5.50 kJ mol^{-1} for the Clausius–Clapeyron approach. The corresponding mean absolute deviations (MADs) equal 2.86 kJ mol^{-1} (12.57%) for the standard QCE approach and 2.79 kJ mol^{-1} (12.84%) for the Clausius–Clapeyron approach, which is within chemical accuracy for the calculation of thermodynamic properties and is, therefore, an acceptable error. Both approaches can thus be considered to perform equally well for the calculation of vaporization enthalpies.

Similar to the total enthalpy, the total entropy of a system can be calculated using the QCE method. Based on that, the vaporization entropy can be obtained in the same manner as the vaporization enthalpy, i.e., by the difference between the total gas phase entropy and the total liquid phase entropy at a given temperature.[32] Yet another possibility to obtain the vaporization entropy of a specific system is its calculation based on the vaporization enthalpy at the boiling point. By exploiting the Gibbs–Helmholtz equation,

$$\Delta G = \Delta H - T \cdot \Delta S, \tag{40}$$

and the fact that ΔG is equal to zero for a phase transition at the boiling point, the vaporization entropy can be expressed as follows:

$$\Delta_{\mathrm{vap}} S = \Delta_{\mathrm{vap}} H / T_{\mathrm{b}}. \tag{41}$$

Here, ΔG, ΔH, and ΔS are the changes in Gibbs energy, enthalpy, and entropy, respectively. Consequently, the enthalpy and entropy changes at the boiling point correspond to the vaporization enthalpy $\Delta_{\mathrm{vap}}H$ and vaporization entropy $\Delta_{\mathrm{vap}}S$. Assuming that the vaporization enthalpy remains constant under temperature changes, vaporization entropies at the boiling point can be calculated based on Eq. (41) as the ratio of the vaporization enthalpy obtained by the Clausius–Clapeyron approach and the boiling temperature. For this reason, we calculated the vaporization entropies solely at the boiling point.

We employed the standard QCE and the Clausius–Clapeyron approach [Eq. (41)] to calculate the vaporization entropies at the boiling points for all seven liquids. The results and the corresponding experimental references are summarized in Table III. The absolute and relative deviations of the calculated entropies with respect to the experimental references are summarized in Table S2. Note that for the aprotic substances, the corresponding values obtained with the standard QCE approach were already calculated in a previous study.[32] Comparing the experimentally observed vaporization entropies of the five aprotic liquids with the value of ≈88 J mol^{-1} K^{-1} predicted by Trouton's rule,[64,65] overall, a good agreement can be observed. Although the experimental references are about 6–8 J mol^{-1} K^{-1} smaller, the application of Trouton's rule seems to be justified here. Considering the vaporization entropies calculated by the standard QCE and the Clausius–Clapeyron approach, both approaches consistently underestimate the experimental references of the five aprotic compounds. Thereby, the

TABLE III. Calculated entropies of vaporization using the standard QCE approach $\Delta_{\mathrm{vap}}^{\mathrm{calc}}S$ [see Eq. (26)] and the Clausius–Clapeyron approach $\Delta_{\mathrm{vap}}^{\mathrm{clau}}S$ based on Eq. (41) as well as experimental vaporization entropies $\Delta_{\mathrm{vap}}^{\mathrm{exp}}S$ in J mol^{-1} K^{-1} and the according transition temperatures T in K.

Substance	$\Delta_{\mathrm{vap}}^{\mathrm{calc}}S$	$\Delta_{\mathrm{vap}}^{\mathrm{clau}}S$	$\Delta_{\mathrm{vap}}^{\mathrm{exp}}S$	T
Ethane	73.13[32]	72.66	79.87[57]	184
Ethylene	77.99[32]	76.82	79.96[58]	169
Propane	65.58[32]	64.81	81.26[60]	231
Propylene	68.95[32]	68.10	81.73[61]	225
Butane	63.08[32]	62.19	82 × 10[62]	272
(*R*)-butan-2-ol	139.27	134.89	109.35[54]	372
Methanol	124.79	123.45	104.25[54]	337

Clausius–Clapeyron approach results in vaporization entropies that are 0.47–1.17 J mol^{-1} K^{-1} (<2%) smaller than the ones obtained with the standard QCE approach. The vaporization entropies obtained with the standard QCE approach differ from the experimental references by 1.97 (2.5%) to 19.02 J mol^{-1} K^{-1} (23.2%). When considering the Clausius–Clapeyron approach on the other hand, the deviations of the obtained vaporization entropies lie within a range of 3.14 (3.9%) to 19.91 J mol^{-1} K^{-1} (24.5%). Thus, it can be concluded that both approaches perform comparably well for the calculation of vaporization entropies in the case of aprotic substances.

The vaporization entropies of the protic liquids are overestimated by both approaches. The experimental reference of butanol is overestimated by 29.92 (27.4%) and 25.54 J mol^{-1} K^{-1} (23.4%) when considering the standard QCE and Clausius–Clapeyron approach, respectively. The reference of methanol is overestimated by 20.54 (19.7%, standard QCE) and 19.20 J mol^{-1} K^{-1} (18.4%, Clausius–Clapeyron). As already mentioned in the last section, this is most likely due to the fact that the gas phase of the polar alcohols is not described properly by a QCE^0-calculation.[46]

In summary, when considering the standard QCE approach, the deviations from the experimental vaporization entropies are within a range of 1.97 (2.5%) to 29.92 J mol^{-1} K^{-1} (27.4%). Considering the Clausius–Clapeyron approach, on the other hand, results in deviations of 3.14 (3.9%) to 25.54 J mol^{-1} K^{-1} (23.4%). The corresponding MADs for the calculated vaporization entropies are 15.23 J mol^{-1} K^{-1} for the standard QCE approach and 15.01 J mol^{-1} K^{-1} for the Clausius–Clapeyron approach. Although these values imply a slightly better performance of the Clausius–Clapeyron approach, the difference between the MADs is negligible and, overall, both approaches can be considered to perform equally well for the calculation of vaporization entropies. However, as an advantage, the QCE approach allows the calculation of vaporization entropies at every temperature, while the Clausius–Clapeyron approach is restricted to the boiling point only. Additionally, the application of the Clausius–Clapeyron approach is computationally more cumbersome compared to the standard QCE approach. As explained earlier, the standard QCE approach requires only two QCE calculations: one of them performing an optimization of a_{mf} and b_{xv} and the other one serving as gas phase reference employing $a_{\mathrm{mf}} = 0.0$ and $b_{\mathrm{xv}} = 1.0$. The Clausius–Clapeyron approach, on the other hand, requires an optimization of a_{mf} and b_{xv} as well; however, these optimized

parameters have to be employed for further QCE calculations at different pressures. Since in the present case, we sample a pressure range from 20 to 500 kPa in increments of 20 kPa, this sampling procedure corresponds to 25 QCE calculations, which sums up to a total of 26 QCE calculations for the present application of the Clausius–Clapeyron approach. Although the computing time of QCE calculations with fixed parameters a_{mf} and b_{xv} is only a matter of seconds, the computational superiority of the standard QCE approach becomes relevant if the calculation of a huge amount of vaporization enthalpies or entropies is desired. Since the quantification of the influence of uncertainties in the physical input quantities on the results of QCE calculations requires the execution of many QCE computations, we will base the following discussion on the standard QCE approach.

Varying the input quantities density and boiling point: Enthalpy

As mentioned above, the two empirical parameters a_{mf} and b_{xv} are optimized in order to reproduce some experimental reference data as accurately as possible. Since these data are prone to measurement errors within the experiments, the uncertainty of the experimental data will inevitably affect the results of a QCE computation and, thus, the calculated thermodynamics of vaporization. In order to investigate the dependence of the calculated vaporization thermodynamics with respect to uncertainties in the experimental input data, we intentionally increased and decreased the employed reference densities and boiling points (see Table I) by 20%, respectively, using increments of 1%. This investigation is necessary in order to verify the smoothness of the thermodynamic functions with respect to the input quantities since this is required for one of the statistical methods used in a later chapter. The large range of ±20% was chosen in order to ensure that there are no discontinuities in these dependencies, even when input values far from the experimental reference are considered. Note that the minimum boiling point that can be employed corresponds to the temperature at which the experimental vaporization enthalpy or entropy was measured. This is due to the fact that further lowering of the input boiling point would lead to an early gas phase in the QCE model for which no vaporization enthalpy can be calculated.

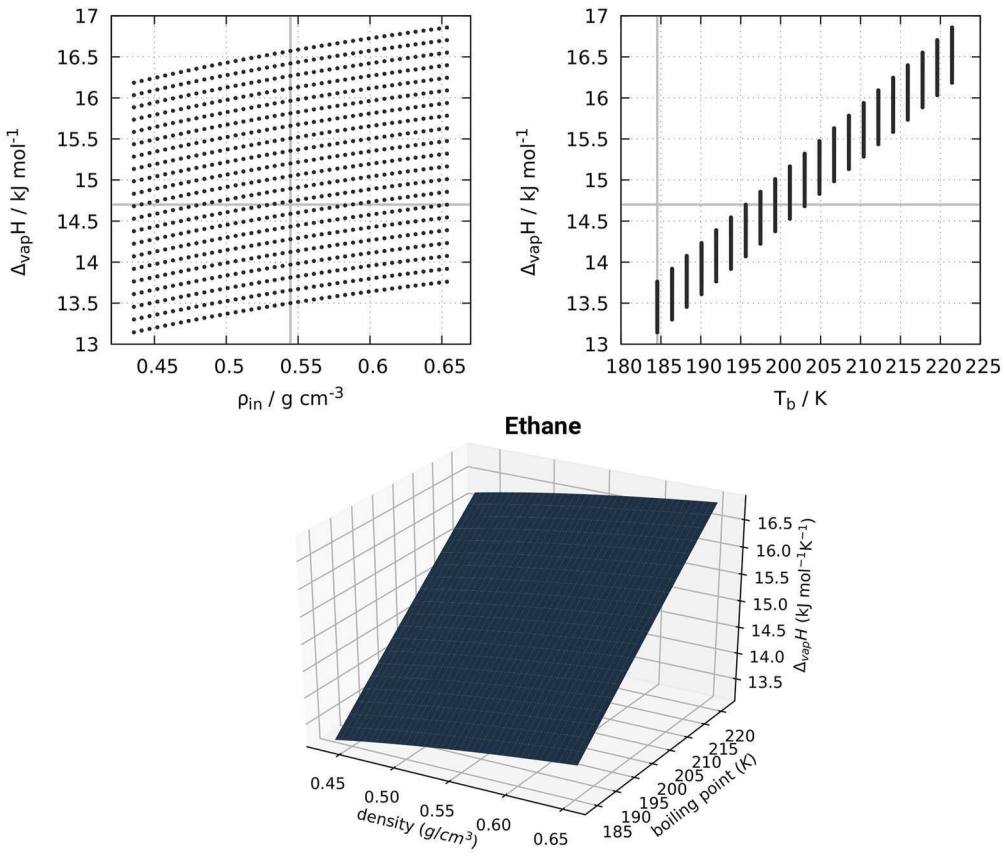

FIG. 2. Enthalpies of vaporization ($\Delta_{vap}H$) of ethane calculated at 184 K using the standard QCE approach [Eq. (25)]. Left: plotted vs input density, each curve represents a constant boiling point (from 184.55 to 221.46 K). Right: plotted vs the input boiling point, each curve represents a constant density (from 0.4357 to 0.6535 g cm^{-3}). Vertical line: reference boiling point (left)[54] and density (right);[54] horizontal lines: experimental $\Delta_{vap}H$ at 184 K.[54,57]

Therefore, for the vaporization enthalpies, the boiling points of butanol and methanol could be decreased by 19% and 11%, respectively, while this was not reasonable for the other solvents. Using these input values, we calculated the corresponding vaporization enthalpies for each resulting combination of boiling point and density. This analysis was performed for all seven investigated compounds and the obtained vaporization enthalpies were plotted against the corresponding densities and boiling points. The results for ethane and butanol are shown in Figs. 2 and 3, respectively. The corresponding graphs for the remaining substances can be found in the supplementary material, Figs. S1–S5. Additionally, Table IV summarizes the vaporization enthalpies obtained with the minimum and maximum densities and boiling points as well as the relative deviations to the vaporization enthalpies obtained with the experimental reference data.

In general, Figs. 2 and 3 show that the vaporization enthalpy changes smoothly upon varying the density and boiling point, which paves the way for the later application of the Gauss–Hermite quadrature rather than the Monte Carlo method for the computation of Eq. (31). This behavior is observed for the other systems as well (see the supplementary material, Figs. S1–S5). Considering the variation of the density in greater detail, both Figs. 2 and 3 as well as the data reported in Table IV suggest that the density variations have only a small influence on the calculated vaporization enthalpies. Considering ethane as an example, when employing its boiling point of 184.55 K combined with densities varying from 0.4357 to 0.6535 g cm^{-3}, the obtained vaporization enthalpies are found to lie within a range of 13.14–13.76 kJ mol^{-1}. The deviations with respect to the vaporization enthalpy obtained with the reference density of 0.5446 g cm^{-3} (13.50 kJ mol^{-1}) are equal to 0.36 (decreased density) and 0.26 kJ mol^{-1} (increased density), respectively. Thus a density variation of ±20% causes a relative decrease/increase of only 2.6%/1.9% in the vaporization enthalpy of ethane. A similar behavior is observed for butanol as well. Here, a combination of the reference boiling point with densities varying from 0.6930 to 1.0396 g cm^{-3} results in vaporization enthalpies lying within a range of 48.81 –49.56 kJ mol^{-1}. The deviations with respect to the vaporization enthalpy obtained with the reference density of 0.8663 g cm^{-3} (49.22 kJ mol^{-1}) are equal to 0.41 (decreased density) and 0.34 kJ mol^{-1} (increased density), respectively, which corresponds

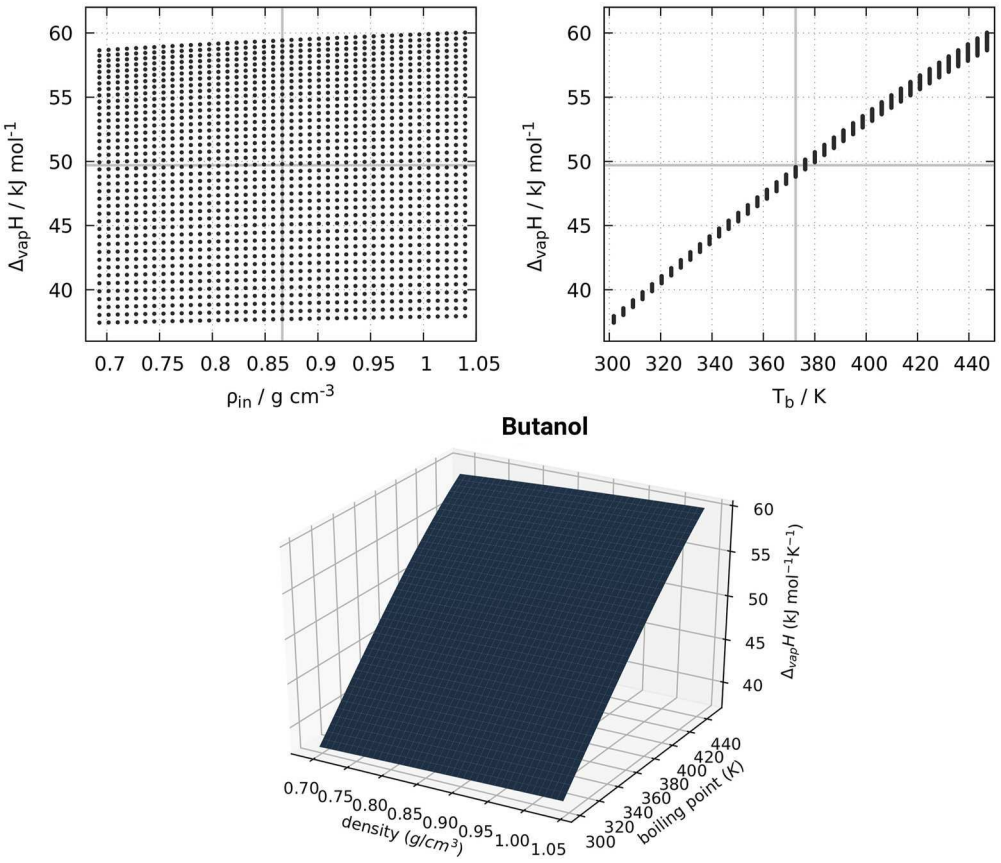

FIG. 3. Enthalpies of vaporization ($\Delta_{vap}H$) of (*R*)-butan-2-ol calculated at 298 K using the standard QCE approach [Eq. (25)]. Left: plotted vs input density, each curve represents a constant boiling point (from 301.77 to 447.06 K). Right: plotted vs the input boiling point, each curve represents a constant density (from 0.6930 to 1.0396 g cm^{-3}). Vertical line: reference boiling point (left)[54] and density (right);[54] horizontal lines: experimental $\Delta_{vap}H$ at 298 K.[54]

TABLE IV. Calculated enthalpies of vaporization (kJ mol^{-1}) obtained from the standard QCE approach [see Eq. (25)] employing the experimental reference densities $\rho_{T\mathrm{ref}}$ and boiling points T_b as well as by 20% decreased and increased reference densities ($\rho_{T\mathrm{ref},-20\%}$ and $\rho_{T\mathrm{ref},+20\%}$) and boiling points [$T_{\mathrm{b,\,min}}$ (as explained in the text) and $T_{\mathrm{b},+20\%}$]. The values in parentheses denote the relative deviation from the enthalpies obtained with $\rho_{T\mathrm{ref}}$ and T_b.

Substance	$\rho_{T\mathrm{ref}}$	$\rho_{T\mathrm{ref},-20\%}$	$\rho_{T\mathrm{ref},+20\%}$	T_b	$T_{\mathrm{b,\,min}}$	$T_{\mathrm{b},+20\%}$
Ethane	13.50	13.14 (2.6%)	13.76 (1.9%)	13.50	⋯	16.57 (22.6%)
Ethylene	13.21	12.81 (3.1%)	13.52 (2.3%)	13.21	⋯	16.27 (23.2%)
Propane	15.15	14.51 (4.2%)	15.62 (3.1%)	15.15	⋯	18.83 (24.3%)
Propylene	15.55	14.87 (4.3%)	16.09 (3.5%)	15.55	⋯	19.35 (24.4%)
Butane	17.20	16.35 (5.0%)	17.65 (2.6%)	17.20	⋯	21.22 (23.4%)
(*R*)-butan-2-ol	49.22	48.81 (0.8%)	49.56 (0.7%)	49.22	37.72 (23.4%)	59.42 (20.7%)
Methanol	43.13	42.90 (0.5%)	43.31 (0.4%)	43.13	38.11 (11.6%)	51.78 (20.1%)

to relative deviations <1%. Given the fact that the uncertainty of experimental densities can be estimated to be around 0.0001 g cm^{-3} (≪1%), it can be expected that these experimental uncertainties will not significantly affect the vaporization enthalpies obtained by the standard QCE approach.

Nevertheless, some interesting trends are recognizable from the data shown in Table IV. It can be observed that for all investigated substances, a decrease in the density consistently causes a decrease in the vaporization enthalpy and vice versa. This is reasonable, since a decrease in the liquid phase density results in the liquid

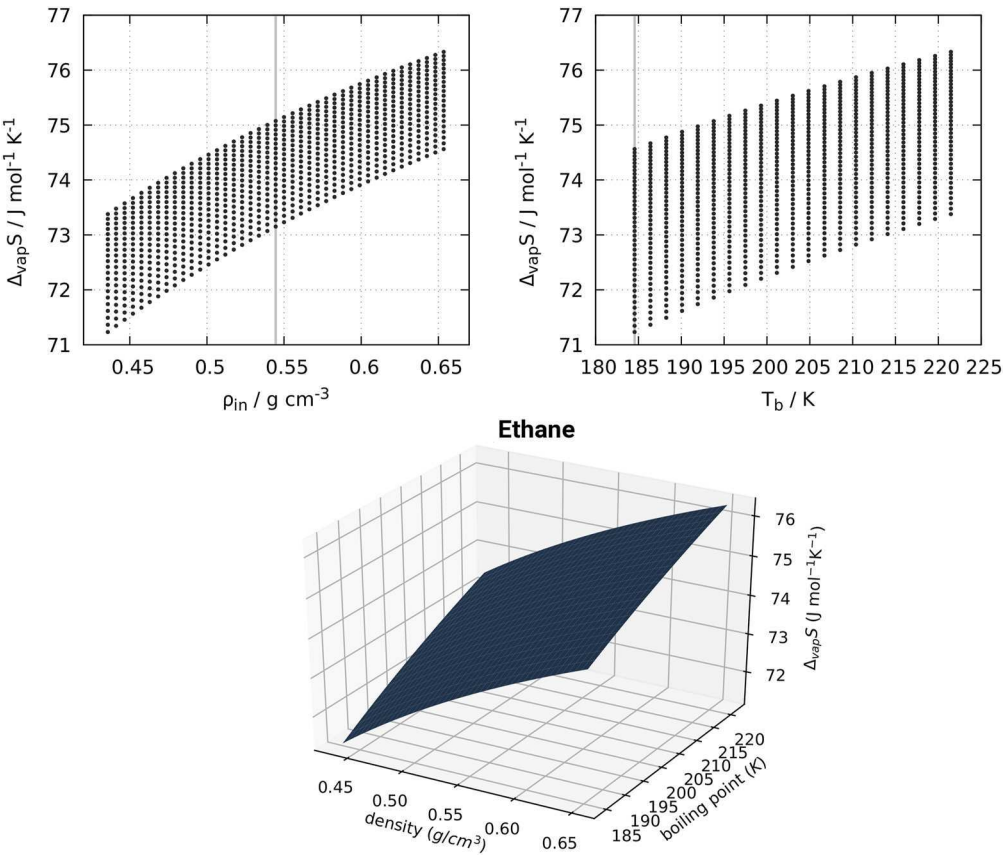

FIG. 4. Entropies of vaporization ($\Delta_\mathrm{vap}S$) of ethane calculated at 184 K using the standard QCE approach [Eq. (26)]. Left: plotted vs input density, each curve represents a constant boiling point (from 184.55 to 221.46 K). Right: plotted vs the input boiling point, each curve represents a constant density (from 0.4357 to 0.6535 g cm^{-3}). Vertical line: reference boiling point (left)[54] and density (right).[54]

phase becoming more similar to the gas phase. However, the aprotic substances seem to be more sensitive to density variations than the protic ones, i.e., a density variation of ±20% induces deviations of 1.9%–5.0% in the vaporization enthalpies of the aprotic liquids while the relative deviations observed for the protic substances are found to lie only between 0.4% and 0.8%. This is due to the fact that the main interactions in the protic substances are hydrogen bonds, which are not affected by the QCE parameters and experimental inputs.

Variations in the boiling points have a significantly larger influence on the calculated vaporization enthalpies, which is immediately recognizable from Figs. 2 and 3. While in the case of ethane, a density increase of 20% causes an increase in the vaporization enthalpy by only 0.26 kJ mol^{-1}, increasing the boiling point by 20% resultes in an increase in the vaporization enthalpy by 3.07 kJ mol^{-1}. For comparison, this corresponds to an almost negligible increase in the vaporization enthalpy by 1.9% upon density variation but to an increase of 22.6% upon variation of the boiling point. A similar behavior is observed for all other investigated substances as well, and an increase in the boiling point by 20% induces an increase in the vaporization enthalpies by more than 20% for all substances investigated. Since a decrease in the boiling point was only reasonable for methanol and butanol, a detailed investigation on how the vaporization enthalpies change upon a boiling point decrease is not feasible here; however, the results obtained for methanol and butanol suggest that a lowering of the boiling point has a similarly strong effect on the vaporization enthalpies as its increase. In the case of butanol, a decrease in the boiling point by 19% results in a decrease in the vaporization enthalpy by 11.50 kJ mol^{-1} (23.4%), and in the case of methanol, a decrease in the boiling temperature by 11% causes a decrease in the vaporization enthalpy by 5.02 kJ mol^{-1} (11.6%).

It can thus be concluded that the high sensitivity of vaporization enthalpies with respect to the employed boiling points necessitates the availability of accurate reference data. However, considering the expanded uncertainties of the experimental boiling temperatures summarized in Table I, the estimated measurement errors are typically below 1 K (<1%). This suggests that typical inaccuracies of experimental boiling points will not significantly affect the calculation of vaporization enthalpies when employing the standard QCE approach.

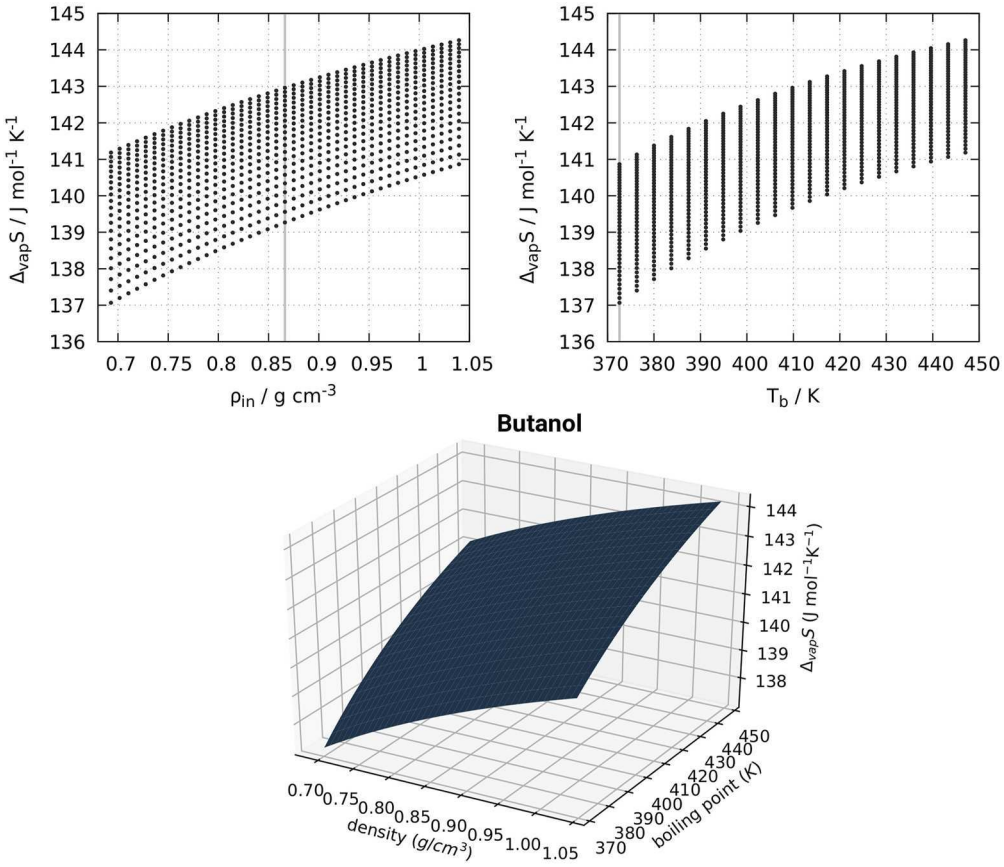

FIG. 5. Entropies of vaporization ($\Delta_{vap}S$) of (*R*)-butan-2-ol calculated at 372 K using the standard QCE approach [Eq. (26)]. Left: plotted vs input density, each curve represents a constant boiling point (from 372.55 to 447.06 K). Right: plotted vs the input boiling point, each curve represents a constant density (from 0.6930 to 1.0396 g cm^{-3}). Vertical line: reference boiling point (left)[54] and density (right).[54]

Varying the two input quantities density and boiling point: Entropy

In order to investigate the dependence of the vaporization entropies with respect to changes in the input densities and boiling points, we performed the analysis employed in the previous section for the calculation of vaporization entropies as well. Note that for the calculation of the vaporization entropies, a decrease in the boiling point is not physically meaningful, since the entropies are calculated at the respective reference boiling temperature. The results for ethane and butanol are shown in Figs. 4 and 5, and Table V summarizes the vaporization entropies obtained with the minimum and maximum densities and boiling points as well as the relative deviations to the vaporization entropies obtained with the experimental reference data. The corresponding graphs for the remaining systems can be found in the supplementary material, Figs. S6–S10.

As already observed for the vaporization enthalpies, the vaporization entropies change smoothly upon varying the density and boiling point. The influence of density variations on the vaporization entropies is comparable to what has been observed for the vaporization enthalpies and a decrease/increase in the density consistently causes a decrease/increase in the vaporization entropy. In case of the investigated aprotic substances, a 20% decrease in the densities causes a decrease in the vaporization entropies by 2.6%–4.9%. A 20% increase in the density on the other hand causes an increase in the vaporization entropies by 2.0%–3.4%. Considering the protic liquids methanol and butanol, density variations have an even smaller influence and the vaporization entropies change by only 0.7%–1.6% when the density is varied by ±20%.

While the variation of the boiling point was found to have a strong influence on the vaporization enthalpies, the vaporization entropies seem to be less prone to changes in the boiling temperature. For instance, increasing the boiling point of ethane by 20% causes an increase in the corresponding vaporization entropy from 73.13 to 75.07 J mol^{-1} K^{-1}. This corresponds to an almost negligible increase of 1.94 J mol^{-1} K^{-1} or 2.7%. The remaining systems show a similar dependence on the variation of the boiling point, and the relative changes of the vaporization entropies induced by a 20% increase of the boiling temperature are found to lie within a range of 1.4%–4.3%.

Overall, it can be concluded that density and boiling point variations have similar effects on the vaporization entropies. While the density has a similar influence on the vaporization enthalpies and entropies, the boiling point has a much stronger effect on the vaporization enthalpies than on the entropies. This effect can be attributed to the fact that the entropy calculated in the QCE model [see Eq. (26)] is not directly dependent on the electronic partition function q_{elec} and, thus, not directly dependent on the mean field parameter a_{mf}. Since the main influence of the variation of the boiling point is observed in a strong change of the a_{mf} parameter, as discussed further in the next section, this results in a smaller dependence of the entropy on the input boiling point. Given the fact that the typical uncertainties of experimental densities and boiling points are <1% (see Table I), these inaccuracies will usually not significantly affect the calculation of vaporization entropies with the standard QCE approach.

Varying the two input quantities density and boiling point: Cluster populations

In order to investigate the dependence of the cluster populations with respect to the input quantities, Figs. 6 and 7 show the respective cluster populations of ethane and butanol obtained with the experimental reference data from Table I as well as the cluster populations obtained with the minimum and maximum densities and boiling points. For the sake of clarity, we summarized the populations of the monomers, dimers, trimers, and larger oligomers (>3 monomers), respectively.

For ethane, the larger oligomers are found to be the dominant species at low temperatures. However, with increasing temperature, the populations of these clusters decrease at the expense of increasing monomer, dimer, and trimer populations. The transition from the condensed to the gas phase manifests as a sharp transition at which the monomers become the dominant species. The dimers are only minorly populated.

Figure 6 shows that an increase or decrease in the density has only a small influence on the cluster populations (compare vertical plots), which explains the small influence of density variations on the calculated vaporization thermodynamics. Nevertheless, some interesting changes can be observed. First of all, an increasing

TABLE V. Calculated entropies of vaporization (J mol^{-1} K^{-1}) obtained from the standard QCE approach [see Eq. (26)] employing the experimental reference densities $\rho_{T\mathrm{ref}}$ and boiling points T_{b} as well as the by 20% decreased and increased reference densities ($\rho_{T\mathrm{ref},-20\%}$ and $\rho_{T\mathrm{ref},+20\%}$) and boiling points ($T_{\mathrm{b},-20\%}$ and $T_{\mathrm{b},+20\%}$). The values in parentheses denote the relative deviation from the enthalpies obtained with $\rho_{T\mathrm{ref}}$ and T_{b}.

Substance	$\rho_{T\mathrm{ref}}$	$\rho_{T\mathrm{ref},-20\%}$	$\rho_{T\mathrm{ref},+20\%}$	T_{b}	$T_{\mathrm{b},-20\%}$	$T_{\mathrm{b},+20\%}$
Ethane	73.13	71.23 (2.6%)	74.56 (2.0%)	73.13	⋯	75.07 (2.7%)
Ethylene	77.99	75.63 (3.0%)	79.83 (2.4%)	77.99	⋯	80.56 (3.3%)
Propane	65.58	62.79 (4.2%)	67.71 (3.2%)	65.58	⋯	68.19 (4.0%)
Propylene	68.95	66.01 (4.3%)	71.32 (3.4%)	68.95	⋯	71.90 (4.3%)
Butane	63.08	59.96 (4.9%)	64.73 (2.6%)	63.08	⋯	65.08 (3.2%)
(*R*)-butan-2-ol	139.27	137.07 (1.6%)	140.86 (1.1%)	139.27	⋯	142.96 (2.7%)
Methanol	124.79	123.70 (0.9%)	125.60 (0.7%)	124.79	⋯	126.59 (1.4%)

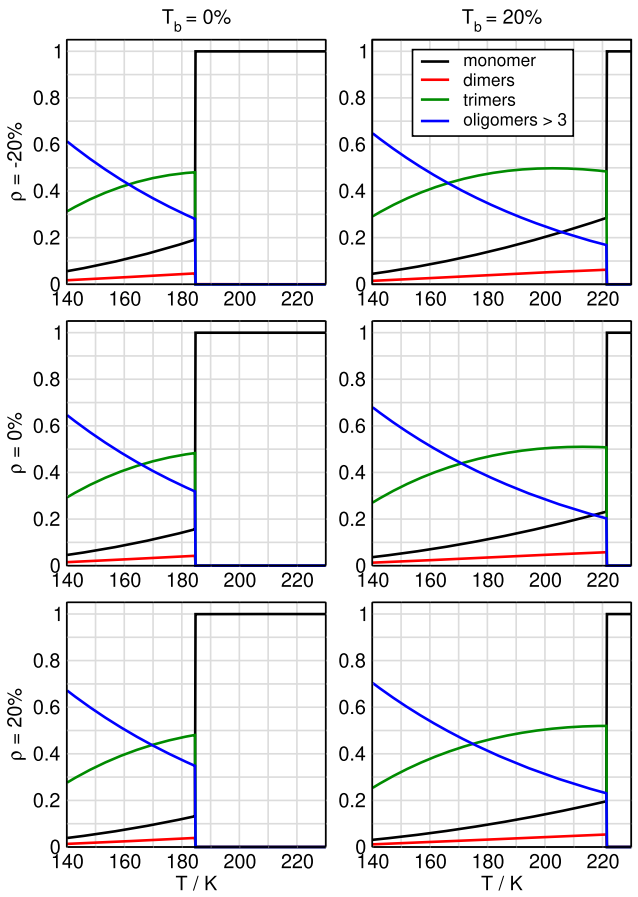

FIG. 6. QCE populations of ethane clusters grouped into monomers, dimers, trimers, and larger oligomers. Every panel resembles a different combination of reference input values.

density causes increasing populations of the larger ethane oligomers, mainly at the expense of trimer populations at low temperatures and at the expense of monomer populations close to the phase transition. The larger oligomers are preferentially occupied since the larger aggregates are better suited for the representation of a liquid with increased density. A decrease in the density on the other hand causes decreasing oligomer populations and increasing monomer and trimer populations, as the small clusters better represent a lower density. The density variation, thus, changes the temperature at which the trimer populations exceed the ones of the larger oligomers, i.e., a decrease/increase in the density shifts the intersection of these populations to lower/higher temperatures. A similar behavior is observed for the other aprotic substances as well. The corresponding population plots are shown in the supplementary material, Figs. S11–S14.

These observations provide a possible explanation for the influence of the density on the vaporization enthalpies. Since a density increase favors the population of larger clusters, an increased amount of energy is required to split these clusters into monomers during the transition from the condensed to the gas phase, which causes an increase in the vaporization enthalpy. The same applies the other way around: A reduced density favors the occupation of small clusters and reduces the amount of energy that is needed to split these clusters into monomers during the phase transition, causing a decrease in the vaporization enthalpy.

A smaller sensitivity with respect to density variations is observed for the butanol populations shown in Fig. 7. Considering the results obtained with the experimental reference temperature, the liquid phase is continuously dominated by the large oligomers. Below 300 K, these clusters make up the entire population, whereas their populations slowly decrease above 300 K at the expense of increasing monomer, dimer, and trimer populations. The phase transition manifests again as a sharp transition and the gas phase is solely composed of monomers. An influence of the density variation on the populations is only recognizable close to the boiling point, where a decrease/increase in the density causes a decrease/increase in the populations of the larger oligomers.

Variations in the boiling temperature have a much more pronounced influence on the cluster populations (compare horizontal plots). In the case of ethane, an increase in the boiling temperature causes a decrease in the monomer population at a given temperature, mainly at the expense of greater oligomer populations. This can be understood in the sense that larger clusters are required to keep the system in the condensed phase over a wider temperature range. Thus, the same effect as observed for the density applies for the boiling temperature: An increase in the respective quantity leads to an increased population of large clusters.

When employing the experimental reference boiling point, the liquid phase of butanol is mainly composed of oligomers, whose populations decrease toward the phase transition at the expense of increasing monomer, dimer, and trimer populations. An increase in the boiling point on the other hand leads to increased monomer, dimer, and trimer populations in the liquid phase close to the phase transition. However, considering the temperature at which the vaporization enthalpy was calculated, i.e., 298 K, variations in the boiling point barely induce any change in the populations at this particular temperature. Here, the larger oligomers are the dominant species and occupy the entire population; thus, a closer look into the oligomer populations is required in order to identify the reasons for the changes in the vaporization enthalpy. We observe that there are three oligomers that make up most of the oligomer populations: a tetramer, an octamer, and a nonamer (see Fig. S16). At 298 K, a decrease in the boiling point leads to an increase in the tetramer population and a simultaneous decrease in the octamer and nonamer populations. An increase in the boiling point on the other hand causes a decreased tetramer population and increased populations of the octamer and nonamer. These findings are in agreement with what has been observed for ethane. Therefore, it can be concluded that a decrease in the boiling temperature induces increased populations of small clusters while an increase in the boiling temperature induces increased populations of larger clusters.

The observations from the last three sections are supported by the changes in the empirical parameters a_{mf} and b_{xv} in dependence of the experimental inputs. All empirical parameters obtained from the QCE calculations with increased/decreased density and boiling point are given in the supplementary material, Tables S3 and S4. For the case of butanol, increasing the boiling point by 20%

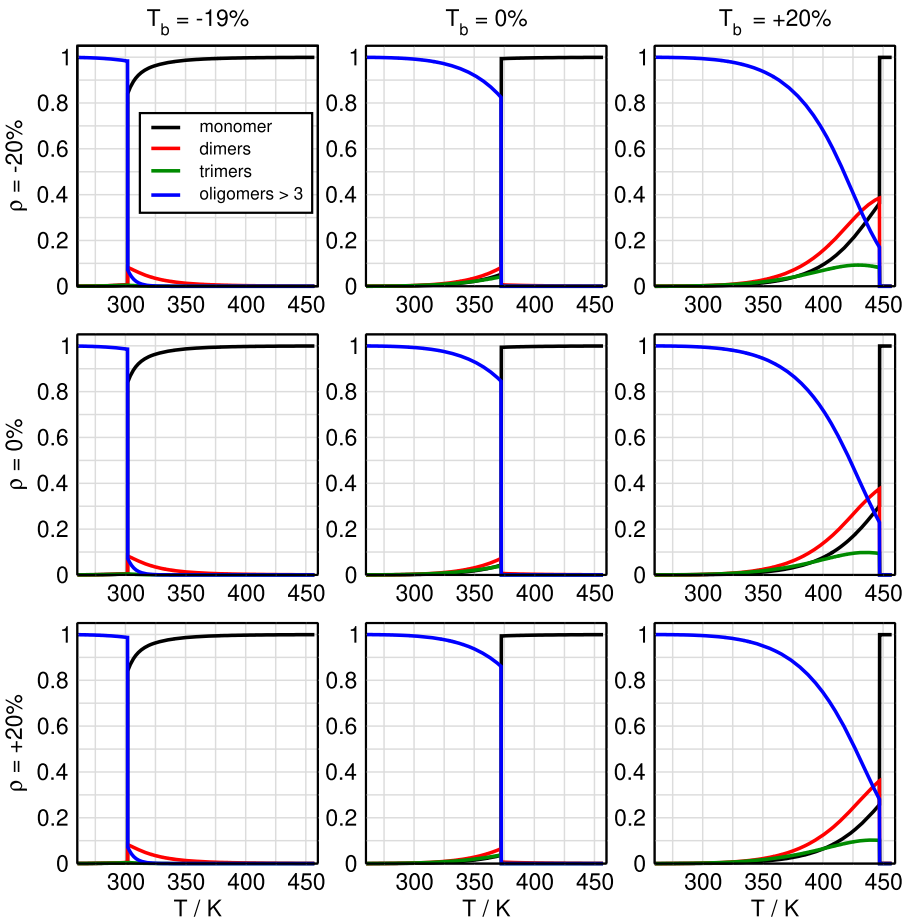

FIG. 7. QCE populations of (*R*)-butan-2-ol clusters grouped into monomers, dimers, trimers, and larger oligomers. Every panel resembles a different combination of reference input values.

increases the mean field parameter a_{mf} from 1.43 to 2.28 J m^3 mol^{-2} while a decrease in the boiling point decreases the parameter to 0.50 J m^3 mol^{-2}. This behavior is in agreement with the previous explanation that stronger interactions between the clusters are required in order to increase the temperature range in which the system stays liquid (and vice versa). Variations in the density influence the mean field parameter much less, decreasing it to 1.21 J m^3 mol^{-2} for an increase in density and increasing it to 1.77 J m^3 mol^{-2} for a decrease in density.

However, the b_{xv} parameter, which scales the cluster volumes, is strongly influenced by density variations. Here, an increase in the density by 20% yields significantly smaller cluster volumes with b_{xv} decreasing from 0.90 to 0.75. A decrease in the density yields a value of 1.12. This is again in agreement with the previous explanations inasmuch as smaller cluster volumes lead to the clusters being closer together, ultimately increasing the density. In contrast to this, b_{xv} seems to be only slightly affected by variations in the boiling temperature, increasing to 0.91 for an increase in the boiling point and decreasing to 0.84 for a decrease in the boiling point. These observations additionally point to the fact that the cluster volume scaling parameter b_{xv} is mainly influenced by the density while the mean field parameter a_{mf} is mainly influenced by the boiling point.

Uncertainty quantification

Up to now, we have examined the sensitivity of the cluster populations and vaporization thermodynamics with respect to changes in the input densities and boiling points. As a last step, we want to quantify the uncertainty that stems from inaccuracies in the experimental input data using the vaporization enthalpy of butanol as an example. Note that we chose butanol as an example because the statistical methods require a slight lowering of the input boiling point, which is physically not meaningful for the investigated apolar systems, as discussed earlier. We considered the density and boiling point as normally distributed quantities with standard deviations equal to the experimental uncertainties (see Table I) and with the experimental values corresponding to the mean of the distribution. Based on the above assumptions, we calculated a realization of the Monte Carlo estimator using different numbers of data points up to $N = 10^6$ as well as the Gauss–Hermite quadrature with up to $N = 9$ quadrature nodes. As a reference, we take the Gauss–Hermite estimator with $N = 10$, which, from the numerical results below, seems to be sufficiently accurate. The random input quantities for the Monte Carlo estimator were created using the Box–Muller transform.

Table VI summarizes some of the calculated estimators. In general, it can be seen that the Monte Carlo estimator approaches the

TABLE VI. Calculated estimators $\mathbb{E}[\Delta_{vap}H]$ in kJ mol^{-1} for the enthalpy of vaporization of (*R*)-butan-2-ol from the Gauss–Hermite quadrature method with $N = 10$ and from the Monte Carlo method using different numbers of data points up to one million. The standard deviation $\sigma[\Delta_{vap}H]$ computed with the Gauss–Hermite quadrature equals $30.951\,207\,76 \cdot 10^{-3}$ kJ mol^{-1}.

Method	$\mathbb{E}[\Delta_{vap}H]$
MC 10	49.208 473 88
MC 100	49.215 525 57
MC 1000	49.217 770 37
MC 10^4	49.217 682 43
MC 10^5	49.217 826 08
MC 10^6	49.217 915 65
G–H quadrature	49.217 945 99

accuracy of the estimator of the Gauss–Hermite quadrature with $N = 10$ with increasing number of data points. However, the Monte Carlo estimator fluctuates, which is due to the random nature of the produced input values. This can be nicely seen when comparing the estimators of MC 1000 and MC 10^4, as the MC 1000 estimator is closer to the estimator of the Gauss–Hermite quadrature than the MC 10^4 estimator. The difference between the MC 10 and Gauss–Hermite $N = 10$ estimators is only about 0.01 kJ mol^{-1}, which, from a chemical point of view, is only a minor difference. This already suggests that the error introduced by the experimental input quantities is rather small.

To finally quantify the uncertainty introduced by the inaccuracies in the experimental reference data, we consider the standard deviation σ [Eq. (32)] computed with the Gauss–Hermite quadrature. The value obtained thus equals to about $30.95 \cdot 10^{-3}$ kJ mol^{-1} and corresponds directly to the uncertainty introduced by the measurement errors of the experimental reference data. From a chemical point of view, this can be considered as negligible for physicochemical properties. Since the dependence of the vaporization enthalpy on the input boiling points is similar for all investigated systems (see Table IV), this uncertainty can be expected to be in the same order of magnitude for the other systems as well.

In Fig. 8, we compare the convergence behavior of the Monte Carlo and Gauss–Hermite estimator. Therefore, we plot the deviation of the calculated Monte Carlo estimators with respect to the Gauss–Hermite estimator with $N = 10$ nodes as a function of the data points. Additionally, Fig. 8 shows the error of the Gauss–Hermite estimators with $N = 1$–9 nodes with respect to the Gauss–Hermite estimator obtained with $N = 10$. Note the logarithmic scale. The classical fluctuations of the Monte Carlo estimator, already seen in Table VI, can be observed here as well. With a convergence behavior of $\mathcal{O}(N^{-1/2})$ (shown by the dashed line), the Monte Carlo estimator shows a rather slow convergence compared to the Gauss–Hermite estimator, which already seems to reach numerical precision at $N = 4$ nodes. The fact that the Gauss–Hermite estimators start to fluctuate for $N = 4$ and larger values is directly connected to this fast convergence. Overall, it can, thus, be concluded that the Gauss–Hermite quadrature is an efficient approach that can be used to estimate uncertainty propagation with low computational cost as long as the investigated quantity behaves smoothly with respect to the inaccurate input quantity.

CONCLUSIONS

In this work, we dealt with how measurement errors in experimental input data influence the outcome of QCE calculations. While the comprehension of uncertainty propagation in complex computer programs is not an easy task, we addressed this issue using two different numerical methods. We investigated the overall dependence of vaporization enthalpies and entropies from the standard QCE approach with respect to variations in the experimental input

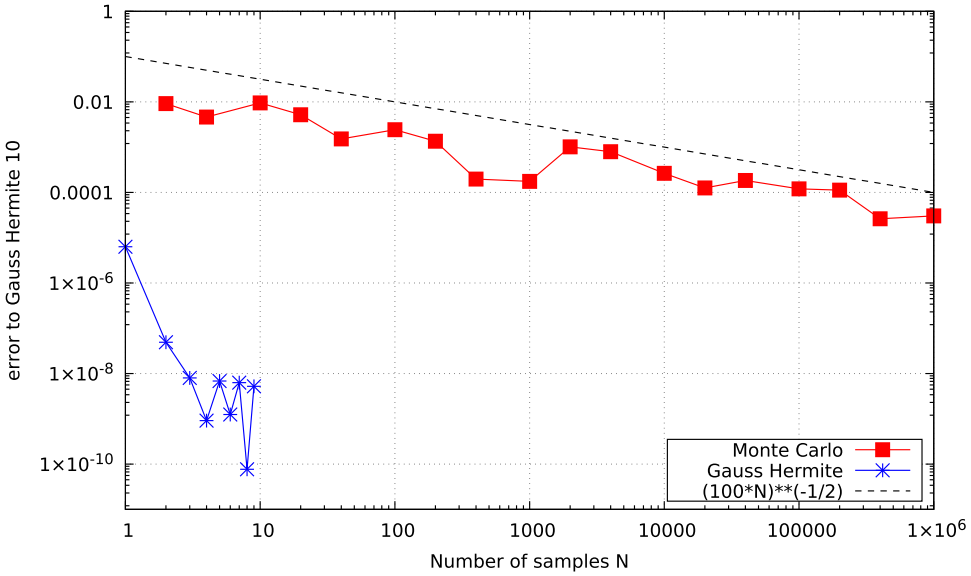

FIG. 8. Convergence behavior of the Monte Carlo estimator and the Gauss–Hermite estimator for the enthalpy of vaporization of (*R*)-butan-2-ol at 298 K plotted against the number of values generated to calculate the estimator. As a reference, the Gauss–Hermite estimator calculated using the tenth Hermite polynomial was chosen.

data and presented an alternative approach for the calculation of both thermodynamic functions.

The alternative approach, termed Clausius–Clapeyron approach, yielded similarly good results as the standard QCE approach. However, there are several drawbacks to this method. One considerable limitation is that the vaporization enthalpy has to be considered as being temperature independent. Moreover, the entropy of vaporization can only be calculated at the boiling point while the standard QCE approach allows the calculation of vaporization entropies at different temperatures. Additionally, the Clausius–Clapeyron requires more calculations, making it computationally more expensive.

By varying the experimental input quantities in ranges of ±20%, we observed a smooth dependence of the vaporization enthalpies and entropies with respect to changes in the input data. This is an important property, since it paves the way for the application of the efficient Gauss–Hermite quadrature method used in this work. In addition, it could be observed that the calculated enthalpies are more prone to inaccuracies in the experimental boiling points than to inaccuracies in the density. The polar liquids show a significantly smaller dependence on the experimental inputs than the nonpolar ones. This is most likely due to the reason that the main interactions in polar liquids are hydrogen bonds, which are less affected by the QCE parameters. In general, the entropies are found to be less prone to inaccuracies in the experimental inputs.

All the observations concerning the thermodynamic functions could be explained by investigating the influence of the experimental inputs on the cluster populations and the two empirical parameters. An increased density leads to increased populations of larger clusters as well as significantly smaller values of b_{xv}. This is reasonable since larger clusters and smaller cluster volumes are required to model higher densities. A similar behavior is observed for the boiling point whose increase leads to higher populations of larger oligomers at the expense of smaller clusters. Moreover, the empirical parameter a_{mf} becomes significantly larger, increasing the intercluster interactions. These effects can be understood based on the fact that stronger interactions are required for the system to stay in the liquid phase over a broader temperature range.

Using both the Monte Carlo method and the Gauss–Hermite quadrature, we addressed the influence of measurement errors in the experimental inputs on the calculated enthalpies of vaporization of polar (*R*)-butan-2-ol. For the uncertainty introduced by the experimental inaccuracies, we obtained a value of about $30.95 \cdot 10^{-3}$ kJ mol^{-1}. This can be considered as negligible in a chemical sense, since most experimental measurement errors are around 4 kJ mol^{-1}. This means that experimental reference data can be used to calculate vaporization enthalpies with QCE without the need to consider measurement errors in greater detail. However, this statement is not necessarily transferable to the calculation of other thermodynamic quantities or to methods based on different theories.

It was also shown that the Monte Carlo estimator slowly converges to the predicted Gauss–Hermite estimator determined with $N = 10$ nodes. The Gauss–Hermite quadrature on the other hand shows fast convergence and, from four nodes on, the estimators start to fluctuate as numerical precision is already reached. This undermines the superior performance of the Gauss–Hermite approach compared to the Monte Carlo approach.

SUPPLEMENTARY MATERIAL

See the supplementary material for additional tables showing the absolute and relative deviations of the calculated enthalpies and entropies of vaporization from the experimentally measured values (Tables S1 and S2); additional figures showing the enthalpy of vaporization plotted against the experimental input density and boiling point for ethylene, propane, propylene, butane, and methanol (Figs. S1–S5); additional figures showing the entropy of vaporization plotted against the experimental input density and boiling point for ethylene, propane, propylene, butane, and methanol (Figs. S6–S10); additional figures showing the cluster populations of ethylene, propane, propylene, butane, and methanol depending on the chosen reference values (Figs. S11–S15); additional figure showing all the cluster populations of (*R*)-butan-2-ol depending on the chosen reference values (Fig. S16); additional tables showing all empirical parameters a_{mf} and b_{xv} for all investigated systems with increased/decreased densities and boiling points (Tables S3 and S4); table showing the nodes and weights for the first ten Gauss–Hermite quadrature rules (Table S5); and additional tables showing the relative cluster binding energies of all clusters used in this work (Tables S6–S8).

ACKNOWLEDGMENTS

The authors acknowledge the DFG for financial support under Project No. 406232243 and the University of Bonn for granting access to the Bonna cluster and the TRA matter for financial support.

AUTHOR DECLARATIONS

Conflict of Interest

The authors have no conflicts to disclose.

Author Contributions

Jan Blasius: Conceptualization (equal); Data curation (equal); Formal analysis (equal); Investigation (equal); Methodology (equal); Validation (equal); Visualization (equal); Writing – original draft (equal); Writing – review and editing (equal). **Paul Zaby:** Conceptualization (equal); Data curation (equal); Formal analysis (equal); Investigation (equal); Methodology (equal); Validation (equal); Visualization (equal); Writing – original draft (equal); Writing – review and editing (equal). **Jürgen Dölz:** Conceptualization (equal); Funding acquisition (equal); Investigation (equal); Methodology (equal); Project administration (equal); Supervision (equal); Validation (equal); Writing – original draft (equal); Writing – review and editing (equal). **Barbara Kirchner:** Conceptualization (equal); Funding acquisition (equal); Investigation (equal); Methodology (equal); Project administration (equal); Supervision (equal); Validation (equal); Writing – original draft (equal); Writing – review and editing (equal).

DATA AVAILABILITY

The data that support the findings of this study are available from the corresponding author upon reasonable request.

REFERENCES

[1] B. Kirchner, P. J. di Dio, and J. Hutter, in *Multiscale Molecular Methods in Applied Chemistry*, Topics in Current Chemistry Vol. 307, edited by B. Kirchner and J. Vrabec (Springer, Berlin, Heidelberg, 2012), pp. 109–153.

[2] A. A. Hassanali, J. Cuny, V. Verdolino, and M. Parrinello, "Aqueous solutions: State of the art in *ab initio* molecular dynamics," Philos. Trans. R. Soc., A **372**, 20120482 (2014).

[3] L. D. M. Peters, J. Kussmann, and C. Ochsenfeld, "Efficient and accurate Born–Oppenheimer molecular dynamics for large molecular systems," J. Chem. Theory Comput. **13**, 5479–5485 (2017).

[4] S. Grimme, A. Hansen, S. Ehlert, and J.-M. Mewes, "r2SCAN-3c: A 'Swiss army knife' composite electronic-structure method," J. Chem. Phys. **154**, 064103 (2021).

[5] F. Neese, A. Hansen, and D. G. Liakos, "Efficient and accurate approximations to the local coupled cluster singles doubles method using a truncated pair natural orbital basis," J. Chem. Phys. **131**, 064103 (2009).

[6] C. Bannwarth, S. Ehlert, and S. Grimme, "GFN2-xTB—An accurate and broadly parametrized self-consistent tight-binding quantum chemical method with multipole electrostatics and density-dependent dispersion contributions," J. Chem. Theory Comput. **15**, 1652–1671 (2019).

[7] A. Severo Pereira Gomes and C. R. Jacob, "Quantum-chemical embedding methods for treating local electronic excitations in complex chemical systems," Annu. Rep. Prog. Chem., Sect. C: Phys. Chem. **108**, 222–277 (2012).

[8] S. Hunkler, T. Lemke, C. Peter, and O. Kukharenko, "Back-mapping based sampling: Coarse grained free energy landscapes as a guideline for atomistic exploration," J. Chem. Phys. **151**, 154102 (2019).

[9] G. Ciccotti, C. Dellago, M. Ferrario, E. R. Hernández, and M. E. Tuckerman, "Molecular simulations: Past, present, and future (a Topical Issue in EPJB)," Eur. Phys. J. B **95**, 3 (2022).

[10] J. VandeVondele, U. Borštnik, and J. Hutter, "Linear scaling self-consistent field calculations with millions of atoms in the condensed phase," J. Chem. Theory Comput. **8**, 3565–3573 (2012).

[11] B. Kirchner, O. Hollóczki, J. N. Canongia Lopes, and A. A. H. Pádua, "Multiresolution calculation of ionic liquids," Wiley Interdiscip. Rev.: Comput. Mol. Sci. **5**, 202–214 (2015).

[12] K. Goloviznina, J. N. Canongia Lopes, M. Costa Gomes, and A. A. H. Pádua, "Transferable, polarizable force field for ionic liquids," J. Chem. Theory Comput. **15**, 5858–5871 (2019).

[13] D. Bedrov, J.-P. Piquemal, O. Borodin, A. D. MacKerell, Jr., B. Roux, and C. Schröder, "Molecular dynamics simulations of ionic liquids and electrolytes using polarizable force fields," Chem. Rev. **119**, 7940–7995 (2019).

[14] B. Kirchner, J. Blasius, V. Alizadeh, A. Gansäuer, and O. Hollóczki, "Chemistry dissolved in ionic liquids. A theoretical perspective," J. Phys. Chem. B **126**, 766–777 (2022).

[15] H. Weber, M. Salanne, and B. Kirchner, "Toward an accurate modeling of ionic liquid–TiO_2 interfaces," J. Phys. Chem. C **119**, 25260–25267 (2015).

[16] L. Scalfi, M. Salanne, and B. Rotenberg, "Molecular simulation of electrode-solution interfaces," Annu. Rev. Phys. Chem. **72**, 189–212 (2021).

[17] A. C. Forse, C. Merlet, J. M. Griffin, and C. P. Grey, "New perspectives on the charging mechanisms of supercapacitors," J. Am. Chem. Soc. **138**, 5731–5744 (2016).

[18] Z. Lin, E. Goikolea, A. Balducci, K. Naoi, P. L. Taberna, M. Salanne, G. Yushin, and P. Simon, "Materials for supercapacitors: When Li-ion battery power is not enough," Mater. Today **21**, 419–436 (2018).

[19] T. Stettner, S. Gehrke, P. Ray, B. Kirchner, and A. Balducci, "Water in protic ionic liquids: Properties and use of a new class of electrolytes for energy-storage devices," ChemSusChem **12**, 3827–3836 (2019).

[20] F. Weinhold, "Quantum cluster equilibrium theory of liquids: General theory and computer implementation," J. Chem. Phys. **109**, 367–372 (1998).

[21] F. Weinhold, "Quantum cluster equilibrium theory of liquids: Illustrative application to water," J. Chem. Phys. **109**, 373–384 (1998).

[22] J. Blasius and B. Kirchner, "Cluster-weighting in bulk phase vibrational circular dichroism," J. Phys. Chem. B **124**, 7272–7283 (2020).

[23] B. Kirchner, "Cooperative versus dispersion effects: What is more important in an associated liquid such as water?," J. Chem. Phys. **123**, 204116 (2005).

[24] G. Matisz, A.-M. Kelterer, W. M. F. Fabian, and S. Kunsági-Máté, "Application of the quantum cluster equilibrium (QCE) model for the liquid phase of primary alcohols using B3LYP and B3LYP-D DFT methods," J. Phys. Chem. B **115**, 3936–3941 (2011).

[25] E. Perlt, M. von Domaros, B. Kirchner, R. Ludwig, and F. Weinhold, "Predicting the ionic product of water," Sci. Rep. **7**, 10244 (2017).

[26] M. Brüssel, E. Perlt, S. B. C. Lehmann, M. von Domaros, and B. Kirchner, "Binary systems from quantum cluster equilibrium theory," J. Chem. Phys. **135**, 194113 (2011).

[27] M. Brüssel, E. Perlt, M. von Domaros, M. Brehm, and B. Kirchner, "A one-parameter quantum cluster equilibrium approach," J. Chem. Phys. **137**, 164107 (2012).

[28] B. Kirchner, C. Spickermann, S. B. C. Lehmann, E. Perlt, J. Langner, M. von Domaros, P. Reuther, F. Uhlig, M. Kohagen, and M. Brüssel, "What can clusters tell us about the bulk?: Peacemaker: Extended quantum cluster equilibrium calculations," Comput. Phys. Commun. **182**, 1428–1446 (2011).

[29] J. Ingenmey, J. Blasius, G. Marchelli, A. Riegel, and B. Kirchner, "A cluster approach for activity coefficients: General theory and implementation," J. Chem. Eng. Data **64**, 255–261 (2019).

[30] J. Blasius, J. Ingenmey, E. Perlt, M. von Domaros, O. Hollóczki, and B. Kirchner, "Predicting mole-fraction-dependent dissociation for weak acids," Angew. Chem., Int. Ed. **58**, 3212–3216 (2019).

[31] J. Blasius, J. Ingenmey, E. Perlt, M. von Domaros, O. Hollóczki, and B. Kirchner, "Dissoziation schwacher säuren über den gesamten molenbruchbereich," Angew. Chem. **131**, 3245–3249 (2019).

[32] P. Zaby, J. Ingenmey, B. Kirchner, S. Grimme, and S. Ehlert, "Calculation of improved enthalpy and entropy of vaporization by a modified partition function in quantum cluster equilibrium theory," J. Chem. Phys. **155**, 104101 (2021).

[33] C. Spickermann, E. Perlt, M. von Domaros, M. Roatsch, J. Friedrich, and B. Kirchner, "Coupled cluster in condensed phase. Part II: Liquid hydrogen fluoride from quantum cluster equilibrium theory," J. Chem. Theory Comput. **7**, 868–875 (2011).

[34] *Handbook of Uncertainty Quantification*, edited by R. Ghanem, D. Higdon, and H. Owhadi (Springer International Publishing, Cham, 2017).

[35] R. E. Caflisch, "Monte Carlo and quasi-Monte Carlo methods," Acta Numer. **7**, 1–49 (1998).

[36] S. Krieg, T. Luu, J. Ostmeyer, P. Papaphilippou, and C. Urbach, "Accelerating Hybrid Monte Carlo simulations of the Hubbard model on the hexagonal lattice," Comput. Phys. Commun. **236**, 15–25 (2019).

[37] D. A. McQuarrie and J. D. Simon, *Physical Chemistry: A Molecular Approach* (University Science Books, 1997), Vol. 1.

[38] M. Abramowitz and I. A. Stegun, *Handbook of Mathematical Functions with Formulas, Graphs, and Mathematical Tables*, National Bureau of Standards Applied Mathematics Series (Dover Publications, North Chelmsford, MA, 1964).

[39] J. Stoer and R. Bulirsch, *Introduction to Numerical Analysis* (Springer, New York, 1993).

[40] J. Dick, F. Y. Kuo, and I. H. Sloan, "High-dimensional integration: The quasi-Monte Carlo way," Acta Numer. **22**, 133–288 (2013).

[41] H.-J. Bungartz and M. Griebel, "Sparse grids," Acta Numer. **13**, 147–269 (2004).

[42] M. B. Giles, "Multilevel Monte Carlo methods," Acta Numer. **24**, 259–328 (2015).

[43] B. Peherstorfer, K. Willcox, and M. Gunzburger, "Survey of multifidelity methods in uncertainty propagation, inference, and optimization," SIAM Rev. **60**, 550–591 (2018).

[44] M. von Domaros, E. Perlt, J. Ingenmey, G. Marchelli, and B. Kirchner, "Peacemaker 2: Making clusters talk about binary mixtures and neat liquids," SoftwareX **7**, 356–359 (2018).

[45] G. Wedler and H.-J. Freund, *Lehrbuch der Physikalischen Chemie* (John Wiley & Sons, 2012), Vol. 1.

[46] G. Marchelli, J. Ingenmey, O. Hollóczki, A. Chaumont, and B. Kirchner, "Hydrogen bonding and vaporization thermodynamics in hexafluoroisopropanol-acetone and -methanol mixtures. A joined cluster analysis and molecular dynamic study," ChemPhysChem **23**, e202100620 (2022).

[47] S. Grimme, "Supramolecular binding thermodynamics by dispersion-corrected density functional theory," Chem. Eur. J. **18**, 9955–9964 (2012).

[48]J.-D. Chai and M. Head-Gordon, "Long-range corrected hybrid density functionals with damped atom–atom dispersion corrections," Phys. Chem. Chem. Phys. **10**, 6615–6620 (2008).
[49]J. M. Dieterich and B. Hartke, "OGOLEM: Global cluster structure optimisation for arbitrary mixtures of flexible molecules. A multiscaling, object-oriented approach," Mol. Phys. **108**, 279–291 (2010).
[50]J. M. Dieterich and B. Hartke, "Composition-induced structural transitions in mixed Lennard-Jones clusters: Global reparametrization and optimization," J. Comput. Chem. **32**, 1377–1385 (2011).
[51]J. Wang, R. M. Wolf, J. W. Caldwell, P. A. Kollman, and D. A. Case, "Development and testing of a general amber force field," J. Comput. Chem. **25**, 1157–1174 (2004).
[52]C. Bannwarth, E. Caldeweyher, S. Ehlert, A. Hansen, P. Pracht, J. Seibert, S. Spicher, and S. Grimme, "Extended tight-binding quantum chemistry methods," Wiley Interdiscip. Rev.: Comput. Mol. Sci. **11**, e1493 (2020).
[53]A. Bondi, "van der Waals volumes and radii," J. Phys. Chem. **68**, 441–451 (1964).
[54]W. M. Haynes, *CRC Handbook of Chemistry and Physics* (CRC Press, Boca Raton, FL, 2014).
[55]E. W. Lemmon, *Thermophysical Properties of Fluid Systems, NIST Chemistry WebBook*, NIST Standard Reference Database Number 69 (National Institute of Standards and Technology, 2005), http://webbook.nist.gov.
[56]J. Ingenmey, M. von Domaros, E. Perlt, S. P. Verevkin, and B. Kirchner, "Thermodynamics and proton activities of protic ionic liquids with quantum cluster equilibrium theory," J. Chem. Phys. **148**, 193822 (2018).
[57]R. K. Witt and J. D. Kemp, "The heat capacity of ethane from 15 K to the boiling point. The heat of fusion and the heat of vaporization," J. Am. Chem. Soc. **59**, 273–276 (1937).
[58]C. J. Egan and J. D. Kemp, "Ethylene. The heat capacity from 15 K to the boiling point. The heats of fusion and vaporization. The vapor pressure of the liquid. The entropy from thermal measurements compared with the entropy from spectroscopic data," J. Am. Chem. Soc. **59**, 1264–1268 (1937).
[59]A. B. Lamb and E. E. Roper, "The vapor pressures of certain unsaturated hydrocarbons," J. Am. Chem. Soc. **62**, 806–814 (1940).
[60]J. D. Kemp and C. J. Egan, "Hindered rotation of the methyl groups in propane. The heat capacity, vapor pressure, heats of fusion and vaporization of propane. Entropy and density of the gas," J. Am. Chem. Soc. **60**, 1521–1525 (1938).
[61]T. M. Powell and W. F. Giauque, "Propylene. The heat capacity, vapor pressure, heats of fusion and vaporization. The third law of thermodynamics and orientation equilibrium in the solid," J. Am. Chem. Soc. **61**, 2366–2370 (1939).
[62]J. G. Aston and G. H. Messerly, "The heat capacity and entropy, heats of fusion and vaporization and the vapor pressure of n-butane," J. Am. Chem. Soc. **62**, 1917–1923 (1940).
[63]A. N. Fletcher, "Self-association of methanol vapor. Evidence for dimers and tetramers," J. Phys. Chem. **75**, 1808–1814 (1971).
[64]F. Trouton, "IV. On molecular latent heat," London, Edinburgh Dublin Philos. Mag. J. Sci. **18**, 54–57 (1884).
[65]C. Spickermann, S. B. C. Lehmann, and B. Kirchner, "Introducing phase transitions to quantum chemistry: From Trouton's rule to first principles vaporization entropies," J. Chem. Phys. **128**, 244506 (2008).

B. Cluster-Weighting in Bulk Phase Vibrational Circular Dichroism

Jan Blasius* and Barbara Kirchner*

Received: 10 July 2020, Published online: 21 July 2020.

Reprinted (adapted) in appendix B with permission† from

J. Blasius and B. Kirchner, *J. Phys. Chem. B* **2020**, *124*, 7272–7283.

doi:10.1021/acs.jpcb.0c06313.

For this article a Supporting Information is available free of charge at:
https://pubs.acs.org/doi/10.1021/acs.jpcb.0c06313.

Contributions to the manuscript

- Development of the concept
- Performance of all calculations
- Interpretation of the results
- Writing of the manuscript

*Mulliken Center for Theoretical Chemistry, Clausius Institute for Physical and Theoretical Chemistry, University of Bonn, Beringstr. 4–6, 53115 Bonn, Germany
†Permission requests to reuse material from this chapter should be directed to the American Chemical Society.

THE JOURNAL OF PHYSICAL CHEMISTRY B

pubs.acs.org/JPCB Article

Cluster-Weighting in Bulk Phase Vibrational Circular Dichroism

Jan Blasius and Barbara Kirchner*

Cite This: J. Phys. Chem. B 2020, 124, 7272–7283 Read Online

ACCESS | Metrics & More | Article Recommendations | Supporting Information

ABSTRACT: We present a cluster-weighting approach for calculating the vibrational circular dichroism (VCD) spectra of bulk phase systems. Based on the quantum cluster equilibrium theory, cluster populations are received via self-consistent field calculations that allow a mixing of differently sized oligomers at the same time. The thereby obtained cluster weights are employed for the weighting of individual cluster VCD spectra in order to calculate an overall gas or bulk phase VCD spectrum. As the mixing of different oligomer sizes is possible, different structural motifs and interactions can be included, and explicit solvation, typically necessary for describing hydrogen bonds, is intrinsically taken care of, however, without neglecting monomeric structures and different conformers. We test the sensitivity of Boltzmann and cluster weights with respect to the level of theory employed and show that cluster weights are less sensitive. By a constant increase of the oligomer sizes included in our cluster sets, combined with a continuous truncation of low populated clusters, we are able to improve the agreement between theory and experiment until we reach an overlap which allows a certain assignment of the absolute configuration based on an experimental bulk phase spectrum. Combined with a computationally cost-efficient level of theory, this approach provides a valuable tool for the fast calculation of VCD spectra for bulk phase systems.

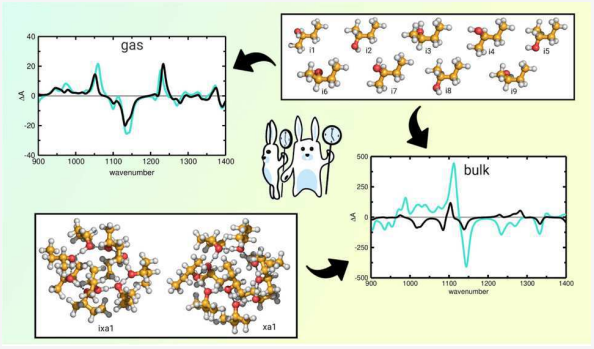

1. INTRODUCTION

Vibrational circular dichroism (VCD) spectroscopy, which measures the different attenuation of left and right circularly polarized infrared (IR) radiation during vibrational transitions, is one of the most powerful techniques for determining the three-dimensional structure of chiral molecules.[1,2] Compared to the more widely known electronic circular dichroism, VCD does not require the presence of any dedicated chromophor as all chemical bonds will serve as probes and thus make this method very sensitive to conformational changes and intermolecular interactions. As the VCD spectra of two enantiomers are the mirror images of each other with respect to the wavenumber axis, this spectroscopic method can be used not only to determine the absolute configurations but also the conformations of molecules or aggregates by comparing experimental data with ab initio predictions from theoretical studies.[3]

The static calculation of VCD spectra on the basis of density functional theory[4] is a common procedure, and the implementations mostly rely on magnetic field perturbation theory[5−8] or on nuclear velocity perturbation theory[9−13] to calculate atomic polar and atomic axial tensors. To reproduce experimental gas phase spectra, usually different conformers have to be taken into account by a reliable conformational averaging, typically achieved by a Boltzmann weighting (BW), of the lowest energy conformers. However, this approach requests high demands to the accuracy of the underlying energy calculations. A new approach based on a genetic algorithm that fits to the experimental spectra was recently suggested by Buma, Nicu, and co-workers.[14] It shows the necessity to develop novel ways to obtain theoretical spectra. As VCD spectra are extremely sensitive to conformational changes,[15,16] accounting for the different conformers is of particular importance. However, as chiroptical measurements are commonly performed on solvated systems, it is often necessary to explicitly account for the environmental effects induced by solute−solvent or solute−solute interactions in order to reproduce the experimental conditions.[3,17] This is of particular importance for solutions in which strong intermolecular contacts occur because such interactions can cause peak shifts or even changes in peak signs compared to the gas phase.[18] In the context of quantum chemistry, the environmental effects are usually modeled by employing implicit solvation models and explicit microsolvation approaches independently[19] or simultaneously.[20] As microsolvation approaches sometimes require the inclusion of differently sized structures, Boltzmann factors cannot be applied for the

Received: July 10, 2020
Revised: July 17, 2020
Published: July 21, 2020

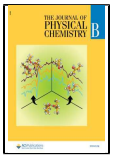

https://dx.doi.org/10.1021/acs.jpcb.0c06313
J. Phys. Chem. B 2020, 124, 7272−7283

weighting procedure as they are limited to one oligomer size at a time and do not yield information about the aggregation behavior of the liquid. An estimation of the degree of self-aggregation can, for instance, be obtained through the evaluation of concentration-dependent IR spectra by the integration of a monomer band and subsequent extrapolation of the intensity to infinite dilution. The integrated intensities allow conclusions about the ratios between monomers and higher oligomers present in the liquid phase and can be applied for weighting the static VCD spectra of different oligomer sizes.[3]

In contrast to static quantum chemistry, dynamic approaches like molecular dynamics simulations[21] are also in wide use for the calculation of vibrational spectra.[22−24] Such simulations model the time development of the system and thus account for the motion of the molecules, conformational changes, and the dynamics of intermolecular interactions which intrinsically yields a credible conformational averaging. If sufficient sampling is not achieved because of inaccuracies in the model or a short and finite simulation time, the conformational ensemble may be refined.[25] The VCD spectra from ab initio molecular dynamics simulations can be obtained by the Fourier transformation of the time cross-correlation function of the electric dipole moment and the magnetic dipole moment.[26−28] Electric dipole moments are accessible via Wannier centers[29] or alternatively by the integration of the electron density over a molecular cell determined by radical Voronoi tessellation.[30] The magnetic dipole moments can be obtained by classical approaches.[22,31] However, as these approaches require knowledge about the electronic structure, they are currently limited to the time-consuming ab initio molecular dynamics simulations.

Herein, we present a new weighting approach for calculating the vibrational spectra of bulk phase systems based on a cluster distribution as in the example of (*R*)-2-butanol. The cluster weights (CWs) are obtained from the quantum cluster equilibrium (QCE) theory[32] which allows a simultaneous weighting of differently sized structures at once. We show that the gas phase spectra can be reproduced with high accuracy and that a successive inclusion of oligomers models the features of the neat bulk phase, which are not accessible by the inclusion of monomers only. Furthermore, we show that a systematic exclusion of structures is possible without worsening the overlap between theory and experiment tremendously, partially even improving the results obtained.

2. METHODS AND COMPUTATIONAL DETAILS

2.1. QCE Method or Cluster-Weighting. The QCE approach starts its description of gaseous and liquid phases by a so-called cluster gas which is in thermodynamic equilibrium and consists of nonpunctiform particles.[32] The chemical equation for the cluster equilibrium of a neat substance reads as

$$\mathrm{C}_1 \rightleftharpoons \frac{\mathrm{C}_2}{i(2)} \rightleftharpoons \frac{\mathrm{C}_3}{i(3)} \rightleftharpoons \ldots \rightleftharpoons \frac{\mathrm{C}_\mathcal{P}}{i(\mathcal{P})} \tag{1}$$

with C_1 and $\mathrm{C}_\mathcal{P}$ being the monomer and a cluster of size $i(\mathcal{P})$, respectively. For a binary system (bQCE),[33] this equilibrium extends to

$$i(\mathcal{P})\mathrm{C}_1 + j(\mathcal{P})\mathrm{C}_2 \rightleftharpoons \mathrm{C}_\mathcal{P} \tag{2}$$

A cluster $\mathrm{C}_\mathcal{P}$ is composed of $i(\mathcal{P})$ and $j(\mathcal{P})$ monomers of the components 1 and 2, respectively. The primary aim of the model is to obtain the equilibrium cluster populations $N_\mathcal{P}$, which minimize the free energy A of a system with volume V, temperature T, and total number of monomers $N^{\mathrm{tot}} = N_1^{\mathrm{tot}} + N_2^{\mathrm{tot}}$, with N_1^{tot} and N_2^{tot} being the number of monomers of the components 1 and 2. Knowing the cluster populations, the system's total partition function Q^{tot} can be calculated as

$$Q^{\mathrm{tot}}(\{N_\mathcal{P}\}, V, T) = \prod_{\mathcal{P}=1}^{N} \frac{1}{N_\mathcal{P}!}[q_\mathcal{P}^{\mathrm{tot}}(V, T)]^{N_\mathcal{P}} \tag{3}$$

where $\{N_\mathcal{P}\}$ denotes the full set of total cluster populations $N_\mathcal{P}$, and $q_\mathcal{P}^{\mathrm{tot}}$ is a single cluster partition function given by

$$q_\mathcal{P}^{\mathrm{tot}}(V, T) = q_\mathcal{P}^{\mathrm{rot}}(T) q_\mathcal{P}^{\mathrm{vib}}(T) q_\mathcal{P}^{\mathrm{trans}}(V, T) q_\mathcal{P}^{\mathrm{elec}}(V, T) \tag{4}$$

The rotational, vibrational, and translational partition functions $q_\mathcal{P}^{\mathrm{rot}}(T)$, $q_\mathcal{P}^{\mathrm{vib}}(T)$, and $q_\mathcal{P}^{\mathrm{trans}}(V, T)$ are calculated from standard equations for the rigid rotator, harmonic oscillator, and particle in a box, respectively.[34]

Based on the nonpunctiform particles, the volume is corrected for the translational partition functions, as the total volume is not accessible for the particles. Therefore, the exclusion volume V_{ex}, given by

$$V_{\mathrm{ex}} = b_{\mathrm{xv}} \sum_{\mathcal{P}=1}^{N} N_\mathcal{P} v_\mathcal{P} \tag{5}$$

is subtracted from the phase volume V. Here, $v_\mathcal{P}$ denotes the volume of the cluster $\mathrm{C}_\mathcal{P}$, and b_{xv} is an empirical parameter which corrects the cluster volumes.

The electronic cluster partition function $q_\mathcal{P}^{\mathrm{elec}}(V, T)$ is calculated from the referenced electronic energy $\varepsilon_\mathcal{P}^{\mathrm{elec}}$ and supplemented by a term accounting for interactions between clusters described by a mean-field-type attractive energy. The electronic partition function reads as

$$q_\mathcal{P}^{\mathrm{elec}}(V, T) = \exp\left(-\frac{\varepsilon_\mathcal{P}^{\mathrm{elec}} - [i(\mathcal{P}) + j(\mathcal{P})]\frac{a_{\mathrm{mf}}}{V}}{k_{\mathrm{B}}T}\right) \tag{6}$$

where k_{B} is the Boltzmann constant, and a_{mf} is the mentioned mean-field parameter, scaling the interactions between clusters. By this, a_{mf} is the second empirical parameter in the theory.

The system's total partition function Q^{tot} is a function of the cluster populations $\{N_\mathcal{P}\}$, which is obtained by minimizing the free energy

$$A = -k_{\mathrm{B}}T \ln Q^{\mathrm{tot}}(\{N_\mathcal{P}\}, V, T) \tag{7}$$

This function shall be minimized under the constraints of a fixed total particle number and a fixed total mass. Based on both constraints, two polynomial equations can be derived, namely the population polynomial

$$0 = -1 + \sum_{\mathcal{P}=1}^{N} \frac{i(\mathcal{P}) + j(\mathcal{P})}{N_1^{\mathrm{tot}} + N_2^{\mathrm{tot}}} \frac{q_\mathcal{P}^{\mathrm{tot}}}{(q_1^{\mathrm{tot}})^{i(\mathcal{P})}(q_2^{\mathrm{tot}})^{j(\mathcal{P})}} N_1^{i(\mathcal{P})} N_2^{j(\mathcal{P})} \tag{8}$$

and the volume polynomial

https://dx.doi.org/10.1021/acs.jpcb.0c06313
J. Phys. Chem. B 2020, 124, 7272−7283

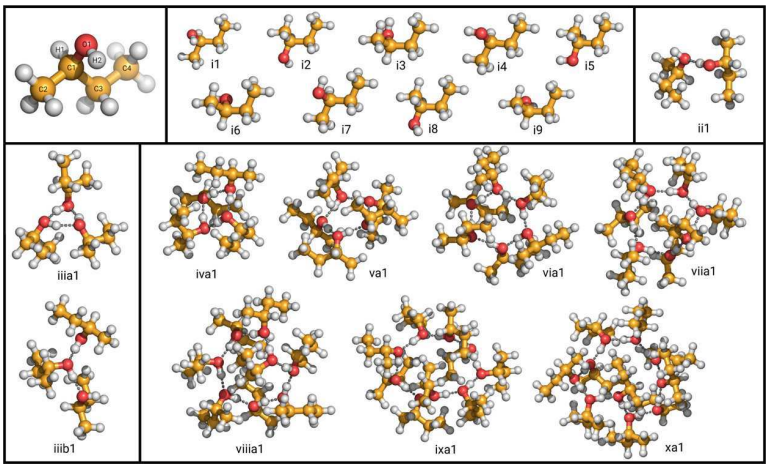

Figure 1. Examples of different clusters employed in this work. Apart from the cluster **iiib1**, which is a linear trimer, all other clusters are included in the cluster set $S4^{gm}$. Note that these are not all clusters employed in this work. Geometries, electronic energies, and vibrational frequencies of all clusters can be obtained upon request.

$$0 = -pV^3 + \left(\sum_{\mathcal{P}=1}^{N} k_B T N_{\mathcal{P}} + p b_{xv}(v_1 N_1^{tot} + v_2 N_2^{tot})\right) V^2 - \left(\sum_{\mathcal{P}=1}^{N} N_{\mathcal{P}}(i(\mathcal{P}) + j(\mathcal{P})) a_{mf}\right) V + \sum_{\mathcal{P}=1}^{N} N_{\mathcal{P}}(i(\mathcal{P}) + j(\mathcal{P})) a_{mf} b_{xv}(v_1 N_1^{tot} + v_2 N_2^{tot}) \quad (9)$$

Both polynomials yield a nonlinear equation system which can be solved numerically.

Since its publication, the method has been applied to many neat and binary systems, including water,[32,35,36] aqueous solutions,[33,37] and even ionic liquids.[38] Recently, the calculation of activity coefficients[39] and ionicity[40,41] has been reported.

2.2. Cluster Generation. For the cluster generation, we employed two methods. For the first approach, we employed a systematic cluster generation based on genetic structure optimization at a classical force field level of theory. Therefore, the OGOLEM[42,43] framework, the AMBER 2016 molecular dynamics package,[44] and the generalized Amber force field (GAFF)[45] were used, and the lowest energy conformers obtained by this procedure were included in the cluster set. However, as this method only yields a very limited number of clusters which are close to global minimum structures, a broad variety of clusters that include different conformations and isomers of the oligomers in various compositions is missing. As it is known that a reliable conformer sampling is especially essential for VCD spectra, many structures with various compositions should be included. In order to construct such clusters which do not represent global minima, we employed the PACKMOL[46] program, fixed all atoms included in the hydrogen bonds, and constructed clusters by attaching the missing carbon chains to the fixed oxygen atoms. With this procedure, iterating over all possible conformer combinations yields a large cluster set including many different binding situations as well as conformer combinations in the clusters. To give an example, assuming nine monomeric conformations, 729 ring trimers can be constructed. However, in the end, not all of them will be employed, as nonlocal minima and similar clusters are deselected.

2.3. Quantum Chemical Calculations. In this work, the low-cost BP86[47,48] functional including the def2-SVP as well as the def2-TZVP basis set[49] has been employed. Dispersion interactions were modeled employing the D3 dispersion correction scheme,[50,51] and except for the gas phase calculations, implicit solvation effects were taken into account by the solvation model COSMO[52] employing the dielectric constant of (*R*)-2-butanol at 293.15 K corresponding to 17.26.[53] All quantum chemical optimizations as well as the calculations of the individual cluster VCD spectra were performed using the Turbomole 7.4 software package,[4,54−56] and the broadening of the VCD spectra was modeled by a Lorentzian band shape, employing a full width at half-maximum of 8 cm^{-1}.

2.4. QCE Calculations with PEACEMAKER. The QCE equilibrium populations were evaluated by PEACEMAKER,[32,33,57,58] which is our publicly available software package for bQCE calculations.[58] All calculations were performed for a fixed pressure of 101.325 kPa and in a temperature range of 200−400 K. The cluster volumes were set as van der Waals volumes, with the radii from Bondi's compilation. As experimental inputs, the boiling point T_b = 372.0 K[53] and the density at 293.15 K $\rho_{293.15}$ = 0.806 g cm^{-3}[53] of (*R*)-2-butanol have been employed. The empirical parameters a_{mf} and b_{xv} have been optimized between values of 0.0 and 2.0 in order to reproduce the boiling point and density at 293.15 K as accurate as possible. The exact values of both parameters are listed in Tables S4 and S5 in the Supporting Information.

3. RESULTS AND DISCUSSION

3.1. Monomers and Gas Phase. Before considering the calculation of the bulk, we first examine the composition of the gas phase and its vibrational spectra. A conformational analysis of (*R*)-2-butanol revealed nine possible conformers induced by the rotations of the hydroxyl and ethyl groups, both rotations exhibiting three minima on the potential energy surface. Thus, the conformation of a single monomer can explicitly be described by a combination of two dihedral angles, including the atoms which are involved in the mentioned rotations. We

https://dx.doi.org/10.1021/acs.jpcb.0c06313
J. Phys. Chem. B 2020, 124, 7272−7283

term these dihedrals as τ_1 (C2−C1−C3−C4 dihedral) and τ_2 (H2−O1−C1−H1 dihedral). For atom labels, see Figure 1, which also shows the most important clusters discussed throughout this study. Herein, we employ the following nomenclature for clusters and cluster sets: Single clusters are printed in boldface type and depicted by lowercase roman numbers in which the roman number gives the oligomer size, for example, **iv** presents a tetramer. The Arabic number behind the roman number is the number of the conformer, whereby the number 1 represents the global minimum. Additionally, lowercase letters represent the isomer of the oligomer, for example, ring or chain. As an example, **iiia1** represents the global minimum of the ring trimers. For cluster sets, we apply a nomenclature relying on this structure; however, we use uppercase roman numbers to give an oligomer size, and separated by a minus sign, we give the number of the cluster of this distinct oligomer size and isomer in the set, for example, IIIa−121 means that 121 ring trimers are included. Combining different cluster sizes in one set yields the following structure: (I−9; II−69; IIIa−121) describing a set including 9 monomers, 69 dimers, and 121 ring trimers. As with the increasing oligomer size, the nomenclature for the cluster sets results in rather long terms, we also shorten the cluster set labels for comparison with the bulk phase to SX^y, where X describes the oligomer sizes and y the kinds of clusters included, for example, just global minima or all clusters. The superscripts imply the following: all—all clusters up to the respective oligomer size have been included; >0.01—only clusters from the respective SX^{all} set with a population greater than 0.01 have been included; gim—only global minima of the isomers have been included; gm—only the global minima have been included. The S1 set includes only monomers, S2 monomers and dimers, S3 monomers up to trimers, S4 monomers up to decamers, and S5 monomers up to decamers but no tetramers. An overview of all sets with their respective labels and clusters included is given in Table S6 in the Supporting Information.

In Table 1 the dihedrals for the idealized conformer structures as well as the ones obtained from structure optimizations at the BP86-D3/def2-SVP level of theory with and without employing COSMO are summarized.

Table 1. Values for the Dihedrals τ_1 and τ_2 Computed at BP86-D3/def2-SVP (Gas) and BP86-D3/def2-SVP/COSMO (Bulk) Levels of Theory as Well as Dihedrals for the Idealized Structures[a]

	idealized		optimized			
			gas		bulk	
	τ_1	τ_2	τ_1	τ_2	τ_1	τ_2
i1	180.0	180.0	178.5	179.1	178.7	−179.3
i2	60.0	180.0	63.3	−179.6	63.8	−180.0
i3	−60.0	180.0	−64.5	174.2	−63.3	174.0
i4	180.0	60.0	178.1	59.9	177.7	59.3
i5	60.0	60.0	65.0	65.7	65.2	64.8
i6	−60.0	60.0	−61.7	69.1	−61.1	68.0
i7	180.0	−60.0	−179.4	−58.7	−179.9	−58.0
i8	60.0	−60.0	63.5	−65.7	64.4	−64.4
i9	−60.0	−60.0	−62.3	−62.0	−62.1	−62.9

[a]Definitions of the dihedrals: τ_1 = C2−C1−C3−C4 and τ_2 = H2−O1−C1−H1; all angles are given in units of degree.

Considering negligible intermolecular interactions, the observable gas phase properties are usually described by a set of all thermally accessible conformers to which some weights are assigned. Such weights are mostly computed by the classical Boltzmann factors (from now on termed as BWs) relying solely on electronic energies. Apart from the electronic energy, the QCE theory also considers vibrational frequencies, the non-negligible particle volume, and the intermolecular interaction between independent structures for the calculation of CW, yielding weights which are somewhat different from the classical Boltzmann factors. Of course, both BW and CW are strongly dependent on the underlying quantum chemical level of theory and the different correction schemes employed because of the uncertainties in the electronic energies and vibrational frequencies. In order to examine the differences between BW and CW as well as the influence of different levels of theory, we calculated both kinds of weights for all the nine conformers of (*R*)-2-butanol, employing different methods. It should be noted that all geometries are optimized at the corresponding level of theory.

In Figures 2 and 3, we present the results obtained at the BP86/def2-SVP and BP86/def2-TZVP levels of theory,

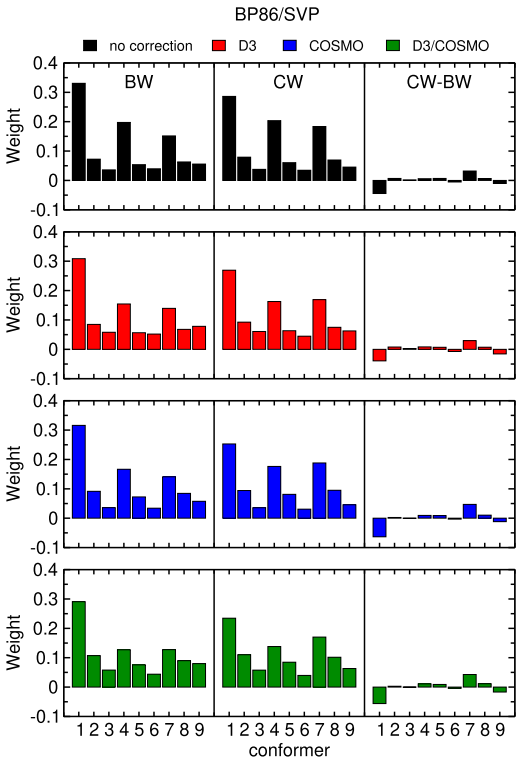

Figure 2. Boltzmann weights (BW) and cluster weights (CW) as well as the difference between CW and BW (CW−BW) for all (*R*)-butanol conformers. Electronic energies and vibrational frequencies have been calculated at the BP86/def2-SVP level of theory with and without employing D3 and COSMO.

including D3 dispersion correction, implicit solvation by COSMO, and the combination of both. Further results employing additional functionals can be found in the Supporting Information. For both basis sets, it is apparent that without including the two correction schemes, the three conformers **i1**, **i4**, and **i7** are dominant in the case of BW as

https://dx.doi.org/10.1021/acs.jpcb.0c06313
J. Phys. Chem. B 2020, 124, 7272−7283

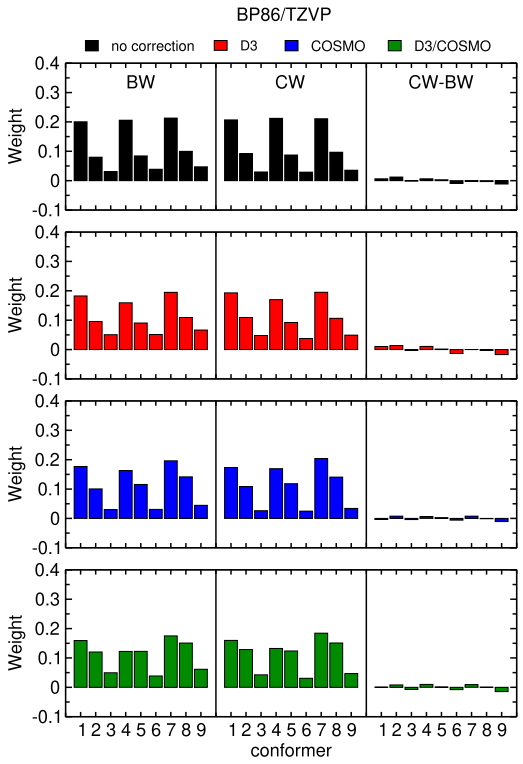

Figure 3. Boltzmann weights (BW) and cluster weights (CW) as well as differences between CW and BW (CW−BW) for all (*R*)-butanol conformers. Electronic energies and vibrational frequencies have been calculated at the BP86/def2-TZVP level of theory with and without employing D3 and COSMO.

well as CW. Although for the larger basis set the weights are more evenly distributed between these three structures, with **i7** being the global minimum, the smaller basis set predicts **i1** as being the highest populated conformer, followed by **i4** and **i7**, respectively. Comparing both types of weights for the def2-SVP basis set, the CWs of **i1** and **i7** differ significantly from the Boltzmann weights. Although the population of **i1** noticeably decreases in the case of CW, the one of **i7** increases, yielding somewhat more evenly distributed weights, as it is also observed for the larger def2-TZVP basis set. This trend is also visible for the weights predicted by including the dispersion correction and implicit solvation. For the larger basis set, only minor differences between BW and CW are observed.

Including a dispersion correction yields only minor differences for BW and CW compared to the calculations without employing any correction. It can be noticed that the weights of **i1**, **i4**, and **i7** are slightly reduced, whereas the ones of the other six conformers increase. However, because of the small size of the monomeric structures, dispersion interactions might be small and do not contribute much to the electronic energy. Nevertheless, the D3 correction scheme will be employed in all the following calculations as dispersion interactions are expected to contribute to the structure and energy of the oligomers and their isomers that will be used for the bulk phase later on.

For the smaller basis set, employing just implicit solvation without a dispersion correction mostly influences the weights of **i1** and **i7** inasmuch as the differences between BW and CW get larger. For the remaining conformers, only minor differences are observed. In the case of the larger def2-TZVP basis set, employing implicit solvation slightly increases the weight of **i7** while decreasing the ones of **i1** and **i4**. Additionally, the weights of **i2**, **i5**, and **i8** increase remarkably, all exhibiting the same dihedral angle of $\tau_1 = 60°$ for the carbon chain. As observed in the previously discussed results, the differences between BW and CW are almost negligible in the case of the def2-TZVP basis set, illustrating for both the sensitivity with respect to the electronic structure.

Finally, employing the dispersion correction and implicit solvation decreases the BW of **i1**, **i4**, and **i7**. Employing this level of theory for the small basis set yields the least dominance of **i1** compared to the other methods. Once more, the CWs somewhat flatten the weights and yield a broader distribution. This effect of leveling out the weights is also observed for the larger basis set for which **i1**, **i2**, **i4**, **i5**, **i8**, and **i9** are similar in their population. Compared to the gas phase calculations without employing any correction scheme, this is a remarkable difference and shows again the sensitivity of the calculated weights with respect to the employed level of theory.

The differences between the respective BW and CW obtained with the def2-SVP and def2-TZVP basis sets, employing dispersion correction and implicit solvation, are compared in Figure 4. As already discussed before, the larger

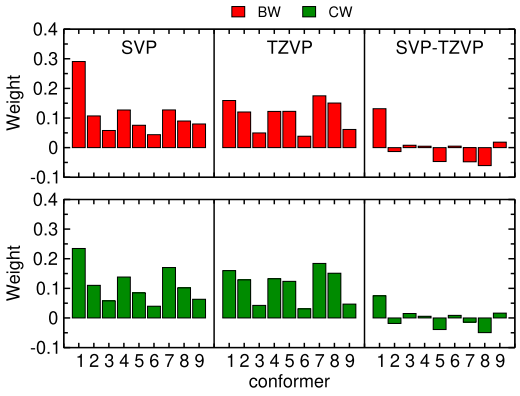

Figure 4. Boltzmann weights (BW), cluster weights (CW), as well as the difference between the respective weights obtained at the BP86-D3/COSMO level of theory, employing either the def2-SVP or the def2-TZVP basis set.

basis set tremendously decreases the population of **i1**, with a stronger extent for the Boltzmann weights. On the other hand, the weights of **i5**, **i7**, and **i8** increase noticeably by enlargening the basis set. Also, for these three conformers, a greater difference between BW is observed for both basis sets compared to CW, although the differences are smaller as for **i1**. For the remaining conformers, only minor changes can be observed for the basis set and type of weight employed. Based on the results discussed above—although still being dependent on the level of theory—we can suggest that the CWs are less sensitive with respect to the employed basis set compared to Boltzmann weights.

After discussing the sensitivity and differences between BW and CW, the weights discussed above will be used in order to calculate the VCD spectra for (*R*)-2-butanol in the gas phase. For this purpose, individual spectra for all conformers have been calculated as described in Section 2.3 and averaged, considering the monomer weights. The overlap σ between the experimental and calculated spectra has been calculated using the SimVCD[59] measure in order to quantify the compliance.

https://dx.doi.org/10.1021/acs.jpcb.0c06313
J. Phys. Chem. B 2020, 124, 7272−7283

Thereby, a value of +1 represents a perfect match between experiment and calculation, and a value of −1 means that both spectra are mirrored with respect to each other, in principle, implying that they represent opposite enantiomers. The resulting overlaps are summarized in Table 2.

Table 2. Overlap between the Experimental Gas Phase and Theoretically Predicted VCD Spectra Based on BW, CW, and WOC Using Monomer Conformers[a]

	def2-SVP			def2-TZVP		
weight	(I−1)	(I−5)	(I−9)	(I−1)	(I−5)	(I−9)
BW	0.264	0.413	0.398	0.313	0.435	0.435
CW	0.264	0.431	0.397	0.313	0.432	0.424
WOC	0.264	0.438	0.327	0.313	0.402	0.368

[a]Set (I−1) includes **i1** (def2-SVP) or **i7** (def2-TZVP); (I−5) includes **i1**, **i2**, **i4**, **i7**, and **i8**; (I−9) includes all conformers.

For the calculations, we considered three different cluster sets. The first one, (I−9), includes all nine conformers. For the second set, (I−5), we excluded all conformers from (I−9) with a value below 0.1 for BW and CW. Fortunately, these are the same four conformers for all different levels of theory employed, namely **i3**, **i5**, **i6**, and **i9**, which are therefore not present in the set (I−5). For (I−1), we just considered the global minimum structures **i1** and **i7** for def2-SVP and def2-TZVP, respectively.

Naively, one would assume the cluster set (I−9) to yield the best representation of the gas phase VCD spectrum as this one is the "most complete" set. However, as it is common practice, comparing the overlaps between (I−9) and (I−5), it is apparent that (I−5) always yields a better or at least the same overlap with the experiment as (I−9). This results in an overall best overlap for the def2-TZVP basis set of 0.435, which is achieved by the sets (I−5) and (I−9). This leads to the assumption that, in some cases, excluding structures can improve the overlap between experiment and calculation, which is, however, expected to be an issue of shifted frequencies based on the underlying level of theory and should be tested further on.

As expected, one trend observed for all methods employed is that including implicit solvation decreases the overlap tremendously (see Table S2 in the Supporting Information). For almost all methods employed, the set (I−1) yields the worst overlap, which is however expected as the conformer distribution of (*R*)-2-butanol is broad and a single conformer which is much lower in energy compared to the remaining conformers does not exist, implying that at least an averaging of some, but not necessarily all conformers, has to be applied.

Altogether, the overlaps obtained using the def2-TZVP basis set are slightly better compared to the def2-SVP results. Comparing the results obtained for BW and CW, it is apparent that both weights mostly yield similar overlaps with a maximum difference of about 0.1. One exception is observed for the set (I−5) employing def2-SVP. In this particular case, the CWs yield an overlap which is 0.18 higher than the one obtained with BW.

Instead of applying weights, we also considered the so-called "wisdom of the crowd" (WOC) approach, which is just taking the arithmetic mean of all conformer spectra. It has been observed before that this approach can yield a good agreement between experiment and theory,[14] and also for the present case, this approach yields reliable overlaps. Although for most sets the overlap is slightly worse compared to employing weights, for the set (I−5) using def2-SVP, the WOC approach yields the best overlap, which is slightly better than BW and CW.

Figure 5 shows the calculated VCD spectra based on the sets (I−1), (I−5), and (I−9), all of them being compared to the

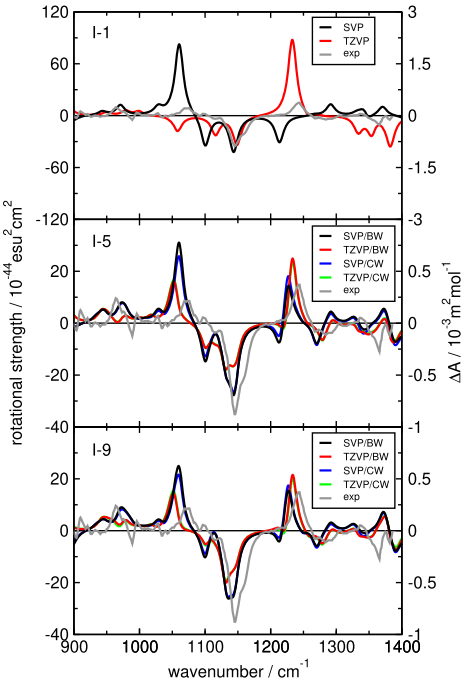

Figure 5. Calculated VCD spectra based on the cluster sets (I−1), (I−5), and (I−9) obtained by weighting with BW as well as CW for the def2-SVP and def2-TZVP basis sets without employing implicit solvation. The gray lines depict the experimental reference measured for a 0.029 M (*R*)-2-butanol solution in carbon disulfide.[15] Note that the green line is covered by the red line.

experimental gas phase reference[15] depicted in gray. The upper panel displays the results for set (I−1), which includes the conformers **i1** and **i7** in the case of def2-SVP and def2-TZVP, respectively. As for the two basis sets different conformers are found to be the global minimum, the predicted spectra display very different features, again exemplifying the role that conformational changes exhibit for the calculation of VCD spectra. The pronounced (+/−/+)-pattern observed between 1050 and 1250 cm^{-1} in the experiment is not reproduced by both conformers. **i1** models a (+/−)-pattern, whereas **i7** models the missing (−/+)-pattern.

Employing set (I−5) already yields spectra which show the characteristic (+/−/+)-pattern, explaining the improvement of the overlap with the experiment compared to the set (I−1). Although the positions of the negative and subsequent positive peaks between 1100 and 1250 cm^{-1} are described with good accuracy, the positive signal around 1050 cm^{-1} is shifted toward lower wavenumbers with a stronger extent for the larger basis set. As it was already observed before that the difference between BW and CW is more pronounced for the smaller basis set, it is not surprising that the def2-SVP basis set yields slightly different spectra for both kinds of weights,

https://dx.doi.org/10.1021/acs.jpcb.0c06313
J. Phys. Chem. B 2020, 124, 7272−7283

whereas with def2-TZVP, basically the same results are obtained.

Comparing the results of (I−5) with the ones of (I−9), just minor differences are observed. This exemplifies, however, that not necessarily all thermally accessible conformers or structures have to be taken into account but just a chosen set of conformers with a significantly high population. We will investigate and discuss this systematic exclusion of single structures later on.

In addition, we also show the calculated IR spectra in Figure 6. As observed for the VCD spectra, just employing the global minimum structures results in different spectra, which can be compared nicely to the VCD spectra. The positive signals of **i1** (def2-SVP, 1050 cm^{-1}) and **i7** (def2-TZVP, 1250 cm^{-1}) correspond to the strong absorption signals in the IR spectrum. Set (I−5) reduces the intensities of these strong absorption peaks, and the wavenumber region above 1000 cm^{-1} matches well with the experiment. However, below 1000 cm^{-1}, the experimental reference cannot be modeled satisfactorily. This issue is also not cured by set (I−9), which yields a similar spectrum as (I−5).

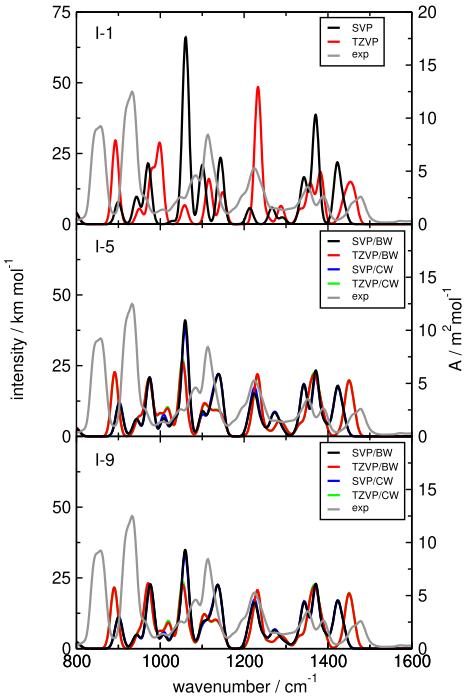

Figure 6. Calculated IR spectra based on the cluster sets (I−1), (I−5), and (I−9) obtained by weighting with BW as well as CW for the def2-SVP and def2-TZVP basis sets without employing implicit solvation. The gray lines depict the experimental reference measured for a 0.029 M (*R*)-2-butanol solution in carbon disulfide.[15] Note that the green line is covered by the red line.

3.2. Bulk Phase Spectra. Bulk phase vibrational spectra usually show different features than the neat gas phase spectra, which is an effect of the occurrence of intermolecular solute−solvent or solute−solute interactions. Especially, bulk phases dominated by intermolecular hydrogen bonds can exhibit remarkable differences compared to the gas phase because of the shifts of vibrational frequencies induced by these interactions. In the following, we will elaborate a protocol which uses CWs from the QCE theory in order to model the bulk phase vibrational spectra of (*R*)-2-butanol by considering differently sized clusters.

A first approach in describing bulk phases is the usage of an implicit solvation model at the monomer conformers. However, as such models just include a continuum, explicit interactions like hydrogen bonds can usually not be described. In order to illustrate this issue for the case of (*R*)-2-butanol, we calculated the overlap between the spectra obtained for the def2-SVP basis set employing implicit solvation and CW of the monomers with the experimental bulk phase VCD spectrum. The results are shown in the first column of Table 3. It is apparent at the first glance that the overlaps of the calculated spectra are much worse for the bulk phase compared to the gas phase, although a solvation model has been applied. The overlaps with the bulk phase spectrum reach a maximum of just 0.036, which would not allow an unambiguous assignment of the absolute configuration. The dramatically reduced overlap is assumed to be a consequence of the frequency shifts observed in the experimental bulk phase spectrum, which cannot be modeled by the monomeric structures and implicit solvation solely. This indicates that the calculated spectra still resemble more the gas and not the bulk phase, and explicit solvation becomes necessary. As an additional observation, no improvement of the overlap is observed when the low populated conformers are excluded, as it was observed for the gas phase, which will be investigated further.

Table 3. Overlap σ of Calculated CW-VCD Spectra for Different Cluster Sets with the Experimental Reference for the Bulk Phase VCD Spectrum[15a]

glob. min.		glob. isom. min.		>0.01		all	
set	σ	set	σ	set	σ	set	σ
$S1^{gm}$	0.019			$S1^{0.01}$	0.028	$S1^{all}$	0.036
$S2^{gm}$	0.019			$S2^{0.01}$	0.042	$S2^{all}$	0.053
$S3^{gm}$	0.222	$S3^{gim}$	0.241	$S3^{0.01}$	0.137	$S3^{all}$	0.136
$S4^{gm}$	0.045	$S4^{gim}$	0.045			$S4^{all}$	0.122
$S5^{gm}$	0.326	$S5^{gim}$	0.326			$S5^{all}$	0.139

[a]All calculations are based on BP86-D3/def2-SVP, employing COSMO. The labels of the sets are described in the text.

The first step for explicit solvation is the inclusion of dimeric structures into the cluster set. By the procedure described in Section 2.2, 81 dimers have been obtained by combining all 9^2 conformers of the monomers. After eliminating similar structures and clusters which did not represent minimum structures, 69 dimers remained. Hence, the set $S2^{all}$ includes all these dimers as well as the nine monomers and yields an overlap of 0.053 with the experimental bulk phase spectrum. Although this already improves the result obtained with the set $S1^{all}$, it would not be convincing to assigning the absolute configuration with certainty in the case of an unknown structure.

In order to continue testing the effect of excluding low populated clusters, we cut all dimers from the set $S2^{all}$ with a population below 0.01. Including the five monomers from the reduced cluster set discussed in Section 3.1 results in set $S2^{0.01}$, which yields an overlap of 0.042. Also, in this case, deleting clusters does not result in an improvement compared to the full set; however, the overlap is still improved compared to the truncated monomer set $S1^{0.01}$. Just applying both global minimum structures (set $S2^{gm}$) yields a rather poor result of 0.019, which is however not surprising as only a very limited

https://dx.doi.org/10.1021/acs.jpcb.0c06313
J. Phys. Chem. B 2020, 124, 7272−7283

part of the conformational space can be explored by these two structures. Nevertheless, the results from considering the dimeric structures are already convincing in that the overlap between calculation and experiment can be improved for the bulk phase by oligomeric structures, which should be included successively in order to improve the overlap steadily.

As a next step, trimers will be added to the cluster set. Compared to the dimers which possess all linear structures connected by hydrogen bonds, there are two possibilities for the construction of trimers, rings (**iiia**) and linear chains (**iiib**). We will term these structures from now on as isomers of the oligomers if we differentiate between different constitutions of the same oligomer size. Again, applying the cluster construction procedure described earlier on, we obtain 121 ring trimers and 118 linear chains. Including all clusters constructed so far results in set $S3^{all}$, which yields an overlap with the experiment of 0.136. Compared to the previously employed sets, this is a remarkable improvement and already approaches a value which is usually said to be required for a confident assignment of the absolute configuration. Excluding the low populated trimers from the full set results in 21 remaining ring structures and no chains. With regard to the lower binding energy of the chains compared to the rings because of a missing hydrogen bond, it is not surprising that the weights of the linear clusters are below our chosen population threshold of 0.01 and thus excluded. The overlap of 0.137 of this cluster set matches the one of the full set. Although this trend was not observed for the sets containing monomers and dimers, this result is again encouraging because it seems to be possible to truncate the cluster set to a collection of chosen structures without losing accuracy.

Because of the two types of isomeric clusters (rings and chains) that occur for the trimers, we introduce a new type of cluster set, which not only includes the global minima of a distinct cluster size but also the global minima of all isomeric clusters, meaning that in the case of the trimers, the global minimum of the ring structures as well as the one of the chains is included (see second column of Table 3). Although just containing these few clusters, this set outperforms all previously employed ones with an overlap of 0.241, which would, in principle, allow a confident assignment of the absolute configuration based on the bulk phase VCD spectrum. This implies that considering many clusters including all combinations of conformers rather worsens the results than improving them similar to overfitting.

As the successive inclusion of oligomers revealed a continuous improvement of the overlap, we will continue by including structures up to decamers at once. However, as the number of possible conformer combinations increases rapidly with the increasing cluster size, we limit the structures constructed for tetramers, pentamers, and hexamers to the global minima of the isomers, and for heptamers and larger just to the global minima. This is also justified by the overlaps obtained for the trimers, which revealed that a cluster set containing those few global minimum structures can yield a good agreement with the experiment. Surprisingly, including all these new structures in the cluster set yields an overlap of 0.122, which is a poorer result compared to the value of 0.136 obtained for the full trimer set. The sets including just the global minima and minima of the isomers perform even worse and yield an overlap of 0.045, which would again not allow a certain assignment of the absolute configuration.

In order to investigate whether this worsening is an issue of some particular clusters, we systematically excluded one cluster size from the set including all global minimum structures and recalculated the spectra and overlaps (see Table S3 in the Supporting Information). What we observe is that as long as the structure of the ring tetramer is included, the overlap always yields a value of 0.045, as in these sets this cluster is by far the one with the highest population, thus dominating the weighted spectrum. On the contrary, once this cluster is excluded from the set and the global minima of all other cluster sizes are taken into account, a remarkable overlap of 0.326 is achieved which allows an assignment of the absolute configuration based on the bulk spectrum with certainty.

We observe that the immense overpopulation of **iv1** might be an issue of the high binding energy (binding energies for the global minima are given in the Supporting Information) and the vibrational frequencies. From the literature, it is known that the ring tetramers of *tert*-butanol are particularly stable because of the structure which allows a favorable up−down alternation of the carbon residues.[60] This structure is present in **iv1**, whereas it is less pronounced for the hexamer, octamer, and decamer, which in principle would also allow an up−down alternation. We observe that a reduction of the binding energy or an upscaling of the frequencies of **iv1** reduces the population. This shows that our approach does not cure the high demands for the energy and frequencies and that further studies in this direction are clearly necessary.

In the lower panel of Figure 7 the spectrum obtained with the set of all global minima including the ring tetramer is

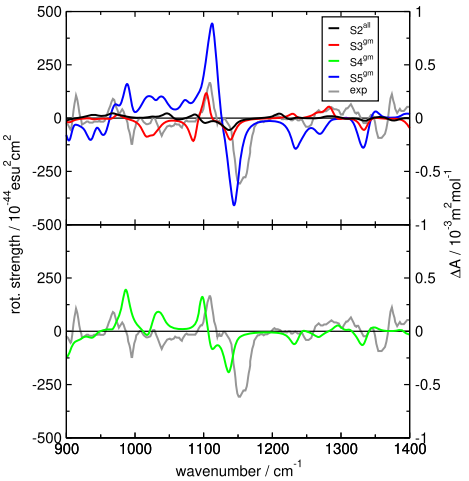

Figure 7. Selection of calculated VCD spectra based on CW obtained with the cluster sets which yielded the best overlap for the respective cluster size. The gray lines depict the experimental reference.[15]

compared to the experimental bulk phase spectrum. Because of the overpopulation of the ring tetramer, the calculated spectrum corresponds in principle to the individual VCD spectrum of this cluster; see Figure 8. It is apparent that the region below 1100 cm^{-1} is simulated rather poor and mostly mirrored and high in intensity compared to the experiment. Additionally, the (+/−)-pattern between 1100 and 1150 cm^{-1} is shifted toward lower wavenumbers. Both phenomena, in combination with the overpopulation of the ring tetramer, result in a poor agreement between calculation and experiment for the set including all global minimum structures. This

https://dx.doi.org/10.1021/acs.jpcb.0c06313
J. Phys. Chem. B 2020, 124, 7272−7283

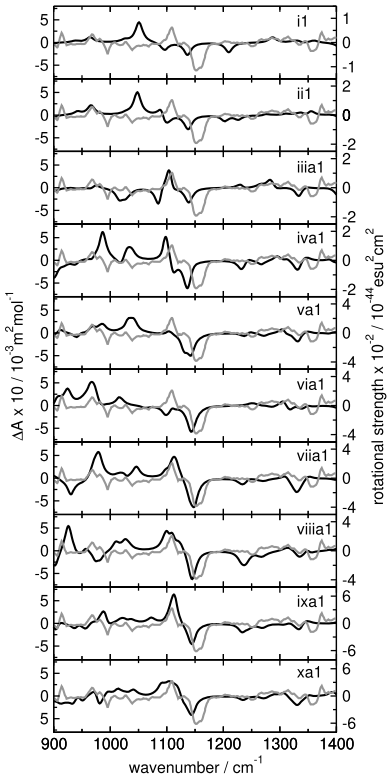

Figure 8. Comparison between the individual VCD spectra of the clusters included in the $S4^{gm}$ cluster set and the experimental reference for the bulk phase. Calculated spectra are shown in black, and gray depicts the experimental reference.[15]

observation exemplifies that in some cases single clusters can worsen the result tremendously and the cluster sets should be chosen carefully. That the choice of the cluster set beyond the CW is important is also visible when comparing the overlaps achieved for sets $S3^{gm}$ and $S3^{gim}$ which contain the same three global minima, but set $S3^{gim}$ is additionally supplemented by a linear trimer. Here, we see clearly room for future studies.

In the upper panel of Figure 7, the calculated spectrum obtained with all global minima excluding the ring tetramer is depicted, which shows a nice agreement with the experiment. Although the lower wavenumber region does not match the experiment adequately, the extremely high intensities observed for the tetramer are flattened. The positive signal at 1100 cm^{-1} matches the experiment almost perfect, and also the subsequent negative signal at around 1150 cm^{-1} fits with the experimentally observed peak, though being slightly shifted toward lower wavenumbers. The positive signal around 1230 cm^{-1} observed in the gas phase VCD spectrum is now turned into a negative peak with low intensity, representing the negative peak at 1250 cm^{-1} observed in the experimental spectrum.

Furthermore, the upper panel in Figure 7 shows the spectra obtained for sets $S2^{all}$ and $S3^{gm}$. The different magnitudes of the intensity are caused by the higher rotational strength of larger clusters; however, the signs and intensity ratios of signals are still comparable. For the set $S2^{all}$, two noticeable mismatches can be observed. First, the calculated spectrum features a negative signal around 1100 cm^{-1}, whereas a positive peak is observed in the experiment; second, a positive peak is simulated around 1200 cm^{-1}, which is observed in the gas phase spectrum but not in the bulk. The trimer set $S3^{gm}$ which already yields an overlap of 0.222 models two negative signals below 1100 cm^{-1} correctly, though being shifted to higher wavenumbers compared to the experiment. However, the main feature of the spectrum, the (+/−)-pattern between 1100 and 1150 cm^{-1}, is modeled with good agreement.

In addition to the VCD spectra, Figure 9 shows the IR spectra obtained for the same sets. As already observed by

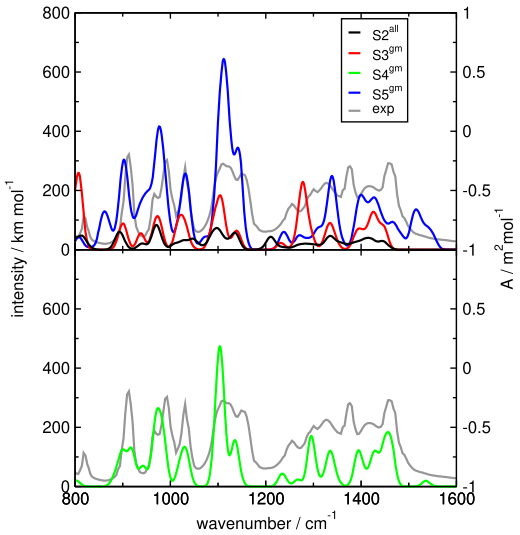

Figure 9. Selection of calculated IR spectra based on CW obtained with the cluster sets which yielded the best overlaps for the VCD spectra for the respective cluster size. The gray lines depict the experimental reference.[15]

others,[61] the IR spectra seem to be less sensitive with respect to the employed cluster set (i.e., the molecular conformation), with all the calculated spectra matching the experiment well. In contrast to the VCD spectra for which the global minimum of the ring tetramer was found to decrease the overlap with the experiment tremendously, the cluster set including this structure maps the experiment with good agreement as well.

From the results discussed in this section, we can conclude the following for the procedure of the cluster construction and weighting process based on the QCE theory if the calculation of VCD spectra is aimed at:

1. Low populated clusters can be excluded based on the threshold of the population without changing the result tremendously. This procedure can accelerate the calculations; however, detailed investigations on how to deselect clusters systematically are still necessary.
2. The inclusion of a broad variety of oligomer clusters which include all various combinations of conformers does not seem to be necessary.
3. Single clusters with an extraordinarily high binding energy can make the cluster weighting redundant because of an overpopulation of these structures causing the weighted spectra to be mainly composed of the clusters' individual spectrum. This might yield a good agreement with the experiment if the single cluster spectrum accidentally matches the experimental one; however, the example discussed above shows that this can also worsen the overlap tremendously and that a variety of oligomers with similar binding energy per

https://dx.doi.org/10.1021/acs.jpcb.0c06313
J. Phys. Chem. B 2020, 124, 7272−7283

monomer should be taken into account. This is related to the first point and also here further studies are needed.

4. Isomeric clusters seem to become less important with increasing cluster size. This might allow a procedure in which just global minimum structures have to be taken into account, which would decrease the effort required for the time-consuming cluster construction by far. Also, this would allow the inclusion of even larger clusters.

3.3. Populations, Self-Aggregation, and Cluster Spectra. In order to investigate the composition of the VCD spectrum calculated with set $S5^{gm}$, we will take a closer look into the respective cluster populations. In Figure 10 the

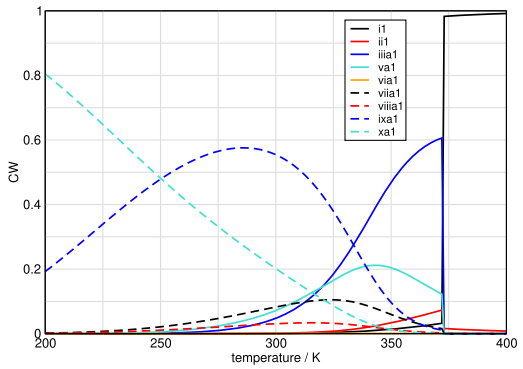

Figure 10. CWs obtained for the cluster set $S5^{gm}$ between 200 and 400 K.

CWs for this particular cluster set are depicted in the temperature range between 200 and 400 K. At low temperatures, the bulk is exclusively composed of the nonamer and decamer, with a stronger extent for the latter one. With an increasing temperature, the weight of the nonamer increases, whereas the one of the decamer decreases. Simultaneously, some smaller clusters start to get populated, which are in particular **iiia1**, **va1**, **viia1**, and **viiia1**. Just below the boiling point **iiia1** is the dominant cluster. The population of all oligomeric clusters drops to zero above the boiling point, with the exception of the dimer which seems to be slightly present in the gas phase.

The calculated bulk spectra discussed in the previous section are composed of the clusters present at 300 K. Thus, the calculated spectrum is mainly composed of the nonamer and decamer; however, other oligomers also contribute about 25% to the spectrum. In order to understand the influence of the single clusters on the weighted spectrum, Figure 8 shows the individual spectra for all clusters included in the set. The monomer and dimer spectra do not match the experimental bulk spectrum at all. The main feature, the (+/−)-pattern observed in the experiment between 1100 and 1150 cm^{-1}, is not pronounced inasmuch as the negative signal is split and low in intensity. Additionally, the positive peak is shifted by about 50 cm^{-1}. For the trimer and larger clusters, this shift is not observed anymore, and all spectra match the positive signal at 1100 cm^{-1} with good agreement, except for the pentamer which just exhibits a low-intensity signal. As discussed before, the tetramer **iva1** fails in the region around 1000 cm^{-1} and is shifted by 20−30 cm^{-1} in the (+/−) region. The best match for the (+/−)-pattern is observed for the heptamer, which agrees almost perfectly with the experiment in this region. On the contrary, this cluster simulates the lower wavenumber region rather poor, which is approximately mirrored compared with the experiment. However, as the CW of this cluster is around 0.1, this mismatch does not affect the weighted spectrum too much. A similar trend is observed for the octamer in the lower wavenumber region, but because of a population of only 0.05, this also does not alter the weighted spectrum excessively. With regard to the two dominant structures, the nonamer and decamer, both are able to model the (+/−)-pattern well, however, with a slight shift of the negative signal toward lower wavenumbers. In addition, the region below 1100 cm^{-1} does not display high intensity signals as observed for the heptamer and octamer. Although the signal signs do not match the experiment in perfection, the absence of high intensity signals at wrong positions or with wrong signs decreases the error sources for the weighted spectrum and thus increases the overlap because of the high population of these clusters.

4. DISCUSSION AND CONCLUSIONS

We introduced a novel cluster-weighting approach based on the QCE theory, which can be used to calculate bulk phase VCD spectra of liquids as in the example of (*R*)-2-butanol. A subsequent inclusion of increasing oligomer sizes allows modeling VCD features induced by intermolecular hydrogen bonds which cannot be modeled by a pure monomeric cluster set, employing an implicit solvation only. As the cluster distribution is calculated intrinsically within the QCE model, it is not necessary to investigate the aggregation behavior of the solution beforehand in order to know which oligomers are necessary for a proper modeling of the spectra.

We have shown that the inclusion of a variety of conformers for the larger oligomeric clusters is not necessary and that low populated clusters can be excluded without losing accuracy. However, including highly populated clusters can also worsen the results, and further studies are needed. With an increasing cluster size, we observe a decrease in the weights of isomeric clusters compared to the global minima of the respective oligomer size. This might allow a procedure in which just global minimum structures have to be taken into account, decreasing the computational effort by far.

Nevertheless, we still see the need for future studies, as indicated above. First of all, we want to test the derived protocol at other substances as well as binary systems, which would allow the calculations of VCD spectra in solution. Although we observed that with increasing oligomer size isomeric clusters become less important, their role for cluster sets including medium-sized clusters is still to be tested further. Additionally, the issue of treating too many clusters which results in a worsening of the spectrum has to be investigated, as intuitively a more complete cluster set should yield a better spectrum. Last but not least, we see a great potential in the combination of our cluster weighting approach with a neural network ansatz[14] which fits to the experimental bulk phase VCD spectra in order to account for uncertainties in the binding energies and vibrational frequencies. Such an approach could improve the obtained CWs further on.

■ ASSOCIATED CONTENT

Supporting Information

The Supporting Information is available free of charge at https://pubs.acs.org/doi/10.1021/acs.jpcb.0c06313.

https://dx.doi.org/10.1021/acs.jpcb.0c06313
J. Phys. Chem. B 2020, 124, 7272−7283

Procedure of solving the QCE equations by PEACEMAKER; dependence of relative energies for the conformers with respect to the level of theory employed; dependence of BW and CW with respect to the level of theory employed; binding energies of global minima; overlaps between calculated and experimental gas phase VCD spectra, employing COSMO; calculated VCD spectra for the monomer sets, employing COSMO; overlaps between calculated and experimental bulk phase VCD spectra when excluding single clusters from the set $S4^{gm}$; optimized QCE parameters; individual cluster VCD spectra for the set $S4^{gim}$; and cluster set labels and clusters included in the sets (PDF)

AUTHOR INFORMATION

Corresponding Author

Barbara Kirchner − *Mulliken Center for Theoretical Chemistry, Rheinische Friedrich-Wilhelms-Universität Bonn, D-53115 Bonn, Germany;* orcid.org/0000-0001-8843-7132; Email: kirchner@thch.uni-bonn.de

Author

Jan Blasius − *Mulliken Center for Theoretical Chemistry, Rheinische Friedrich-Wilhelms-Universität Bonn, D-53115 Bonn, Germany*

Complete contact information is available at: https://pubs.acs.org/10.1021/acs.jpcb.0c06313

Notes

The authors declare no competing financial interest.

ACKNOWLEDGMENTS

The authors thank DFG under the grant project number 406232243.

REFERENCES

(1) Nafie, L. A. Infrared and Raman vibrational optical activity: theoretical and experimental aspects. *Annu. Rev. Phys. Chem.* **1997**, *48*, 357−386.

(2) Merten, C.; Golub, T. P.; Kreienborg, N. M. Absolute configurations of synthetic molecular scaffolds from vibrational CD spectroscopy. *J. Org. Chem.* **2019**, *84*, 8797−8814.

(3) Weirich, L.; Merten, C. Solvation and self-aggregation of chiral alcohols: how hydrogen bonding affects their VCD spectral signatures. *Phys. Chem. Chem. Phys.* **2019**, *21*, 13494−13503.

(4) Reiter, K.; Kühn, M.; Weigend, F. Vibrational circular dichroism spectra for large molecules and molecules with heavy elements. *J. Chem. Phys.* **2017**, *146*, 054102.

(5) Stephens, P. J. Theory of vibrational circular dichroism. *J. Phys. Chem.* **1985**, *89*, 748−752.

(6) Stephens, P. J. Gauge dependence of vibrational magnetic dipole transition moments and rotational strengths. *J. Phys. Chem.* **1987**, *91*, 1712−1715.

(7) Cheeseman, J. R.; Frisch, M. J.; Devlin, F. J.; Stephens, P. J. Ab initio calculation of atomic axial tensors and vibrational rotational strengths using density functional theory. *Chem. Phys. Lett.* **1996**, *252*, 211−220.

(8) Nicu, V. P.; Neugebauer, J.; Wolff, S. K.; Baerends, E. J. A vibrational circular dichroism implementation within a Slater-type-orbital based density functional framework and its application to hexa- and hepta-helicenes. *Theor. Chem. Acc.* **2008**, *119*, 245−263.

(9) Nafie, L. A.; Freedman, T. B. Vibronic coupling theory of infrared vibrational transitions. *J. Chem. Phys.* **1983**, *78*, 7108−7116.

(10) Nafie, L. A. Adiabatic molecular properties beyond the Born−Oppenheimer approximation. Complete adiabatic wave functions and vibrationally induced electronic current density. *J. Chem. Phys.* **1983**, *79*, 4950−4957.

(11) Buckingham, A. D.; Fowler, P. W.; Galwas, P. A. Velocity-dependent property surfaces and the theory of vibrational circular dichroism. *Chem. Phys.* **1987**, *112*, 1−14.

(12) Scherrer, A.; Vuilleumier, R.; Sebastiani, D. Nuclear velocity perturbation theory of vibrational circular dichroism. *J. Chem. Theory Comput.* **2013**, *9*, 5305−5312.

(13) Scherrer, A.; Agostini, F.; Sebastiani, D.; Gross, E. K. U.; Vuilleumier, R. Nuclear velocity perturbation theory for vibrational circular dichroism: An approach based on the exact factorization of the electron-nuclear wave function. *J. Chem. Phys.* **2015**, *143*, 074106.

(14) Koenis, M. A. J.; Xia, Y.; Domingos, S. R.; Visscher, L.; Buma, W. J.; Nicu, V. P. Taming conformational heterogeneity in and with vibrational circular dichroism spectroscopy. *Chem. Sci.* **2019**, *10*, 7680−7689.

(15) Wang, F.; Polavarapu, P. L. Vibrational circular dichroism: Predominant conformations and intermolecular interactions in (R)-(-)-2-butanol. *J. Phys. Chem. A* **2000**, *104*, 10683−10687.

(16) Shin, S.; Nakata, M.; Hamada, Y. Analysis of vibrational circular dichroism spectra of (S)-(+)-2-butanol by rotational strengths expressed in local symmetry coordinates. *J. Phys. Chem. A* **2006**, *110*, 2122−2129.

(17) Nicu, V. P.; Baerends, E. J.; Baerends, E. J. Effects of complex formation on vibrational circular dichroism spectra. *J. Phys. Chem. A* **2008**, *112*, 6978−6991.

(18) Perera, A. S.; Thomas, J.; Poopari, M. R.; Xu, Y. The clusters-in-a-liquid approach for solvation: new insights from the conformer specific gas phase spectroscopy and vibrational optical activity spectroscopy. *Front. Chem.* **2016**, *4*, 9.

(19) Poopari, M. R.; Dezhahang, Z.; Xu, Y. A comparative VCD study of methyl mandelate in methanol, dimethyl sulfoxide, and chloroform: explicit and implicit solvation models. *Phys. Chem. Chem. Phys.* **2013**, *15*, 1655−1665.

(20) Bünnemann, K.; Pollok, C. H.; Merten, C. Explicit solvation of carboxylic acids for vibrational circular dichroism studies: Limiting the computational efforts without losing accuracy. *J. Phys. Chem. B* **2018**, *122*, 8056−8064.

(21) Gaigeot, M.-P.; Sprik, M. Ab initio molecular dynamics computation of the infrared spectrum of aqueous uracil. *J. Phys. Chem. B* **2003**, *107*, 10344−10358.

(22) Choi, J.-H.; Cho, M. Direct calculations of mid-and near-IR absorption and circular dichroism spectra of chiral molecules using QM/MM molecular dynamics simulation method. *J. Chem. Theory Comput.* **2011**, *7*, 4097−4103.

(23) Thomas, M.; Brehm, M.; Fligg, R.; Vöhringer, P.; Kirchner, B. Computing vibrational spectra from ab initio molecular dynamics. *Phys. Chem. Chem. Phys.* **2013**, *15*, 6608−6622.

(24) Thomas, M.; Brehm, M.; Hollóczki, O.; Kelemen, Z.; Nyulászi, L.; Pasinszki, T.; Kirchner, B. Simulating the vibrational spectra of ionic liquid systems: 1-ethyl-3-methylimidazolium acetate and its mixtures. *J. Chem. Phys.* **2014**, *141*, 024510.

(25) Bottaro, S.; Bengtsen, T.; Lindorff-Larsen, K. *Structural Bioinformatics*; Springer, 2020; pp 219−240.

(26) Abbate, S.; Longhi, G.; Kwon, K.; Moscowitz, A. The use of cross-correlation functions in the analysis of circular dichroism spectra. *J. Chem. Phys.* **1998**, *108*, 50−62.

(27) Horníček, J.; Kaprálová, P.; Bouř, P. Simulations of vibrational spectra from classical trajectories: Calibration with ab initio force fields. *J. Chem. Phys.* **2007**, *127*, 084502.

(28) Yang, S.; Cho, M. Direct calculations of vibrational absorption and circular dichroism spectra of alanine dipeptide analog in water: Quantum mechanical/molecular mechanical molecular dynamics simulations. *J. Chem. Phys.* **2009**, *131*, 135102.

(29) Kirchner, B.; Hutter, J. Solvent effects on electronic properties from Wannier functions in a dimethyl sulfoxide/water mixture. *J. Chem. Phys.* **2004**, *121*, 5133−5142.

(30) Thomas, M.; Brehm, M.; Kirchner, B. Voronoi dipole moments for the simulation of bulk phase vibrational spectra. *Phys. Chem. Chem. Phys.* **2015**, *17*, 3207−3213.
(31) Thomas, M.; Kirchner, B. Classical magnetic dipole moments for the simulation of vibrational circular dichroism by ab initio molecular dynamics. *J. Phys. Chem. Lett.* **2016**, *7*, 509−513.
(32) Kirchner, B. Cooperative versus dispersion effects: What is more important in an associated liquid such as water? *J. Chem. Phys.* **2005**, *123*, 204116.
(33) Brüssel, M.; Perlt, E.; Lehmann, S. B. C.; von Domaros, M.; Kirchner, B. Binary systems from quantum cluster equilibrium theory. *J. Chem. Phys.* **2011**, *135*, 194113.
(34) McQuarrie, D. A.; Simon, J. D. *Physical Chemistry: A Molecular Approach*; University Science Books, 1997.
(35) Lehmann, S. B. C.; Spickermann, C.; Kirchner, B. Quantum cluster equilibrium theory applied in hydrogen bond number studies of water. 1. Assessment of the quantum cluster equilibrium model for liquid water. *J. Chem. Theory Comput.* **2009**, *5*, 1640−1649.
(36) Lehmann, S. B. C.; Spickermann, C.; Kirchner, B. Quantum cluster equilibrium theory applied in hydrogen bond number studies of water. 2. Icebergs in a two-dimensional water continuum? *J. Chem. Theory Comput.* **2009**, *5*, 1650−1656.
(37) Matisz, G.; Kelterer, A.-M.; Fabian, W. M. F.; Kunsági-Máté, S. Structural properties of methanol−water binary mixtures within the quantum cluster equilibrium model. *Phys. Chem. Chem. Phys.* **2015**, *17*, 8467−8479.
(38) Ingenmey, J.; von Domaros, M.; Perlt, E.; Verevkin, S. P.; Kirchner, B. Thermodynamics and proton activities of protic ionic liquids with quantum cluster equilibrium theory. *J. Chem. Phys.* **2018**, *148*, 193822.
(39) Ingenmey, J.; Blasius, J.; Marchelli, G.; Riegel, A.; Kirchner, B. A cluster approach for activity coefficients: General theory and implementation. *J. Chem. Eng. Data* **2018**, *64*, 255−261.
(40) Perlt, E.; von Domaros, M.; Kirchner, B.; Ludwig, R.; Weinhold, F. Predicting the ionic product of water. *Sci. Rep.* **2017**, *7*, 10244.
(41) Blasius, J.; Ingenmey, J.; Perlt, E.; von Domaros, M.; Hollóczki, O.; Kirchner, B. Predicting mole-fraction-dependent dissociation for weak acids. *Angew. Chem., Int. Ed.* **2019**, *58*, 3212−3216.
(42) Dieterich, J. M.; Hartke, B. OGOLEM: global cluster structure optimisation for arbitrary mixtures of flexible molecules. A multi-scaling, object-oriented approach. *Mol. Phys.* **2010**, *108*, 279−291.
(43) Dieterich, J. M.; Hartke, B. Composition-induced structural transitions in mixed Lennard-Jones clusters: Global reparametrization and optimization. *J. Comput. Chem.* **2011**, *32*, 1377−1385.
(44) Case, D. A.; Betz, R. M.; Cerutti, D. S.; Cheatham, T. E.; Darden, T. A.; Duke, R. E.; Giese, T. J.; Gohlke, H.; Goetz, A. W.; Homeyer, N.; et al. *AMBER 2016*; University of California: San Francisco, 2016.
(45) Wang, J.; Wolf, R. M.; Caldwell, J. W.; Kollman, P. A.; Case, D. A. Development and testing of a general amber force field. *J. Comput. Chem.* **2004**, *25*, 1157−1174.
(46) Martínez, L.; Andrade, R.; Birgin, E. G.; Martínez, J. M. PACKMOL: a package for building initial configurations for molecular dynamics simulations. *J. Comput. Chem.* **2009**, *30*, 2157−2164.
(47) Becke, A. D. Density-functional exchange-energy approximation with correct asymptotic behavior. *Phys. Rev. A: At., Mol., Opt. Phys.* **1988**, *38*, 3098−3100.
(48) Perdew, J. P. Density-functional approximation for the correlation energy of the inhomogeneous electron gas. *Phys. Rev. B: Condens. Matter Mater. Phys.* **1986**, *33*, 8822−8824.
(49) Weigend, F.; Ahlrichs, R. Balanced basis sets of split valence, triple zeta valence and quadruple zeta valence quality for H to Rn: Design and assessment of accuracy. *Phys. Chem. Chem. Phys.* **2005**, *7*, 3297−3305.
(50) Grimme, S.; Antony, J.; Ehrlich, S.; Krieg, H. A consistent and accurate ab initio parametrization of density functional dispersion correction (DFT-D) for the 94 elements H-Pu. *J. Chem. Phys.* **2010**, *132*, 154104.
(51) Grimme, S.; Ehrlich, S.; Goerigk, L. Effect of the damping function in dispersion corrected density functional theory. *J. Comput. Chem.* **2011**, *32*, 1456−1465.
(52) Klamt, A.; Schüürmann, G. COSMO: a new approach to dielectric screening in solvents with explicit expressions for the screening energy and its gradient. *J. Chem. Soc., Perkin Trans. 2* **1993**, 799−805.
(53) Haynes, W. M. *CRC Handbook of Chemistry and Physics*; CRC press: Boca Raton, Florida, 2014.
(54) TURBOMOLE V7.4 2017, A Development of University of Karlsruhe and Forschungszentrum Karlsruhe GmbH, 1989−2007; TURBOMOLE GmbH, since 2007, available from http://www.turbomole.com.
(55) Ahlrichs, R.; Bär, M.; Häser, M.; Horn, H.; Kölmel, C. Electronic structure calculations on workstation computers: The program system turbomole. *Chem. Phys. Lett.* **1989**, *162*, 165−169.
(56) Balasubramani, S. G.; Chen, G. P.; Coriani, S.; Diedenhofen, M.; Frank, M. S.; Franzke, Y. J.; Furche, F.; Grotjahn, R.; Harding, M. E.; Hättig, C.; et al. TURBOMOLE: Modular program suite for ab initio quantum-chemical and condensed-matter simulations. *J. Chem. Phys.* **2020**, *152*, 184107.
(57) Kirchner, B.; Spickermann, C.; Lehmann, S. B. C.; Perlt, E.; Langner, J.; von Domaros, M.; Reuther, P.; Uhlig, F.; Kohagen, M.; Brüssel, M. What can clusters tell us about the bulk? *Comput. Phys. Commun.* **2011**, *182*, 1428−1446.
(58) von Domaros, M.; Perlt, E.; Ingenmey, J.; Marchelli, G.; Kirchner, B. Peacemaker 2: Making clusters talk about binary mixtures and neat liquids. *SoftwareX* **2018**, *7*, 356−359.
(59) Shen, J.; Zhu, C.; Reiling, S.; Vaz, R. A novel computational method for comparing vibrational circular dichroism spectra. *Spectrochim. Acta, Part A* **2010**, *76*, 418−422.
(60) Zimmermann, D.; Häber, T.; Schaal, H.; Suhm, M. A. Hydrogen bonded rings, chains and lassos: the case of t-butyl alcohol clusters. *Mol. Phys.* **2001**, *99*, 413−425.
(61) Nicu, V. P.; Domingos, S. R.; Strudwick, B. H.; Brouwer, A. M.; Buma, W. J. Interplay of exciton coupling and large-amplitude motions in the vibrational circular dichroism spectrum of dehydroquinidine. *Chem.—Eur. J.* **2016**, *22*, 704−715.

https://dx.doi.org/10.1021/acs.jpcb.0c06313
J. Phys. Chem. B 2020, 124, 7272−7283

C. Predicting Vibrational Spectroscopy for Flexible Molecules and Molecules with Non-Idle Environments

Barbara Kirchner,[*] Jan Blasius,[*] Lars Esser,[*] and Werner Reckien[*]

Received: 22 September 2020, Published online: 16 December 2020.

Reprinted (adapted) in appendix C with permission[†] from

B. Kirchner, J. Blasius, L. Esser, and W. Reckien, *Adv. Theory Simul.* **2021**, *4*, 2000223.

doi:10.1002/adts.202000223.

For this article a Supporting Information is available free of charge at:
https://onlinelibrary.wiley.com/doi/full/10.1002/adts.202000223.

Contributions to the manuscript

- Development of the concept
- Performance of all calculations except for the SCF convergence and DFT integration grid tests
- Interpretation of the results
- Co-writing of the manuscript

[*] Mulliken Center for Theoretical Chemistry, Clausius Institute for Physical and Theoretical Chemistry, University of Bonn, Beringstr. 4–6, 53115 Bonn, Germany
[†] Permission requests to reuse material from this chapter should be directed to Wiley-VCH GmbH.

ADVANCED THEORY AND SIMULATIONS
www.advtheorysimul.com

Predicting Vibrational Spectroscopy for Flexible Molecules and Molecules with Non-Idle Environments

Barbara Kirchner, Jan Blasius, Lars Esser, and Werner Reckien*

Flexible molecules and non-idle environments can present severe problems in the prediction of vibrational spectra. This work focuses on infrared and vibrational circular dichroism for which the latter is extremely sensitive to such complicated situations. Here two possible ways to perform spectroscopy calculations for such situations are investigated. The first approach is based on static quantum chemical calculations employing cluster-weighting. The second approach is rooted in ab initio molecular dynamics simulations using the time correlations approach. For the present example ((*R*)-butan-2-ol), excellent spectra from simulations are obtained for gas and bulk, when the former is averaged over trajectories with all possible starting conformers and these are scaled to match the experimental spectrum. The cluster-weighted approach is inferior to the simulations but still reaches very good results at much less computational cost. A simplified, but computationally less expensive simulation approach is considered by approximating the electric and magnetic moments, which are input quantities in the correlation function, by classical equations and different populations analysis for the required partial charges. The results are inferior to the full simulations but still give satisfying results at the advantage of being much faster to calculate.

1. Introduction

The calculation of bulk phase spectra[1] often requires the accurate treatment of the environment. This is especially the case if the environment behaves non-idle towards the solute or observed molecules. Consequently, two questions arise, first what is considered an "accurate treatment" and second what counts as a "non-idle environment"? As non-idle environment we simply refer to such an environment that directly or indirectly changes the properties (here the spectrum) of the solute or the molecule under investigation. Therefore, it needs to be considered in the calculations on a certain level of method and model — often on the same level as the observed molecule or only on a slightly reduced one. Examples for such an environmental influence can be electronic or geometrical effects due to non-negligible intermolecular interactions between solute and media as for example hydrogen bonds.[2] However, the accurate treatment of these influences is not always trivial. For instance a large size of the observed molecule (mostly biomolecules) may cause the environment to be not only around the molecule but contained within it. Already in isolated systems, complicated cases occur where large amplitude motion[3] plays a role which becomes even more complicated when an active environment has to be considered.

Coming back to the first point of the accurate treatment, there are several ways to deal with such an intrusive environment. In this work we will consider two approaches, the first being based on static quantum chemical calculations of the observed molecules including explicitly some of the media molecules or fragments. We call the whole assembly a cluster.[4,5] The individual properties of several clusters can be calculated and averaged to arrive at the desired observable property. Besides the method of quantum cluster equilibrium (QCE)[4–6] or cluster weighting (CW)[7] there are many variants of cluster models. The first work, which utilized clusters obtained from snapshots of trajectories, was carried out by the Hermansson et al.[8] and little later by the Huber group.[9] Pliego and Riveros[10] call their approach a cluster-continuum model, while Xu and coworkers[11] have developed the cluster-in-a-solvent method. A cluster can contain explicit (micro-solvation) or implicit (continuum) solvent molecules[12] and the best results are obtained by the combination of both,[13] for an excellent review see ref. [11]. A crucial step in the application of all these different models is the construction of the clusters since the description of the often very involved bulk phase has to be reduced to a small set of representative structures. For this reason, several construction schemes for clusters have been proposed. The clusters can be generated based on approaches of neural network or machine learning, they can be intuitively guessed or extracted from molecular dynamics simulations.[8,9] Alternatively they can be obtained by conformer rotamer ensemble sampling as recently presented by Grimme.[14] When subsequently the Boltzmann weighting (BW) is applied, clusters of equal size and composition are usually selected. However, in the case of QCE, clusters of different size and composition[15] can serve as input for the

Prof. B. Kirchner, J. Blasius, L. Esser, Dr. W. Reckien
Mulliken Center for Theoretical Chemistry
Rheinische Friedrich-Wilhelms-Universität Bonn
Beringstr. 4+6, D-53115 Bonn, Germany
E-mail: kirchner@thch.uni-bonn.de

The ORCID identification number(s) for the author(s) of this article can be found under https://doi.org/10.1002/adts.202000223

DOI: 10.1002/adts.202000223

calculations and the weighting is applied to all of them at the same time. Besides the calculation of properties to which clusters of different sizes can contribute simultaneously, this method opens the door for concentration-dependent calculations.[16–18]

Apart from the static approach, we will secondly focus on ab initio molecular dynamics simulations[19] (AIMD) of a complete but "small" system. The Delle Site group showed a specific locality for the properties applied here such as the electric dipole moment, which justifies the small system size.[20] For the overall system, AIMD calculates the electronic structure on the fly, that is, at each time step. This in turn allows the spectra to be determined from the Green–Kubo or correlation function approach[21,22] and the subsequent Fourier transformation as applied in molecular dynamics simulations by directly collecting the correlated quantities in each time step. In the case of the infrared (IR) spectrum the auto-correlation functions of the electric dipole moments are required,[1,23,24] Raman spectroscopy employs auto-correlation of polarization,[25] while vibrational circular dichroism (VCD) cross-correlates magnetic with electric dipole moment.[26] Recently, an excellent study compared a cluster approach based on Boltzmann weighting to an AIMD ansatz of the substance trans-1-amino-2-indanol solvated in dimethyl sulfoxide.[27] Several solvent approaches are rarely discussed or compared in one study. Thus, Zehnacker and co-workers offered a significant insight into the advantages and disadvantages of the individual approaches.[27]

We would like to briefly mention other spectroscopy calculations based on AIMD, namely, resonance Raman, [28] Raman optical activity, [29] and sum frequency generation.[30,31] Furthermore, some important routes based on polarizable force field molecular dynamics simulations [32–36] also allow to obtain the quantity which enters the Green–Kubo relation on the fly. Another approach operates with hybrid simulation techniques (QM/MM) [37,38] where the observed molecule forms the quantum mechanical (QM) part and the non-idle environment the molecular mechanics (MM or MD) part. Chiral molecules in the amorphous solid encounter were tackled by a fragmentation approach involving MD simulations.[39] Furthermore, Raman optical activity [40,41] was investigated in ab initio calculations by the Pecul group. A polarizable MD/QM approach was focused by the Capelli group.[42,43]

In the present work we focus on IR and VCD spectroscopy, the latter one being considered the chiral version of IR spectroscopy, which measures the different attenuation of left- and right-circularly polarized infrared radiation. While the static calculation of IR spectra is well described in several textbooks, the calculations of VCD spectra [44,45] can be based on magnetic field perturbation theory [46–49] or rely on nuclear velocity perturbation theory [50–54] to calculate atomic polar and atomic axial tensors. When considering an ensemble of different structures (different conformers or clusters) some kind of weighting is usually necessary to obtain a correctly averaged spectrum that corresponds to the experiment. The most commonly used weighting scheme are the Boltzmann factors. However, since these weights depend on the electronic energy, they are very sensitive to the underlying theory level. A new approach based on a genetic algorithm that fits the conformer weights to the experimental spectra and thus takes into account uncertainties in the electronic energies has recently been proposed by Buma, Nicu and co-workers.[55] Unlike IR, [3] VCD spectra are extremely sensitive to conformational changes [56,57] and environmental effects induced by solute-solvent or solute-solute interactions which thus have to be included in the calculations to match the experiment.[58,59] Since the calculation of VCD spectra based on AIMD simulations relies on the Fourier transformed cross-correlation function of the electric dipole moment and the magnetic dipole moment,[37,60,61] these properties have to be calculated. Traditionally, the electric dipole moments are accessible via Wannier centers [62,63] and more recently by integrating the electron density over a molecular cell, which is determined by a radical Voronoi tessellation.[64] The magnetic dipole moments can be obtained by classical approaches [26,38] or by quantum mechanical approaches.[53,54] To quantify the compliance, the overlap σ between the experimental and calculated spectra can be calculated, for example, with the SimVCD measure.[65] A value of +1 represents a perfect agreement between experiment and calculation, and a value of −1 indicates that both spectra are mirrored to each other. Thus, −1 implies, in principle, opposite enantiomers. Starting from 0.2, the value allows a safe (>90%) determination of the absolute configuration.

The article is structured as follows: The cluster weighting methodology, cluster generation, cluster weighting input details, and the quantum chemical methodology used are described in detail in Section 2. We then give details about the AIMD simulations and the trajectory analysis (Section 3). In Section 4, we present the results. The following Section 4.1 gives a detailed analysis of the AIMD spectra for the gas phase and the bulk. In Section 4.2, we discuss functional and basis set including CW input parameter dependencies on the spectra obtained from CW in order to compare in Section 4.3 AIMD with CW spectrum. An analysis of the moments in Section 4.4 follows. Finally, Section 5 gives a general discussion and conclusions.

2. Cluster Weighting Method and Computational Details

2.1. The Cluster-Weighting Method

The QCE approach [4,6] begins its description of gaseous and liquid phases by a so-called cluster gas, which is in thermodynamic equilibrium and consists of non-point particles.[4] The chemical equation for the cluster equilibrium of a pure substance is

$$C_1 \rightleftharpoons \frac{C_2}{i(2)} \rightleftharpoons \frac{C_3}{i(3)} \rightleftharpoons \cdots \rightleftharpoons \frac{C_{\wp}}{i(\wp)} \tag{1}$$

with C_1 and $C_{\wp}$ being the monomer and a cluster of size $i(\wp)$, respectively. In 2011 we extended the QCE to binary systems (bQCE) [15]:

$$i(\wp)C_1 + j(\wp)C_2 \rightleftharpoons C_{\wp} \tag{2}$$

A cluster $C_{\wp}$ is composed of $i(\wp)$ and $j(\wp)$ monomers of the components 1 and 2. The primary goal of the model is to obtain the equilibrium cluster populations $N_{\wp}$ that minimize the free energy A of a system with volume V, temperature T and total number of monomers $N^{\text{tot}} = N_1^{\text{tot}} + N_2^{\text{tot}}$, where N_1^{tot} and N_2^{tot} is the number of monomers of the components 1 and 2. If the cluster

populations are known, the systems' total partition function Q^{tot} can be calculated as follows

$$Q^{\text{tot}}(\{N_{\wp}\}, V, T) = \prod_{\wp=1}^{N} \frac{1}{N_{\wp}!}[q_{\wp}^{\text{tot}}(V,T)]^{N_{\wp}} \tag{3}$$

where $\{N_{\wp}\}$ denotes the full set of total cluster populations $N_{\wp}$ and $q_{\wp}^{\text{tot}}$ is a single cluster partition function given by

$$q_{\wp}^{\text{tot}}(V,T) = q_{\wp}^{\text{rot}}(T) q_{\wp}^{\text{vib}}(T) q_{\wp}^{\text{trans}}(V,T) q_{\wp}^{\text{elec}}(V,T) \tag{4}$$

The rotational, vibrational and translational partition functions $q_{\wp}^{\text{rot}}(T)$, $q_{\wp}^{\text{vib}}(T)$ and $q_{\wp}^{\text{trans}}(V,T)$ are calculated from standard equations for the rigid rotator, harmonic oscillator and particle in a box, respectively.[66]

Based on the non-point-shaped particles, the volume is corrected by the translational partition functions, since the total volume is not accessible for the particles. Therefore, the exclusion volume V_{ex}, given by

$$V_{\text{ex}} = b_{\text{xv}} \sum_{\wp=1}^{N} N_{\wp} v_{\wp} \tag{5}$$

is subtracted from the phase volume V. Thereby $v_{\wp}$ denotes the volume of cluster $C_{\wp}$ and b_{xv} is an empirical parameter which corrects the cluster volumes.

The electronic cluster partition function $q_{\wp}^{\text{elec}}(V,T)$ is calculated from the referenced electronic energy $\epsilon_{\wp}^{\text{elec}}$ and is supplemented by a term that takes into account interactions between clusters described by a mean-field-type attractive energy. The electronic partition function reads as follows

$$q_{\wp}^{\text{elec}}(V,T) = \exp\left(-\frac{\epsilon_{\wp}^{\text{elec}} - [i(\wp)+j(\wp)]\frac{a_{\text{mf}}}{V}}{k_{\text{B}}T}\right) \tag{6}$$

where k_{B} is the Boltzmann constant and a_{mf} is the mentioned mean-field parameter, thus scaling the interactions between clusters. Thus, a_{mf} is the second empirical parameter in the theory.

The systems' total partition function Q^{tot} is a function of the cluster populations $\{N_{\wp}\}$ obtained by minimizing the free energy

$$A = -k_{\text{B}}T \ln Q^{\text{tot}}(\{N_{\wp}\}, V, T) \tag{7}$$

This function should be minimized under the conditions of a fixed total number of particles and a fixed total mass. Two polynomial equations can be derived from both constraints, namely the population polynomial

$$0 = -1 + \sum_{\wp=1}^{N} \frac{i(\wp)+j(\wp)}{N_1^{\text{tot}}+N_2^{\text{tot}}} \frac{q_{\wp}^{\text{tot}}}{\left(q_1^{\text{tot}}\right)^{i(\wp)}\left(q_2^{\text{tot}}\right)^{j(\wp)}} N_1^{i(\wp)} N_2^{j(\wp)} \tag{8}$$

and the volume polynomial

$$\begin{aligned} 0 = &-pV^3 + \left(\sum_{\wp=1}^{N} k_B T N_{\wp} + p b_{\text{xv}}(v_1 N_1^{\text{tot}} + v_2 N_2^{\text{tot}})\right) V^2 \\ &-\left(\sum_{\wp=1}^{N} N_{\wp}(i(\wp)+j(\wp)) a_{\text{mf}}\right) V \\ &+\sum_{\wp=1}^{N} N_{\wp}(i(\wp)+j(\wp)) a_{\text{mf}} b_{\text{xv}} (v_1 N_1^{\text{tot}} + v_2 N_2^{\text{tot}}) \end{aligned} \tag{9}$$

Both polynomials result in a non-linear equation system, which can be solved numerically. The two empirical parameters a_{mf} and b_{xv} are optimized on the experimental reference (usually one density and the boiling point). The obtained partition functions and populations can be used in further calculations.

Applications of the QCE method involve many neat and binary systems, including water,[4,67,68] aqueous solutions [15,69] and even ionic liquids.[70] In addition, we calculated activity coefficients [71] and ionicity [17,18,72] with binary QCE and we applied QCE or cluster weighting CW to vibrational circular dichroism [7].

2.2. Cluster Generation

Since the description of the complex bulk phase is based on a limited set of clusters, the choice of the input structures for the cluster-weighting is an essential step [7]. First, it was shown that for the calculation of VCD spectra of conformationally flexible molecules more than one conformer has to be considered.[55] Furthermore, the CW calculation allows the simultaneous inclusion of different oligomers and for these, constitutional isomers can be selected. As constitutional isomers we consider such clusters with different motifs, that is, for a trimer a ring and a chain can be constructed, for larger clusters even more structure motifs appear. All clusters considered are taken from our previous work.[7]

We created the global minimum structure for the monomer up to the decamer by applying a structure optimization based on genetic algorithms on the classical force field level of theory. For this purpose we combined the software Ogolem,[73,74] with the Amber 2016 molecular dynamics package [75] and the generalized Amber force field (GAFF).[76]

2.3. Quantum Chemical Calculations

Since the goal of the work is to compare CW to AIMD, we calculated the clusters quantum chemically on different theoretical levels. All clusters were optimized using the BP86,[77,78] the BLYP, [77,78] and the B3LYP [77,78] functional. For the generalized gradient approximation (GGA) functionals we used both the def2-SVP and the def2-TZVP basis set,[79] for the B3LYP functional only the def2-TZVP basis set. For each calculation dispersion corrections according to the D3 dispersion scheme [80,81] were used. The neglect of these corrections was tested and some examples show improved results, but these results were found for the conformers of rotaxanes.[82] Nevertheless, we expect in principle that the dispersion correction will play an important role already for a dimer. All clusters were treated with implicit solvation, which was considered by the solvation model Cosmo [83] using the dielectric constant of (*R*)-butan-2-ol at 293.15 K corresponding to 17.26.[84] In general, we have chosen 10^{-4} a.u. as convergence criteria for the maximum norm of the cartesian gradient and 10^{-8} a.u. for the energy of the SCF. We use a fine multigrid (m4) [85] for the numerical integration of the functional. Some tests for the sensitivity of the electronic energy with respect to the mentioned parameters are given in **Table 1**. Note that in some problematic cases we increased the multi-grid to m5 for some larger clusters, all information is given in the supporting information.

Table 1. Tests of the various SCF convergence criteria of 10^{-6}, 10^{-8}, and 10^{-9}, as well as various selections of DFT integration grids m3, m4 and m5.

		Continuum			No continuum		
Basis	SCF/grid	Monomer	Dimer	ΔE	Monomer	Dimer	ΔE
SVP	6/m3	−233.520995	−467.058865	−44.3	−233.514891	-467.049110	−50.7
	6/m4	−233.520999	−467.058803	−44.1	−233.514896	−467.049133	−50.8
	6/m5	−233.520999	−467.058722	−43.9	−233.514895	−467.049126	−50.8
	8/m3	−233.520995	−467.058879	−44.3	−233.514891	−467.049180	−50.9
	8/m4	−233.520999	−467.058814	−44.1	−233.514896	−467.049235	−51.1
	8/m5	−233.520999	−467.058803	−44.1	−233.514895	−467.049203	−51.0
	9/m3	−233.520995	−467.058879	−44.3	−233.514891	−467.049180	−50.9
	9/m4	−233.520999	−467.058814	−44.1	−233.514896	−467.049235	−51.1
	9/m5	−233.520999	−467.058798	−44.1	−233.514895	−467.049203	−51.0
TZVP	6/m3	−233.788351	−467.587266	−27.7	−233.781298	−467.576607	−36.8
	6/m4	−233.788347	−467.587263	−27.8	−233.781298	−467.576661	−36.9
	6/m5	−233.788348	−467.587265	−27.8	−233.781298	−467.576658	−36.9
	8/m3	−233.788348	−467.587267	−27.8	−233.781298	−467.576608	−36.8
	8/m4	−233.788347	−467.587265	−27.8	−233.781298	−467.576660	−36.9
	8/m5	−233.788348	−467.587267	−27.8	−233.781298	−467.576659	−36.9
	9/m3	−233.788348	−467.587266	−27.8	−233.781298	−467.576608	−36.8
	9/m4	−233.788347	−467.587265	−27.8	−233.781298	−467.576660	−36.9
	9/m5	−233.788348	−467.587267	−27.8	−233.781298	−467.576659	−36.9

For all calculations, we list the total energy E_h in Hartree and (ΔE) interaction energy in kJ mol^{-1} with one digit after the decimal. All calculations were performed with the BP86 functional and the SVP as well as the TZVP basis set.

The results of the BLYP functional and some results of the BP86 functional were compared with unscaled and scaled AIMD calculations. For details see methodology of AIMD calculations.

All quantum chemical optimizations as well as the calculations of the individual cluster VCD spectra were performed using the Turbomole 7.4 software package [44,86–88] and the broadening of the VCD spectra was modeled by a Lorentzian band shape employing a full width at half maximum of 8 cm^{-1}.

Since both the Boltzmann and the cluster weighting are very sensitive to the energy gained, we also tested various parameters of the quantum chemical calculations for the dimer. The corresponding spectra are shown in the supporting information (Figures S4 and S5, Supporting Information) and do not show a pronounced sensitivity. Table 1 shows the absolute interaction energies for the dimer and monomer and the interaction energies for the dimer. We observe a good agreement between the different energies, so we are sure that our parameters are adequately chosen. The interaction energies show deviations of less than 1 kJ mol^{-1} when comparing the different criteria.

2.4. Cluster Weighting Calculations

The QCE equilibrium populations were evaluated with Peacemaker,[4,5,89,90] a publicly available software package for neat and binary QCE calculations.[90] All calculations were performed for a fixed pressure of 101.325 kPa and in a temperature range of 200–500 K. The cluster volumes were defined as van der Waals volumes with radii from Bondi's compilation.[91] As experimental input the boiling point $T_b = 372.0$ K [84] and the density at 293.15 K $\rho_{293.15} = 0.806$ g cm^{-3} [84] of (*R*)-butan-2-ol were employed. The empirical parameters a_{mf} and b_{xv} were optimized between values of 0.0 and 3.0 to reproduce the boiling point and density at 293.15 K as accurately as possible.

3. Spectra from Ab Initio Molecular Dynamics Simulations and Computational Details

3.1. AIMD Simulations

Several systems were simulated from AIMD, nine single molecules (based on all possible monomer conformations, referenced as gas) and 16 molecules (coined bulk) of (*R*)-butan-2-ol. While the single molecule trajectories were created in this work, the 16 molecule trajectory we took from ref. [26]. The starting conformations can be understood according to the dihedral angles defined in **Figure 1** with gas1 ≡ ($\tau_1 = 300$; $\tau_2 = 300$), gas2 ≡ ($\tau_1 = 180$; $\tau_2 = 180$), gas3 ≡ ($\tau_1 = 300$; $\tau_2 = 180$), gas4 ≡ ($\tau_1 = 180$; $\tau_2 = 60$), gas5 ≡ ($\tau_1 = 60$; $\tau_2 = 60$), gas6 ≡ ($\tau_1 = 300$; $\tau_2 = 60$), gas7 ≡ ($\tau_1 = 180$; $\tau_2 = 300$), gas8 ≡ ($\tau_1 = 60$; $\tau_2 = 300$), gas9 ≡ ($\tau_1 = 60$; $\tau_2 = 180$) and angles in degrees. Of course these rearrange partly in the equilibration runs and partly stay close to their local minima. All AIMD simulations are based on density functional theory using the QUICKSTEP module [92] within the CP2K [93] program package. The hybrid Gaussian and plane waves (GPW) approach was used to calculate the energies and forces on the atoms. As basis set we choose the molecularly optimized double-ζ basis set (MOLOPT-DZVP-SR-GTH).[94] Note that this generally contracted basis set contains diffuse primitives and is

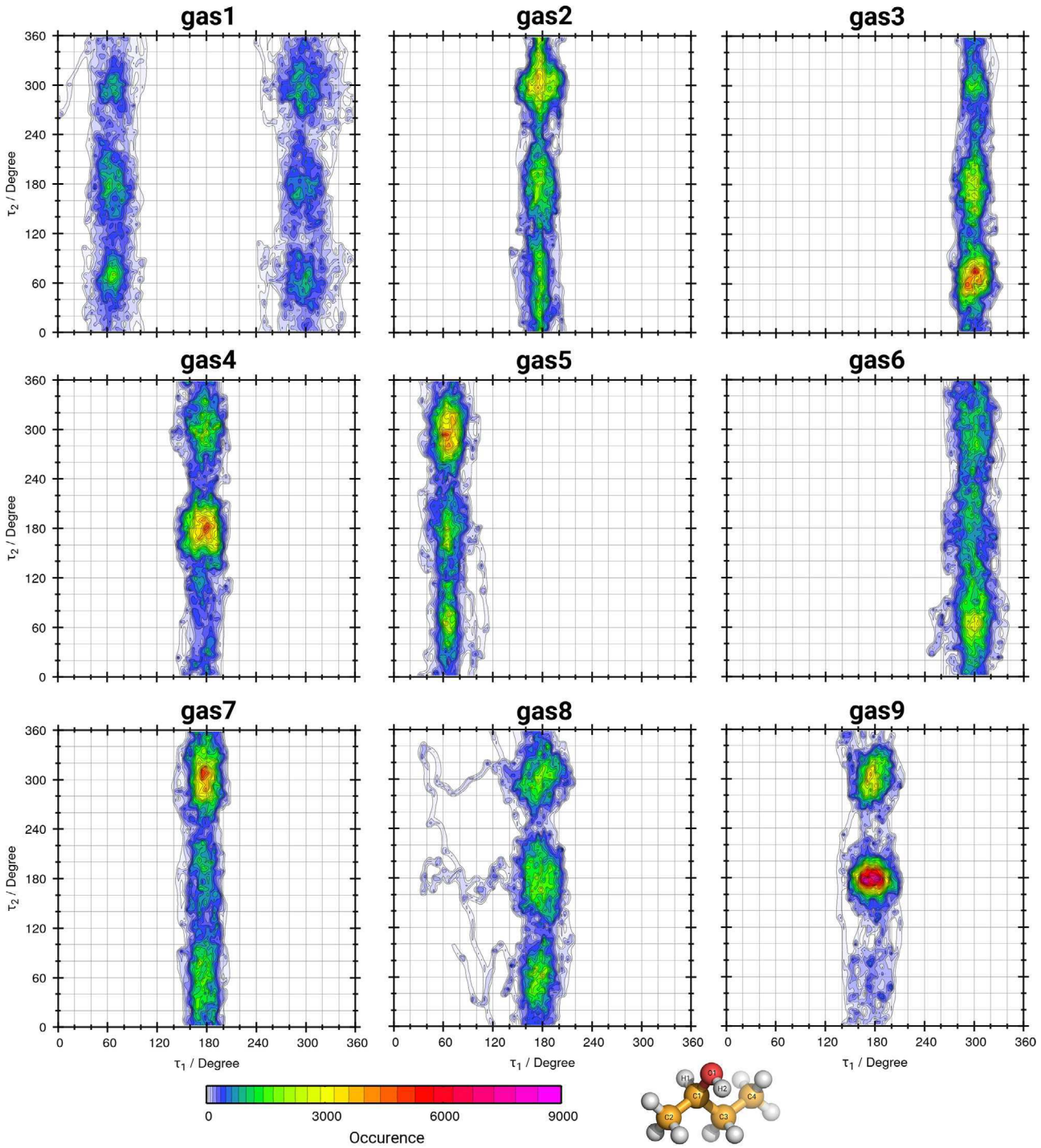

Figure 1. Conformation plots showing which of the nine minima of the potential energy surface are visited by the gas phase simulations gas1 to gas9. Plotted is τ_1:C2-C1-C3-C4 dihedral angle versus τ_2:H2-O1-C1-H1 dihedral angle.

obtained by minimizing a linear combination of the total energy and the condition number of the overlap matrix. It is used in combinations with pseudopotentials and the hybrid approach and is therefore not comparable with standard quantum chemical basis sets. Therefore, for a given accuracy in the total energy, considerably fewer basis functions are required than in the usual split valence scheme. This can make the MOLOPT-DZVP-SR-GTH comparable to the def2-TZVP basis set, which is important for the comparison between CW and AIMD spectra. For the functional we choose here and in the previous work [26] the generalized gradient approximations (GGA) functional BLYP [77,78] and the corresponding BLYP Goedecker–Teter–Hutter

pseudopotentials for core electrons,[95–97] since hybrid functionals are outside the scope of standard AIMD simulations and BLYP showed good performance for condensed phase systems in several comparative studies.[98,99] The choice of this functional in the AIMD simulations is the reason why we have also repeated the static quantum chemical calculations of all clusters with the same BLYP functional. A 280 Ry density CUTOFF criterion with the finest grid level was used together with multi-grids number 5 (NGRID 5 and REL_CUTOFF 40) using the smoothing for the electron density (NN10_SMOOTH) and its derivative (NN10).[92] Dispersion interactions were accounted for by applying the DFT-D3 type of a pair potential van der Waals density functional.[80,81] For the SCF calculation, the default value (10^{-5}) was used as target accuracy for the SCF convergence. The DIIS minimizer [93] was employed to achieve a faster orbital transformation by direct inversion in the iterative subspace. The maximum number of SCF iterations to be performed for one iteration was set to 200.

The following equilibration and production runs were carried out applying periodic boundary conditions to avoid boundary effects. The canonical (NVT) ensemble was applied using the Nosé–Hoover-chain thermostats [100,101] with a time constant of the thermostat chain of 50 fs (first equilibrium run), 10 fs (second equilibrium run), and 50 fs (production run). The first equilibration runs were performed over 5 ps (10 000 steps with a time step of 0.5 fs) and the temperature was increased to 600 K to achieve faster equilibration. The second equilibration runs were performed over 5 ps (10 000 steps with a time step of 0.5 fs) defining the keyword REGION MASSIVE (thermostating each individual atom) and lowering the temperature to 400 K to relax the system to the correct temperature. The subsequent production runs were performed over 30 ps (60 000 steps à 0.5 fs) for the bulk and gas2 to gas9 systems and over 50 ps (100 000 steps) for the gas1 system at a temperature of 400 K. Electric and magnetic dipole moments were analyzed for the gas1 trajectory. For this trajectory also different populations analysis were carried out to obtain partial charges, namely Blöchl, [102] Mulliken,[103] and Löwdin [104] as implemented in the CP2K package.[93]

Please note here that the temperature has been set to 400 K to improve the sampling. In addition, several AIMD studies [99,105] have shown that the temperature is 20–50 K too low compared to experiment. The box length for the bulk system was set to 13.45 Å, which corresponds to a density of 0.81 g cm^{-3} at 293.15 K. For the gas phase simulation, the box length was set to 12.00 Å.

3.2. Analysis

Our open source program TRAVIS (Trajectory Analyzer and Visualizer) was used to investigate the time-dependent structural evolution of the simulated systems and to calculate IR and VCD spectra from the AIMD trajectories.[106,107] The results are visualized with the Xmgrace software [108] or, alternatively with the program gnuplot (version 5.0) [109] to generate 3D data plots.

3.2.1. Calculation of Vibrational Spectra

The AIMD calculation of different spectroscopic properties is based on the Green and Kubo, [21,22] approach. To transfer the correlation functions into a frequency spectrum, a Fourier transformation according to the Wiener-Khintchine theorem is applied: [110,111] Using the time derivative, which is advantageous for numerical reasons, the IR intensities $A(\omega)$ are then given by

$$A(\omega) = \frac{N_A}{24\pi\varepsilon_0 c^2 k_B T} \int \langle \dot{\mu}(\tau) \cdot \dot{\mu}(t+\tau) \rangle_\tau e^{-i\omega t} dt \tag{10}$$

For the comparison with experimental data the corresponding wavenumber-dependent representation is

$$A(\tilde{\nu}) = \frac{N_A}{12\varepsilon_0 c k_B T} \int \langle \dot{\mu}(\tau) \cdot \dot{\mu}(t+\tau) \rangle_\tau e^{-2\pi i c\tilde{\nu} t} dt \tag{11}$$

With the Avogadro constant N_A (in mol^{-1}), the dielectric constant ε_0 (in $C^2\ s^2\ kg^{-1}\ m^{-1}$), the speed of light c (in m s^{-1}), the Boltzmann constant k_B (in $m^2\ kg\ s^{-2}\ K^{-1}$), the temperature T (in K), the electric dipole moment μ (in C m), the time t/τ (in s) and the wavenumber $\tilde{\nu}$ (in m^{-1}) the IR intensity has the unit $m^2\ mol^{-1}$. For further details see ref. [1]

Abbate et al.[60] developed the time-correlation ansatz for the calculation of VCD spectra from molecular dynamics trajectories, which is based on a cross-correlation of the electric and magnetic dipole moment:

$$A(\omega) = \frac{N_A}{24\pi\varepsilon_0 c^3 k_B T} \int \langle \dot{\mu}(\tau) \cdot \dot{M}(t+\tau) \rangle_\tau - \langle \dot{M}(\tau) \cdot \dot{\mu}(t+\tau) \rangle_\tau e^{-i\omega t} dt \tag{12}$$

The corresponding wavenumber-dependent expression is

$$A(\omega) = \frac{N_A}{12\varepsilon_0 c^2 k_B T} \int \langle \dot{\mu}(\tau) \cdot \dot{M}(t+\tau) \rangle_\tau - \langle \dot{M}(\tau) \cdot \dot{\mu}(t+\tau) \rangle_\tau e^{-2\pi i c\tilde{\nu} t} dt \tag{13}$$

Please note that the VCD intensity has a slightly different prefactor with respect to the speed of light c compared to the IR intensity due to the unit of the magnetic moment (which is A m^2). Nevertheless, also the VCD intensity has the unit $m^2\ mol^{-1}$. The magnetic dipole moment is calculated by the electric current density, for more details, see ref. [26]

The radical Voronoi tessellation is used to calculate the electric dipole moments.[64] All Voronoi cells C_i of all atoms belonging to the same molecule are united to obtain molecular cells M_k. The recognition of the molecules is available in TRAVIS.[106,107] Molecular dipole moments are obtained by integrating the electron density $\rho(r)$, which is accessible for each time step in an AIMD simulation, as a function of the spatial coordinate r over the previously defined molecular cells:

$$\mu = \int_{M_k} r \cdot \rho(r)\, dr;\ k = 1, \ldots, N \tag{14}$$

Table 2. Overlap of σ from SimVCD tool[65] between experimental gas and bulk phase VCD spectra of (*R*)-butan-2-ol with calculated VCD spectra from AIMD simulations.

	0.95	0.96	0.97	0.98	0.99	1.00	1.01	1.02	1.03	1.04	1.05
σ_{gas}	−0.197	−0.100	−0.038	−0.011	0.049	0.248	0.509	**0.536**	0.363	0.193	0.091
σ_{bulk}	−0.023	−0.047	−0.145	−0.234	−0.216	−0.015	0.181	0.415	**0.456**	0.222	0.069

The calculated frequencies were scaled with factors between 0.95 and 1.05, which are given in the first row. Bold marked overlaps show the best agreement with the experimental references. Please note, that gas is the mean of the nine trajectories gas1 to gas9. Conformational plots for the simulations gas1 to gas9 can be found in Figure 1.

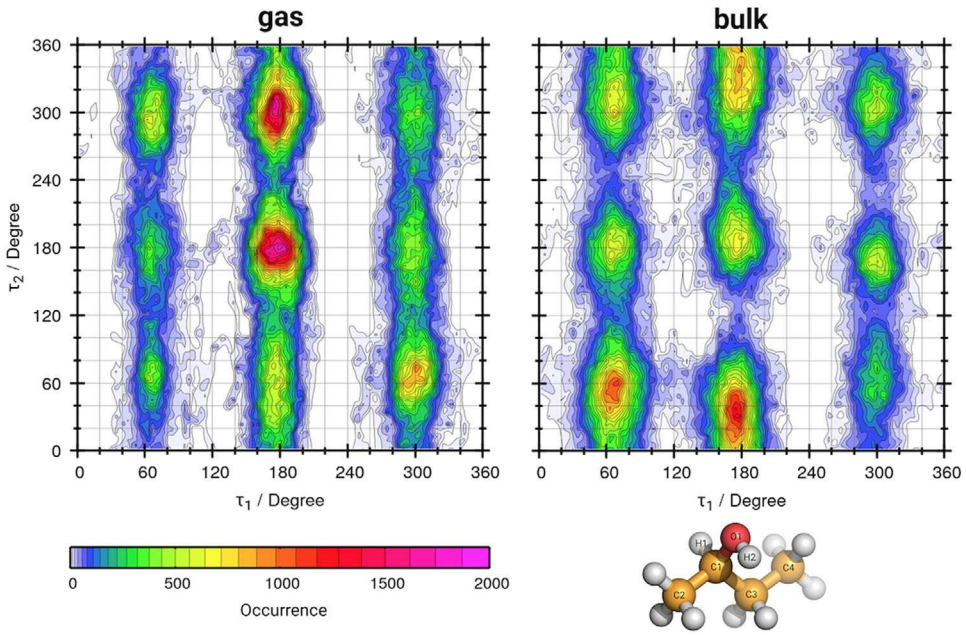

Figure 2. Conformation plot indicating whether all nine minima of the potential energy surface are visited. The plot shows the dihedral angle τ_1:C2-C1-C3-C4 against the dihedral angle τ_2:H2-O1-C1-H1. Left: Gas and right: Bulk phase. Please note, that gas is the mean of the nine trajectories gas1 to gas9.

4. Results and Discussion

4.1. Comparison of Ab Initio Molecular Dynamics Simulations and Experiment

In general, ab initio (and traditional) molecular dynamics simulations take anharmonicity into account, since molecular dynamics does not use a harmonic potential approximation as in frequency analysis in standard static quantum chemical calculations. However, the motion of the nuclei in standard simulations is treated classically. Therefore, nuclear quantum effects are not considered. The electronic structure is based on the Born–Oppenheimer approximation and the electronic structure is based on generalized gradient approximation (GGA) DFT, which has been shown to introduce another error to AIMD (see e.g., the work of Klein[99] and the discussion of the self-interaction error therein). The influence of the electronic structure on the spectrum (BLYP vs BLYP-D3) was also demonstrated.[98] In addition, the step-wise integration of the equation of motion has an influence over the time step size, which was demonstrated, for example, by Bourănd co-workers.[61] In quantum chemistry, besides the treatment of anharmonicity, such problems are sometimes solved by a simple approach using frequency scaling.[43,112]

To maximize the overlap with the experiment, we have also determined scaling factors for the calculated frequencies in the gas and in the bulk phase. The results are listed in **Table 2**.

Our scaling factors for the gas (1.02) and for the bulk (1.03) lead to overlaps of $\sigma_{gas} = 0.536$ and $\sigma_{bulk} = 0.456$, indicating a quite satisfactory agreement with the experiment. The gas phase spectrum was obtained from nine simulations with different initial conditions using all possible conformers (see Figure 1 and computational details) as the arithmetic mean between the nine trajectories (see **Figure 2**). Both the C–O bond and the central C–C bond exhibit three distinct torsional minima on the potential energy surface, resulting in nine conformations of the molecule, all of which seem to be sufficiently visited in the AIMD simulations, as can be seen from the conformation plots previously created in ref. [113], see Figure 2.

The excellent agreement between the averaged gas phase simulations and experiment suggests to follow this approach, where the simulations are started from all possible monomer conformations in order to correctly sample the conformational space. It is also clear that only averaging leads to the complete exploration of the conformational space, compare Figure 1 with 2. This is in line with the philosophy of the more recent research topic

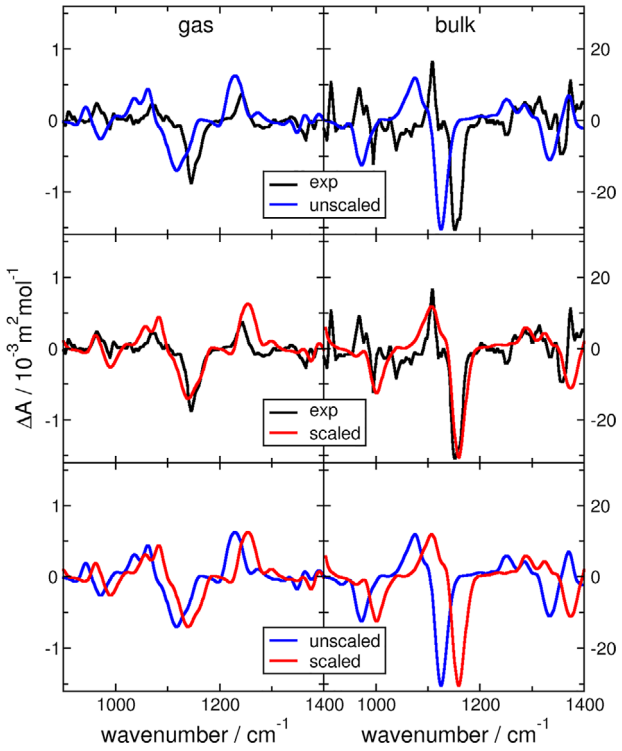

Figure 3. VCD spectra for gas (left) and bulk (right) in the range between 900 and 1400 cm^{-1}. The experimental gas spectrum is a diluted solution of (*R*)-butan-2-ol in carbon disulfide, both experimental gas and bulk are from ref. [56] Top: Comparison between experiment and unscaled AIMD data. Middle: Experiment and scaled AIMD data. Bottom: Scaled and unscaled AIMD data. Note that the gas indicates the mean of the nine trajectories from gas1 and gas9. Blue: unscaled; red: scaled; black: experiment. For corresponding overlaps see Table 2.

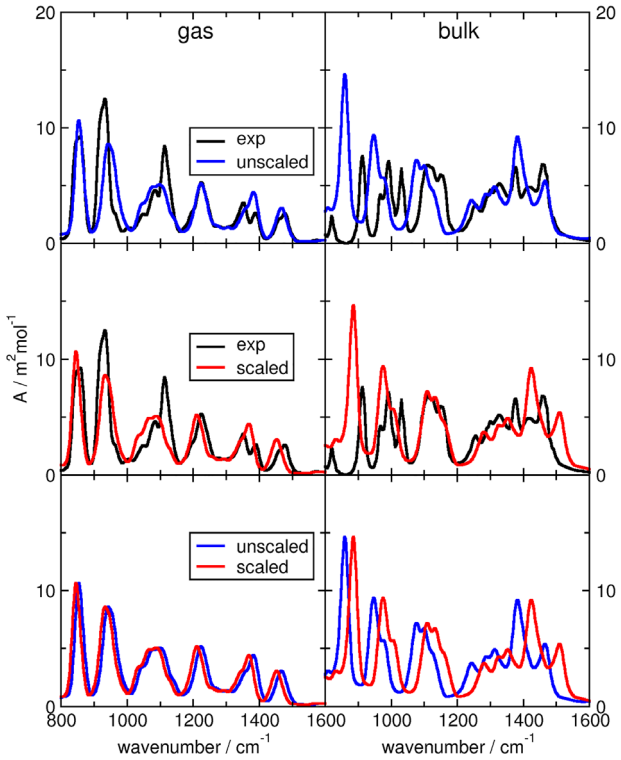

Figure 4. IR spectra for gas (left) and bulk (right) in the range between 800 and 1600 cm^{-1}. The experimental gas spectrum is a diluted solution of (*R*)-butan-2-ol in carbon disulfide, both experimental gas and bulk are from ref. [56]. Top: Comparison between experiment and unscaled AIMD data. Middle: Experiment and scaled AIMD data with scaling factors: gas = 0.99 (σ = 0.786); bulk = 1.03 σ = 0.7800). Bottom: Scaled and unscaled AIMD data. Blue: unscaled; red: scaled; black: experiment.

of enhanced sampling.[114–119] For the averaged simulations, it is obvious that the conformation with $\tau_1 = 180°$ and $\tau_2 = 300$ and 180° are the most frequently visited conformations. This is fully consistent with our previously published results from applying cluster weighting to the monomer conformations in static quantum chemical calculations.[7] Interestingly, due to intermolecular interactions, the dominance of the conformers shifts in the bulk to those with $\tau_1 = 60$ and 180° and $\tau_2 = 60°$.

In **Figure 3**, we show the gas and bulk AIMD and experimental VCD spectra for the scaled and unscaled results. As discussed earlier,[26] due to the theoretical standard, a noticeable red-shift of the calculated data occurs (Figure 3 top and bottom panels). However, we observe an excellent agreement between experiment and calculations, when applying our scaling factors. In particular, AIMD agrees exceptionally well with the −/+ VCD pattern in the gas phase at 1145 and 1242 cm^{-1}. For the bulk AIMD, the spectrum agrees well with a positive peak at around 1109 cm^{-1} followed by a strong negative peak at 1152 cm^{-1} and another weak positive peak at 1290 cm^{-1} of the experiment. However, below 1100 cm^{-1} the agreement between experiment and simulation is worse. The calculated overlap between bulk simulation and experiment in this range is only 0.112. One of the influences for the lack of the correct description of the bandwidth could be the length of the simulations. In Figure S2, Supporting Information, we confirm the change of the bands with simulation time. We also show that our trajectory length appears sufficiently converged for bands above 1100 cm^{-1}. Furthermore, the intensity ratios are also very well reproduced in the bulk. This is also reflected in the high overlaps of 0.536 (gas) and 0.456 (bulk) (Table 2). That the overlap numbers should be treated with caution and can only be interpreted in combination with the spectrum is shown by the small overlaps between the scaled and the unscaled spectrum (see Table S1, Supporting Information, bulk value), which are the same spectra shifted only by the scaling factor. Overall, given the short simulation time (30 ps) and system size (16 molecules) the agreement between AIMD simulation and experiment is excellent. Such a locality behavior of the electric dipole moment has been investigated previously.[120] It seems that all important conformations are sampled (see Figures 1 and 2), especially in the averaged gas phase.

Finally, we show the gas and bulk IR spectra in **Figure 4**. Again, we observe that scaling leads to a better agreement between bulk and experiment. Since AIMD covers anharmonicity effects the discrepancy between experiment and simulations can be attributed to the incorrect description of GGA functionals, the small basis set or the choice of time step.

The full scaling range from 0.95 to 1.05 for the gas and the bulk AIMD is given in Table S2, Supporting Information. Furthermore, the comparison between VCD and IR is possible in

Table 3. Overlap of σ from SimVCD tool[65] between experimental bulk phase VCD spectrum and calculated VCD spectra employing CW for different sized cluster sets on different theoretical levels.

Cluster	B3LYP TZVP	BLYP SVP	BLYP TZVP	BP86 SVP	BP86 TZVP	BLYP* TZVP	BP86* TZVP
i1	0.102	0.015	0.003	0.019	−0.003	0.003	−0.003
ii1	0.104	0.000	0.001	0.019	−0.007	−0.005	−0.009
iiia1	0.125	0.175	0.035	0.222	0.040	0.047	0.058
iva1	0.075	0.030	0.039	0.045	0.040	0.046	0.058
va1	0.118	0.114	0.112	0.045	0.040	0.114	0.182
via1	0.108	0.109	0.119	0.045	0.040	0.125	0.208
viia1	0.107	0.114	0.120	0.045	0.040	0.130	0.320
viiia1	0.107	0.123	0.120	0.045	0.040	0.130	0.320
ixa1	0.107	0.206	0.120	0.045	0.040	0.131	0.340
xa1	0.107	0.207	0.120	0.045	0.040	0.131	0.239

* indicates that the referenced binding energies have been doubled in the calculation of CW. The labeling of the clusters is taken from ref. [7]. The Roman number terms the size of the cluster. The remainder indicates the conformation.

Figure S1, Supporting Information, where we have plotted the spectra together.

4.2. Comparison of Different Functionals in Cluster Weighting

We now turn to the results of the cluster weighting, that is, static quantum chemical calculations based on the QCE approach, and in this section we compare the performance of different functionals. Previously,[7] we build a cluster set, which we have coined S4^{gm}. The superscript "gm" stands for global minimum and the four stands only for the fourth. It is important, that this cluster set contains all global minimum oligomers from one to ten. Furthermore it is important to understand, that all clusters included in the calculation are given a weight by the QCE calculation. The individual spectrum of each cluster is then weighted to obtain a total spectrum. For these clusters, we tested the agreement with the experiment step by step, that is, by increasing the oligomers contained.

In **Table 3**, the cluster label in the cluster column indicates the largest cluster included for the overlap calculations, all smaller clusters are always included.

The clusters were calculated using the D3 dispersion correction and implicit solvation with Cosmo, see Section 2.3. It is disappointing that a strict systematic trend is missing, although increasing the cluster size seems to lead to slightly better results. Compared to the unscaled bulk AIMD, the overlaps are much better, with the BLYP/SVP combination performing best. The early convergence of the SimVCD value for some level of theory suggests that inclusion of clusters up to the decamer is unnecessary. Indeed, visual inspection of the AIMD bulk trajectories shows that mainly bent chain trimers and tetramers are formed, a pentamer and a hexamer occur only rarely. Table 3 contains two more columns, in which we artificially overbind the interaction energy of the clusters by a factor of two. The reason is simply that the worse basis set SVP exceeds the TZVP basis set, see column two and three as well as four and five in Table 3, and one difference is

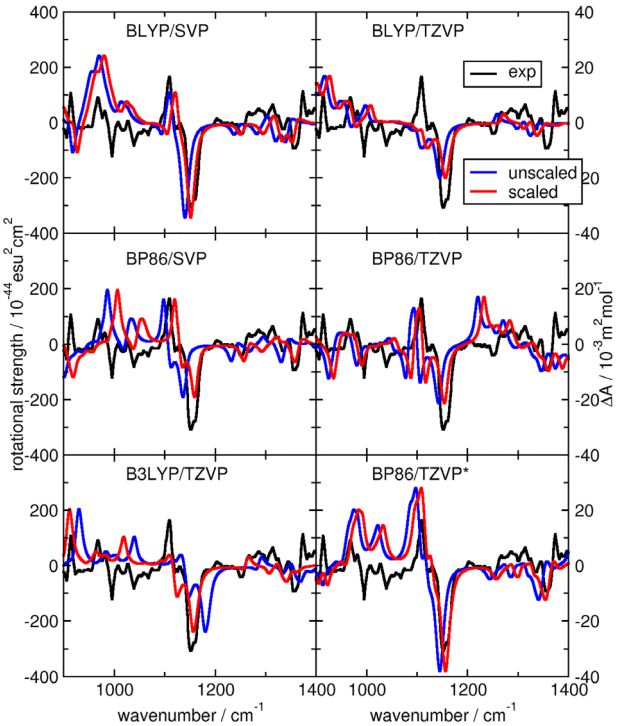

Figure 5. Cluster weighting bulk VCD spectra for different level of theory in the range between 900 and 1400 cm^{-1}. The experimental spectrum is from ref. [56]. Blue: unscaled; red: scaled; black: experiment. For corresponding overlaps see **Table 4**.

the overbinding of SVP compared to TZVP. As a result both functionals BLYP and BP86 perform better than the original TZVP data, but only in the case of BP86 an extreme improvement (even compared to SVP) can be observed. These trends are also not systematic, which is easy to understand. In QCE calculations a difficult equilibrium of the input data leads to significantly different populations (see Supporting Information), making error tracking and the understanding error compensation more difficult than in a case where only electronic energies of one molecule are compared.

The corresponding spectra of the S4^{gm} set for different level of theory are exhibited in **Figure 5** blue curves.

Similar to the AIMD simulations we also scale the spectra, which is even more serious, because here we counteract the missing description of the anharmonicity besides incompleteness of the basis set, level of theory, and remaining errors. The results are presented in Table 4 and in Figure 5, red curves.

All spectra based on GGA functionals have to be shifted to higher wavenumbers, while the B3LYP data have to be scaled by a factor lower than one. The best performance can be found for the B3LYP/TZVP closely followed by the BP86/TZVP results. This is in accordance with the findings found in the literature for gas phase calculations.[121] Besides this the artificially doubled energy BP86/TZVP* slightly exceeds the good B3LYP/TZVP performance, but this is not the case for the BLYP/TZVP*, which shows that there is an important influence besides the energy. The overall very good performance of BP86/TZVP* and BP86/TZVP is interesting and could be due to the good frequency calculation

Table 4. Overlap of σ from SimVCD tool[65] between bulk experimental and calculated VCD spectra employing CW for different levels of theory.

level of theory	0.97	0.98	0.99	1.00	1.01	1.02	1.03	1.04	1.05
B3LYP/TZVP	0.162	**0.381**	0.229	0.107	0.028	−0.026	−0.023	0.037	0.051
BLYP/SVP	–	–	–	0.207	**0.278**	0.185	0.022	−0.107	−0.114
BLYP/TZVP	–	–	–	0.120	**0.226**	0.201	0.158	0.097	0.086
BP86/SVP	–	–	–	0.045	0.206	**0.213**	0.096	−0.018	−0.144
BP86/TZVP	–	–	–	0.040	**0.311**	0.245	0.077	0.112	0.016
BLYP/TZVP*	–	–	–	0.131	**0.248**	0.219	0.149	0.071	0.067
BP86/TZVP*	–	–	–	0.239	**0.410**	0.194	0.120	−0.111	−0.245

For all CW spectra the complete S4^{gm} set has been employed. * indicates that the referenced binding energies have been doubled in the CW calculation. Bold marked overlaps show the best agreement with the experiment.

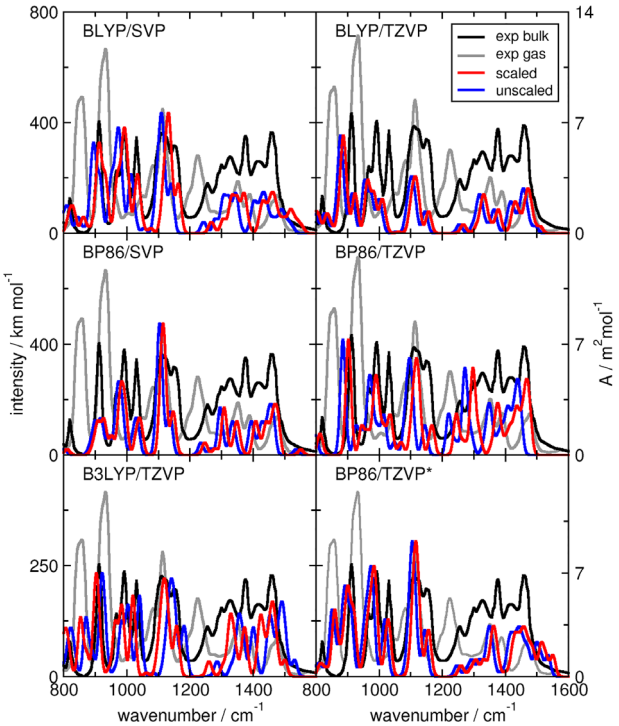

Figure 6. Cluster weighting bulk IR spectra for different levels of theory in the range between 900 and 1400 cm^{-1}. The experimental spectrum is taken from ref. [56]. Blue: unscaled; red: scaled; black: experiment.

rather than in overbinding, that is not observed for these levels of theory compared to the other methods, see Table S5, Supporting Information. The remaining data from different level of theory are also above an overlap with experiment of 0.2. Therefore all cluster weighting calculations are sufficient and serve well to determine the absolute configuration in bulk phase systems. As with the AIMD calculations the performance of the CW below 1100 cm^{-1} is not as good as when considering the whole range. To give an estimate of Table S4, Supporting Information, we list the overlaps below 1100 cm^{-1}. Interestingly, BP86/TZVP outperforms the AIMD simulation and B3LYP/TZVP is in the same range. For completeness, **Figure 6** displays the corresponding IR spectra.

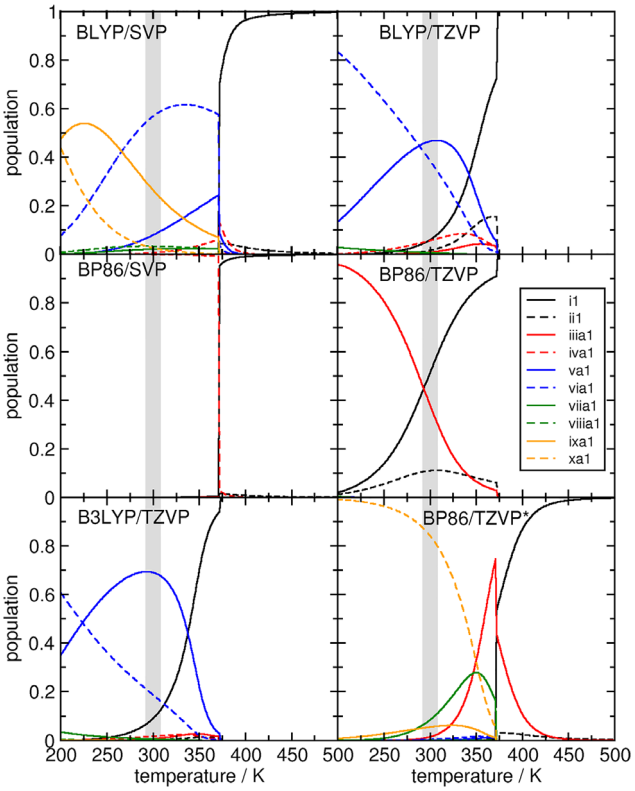

Figure 7. Plotted are the different CW populations obtained in dependency of functional and basis set. Different colors and lines indicate the different clusters. The gray bar marks a range around 300 K temperature, where the spectra were calculated.

Finally, we show in **Figure 7** the received CW populations based on different functionals and basis set.

The variety of curves is deflating, but also not surprising considering that the variety already exists only for the interaction energies (Table S5, Supporting Information). On closer examination, however, some systematic trends can be derived from this. All methods occupy only the monomer in the gas phase with the exception of BLYP/SVP, which also occupy a majority of monomer population, but still have a certain amount of dimer, tetramer, and pentamer in the gas phase and BP86/TZVP* which occupies the dimer and the trimer. In the liquid phase the clusters above the hexamer (at 300 K) seem to be insignificant—again with the BLYP/SVP and BP86/TZVP* exception. This strongly suggests that higher clusters than the hexamer are dispensable for calculations of hydrogen bonded systems. Unfortunately, the most well-performing functional/basis set combinations, where certain clusters play a role, do not agree. While B3LYP/TZVP populates the pentamer followed by the hexamer and slightly followed by the trimer and tetramer, the BP86/TZVP combination favors the monomer, trimer, and dimer. These results are certainly due to the slightly different structures obtained by geometry optimizations (Table S3, Supporting Information) together with the extreme differences in interaction energies, but they also suggest what was observed before.[68,122] Namely, that structural motifs contained in clusters are more important than a certain cluster size, that is, a particular

oligomer. The artificially increased energy combination BP86/TZVP* apparently contributes to the curiosity of this graph in that here the decamer is highly and the heptamer and trimer are slightly populated. But this is also understandable if one considers the interaction energies (Table S5, Supporting Information). It reflects that higher energies contribute to populate certain clusters, see BLYP/SVP and BP86/TZVP*. The outlier BP86/SVP behaves differently because of very low frequencies. Frequencies are also an input quantity in the vibrational partition function for QCE calculations, but Grimme showed that these low frequencies must enter the rotational partition function instead of the vibrational because they are prevented from rotating.[123]

Therefore, it is not justified to believe that a certain cluster or the choice of a large size of clusters makes the spectrum good. It remains to be seen how much other isomeric clusters, that is, other local minima for a particular oligomer, or clusters with more conformations change the picture. However, since CW is strongly dominated by energies an improvement by isomeric clusters with higher-energies (at least much higher energies) seems unlikely.

In summary, we can give the following advice when performing static quantum chemical calculations with cluster weighting: Given that it is affordable in terms of computer time, it is best to choose the hybrid functional B3LYP/TZVP combination, followed by the BP86/TZVP combination for bulk calculations. If computer time is a problem, BLYP/SVP calculation may be an alternative. This relatively good performance of BLYP/SVP for the bulk strongly suggests that large error compensations are involved.

4.3. Comparison of Ab Initio Molecular Dynamics Simulations with Cluster Weighting

We now compare the CW and the AIMD VCD spectra to see how much the former can model the latter, see **Figure 8**. To reduce the influence of different parameters, we mainly compare the AIMD bulk simulation (scaled and unscaled) with the BLYP/SVP and BLYP/TZVP, but we also add the B3LYP/TZVP data, since it achieved the best overlap values with the experiment.

All CW data compare well with the AIMD in the strong negative peak at around 1152 cm^{-1}. While the BLYP with smaller SVP basis set shows at least a hint of the positive peak at 1109 cm^{-1}, this hint is missing in the BLYP/TZVP combination, which already in the previous subsection 4.2 led to a bad comparison to the experiment. An exception to the poor performance of BLYP/TZVP with respect to AIMD is the weak peak at 1290 cm^{-1}, which is almost reached by it. All three static calculations strongly disagree with AIMD in the lower wavenumber region, showing an opposite (positive) peak to the negative one at around 975 cm^{-1}. While B3LYP/TZVP-CW also lacks these negative peaks, it shows on the other hand a weak positive peak at around 965 cm^{-1} which is missing in the AIMD. It remains to be seen whether AIMD, which is based on other functionals changes the spectrum extensively and for the better, but for the time being the CW approach is better based on the BP86 or B3LYP functional, as has been shown several times in literature for Boltzmann weighting in the gas phase.[55]

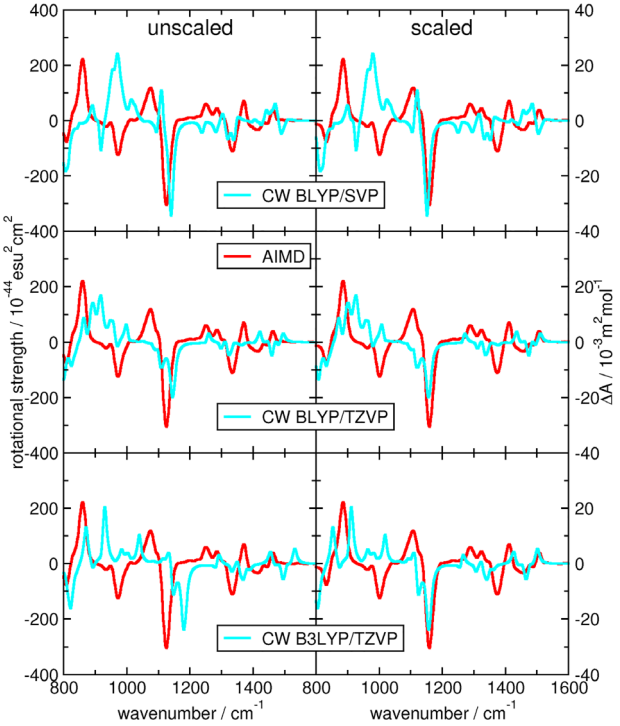

Figure 8. Cluster weighting (cyan) and AIMD (red) bulk VCD spectra for different levels of theory in the range between 900 and 1400 cm^{-1}.[56]

4.4. Magnetic Moments from Ab Initio Molecular Dynamics Simulations

The calculation of the VCD spectra from the correlation approach requires the knowledge of the moments along the trajectories. In **Figure 9**, we show a short snapshot of the moments' time development (upper panels) together with their distribution (middle panels) and the x-, y-, and z-component distributions (lower panels) for the gas1 trajectory.

Since the Thomas-Kirchner ansatz[26] to obtain the magnetic moments is quite computationally intensive, we also test here Cho's long established approach for classical or QM/MM trajectories. Instead of using QM/MM or classical simulations, we apply Cho's ansatz to AIMD trajectories, where the electric dipole moment $\vec{\mu}(t)$ is obtained via:

$$\vec{\mu}(t) = \sum_i q_i(t) \cdot \vec{r}_i(t) \tag{15}$$

with $q_i(t)$ being the partial charges at time t and $\vec{r}_i(t)$ the position vector of the molecular atoms. Similarly, the magnetic dipole moment $\vec{M}(t)$ is given by:

$$\vec{M}(t) = \frac{1}{2c} \sum_i q_i(t) \cdot \vec{r}_i(t) \times \vec{v}_i(t) \tag{16}$$

with c being the speed of light and $\vec{v}_i$ being the according velocity.

In Figure 9, we show on the left side the corresponding electric dipole moments μ based on various population analysis marked in different colors. In the upper picture we see that all population methods follow the same trends for μ, with the largest dispersion

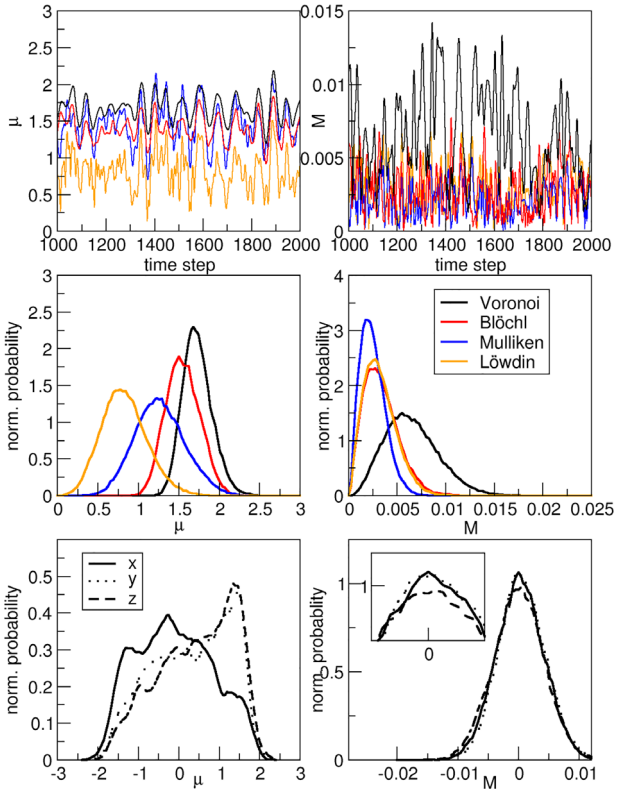

Figure 9. Shown are the magnetic moments. Left: electric (in D) and right: the magnetic moment (in Bohr magneton). Upper panel exhibits a snapshot from time step 1000 to 2000 of the trajectory. Middle panels show the histograms of the absolute value and lower panels show the distribution of x-, y-, and z-component. Black from the Voronoi approach.[26] Red, blue and orange are the classical approach developed by Cho and co-workers[37,38] on the basis of Blöchl,[102] Mulliken,[103] and Löwdin[104] partial charges.

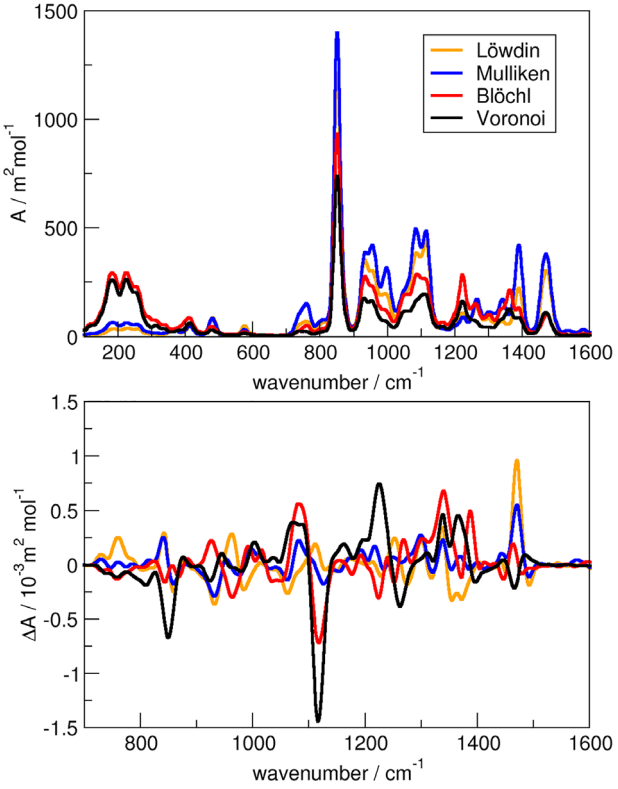

Figure 10. IR and VCD AIMD gas spectra. Black from the Voronoi approach.[26] Red, blue and orange are the classical approach established by Cho and co-workers[37,38] based on Blöchl,[102] Mulliken,[103] and Löwdin[104] partial charges.

from the main trends coming from the Löwdin population analysis. This agreement is not surprising since we choose the same trajectory and electronic structure method on which the analysis is based. For the Voronoi approach we observe a dipole moment in the range of 1 and 2.5 D with a mean of 1.71 D, Blöchl lies between 1 and 2.25 D with a mean of 1.53 D, Mulliken occupies the range between 0.5 and 2 D with the average of 1.25 D, and Löwdin provides the lowest dipole moment distribution between zero and 1.5 D and an average of 0.81 D. A comparison of these values with the experiment of 1.66 D[124] clearly shows the superiority of the Voronoi together with the Blöchl approach.

The situation is different with the magnetic moment. The agreement between Voronoi and the three other approaches is no longer in phase, because the calculation of the moment in the case of Voronoi is based on a completely different method. Nevertheless the range covered seems to be comparable and the moments based on the population analysis obviously fluctuate. Therefore, we now focus on the calculated spectra in **Figure 10**.

Again, the IR spectrum based on electric dipole moments shows a large agreement between the different approaches for the peak locations. Only the intensities differ more between both the Mulliken and the Löwdin compared to the Voronoi approach. Blöchl,[102] and Voronoi compare very well in both location and intensity. The difference in the intensity for different electric dipole moment methods is nothing new. It was observed earlier, when we compared our Voronoi and the Wannier function approach.[64] This intensity problem is naturally more pronounced in the VCD case. While our Thomas-Kirchner[26] approach has the experimental +/− feature between 1020 and 1150 cm^{-1}, Löwdin fails completely, Mulliken underestimates the extremity in the second peak and Blöchl performs well. The second positive peak around 1200 cm^{-1} is only slightly reproduced by Mulliken, the other two approaches of population analysis neglect to show this peak. In summary, we can say that these tests are very promising, since the computer time and data handling are much less complex. Furthermore, the outcome especially the case of the Blöchl charges[102] is very satisfactory.

5. Discussion and Conclusion

Using the example of (*R*)-butan-2-ol in the gas and bulk phase, we investigate the problems that arise when predicting the vibrational spectrum of a flexible molecule in a non-idle environment. Two approaches are investigated in detail. The methods used are ab initio molecular dynamics simulations and cluster weighting based on static quantum chemical calculations.

From AIMD simulations we calculated the gas and the bulk phase spectra, with excellent agreement when we applied a scaling factor of 1.03 (bulk) and 1.02 (gas) for the selected

BLYP/MOLOPT-DZVP-SR-GTH basis set combination. (*R*)-butan-2-ol shows several conformations connected by barriers low enough to be influential in experiment but too high to be visited by only one initial conformation in the ab initio simulation. To scan all the important conformational regions, we simulated from the different initial conditions of all monomer conformers. A subsequent conformation analysis shows, that taking the average of all trajectories covers the whole conformation range apparently with the right proportion resulting in an excellent spectrum. Therefore, this ansatz, where multiple trajectories are simulated starting from all monomer conformers and then averaged over them, is a valid approach for an accurate spectrum when considering a flexible species in gas phase or a single solute molecule is solvated in a different solvent than the solute molecule. It should be noted that AIMD is computationally very demanding.

The second approach used in this work, is much less computationally demanding. Therefore, we could compare different functionals (BP86, BLYP, B3LYP) and basis sets (SVP and TZVP) and confirm for the bulk, what is valid and already known for the gas phase infrared and vibrational circular dichroism spectra calculation. The best results are obtained for the BP86/TZVP and B3LYP/TZVP functional and basis set combination. This superiority of these two level of theory may be due more to the good frequencies (input for cluster weighting) than the energies and geometries. We found a rough converging trend with increasing cluster size indicating that for hydrogen bonded systems clusters up to tetramers or hexamers might be sufficient. Again the scaling leads to very good agreement with the experiment. In total, all methods resulted in an agreement with the experiment above 0.2, which allows a safe assignment of the absolute configuration.

In the last part we analyzed the moments of one gas phase trajectory based on our previously developed method and on different population analyses. The Voronoi electric dipole moment is well matched to the experiment followed by that of the Blöchl charges. There is a perfect agreement between Voronoi and population analysis even in the time development and the resulting IR spectra agree very well in peak location. The magnetic moments from the population analysis and from our Voronoi approach do not fluctuate in phase, but still show a similar distributions. Interestingly, the Blöchl vibrational circular dichroism spectrum reproduces the Voronoi characteristics very well with much less computer time and makes it a valuable approach for the calculation of such spectra.

Supporting Information

Supporting Information is available from the Wiley Online Library or from the author.

Acknowledgements

The authors thank the DFG under the grant project number 406232243 and Prof. A. Schweitzer as well as Prof. C. Urbach for discussion with respect to the Bonna cluster. They also thank the Bonn University for granting access to Bonna.

Conflict of Interest

The authors declare no conflict of interest.

Keywords

ab initio molecular dynamics, cluster weighting, infrared spectroscopy, vibrational circular dichroism

Received: September 22, 2020
Revised: November 26, 2020
Published online: December 16, 2020

[1] M. Thomas, M. Brehm, R. Fligg, P. Vöhringer, B. Kirchner, *Phys. Chem. Chem. Phys.* **2013**, *15*, 6608.
[2] K. Wendler, J. Thar, S. Zahn, B. Kirchner, *J. Phys. Chem. A* **2010**, *114*, 9529.
[3] V. P. Nicu, S. R. Domingos, B. H. Strudwick, A. M. Brouwer, W. J. Buma, *Chem. Eur. J.* **2016**, *22*, 704.
[4] B. Kirchner, *J. Chem. Phys.* **2005**, *123*, 204116.
[5] B. Kirchner, C. Spickermann, S. B. Lehmann, E. Perlt, J. Langner, M. von Domaros, P. Reuther, F. Uhlig, M. Kohagen, M. Brüssel, *Comput. Phys. Commun.* **2011**, *182*, 1428.
[6] F. Weinhold, *J. Chem. Phys.* **1998**, *109*, 367.
[7] J. Blasius, B. Kirchner, *J. Phys. Chem. B* **2020**, *124*, 7272.
[8] K. Hermansson, S. Knuts, J. Lindgren, *J. Chem. Phys.* **1991**, *95*, 7486.
[9] R. Eggenberger, S. Gerber, H. Huber, D. Searles, M. Welker, *J. Chem. Phys.* **1992**, *97*, 5898.
[10] J. R. Pliego, J. M. Riveros, *J. Phys. Chem. A* **2001**, *105*, 7241.
[11] A. S. Perera, J. Thomas, M. R. Poopari, Y. Xu, *Front. Chem.* **2016**, *4*, 9.
[12] B. Mennucci, J. Tomasi, R. Cammi, J. R. Cheeseman, M. J. Frisch, F. J. Devlin, S. Gabriel, P. J. Stephens, *J. Phys. Chem. A* **2002**, *106*, 6102.
[13] A. Marini, A. Muñoz-Losa, A. Biancardi, B. Mennucci, *J. Phys. Chem. B* **2010**, *114*, 17128.
[14] S. Grimme, *J. Chem. Theory Comput.* **2019**, *15*, 2847.
[15] M. Brüssel, E. Perlt, S. B. C. Lehmann, M. von Domaros, B. Kirchner, *J. Chem. Phys.* **2011**, *135*, 194113.
[16] M. Brüssel, E. Perlt, M. von Domaros, M. Brehm, B. Kirchner, *J. Chem. Phys.* **2012**, *137*, 164107.
[17] J. Blasius, J. Ingenmey, E. Perlt, M. von Domaros, O. Hollóczki, B. Kirchner, *Angew. Chem. Int. Ed.* **2019**, *58*, 3212.
[18] J. Blasius, J. Ingenmey, E. Perlt, M. von Domaros, O. Hollóczki, B. Kirchner, *Angew. Chem.* **2019**, *131*, 3245.
[19] B. Kirchner, P. J. di Dio, J. Hutter, in *Multiscale Molecular Methods in Applied Chemistry* (Eds: B. Kirchner, J. Vrabec), Topics in Current Chemistry, Vol. *307*, Springer, Berlin, pp. 109–153.
[20] K. Wendler, M. Brehm, F. Malberg, B. Kirchner, L. Delle Site, *J. Chem. Theory Comput.* **2012**, *8*, 1570.
[21] M. S. Green, *J. Chem. Phys.* **1954**, *22*, 398.
[22] R. Kubo, *J. Phys. Soc. Jpn.* **1957**, *12*, 570.
[23] M.-P. Gaigeot, M. Martinez, R. Vuilleumier, *Mol. Phys.* **2007**, *105*, 2857.
[24] M.-P. Gaigeot, *Phys. Chem. Chem. Phys* **2010**, *12*, 10198.
[25] A. Putrino, D. Sebastiani, M. Parrinello, *J. Chem. Phys.* **2000**, *113*, 7102.
[26] M. Thomas, B. Kirchner, *J. Phys. Chem. Lett.* **2016**, *7*, 509.
[27] K. Le Barbu-Debus, J. Bowles, S. Jähnigen, C. Clavaguéra, F. Calvo, R. Vuilleumier, A. Zehnacker, *Phys. Chem. Chem. Phys.* **2020**, *22*, 26047.
[28] M. Brehm, M. Thomas, *J. Chem. Theory Comput.* **2019**, *15*, 3901.
[29] M. Brehm, M. Thomas, *J. Phys. Chem. Lett.* **2017**, *8*, 3409.
[30] S. Pezzotti, D. R. Galimberti, Y. R. Shen, M.-P. Gaigeot, *Minerals* **2018**, *8*, 305.
[31] O. Kroutil, S. Pezzotti, M.-P. Gaigeot, M. Predota, *J. Phys. Chem. C* **2020**, *124*, 15253.

[32] C. Schröder, A. Lyons, S. W. Rick, *Phys. Chem. Chem. Phys.* **2020**, *22*, 467.
[33] M. Salanne, B. Rotenberg, S. Jahn, R. Vuilleumier, C. Simon, P. A. Madden, *Theo. Chem. Acc.* **2012**, *131*, 1143.
[34] W. J. Glover, P. A. Madden, *J. Chem. Phys.* **2004**, *121*, 7293.
[35] M. Salanne, P. A. Madden, *Mol. Phys.* **2011**, *109*, 2299.
[36] M. Wilson, P. A. Madden, M. Hemmati, C. A. Angell, *Phys. Rev. Lett.* **1996**, *77*, 4023.
[37] S. Yang, M. Cho, *J. Chem. Phys.* **2009**, *131*, 135102.
[38] J.-H. Choi, M. Cho, *J. Chem. Theory Comput.* **2011**, *7*, 4097.
[39] N. Jiang, R. X. Tan, J. Ma, *J. Phys. Chem. B* **2011**, *115*, 2801.
[40] M. Pecul, A. Rizzo, J. Leszczynski, *J. Phys. Chem. A* **2002**, *106*, 11008.
[41] M. Kamiński, A. Kudelski, M. Pecul, *J. Phys. Chem. B* **2012**, *116*, 4976.
[42] T. Giovannini, M. Olszówka, C. Cappelli, *J. Chem. Theory Comput.* **2016**, *12*, 5483.
[43] T. Giovannini, G. Del Frate, P. Lafiosca, C. Cappelli, *Phys. Chem. Chem. Phys.* **2018**, *20*, 9181.
[44] K. Reiter, M. Kühn, F. Weigend, *J. Chem. Phys.* **2017**, *146*, 054102.
[45] G. Magyarfalvi, G. Tarczay, E. Vass, *Wiley Interdiscip. Rev.: Comput. Mol. Sci.* **2011**, *1*, 403.
[46] P. J. Stephens, *J. Phys. Chem.* **1985**, *89*, 748.
[47] P. Stephens, *J. Phys. Chem.* **1987**, *91*, 1712.
[48] J. Cheeseman, M. Frisch, F. Devlin, P. Stephens, *Chem. Phys. Lett.* **1996**, *252*, 211.
[49] V. P. Nicu, J. Neugebauer, S. K. Wolff, E. J. Baerends, *Theor. Chem. Acc.* **2008**, *119*, 245.
[50] L. A. Nafie, T. B. Freedman, *J. Chem. Phys.* **1983**, *78*, 7108.
[51] L. A. Nafie, *J. Chem. Phys.* **1983**, *79*, 4950.
[52] A. Buckingham, P. Fowler, P. Galwas, *Chem. Phys.* **1987**, *112*, 1.
[53] A. Scherrer, R. Vuilleumier, D. Sebastiani, *J. Chem. Theory Comput.* **2013**, *9*, 5305.
[54] A. Scherrer, F. Agostini, D. Sebastiani, E. Gross, R. Vuilleumier, *J. Chem. Phys.* **2015**, *143*, 074106.
[55] M. A. Koenis, Y. Xia, S. R. Domingos, L. Visscher, W. J. Buma, V. P. Nicu, *Chem. Sci.* **2019**, *10*, 7680.
[56] F. Wang, P. L. Polavarapu, *J. Phys. Chem. A* **2000**, *104*, 10683.
[57] S. Shin, M. Nakata, Y. Hamada, *J. Phys. Chem. A* **2006**, *110*, 2122.
[58] V. P. Nicu, J. Neugebauer, E. J. Baerends, *J. Phys. Chem. A* **2008**, *112*, 6978.
[59] L. Weirich, C. Merten, *Phys. Chem. Chem. Phys.* **2019**, *21*, 13494.
[60] S. Abbate, G. Longhi, K. Kwon, A. Moscowitz, *J. Chem. Phys.* **1998**, *108*, 50.
[61] J. Horníček, P. Kaprálová, P. Bouř, *J. Chem. Phys.* **2007**, *127*, 084502.
[62] B. Kirchner, J. Hutter, *J. Chem. Phys.* **2004**, *121*, 5133.
[63] R. Iftimie, M. E. Tuckerman, *J. Chem. Phys.* **2005**, *122*, 214508.
[64] M. Thomas, M. Brehm, B. Kirchner, *Phys. Chem. Chem. Phys.* **2015**, *17*, 3207.
[65] J. Shen, C. Zhu, S. Reiling, R. Vaz, *Spectrochim. Acta Part A: Mol. Biomol. Spectrosc.* **2010**, *76*, 418.
[66] D. A. McQuarrie, J. D. Simon, *Physical Chemistry: A Molecular Approach*, University Science Books, Sausalito, CA **1997**.
[67] S. Lehmann, C. Spickermann, B. Kirchner, *J. Chem. Theory Comput.* **2009**, *5*, 1640.
[68] S. Lehmann, C. Spickermann, B. Kirchner, *J. Chem. Theory Comput.* **2009**, *5*, 1650.
[69] G. Matisz, A.-M. Kelterer, W. Fabian, S. Kunsági-Máté, *Phys. Chem. Chem. Phys.* **2015**, *17*, 8467.
[70] J. Ingenmey, M. von Domaros, E. Perlt, S. P. Verevkin, B. Kirchner, *J. Chem. Phys.* **2018**, *148*, 193822.
[71] J. Ingenmey, J. Blasius, G. Marchelli, A. Riegel, B. Kirchner, *J. Chem. Eng. Data* **2018**, *64*, 255.
[72] E. Perlt, M. von Domaros, B. Kirchner, R. Ludwig, F. Weinhold, *Sci. Rep.* **2017**, *7*, 10244.
[73] J. M. Dieterich, B. Hartke, *Mol. Phys.* **2010**, *108*, 279.
[74] J. M. Dieterich, B. Hartke, *J. Comput. Chem.* **2011**, *32*, 1377.
[75] D. A. Case, R. M. Betz, D. S. Cerutti, T. E. Cheatham, T. A. Darden, R. E. Duke, T. J. Giese, H. Gohlke, A. W. Goetz, N. Homeyer, S. Izadi, P. Janowski, J. Kaus, A. Kovalenko, T. S. Lee, S. LeGrand, P. Li, C. Lin, T. Luchko, R. Luo, B. Madej, D. Mermelstein, K. M. Merz, G. Monard, H. Nguyen, H. T. Nguyen, I. Omelyan, A. Onufriev, D. R. Roe, A. Roitberg, C. Sagui, C. L. Simmerling, W. M. Botello-Smith, J. Swails, R. C. Walker, J. Wang, R. M. Wolf, X. Wu, L. Xiao, P. A. Kollman, *AMBER 2016*, University of California, San Francisco **2016**.
[76] J. Wang, R. M. Wolf, J. W. Caldwell, P. A. Kollman, D. A. Case, *J. Comput. Chem.* **2004**, *25*, 1157.
[77] A. D. Becke, *Phys. Rev. A* **1988**, *38*, 3098.
[78] J. P. Perdew, *Phys. Rev. B* **1986**, *33*, 8822.
[79] F. Weigend, R. Ahlrichs, *Phys. Chem. Chem. Phys.* **2005**, *7*, 3297.
[80] S. Grimme, J. Antony, S. Ehrlich, H. Krieg, *J. Chem. Phys.* **2010**, *132*, 154104.
[81] S. Grimme, S. Ehrlich, L. Goerigk, *J. Comput. Chem.* **2011**, *32*, 1456.
[82] M. A. J. Koenis, O. Visser, L. Visscher, W. J. Buma, V. P. Nicu, *J. Chem. Inf. Model.* **2020**, *60*, 259.
[83] A. Klamt, G. Schüürmann, *J. Chem. Soc., Perkin Trans.* **1993**, *2*, 799.
[84] W. M. Haynes, *CRC Handbook of Chemistry and Physics*, CRC Press, Boca Raton, FL **2014**.
[85] K. Eichkorn, F. Weigend, O. Treutler, R. Ahlrichs, *Theor. Chem. Acc.* **1997**, *97*, 119.
[86] TURBOMOLE V7.4 2017, a development of University of Karlsruhe and Forschungszentrum Karlsruhe GmbH, 1989-2007, http://www.turbomole.com (accessed: July 2019).
[87] R. Ahlrichs, M. Bär, M. Häser, H. Horn, C. Kölmel, *Chem. Phys. Lett.* **1989**, *162*, 165.
[88] S. G. Balasubramani, G. P. Chen, S. Coriani, M. Diedenhofen, M. S. Frank, Y. J. Franzke, F. Furche, R. Grotjahn, M. E. Harding, C. Hättig, A. Hellweg, B. Helmich-Paris, C. Holzer, U. Huniar, M. Kaupp, A. M. Khah, S. K. Khani, T. Müller, F. Mack, B. D. Nguyen, S. M. Parker, E. Perlt1, D. Rappoport, K. Reiter, S. Roy, M. Rückert, G. Schmitz, M. Sierka, E. Tapavicza, D. P. Tew, C. van Wüllen, V. K. Voora, F. Weigend, A. Wodyński, J. M. Yu, *J. Chem. Phys.* **2020**, *152*, 184107.
[89] M. Brüssel, E. Perlt, S. B. Lehmann, M. von Domaros, B. Kirchner, *J. Chem. Phys.* **2011**, *135*, 194113.
[90] M. von Domaros, E. Perlt, J. Ingenmey, G. Marchelli, B. Kirchner, *SoftwareX* **2018**, *7*, 356.
[91] A. v. Bondi, *J. Phys. Chem.* **1964**, *68*, 441.
[92] J. VandeVondele, M. Krack, F. Mohamed, M. Parrinello, T. Chassaing, J. Hutter, *Comput. Phys. Commun.* **2005**, *167*, 103.
[93] CP2k developers group under the terms of the GNU General Public License; see http://www.cp2k.org.
[94] J. VandeVondele, J. Hutter, *J. Chem. Phys.* **2007**, *127*, 114105.
[95] S. Goedecker, M. Teter, J. Hutter, *Phys. Rev. B* **1996**, *54*, 1703.
[96] C. Hartwigsen, S. Goedecker, J. Hutter, *Phys. Rev. B* **1998**, *58*, 3641.
[97] M. Krack, *Theor. Chem. Acc.* **2005**, *114*, 145.
[98] D. S. Firaha, M. Thomas, O. Hollóczki, M. Korth, B. Kirchner, *J. Chem. Phys.* **2016**, *145*, 204502.
[99] A. Bankura, A. Karmakar, V. Carnevale, A. Chandra, M. L. Klein, *J. Phys. Chem. C* **2014**, *118*, 29401.
[100] S. Nosé, *J. Chem. Phys.* **1984**, *81*, 511.
[101] W. G. Hoover, *Phys. Rev. A* **1985**, *31*, 1695.
[102] P. Blöchl, *J. Chem. Phys.* **1995**, *103*, 7422.
[103] R. S. Mulliken, *J. Chem. Phys.* **1955**, *23*, 1833.
[104] P. Löwdin, *J. Chem. Phys.* **1950**, *18*, 365.
[105] E. Schwegler, J. C. Grossman, F. Gygi, G. Galli, *J. Chem. Phys.* **2004**, *121*, 5400.
[106] M. Brehm, B. Kirchner, *J. Chem. Inf. Model.* **2011**, *51*, 2007.
[107] M. Brehm, M. Thomas, S. Gehrke, B. Kirchner, *J. Chem. Phys.* **2020**, *152*, 164105.
[108] http://plasma-gate.weizmann.ac.il/Grace/.

[109] http://www.gnuplot.info/.
[110] N. Wiener, *Acta Math.* **1930**, *55*, 117.
[111] A. Khintchine, *Math. Ann.* **1934**, *109*, 604.
[112] M. L. Laury, M. J. Carlson, A. K. Wilson, *J. Comp. Chem.* **2012**, *33*, 2380.
[113] J. Blasius, *M.Sc. Thesis*, University of Bonn, **2019**.
[114] O. Kukharenko, K. Sawade, J. Steuer, C. Peter, *J Chem. Theo. Comp.* **2016**, *12*, 4726.
[115] O. Bezkorovaynaya, A. Lukyanov, K. Kremer, C. Peter, *J. Comp. Chem.* **2012**, *33*, 937.
[116] T. Lemke, C. Peter, O. Kukharenko, *J. Chem. Theo. Comp.* **2018**, *14*, 5476.
[117] J. B. Abrams, M. E. Tuckerman, *J. Phys. Chem. B* **2008**, *112*, 15742.
[118] A. Rodriguez, A. Laio, *Science* **2014**, *344*, 1492.
[119] M. Ceriotti, G. A. Tribello, M. Parrinello, *Proc. Natl. Acad. Sci. U.S.A.* **2011**, *108*, 13023.
[120] K. Wendler, S. Zahn, F. Dommert, R. Berger, C. Holm, B. Kirchner, L. Delle Site, *J. Chem. Theory Comput.* **2011**, *7*, 3040.
[121] M. K. Kesharwani, B. Brauer, J. M. L. Martin, *J. Phys. Chem. A* **2015**, *119*, 1701.
[122] E. Perlt, J. Friedrich, M. von Domaros, B. Kirchner, *ChemPhysChem* **2011**, *12*, 3474.
[123] S. Grimme, *Chem.–Eur. J.* **2012**, *18*, 9955.
[124] J. A. Dean, *Handbook of Organic Chemistry*, New York **1987**.

D. Efficient Prediction of Mole Fraction Related Vibrational Frequency Shifts

Jan Blasius,[*] Katrin Drysch,[*] Frank Hendrik Pilz,[†] Tom Frömbgen,[*] Patrycja Kielb,[†‡] and Barbara Kirchner[*]

Submitted for publication in J. Phys. Chem. Lett.

Printed in appendix D.

Contributions to the manuscript

- Development of the concept
- Supervision and performance of all calculations
- Interpretation of the results
- Writing of the manuscript

[*] Mulliken Center for Theoretical Chemistry, Clausius Institute for Physical and Theoretical Chemistry, University of Bonn, Beringstr. 4–6, 53115 Bonn, Germany
[†] Clausius Institute of Physical and Theoretical Chemistry, University of Bonn, Wegelerstraße 12, 53115 Bonn, Germany
[‡] Transdisciplinary Research Area "Building Blocks of Matter and Fundamental Interactions" (TRA Matter), University of Bonn, Bonn, Germany

Efficient Prediction of Mole Fraction Related Vibrational Frequency Shifts

Jan Blasius,[†] Katrin Drysch,[†] Frank Hendrik Pilz,[‡] Tom Frömbgen,[†,¶] Patrycja Kielb,[§,‡] and Barbara Kirchner[*,†]

[†]*Mulliken Center for Theoretical Chemistry, Clausius Institute of Physical and Theoretical Chemistry, University of Bonn, Beringstraße 4–6, D-53115 Bonn, Germany*
[‡]*Clausius Institute of Physical and Theoretical Chemistry, University of Bonn, Wegelerstraße 12, D-53115 Bonn, Germany*
[¶]*Max-Planck-Institut für Chemische Energiekonversion, Stiftstrasse 34-36, D-45470 Mülheim an der Ruhr, Germany*
[§]*Transdisciplinary Research Area "Building Blocks of Matter and Fundamental Interactions" (TRA Matter), University of Bonn, Bonn, Germany*

E-mail: kirchner@thch.uni-bonn.de

Abstract

While so far it has been possible to calculate vibrational spectra of mixtures at a particular composition, we present here a novel cluster approach for a fast and robust calculation of mole fraction dependent infrared and vibrational circular dichroism spectra at the example of acetonitrile/(*R*)-butan-2-ol mixtures. By assigning weights to a limited number of quantum chemically calculated clusters, vibrational spectra can be obtained at any desired composition by a weighted average of the single cluster spectra. In this way, peak positions carrying information about intermolecular interactions can be predicted. We show that mole fraction dependent peak shifts can be accurately modeled and that experimentally recorded infrared spectra can be reproduced with high accuracy over the entire mixing range. Since only a very limited number of clusters is required, the presented approach is a valuable and computationally efficient tool to access mole fraction dependent spectra of mixtures on a routine basis.

TOC Graphic

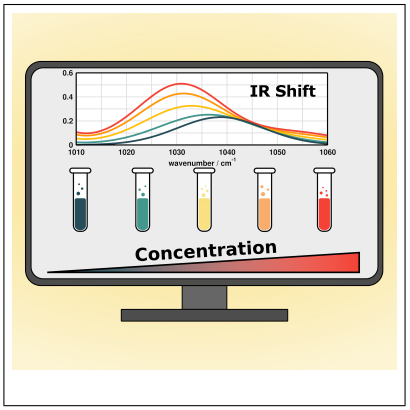

Infrared (IR) and vibrational circular dichroism[1–3] (VCD) spectroscopy are essential techniques for detecting the molecular structure of (chiral) compounds by determining functional groups, conformation and handedness of a molecule.[4–7] Due to their high sensitivity to structures of atomic-scale resolution, the most widespread applications of IR and VCD are in qualitative analytical (bio)chemistry, including detailed investigations of reaction mechanisms[8,9] and the determination of (chiral) products or intermediates in catalytic reactions.[10,11] Furthermore, they are valuable techniques for probing atomic and molecular interactions, e.g. hydrogen bonds,[12,13] intra- and intermolecular couplings in crystals[14,15] or contacts between metals and (bio)molecules.[16]

However, both methods also serve as valuable tools in quantitative analytical chemistry, as they show a pronounced concentration dependence.[17] Such quantitative spectroscopy analyses rely mostly on the Lambert–Beer law, that relates spectroscopic intensities to the concentrations of the absorbing species. While primarily used to determine the concentrations of molecules in samples, quantitative spectroscopy is also a powerful tool for studying diffusion coefficients[18] and the aggregation behavior of molecules.[19] IR and VCD have for instance been used by Stephens and coworkers to study the concentration dependent oligomerization of *S*-2,2'-dimethyl-biphenyl-6,6'-dicarboxylic acid, proving the existence of supramolecular cyclotetramers in solution.[19]

The interpretation of vibrational spectra generally requires an accurate theoretical modeling of the system of interest.[3,6] This can be particularly challenging for the condensed phase, as an explicit treatment of the (non-idle) environment is often necessary.[2,13,20–22] Common computational approaches for the calculation of liquid phase vibrational spectra are based on either molecular dynamics (MD) simulations[2,20,23] or Boltzmann weighted ensembles of quantum chemically calculated clusters.[24] Both approaches have been successfully applied for the calculation of liquid phase spectra of neat substances and mixtures, but the need to run individual MD simulations[17] or to construct different cluster sets for each composition of interest[24] limits their applicability for the calculation of mole fraction dependent spectra. To date, a low-cost computational method for a fast and robust calculation of mole fraction dependent vibrational spectra is still missing, yet the development of such a tool is highly desirable to support quantitative analyses and investigate the molecular structure of unknown mixtures.

Herein, we demonstrate that the IR and VCD spectra of acetonitrile/(*R*)-butan-2-ol mixtures can be accurately described at mole fractions of 0.2, 0.5 and 0.8 by treating the mixtures within the binary quantum cluster equilibrium (bQCE or cluster weighting) theory.[25,26] This cluster ansatz provides an extension to Boltzmann weighting and allows for a simultaneous weighting of clusters of different sizes and compositions by deriving a mole fraction dependent system partition function from a set of quantum chemically calculated clusters. The requirement of Boltzmann weighting to construct different cluster sets for different compositions is thus circumvented and a single cluster set is sufficient to describe the entire mole fraction range,[27,28] reducing the computational effort by far. By self-consistently solving a set of polynomial equations, the bQCE theory assigns populations (i.e., cluster weights) to the clusters. The system's IR and VCD spectra can then be obtained by a weighted average of the individual clusters' spectra. Detailed derivations of the bQCE theory can be found in earlier works[25,26] and the Supporting Information. All bQCE calculations were carried out with our own Peacemaker software,[26,29] for further details, the reader is referred to the Supporting Information.

The employed clusters were constructed to contain either only acetonitrile or (*R*)-butan-2-ol molecules (neat clusters) or a combination of both (mixed clusters). It is important to consider different conformers for each cluster size to account for different bonding motifs and interactions between the molecules. Some of the most important clusters in our cluster set are shown in fig. 1, together with relevant interactions found between the molecules. Acetonitrile is known to interact mainly by dipole–dipole and CH···N interactions (see fig. 1, top left and center). The dipole–dipole interactions of the nitrile groups are known to affect the C≡N stretching vibration, greatly enhancing its IR intensity in the liquid phase as compared to the gas phase. The vibrational frequencies of acetonitrile are, however, hardly changed under aggregation. We applied the cluster weighting to acetonitrile and calculated the corresponding liquid phase IR spectrum, which shows an excellent agreement with the experimental reference, see fig. S1, table S1 and the corresponding discussion in the Supporting Infor-

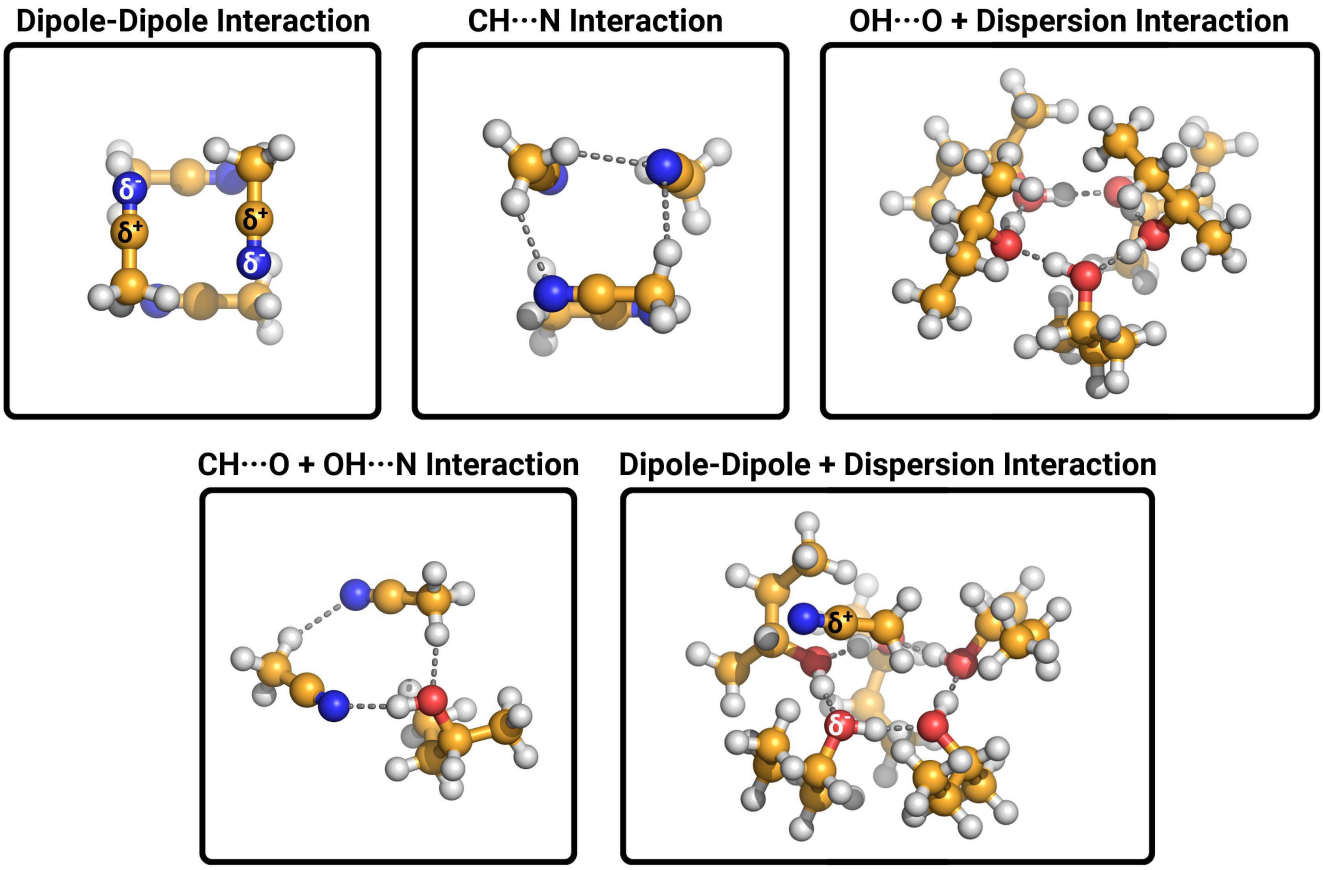

Figure 1: Ball-and-stick images of some clusters showing the different kinds of interactions that are present in the neat acetonitrile and (*R*)-butan-2-ol liquids and in the mixtures of both. The color code for the atoms is: carbon: orange; nitrogen: blue; hydrogen: white; oxygen: red.

mation. The main feature of the acetonitrile liquid phase spectrum, i.e., the high intensity of the C≡N stretching mode at 2252 cm^{-1}, is nicely captured by the calculated spectrum and can not be modeled by using an isolated acetonitrile monomer only (see fig. S4).

(*R*)-butan-2-ol molecules form homodromic structures and interact mainly through OH···O hydrogen bonds and dispersion interactions between the hydrocarbon chains (see fig. 1, top right). Liquid phase IR and VCD spectra of (*R*)-butan-2-ol have been investigated by cluster weighting before[13,22] and we were able to reproduce these results with the cluster set employed herein (see figs. S2–S3, table S1 and the corresponding discussion in the Supporting Information). These successful applications to the neat liquids justify the application of the cluster weighting approach for the calculation of mole fraction dependent liquid phase spectra of mixtures.

To obtain mole fraction dependent spectra of mixtures, we performed bQCE calculations of acetonitrile/(*R*)-butan-2-ol mixtures with mole fractions of x_b = 0.2, 0.5 and 0.8, with x_b being the mole fraction of (*R*)-butan-2-ol. In these calculations, the cluster weighting is applied to the complete ensemble of neat and mixed clusters simultaneously. The thereby obtained IR and VCD spectra are shown in fig. 2 together with the calculated spectra for the neat substances and experimental IR spectra at the same mole fractions (information about the experimental setup details are provided in the Supporting Information). Overall we observe a very good agreement between the calculated and experimental IR spectra, despite in the region around 1400 cm^{-1} where no IR intensity occurs in the calculated spectra. We observe that increasing the (*R*)-butan-2-ol mole fraction from 0.0 to 0.2 results in the occurrence of peaks around 1080–1180 cm^{-1} (C−C stretching, C−O stretching and C−C−H bending, peaks **2** and **3**) and between 1240–1350 cm^{-1} (C−C−H bending, peaks **4**–**6**) and the intensities of these peaks further increase with increasing (*R*)-butan-2-ol mole frac-

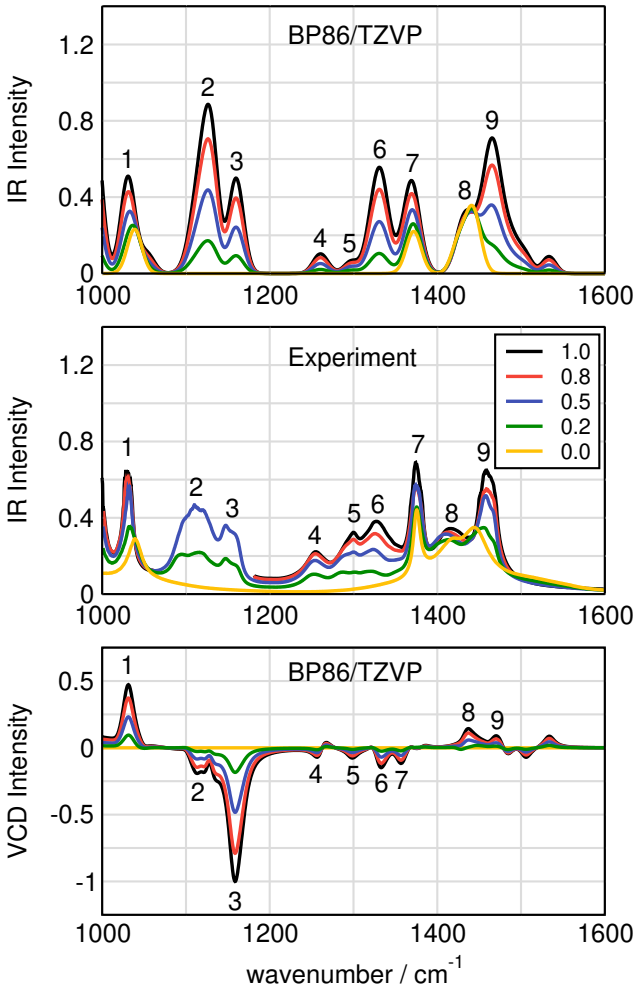

Figure 2: Vibrational spectra of acetonitrile/(*R*)-butan-2-ol mixtures with varying compositions. The composition is given by the mole fraction x_b of (*R*)-butan-2-ol. Top: Cluster weighted IR spectra at the BP86/def2-TZVP level of theory. Middle: Experimental IR spectra recorded in transmission mode. Note that for 1.0 and 0.8 the experimental data between 1060–1180 cm^{-1} had to be excluded due to an oversaturation of the detector. Bottom: Cluster weighted VCD spectra at the BP86/def2-TZVP level of theory.

tion.

The most interesting spectral features are observed in the wavenumber regions where the IR spectra of the neat liquids overlap. In the experimental spectra, the symmetric CH_3 bending modes of both components are located at 1375 cm^{-1} (peak **7**). The calculated spectra predict the correct peak position and it remains unchanged with varying composition of the mixtures.

The C−O−H bending of (*R*)-butan-2-ol occurs at 1460 cm^{-1} (peak **9**). Increasing the mole fraction of (*R*)-butan-2-ol from 0.0 to 0.2 results in increased spectral intensity between 1450–1500 cm^{-1} which manifests as a shoulder of the asymmetric CH_3 bending peak of acetonitrile (1440 cm^{-1}, peak **8**). Further increasing the (*R*)-butan-2-ol mole fraction leads to an increasing intensity of this shoulder until it transforms into a distinct peak. This transformation is well captured by the cluster weighted spectra, although the peak width is overestimated.

One discrepancy is observed for the asymmetric CH_3 bending (peak **8**), which is located at around 1440 cm^{-1} for acetonitrile whereas it appears at 1420 cm^{-1} in the case of (*R*)-butan-2-ol. This redshift is unfortunately not properly modeled by the cluster weighted IR spectra which is due to the lack of intensity around 1400 cm^{-1}. Another important redshift is, however, observed for the CH_3 rocking (peak **1**) which is located at 1040 cm^{-1} in the experimental acetonitrile spectrum but shifted to 1030 cm^{-1} in the experimental spectrum of (*R*)-butan-2-ol. A magnification of the corresponding wavenumber region is depicted in fig. 3 together with fitted experimental spectra obtained from a component data analysis. The redshift is modeled almost perfectly by the cluster weighted IR spectra and the deviations between the calculated and experimental peak maxima are in the range of 1 cm^{-1} with the exception of $x_b = 0.0$.

Figure 2 also depicts cluster weighted VCD spectra. As acetonitrile is achiral, the chiral (*R*)-butan-2-ol is the only VCD active molecule in the mixtures. Therefore, there should be no VCD intensity observable for neat acetonitrile which is the case for the cluster weighted spectrum of $x_b = 0.0$. As soon as some (*R*)-butan-2-ol molecules are present, the mixtures show VCD activity and the intensity increases with increasing (*R*)-butan-2-ol mole fraction. However, the peak shapes and positions remain basically unchanged with varying composition (see also fig. S10). The VCD spectra of the mixtures therefore resemble the calculated VCD spectra of neat (*R*)-butan-2-ol ($x_b = 1.0$) and the VCD intensities are roughly proportional to the concentration (mole fraction) of the chiral compound (see table S2). These results may indicate that acetonitrile–(*R*)-butan-2-ol interactions are only weakly pronounced in the mixtures.

Interactions between (*R*)-butan-2-ol and acetonitrile can occur by hydrogen bonding, dipole–dipole interactions and dispersion interactions (see fig. 1, bottom). However, a relevant amount of mixed

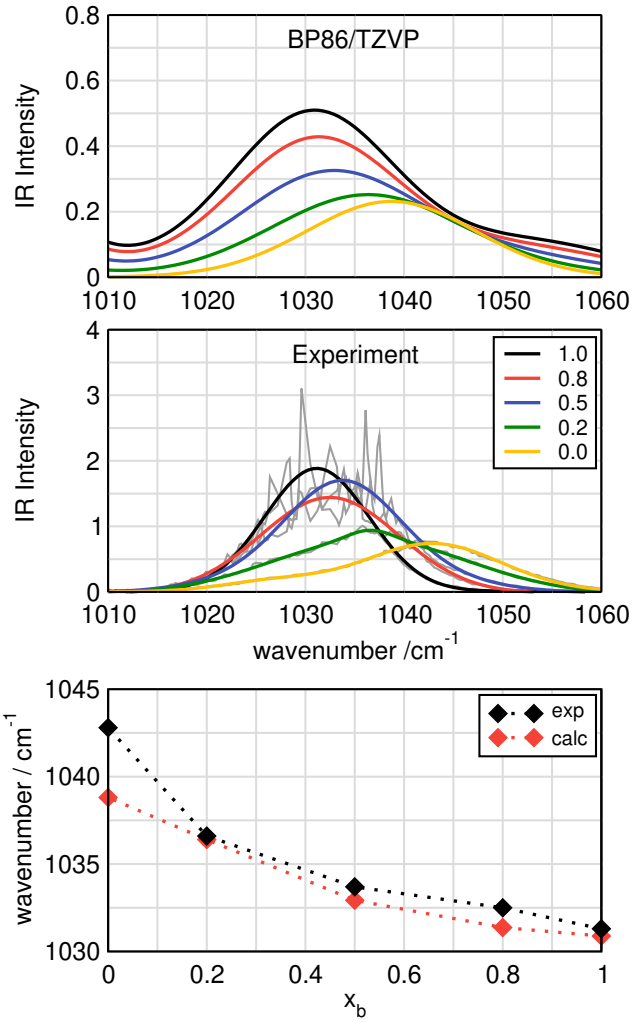

Figure 3: Vibrational spectra of acetonitrile/(*R*)-butan-2-ol mixtures with varying compositions between 1010–1060 cm^{-1}. The composition is given by the mole fraction x_b of (*R*)-butan-2-ol. Top: Cluster weighted IR spectra at the BP86/def2-TZVP level of theory. Middle: Fitted experimental spectra obtained from component data analysis. The raw experimental data are shown in gray. Bottom: Positions of the peak maxima as function of x_b.

clusters will only form if these heteromolecular interactions are strong enough to break the dipole–dipole interactions between acetonitrile molecules and the hydrogen bonds between (*R*)-butan-2-ol molecules. Although the pronounced dipole moments μ and polarizabilities α of acetonitrile ($\mu = 3.93\,\mathrm{D}$, $\alpha = 4.4 \times 10^{-24}\,\mathrm{cm}^3$)[30] and (*R*)-butan-2-ol ($\mu = 1.80\,\mathrm{D}$, $\alpha = 8.9 \times 10^{-24}\,\mathrm{cm}^3$)[30] may promote the formation of dipole–dipole and dispersion interactions, the large size difference between both molecules limits this heteroassociation.[31] The tendency toward a hydrogen bond formation can

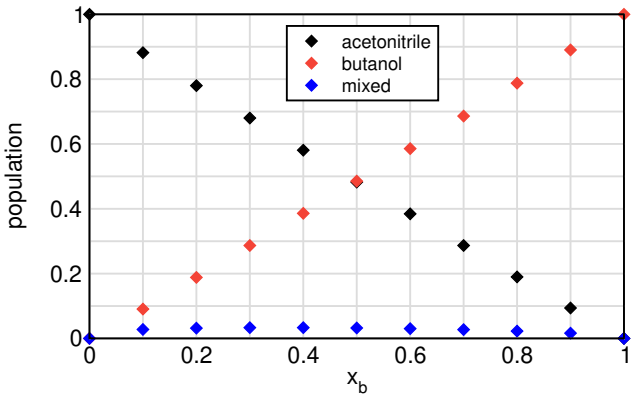

Figure 4: Summed cluster weights of neat and mixed clusters of the acetonitrile/(*R*)-butan-2-ol mixtures at 298.15 K.

be estimated from the electronic binding energies of hydrogen bonded dimers.[32,33] From the calculations of such clusters we observe binding energies of $-29.08\,\mathrm{kJ\,mol}^{-1}$ for a (*R*)-butan-2-ol dimer and only $-20.61\,\mathrm{kJ\,mol}^{-1}$ for a mixed acetonitrile/(*R*)-butan-2-ol dimer. The same trends are observed for larger cluster sizes and suggest that hydrogen bonds between acetonitrile and (*R*)-butan-2-ol are not strong enough to break the hydrogen bonds between (*R*)-butan-2-ol molecules.

These findings suggest that the binary acetonitrile/(*R*)-butan-2-ol system is dominated by self-association of the neat compounds. This assumption is supported by fig. 4 which shows that the mixed clusters are populated only to a minor extent in the bQCE calculations. A maximum population of 3.33 % is reached at $x_b = 0.4$. The most populated mixed cluster is shown in fig. 1, bottom right, and illustrates the problems of the heteroassociation as described above, that is, the hydrogen bonds between (*R*)-butan-2-ol molecules can not be broken by acetonitrile. The ring-shaped (*R*)-butan-2-ol pentamer thus retains its structure and the acetonitrile monomer is located on top of the ring.

In summary we have introduced a novel approach for the prediction of mole fraction dependent IR and VCD spectra at the example of acetonitrile/(*R*)-butan-2-ol mixtures. By assigning weights to a set of simple and easily accessible quantum chemically calculated clusters, the mole fraction dependent spectra are obtained as a weighted average of the individual cluster spectra. The simultaneous weighting of differently sized clusters makes it possible to investigate the entire mole fraction range of a mixture with only one sin-

gle cluster set. This simplicity makes this novel approach computationally very efficient and allows for routine investigations of mole fraction dependent vibrational spectra of mixtures. We have shown that mole fraction related vibrational frequency shifts can be modeled with high accuracy and that the obtained cluster weights provide detailed information about the molecular structure and interactions present in the mixtures.

Acknowledgements

This project (EOS 40007515) has received funding from the FWO and F.R.S.-FNRS under the Excellence of Science (EOS) programme. T.F. acknowledges financial support by the International Max Planck Research School on Reactive Structure Analysis for Chemical Reactions (IMPRS-RECHARGE). P.K. acknowledges financial support by the TRA Matter. The authors also thank the university of Bonn for granting access to the Bonna cluster.

Supporting Information

Derivation of the bQCE theory; methodological details on the cluster generation, quantum chemical calculations, bQCE calculations, and experimental measurements; discussion about the cluster weighted spectra of neat acetonitrile and (*R*)-butan-2-ol; cluster weighted spectra of the investigated acetonitrile/(*R*)-butan-2-ol mixtures at additional levels of theory

References

(1) Nafie, L. A. Vibrational optical activity: From discovery and development to future challenges. *Chirality* **2020**, *32*, 667–692.

(2) Thomas, M.; Kirchner, B. Classical magnetic dipole moments for the simulation of vibrational circular dichroism by ab initio molecular dynamics. *J. Phys. Chem. Lett.* **2016**, *7*, 509–513.

(3) Merten, C.; Bloino, J.; Barone, V.; Xu, Y. Anharmonicity effects in the vibrational CD spectra of propylene oxide. *J. Phys. Chem. Lett.* **2013**, *4*, 3424–3428.

(4) Merten, C.; Golub, T. P.; Kreienborg, N. M. Absolute configurations of synthetic molecular scaffolds from vibrational CD spectroscopy. *J. Org. Chem.* **2019**, *84*, 8797–8814.

(5) Bakels, S.; Gaigeot, M.-P.; Rijs, A. M. Gas-phase infrared spectroscopy of neutral peptides: Insights from the far-IR and THz domain. *Chem. Rev.* **2020**, *120*, 3233–3260.

(6) Panek, P. T.; Jacob, C. R. Anharmonic theoretical vibrational spectroscopy of polypeptides. *J. Phys. Chem. Lett.* **2016**, *7*, 3084–3090.

(7) Nieto-Ortega, B.; Rodríguez, R.; Medina, S.; Quiñoá, E.; Riguera, R.; Casado, J.; Freire, F.; Ramírez, F. J. Sequential Induction of Chirality in Helical Polymers: From the Stereocenter to the Achiral Solvent. *J. Phys. Chem. Lett.* **2018**, *9*, 2266–2270.

(8) Zaera, F. New advances in the use of infrared absorption spectroscopy for the characterization of heterogeneous catalytic reactions. *Chem. Soc. Rev.* **2014**, *43*, 7624–7663.

(9) Wang, C.; Li, Q.; Kong, X.; Zheng, H.; Wang, T.; Zhao, Y.; Li, G.; Xie, H.; Yang, J.; Wu, G. et al. Observation of carbon–carbon coupling reaction in neutral transition-metal carbonyls. *J. Phys. Chem. Lett.* **2021**, *12*, 1012–1017.

(10) Merten, C. Recent Advances in the Application of Vibrational Circular Dichroism Spectroscopy for the Characterization of Asymmetric Catalysts. *Eur. J. Org. Chem.* **2020**, *2020*, 5892–5900.

(11) Guo, C.; Shah, R. D.; Dukor, R. K.; Cao, X.; Freedman, T. B.; Nafie, L. A. Determination of enantiomeric excess in samples of chiral molecules using Fourier transform vibrational circular dichroism spectroscopy: simulation of real-time reaction monitoring. *Anal. Chem.* **2004**, *76*, 6956–6966.

(12) Jiang, S.; Su, M.; Yang, S.; Wang, C.; Huang, Q.-R.; Li, G.; Xie, H.; Yang, J.; Wu, G.; Zhang, W. et al. Vibrational Signature of Dynamic Coupling of a Strong Hydrogen Bond. *J. Phys. Chem. Lett.* **2021**, *12*, 2259–2265.

(13) Kirchner, B.; Blasius, J.; Esser, L.; Reckien, W. Predicting Vibrational Spectroscopy for Flexible Molecules and Molecules with Non-Idle Environments. *Adv. Theory Simul.* **2021**, *4*, 2000223.

(14) Jähnigen, S.; Zehnacker, A.; Vuilleumier, R. Computation of solid-state vibrational circular dichroism in the periodic gauge. *J. Phys. Chem. Lett.* **2021**, *12*, 7213–7220.

(15) Jähnigen, S.; Scherrer, A.; Vuilleumier, R.; Sebastiani, D. Chiral crystal packing induces enhancement of vibrational circular dichroism. *Angew. Chem. Int. Ed.* **2018**, *57*, 13344–13348.

(16) Pescitelli, G.; Lüdeke, S.; Gorecki, M.; Di Bari, L. Symmetry-Dependent Vibrational Circular Dichroism Enhancement in Co (II) Salicylaldiminato Complexes. *J. Phys. Chem. Lett.* **2019**, *10*, 650–654.

(17) Zhu, Z.; Tuckerman, M. E. Ab initio molecular dynamics investigation of the concentration dependence of charged defect transport in basic solutions via calculation of the infrared spectrum. *J. Phys. Chem. B* **2002**, *106*, 8009–8018.

(18) Karimi, M.; Tashvigh, A. A.; Asadi, F.; Ashtiani, F. Z. Determination of concentration-dependent diffusion coefficient of seven solvents in polystyrene systems using FTIR-ATR technique: experimental and mathematical studies. *RSC Adv.* **2016**, *6*, 9013–9022.

(19) Urbanová, M.; Setnicka, V.; Devlin, F.; Stephens, P. Determination of molecular structure in solution using vibrational circular dichroism spectroscopy: the supramolecular tetramer of S-2, 2'-Dimethyl-Biphenyl-6, 6'-dicarboxylic acid. *J. Am. Chem. Soc.* **2005**, *127*, 6700–6711.

(20) Cappelli, C.; Bloino, J.; Lipparini, F.; Barone, V. Toward ab initio anharmonic vibrational circular dichroism spectra in the condensed phase. *J. Phys. Chem. Lett.* **2012**, *3*, 1766–1773.

(21) Brehm, M.; Thomas, M. Computing bulk phase Raman optical activity spectra from ab initio molecular dynamics simulations. *J. Phys. Chem. Lett.* **2017**, *8*, 3409–3414.

(22) Blasius, J.; Kirchner, B. Cluster-weighting in bulk phase vibrational circular dichroism. *J. Phys. Chem. B* **2020**, *124*, 7272–7283.

(23) Thomas, M.; Brehm, M.; Fligg, R.; Vöhringer, P.; Kirchner, B. Computing vibrational spectra from ab initio molecular dynamics. *Phys. Chem. Chem. Phys.* **2013**, *15*, 6608–6622.

(24) Perera, A. S.; Cheramy, J.; Merten, C.; Thomas, J.; Xu, Y. IR, Raman, and Vibrational Optical Activity Spectra of Methyl Glycidate in Chloroform and Water: The Clusters-in-a-liquid Solvation Model. *ChemPhysChem* **2018**, *19*, 2234–2242.

(25) Brüssel, M.; Perlt, E.; Lehmann, S. B.; von Domaros, M.; Kirchner, B. Binary systems from quantum cluster equilibrium theory. *J. Chem. Phys.* **2011**, *135*, 194113.

(26) Kirchner, B.; Spickermann, C.; Lehmann, S. B.; Perlt, E.; Langner, J.; von Domaros, M.; Reuther, P.; Uhlig, F.; Kohagen, M.; Brüssel, M. What can clusters tell us about the bulk?: Peacemaker: Extended quantum cluster equilibrium calculations. *Comput. Phys. Commun.* **2011**, *182*, 1428–1446.

(27) Blasius, J.; Ingenmey, J.; Perlt, E.; von Domaros, M.; Hollóczki, O.; Kirchner, B. Predicting Mole-Fraction-Dependent Dissociation for Weak Acids. *Angew. Chem. Int. Ed.* **2019**, *58*, 3212–3216.

(28) Blasius, J.; Ingenmey, J.; Perlt, E.; von Domaros, M.; Hollóczki, O.; Kirchner, B. Dissoziation schwacher Säuren über den gesamten Molenbruchbereich. *Angew. Chem.* **2019**, *131*, 3245–3249.

(29) von Domaros, M.; Perlt, E.; Ingenmey, J.; Marchelli, G.; Kirchner, B. Peacemaker 2: Making clusters talk about binary mixtures and neat liquids. *SoftwareX* **2018**, *7*, 356–359.

(30) Haynes, W. M. *CRC Handbook of Chemistry and Physics*; CRC press: Boca Raton, Florida, 2014.

(31) Rastrelli, F.; Saielli, G.; Bagno, A.; Wakisaka, A. Preferential Solvation and Self-Association in Alcohol- Acetonitrile Mixtures Observed through Mass Spectrometric Analysis of Clusters: Influence of Alkyl Chain Length. *J. Phys. Chem. B* **2004**, *108*, 3479–3487.

(32) Thar, J.; Kirchner, B. Hydrogen bond detection. *J. Phys. Chem. A* **2006**, *110*, 4229–4237.

(33) Wendler, K.; Thar, J.; Zahn, S.; Kirchner, B. Estimating the hydrogen bond energy. *J. Phys. Chem. A* **2010**, *114*, 9529–9536.

Supporting Information: Efficient Prediction of Mole Fraction Related Vibrational Frequency Shifts

Jan Blasius,[†] Katrin Drysch,[†] Frank Hendrik Pilz,[‡] Tom Frömbgen,[†,¶] Patrycja Kielb,[§,‡] and Barbara Kirchner[*,†]

†*Mulliken Center for Theoretical Chemistry, Clausius Institute of Physical and Theoretical Chemistry, University of Bonn, Beringstraße 4–6, D-53115 Bonn, Germany*
‡*Clausius Institute of Physical and Theoretical Chemistry, University of Bonn, Wegelerstraße 12, D-53115 Bonn, Germany*
¶*Max-Planck-Institut für Chemische Energiekonversion, Stiftstrasse 34-36, D-45470 Mülheim an der Ruhr, Germany*
§*Transdisciplinary Research Area "Building Blocks of Matter and Fundamental Interactions" (TRA Matter), University of Bonn, Bonn, Germany*

E-mail: kirchner@thch.uni-bonn.de

1 Methods

1.1 QCE Method or Cluster-Weighting

The theory of the quantum cluster equilibrium method (QCE) and its extension to binary systems (bQCE) has been extensively described in several earlier works.[1–5] In general, this method considers the liquid phase as an ensemble of interacting molecular clusters. The cluster distribution of this ensemble is obtained through expressions of statistical thermodynamics and by introducing extensions in the cluster partition functions. Based on the obtained cluster populations and the system's total partition function, the thermodynamic properties of the system are accessible in a selected temperature range. Herein we will only provide an overview of the basic aspects of QCE and bQCE and discuss the most recent modifications of the partition functions.

Within the QCE method, the cluster ensemble is considered to be in thermodynamic equilibrium. This equilibrium can be expressed as

$$\mathrm{C}_1 \rightleftharpoons \frac{\mathrm{C}_2}{i(2)} \rightleftharpoons \frac{\mathrm{C}_3}{i(3)} \rightleftharpoons \cdots \rightleftharpoons \frac{\mathrm{C}_\wp}{i(\wp)} \tag{1}$$

for a neat substance and extends to

$$i(\wp)\mathrm{C}_1 + j(\wp)\mathrm{C}_2 \rightleftharpoons \mathrm{C}_\wp \tag{2}$$

for a binary mixture. Therein, a cluster $\mathrm{C}_\wp$ is formed by $i(\wp)$ and $j(\wp)$ monomers of the components C_1 and C_2. Assuming independent clusters and independent translational, vibrational, rotational and electronic degrees of freedom, the system's total partition function is given by

$$Q^{\mathrm{tot}}(\{N_\wp\}, V, T) = \prod_{\wp=1}^{N} \frac{1}{N_\wp!}[q_\wp^{\mathrm{tot}}(V,T)]^{N_\wp}, \tag{3}$$

with

$$q_\wp^{\mathrm{tot}}(V,T) = q_\wp^{\mathrm{trans}}(V,T) q_\wp^{\mathrm{vib}}(T) q_\wp^{\mathrm{rot}}(T) q_\wp^{\mathrm{elec}}(V,T). \tag{4}$$

Therein, $\{N_\wp\}$ is the full set of cluster populations $N_\wp$, T and V are the temperature and volume, respectively, and $q_\wp^{\mathrm{tot}}$ is the partition function of a single cluster $\mathrm{C}_\wp$. The translational, vibrational and rotational partition functions, $q_\wp^{\mathrm{trans}}$, $q_\wp^{\mathrm{vib}}$ and $q_\wp^{\mathrm{rot}}$ are based on standard expressions for the particle in a box, the harmonic oscillator and the rigid rotor, respectively. The electronic partition func-

tion $q_{\wp}^{\mathrm{elec}}$ is calculated from the referenced binding energy $\varepsilon_{\wp}^{\mathrm{elec}}$ of the respective cluster.

Up to this point, the system consists of non-interacting and point-shaped particles. However, to achieve a proper description of the liquid phase, inter-cluster interactions as well as the finite cluster volumes need to be considered. The finite cluster volumes are taken into account by introducing an exclusion volume

$$V^{\mathrm{excl}} = b_{\mathrm{xv}} \sum_{\wp=1}^{N} N_{\wp} v_{\wp} \tag{5}$$

which is subtracted from the phase volume V in the translational partition function. The empirical exclusion volume parameter b_{xv} scales the cluster volumes $v_{\wp}$, which are known to be sensitive with respect to the choice of the atomic radii. A recent extension[6] of the QCE theory introduced a linear temperature dependence of b_{xv}:

$$b_{\mathrm{xv}}(T) = T \cdot \beta_{\mathrm{xv}} + b_{\mathrm{xv}}^{0}. \tag{6}$$

Here, β_{xv} and b_{xv}^{0} are the exclusion volume expansion coefficient and the base of the intercept, respectively.

The inter-cluster interactions are taken into account by introducing a volume dependent mean-field-like attractive energy term in the electronic partition function, which therefore reads as

$$q_{\wp}^{\mathrm{elec}}(V,T) = \exp\left(-\frac{\epsilon_{\wp}^{\mathrm{elec}} - [i(\wp)+j(\wp)]\frac{a_{\mathrm{mf}}}{V}}{k_{\mathrm{B}}T}\right). \tag{7}$$

Therein, the empirical mean-field parameter a_{mf} scales the strength of the inter-cluster interactions and k_{B} is the Boltzmann constant.

Another recently introduced modification[7] targets the vibrational partition function, whose combination with the rotational partition function is usually referred to as the rigid-rotor–harmonic-oscillator approximation. However, since the vibrational partition function diverges for $\nu_i \longrightarrow 0$, with ν_i being a vibrational mode,[8] the modified rigid-rotor–harmonic-oscillator (mRRHO) approximation introduces the vibrational partition function as

$$q_i^{\mathrm{vib}} = \prod_{\nu_i}^{N_i^{\mathrm{vib}}} \left(q_{\mathrm{HO}}^{\mathrm{vib}}(\nu_i)\right)^{f(\nu_i)} \cdot \left(q_{\mathrm{HR}}^{\mathrm{vib}}(\nu_i)\right)^{1-f(\nu_i)}. \tag{8}$$

Within this modified vibrational partition function, $q_{\mathrm{HO}}^{\mathrm{vib}}$ is the partition function of the harmonic oscillator and $q_{\mathrm{HR}}^{\mathrm{vib}}$ is the partition function of the hindered rotor

$$q_{\mathrm{HR}}^{\mathrm{vib}}(\nu_i) = \sqrt{\frac{2\mu'(\nu_i)}{\pi\hbar^2\beta}} \tag{9}$$

with

$$\mu'(\nu_i) = \frac{\mu(\nu_i)\bar{I}}{\mu(\nu_i)+\bar{I}} \tag{10}$$

and

$$\mu(\nu_i) = \frac{\hbar}{4\pi\nu_i}. \tag{11}$$

Therein, $\bar{I}$ corresponds to the average moment of inertia of the cluster, μ is the moment of inertia corresponding to the normal mode, and $\hbar$ is the reduced Planck constant. The Chai–Head-Gordon damping function[9]

$$f(\nu_i) = \left(1 + \left(\frac{\nu_0}{\nu_i}\right)^4\right)^{-1} \tag{12}$$

is chosen as switching function, where ν_0 is the user defined rotor cutoff value, typically set between 20 and 100 cm^{-1}. The modified vibrational partition function thus corresponds to the partition function of a harmonic oscillator for high-frequency modes and to that of a hindered rotor for low-frequency modes.

1.2 Cluster Generation

The structures for the neat acetonitrile and (*R*)-butan-2-ol clusters were taken from previous studies[10,11] and reoptimized at the respective levels of theory. The mixed acetonitrile/(*R*)-butan-2-ol clusters were created in a systematic cluster generation based on a genetic structure optimization at a classical force field level. For this purpose, we interfaced the Ogolem[12,13] framework with the Amber 2016 molecular dynamics package[14] and employed the generalized Amber force field (GAFF).[15] From all generated clusters, the three lowest energy conformers were included in the cluster set. The maximum cluster size corresponds to six monomers for the neat as well as for the mixed clusters. Throughout this work, the clusters will be labeled as aXbY-Z, with X being the number of acetonitrile (a) monomers and Y being the number

of (*R*)-butan-2-ol (b) monomers that are contained in the respective cluster. Z numbers clusters that have the same composition.

1.3 Quantum Chemical Calculations

All quantum chemical calculations were performed using the Turbomole 7.5 software package.[16–18] Four different levels of theory were employed for the geometry optimizations and frequency calculations: BP86[19,20]/def2-SVP,[21] BP86/def2-TZVP,[21] B3LYP[19,20]/def2-SVP and B3LYP/def2-TZVP. London dispersion interactions were modeled by the D3 dispersion correction employing Becke–Johnson damping[22,23] and the geometrical counterpoise correction[24] was used in order to correct for the inter- as well as intramolecular basis set superposition error. The convergence criteria for the self-consistent field energy and the maximum norm of the Cartesian gradient were set to 10^{-8} a.u. and 10^{-4} a.u., respectively. All clusters were verified as minimum structures by having no negative eigenvalues of the Hessian. The IR and VCD spectra were broadened with Gaussian and Lorentzian band shapes, respectively, using a full width at half-maximum of 8 cm^{-1}. To achieve a better agreement with the experimental references, the calculated spectra have been scaled according to the scaling factors reported in Ref.[25]

1.4 Cluster Weighting Calculations

The QCE and bQCE equilibrium populations or so called cluster weights (CWs) were calculated with our publicly available software package PEACEMAKER 2.8.[2–5] All calculations were performed within a temperature range of 200–500 K using increments of 1 K and a fixed pressure of 101.325 kPa. The cluster volumes were defined based on van der Waals radii from Bondi's compilation[26] and the mRRHO rotor cutoff value was set to 50 cm^{-1}, which is a robust choice for the calculation of QCE populations.[27] In this work, we consider a linear temperature dependence of b_{xv} (see eq. (6)),[6] which means that the three empirical QCE parameters a_{mf}, β_{xv} and b^0_{xv} are optimized such that the deviation from the given reference data is minimized. For this purpose, the PEACEMAKER 2.8 code is interfaced with the Differential Evolution algorithm[28] from the SciPy library[29] for PYTHON 3.4. The corresponding script can be provided on request. As experimental reference data, the density at 293.15 K, the boiling temperature, and an isobar of the molar volume were employed. The composition of the investigated mixtures is given by the mole fraction x_b of (*R*)-butan-2-ol which has been scanned from $x_b = 0.0$ to $x_b = 1.0$ in steps of 0.1. The exact values of the reference data and optimized QCE parameters are provided in the Supporting Information. For the weighting of the individual cluster spectra, the cluster weights at 298.15 K have been employed.

1.5 Experimental Setup

Fourier-Transform infrared (FTIR) spectra were recorded at room temperature on a Nicolet 5700 FTIR spectrometer (Thermo Electron Corp.) in transmission mode. Each spectrum is the average of 128 scans measured from 1000 to 7400 cm^{-1} at a frequency resolution of 0.5 cm^{-1}. Measurements were repeated three times with freshly prepared samples to ensure reproducibility. The sample cells had a thickness of ≈50 µm and were equipped with CaF_2 windows.

Samples at different molar fractions were prepared from neat solutions of (*R*)-butan-2-ol (98 %, Thermo Scientific Chemicals, 10.9 mol L^{-1}) and acetonitrile (≥99.9 %, VWR Chemicals, 19.0 mol L^{-1}) which were used without further purification. The concentration of (*R*)-butan-2-ol in mixtures with mole fractions of 0.2, 0.5 and 0.8 corresponds to 3.31 mol L^{-1}, 6.94 mol L^{-1} and 9.56 mol L^{-1}, respectively.

2 Cluster Weighted Spectra of Neat Substances

2.1 Infrared

Here we want to examine the neat liquid states of both solvents. Intermolecular interactions are known to have a huge influence on the vibrational modes of a molecule, causing observable differences between the gas phase and liquid phase vibrational spectra.[11,25,30] In the case of liquid acetonitrile, dipole–dipole interactions of the nitrile groups are known to affect the C≡N stretching vibration, greatly enhancing its IR intensity in the

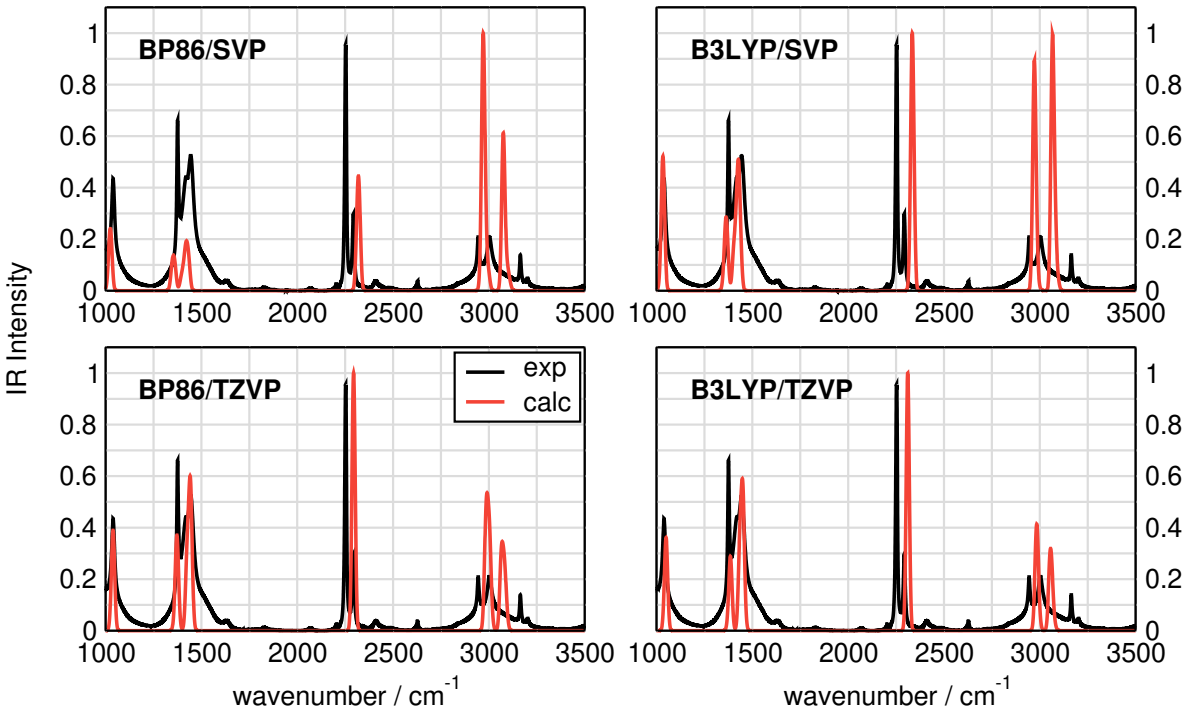

Figure S1: Calculated IR spectra of acetonitrile obtained from cluster weighting compared to the experimental IR spectrum of liquid acetonitrile.

liquid phase as compared to the gas phase. The vibrational frequencies of acetonitrile are, however, hardly changed under aggregation.[30]

Figure S1 shows the calculated IR spectra of acetonitrile based on the CWs that were obtained from the PEACEMAKER calculation with $x_b = 0.0$. The calculated spectra show an overall good agreement with the experimentally measured IR spectrum of liquid acetonitrile. Almost all peak positions are modeled correctly and the deviations from the experimentally observed peak locations are mostly less than $10\,cm^{-1}$. Two exceptions are the symmetric C≡N and the symmetric/asymmetric C−H stretching vibrations which are experimentally observed at around $2252\,cm^{-1}$ and $2942/3001\,cm^{-1}$, respectively.[33] These modes are shifted to higher wavenumbers, the symmetric C−H stretching by 25–$45\,cm^{-1}$, and the symmetric C≡N and asymmetric C−H stretching by 40–$80\,cm^{-1}$, depending on the level of theory.

Despite the good agreement of the frequencies, some discrepancies are observed for the intensity ratios, e.g., the intensities in the C−H stretching region around $3000\,cm^{-1}$ are consistently overestimated at all levels of theory. Accurate and quantitative predictions of vibrational intensities usually require a sophisticated treatment of the electron correlation and large basis sets.[34] However, as we are aiming for a low cost approach that can model the main features of liquid phase spectra, we focus more on using computationally fast quantum chemical methods and consider intensity ratios only qualitatively. The main feature of the acetonitrile liquid phase spectrum, i.e., the high intensity of the C≡N stretching mode at $2252\,cm^{-1}$, is nicely captured by the BP86/TZVP and B3LYP/TZVP spectra. This high intensity can not be modeled by using an isolated acetonitrile monomer only (see fig. S4). The two levels using the smaller SVP basis set produce a worse agreement in this regard, showing that an increase of the basis set indeed improves the intensity ratios of the calculated spectra. Additionally, the intensity of the symmetric CH_3 deformation at $1374\,cm^{-1}$[33] is increased in the cluster weighted spectrum as compared to the monomer spectrum (see fig. S4), further improving the overlap with the experiment significantly.

To quantify the quality of the cluster weighting approach, table S1 summarizes the overlaps σ between the experimental liquid phase and the calculated CW spectra. The overlaps are calculated using the SimVCD measure and can range from 0 to +1 in the case of IR and from −1 to +1 in the case of VCD spectra.[31] The best agreement with the experiment is observed for BP86/TZVP with an overlap of 0.614, followed by an overlap

Table S1: Overlap σ between the experimental bulk phase and calculated CW spectra of neat acetonitrile (IR_a) and (R)-butan-2-ol (IR_b and VCD_b). The values in parentheses correspond to the overlaps between the experimental bulk phase spectra and calculated monomer spectra. The overlap is calculated with the SimIR/VCD tool[31] and can range from 0 to +1 for IR and from −1 to +1 for VCD.

	BP86/SVP	BP86/TZVP	B3LYP/SVP	B3LYP/TZVP
IR_a	0.429 (0.279)	0.614 (0.307)	0.519 (0.224)	0.533 (0.274)
IR_b	0.570 (0.400)	0.653 (0.377)	0.571 (0.385)	0.584 (0.343)
VCD_b	0.166 (0.184)	0.240 (0.129)	0.296 (0.181)	0.290 (0.163)

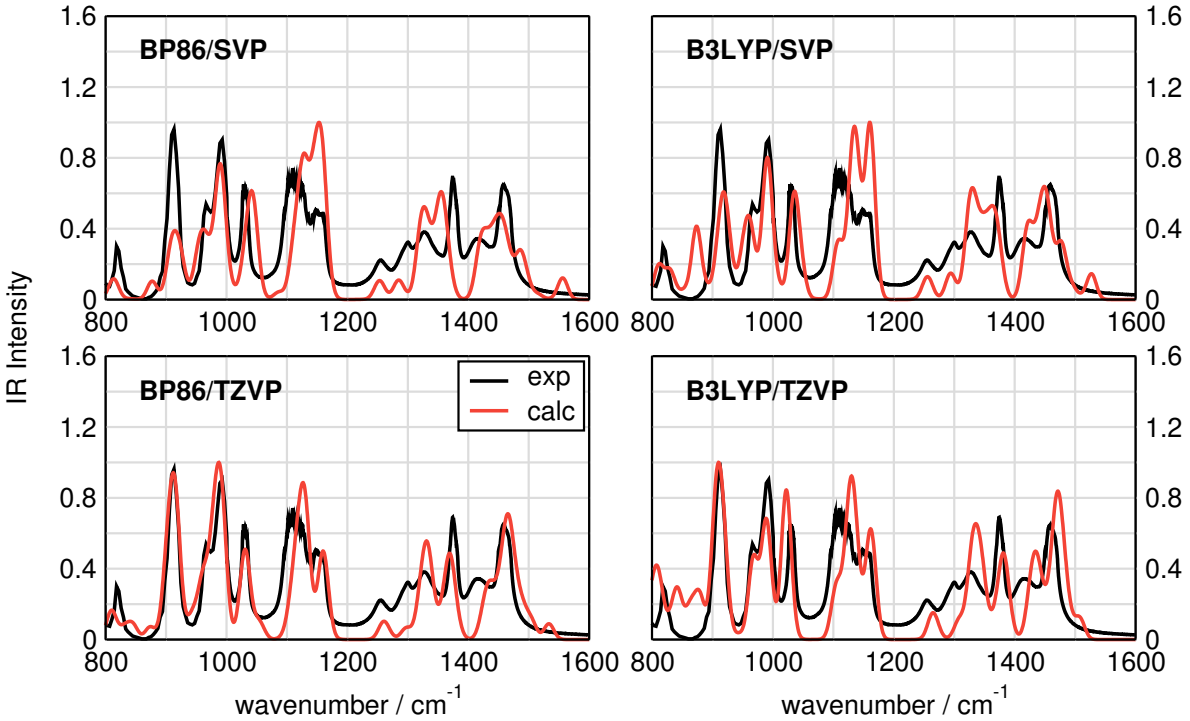

Figure S2: Calculated IR spectra of (R)-butan-2-ol obtained from cluster weighting compared to the experimental IR spectrum of liquid (R)-butan-2-ol. The experimental spectrum below 1000 cm^{-1} is reproduced from Ref.[32]

of 0.533 for the B3LYP/TZVP spectrum. As already concluded from the visual inspection, the two levels of theory using the small SVP basis set yield a poorer overlap with the experiment, which is mostly caused by the inaccurate intensity ratios. Table S1 additionally summarizes the overlaps between the experimental bulk phase spectra and calculated monomer spectra (see fig. S4). Based on these overlaps, it becomes clear that using only the acetonitrile monomer yields a much poorer overlap with the experimental bulk phase spectrum, justifying the application of our cluster weighting approach for the calculation of liquid phase spectra.

(R)-butan-2-ol molecules are known to aggregate in the liquid phase, mainly by hydrogen bonds. These hydrogen bonds usually induce large frequency shifts and intensity perturbations in liquid phase spectra compared to the gas phase. The most pronounced frequency shifts are observed for the C−O stretching and C−O−H bending modes which are shifted from 1076 cm^{-1} and 1241 cm^{-1} to the region of H−C−H bending modes around 1450 cm^{-1}.[32] We have already discussed the functional and basis set dependence of cluster weighted IR and VCD spectra of (R)-butan-2-ol in an earlier study.[25] Although we are using a different cluster set herein, we observe the same trends and will therefore only briefly discuss the spectra of neat (R)-butan-2-ol in the following. For a more detailed discussion the reader is referred to refs.[11,25]

Figure S2 shows the calculated IR spectra of (R)-butan-2-ol based on the CWs that were ob-

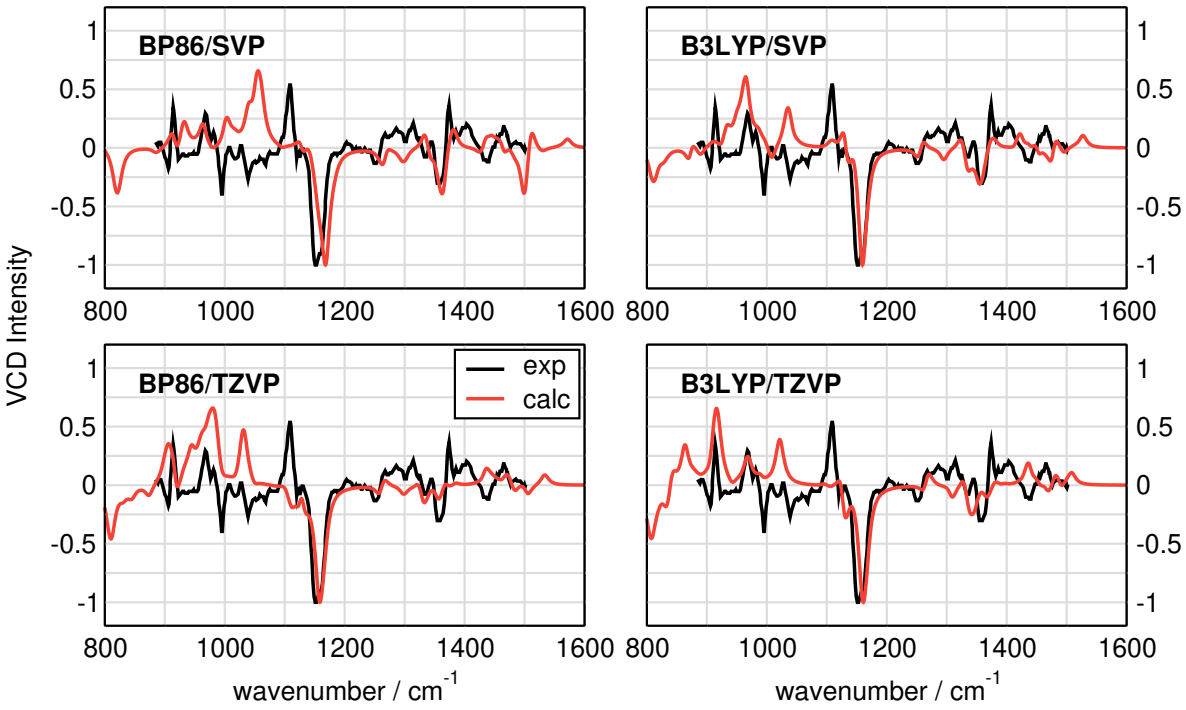

Figure S3: Calculated VCD spectra of (*R*)-butan-2-ol obtained from cluster weighting compared to the experimental VCD spectrum[32] of liquid (*R*)-butan-2-ol.

tained from the PEACEMAKER calculation with x_b = 1.0. The spectra show a good agreement with the experimental spectrum of liquid (*R*)-butan-2-ol and the peak positions and intensities below 1200 cm^{-1} are reproduced almost perfectly, especially for BP86/TZVP and B3LYP/TZVP. For the broader band between 1200 and 1500 cm^{-1} we observe some discrepancies, mainly underestimated intensities for the H−C−H bending modes between 1200 and 1300 cm^{-1} and around 1400 cm^{-1}. Performing a normal mode analysis of the (*R*)-butan-2-ol monomers reveals, that the C−O−H bending modes are located between 1200 and 1300 cm^{-1}, see fig. S5 for the monomer IR spectra of (*R*)-butan-2-ol. This agrees well with experimentally recorded IR spectra of a 0.029 M (*R*)-butan-2-ol solution in carbon disulfide,[32] which can be seen as a gas phase reference. However, a normal mode analysis of the clusters that contribute to the IR spectra shown in fig. S2 reveals that their C−O−H bending modes are shifted to 1450 cm^{-1}, just as it is observed in the experimental spectrum of the liquid phase. We observed earlier that the sole application of an implicit solvation model to the (*R*)-butan-2-ol monomers is not sufficient to model this hydrogen bond induced frequency shift,[11] showing that it is necessary to use clusters here. This is further exemplified by the overlaps summarized in table S1, which show that the monomer spectra have a worse overlap with the liquid phase experiment than the cluster weighted spectra. Again, the best agreement with the experiment is observed for BP86/TZVP with an overlap of $\sigma = 0.653$, the remaining levels of theory perform similarly well and yield overlaps between 0.570 and 0.584.

2.2 Vibrational Circular Dichroism

Figure S3 depicts the cluster weighted VCD spectra for (*R*)-butan-2-ol which show a satisfactory agreement with the experiment between 1120 and 1500 cm^{-1} and the intense negative peak around 1150 cm^{-1} is nicely captured by all levels of theory. Compared to the calculated monomer VCD spectra (see fig. S6), i.e., the gas phase reference, the most important change in the cluster weighted spectra is the vanishing positive peak around 1250 cm^{-1}. In the gas phase, this peak corresponds to the C−O−H bending mode and its shift to the region of H−C−H bending modes around 1450 cm^{-1} leads to the disappearance of this peak in the liquid phase. This main characteristics of the experimental liquid phase VCD spectrum is nicely reproduced by the cluster weighted spectra. Again, we observed earlier that the sole application of a contin-

uum solvation model is not sufficient to model this feature of the liquid phase VCD spectrum.[11] Below 1150 cm^{-1} the agreement with the experiment is worse. Especially the intense positive peak at 1110 cm^{-1}, corresponding to C−O stretching and C−C−H bending motions, is barely reproduced by any level of theory but rather redshifted by 60–80 cm^{-1}.

In the case of VCD, overlaps of 0.2 and greater usually allow for a safe (> 90%) determination of the absolute configuration. The overlaps of the calculated monomer VCD spectra (see fig. S6) with the liquid phase experiment are, however, consistently smaller than 0.2 (see table S1). The cluster weighted VCD spectra improve the overlap with the experiment with the exception of BP86/SVP. In the case of BP86/SVP, the poor overlap is most likely caused by the high intensity of the positive peak around 1050 cm^{-1}. Besides that, the overlaps achieved by the other levels of theory are greater than 0.2, which allows for a certain assignment of the absolute configuration based on the liquid phase VCD spectrum.

2.3 Monomer Spectra

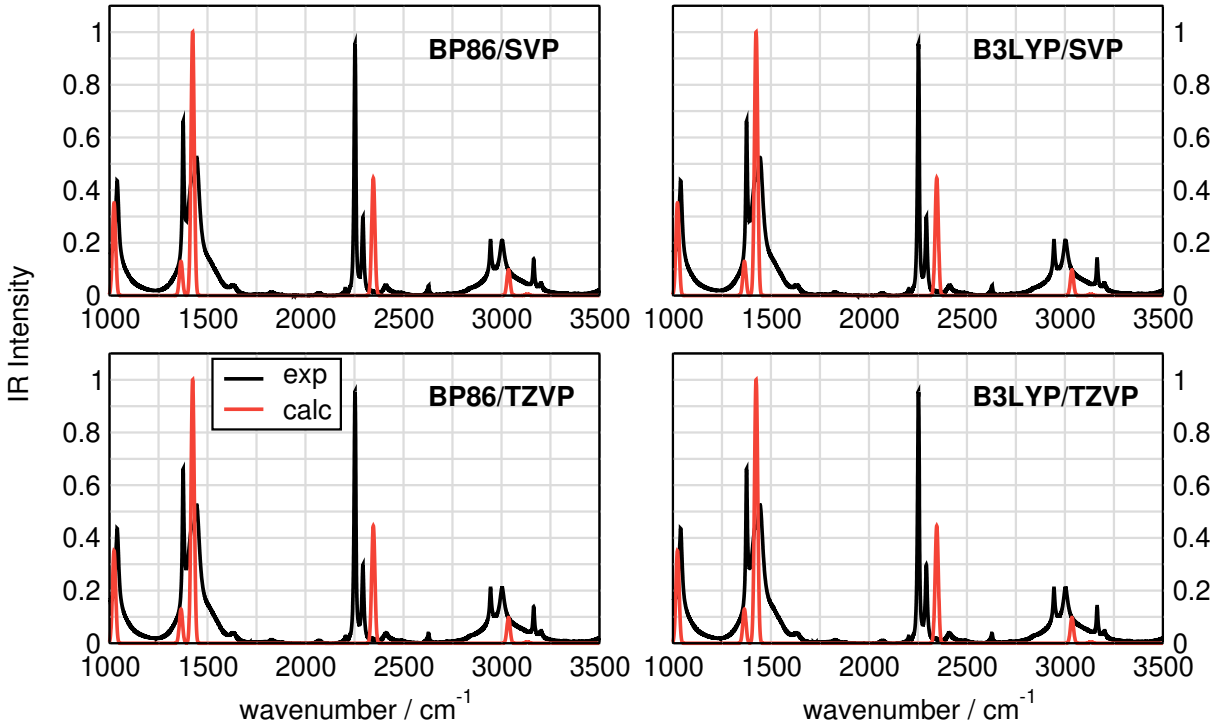

Figure S4: IR spectrum of the acetonitrile monomer at different levels of theory compared to the experimental IR spectrum of liquid acetonitrile.

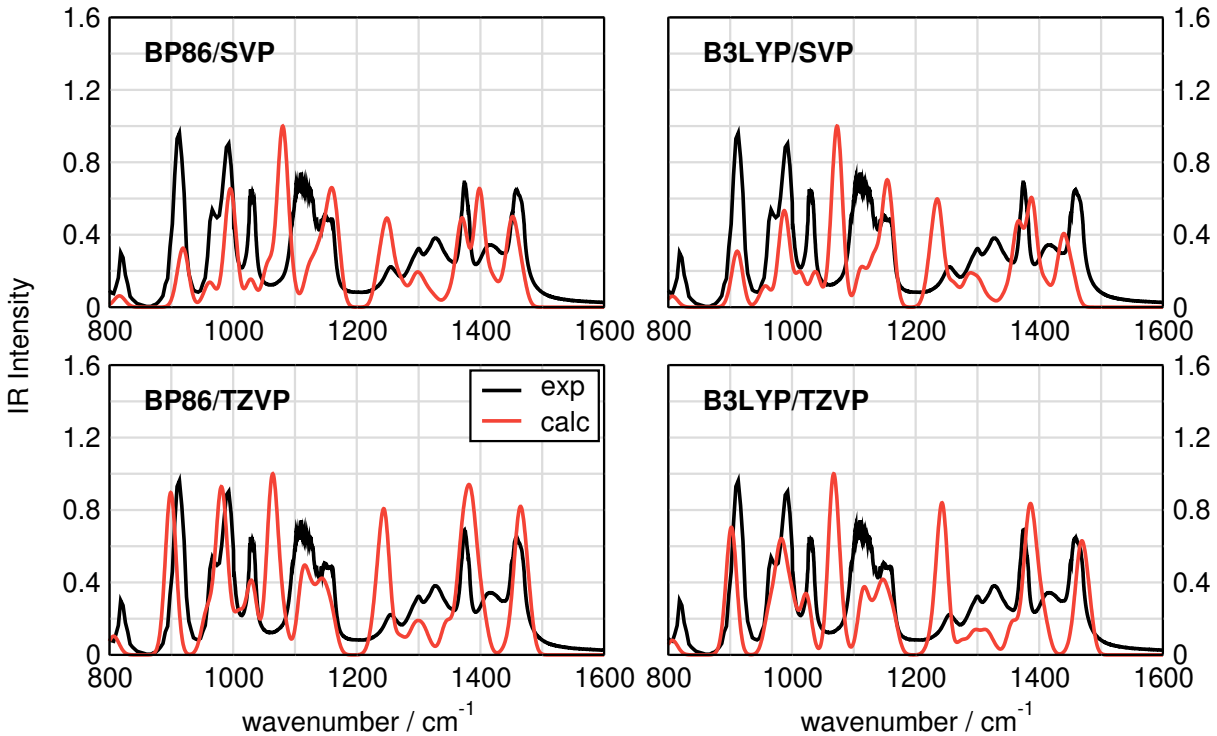

Figure S5: Cluster weighted IR spectrum of the (*R*)-butan-2-ol monomers at different levels of theory compared to the experimental IR spectrum of liquid (*R*)-butan-2-ol. The CWs were obtained from a PEACEMAKER calculation with $x_b = 1.0$ employing only the monomer conformers in the cluster set.

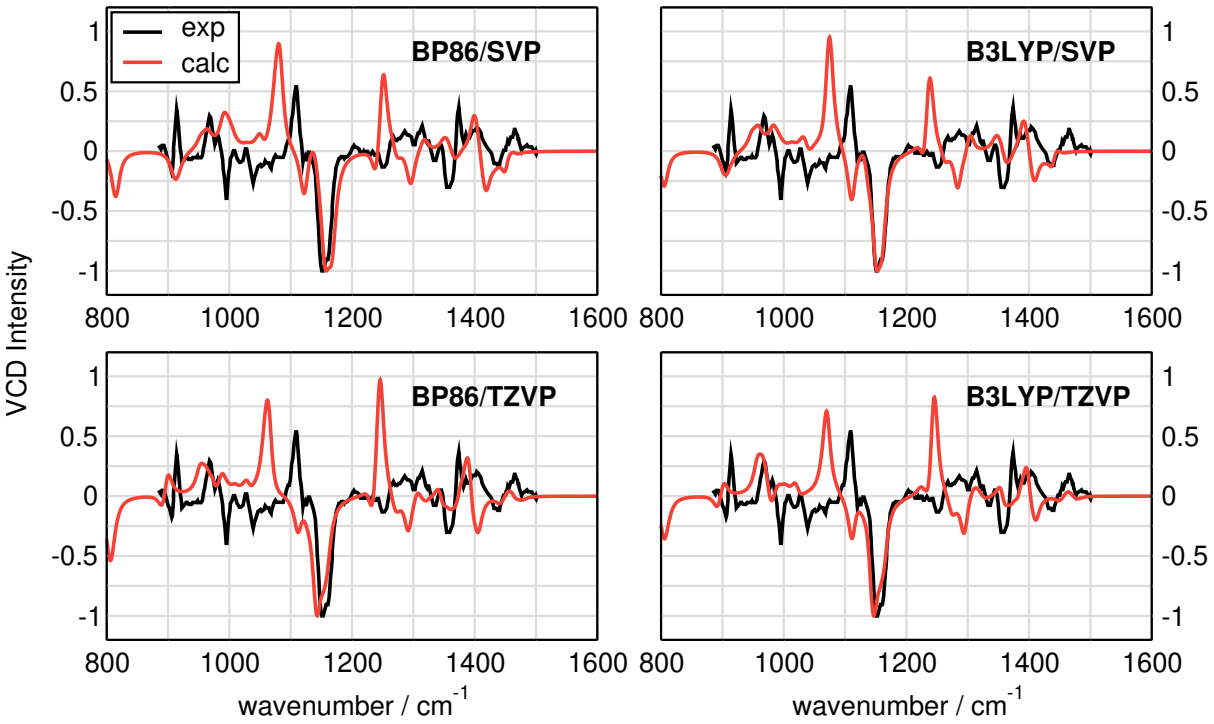

Figure S6: Cluster weighted VCD spectrum of the (*R*)-butan-2-ol monomers at different levels of theory compared to the experimental VCD spectrum of liquid (*R*)-butan-2-ol.[32] The CWs were obtained from a PEACEMAKER calculation with $x_b = 1.0$ employing only the monomer conformers in the cluster set.

3 Cluster Weighted Spectra of Mixtures

Table S2: Averaged relative peak intensities for the VCD spectra obtained at different mole fractions with respect to the VCD spectra obtained at $x_b = 1.0$.

x_b	BP86/SVP	BP86/TZVP	B3LYP/SVP	B3LYP/TZVP
0.2	0.22	0.20	0.21	0.22
0.5	0.50	0.48	0.45	0.51
0.8	0.79	0.79	0.77	0.81
1.0	1.00	1.00	1.00	1.00

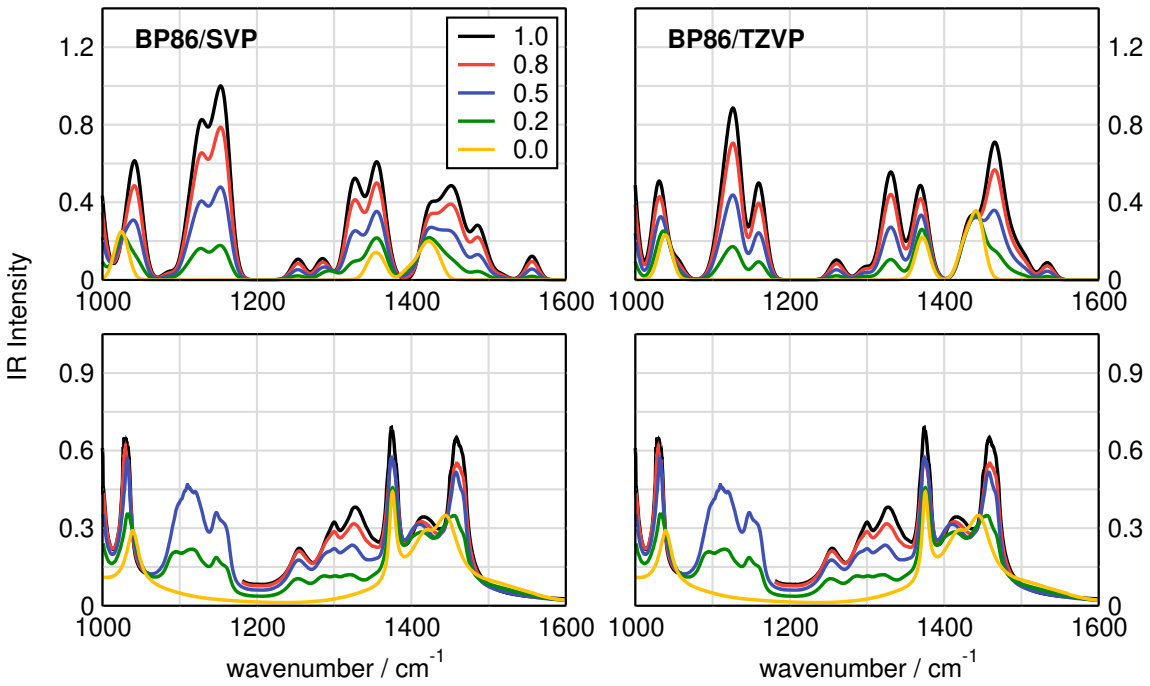

Figure S7: Top: Cluster weighted IR spectra of acetonitrile/(*R*)-butan-2-ol mixtures with varying composition obtained at the BP86/SVP and BP86/TZVP levels of theory. The composition is given by the mole fraction x_b of (*R*)-butan-2-ol. Bottom: Experimental IR spectra recorded in transmission mode. Note that for 1.0 and 0.8 the experimental data between 1060–1180 cm^{-1} had to be excluded due to an oversaturation of the detector..

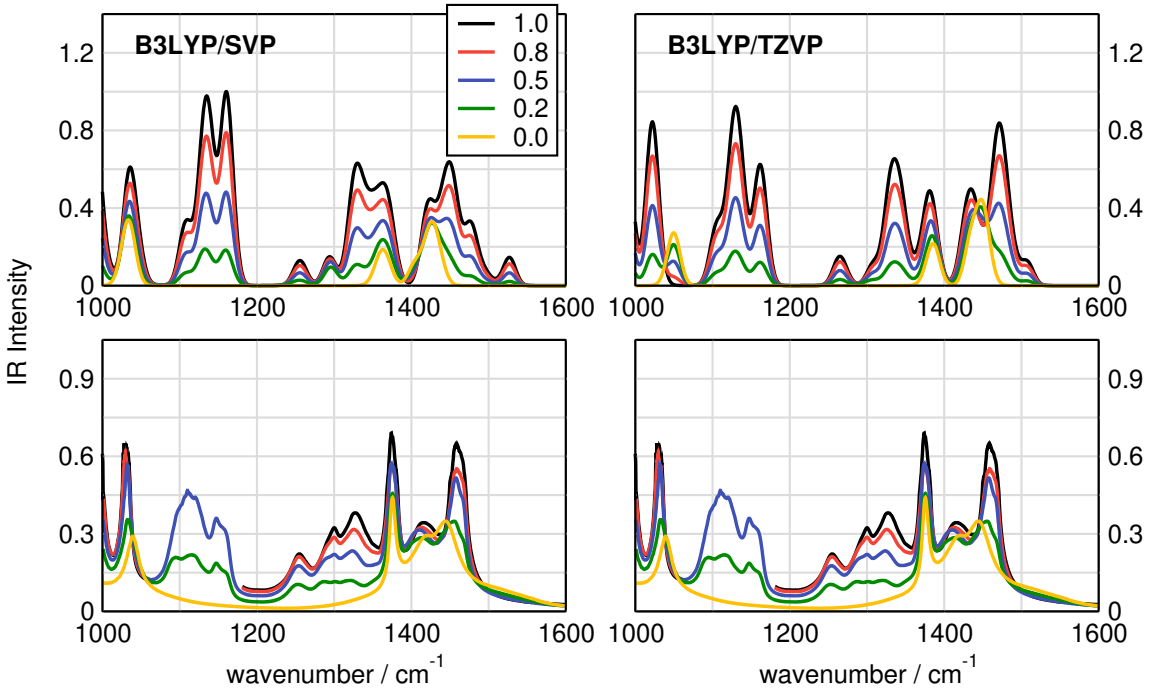

Figure S8: Top: Cluster weighted IR spectra of acetonitrile/(*R*)-butan-2-ol mixtures with varying composition obtained at the B3LYP/SVP and B3LYP/TZVP levels of theory. The composition is given by the mole fraction x_b of (*R*)-butan-2-ol. Bottom: Experimental IR spectra recorded in transmission mode. Note that for 1.0 and 0.8 the experimental data between 1060–1180 cm^{-1} had to be excluded due to an oversaturation of the detector.

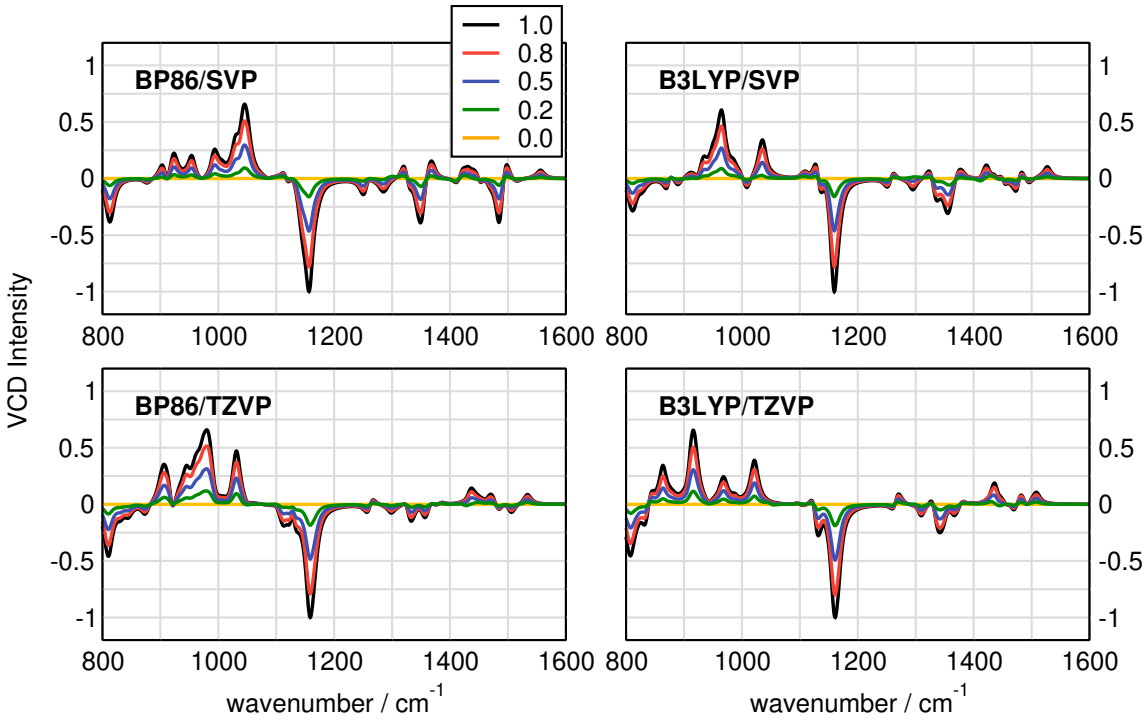

Figure S9: Cluster weighted VCD spectra of acetonitrile/(*R*)-butan-2-ol mixtures with varying composition obtained at different levels of theory. The composition is given by the mole fraction x_b of (*R*)-butan-2-ol.

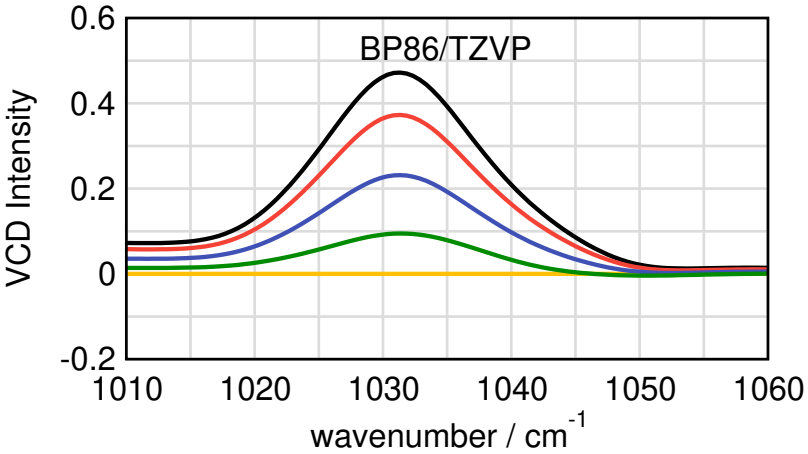

Figure S10: Cluster weighted VCD spectra of acetonitrile/(*R*)-butan-2-ol mixtures with varying compositions between 1010–1060 cm^{-1}. The composition is given by the mole fraction x_b of (*R*)-butan-2-ol.

References

(1) Weinhold, F. Quantum cluster equilibrium theory of liquids: General theory and computer implementation. *J. Chem. Phys.* **1998**, *109*, 367–372.

(2) Kirchner, B. Cooperative versus dispersion effects: What is more important in an associated liquid such as water? *J. Chem. Phys.* **2005**, *123*, 204116.

(3) Brüssel, M.; Perlt, E.; Lehmann, S. B.; von Domaros, M.; Kirchner, B. Binary systems from quantum cluster equilibrium theory. *J. Chem. Phys.* **2011**, *135*, 194113.

(4) Kirchner, B.; Spickermann, C.; Lehmann, S. B.; Perlt, E.; Langner, J.; von Domaros, M.; Reuther, P.; Uhlig, F.; Kohagen, M.; Brüssel, M. What can clusters tell us about the bulk?: Peacemaker: Extended quantum cluster equilibrium calculations. *Comput. Phys. Commun.* **2011**, *182*, 1428–1446.

(5) von Domaros, M.; Perlt, E.; Ingenmey, J.; Marchelli, G.; Kirchner, B. Peacemaker 2: Making clusters talk about binary mixtures and neat liquids. *SoftwareX* **2018**, *7*, 356–359.

(6) Marchelli, G.; Ingenmey, J.; Hollóczki, O.; Chaumont, A.; Kirchner, B. Hydrogen Bonding and Vaporization Thermodynamics in Hexafluoroisopropanol-Acetone and-Methanol Mixtures. A Joined Cluster Analysis and Molecular Dynamic Study. *ChemPhysChem* **2022**, *23*, 50–62.

(7) Zaby, P.; Ingenmey, J.; Kirchner, B.; Grimme, S.; Ehlert, S. Calculation of improved enthalpy and entropy of vaporization by a modified partition function in quantum cluster equilibrium theory. *J. Chem. Phys.* **2021**, *155*, 104101.

(8) Grimme, S. Supramolecular binding thermodynamics by dispersion-corrected density functional theory. *Chem. Eur. J.* **2012**, *18*, 9955–9964.

(9) Chai, J.-D.; Head-Gordon, M. Long-range corrected hybrid density functionals with damped atom–atom dispersion corrections. *Phys. Chem. Chem. Phys.* **2008**, *10*, 6615–6620.

(10) Ingenmey, J.; Blasius, J.; Marchelli, G.; Riegel, A.; Kirchner, B. A Cluster Approach for Activity Coefficients: General Theory and Implementation. *J. Chem. Eng. Data* **2019**, *64*, 255–261.

(11) Blasius, J.; Kirchner, B. Cluster-weighting in bulk phase vibrational circular dichroism. *J. Phys. Chem. B* **2020**, *124*, 7272–7283.

(12) Dieterich, J. M.; Hartke, B. OGOLEM: global cluster structure optimisation for arbitrary mixtures of flexible molecules. A multiscaling, object-oriented approach. *Mol. Phys.* **2010**, *108*, 279–291.

(13) Dieterich, J. M.; Hartke, B. Composition-induced structural transitions in mixed Lennard-Jones clusters: Global reparametrization and optimization. *J. Comput. Chem.* **2011**, *32*, 1377–1385.

(14) Case, D. A.; Betz, R. M.; Cerutti, D. S.; Cheatham, T. E.; Darden, T. A.; Duke, R. E.; Giese, T. J.; Gohlke, H.; Goetz, A. W.; Homeyer, N.; et al., AMBER 2016 (University of California). *San Francisco* **2016**,

(15) Wang, J.; Wolf, R. M.; Caldwell, J. W.; Kollman, P. A.; Case, D. A. Development and testing of a general amber force field. *J. Comput. Chem.* **2004**, *25*, 1157–1174.

(16) Reiter, K.; Kühn, M.; Weigend, F. Vibrational circular dichroism spectra for large molecules and molecules with heavy elements. *J. Chem. Phys.* **2017**, *146*, 054102.

(17) Balasubramani, S. G.; Chen, G. P.; Coriani, S.; Diedenhofen, M.; Frank, M. S.; Franzke, Y. J.; Furche, F.; Grotjahn, R.; Harding, M. E.; Hättig, C.; et al., TURBOMOLE: Modular program suite for ab initio quantum-chemical and condensed-matter simulations. *J. Chem. Phys.* **2020**, *152*, 184107.

(18) TURBOMOLE V7.5 2020, a development of University of Karlsruhe and Forschungszentrum Karlsruhe GmbH, 1989-2007, TURBOMOLE GmbH, since 2007; available from `https://www.turbomole.org`.

(19) Becke, A. D. Density-functional exchange-energy approximation with correct asymptotic behavior. *Phys. Rev. A* **1988**, *38*, 3098–3100.

(20) Perdew, J. P. Density-functional approximation for the correlation energy of the inhomogeneous electron gas. *Phys. Rev. B* **1986**, *33*, 8822–8824.

(21) Weigend, F.; Ahlrichs, R. Balanced basis sets of split valence, triple zeta valence and quadruple zeta valence quality for H to Rn: Design and assessment of accuracy. *Phys. Chem. Chem. Phys.* **2005**, *7*, 3297–3305.

(22) Grimme, S.; Antony, J.; Ehrlich, S.; Krieg, H. A consistent and accurate ab initio parametrization of density functional dispersion correction (DFT-D) for the 94 elements H-Pu. *J. Chem. Phys.* **2010**, *132*, 154104.

(23) Grimme, S.; Ehrlich, S.; Goerigk, L. Effect of the damping function in dispersion corrected density functional theory. *J. Comput. Chem.* **2011**, *32*, 1456–1465.

(24) Kruse, H.; Grimme, S. A geometrical correction for the inter-and intra-molecular basis set superposition error in Hartree-Fock and density functional theory calculations for large systems. *J. Chem. Phys.* **2012**, *136*, 154101.

(25) Kirchner, B.; Blasius, J.; Esser, L.; Reckien, W. Predicting Vibrational Spectroscopy for Flexible Molecules and Molecules with Non-Idle Environments. *Adv. Theory Simul.* **2021**, *4*, 2000223.

(26) Bondi, A. v. van der Waals volumes and radii. *J. Phys. Chem.* **1964**, *68*, 441–451.

(27) Taherivardanjani, S.; Blasius, J.; Brehm, M.; Dötzer, R.; Kirchner, B. Conformer Weighting and Differently Sized Cluster Weighting for Nicotine and Its Phosphorus Derivatives. *J. Phys. Chem. A* **2022**,

(28) Storn, R.; Price, K. Differential evolution–a simple and efficient heuristic for global optimization over continuous spaces. *J. Glob. Optim.* **1997**, *11*, 341–359.

(29) Virtanen, P.; Gommers, R.; Oliphant, T. E.; Haberland, M.; Reddy, T.; Cournapeau, D.; Burovski, E.; Peterson, P.; Weckesser, W.; Bright, J., et al. SciPy 1.0: fundamental algorithms for scientific computing in Python. *Nat. Methods* **2020**, *17*, 261–272.

(30) Mathieu, D.; Defranceschi, M.; Delhalle, J. Ab initio study of the influence of aggregation on the infrared spectrum of acetonitrile. *Int. J. Quantum Chem.* **1993**, *45*, 735–746.

(31) Shen, J.; Zhu, C.; Reiling, S.; Vaz, R. A novel computational method for comparing vibrational circular dichroism spectra. *Spectrochim. Acta Part A: Mol. Biomol. Spectrosc.* **2010**, *76*, 418–422.

(32) Wang, F.; Polavarapu, P. L. Vibrational circular dichroism: Predominant conformations and intermolecular interactions in (R)-(-)-2-butanol. *J. Phys. Chem. A* **2000**, *104*, 10683–10687.

(33) Pace, E.; Noe, L. J. Infrared Spectra of Acetonitrile and Acetonitrile-d3. *J. Chem. Phys.* **1968**, *49*, 5317–5325.

(34) Galabov, B.; Yamaguchi, Y.; Remington, R. B.; Schaefer, H. F. High level ab initio quantum mechanical predictions of infrared intensities. *J. Phys. Chem. A* **2002**, *106*, 819–832.

E. Glucose in Dry and Moist Ionic Liquid: Vibrational Circular Dichroism, IR, and Possible Mechanisms

Jan Blasius,[*] Roman Elfgen,[*] Oldamur Hollóczki,[†*] and Barbara Kirchner[*]

Received: 17 December 2019, Published online: 28 February 2020.

Reprinted (adapted) in appendix E with permission[‡] from

J. Blasius, R. Elfgen, O. Hollóczki, and B. Kirchner, *Phys. Chem. Chem. Phys.* **2020**, *22*, 10726–10737.

doi:10.1039/c9cp06798a.

For this article a Supporting Information is available free of charge at:
https://pubs.rsc.org/en/content/articlelanding/2020/cp/c9cp06798a.

Contributions to the manuscript

- Performance of the analyses
- Interpretation of the results
- Co-writing of the manuscript

[*] Mulliken Center for Theoretical Chemistry, Clausius Institute for Physical and Theoretical Chemistry, University of Bonn, Beringstr. 4–6, 53115 Bonn, Germany
[†] Department of Physical Chemistry, Faculty of Science and Technology, University of Debrecen, 4010 Debrecen, Hungary
[‡] Permission requests to reuse material from this chapter should be directed to the Royal Society of Chemistry.

PCCP

PAPER

View Article Online
View Journal | View Issue

Cite this: *Phys. Chem. Chem. Phys.*, 2020, **22**, 10726

Glucose in dry and moist ionic liquid: vibrational circular dichroism, IR, and possible mechanisms†

Jan Blasius, Roman Elfgen, Oldamur Hollóczki and Barbara Kirchner *

Ionic liquids and their mixtures with water show remarkable features in cellulose processing. For this reason, understanding the behavior of carbohydrates in ionic liquids is important. In the present study, we investigated three D-glucose isomers (α, β and open-chain) in 1-ethyl-3-methylimidazolium acetate in the presence and absence of water, through *ab initio* molecular dynamics simulations. In the complex hydrogen bonding network of these mixtures, the most interesting observation is that upon water addition every hydrogen bond elongates, except the glucose–glucose hydrogen bond for the open-chain and the α-form which shortens, clearly showing the beginning of the crystallization process. The ring glucose rearranges from on-top to in-plane and the open form changes from a coiled to a more linear arrangement when adding water which explains the contradiction that the center of mass distances of the glucose molecules with other glucose molecules grow while the hydrogen bonds shorten. The appearance of coiled open forms indicates that the previously suggested isomerization between these forms is possible and might play a role in the solubility of the related carbohydrates. The calculated IR and VCD spectra reveal insight into the intermolecular interactions, with good to excellent agreements with experimental spectra. Investigating the role of the cation, distances between the acidic carbon atom of the cation and the glucose carbon atom where ring closure and opening occurs are found, which are way shorter than dispersion-like interactions between aliphatic hydrocarbons.

Received 17th December 2019,
Accepted 28th February 2020

DOI: 10.1039/c9cp06798a

rsc.li/pccp

Introduction

Due to its abundance in biomass, cellulose has a great potential as an alternative feedstock for polymers, chemicals and fuels.[1] Ionic liquids (ILs) – liquids that are entirely composed of ions[2–6] – have shown superb features as solvents for processing this biopolymer,[7–9] promising simple and clean technologies for the future. Nonetheless, large-scale industrial applications of these advanced liquids in this field have not yet been introduced. To achieve such a breakthrough, it is paramount that the details of cellulose dissolution are fully revealed, so that efficient and economically viable technologies can be developed for these purposes.

The still open questions in the field include the molecular picture of the dissolution process, especially the particular role played by the cation and anion of the IL. Since cellulose chains are held together in a highly ordered structure by a network of hydrogen bonds, hydrogen bond acceptor strength of the anion is decisive, which breaks up these interchain connections.[9–11] Furthermore, it has been recently demonstrated that by breaking the intramolecular hydrogen bonds within each cellulose chain, a well-chosen solvent induces a higher conformational flexibility to these compounds, which increases solubility through entropic effects.[12] The role of the cations, however, is less obvious, as pointed out by Teles *et al.*[8] Cations have been observed to interact with glucose through dispersion interactions, and with the anions in the first solvent shell of the carbohydrate through hydrogen bonding.[13] The resulting alternating network of anions and cations in the solvent shell should also decrease the repulsive coulombic interactions between the solvating anions through charge screening, and thereby allowing more of them to interact with the polymer. The effect of cations is dependent on how acidic their protons are, if a participation in the hydrogen bond network is anticipated, or how large the space requirements are if it is to be situated in between the chains. On the other hand, if the strength of anion–cation interactions becomes too strong, the cation will compete with the cellulose for the anion, hindering the solubility. Steric effects of the cation and nanosegregation[14,15] seem to have a negative influence on the dissolution of cellulose.[9] It has been also shown that by adding water to the solution the solubility of cellulose in the ionic liquid drops.[9] This does not only underline the necessity to use sufficiently dried biomass and ILs, but also provides a facile technological possibility for the recovery of the biopolymer from the solution.

Mulliken Center for Theoretical Chemistry, University of Bonn, Beringstraße 4 + 6, D-53115 Bonn, Germany. E-mail: kirchner@thch.uni-bonn.de

† Electronic supplementary information (ESI) available. See DOI: 10.1039/c9cp06798a

The capacity of basic imidazolium salts, such as imidazolium acetate ionic liquids (especially 1-ethyl-3-methylimidazolium acetate, [C_2C_1Im][OAc]), to exhibit N-heterocyclic carbene-like activity[16–22] has been shown to be disadvantageous in terms of the stability of the recovered biopolymer.[23] It was demonstrated that the isomerization of the terminal glucose rings of cellulose produces the open-chain aldose isomer of these units, which possesses an active carbonyl group. N-Heterocyclic carbenes (NHCs) react readily with carbonyl groups to give various products.[24] In [C_2C_1Im][OAc] a reverse benzoin reaction was observed, which cleaves off a single H_2CO unit from the carbohydrate, producing thereby a shorter aldose molecule.[23] This reaction was suggested to cause a slow degradation and disintegration of the biopolymer.[23] It is, however, yet unknown, how the glucose isomerization – necessary for the aforementioned reactivity – might take place, and what the role of the IL in that could be.

We have proven that the NHC formation is not necessary for cellulose dissolution, so in principle IL solvents that dissolve but do not degrade cellulose can be designed.[25] Furthermore, it has been observed that this hydrogen bond donor biopolymer – unlike CO_2[17] – suppresses the proton transfer between cation and anion, thus, the NHC formation.[25] However, the suppression of NHC accessibility by the carbohydrate seemingly contradicts the degradation mechanism established by Welton: How could carbene-like reactions possibly occur, if the formation of these species is hindered? A possible resolution for this contradiction might be a recently discovered alternative concerted mechanism for these reactions, which fully avoids the formation of carbenes.[26–28] In this process, the proton transfer from the azolium cation to the base, and the NHC-substrate bond formation occur in a single elementary step, requiring the presence of no free NHCs in solution. It is not yet clearly understood what role the concerted mechanism might play in this process.

In order to elucidate the molecular level pictures a vast amount of studies on glucose in ILs were carried out of which we summarize here only a few representative examples mainly focusing on theoretical work[29–34] and spectroscopy.[35–37] Kiefer and coworkers presented a quantitative analysis of α-D-glucose in 1-ethyl-3-methylimidazolium acetate [C_2C_1Im][OAc] using infrared (IR) spectroscopy.[35] They managed to establish a protocol to monitor the concentrations of the monosaccharide in the IL. Youngs and coworkers showed from classical molecular dynamics simulations that a strong organisation of negatively charged ions around the hydrogen atoms of the glucose occur.[33] Brehm *et al.* presented a combined experimental and theoretical work of triazolium-based ionic liquids in which strong hydrogen bonds between the cellulose and anion, but much weaker ones between cellulose and the cations form.[30] Rabideau, Agarwal and Ismael presented a seminal study of the side chain length (up to pentyl) effect on the interaction energies, hydrogen bonding and solvation structure.[29] They found that the tail length of the cation has only a minor influence on these quantities. They observe that cations interact directly with anions at the cellulose surface *via* electrostatic interactions, but they also fill the gaps between these successive sites, providing coverage of and favorable van der Waals interactions with the nonpolar groups of the cellulose. As the imidazolium ring group size is approximately equal to the distance between successive cellulose-bound anions, hydrophobic interactions with cellulose are possible. This also contains the anion–cation network at the surface of cellulose.[29] Li *et al.*[31] focused on cellulose dissolution in ILs containing cations with an unsaturated heterocyclic ring. They explained the good solubility by the π-electron delocalization which would make the cations more likely to interact and provide space for the anions.[31] The solvation of cellobiose in [C_2C_1Im][OAc] at the presence of small water contents was studied by Payal and Balasubramanian from *ab initio* molecular dynamics (AIMD) simulations.[38] The AIMD study found that anions are in the first solvent shell of the cellobiose molecule, however cations were present to a minor content too, thus leading to the conclusion that their role cannot be completely ignored. The authors also added small amounts of water (30 ion pairs of IL with 5 water molecules) and found that this did not alter the overall picture. Regarding the ionic liquids, our group analyzed the vibrational spectra of [C_2C_1Im][OAc] and its mixtures with water and carbon dioxide using AIMD simulations in comparison to experiment. With the aid of a normal coordinate analysis the experimentally observed bands were assigned to specific molecular vibrations.[39] In 2015[40] we introduced an alternative approach for calculating bulk phase vibrational spectra from AIMD simulations based on cross-correlations.[41] Instead of the well-known approach of maximally localized Wannier functions,[42] we applied the Voronoi tessellation of electron density to receive molecular dipole moments. We applied this approach also to a mixture of [C_2C_1Im][OAc] with water. Furthermore, we used this approach in order to obtain vibrational circular dichroism spectra by AIMD[43] instead of from static quantum chemical calculations[44–47] or other AIMD approaches.[48–51] In VCD spectroscopy[45] the differential absorbance of left- and right-circularly polarized light during vibrational transitions is measured. In the spectrum of an enantiomer positive or negative features allow the distinction from its mirror image and intermolecular interactions similar as in IR spectroscopy can be probed.[52,53]

Thus, beside the direct chemical questions, the theoretical modeling of the corresponding systems also poses a hitherto unprecedented challenge. In this work we aim at elucidating the molecular level picture of glucose solvation in 1-ethyl-3-methylimidazolium acetate without and with added water, composition see Table 1 and Fig. 1. We investigate the monosaccharide in the open form, as α-D-glucose and β-D-glucose in the pure and moist IL. We calculate the IR-spectrum from AIMD in these mixtures as has been done previously by many researchers for other systems.[54] We also calculate the vibrational circular dichroism (VCD) spectra. The present article reports on a very comprehensive study, its novelty lies in the following aspects:

(1) Different anomers and their potential conversion have yet not been studied and compared from molecular dynamics simulations, especially not from AIMD simulations.

(2) The high water content has not yet been studied from AIMD simulations. This enforces the application of at least polarizable force fields or even better of AIMD (used in the present study).

Table 1 Compositions of the simulation boxes and simulation duration t_{sim} in ps. Concentration c(glu) is given in g(glu)/mol(IL). Abbreviations **O**, **A** and **B** as well as **OW**, **AW** and **BW** defined in Fig. 1

Quantity	O	A	B	OW	AW	BW
No(IP)	48			36		
No(glu)	8			6		
No(wat)	—			100		
wt%(wat)	—			20		
c(glu)	30.0267			30.0267		
wt%(glu)	15			11		
t_{sim}	43	38	40	47	39	49

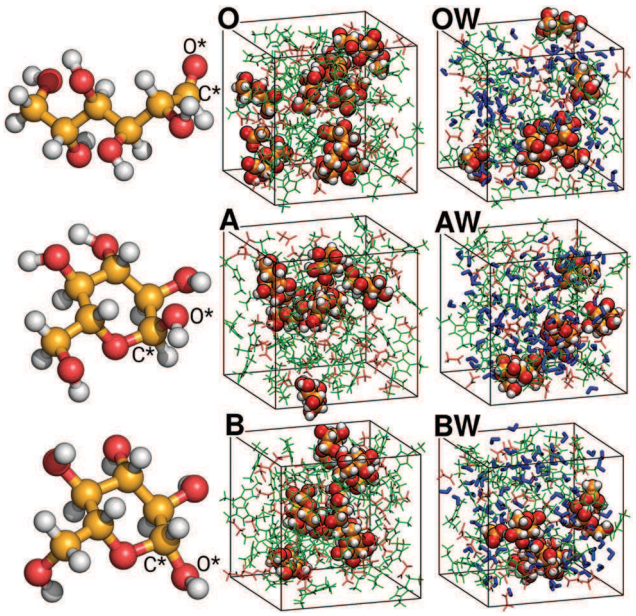

Fig. 1 Ball-and-stick images of different glucose molecules and snapshots of simulation boxes without water (**O**, **A** and **B**) and with water (**OW**, **AW** and **BW**). The upper row shows the open chain glucose, the middle row α-D-glucose and the bottom row β-D-glucose. O* (C*) marks the oxygen (carbon) atom at the anomeric center in the case of the ring isomers and the aldehyde oxygen (carbon) atom in the case of the open form. Color code for the left is carbon: orange; oxygen: red and hydrogen atom: white. Within the simulation boxes the IL cations are colored in green, the IL anions in red and the water molecules in blue.

(3) The vibrational spectra of the monosaccharide molecules in dry and moist IL have not yet been calculated. Especially the VCD spectra of chiral solutes have never been modeled before.

Results and discussion

Overall structure

In order to discuss the overall structure of the present solutions, we show in Fig. 2 and 3 the radial pair distribution functions and the corresponding number integrals (RDF and NI) between centers of mass of each molecular compounds (center of ring in the case of the cation) in absence (left) and presence of water (right). Focusing first on the dry systems, the cation interacts strongly with the anion as observed before,[55,56] and this interaction shows only slight differences between the three glucose isomers.

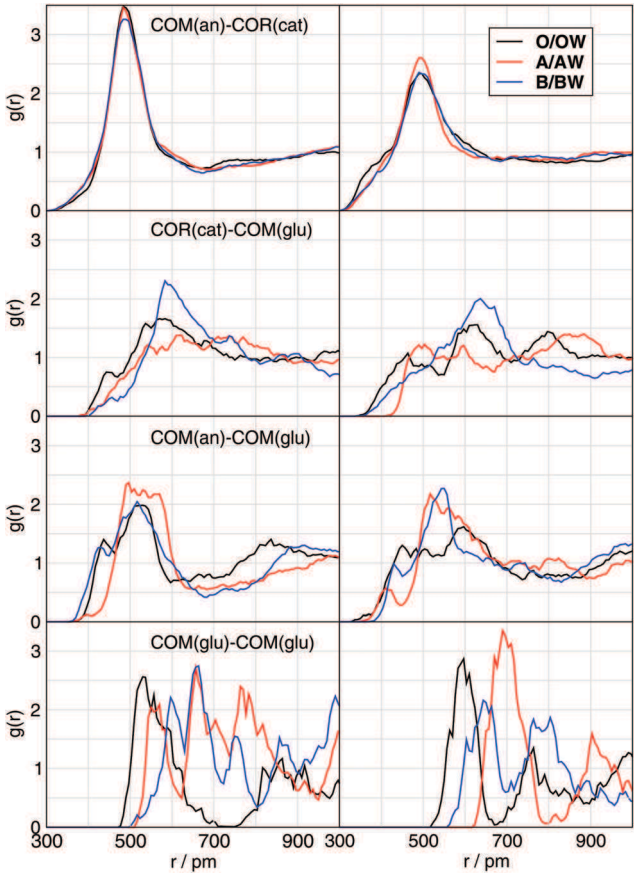

Fig. 2 Radial distribution functions (RDFs) between the center of mass (COM) of the anion and the center of ring (COR) of the cation (above); between the COM of glucose and the COR of the cation (second plots), and the COM of the anion (third plots), and of the COM of other glucose molecules (bottom plots), respectively. The different letters **O**, **A** and **B** (water free) as well as **OW**, **AW** and **BW** (with water) mark the different systems and are defined in Fig. 1.

In all solutions, the solvation of the carbohydrate is influenced by all species in the system, as significant first peaks at relatively short distances in the RDFs of glucose with the anion, cation and other glucose molecules can be observed. The anion–glucose interaction seems to be somewhat more pronounced than the cation–glucose interaction. In the first solvent shell – which is situated at 700 pm according to the RDFs – we observe approximately four to five anions for each glucose molecule of each isomer, which is in good agreement with the experimental results of Teles and coworkers.[8]

Interestingly, in their solvation, distinct differences can be observed between the different isomers of the sugar molecule. The open-chain form of glucose shows the highest correlation for self-interaction, with a single peak in contrast to the other isomers that exhibit multiple peaks. This can be explained by the larger flexibility of these structures as opposed to the rigid rings, which allows more efficient alignment, and multiple favorable interactions.

The presence of water (right panels in Fig. 2) reduces the cation–anion interaction and both the cation– as well as the anion–glucose interaction with a stronger extent for the former interaction.

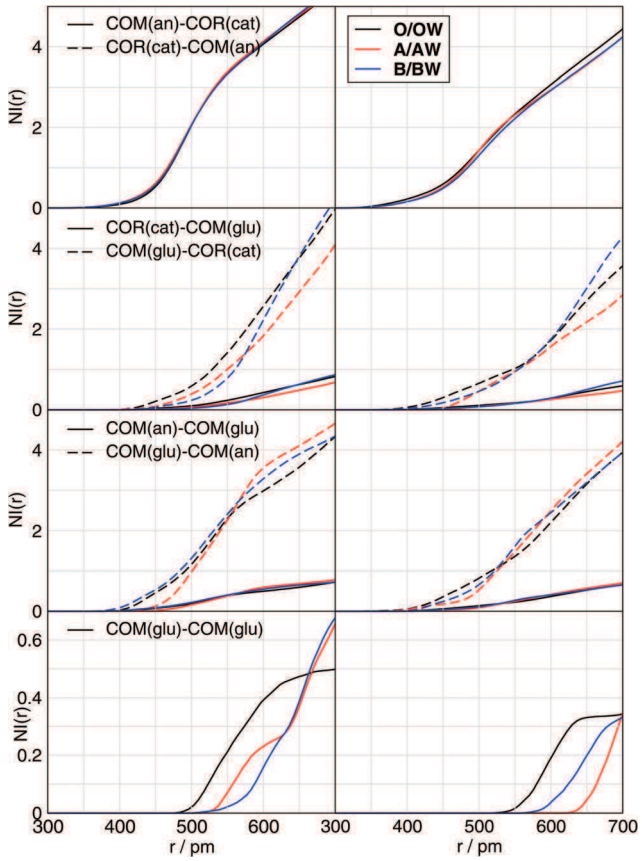

Fig. 3 Number integrals (NIs) between the center of mass (COM) of the anion and the center of ring (COR) of the cation (above); between the COM of glucose and the COR of the cation (second plots), and the COM of the anion (third plots), and of the COM of other glucose molecules (bottom plots), respectively. Solid lines (top): amount of cations that surround the anions; dashed lines: *vice versa*. Please note that solid and dashed are here identical. Second and third panel: solid lines: amount of glucose molecules that surround the ions; dashed lines: amount of ions that surround the glucose molecules.

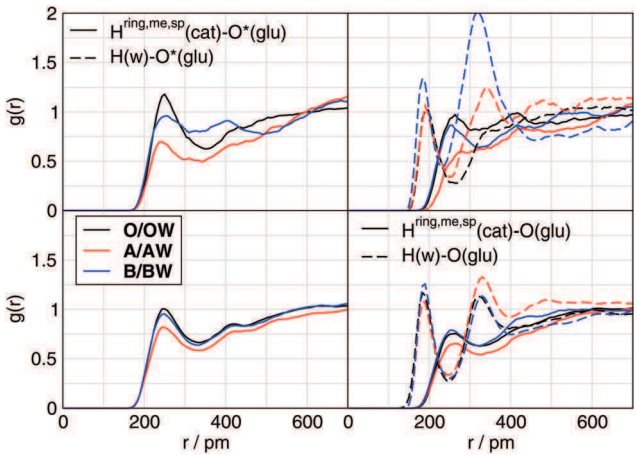

Fig. 4 RDFs between the ring protons H^{ring}, the methyl group protons (me) as well as the protons of the spacer (sp) of the cation and the oxygen atom (O*) bound to the specific stereo center of glucose (upper plots) and all glucose oxygen atoms (bottom plots). Dashed lines are the same for the water protons H(w). RDFs for only the ring protons of the cation are given in the ESI.†

This effect is also reflected in the number integrals in Fig. 3 showing that fewer cations surround the anions and *vice versa*, while the ion–glucose contacts also decrease. The graphs in Fig. 2 also show that water induces larger distances for the glucose–glucose interplay, while the multiple peaks observed in the dry systems merge into fewer, but higher or wider peaks. The variations in the amount of neighbors are very diverse (lowest panels in Fig. 3). While the amount of neighbours decreases for the open form glucose from 0.5 to 0.3 in the first solvent shell, the alterations for α-D-glucose are difficult to discuss. This is due to a transformation from stacked arrangement to an in-plane arrangement when considering wet instead of dry ionic liquids, see discussion below and Fig. S2 in ESI.† Turning to β-D-glucose: at the first minimum of 630 pm 0.3 neighbours are found which remain approximately the same at the first shell minimum of 700 pm in **BW**. This illustrates how complex these systems are and that they are far from fully understood.

Hydrogen bond structure

Considering now the hydrogen bonding in particular under participation of the glucose molecules we present in Fig. 4–6 selected H···O radial distribution functions and in Table 2 the corresponding first peak positions. Since there is a multitude of hydrogen bond donor and acceptor sites in the system, for the sake of clarity we discuss some groups of them together. Starting with the most relevant protons of the cation, namely the ring protons (H^{ring}), the methyl and methylene groups (abbreviated sp for spacer) of the side chain adjacent to the nitrogen atoms (H^{me}, and H^{sp}, respectively), we observe hydrogen bonds with all other components, with H···O distances below 250 pm (Table 2) and peaks reaching above or close to $g(r) = 1$ in the corresponding RDFs. The only exception in this regard is the α-D-glucose acceptor, which exhibits notably lower peak heights than the other two isomers, indicating a relatively rare connection with the aforementioned hydrogen atoms of the cation.

The three glucose isomers are all different in the position of the oxygen atom O*, hence when comparing the solvation of these molecules, this site deserves special attention. In agreement, the differences between the three compounds in the hydrogen bonding situation of the O* are higher, than for the

Table 2 Oxygen-proton distance in pm at the first peak in each obtained radial pair distribution function, with an expected accuracy of ±5 pm. For labels see Fig. 1

H	glu	O(an)	O*(glu)	O(glu)	O(W)
$H^{ring,me,sp}$	**O/OW**	225/247	250/263	246/255	—/265
$H^{ring,me,sp}$	**A/AW**	222/242	242/—	246/255	—/265
$H^{ring,me,sp}$	**B/BW**	223/245	254/253	246/255	—/265
H^{ring}	**O/OW**	204/219	250/—	243/243	—/253
H^{ring}	**A/AW**	206/216	230/257	236/243	—/253
H^{ring}	**B/BW**	206/222	237/—	234/246	—/242
HO(glu)	**O/OW**	170/170	—/—	190/175	—/178
HO(glu)	**A/AW**	170/170	—/—	182/172	—/177
HO(glu)	**B/BW**	170/170	—/—	176/195	—/178
H(w)	**O/OW**	—/176	—/193	—/186	—/180
H(w)	**A/AW**	—/176	—/190	—/186	—/180
H(w)	**B/BW**	—/176	—/184	—/186	—/180

other oxygen atoms. In the open-chain form this atom is an oxo-group, making it a strong hydrogen bond acceptor, producing the highest RDF first peaks with the cation. In the α-D-glucose, O* is spatially closer to the adjacent hydroxyl group, allowing an intramolecular hydrogen bond between them, while such an interplay within β-D-glucose is not feasible. Consequently, the aforementioned lower probability of intermolecular hydrogen bond acceptor strength for the α-D-glucose can be explained through these structural differences, the resulting competing intramolecular hydrogen bonds, and the competition between these two neighboring hydrogen bond acceptor sites for the hydrogen bond donor molecules.

For every hydrogen bond involving the cation, water addition significantly raises the distances by 10 pm and even sometimes by 20 pm, including the very strong hydrogen bonds between the cation and the anion (Table 2) with the exception of the hydrogen bond between cation as donor and the open form glucose molecules as acceptor. This hydrogen bond distance remains unaffected. The increased hydrogen bonds are in line with the lower hydrogen bond donor strength of the imidazolium cation compared to that of water, which allows the latter species to effectively compete for the acceptor sites with the cation. The contacts of the cation to water also possess hydrogen bond-like geometries, however, the corresponding O···H distances are almost always significantly longer than the ones of the other hydrogen bonds.

Much stronger hydrogen bonds are provided by the anions with the glucose molecules, as indicated by shorter distances (170 pm) and higher first peaks. Since the open-chain isomer lacks a proton at O*, this (black) curve is missing in Fig. 5. Even if the characteristic O···H distances are unaffected by moisture, water reduces the occurrence of these interactions (see number integrals NI in the ESI†). In the dry system the oxygen is up to 250 pm in contact with one hydrogen of the glucose, it changes to statistically half a hydrogen atom of glucose and half a hydrogen of water in the moist system at the same distance.

It is noteworthy that a proton transfer from a hydroxyl group of the glucose to the anion is observed in the system **OW**, which gives rise to a peak in the corresponding RDF at a distance of 100 pm (Fig. 5 bottom right). Although this reaction took place during the high temperature equilibration of the system, therefore it should be interpreted with high care, the proton fails to return in the later simulation steps from the acetate to the carbohydrate, showcasing the high basicity of the anion in the system.

Between the hydroxyl groups of the glucose molecules, we also find very short hydrogen bonds (below 200 pm), both intra- and intermolecularly. The intramolecular interactions (Fig. 6 above) occur most in the open form, while for the other two isomers, due to the spatial inaccessibility of most neighboring hydroxyl groups, these interactions are negligible. The only exceptions in this regard are the –CH_2–OH groups of the α- and β-D-glucose, and the aforementioned hydrogen bond between the O* and its adjacent hydroxyl moiety in the α-D-glucose. These two kinds of interactions produce a very low (*i.e.*, statistically somewhat irrelevant) peak at *ca.* 200 pm for the β-D-glucose, and a somewhat higher shoulder for the first peak in case of α-D-glucose. Interestingly, upon adding water to the system, the intramolecular hydrogen bonds of both the open-chain isomer and α-D-glucose increase in occurrence. However, this is not the case for β-D-glucose where the events of intramolecular hydrogen bonding become rarer when water is present.

For the intermolecular hydrogen bonding between glucose molecules in the dry system (Fig. 6 below) it is apparent that they are significantly less pronounced for the open form than for the other two compounds, producing a first peak with a height far below $g(r) = 1$. The other two molecules show intensive intermolecular hydrogen bonding between the carbohydrates,

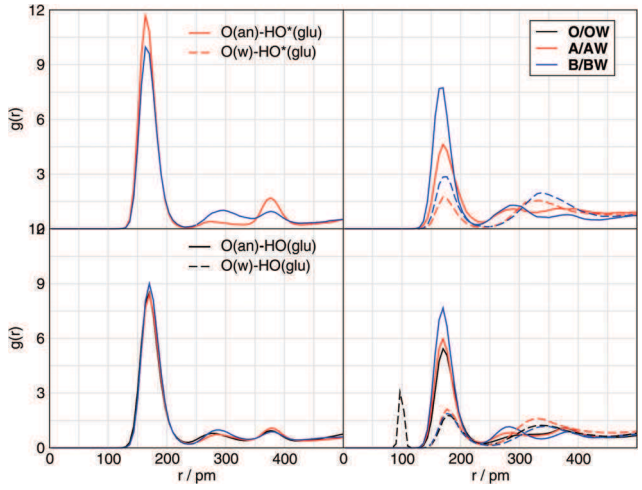

Fig. 5 RDFs between the anion oxygen atoms and the glucose hydrogen atom associated with the stereo center of the molecule (upper plots) and all alcohol-hydrogen atoms at the glucose molecules (bottom plots). Please note, the open form stereo center oxygen atom is transformed into an aldehyde group which is why the curves for the open form are missing above.

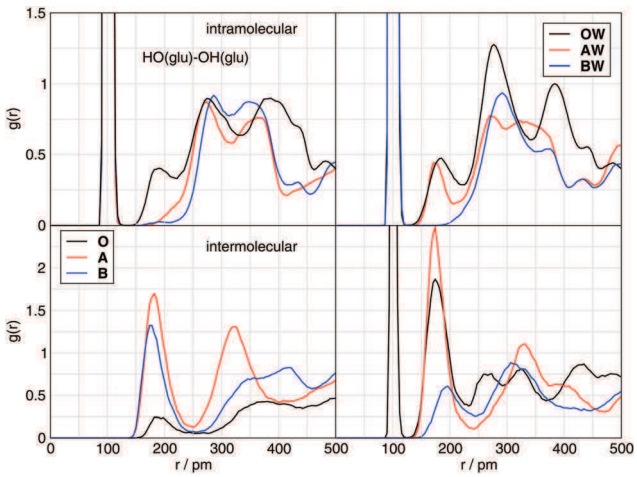

Fig. 6 RDFs between the acidic protons of the glucose and the oxygen atoms O of the monosaccharide. Above we show the intramolecular contributions and below we show the intermolecular contributions. Left is the dry and right is the moist system.

with the α-isomer being somewhat stronger. Upon adding water to the system, the RDFs representing the intermolecular glucose–glucose interactions for the open chain form and α-D-glucose show higher first peaks at *ca.* 15 pm shorter distances, which is a very interesting result given that every other hydrogen bond increases upon water addition. This seems to be in contrast to the increased "center of mass"-distances of the glucose molecules observed in the COM RDFs. However, closer inspection (see Fig. S2 in the ESI†) shows that the arrangement between the α-D-glucose molecules changes from a ring stacking (dry) to an "in-plane" (moist) contact. For the open form we observe more coiled arrangements in the dry liquid compared to the moist solution, see Fig. S3 in the ESI,† and distribution plot in Fig. 12 below and the according discussion. These shortened hydrogen bonds and higher peaks indicate both stronger hydrogen bonding, and a higher degree of association, because in agreement, the number integrals for the open form increase tremendously, see Fig. 7. Although we are considering only monosaccharides here, these results show that the α-D-glucose and open-chain glucose both behave similarly to cellulose, and potentially precipitate from moist IL solutions. The peak for β-D-glucose, however, seems to drop in height, and shifts to larger distances, which infers a more loose association of these molecules in solution, thus, the water content in fact solubilizes these molecules. These results also point to the possibility that if glucose units of the cellulose can rearrange into the open-chain isomer in the IL solution, as suggested by Welton and coworkers,[23] they may initiate the precipitation. While this clearly aids the recovery of cellulose from the solvent, the higher conformational flexibility of this isomer will produce a lower order in the cellulose solid, which can affect its stability and integrity.

Vibrational spectra: infrared

We focus now on the calculated infrared spectra for the different systems. Pioneering work in IL spectroscopy was carried out by Kazarian and coworkers from the beginning of 2000 on.[57,58]

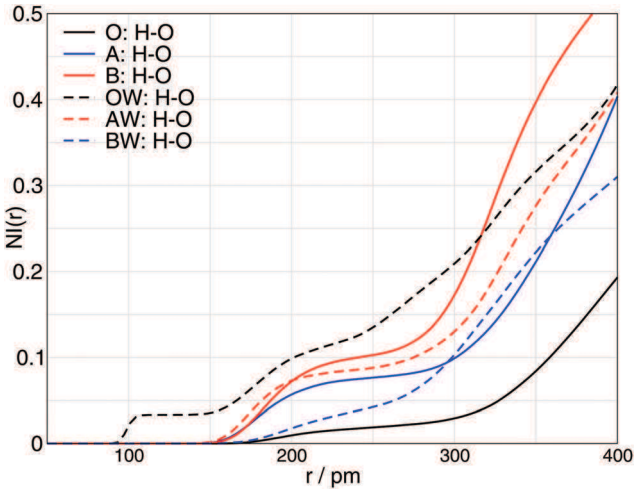

Fig. 7 Number integrals of the intermolecular distances between all alcohol-hydrogens and all oxygen atoms of glucose. Shown are only the numbers for oxygen atoms surrounding the hydrogen atoms. The complete data is given in the ESI,† Fig. S7.

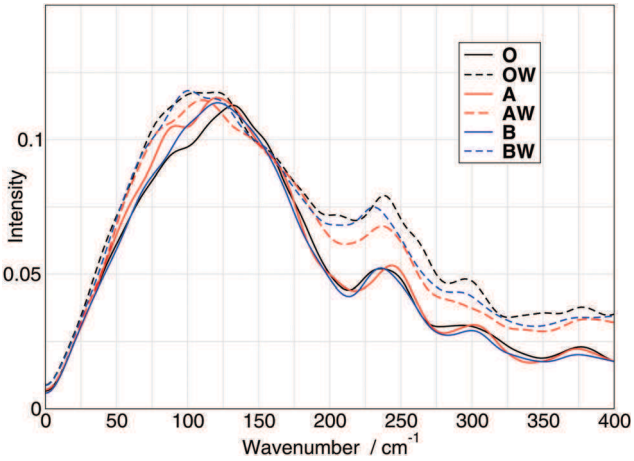

Fig. 8 Infrared spectra of the different systems including the different glucose molecules with and without water disentangled for the ionic liquid $[C_2C_1Im][OAc]$ contribution in the low cm^{-1} region in which Ludwig identified vibrational modes of the cation–anion interaction.[59] Intensity units are given in the ESI.†

Later, Ludwig and coworkers investigated the cation–anion interaction probed by far-infrared spectroscopy.[59] Bands with lowest frequencies (between 50 and 150 cm^{-1}) were assigned to the bending and stretching vibrational modes of the cation–anion interaction, reflecting a C–H···A^- hydrogen bond. They were able to demonstrate that the intermolecular stretching modes are shifted to higher wavenumbers with increasing ionic strength of the anion.[59] In Fig. 8 we show the same region as in ref. 59. Little changes are visible, as from the dry system with the closed α-D-glucose, through that with the β-D-glucose to the one with the open-chain isomer, in analogy to the hydrogen bond distances (Table 2), the anion–cation modes are gradually shifting to higher wave numbers, implying increased strengths of interactions between the counterions. Interestingly, water does not show this effect, rather no shift within the different anomers, but an approximate 60 cm^{-1} shift to lower wavenumber compared to the dry system is observed. This indicates – in agreement with the RDFs shown above and in literature[55,56] – a weakening of the cation–anion interaction when adding water to the ionic liquid.

In Fig. 9 we give a broader range of wavenumbers (500 to 1700 cm^{-1}) and all disentangled (glucose, IL, cation and anion) spectra together with the total spectra. The ionic liquid contributions can be seen in Fig. 9 in the lowest panel and one above. Due to the resemblance of the disentangled IL and ion spectra for all systems we show only the one for system **B**. The comparison between calculation and experiment with very good agreement for the neat and moist IL was presented in our previous study.[39] Compared to our previous AIMD calculation of $[C_2C_1Im][OAc]$ (and experiment)[39] carried out at the same temperature of 350 K and with the same computational set-up, we find interesting differences. Several peaks are slightly shifted to higher wavenumbers compared to the previous neat IL simulation which is due to the addition of glucose molecules. Especially the cation "in-plane ring deformation + $C_{Et}N$ stretching + $C_{Me}N$ stretching" at 682 cm^{-1} and the "OCO bending + CC

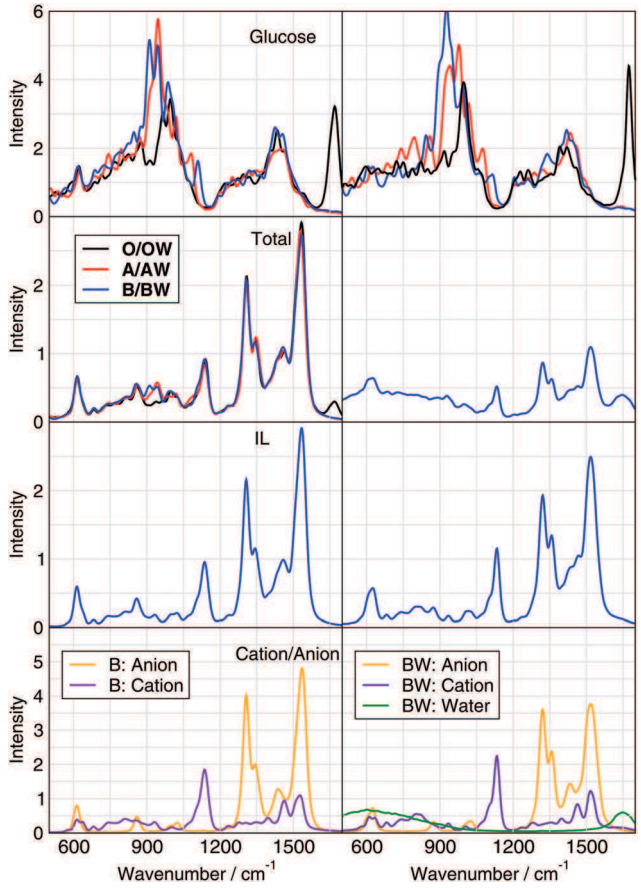

Fig. 9 Infrared spectra of the different systems including the different glucose molecules with and without water. The first panel shows the disentangled spectra for the glucose molecules, followed by the total spectra. The disentangled IL and cation and anion spectra are depicted in the lowest panels. Note, the color code is like in the previous pictures except for the lowest panel. Intensity units are given in the ESI.†

stretching" at 613 cm^{-1} as well as the "CH_3 bending" of the anion at 1024 cm^{-1} are affected. In addition the intensity of the anion "symmetric CO stretching" increases while the "CH_3 bending" intensity decreases a lot (1307 and 1343 cm^{-1}, respectively). When adding water similar effects as observed before can be detected.[39] Above 3000 cm^{-1} (see ESI†) the O–H stretching vibrations add to the peak of the C–H stretching bands of both the cation and the anion. New bands due to water show up at 1646 cm^{-1} and at around 600 cm^{-1}. Some peaks are blue-shifted (1518 cm^{-1} and 1133 cm^{-1}) and some are red-shifted (above 3000 cm^{-1} and at 1320 and 1358 cm^{-1}).

Considering now the disentangled spectrum of the glucose molecules, we observe large contributions at around 3000 cm^{-1}, see ESI.† This is in agreement with the experiments from the Kiefer (α-D-glucose in [C_2C_1Im][OAc]) and from the Champagne group (cellulose in [C_2C_1Im][OAc]).[35,36,60] While the different glucose isomers exhibit many similarities, there are also remarkable differences. For example the open-chain form provides a strong additional peak at 1669 cm^{-1}, due to the valence vibration of the C=O bond. At *ca.* 1450 cm^{-1} the characteristic bands exhibit very different shapes. Furthermore between 900 and 950 cm^{-1}, where β has two peaks and α shows one, the open form has no contribution. Comparing the disentangled glucose spectra to that from Bose and Polavarapu,[61] who measured vibrational absorption and circular dichroism spectra of several monosaccharides in the 1500–1180 cm^{-1} region in DMSO, we find many similarities despite the different solvent. This comparison is important since we observe important influences due to water and – as discussed below – the IL is never fully dry in experiments. Between 1300 and 1500 cm^{-1} a distinct feature, namely a double peak (see ESI†) appears and there are differences between α-glucose and β-glucose in the experimental spectrum which are reflected in the calculations as well.[61] The intensities are of the same size for the α-D-glucose while the lower wavenumber peak is higher for the β-D-glucose which is nicely covered in the calculated spectrum.

For the total spectrum the increase of the bands above 3000 cm^{-1} due to additional OH groups and CH groups is visible in agreement with the results of Kiefer and coworkers.[35,60] Residual water traces are inferred by the experimentalists to add to the spectrum. More changes are found in the fingerprint region (experimentally between 1000 and 1100 cm^{-1}) between 950 and 1050 cm^{-1}. The total spectrum resembles the one of Champagne *et al.* in the region of 500 to 1700 cm^{-1} apart from the usual shifts between calculation and experiment.[36] The five bands (at around ∼1540, 1311, 1150, 900, and 600 cm^{-1}) agree reasonably in form and location.

Vibrational spectra: circular dichroism

After having observed the key features of the IR spectra, we present calculated vibrational circular dichroism spectra[45] of the different monosaccharides in the wet and dry ionic liquid at distinct regions (Fig. 10 and 11). For these calculations we employed our software TRAVIS,[40,62] in which we implemented recently an alternative route for calculating the VCD spectra from classical magnetic dipole moments.[43] The complete spectra are presented in the ESI† (Fig. S15).

The different forms of glucose give rise to very different VCD spectra. Comparing the total spectra with the monosaccharide spectra, it is apparent that the main contributions are governed by the chiral carbon atom containing molecules, namely the glucose molecules. However, some contributions seem to be originating from the IL due to intermolecular interactions[45] between the monosaccharide and the IL, transferring the chiral structure of the sugar molecule to its solvent shell. In all wavenumber regions the solvent contributions to the VCD spectra are mainly due to cationic contributions, showing again the significant role the cation is playing.

In order to be able to compare between experiments and calculations we further restrict the region to between 1200 and 1500 cm^{-1}. Bose and Polavarapu published the experimental VCD spectra of many monosaccharides, especially α-glucose and β-glucose, in the region of 1200 and 1500 cm^{-1}.[61] The overall agreement is excellent between theory and experiment, the patterns of the experimental *versus* the theoretical spectra resemble each other extraordinarily (especially α-glucose) given that different solvents are considered.

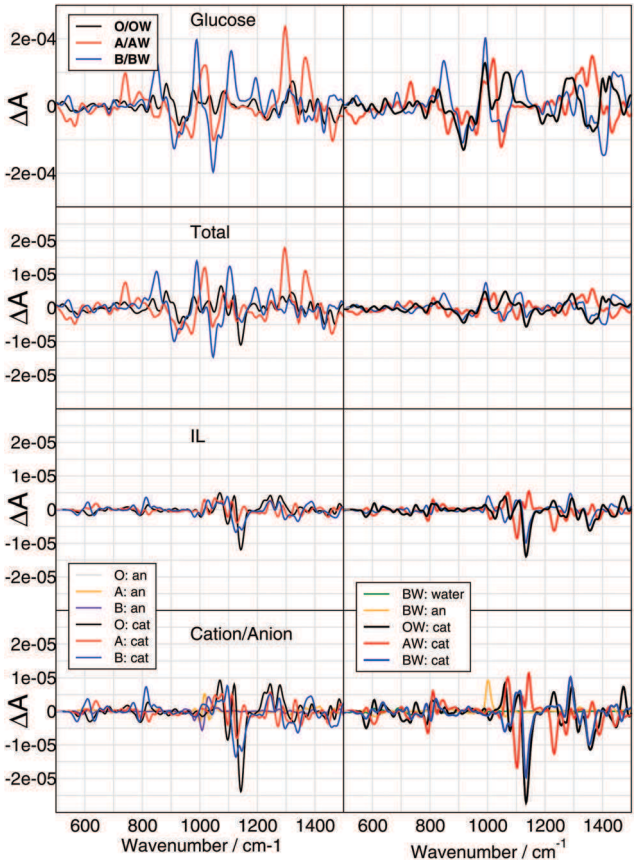

Fig. 10 VCD spectra of different glucose molecules in $[C_2C_1Im][OAc]$ with and without water. We show above the entangled spectrum for the monosaccharides, below the total spectrum, after this the IL and the cation as well as the anion contribution. In the right panels the water contribution is also given in the lowest panel.

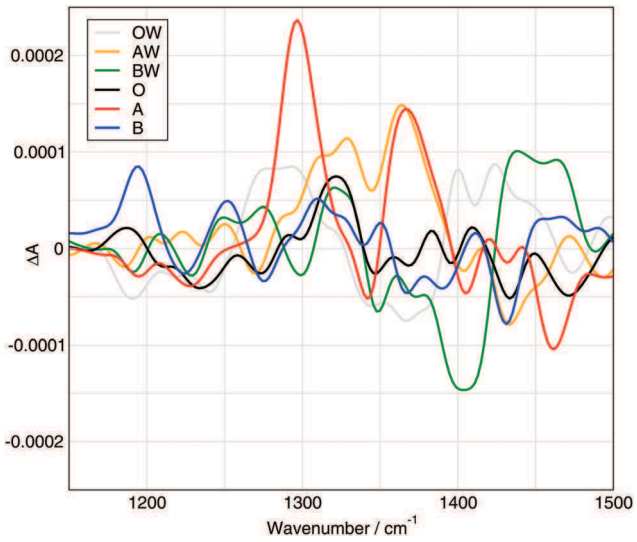

Fig. 11 VCD spectra of different glucose molecules in $[C_2C_1Im][OAc]$ with and without water between 1200 and 1500 cm^{-1}.

In comparison to these experimental spectra in DMSO we also find strong peaks for α-D-glucose and weaker to almost no spectral intensities for the β-D-glucose. As in the experimental spectrum α-glucose exhibits a negative pattern at 1405 cm^{-1} compared to the peak at 1455 cm^{-1}. Shifts between experimental and theoretical spectra have been discussed before not only in the context of VCD spectra, please note that these shifts can also be due to the different choice of solvents.[45] The negative entry is followed by a weak positive (theor. 1366 *versus* exp. 1416 cm^{-1}), a negative (1342 *versus* 1361 cm^{-1}), a strong positive (1297 *versus* 1323 cm^{-1}) and after this a weak negative (1228 *versus* 1247 cm^{-1}), and a weak negative (1195 *versus* 1196 cm^{-1}) pattern. The spectrum of β-D-glucose exhibits weak positive (1410 *versus* 1476 cm^{-1}), a negative (1395 *versus* 1420 cm^{-1}), negative (1366 *versus* 1373 cm^{-1}), positive (1350–1288 *versus* 1355–1281 cm^{-1}), negative (1275 *versus* 1238 cm^{-1}) peaks. Interestingly, adding water changes the spectrum tremendously. For example for β-D-glucose, the positive weak peak at 1410 cm^{-1} turns into the strong negative one, or the negative pattern at 1275 cm^{-1} changes to a positive one.

Anomeric conversion and role of the cation

In order to evaluate the stability of the different anomers compared to each other and compared to the open form, we carried out quantum chemical calculations applying the COSMO-RS solvent model (details see ESI†) and we considered the average Kohn–Sham energy from the AIMD simulations. The results are listed in Table 3. In the dry IL the α-D-glucose is more stable than the open form and so is the β-D-glucose. Within the error of this approach both the α- and β-D-glucose are similarly stable with a slight preference of the former one in dry and the latter one in the wet system (at least for the AIMD data). Furthermore the stability of the ring anomers over the open form of glucose is reduced in the moist IL. This indicates that the presence of water might enable the conversion of the different forms given that the barriers show similar trends.

The conversion of the open form to either of the two rings can proceed *via* a nucleophilic attack of a hydroxyl group at the carbonyl carbon atom, and the simultaneous deprotonation of the attacking group, followed by the subsequent protonation at the carbonyl oxygen. The distributions of the specific intramolecular C–O distance, which is involved in the ring closure, we show for each molecules in Fig. 12, while the corresponding temporal developments are presented in Fig. S3 in the ESI.† As

Table 3 Energy differences between all anomers in kJ mol^{-1}. For labels see Fig. 1. ΔG^{COSMO} are Gibbs free energies obtained quantum chemically, see ESI. ΔE^{AIMD} indicates the difference in the potential energy of the different AIMD trajectories. The errors for the AIMD values are evaluated as propagation of uncertainty in standard deviations

	ΔG^{COSMO}		ΔE^{AIMD}	
	Dry	Wet	Dry	Wet
α → open	63.0	37.4	177.0 ± 18.0	131.5 ± 0.7
β → open	60.2	36.9	142.6 ± 9.8	133.8 ± 16.2
α → β	2.9	0.5	34.4 ± 8.2	−2.3 ± 17.0

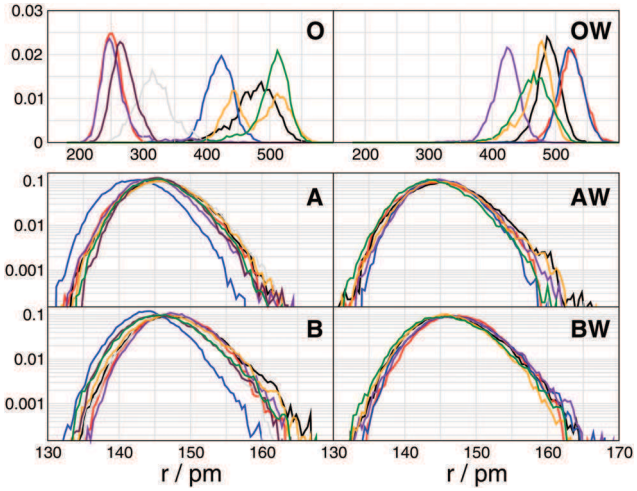

Fig. 12 Distribution of specific C–O intra-distance in the 8/6 glucose molecules of the simulated systems. For the open form this is the distance modeling the ring closure and for the α- and β-D-glucose (logarithmic scale to show extrema) it is the distance modeling the ring opening. The input data is plotted in Fig. S3 of the ESI.† Colors represent different molecules.

it can be seen in the distributions, four of the open glucose molecules assume a ring-like arrangement in system **O**. Additionally, two molecules show intramolecular C–O distances slightly below 450 pm (blue curve and short-distance peak of the orange curve), indicating the close proximity of both atoms which might lead to further conformations with C–O distances significantly shorter than 400 pm. Interestingly, in the moist system such conformations cannot be observed on the time scale of our simulations.

The ring-like arrangement in system **O** is illustrated in Fig. 13, displaying the ball-and-stick representation for different subsequent snapshots. While an intramolecular C–O distance below 200 pm for the ring-like open form is observed, both an anion as well as a cation seem to participate in this process. The anion forms a short hydrogen bond with the hydroxyl group that is to lose a proton for the ring formation, while the cation donates a hydrogen atom to the carbonyl oxygen atom (first panel). Interestingly, this cationic hydrogen atom is not donated from the ring carbon atoms, but from the C–H units of the cation, adjacent to the nitrogen atoms. Even more interestingly, the cationic ring approaches the formyl group of the glucose molecule. These interactions suggest that the hydroxyl and carbonyl groups are both polarized by the IL in a manner, which facilitates the reaction: The partial abstraction of the proton by the

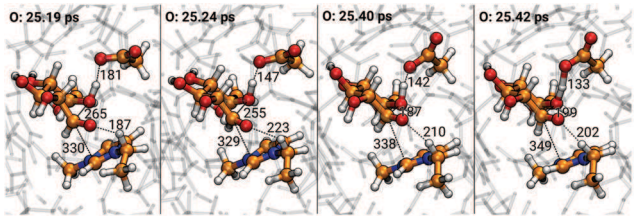

Fig. 13 Snapshots from the trajectory of system **O** showcasing one coiled open form glucose molecule and the contact to an anion as well as to a cation. Distances are marked in black.

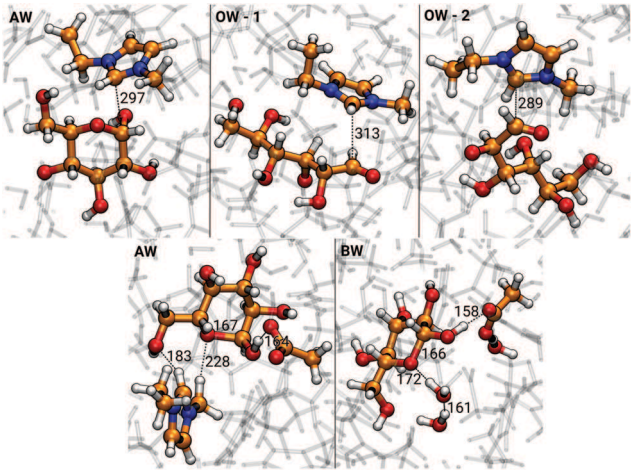

Fig. 14 Different snapshots from the trajectory of the systems **AW**, **BW** and **OW** showcasing the contacts between one glucose molecule and surrounding molecules or ions. Distances are marked in black.

anion makes the corresponding hydroxyl group more negative, and thereby more nucleophilic, while the interaction of the carbonyl oxygen atom with the cation should polarize the C=O bond, resulting in an improvement of the electrophilicity at the carbon atom. The latter effect is well-known, and exploited in hydrogen bond-supported catalysis.[63–66] Such slight, but chemically nonetheless highly important changes in bonding and in the electronic structure cannot be properly described by classical molecular dynamics simulations, which makes applying the present *ab initio* molecular dynamics approach essential, if the behavior of carbohydrates in these ILs is to be understood (see also Fig. 14).

To further gain insight into this C*(glucose)–C2(cation) arrangement (labels see Fig. 1 and 15), we analyzed the corresponding RDFs and NIs, see Fig. 15. Interestingly, we observe a strong correlation at 380 pm for the dry open form system with shortest distances of around 300 pm. In the first solvent shell of 460 pm the glucose carbon atom C* sees one such cationic carbon atom C2. Furthermore, α-D-glucose shows a pre-peak at around 380 pm. In the wet systems this correlation is increased (more entries at shorter distances below 300 pm) for the open form and emerges at around 400 pm for α-D-glucose with shortest distances at around 340 pm. The number integrals for the wet system indicate more than one C2 and one for the open form and the α-D-glucose in the first shell, respectively. It has been shown before that structurally relevant interactions reach to even longer distances than these in case of aromatic rings, and cyclic aliphatic systems as well.[67] For instance, in the optimized geometry of two cyclohexane molecules in interaction, the distance between the centers of mass is 430 pm. This implies that the distances described above for the cation–glucose RDFs relate to an even stronger interplay, which has structural and chemical consequences.

The interplay between the cation and the sugar molecules is interesting to consider in detail, also to assess the mechanism of previously observed[23] carbene catalysis-like decomposition reactions in such solutions. As mentioned in the Introduction,

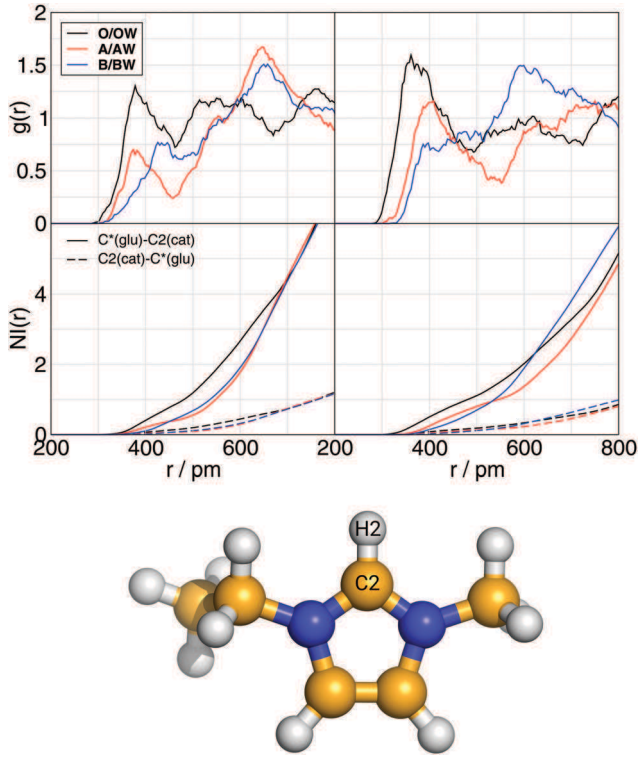

Fig. 15 RDFs and NIs for the correlation between the C2 atom of cation ring and the C of the glucose, see Fig. 1. Below is a ball-and-stick representation of the cation with the H2 and C2 atom marked.

the theoretically suggested destabilization of the carbene in the presence of cellulose[25] seemingly contradicts the occurrence of these decomposition reactions, unless the formation of the carbene can be bypassed by an alternative reaction mechanism. In this alternative path, the deprotonation of the cation by the acetate anion, and the bond formation between the carbohydrate and the cation occurs in a concerted fashion in a single elementary step, as has been shown for organocatalytic reactions catalyzed by azolium cations in general,[26] and by this ionic liquid in particular.[27] The mechanism relies on the capacity of N-heterocyclic carbenes to accommodate two electrophilic compounds at their single lone pair,[68] allowing the leaving proton and the electrophilic substrate to approach the active site simultaneously. Surprisingly, in all systems we observe hydrogen bond donor molecules approaching the carbon atoms of the imidazolium cation with their acidic hydrogen atoms to a distance as close as 200–225 pm (Fig. S13 of the ESI†), which suggests a hydrogen bond-like interplay with the cation as an acceptor. This unusual finding is, however, fully consistent with the aforementioned characteristic behaviour of azolium salts and N-heterocyclic carbenes, already suggesting that the concerted, carbene-free mechanism might be at play in these systems.

Moreover, in system **OW** the C2 atom of the imidazolium cation approaches the positively polarized carbonyl carbon atom to a distance of 289–313 pm, while in system **AW** the C2 atom of the cation is occasionally as close as 297 pm to a carbon atom of the glucose ring that is adjacent to the etheric oxygen atom. In all these cases we observe an acetate anion in hydrogen bond with the H2 of the cation, suggesting that the abstraction of the proton could be feasible, should the C–C bond formation between the glucose and the cation succeed. Even if the reaction itself cannot be observed directly in the present simulations, since it is, in fact, beyond the reach of this method, the observations above clearly point to the previously suggested concerted reaction pathway[25,27] to be occurring in these solutions. In case of the open form of glucose the reaction would result in the degradation reactions as reported earlier,[23] while the reaction with the α-D-glucose would probably cleave the ether bond of the glucose ring through an S_N2 reaction. In agreement, the corresponding C–O bond was observed to occasionally elongate to *ca.* 170 pm (see Fig. S3 in the ESI†), showing that the ring opening is somewhat facilitated by the IL. This process opens even more interesting possibilities. If the cations can indeed attack such an ether unit, and cleave them, the decomposition of cellulose into shorter chains can occur also through this mechanism, breaking the C–O–C bonds that hold the glucose units within a cellulose chain together. Unlike the reaction with the open chain form that can take effect only at one end of the polymer, the only location where the isomerization to the open form might occur, this degradation mechanism could break the cellulose at any point, resulting in a significantly faster and more effective degradation.

Conclusions

In this article we studied three different forms of glucose molecules, the open chain glucose, and the closed ring α- and β-D-glucose in the dry and wet ionic liquid (IL) 1-ethyl-3-methylimidazolium acetate ([C_2C_1Im][OAc]) from *ab initio* molecular dynamics (AIMD) simulations in order to get insight into the hydrogen bond pattern, the IR and VCD spectra, as well as many potential reaction mechanisms. These reaction mechanisms comprise (a) the onset of the glucose-crystallization in moist IL, (b) onset of ring closure in the open form through hydrogen bond supported catalysis, (c) onset of the ring opening of the two cyclic forms of glucose, and (d) onset of carbene catalysis that can either attack the carbonyl group of the open form, or the C–O bond of the rings, taking effect through a mechanism that avoids the explicit carbene formation in the solution. Observing these processes is only possible due to the choice of AIMD simulations that considers the full electronic structure at every timestep, and allows such spontaneous events to occur, provided that the barriers are low enough.

For the overall structure we find correlations of all ions and molecules with glucose. On average four to five anions surround the glucose in accordance with experimental studies of Teles *et al.*[8] The cations form long hydrogen bonds (250 pm) with the monosaccharides showing distinct differences when the α- or β-anomeric-oxygen atom is considered. Water addition decreases all interactions, which is reflected in lower RDF peaks and longer hydrogen bond distances with the exception of the cationic ring protons accepted by the hydroxyl groups of the glucose, which remain unaffected.

The H···O contacts between water and the cations are even longer (265 pm) which was observed several times before.[69,70] The strongest hydrogen bonds in terms of distance (170 pm) and peak height for the glucose molecules are found to the anion. The hydrogen bonding within and between different glucose molecules provides a complementary picture. When the intramolecular bonds are present, then the intermolecular bonds are less apparent. Short hydrogen bond distances (170–190 pm) are present, and as opposed to any other hydrogen bonds in water, the distances decrease and the heights increase for the first peaks in the RDFs for the α-isomer, and even more extreme for the open-form isomer. The number integrals reflecting the amount of neighbors increase tremendously upon water addition only for the open form glucose which infers their possible presence in the cellulose IL solution, as suggested by Welton and coworkers,[23] and also that the crystallization might follow a path *via* the open form.

We also calculated the IR spectra and could observe trends in agreement with the idea of Ludwig to correlate anion–cation strength with low wavenumber bands in the IR spectrum. The cation–anion bands shift in agreement with their hydrogen bond length when different glucose isomers are present. When water is added the bands are shifted slightly to even lower wavenumbers showing the weakening of the cation–anion interaction which is also reflected in our hydrogen bond lengths. Considering the complete spectrum we obtain good agreement to experiment and due to the different isomers different contributions in the spectra are visible. We find shifted peaks due to the glucose and above 3000 cm^{-1} large contributions due to additional O–H stretching frequencies and additional bands due to water appear.

In the calculated VCD spectra we observed that the major contributions are obviously due to the glucose molecules with their chiral carbon atoms. The agreement between experiment and calculation is very good given the fact that different solvents are chosen. We also see that some contributions are due to the ionic liquid and these stem solely from the cations, showing again that the role of them should not be underestimated. Also important is the fact that adding water changes the entangled spectrum of the glucose isomers completely.

Considering energies shows that the anomeric conversion might be possible with a slightly higher probability in the moist than in the dry system, since opening the cyclic forms of glucose to the open isomer is energetically less demanding. Interestingly, in the dry ionic liquids the open form in many cases coils in a manner that the distance between those very oxygen and carbon atoms decreases to as low as 250 pm, which should form the bond to produce the cyclic glucose molecules. Apparently, the ring closure is facilitated through hydrogen abstraction by the anion to the reacting hydroxyl group, which increases the nucleophilicity of the oxygen atom, and through various interactions by the cation, which increases the electrophilicity of the carbonyl group.

We also observe the onset of carbene-like reactions of the IL, in which the cation apparently reacts directly with the carbonyl group of the open form, or with the etheric bond of the glucose ring in the other two isomers. This latter reaction implies that the present ionic liquid might not only degrade cellulose through a reverse benzoin reaction, but also possibly *via* cleaving etheric units that hold the glucose units of cellulose together. The importance of this novel mechanism lies in the efficiency of the degradation process, since while the reverse benzoin reaction is limited to the end of the biopolymer chain, the C–O–C bond cleaving might occur at any location, creating shorter cellulose polymers.

Conflicts of interest

There are no conflicts to declare.

Acknowledgements

We would like to thank the DFG under the grant project number 406232243.

References

1 R. D. Perlack, *Biomass as feedstock for a bioenergy and bioproducts industry: the technical feasibility of a billion-ton annual supply*, Oak Ridge National Laboratory, 2005.
2 R. D. Rogers and K. R. Seddon, *Science*, 2003, **302**, 792–793.
3 J. F. Brennecke, R. D. Rogers and K. R. Seddon, *Ionic liquids IV. Not just solvents anymore*, American Chemical Society, Washington, 2007.
4 J. P. Hallett and T. Welton, *Chem. Rev.*, 2011, **111**, 3508–3576.
5 B. Kirchner, O. Hollóczki, J. N. Canongia Lopes and A. A. H. Pádua, *Wiley Interdiscip. Rev.: Comput. Mol. Sci.*, 2014, 202–214.
6 R. Hayes, G. G. Warr and R. Atkin, *Chem. Rev.*, 2015, **115**, 6357–6426.
7 F. Hermanutz, M. P. Vocht, N. Panzier and M. R. Buchmeiser, *Macromol. Mater. Eng.*, 2019, **304**, 1800450.
8 A. R. R. Teles, T. B. V. Dinis, E. V. Capela, L. M. N. B. F. Santos, S. P. Pinho, M. G. Freire and J. A. P. Coutinho, *Phys. Chem. Chem. Phys.*, 2016, **18**, 19722–19730.
9 H. Wang, G. Gurau and R. D. Rogers, *Chem. Soc. Rev.*, 2012, **41**, 1519–1537.
10 Y. Fukaya, K. Hayashi, M. Wada and H. Ohno, *Green Chem.*, 2008, **10**, 44–46.
11 B. D. Rabideau, A. Agarwal and A. E. Ismail, *J. Phys. Chem. B*, 2013, **117**, 3469–3479.
12 A. Parviainen, A. W. King, I. Mutikainen, M. Hummel, C. Selg, L. K. Hauru, H. Sixta and I. Kilpeläinen, *ChemSusChem*, 2013, **6**, 2161–2169.
13 B. D. Rabideau, A. Agarwal and A. E. Ismail, *J. Phys. Chem. B*, 2014, **118**, 1621–1629.
14 M. Brehm, H. Weber, M. Thomas, O. Hollóczki and B. Kirchner, *ChemPhysChem*, 2015, **16**, 3271–3277.
15 R. Elfgen, O. Hollóczki and B. Kirchner, *Acc. Chem. Res.*, 2017, **50**, 2949–2957.
16 O. Hollóczki, D. Gerhard, K. Massone, L. Szarvas, B. Németh, T. Veszprémi and L. Nyulászi, *New J. Chem.*, 2010, **34**, 3004–3009.

17 O. Hollóczki, D. S. Firaha, J. Friedrich, M. Brehm, R. Cybik, M. Wild, A. Stark and B. Kirchner, *J. Phys. Chem. B*, 2013, **117**, 5898–5907.
18 O. Hollóczki and L. Nyulászi, *Top. Curr. Chem.*, 2013, **341**, 1–24.
19 O. Hollóczki, *Inorg. Chem.*, 2014, **53**, 835–846.
20 Z. Kelemen, O. Hollóczki, J. Nagy and L. Nyulászi, *Org. Biomol. Chem.*, 2011, **9**, 5362–5364.
21 H. Rodriguez, G. Gurau, J. D. Holbrey and R. D. Rogers, *Chem. Commun.*, 2011, **47**, 3222–3224.
22 G. Gurau, H. Rodríguez, S. P. Kelley, P. Janiczek, R. S. Kalb and R. D. Rogers, *Angew. Chem., Int. Ed.*, 2011, **50**, 12024–12026.
23 M. T. Clough, K. Geyer, P. A. Hunt, S. Son, U. Vagt and T. Welton, *Green Chem.*, 2015, **17**, 231–243.
24 D. Enders, O. Niemeier and A. Henseler, *Chem. Rev.*, 2007, **107**, 5606–5655.
25 S. Gehrke, K. Schmitz and O. Hollóczki, *J. Phys. Chem. B*, 2017, **121**, 4521–4529.
26 S. Gehrke and O. Hollóczki, *Angew. Chem., Int. Ed.*, 2017, **56**, 16395–16398.
27 S. Gehrke, W. Reckien, I. Palazzo, T. Welton and O. Hollóczki, *Eur. J. Org. Chem.*, 2019, 504–511.
28 O. Hollóczki, *Chem. – Eur. J.*, 2019, DOI: 10.1002/chem.201903021.
29 B. D. Rabideau and A. E. Ismail, *Phys. Chem. Chem. Phys.*, 2015, **17**, 5767–5775.
30 M. Brehm, M. Pulst, J. Kressler and D. Sebastiani, *J. Phys. Chem. B*, 2019, **123**, 3994–4003.
31 Y. Li, X. Liu, Y. Zhang, K. Jiang, J. Wang and S. Zhang, *ACS Sustainable Chem. Eng.*, 2017, **5**, 3417–3428.
32 Z. Jarin and J. Pfaendtner, *J. Chem. Theory Comput.*, 2014, **10**, 507–510.
33 T. G. A. Youngs, C. Hardacre and J. D. Holbrey, *J. Phys. Chem. B*, 2007, **111**, 13765–13774.
34 T. G. Youngs, J. D. Holbrey, C. L. Mullan, S. E. Norman, M. C. Lagunas, C. D'Agostino, M. D. Mantle, L. F. Gladden, D. T. Bowron and C. Hardacre, *Chem. Sci.*, 2011, **2**, 1594–1605.
35 J. Kiefer, K. Obert, A. Bösmann, T. Seeger, P. Wasserscheid and A. Leipertz, *ChemPhysChem*, 2008, **9**, 1317–1322.
36 M. FitzPatrick, P. Champagne and M. F. Cunningham, *Carbohydr. Polym.*, 2012, **87**, 1124–1130.
37 N. R. Dhumal, H. J. Kim and J. Kiefer, *J. Phys. Chem. A*, 2009, **113**, 10397–10404.
38 R. S. Payal and S. Balasubramanian, *Phys. Chem. Chem. Phys.*, 2014, **16**, 17458–17465.
39 M. Thomas, M. Brehm, O. Hollóczki, Z. Kelemen, L. Nyulászi, T. Pasinszki and B. Kirchner, *Chem. – Eur. J.*, 2014, **20**, 1622–1629.
40 M. Thomas, M. Brehm and B. Kirchner, *Phys. Chem. Chem. Phys.*, 2015, **17**, 3207–3213.
41 S. Abbate, G. Longhi, K. Kwon and A. Moscowitz, *J. Chem. Phys.*, 1998, **108**, 50–62.
42 B. Kirchner and J. Hutter, *J. Chem. Phys.*, 2004, **121**, 5133–5142.
43 M. Thomas and B. Kirchner, *J. Phys. Chem. Lett.*, 2016, **7**, 509–513.
44 K. Reiter, M. Kühn and F. Weigend, *J. Chem. Phys.*, 2017, **146**, 054102.
45 C. Merten, T. P. Golub and N. M. Kreienborg, *J. Org. Chem.*, 2019, **84**, 8797–8814.
46 T. Q. Teodoro, M. A. J. Koenis, R. Rueger, S. E. Galembeck, W. J. Buma, V. P. Nicu and L. Visscher, *J. Phys. Chem. A*, 2018, **122**, 9435–9445.
47 B. Nieto-Ortega, J. Casado, J. T. López Navarrete, F. J. Ramírez, M. Tommasini, G. Longhi, G. Mazzeo and S. Abbate, *J. Chem. Theory Comput.*, 2015, **11**, 2633–2641.
48 A. Scherrer, F. Agostini, D. Sebastiani, E. Gross and R. Vuilleumier, *J. Chem. Phys.*, 2015, **143**, 074106.
49 A. Scherrer, R. Vuilleumier and D. Sebastiani, *J. Chem. Phys.*, 2016, **145**, 084101.
50 P. Oulevey, S. Luber, B. Varnholt and T. Bürgi, *Angew. Chem., Int. Ed.*, 2016, **55**, 11787–11790.
51 S. Jähnigen, A. Scherrer, R. Vuilleumier and D. Sebastiani, *Angew. Chem., Int. Ed.*, 2018, **57**, 13344–13348.
52 Y. He, W. Bo, R. K. Dukor and L. A. Nafie, *Appl. Spectrosc.*, 2011, **65**, 699–723.
53 T. B. Freedman, X. Cao, R. K. Dukor and L. A. Nafie, *Chirality*, 2003, **15**, 743–758.
54 M.-P. Gaigeot and M. Sprik, *J. Phys. Chem. B*, 2003, **107**, 10344–10358.
55 M. Brehm, H. Weber, A. S. Pensado, A. Stark and B. Kirchner, *Phys. Chem. Chem. Phys.*, 2012, **14**, 5030–5044.
56 M. Brehm, H. Weber, A. S. Pensado, A. Stark and B. Kirchner, *Z. Phys. Chem.*, 2013, **227**, 177–203.
57 S. G. Kazarian, B. J. Briscoe and T. Welton, *Chem. Commun.*, 2000, 2047–2048.
58 L. Cammarata, S. G. Kazarian, P. A. Salter and T. Welton, *Phys. Chem. Chem. Phys.*, 2001, **3**, 5192–5200.
59 K. Fumino, A. Wulf and R. Ludwig, *Angew. Chem., Int. Ed.*, 2008, **47**, 3830–3834.
60 J. Kiefer, K. Obert, J. Fries, A. Bösmann, P. Wasserscheid and A. Leipertz, *Appl. Spectrosc.*, 2009, **63**, 1041–1049.
61 P. K. Bose and P. L. Polavarapu, *Carbohydr. Res.*, 1999, **319**, 172–183.
62 M. Brehm and B. Kirchner, *J. Chem. Inf. Model.*, 2011, **51**, 2007–2023.
63 M. S. Taylor and E. N. Jacobsen, *Angew. Chem., Int. Ed.*, 2006, **45**, 1520–1543.
64 P. R. Schreiner, *Chem. Soc. Rev.*, 2003, **32**, 289–296.
65 R. R. Knowles and E. N. Jacobsen, *Proc. Natl. Acad. Sci. U. S. A.*, 2010, **107**, 20678–20685.
66 A. G. Doyle and E. N. Jacobsen, *Chem. Rev.*, 2007, **107**, 5713–5743.
67 S. Grimme, *Angew. Chem., Int. Ed.*, 2008, **47**, 3430–3434.
68 O. Hollóczki, *Phys. Chem. Chem. Phys.*, 2016, **18**, 126–140.
69 R. Macchieraldo, L. Esser, R. Elfgen, P. Voepel, S. Zahn, B. M. Smarsly and B. Kirchner, *ACS Omega*, 2018, **3**, 8567–8582.
70 C. Spickermann, J. Thar, S. B. C. Lehmann, S. Zahn, J. Hunger, R. Buchner, P. A. Hunt, T. Welton and B. Kirchner, *J. Chem. Phys.*, 2008, **129**, 104505.

F. Recognition in Chiral Ionic Liquids: The Achiral Cation Makes the Difference!

Jan Blasius,[*] Paul Zaby,[*] Oldamur Hollóczki,[†*] and Barbara Kirchner[*]

Received: 22 April 2021, Published online: 28 July 2021.

Reprinted (adapted) in appendix F with permission[‡] from

J. Blasius, P. Zaby, O. Hollóczki, and B. Kirchner, *J. Org. Chem.* **2022**, *87*, 1867–1873.

doi: 10.1021/acs.joc.1c00939.

For this article a Supporting Information is available free of charge at:
https://pubs.acs.org/doi/10.1021/acs.joc.1c00939.

Contributions to the manuscript

- Development of the concept
- Performance of all calculations
- Interpretation of the results
- Writing of the manuscript

[*] Mulliken Center for Theoretical Chemistry, Clausius Institute for Physical and Theoretical Chemistry, University of Bonn, Beringstr. 4–6, 53115 Bonn, Germany
[†] Department of Physical Chemistry, Faculty of Science and Technology, University of Debrecen, 4010 Debrecen, Hungary
[‡] Permission requests to reuse material from this chapter should be directed to the American Chemical Society.

JOC The Journal of Organic Chemistry

pubs.acs.org/joc Note

Recognition in Chiral Ionic Liquids: The Achiral Cation Makes the Difference!

Jan Blasius, Paul Zaby, Oldamur Hollóczki, and Barbara Kirchner*

Cite This: J. Org. Chem. 2022, 87, 1867−1873 Read Online

ACCESS | Metrics & More | Article Recommendations | Supporting Information

ABSTRACT: By simulating butan-2-ol dissolved in the chiral ionic liquid 1-ethyl-3-methylimidazolium (*S*)-alaninate, we investigate the chiral recognition of butan-2-ol in the ionic liquid. The hydrogen bonding between the chiral anion and both enantiomers of butan-2-ol is similar; however, both chiral molecules (anion and alcohol) induce an asymmetry in the achiral cation which leads to a more favorable environment for the alcohol in the heterochiral system as compared to the homochiral system and hence provides an energetic stabilization of the former.

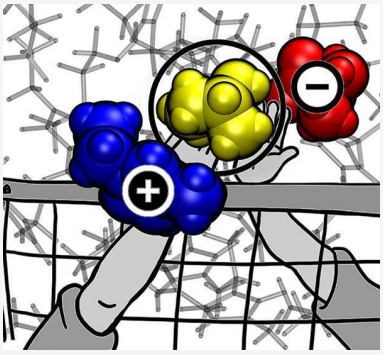

The increasing demand for chiral compounds poses severe challenges for industrial applications.[1] Especially in the case of pharmaceuticals, significant attention has been drawn by chiral separation and recognition[2−4] methods to ensure enantiomeric purity prior to medicinal use. In general, enantiopure compounds are accessible via crystallization,[5] chromatographic[5] or membrane-based separation,[6] asymmetric catalysis[7] or kinetic resolution.[8] However, requirements for complicated operations or expensive equipment might limit some of these techniques. Among these possibilities, the importance of the liquid medium is the most conspicuous in liquid−liquid extraction, where an additive[9] or the solvent itself acts as selector,[10] resulting in an efficient and low-cost process that is easy to scale up. Furthermore, asymmetric synthesis can be directed by a chiral solvent.[11,12] Even more interestingly, significant solvent effects on enantioselectivity have been observed also in nonchiral solvents.[13] These examples clearly underscore the paramount importance of understanding the behavior of the medium in processes that involve chiral compounds and the ways solvents can aid in discriminating enantiomers.

Through their potential properties like low melting point, negligible vapor pressure, efficient reusability and ionic character,[14] ionic liquids (ILs)[15,16] have proven to be valuable for numerous applications.[17] Most notably, ILs have been applied as highly efficient solvents in asymmetric synthesis. An outstanding feature of ILs is their infinite tunability, enabling the adjustment to a specific task through functionalization.[18] Through the introduction of chiral substituents, the subgroup chiral ionic liquids (CILs) were derivatized.[19−27] The few attempts that considered enantiomeric separation with CILs to date aimed at enantiomeric compounds with long-chained or cross-linked substituents.[25,28−30] Due to great variations of the different residues in polarity or size, such complex molecules with substantial differences around the stereogenic center can usually be separated by a variety of chiral selectors, being thereby significantly less restrictive in the choice of the solvent and its properties. It remains, however, a challenge to separate small enantiomers such as butan-2-ol, often requiring the attachment of further functional groups to enhance the separation.[31] Hence there is a need for neoteric selectors and processes for such cases in order to avoid the costs and waste of the additional synthetic steps. Highly efficient enantioselective processes usually involve enantiomeric recognition via homo- or heterochiral encounter complexes formed by the selector and the enantiomer, which is easily described by the three-point model[32] within a chiral host−guest system. Based on geometry, this model states that one enantiomer of a chiral guest molecule shows favored interactions with a host via three residues attached to the chiral center. However, already simple, achiral ILs show an involved structure,[14,33−35] and they solvate *n*-butanol through a complex interplay of interactions.[35] Thus, the additional complexity of a CIL combined with the wide variety of potential discriminative interactions complicates the application of such idealized models for these systems. On the

Special Issue: Solvation Effects in Organic Chemistry

Received: April 22, 2021
Published: July 28, 2021

https://doi.org/10.1021/acs.joc.1c00939
J. Org. Chem. 2022, 87, 1867−1873

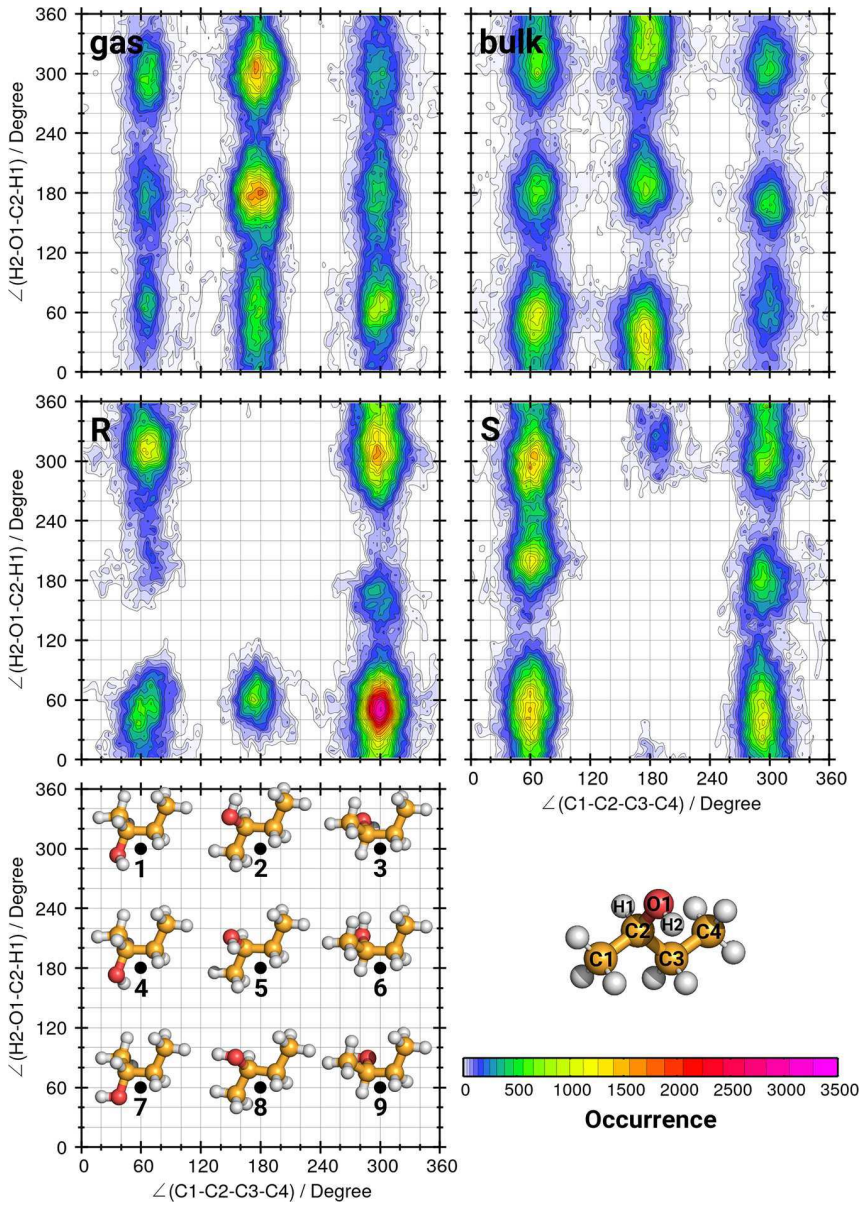

Figure 1. Conformational plots showing the populations of the nine conformers of (*R*)- and (*S*)-butan-2-ol. Plotted are the dihedral angles ∠C1−C2−C3−C4 versus ∠H2−O1−C2−H1. Above: gas phase (left) and the bulk (right). Middle: butan-2-ol dissolved in the CIL (all from AIMD simulations). Bottom: ball-and-stick representations of (*R*)-butan-2-ol in different conformations.

other hand, this very complexity opens novel routes for chiral recognition.

It has been recently shown that the achiral cation of the amino acid based chiral ionic liquid[26,27,36] 1-ethyl-3-methylimidazolium L-alaninate (i.e., (*S*)-alaninate) is prone to symmetry breaking due to the presence of the chiral anion.[37,38] This induced chirality amplifies the asymmetry within the liquid, which may have significant effects on the solvation of chiral compounds in these CILs. In light of the aforementioned necessity to develop novel strategies for chiral recognition and separation, it is of paramount importance to gain full control over any potential enhancement, and eventually exploit it in highly efficient applications. To this end, we investigated (*R*)- and (*S*)-butan-2-ol dissolved in 1-ethyl-3-methylimidazolium (*S*)-alaninate, in order to obtain detailed information on the effects of the asymmetric behavior of the cation on chiral recognition.

As the high conformational flexibility necessitates an adequate exploration of the potential energy surface, we performed ab initio molecular dynamics (AIMD) simulations, starting from all nine possible conformers of butan-2-ol, and analyzed the obtained trajectories with Travis.[39,40] The simulation boxes were set up with PACKMOL[41,42] and pre-equilibrated at a classical force field level of theory employing the OPLS-AA[43] as well as the Pádua and Canongia Lopes[44−46] force field parameters and the Lammps[47] program package. The last snapshot of each classical simulation has been taken as input structure for the following AIMD simulations which were performed using the CP2K[48] program package employing the BLYP[49,50] functional and the corresponding BLYP Goedecker−Teter−Hutter pseudopotentials[51−53] with the molecularly optimized double-ζ basis set (MOLOPT-DZVP-SR-GTH).[54] Dispersion interactions were taken care of by the DFT-D3[55,56] scheme. The AIMD simulations were set up for 10 ps of

https://doi.org/10.1021/acs.joc.1c00939
J. Org. Chem. 2022, 87, 1867−1873

equilibration followed by a 30 ps production run for each simulation. For further details, see Supporting Information (SI).

The conformational flexibility of butan-2-ol arises from two rotatable dihedral angles (Figure 1, lower panel left), resulting in nine conformers all being present in the gas and neat bulk phase (Figure 1 upper panels) with a preference for structures that feature a stretched carbon chain (∠C1−C2−C3−C4 = 180°, **2**, **5**, and **8**).[57] Considering the dominance of conformers with stretched carbon chains in the neat environment, a strong solvent effect is observed in the CIL. Surprisingly, not only are the populations reduced, but two of these conformers being distinctively present in the neat systems completely disappear, implying mainly curled structures of butan-2-ol (**3**, **6**, and, **9** in Figure 1 lower left panel). The prevalence of curled structures in the CIL compared to the neat bulk phase is further underlined by the averaged exposed surface area of butan-2-ol which equals 164 Å^2 in systems **R** and **S** compared to 174 Å^2 in the neat bulk phase (see also Figure S1 in the SI). As for both enantiomers the same conformers are absent; no signs for enantiomeric recognition can be deduced yet. However, indications for chiral discrimination are observed when comparing the occurrence of conformers between the homo- and heterochiral systems, as for the (*R*)-enantiomer one conformation is conspicuously dominant. We observed that while the dominant conformer of system **R** features a population of 39%, its mirror-imaged counterpart in system **S** is only populated by 23%. Among the curled structures, this distinct conformer (**9** in Figure 1 lower left panel) exposes its hydrogen atom at the hydroxyl group the most to the neighboring molecules. Thus, the contribution of the hydroxyl group to the CIL's hydrogen bond network is more likely for this structure compared to the other conformers. Besides the general hydrogen bonding features (see SI) of ionic liquids[27,33,58,59]—i.e. hydrogen bonding between ring hydrogen atom of the cation and the carboxylate oxygen and amino nitrogen atom of the anion[27]—the present CIL exhibits amino group donated and carboxylate group accepted intramolecular hydrogen bonding within one anion and hydrogen bonding between two anions in analogy to the cation−cation interaction observed in functionalized ILs.[60]

In this complex network of interactions, butan-2-ol adopts distinct geometries in order to fit best to the binding partners within the solvent. The efficiency of this induced fit[10] is different for the two enantiomers, as shown by the difference in the averaged electronic energies of the two systems, further underlining enantiomeric discrimination: The heterochiral system **R** is stabilized by a substantial ΔE = 18.8 kJ mol^{-1} compared to the homochiral system **S**. Thus, the CIL employed seems to serve as an excellent enantiophobic selector, raising questions about the detailed mechanism of the recognition.

Radial distribution functions (RDFs) indicate that solvation by the anions' carboxylate group barely alters between the enantiomers (Figure 2, top, r(O···H) = 174 pm for both systems). However, discriminative interactions seem to be induced by the amino group which only acts as a donor in the case of the (*R*)-enantiomer but on rare occasion also as an acceptor for (*S*)-butan-2-ol (Figure 2, middle). Despite butan-2-ol having only one contact point, we observe hydrogen bonds to both the oxygen and nitrogen atoms of the anion in the case of the homochiral system. The chiral center of the anion approaches the (*S*)-butan-2-ol somewhat closer than the

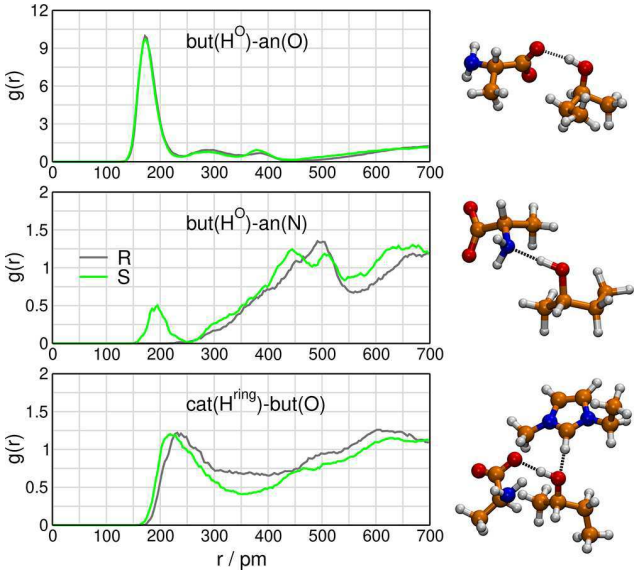

Figure 2. Radial distribution functions between the hydroxyl hydrogen atom of butan-2-ol and the anion's oxygen atom (top) or the nitrogen atom of the anion (middle); between the ring hydrogen atoms of the cation and the hydroxyl oxygen (bottom). Gray: **R**. Green: **S**. Right panels: ball-and-stick representations of (*S*)-butanol clusters illustrating the corresponding interplay.

(*R*)-alcohol on these rare occasions where the nitrogen atom accepts the hydroxyl hydrogen atom in the **S** system.

However, these two hydrogen bonds cannot occur simultaneously; they compete with each other. Since it has been found for similar systems[61] that at least two interactions are necessary for achieving chiral discrimination, interplay with the cation seems to be essential in the present case. The RDFs representing the interactions between the ring hydrogen atoms of the cation and the oxygen atom of the alcohol clearly show the occurrence of such hydrogen bonds, and that these could serve as additional interaction guiding the chiral discrimination. On the other hand, these interactions show almost no differences between systems **S** and **R** and rather point to stronger interaction (shorter distances, Figure 2 bottom and Table 1) of the (*S*)- than the (*R*)-alcohol. This is due to the

Table 1. Relevant Distances (in pm) Obtained at the Maximum of the First Peak of the Radial Distribution Functions Discussed

	R	S
but(H^O)−an(O)	174	174
cat(H^{ring})−but(O)	235	221
an(C*)−cat(N^{et})	448	457
but(C*)−cat(N^{et})	438	493

fact that the most acidic proton of the imidazolium cation (the one attached to C2; see Figure 3) is only accepted by the (*S*)-butan-2-ol oxygen which contradicts the lower energy of system **R**. Therefore, the source of discriminating interactions lies somewhere else than those above.

The alcohol donates one hydrogen bond to an anion (see Figure S3). While this interplay seems rather ordered (Figures 2 and 4) for the (*R*)-alcohol, it appears to be more diversified in the case of the (*S*)-alcohol. However, this higher order in the anion's spatial arrangement around the alcohol in system **R**

https://doi.org/10.1021/acs.joc.1c00939
J. Org. Chem. 2022, 87, 1867−1873

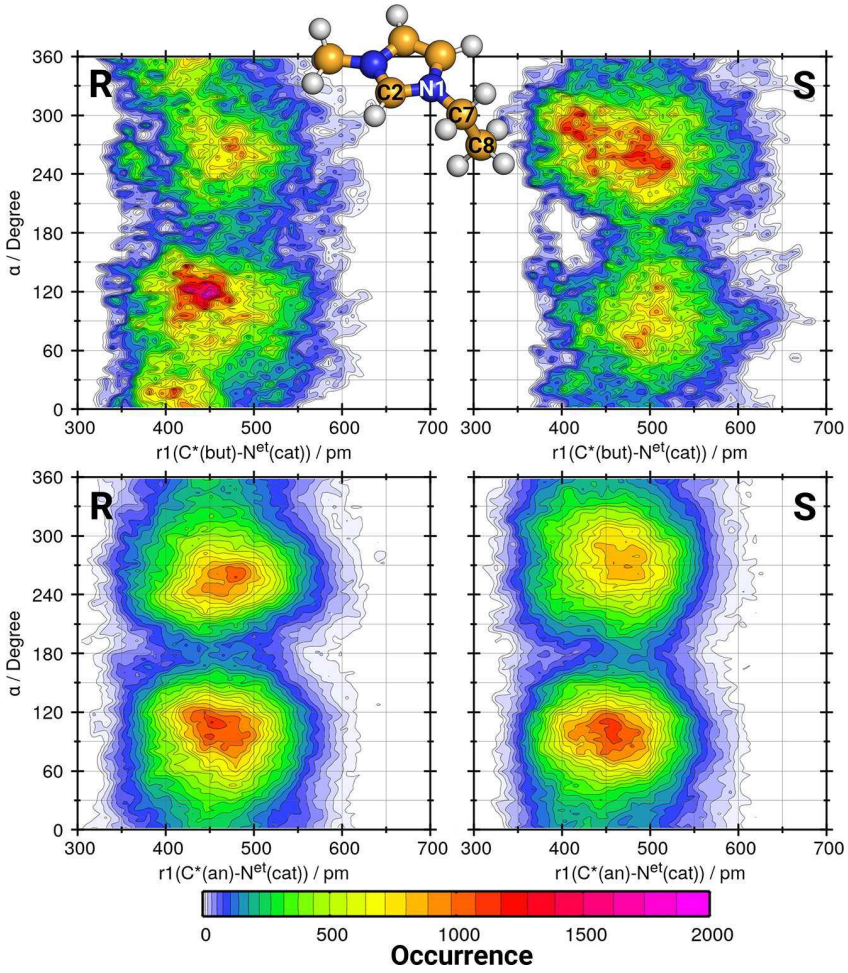

Figure 3. Combined distribution functions correlating the dihedral angle α (C2−N1−C7−C8) of the cation with the distance between the chiral center of butan-2-ol and the nitrogen atom of the cation bound to the ethyl group only considering the closest cation with respect to butan-2-ol.

restricts the anion to one side of the (*R*)-butan-2-ol and leaves more room for the cations to adjust to the rest of the alcohol.

The conformational flexibility of 1-ethyl-3-methylimidazolium arises solely from the ethyl group rotation. As indicated before, 1-ethyl-3-methylimidazolium has been observed to break symmetry in chiral environments, becoming chiral itself.[37,38] A distorted equilibrium of the ethyl group rotation—induced by a neighboring chiral molecule(s)—breaks the enantiotopic faces of the cation. In contrast to employing a permanently chiral cation with diastereotopic faces, employing the achiral 1-ethyl-3-methylimidazolium will result in enantiomeric pairs instead of diastereomers, depending on the approaching site of the permanently chiral molecule. This effect is often referred to as chirality induction.[2,62] The interaction of the chiral anion with the cation has this very effect,[37,38] which is visible in Figure 3 (below). In this plot the combined distribution functions correlating the dihedral angle α of the cation with the distance between the stereocenter of the anion and the nitrogen atom of the cation bound to the ethyl group are shown. It is clearly visible that—in agreement with earlier reports[37,38]—one of the rotamers has a higher occurrence, breaking the symmetry of the cation. Importantly, this enrichment of the conformation with the dihedral angle being around 120° is the same in both systems **R** and **S**, independently from which enantiomer of the alcohol is present.

Performing the same analysis for the chiral induction effects of the alcohol results in the combined distribution functions given in Figure 3 (above) in which the correlation of the dihedral angle α of the cation with the distance between the stereocenter of the butan-2-ol and the nitrogen atom of the cation bound to the ethyl group is shown. When comparing systems **R** and **S**, stark differences can be observed. While (*R*)-butan-2-ol induces conformations with $\alpha \approx 120°$ on the cation, resembling the conformation indicated by the ball-and-stick model in Figure 3, with (*S*)-butan-2-ol, cation structures with the opposite chirality, i.e. $\alpha \approx 270°$, occur with higher probability.

Thus, remarkably, (*S*)-alaninate induces the same chirality in the cation as (*R*)-butan-2-ol, and the opposite of that induced by (*S*)-butan-2-ol. Accordingly, while (*R*)-butan-2-ol fits well into the environment created by the anion, in system **S** the anion competes with the alcohol for enforcing that conformation on the cation, which is the most advantageous for each of the chiral components. This finding is in good qualitative agreement with the relative energies obtained for the two systems which state that system **R** is stabilized by ΔE = 18.8 kJ mol^{-1} compared to **S**.

Besides this induction effect, another remarkable difference between the systems is the distance between the stereocenter of butan-2-ol and the nitrogen of the cation bound to the ethyl group. In the complex formed by the cation with the (*R*)-

https://doi.org/10.1021/acs.joc.1c00939
J. Org. Chem. 2022, 87, 1867−1873

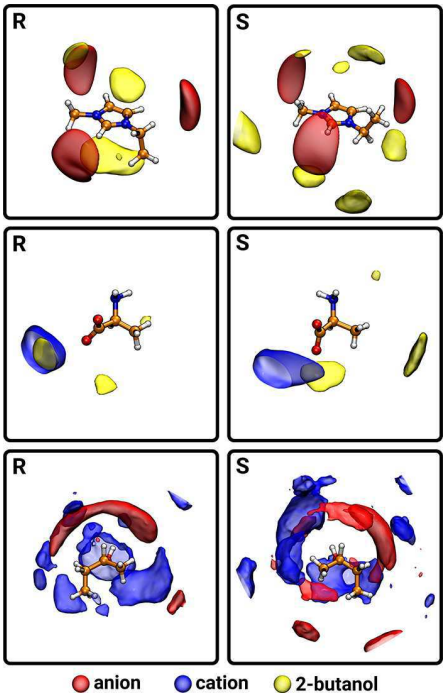

Figure 4. Spatial distribution functions of the anions, and butan-2-ol around the cation (top), all units around the anion (middle) and of the ions around butan-2-ol (bottom).

butan-2-ol, these two atoms approach each other much closer compared to the one formed with the (*S*)-enantiomer, on average by about 40 pm (see Figure 3 above and Table 1). When the hydrogen bonding situation of the anion around the two butan-2-ol enantiomers is considered, the distribution was much more disordered around (*S*)-butan-2-ol with the anion accepting the hydroxyl hydrogen of the (*S*)-alcohol by both the nitrogen and oxygen atoms. Consequently, as found for the anion, also the arrangement of the cation around the (*R*)-enantiomer will be more ordered, resulting in a more pronounced conformational preference for the ethyl group rotation, which becomes clear when having a closer look at the intensities and widths of the occurrence graphs in Figure 3. Compared to the (*S*)-enantiomer, the structural imprint of (*R*)-butan-2-ol makes the cation much more rigid, underlining the existence of this distinct cation conformation that supports the chiral recognition. All the data above point toward the fact that the cation plays an important role in the discrimination between system **R** and **S**.

To complete the molecular picture of the solvation mechanisms, the spatial distribution functions of all three components around each other have been plotted. Based on these data (Figure 4), it can be seen how the arrangement of butan-2-ol around the cation differs for the two enantiomers. While the (*R*)-enantiomer is preferably located above or beneath the cation's ring plane (see also Figure S3), the (*S*)-enantiomer is more frequently observed in-plane around the methyl and ethyl residues. From this it can be concluded that, in contrast to the (*S*)-enantiomer, the (*R*)-enantiomer preferably interacts with the π-system of the cation. As the ring hydrogens of the cation exhibit an acidic nature (see also lower RDFs of Figure 2), the basic anions mainly approach these atoms. The arrangement around the anion and the alcohol fit this picture: The interaction is more ordered and distinctly located in the case of the **R** as compared to the **S** system.

In summary, we shed light on the working principles of the chiral recognition mechanism of (*R*)- and (*S*)-butan-2-ol in the chiral ionic liquid 1-ethyl-3-methylimidazolium (*S*)-alaninate. Although hydrogen bonding shows shorter distances and is more diverse in the homochiral system, the heterochiral variant is energetically stabilized by 18.8 kJ mol^{-1}. We observed that this clear discrimination between the two enantiomers originates from a very unusual chiral induction. Due to the presence of the chiral substances in the system—that is, the anion and the solute—the cation becomes asymmetric due to a distorted equilibrium of the ethyl group rotation. This asymmetry is the opposite for the two alcohol enantiomers, underlining the physical relevance of this effect. Remarkably, the asymmetrization (or chiral induction) effects by the anion and the solute are conflicting in the homochiral, and harmonious for the heterochiral combination of these two species, explaining the differences in stability. The better fitting in the heterochiral system results in 40 pm shorter distances between the cation and the alcohol, and thus tighter cation-alcohol aggregates than in the homochiral solution. Interactions that govern chiral recognition in this system emanate not only from the anion-alcohol hydrogen bonds, but also from the cation-alcohol interplay. Our results open doors for the design of fundamentally new chiral ionic liquid selectors for extraction and synthesis, which in addition to the chiral anionic part also include either modified side chains of the cation or a permanently chiral cation resembling the structures imprinted by the respective solute molecule.

■ ASSOCIATED CONTENT

Supporting Information

The Supporting Information is available free of charge at https://pubs.acs.org/doi/10.1021/acs.joc.1c00939.

Details about systems investigated; setting up of the simulation boxes; computational details about the ab initio molecular dynamics simulations; details about the tools used for the analysis; distribution of the exposed surface area of butan-2-ol in the different systems; radial distribution functions and discussion about the hydrogen bonds of the ionic liquid; trajectory snapshots illustrating intermolecular interaction pattern; spatial distribution functions of the 2-butanol oxygen atoms around the cation; RDFs between chiral center of butan-2-ol and the nitrogen atom of the cation bound to the ethylgroup (PDF)

■ AUTHOR INFORMATION

Corresponding Author

Barbara Kirchner − *Mulliken Center for Theoretical Chemistry, Rheinische Friedrich-Wilhelms-Universität Bonn, D-53115 Bonn, Germany;* orcid.org/0000-0001-8843-7132; Email: kirchner@thch.uni-bonn.de

Authors

Jan Blasius − *Mulliken Center for Theoretical Chemistry, Rheinische Friedrich-Wilhelms-Universität Bonn, D-53115 Bonn, Germany*

Paul Zaby − *Mulliken Center for Theoretical Chemistry, Rheinische Friedrich-Wilhelms-Universität Bonn, D-53115 Bonn, Germany*

Oldamur Hollóczki − *Mulliken Center for Theoretical Chemistry, Rheinische Friedrich-Wilhelms-Universität Bonn, D-53115 Bonn, Germany;* orcid.org/0000-0003-3105-7176

Complete contact information is available at: https://pubs.acs.org/10.1021/acs.joc.1c00939

Notes

The authors declare no competing financial interest.

■ ACKNOWLEDGMENTS

The authors thank the DFG under the Grant Project Number 406232243.

■ REFERENCES

(1) Blaser, H. U.; Federsel, H.-J. *Asymmetric Catalysis on Industrial Scale: Challenges, Approaches and Solutions*; John Wiley & Sons: 2011.
(2) Zehnacker, A.; Suhm, M. A. Chirality recognition between neutral molecules in the gas phase. *Angew. Chem., Int. Ed.* **2008**, *47*, 6970−6992.
(3) Schopohl, M. C.; Siering, C.; Kataeva, O.; Waldvogel, S. R. Reversible enantiofacial differentiation of a single heterocyclic substrate by supramolecular receptors. *Angew. Chem., Int. Ed.* **2003**, *42*, 2620−2623.
(4) Schopohl, M. C.; Siering, C.; Kataeva, O.; Waldvogel, S. R. Reversible enantiofaciale Differenzierung eines einzelnen heterocyclischen Substrates durch supramolekulare Rezeptoren. *Angew. Chem.* **2003**, *115*, 2724−2727.
(5) Lorenz, H.; Seidel-Morgenstern, A. Processes to separate enantiomers. *Angew. Chem., Int. Ed.* **2014**, *53*, 1218−1250.
(6) Afonso, C. A.; Crespo, J. G. Recent advances in chiral resolution through membrane-based approaches. *Angew. Chem., Int. Ed.* **2004**, *43*, 5293−5295.
(7) Mohr, J. T.; Krout, M. R.; Stoltz, B. M. Natural products as inspiration for the development of asymmetric catalysis. *Nature* **2008**, *455*, 323−332.
(8) Vedejs, E.; Jure, M. Efficiency in nonenzymatic kinetic resolution. *Angew. Chem., Int. Ed.* **2005**, *44*, 3974−4001.
(9) Cui, X.; Ding, Q.; Shan, R.-N.; He, C.-H.; Wu, K.-J. Enantioseparation of flurbiprofen enantiomers using chiral ionic liquids by liquid-liquid extraction. *Chirality* **2019**, *31*, 457−467.
(10) Schuur, B.; Verkuijl, B. J.; Minnaard, A. J.; De Vries, J. G.; Heeres, H. J.; Feringa, B. L. Chiral separation by enantioselective liquid−liquid extraction. *Org. Biomol. Chem.* **2011**, *9*, 36−51.
(11) Nagata, Y.; Takeda, R.; Suginome, M. Asymmetric catalysis in chiral solvents: chirality transfer with amplification of homochirality through a helical macromolecular scaffold. *ACS Cent. Sci.* **2019**, *5*, 1235−1240.
(12) Laarhoven, W. H.; Cuppen, T. J. Chiral solvent-induced asymmetric synthesis. Part 2. Photosynthesis of optically enriched hexahelicenes. *J. Chem. Soc., Perkin Trans. 2* **1978**, *2*, 315−318.
(13) Nishiyama, K.; Inouye, Y. Solvent Effect in a Partial Asymmetric Synthesis. III. *Bull. Chem. Soc. Jpn.* **1971**, *44*, 2795−2797.
(14) Zahn, S.; Uhlig, F.; Thar, J.; Spickermann, C.; Kirchner, B. Intermolecular forces in an ionic liquid ([Mmim][Cl]) versus those in a typical salt (NaCl). *Angew. Chem., Int. Ed.* **2008**, *47*, 3639−3641.
(15) Earle, M. J.; Seddon, K. R. Ionic liquids. Green solvents for the future. *Pure Appl. Chem.* **2000**, *72*, 1391−1398.
(16) Seddon, K. R. Ionic liquids for clean technology. *J. Chem. Technol. Biotechnol.* **1997**, *68*, 351−356.
(17) Welton, T. Room-temperature ionic liquids. Solvents for synthesis and catalysis. *Chem. Rev.* **1999**, *99*, 2071−2083.
(18) Davis, J. H. Task-specific ionic liquids. *Chem. Lett.* **2004**, *33*, 1072−1077.
(19) Earle, M. J.; McCormac, P. B.; Seddon, K. R. Diels−Alder reactions in ionic liquids. A safe recyclable alternative to lithium perchlorate−diethyl ether mixtures. *Green Chem.* **1999**, *1*, 23−25.
(20) Wasserscheid, P.; Bösmann, A.; Bolm, C. Synthesis and properties of ionic liquids derived from the 'chiral pool'. *Chem. Commun.* **2002**, 200−201.
(21) Baudequin, C.; Brégeon, D.; Levillain, J.; Guillen, F.; Plaquevent, J.-C.; Gaumont, A.-C. Chiral ionic liquids, a renewal for the chemistry of chiral solvents? Design, synthesis and applications for chiral recognition and asymmetric synthesis. *Tetrahedron: Asymmetry* **2005**, *16*, 3921−3945.
(22) Schulz, P. S.; Müller, N.; Bösmann, A.; Wasserscheid, P. Effective chirality transfer in ionic liquids through ion-pairing effects. *Angew. Chem., Int. Ed.* **2007**, *46*, 1293−1295.
(23) Bica, K.; Gaertner, P. Applications of chiral ionic liquids. *Eur. J. Org. Chem.* **2008**, *2008*, 3235−3250.
(24) Chen, X.; Li, X.; Hu, A.; Wang, F. Advances in chiral ionic liquids derived from natural amino acids. *Tetrahedron: Asymmetry* **2008**, *19*, 1−14.
(25) Payagala, T.; Armstrong, D. W. Chiral ionic liquids: A compendium of syntheses and applications (2005−2012). *Chirality* **2012**, *24*, 17−53.
(26) Ohno, H. In *Application of Ionic Liquids in Biotechnology*; Itoh, T., Koo, Y., Eds.; Springer: 2018; Chapter Synthesis of Ionic Liquids Originated from Natural Products.
(27) Ruivo, D.; Lopes, J. N. C.; Deive, F. J.; Esperança, J. M.; Rebelo, L. P. N.; Rodriguez, A.; Shimizu, K. Molecular dynamics studies on the structure and interactions of ionic liquids containing amino-acid anions. *Phys. Chem. Chem. Phys.* **2018**, *20*, 23864−23872.
(28) Ding, J.; Welton, T.; Armstrong, D. W. Chiral ionic liquids as stationary phases in gas chromatography. *Anal. Chem.* **2004**, *76*, 6819−6822.
(29) Yu, S.; Lindeman, S.; Tran, C. D. Chiral ionic liquids: synthesis, properties, and enantiomeric recognition. *J. Org. Chem.* **2008**, *73*, 2576−2591.
(30) Sintra, T. E.; Gantman, M. G.; Ventura, S. P.; Coutinho, J. A.; Wasserscheid, P.; Schulz, P. S. Synthesis and characterization of chiral ionic liquids based on quinine, l-proline and l-valine for enantiomeric recognition. *J. Mol. Liq.* **2019**, *283*, 410−416.
(31) Berthod, A. Chiral recognition mechanisms. *Anal. Chem.* **2006**, *78*, 2093−2099.
(32) Easson, L. H.; Stedman, E. Studies on the relationship between chemical constitution and physiological action: Molecular dissymmetry and physiological activity. *Biochem. J.* **1933**, *27*, 1257−1266.
(33) Fumino, K.; Wulf, A.; Ludwig, R. The Cation−Anion Interaction in Ionic Liquids Probed by Far-Infrared Spectroscopy. *Angew. Chem., Int. Ed.* **2008**, *47*, 3830−3834.
(34) Weber, H.; Kirchner, B. Complex Structural and Dynamical Interplay of Cyano-Based Ionic Liquids. *J. Phys. Chem. B* **2016**, *120*, 2471−2483. PMID: 26882454.
(35) Elfgen, R.; Hollóczki, O.; Kirchner, B. A molecular level understanding of template effects in ionic liquids. *Acc. Chem. Res.* **2017**, *50*, 2949−2957.
(36) Ohno, H.; Fukumoto, K. Amino acid ionic liquids. *Acc. Chem. Res.* **2007**, *40*, 1122−1129.
(37) Oulevey, P.; Luber, S.; Varnholt, B.; Bürgi, T. Symmetry breaking in chiral ionic liquids evidenced by vibrational optical activity. *Angew. Chem., Int. Ed.* **2016**, *55*, 11787−11790.
(38) Blasius, J.; Elfgen, R.; Hollóczki, O.; Kirchner, B. Glucose in dry and moist ionic liquid: vibrational circular dichroism, IR, and possible mechanisms. *Phys. Chem. Chem. Phys.* **2020**, *22*, 10726−10737.
(39) Brehm, M.; Kirchner, B. TRAVIS-a free analyzer and visualizer for Monte Carlo and molecular dynamics trajectories. *J. Chem. Inf. Model.* **2011**, *51*, 2007−2023.
(40) Brehm, M.; Thomas, M.; Gehrke, S.; Kirchner, B. TRAVIS-A free analyzer for trajectories from molecular simulation. *J. Chem. Phys.* **2020**, *152*, 164105.
(41) Martínez, J. M.; Martínez, L. Packing optimization for automated generation of complex system's initial configurations for molecular dynamics and docking. *J. Comput. Chem.* **2003**, *24*, 819−825.

(42) Martínez, L.; Andrade, R.; Birgin, E. G.; Martínez, J. M. PACKMOL: a package for building initial configurations for molecular dynamics simulations. *J. Comput. Chem.* **2009**, *30*, 2157−2164.
(43) Jorgensen, W. L.; Maxwell, D. S.; Tirado-Rives, J. Development and testing of the OPLS all-atom force field on conformational energetics and properties of organic liquids. *J. Am. Chem. Soc.* **1996**, *118*, 11225−11236.
(44) Canongia Lopes, J. N.; Deschamps, J.; Pádua, A. A. Modeling ionic liquids using a systematic all-atom force field. *J. Phys. Chem. B* **2004**, *108*, 2038−2047.
(45) Canongia Lopes, J. N.; Pádua, A. A. Molecular force field for ionic liquids composed of triflate or bistriflylimide anions. *J. Phys. Chem. B* **2004**, *108*, 16893−16898.
(46) Canongia Lopes, J. N.; Pádua, A. A. Molecular force field for ionic liquids III: Imidazolium, pyridinium, and phosphonium cations; chloride, bromide, and dicyanamide anions. *J. Phys. Chem. B* **2006**, *110*, 19586−19592.
(47) Plimpton, S. Fast parallel algorithms for short-range molecular dynamics. *J. Comput. Phys.* **1995**, *117*, 1−19.
(48) CP2k, A General Program to Perform Molecular Dynamics Simulations. CP2k developers group under the terms of the GNU General Public License; see http://www.cp2k.org.
(49) Becke, A. D. Density-functional exchange-energy approximation with correct asymptotic behavior. *Phys. Rev. A: At., Mol., Opt. Phys.* **1988**, *38*, 3098−3100.
(50) Perdew, J. P. Density-functional approximation for the correlation energy of the inhomogeneous electron gas. *Phys. Rev. B: Condens. Matter Mater. Phys.* **1986**, *33*, 8822−8824.
(51) Goedecker, S.; Teter, M.; Hutter, J. Separable dual-space Gaussian pseudopotentials. *Phys. Rev. B: Condens. Matter Mater. Phys.* **1996**, *54*, 1703.
(52) Hartwigsen, C.; Gœdecker, S.; Hutter, J. Relativistic separable dual-space Gaussian pseudopotentials from H to Rn. *Phys. Rev. B: Condens. Matter Mater. Phys.* **1998**, *58*, 3641.
(53) Krack, M. Pseudopotentials for H to Kr optimized for gradient-corrected exchange-correlation functionals. *Theor. Chem. Acc.* **2005**, *114*, 145−152.
(54) VandeVondele, J.; Hutter, J. Gaussian basis sets for accurate calculations on molecular systems in gas and condensed phases. *J. Chem. Phys.* **2007**, *127*, 114105.
(55) Grimme, S.; Antony, J.; Ehrlich, S.; Krieg, H. A consistent and accurate ab initio parametrization of density functional dispersion correction (DFT-D) for the 94 elements H-Pu. *J. Chem. Phys.* **2010**, *132*, 154104.
(56) Grimme, S.; Ehrlich, S.; Goerigk, L. Effect of the damping function in dispersion corrected density functional theory. *J. Comput. Chem.* **2011**, *32*, 1456−1465.
(57) Kirchner, B.; Blasius, J.; Esser, L.; Reckien, W. Predicting Vibrational Spectroscopy for Flexible Molecules and Molecules with Non-Idle Environments. *Adv. Theory Simul.* **2021**, *4*, 2000223.
(58) Fumino, K.; Wulf, A.; Ludwig, R. Strong, localized, and directional hydrogen bonds fluidize ionic liquids. *Angew. Chem., Int. Ed.* **2008**, *47*, 8731−8734.
(59) Fumino, K.; Reichert, E.; Wittler, K.; Hempelmann, R.; Ludwig, R. Low-Frequency Vibrational Modes of Protic Molten Salts and Ionic Liquids: Detecting and Quantifying Hydrogen Bonds. *Angew. Chem., Int. Ed.* **2012**, *51*, 6236−6240.
(60) Niemann, T.; Strate, A.; Ludwig, R.; Zeng, H. J.; Menges, F. S.; Johnson, M. A. Spectroscopic Evidence for an Attractive Cation−Cation Interaction in Hydroxy-Functionalized Ionic Liquids: A Hydrogen-Bonded Chain-like Trimer. *Angew. Chem., Int. Ed.* **2018**, *57*, 15364−15368.
(61) Scuderi, D.; Le Barbu-Debus, K.; Zehnacker, A. The role of weak hydrogen bonds in chiral recognition. *Phys. Chem. Chem. Phys.* **2011**, *13*, 17916−17929.
(62) Hembury, G. A.; Borovkov, V. V.; Inoue, Y. Chirality-sensing supramolecular systems. *Chem. Rev.* **2008**, *108*, 1−73.

https://doi.org/10.1021/acs.joc.1c00939
J. Org. Chem. 2022, 87, 1867−1873

G. Chemistry Dissolved in Ionic Liquids. A Theoretical Perspective

Barbara Kirchner,[*] Jan Blasius,[*] Vahideh Alizadeh,[*] Andreas Gansäuer,[†] and Oldamur Hollóczki[‡*]

Received: 19 October 2021, Published online: 17 January 2022.

Reprinted (adapted) in appendix G with permission[§] from

B. Kirchner, J. Blasius, V. Alizadeh, A. Gansäuer, and O. Hollóczki, *J. Phys. Chem. B* **2022**, *126*, 766–777.

doi:10.1021/acs.jpcb.1c09092.

For this article a Supporting Information is available free of charge at:
https://pubs.acs.org/doi/abs/10.1021/acs.jpcb.1c09092.

Contributions to the manuscript

- Performance of all calculations presented in chapter "Chirality: Complications from Asymmetry"
- Interpretation of the results presented in chapter "Chirality: Complications from Asymmetry"
- Writing of chapter "Chirality: Complications from Asymmetry"
- Co-writing of the other chapters

[*] Mulliken Center for Theoretical Chemistry, Clausius Institute for Physical and Theoretical Chemistry, University of Bonn, Beringstr. 4–6, 53115 Bonn, Germany
[†] Kekulé-Institut für Organische Chemie und Biochemie, Gerhard-Domagk-Str. 1, University of Bonn, 53121 Bonn, Germany
[‡] Department of Physical Chemistry, Faculty of Science and Technology, University of Debrecen, 4010 Debrecen, Hungary
[§] Permission requests to reuse material from this chapter should be directed to the American Chemical Society.

THE JOURNAL OF PHYSICAL CHEMISTRY B
A JOURNAL OF THE AMERICAN CHEMICAL SOCIETY

pubs.acs.org/JPCB

Perspective

Chemistry Dissolved in Ionic Liquids. A Theoretical Perspective

Barbara Kirchner,* Jan Blasius, Vahideh Alizadeh, Andreas Gansäuer, and Oldamur Hollóczki

Cite This: *J. Phys. Chem. B* 2022, 126, 766–777

Read Online

ACCESS | Metrics & More | Article Recommendations

ABSTRACT: The theoretical treatment of ionic liquids must focus now on more realistic models while at the same time keeping an accurate methodology when following recent ionic liquids research trends or allowing predictability to come to the foreground. In this Perspective, we summarize in three cases of advanced ionic liquid research what methodological progress has been made and point out difficulties that need to be overcome. As particular examples to discuss we choose reactions, chirality, and radicals in ionic liquids. All these topics have in common that an explicit or accurate treatment of the electronic structure and/or intermolecular interactions is required (accurate methodology), while at the same time system size and complexity as well as simulation time (realistic model) play an important role and must be covered as well.

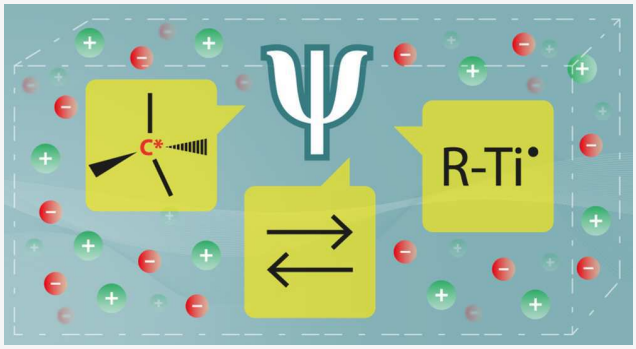

INTRODUCTION

Sustainable chemistry is a broad field with many materials and processes of interest, which may open possibilities to decrease our impact on the environment.[1−4] Among these, ionic liquids (ILs) have received particular scientific attention, leading to comprehensive discussions about their toxicity.[5,6] The research on ionic liquids was for a long time of two extremes: aiming at either very fundamental or very application-oriented questions. Interestingly, throughout the past years these two extremes started to approach each other to merge into interesting advanced academic ionic liquid applications. This bears significant challenges for theoretical chemists in many aspects if they are to follow or assist the experiments, such as the size of the systems[7] to consider and the accuracy of the results that are needed. Moreover, recently a new field related to ILs has emerged, deep eutectic solvents (DESs). In the theoretical research on DESs, the complexity of the system is a burdensome necessity, since this very property gives these mixtures their practically most important feature: their low melting point compared to the primary substances.[8]

Traditionally, ionic liquids (and DESs) have been studied computationally mainly from classical molecular dynamics simulations based on force fields.[9−22] Car−Parrinello or Born−Oppenheimer *ab initio* molecular dynamics (AIMD) simulations[23] based on the explicit description of the electronic structure concerning ionic liquids[24,25] and deep eutectic solvents[8,26−30] also appeared in the literature. Many contributions and clarifications came from static quantum chemical calculations.[31−37] As usual in static quantum chemistry, density functional theory (DFT) serves as workhorse for many calculations;[38,39] however, different methods were applied as well.[40−42] Polarizable force fields in all forms receive always special attention because they overcome many problems of traditional MD simulations.[43−47]

As Sharma et al. point out in their perspective about the differences of molten salts and ionic liquids,[48] general ionic liquid research tends to be always very broad and a myriad of excellent reviews exists for every special topic. In this Perspective we aim at considering only three wider ionic liquid applications without covering the literature completely as examples, which are not completely unaffected by each other, and they do not necessarily lead to industrial applications. These topics will, in our opinion, help identify and recognize the difficulties theoreticians face and will also highlight the accomplishments of computational chemistry in following the research to the aforementioned newly besieged more advanced stage.

Probably the most prominent applications of ionic liquids are related to energy devices.[49−51] The obvious connection of our three discussed examples to electrochemistry (echem) will be underscored where we deem it necessary. This will be, of course, far from being complete. Besides, several reviews with respect to calculations in echem applications and ionic liquids exist already.[52−56]

Received: October 19, 2021
Revised: January 2, 2022
Published: January 17, 2022

https://doi.org/10.1021/acs.jpcb.1c09092
J. Phys. Chem. B 2022, 126, 766−777

As first example, we would like to recall that ionic liquids can be attractive solvents for reactions.[57,58] They can be used to dissolve substances, stabilize transition states and intermediates, or simply change the selectivity for different reasons. Early (experimental) studies with a molecular level focus were performed by the groups of Welton,[59] Croft and Harper,[60−63] D'Anna,[64,65] and Chiappe.[66] Connected to this are the IL applications regarding chirality. Chiral ionic liquids (CILs) were studied experimentally very early on by Seddon, Wasserscheid, and others, who introduced the possibility to include chirality in IL ions.[67−71] In amino acid-based ILs, the amino acid group can provide the cation and/or the anion.[72] A further challenge for theory is our third topic, "radicals in ionic liquids".[73,74] The difficulties lie in the complex electronic structure of these compounds, next to the intricacies of solvation in these highly structured solvents. Nonetheless, their importance is shown by the myriad of reactions in which radicals are involved, as will be shown below.

RESULTS AND DISCUSSION

Ionic Liquids as Reaction Media. An excellent review article about the main properties, i.e., the bulk polarity and the nanostructure[75] or that they are microheterogeneous liquids,[76] which make ILs good solvents, was provided by the D'Anna group recently.[65] One of the most important messages of their review is that the IL effect[59] can be influenced not only by the nature of the IL but also by the nature of the substrate, highlighting the complexity of the factors that govern reactivity in such media. Examples for a mechanism switch are provided.[65]

As trivial as it may sound, let us recall that, in describing reactivity, the challenge for theoretical studies is the need to treat the electronic structure explicitly, if a proper description of bond breaking and formation is to be achieved. Furthermore, describing the peculiar solvent effects of ionic liquids—often dependent on amphiphilic interactions and mesoscale microsegregation—necessitates dealing with a large amount of particles. Several reactions in explicit ionic liquid solvents were studied from theory by the Acevedo group.[77,78] Acevedo and coworkers apply to this end mixed *ab initio* and molecular mechanics simulations (QM/MM), where the QM part delivers the explicit electronic structure, whereas the MM part—that can deal with the huge number of particles—can provide the description of influential long-range solvation effects. Large improvements of the results were observed if the QM part for the solute was described through exact exchange functionals of density functional theory[78] instead of only semiempirical methods.[77] Similarly, much effort was also put into improving the MM part that definitively leads to a superior solvent structure.[9−11]

Recently, the anion $[BF_4]^-$ is gaining interest in electrochemical applications. Already in the early days of the renaissance of ILs, Ken Seddon warned of the instability of $[BF_4]^-$ and $[PF_6]^-$, especially in aqueous solution.[79] This does not only raise questions about the inertness of the corresponding materials and their use in sustainable processes but also makes the simulation of such systems from classical MD nontrivial, considering that their spontaneous reactivity is their inherent feature. Standard classical simulations cannot describe reactivity, while in AIMD simulations, without the use of free energy methods, they can be observed only if the barrier is not higher than ca. k_BT (Boltzmann constant times temperature). Nonetheless, if this criterion is met, simple spontaneous reactions of or in ILs can be captured from full AIMD simulations. These include, for example, CO_2 absorption studies in ILs,[80−82] Grotthuss type mechanisms that are closely related to echem,[83] or decomposition reactions.[84]

CO_2−IL mixtures were studied from AIMD by Bhargava and Balasubramanian[81] where no chemical reaction occurred because the chosen ionic liquid (1-*n*-butyl-3-methylimidazolium hexafluorophosphate ($[C_4C_1Im][PF_6]$)) absorbs this gas physically.[85,86] Similarly, in a study of ethylammonium nitrate ($[N_{2HHH}][NO_3]$) a rationale could be provided for the missing swelling when CO_2 is being physically absorbed, but a chemical reaction did not occur.[87] Furthermore, AIMD simulations at 1 and 5 MPa were performed to investigate the CO_2 absorption in the choline chloride:ethylene glycol DES. While at lower pressure the cation and the ethylene glycol played the major role, at higher pressure the anion was more important in the physical absorption of CO_2.[26]

The chemical absorption of CO_2 by amino acid-based ionic liquids was studied from AIMD and static quantum chemical methods.[80,88] Reaction mechanisms were discussed, and the modification of the CO_2 adduct formation barrier (rate-determining step) was tested. It can be increased by side-chain elongation, the introduction of an aromatic π-system, and perfluorination.[80] The chemical absorption of CO_2 in imidazolium acetate ionic liquids has also been studied through AIMD.[88] It was found that CO_2 does not hinder the mobility of the most acidic ring proton and it seemed to rather induce it. It is worth mentioning that a couple of static quantum chemical investigations about CO_2 absorption in ILs exist as well, for example in refs 85, 86, and 88−91. First principles Monte Carlo simulations were applied by the Rai group to test the applicability of different functionals for the calculations of vapor−liquid equilibria of CO_2 in ILs.[82] Interestingly, the authors have a very good point about that classical MD can fail "when/where they are needed the most, i.e., when experiments are either difficult or nearly impossible to perform", which appears for systems under extreme pressure or temperature, or chemicals that are toxic, or for unknown materials.[82]

The Grotthuss diffusion of protons in aqueous solutions is a typical case for the applicability of AIMD. In certain ILs, similar structural diffusion can occur; thus, charge can move in space with a minimal movement of the atoms, if bonds can rearrange within a network of covalent and noncovalent interactions. The first Grotthuss diffusion process that was observed in ionic liquids from AIMD was that in mixtures of $[C_2C_1Im][Cl]$ and aluminum trichloride.[83] In these liquids, the anionic clusters of aluminum can transfer a chloride anion to a neutral cluster. Because the newly formed charged cluster can transfer another chloride at a different site, this mechanism provides a shortcut for charge transport. These theoretical findings, obtained by AIMD, gave a feasible explanation for the superb performance of these ILs in echem applications.[83] Analogously to aqueous solutions of acids and bases, a proton conduction mechanism for imidazole−acid mixtures has been observed.[92] These mixtures are often termed pseudo-ILs since they are not fully ionic but contain many neutral imidazole and acid molecules.[92] The proton transfer from one basic site to the other can therefore be conducted through a chain of acids and imidazolium compounds. By altering the substituents of the acid and the base, further pseudo-ILs were designed, which should show similarly remarkable conductive processes.[92] An interesting work of Bodo and co-workers considered the Grotthuss diffusion in amino acid-based ionic liquids. They observed in their AIMD simulations that the repulsive anion−anion

https://doi.org/10.1021/acs.jpcb.1c09092
J. Phys. Chem. B 2022, 126, 766−777

interplay can be weakened to such an extent that a proton migration becomes possible also within the anionic component of the liquid.[93] Recently, a similar dynamic bond breaking and bond formation process has been observed for the mixtures of imidazolium halide ILs and phosphorus trihalides. It was observed through experiments and AIMD simulations that the anion coordinates to the phosphorus atom, forming a complex anion in a dynamic equilibrium. This process was suggested to offer a way for Grotthuss diffusion of anions.[94] The actual Grotthuss diffusion process was observed later in a PCl_3:$[C_4C_1Im][Cl]$ 3:1 mixture with AIMD[95] (see Figure 1). Through static calculations, the possible mechanisms of further anionic structural diffusion processes of ionic liquids have been comprehensively explored.[95]

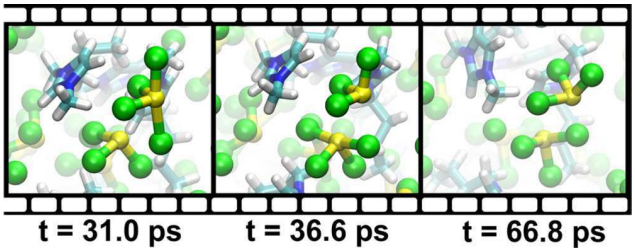

Figure 1. Selected snapshots from a simulation of a PCl_3:$[C_4C_1Im][Cl]$ 3:1 mixture: (P, yellow; C, cyan; Cl, green; H, white; N, blue). The transfer of a chloride from a $[PCl_4]^-$ complex anion to a PCl_3 can be observed, which is followed by the break of another P−Cl bond in the latter molecule, releasing a free chloride at the opposite end of the molecule. To highlight the time scale of the process, the physical time in the simulation is given for each snapshot. Reproduced with permission from ref 95.

An obvious drawback in all AIMD simulations is that the time scales are far below those of classical simulations. There are some promising approaches that we want to mention here. Sebastiani and co-workers[96,97] derived in the spirit of Monte Carlo simulations[98] a matrix formalism to be able to simulate proton dynamics for extended systems and time scales. This involves the construction of a Markov chain based on an AIMD run and the subsequent propagation of the proton distribution by means of transition matrices, which contain kinetic data from both ultrashort and intermediate (picoseconds) time scales.[96,97] Second, improved tight-binding semiempirical methods[99] that have been applied in ILs[100−102] may lead to larger and longer investigations of (organic) reactions in ILs and DESs due to the reduced costs of the electronic structure method. Quantum embedding for material chemistry based on domain separation and open subsystems might be another solution to these problems.[103] As such methods can provide a more sufficient sampling than traditional AIMD of wide conformational spaces, they enable theoretical investigations of, for example, the reactivity of large and flexible molecules. Moreover, they can contribute to the investigation of chiral phenomena like chiroptical response or chirality transfer, which necessitate the consideration of the electronic structure and a proper sampling of all relevant conformers.

Chirality: Complications from Asymmetry. Chiral induction effects in the amino acid-based ionic liquid 1-ethyl-3-methylimidazolium L-alaninate ($[C_2C_1Im][$L-ala$]$) were detected by Oulevey and co-workers.[104,105] Experimental vibrational circular dichroism (VCD) spectra were found to be dominated by the chiral anion, but Raman optical activity measurements revealed chiroptical activity of the achiral cation, thereby proving chirality transfer.[104,105] With the aid of theoretical investigations, a symmetry breaking in the conformational distribution of the cation was found to be the source for the chiroptical response, inasmuch as the energetic degeneration of two mirror-imaged conformations gets perturbed by the chiral anion.[104,105] This study exemplifies that experiments can definitely prove the occurrence of chiral induction effects, but theoretical methods can provide valuable mechanistic insights, not least with the aid of theoretical spectra which can be decomposed into contributions of different components.

However, an accurate modeling of phenomena like chiral induction poses severe challenges. The assessment through static approaches[106−109] can be achieved by calculations of diastereomeric complexes, that is, clusters in which a permanently chiral species interacts with different conformations of an achiral molecule. Based on the electronic energies of the clusters, indications for the most stable conformations of the achiral molecule in the presence of the chiral species can be obtained. However, since chiral induction is often a dynamic process[110,111] influenced by many species, the search for a representative ensemble of clusters is desirable but far from being straightforward. Although MD simulations can circumvent this ensemble issue,[112,113] great care has to be taken with respect to the force field employed. As discussed above, classical force fields are usually fitted to macroscopic properties of known substances, meaning they do not necessarily apply to unknown substances or deliver a reliable description of the correct intermolecular interactions and hence molecular-level speciation. Chirality transfer is often related to the formation of intermolecular complexes involving many particles. Therefore, the usage of either polarizable force fields or AIMD simulations is recommended, at the cost of limiting the system size to fewer molecules and restricting the analysis of the trajectories to local phenomena in the case of AIMD.

If the calculation of vibrational spectra and their decomposition into contributions of different species is desired, correlation functions can be employed in nonstatic approaches. A VCD spectrum can for instance be calculated from an MD trajectory by taking the Fourier transform of the time cross-correlation function of the electric dipole moment $\mu(t)$ and the magnetic dipole moment $m(t)$:[114]

$$\Delta A_{\mathrm{VCD}}(\tilde{\nu}) = \frac{N_{\mathrm{A}}}{12\varepsilon_0 c^2 k_{\mathrm{B}} T} \int_{-\infty}^{\infty} [\langle \dot{\mu}(\tau)\cdot\dot{m}(\tau + t)\rangle_\tau - \langle \dot{m}(\tau)\cdot\dot{\mu}(\tau + t)\rangle_\tau] \exp(-2\pi i c\tilde{\nu}t)\, \mathrm{d}t \quad (1)$$

Herein, N_A is the Avogadro constant, t and τ represent the time, c is the speed of light, ε_0 is the vacuum permittivity, k_B is the Boltzmann constant, T is the average temperature of the simulation, and $\langle \dot{\mu}(\tau)\cdot\dot{m}(\tau + t)\rangle_\tau$ is the cross-correlation function[114] of the electric and magnetic dipole moments. For the calculation of the electric dipole moments we presented the so-called Voronoi tessellation which partitions the electron density in space.[115] Based on this partitioning scheme also the magnetic dipole moments can be obtained by solving the according partial differential equation.[116]

Following this approach, our investigations of different D-glucose isomers dissolved in the nonchiral ionic liquid 1-ethyl-3-methylimidazolium acetate ($[C_2C_1Im][OAc]$) revealed the occurrence of chiral induction effects with the aid of theoretical VCD spectra.[117] While the global spectra were dominated by the chiral D-glucose molecules, a decomposition into the contribu-

https://doi.org/10.1021/acs.jpcb.1c09092
J. Phys. Chem. B 2022, 126, 766−777

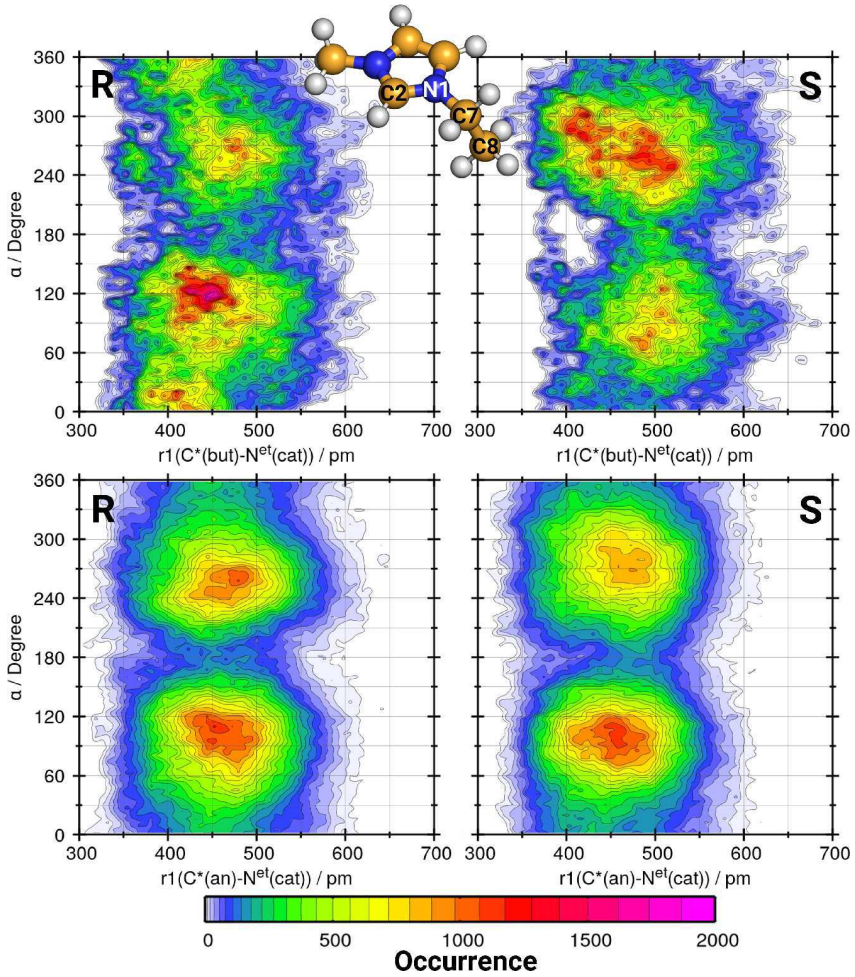

Figure 2. Combined distribution functions correlating the dihedral angle α (C2−N1−C7−C8) of the cation 1-ethyl-3-methylimidazolium with the distance between the chiral center of butan-2-ol (top) or the chiral center the anion L-alaninate (bottom) and the nitrogen atom N1 of the cation bound to the ethyl group. Note that only the closest cation with respect to butan-2-ol or the anion was taken into account. Reproduced with permission from ref 24.

tions of the different components clearly confirmed chiroptical activity of the achiral IL components. Opposed to the chirality transfer observed in neat $[C_2C_1Im][$L-ala$]$, the chiral information does not stem from one of the IL components but from a solute. A deeper investigation of the intermolecular interactions revealed an involved network, causing the formation of tight complexes between the different species which can promote the chirality transfer. This highlights the importance to use computational methods that can describe the intermolecular speciation properly.

To investigate the influence of chiral induction on enantiomeric recognition, we performed AIMD simulations of (*R*)- and (*S*)-butan-2-ol dissolved in the chiral ionic liquid $[C_2C_1Im][$L-ala$]$.[24] Depending on the chirality of the solute, the systems were termed as **R** (heterochiral) and **S** (homochiral). We observed that the heterochiral system is stabilized by ΔE = 18.8 kJ/mol compared to the homochiral one, indeed indicating the occurrence of chiral discrimination induced by the IL. Although this could be attributed to diastereomeric complexes formed between the permanently chiral $[$L-ala$]^-$ anion and the butan-2-ol enantiomers, chiral information induced on the cation might amplify this process.

A more detailed investigation of the effects of the $[$L-ala$]^-$ anions and the enantiomers of butan-2-ol on the structure of the cation is presented in Figure 2, which depicts combined distribution functions that correlate the dihedral angle α (C2−N1−C7−C8) of the cation (see sketch in Figure 2) with the distance between the nitrogen atom N1 of the cation and the chiral center of butan-2-ol (top) or the chiral center of the $[$L-ala$]^-$ anion (bottom).[24] To capture the local effects of the permanently chiral species on the achiral cation, only the closest cation with respect to butan-2-ol or the anion was taken into account. Around the $[$L-ala$]^-$ anion, the cation shows a slight preference to adopt structures with α around 120° (bottom panel). A preference for the same cation structure is observed around (*R*)-butan-2-ol (top left); however, around (*S*)-butan-2-ol we observe a preference for cation structures with opposite chirality, i.e., α around 270° (top right). Thus, the $[$L-ala$]^-$ anion and (*R*)-butan-2-ol induce the same chirality within the cation. As a consequence, the IL itself creates an environment in which (*R*)-butan-2-ol fits well, while (*S*)-butan-2-ol does not, ultimately leading to chiral discrimination effects caused by chiral induction.

To verify the observed chiral induction effects, we present in Figure 3 the calculated VCD spectra obtained from the AIMD trajectories. As observed in our previous study of D-glucose dissolved in $[C_2C_1Im][OAc]$,[117] the global spectrum is dominated by the chiral compound in excess, here the $[$L-ala$]^-$

https://doi.org/10.1021/acs.jpcb.1c09092
J. Phys. Chem. B 2022, 126, 766−777

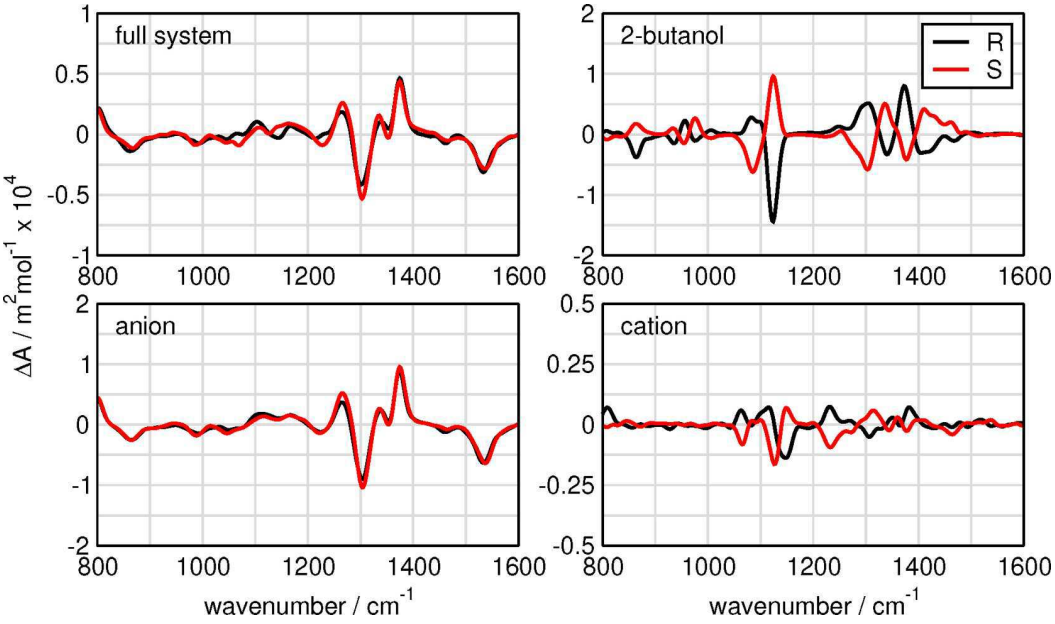

Figure 3. Vibrational circular dichroism spectra obtained from *ab initio* molecular dynamics simulations of (*R*)- and (*S*)-butan-2-ol in the ionic liquid 1-ethyl-3-methylimidazolium L-alaninate.

anion. Both butan-2-ol enantiomers show mirror-imaged spectra, as it is expected due to their opposite chirality. However, mirror-imaged VCD spectra are also observed for the achiral cation, clearly proving the existence of enantiomeric conformers and the occurrence of chirality transfer. The decreased intensity as compared to the $[\text{L-ala}]^-$ anion and butan-2-ol can be explained by the conformational analysis presented in Figure 2. Although the cation preferably adopts specific conformations around either the anion or butan-2-ol, conformations with opposite chirality are still present in the solution. Thus, the chiroptical response of those enantiomeric structures cancels out to some extent, and only chiral conformations being present in excess contribute to the spectrum.

While this study exemplifies that the approach presented above allows a theoretical investigation of chirality transfer from spectroscopy, it requires knowledge about the electronic structure whose calculation is computationally rather intense. As a computationally less expensive alternative for calculating bulk-phase spectra, we introduced a cluster weighting approach[109] based on the quantum cluster equilibrium theory,[118] and we are currently investigating the calculation of dipole moments based on partial charges.[113] Provided that a reliable description of dipole moments from partial charges can be achieved, polarizable force fields[43] could be employed for the calculation of bulk phase spectra. As another alternative, force fields specially fitted for the description of spectroscopic properties or reaction dynamics can be employed.[119] The development of such specialized force fields might also be a promising approach for the theoretical description of radicals and their dynamics in solution.

Radical Problems in Ionic Liquids. Early experimental studies by the Lagrost group considered the dimerization of acetophenone anion radicals in ionic liquids.[120] Interestingly, they found an increased kinetics in 1,3-dialkylimidazolium salts as compared to 1,2,3-trialkylimidazolium salts, which they could attribute to hydrogen bonding to the acidic proton of the imidazolium ring and hence to charge transfer between the radical anion and the cation.[120]

As pointed out by the López group,[4] DFT calculations can run into problems if the electronic structure becomes too complicated such as in complex spin configurations. A remedy can be the use of hybrid functionals in which the exchange term is based on Hartree−Fock, however, at the cost of computationally expensive calculations. For repeated force calculations (when molecular dynamics simulations are involved) of solvent effects in large systems, this might not pose a realistic possibility, and other approaches like the Hubbard model which is often abbreviated as DFT+U[4] must be sought for.

Izgorodina and co-workers pioneered quantum chemical calculations of radicals in ionic liquids by considering radicals combined with ion pairs in multiple conformations.[31,32,121,122] To be able to study the complicated electronic structure of such systems in ILs, they specifically developed a spin ratio scaled MP2 method termed SRS-MP2.[123]

It is worth mentioning that excess electrons[124,125] in ionic liquids have been studied from AIMD simulations as well. As Unterreiner and co-workers point out, a major task is to understand "the fate of excess electrons (and holes)", which needs the consideration of "various formation mechanisms considering structural and dynamical aspects".[125] Wang et al. investigated an excess electron in eight ion pairs of 1-methylpyridinium chloride already in 2010.[126] While they used the generalized gradient approximation (GGA) functional BLYP[127,128] to generate the trajectory, they added calculations employing exact exchange density functionals on top of these simulations at certain snapshots of the BLYP trajectory. Their analysis contained energy level plots, the density of states, and orbital analysis next to radial pair distribution functions. A similar choice (PBE[129] and B3LYP[127,128]) was taken by Margulis and co-workers[130] when studying a dry excess electron in ethyltrimethylammonium bis(trifluoromethane)sulfonimide ($[N_{1113}][Tf_2N]$). The reasons for this are that the unpaired electron in the singly occupied molecular orbital could suffer under the self-interaction error, and the valence-conduction

https://doi.org/10.1021/acs.jpcb.1c09092
J. Phys. Chem. B 2022, 126, 766−777

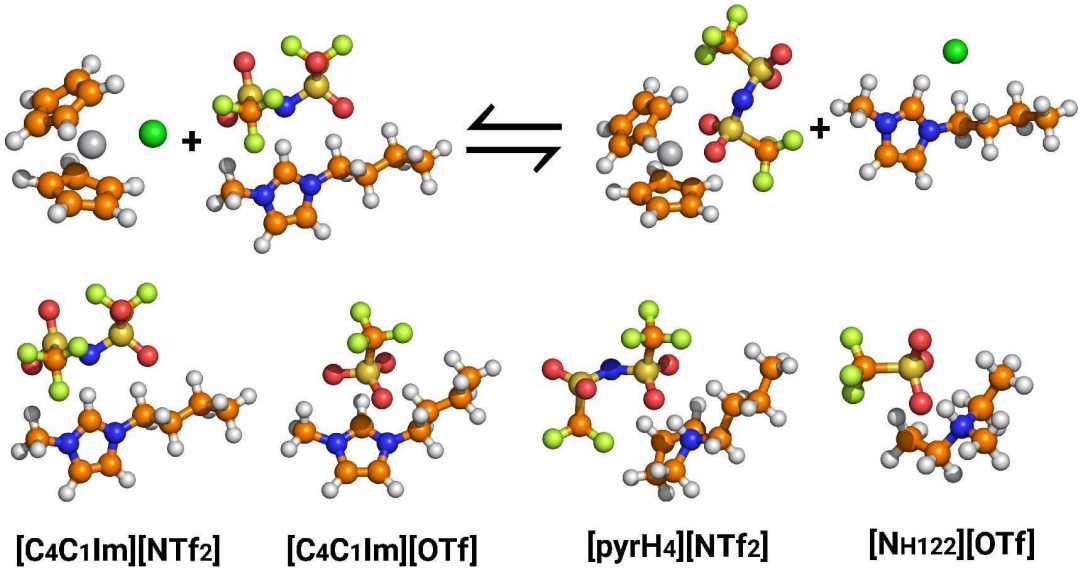

Figure 4. Top: illustration in ball-and-stick representation of the exchange reaction between the chloride ligand of a titanocene complex[138,139] and the $[NTf_2]^-$ anion of the 1-*n*-butyl-3-methylimidazolium bis(trifluoromethylsulfonyl)imide $[C_4C_1Im][NTf_2]$ ion pair. Bottom: different ion pairs as used in the calculations, from left to right: $[C_4C_1Im][NTf_2]$; $[C_4C_1Im][OTf]$ ([OTf]: trifluoromethanesulfonate anion), [pyrH4][NTf_2] (cation: *N*-butylpyrrolidinium), and $[N_{H122}][OTf]$ (cation: diethylmethylammonium).

Table 1. Reaction Energy E^{IP} in kJ/mol of the Exchange Reaction (2)[a]

method	$E^{[C_4C_1Im][NTf_2]}$	$E^{[C_4C_1Im][OTf]}$	$E^{[pyrH4][NTf_2]}$	$E^{[N_{H122}][OTf]}$	RAD	$t(TiCp_2X)$
			DZVP[134] basis set			
BLYP	97.8 (1.3)	41.8 (4.4)	69.6 (1.1)	31.7 (3.9)	2.7	371
PBE	97.5 (1.6)	35.1 (2.3)	65.0 (3.5)	24.6 (3.2)	2.7	475
revPBE	100.7 (1.6)	43.6 (6.2)	67.5 (1.0)	30.5 (2.7)	9.5	393
PBE+U (U = 5 eV)	78.1 (21.0)	21.4 (16.0)	45.7 (22.8)	10.8 (17.0)	19.2	558
PBE+U (U = 2 eV)	99.6 (0.5)	32.8 (4.6)	67.2 (1.3)	22.3 (5.5)	3.0	382
TPSS	91.5 (7.6)	34.3 (3.1)	63.2 (5.3)	26.0 (1.8)	4.5	617
B3LYP(ADMM)	105.2 (6.1)	49.7 (12.3)	77.0 (8.5)	39.7 (11.9)	9.7	1266
PBE0(ADMM)	104.2 (5.1)	42.8 (5.4)	71.5 (3.0)	26.0 (1.8)	3.8	1380
PBE0	99.1 (−)	37.4 (−)	68.5 (−)	27.8 (−)		60640
			TZVP[134,145] basis set			
BLYP	89.1 (4.9)	32.8 (0.9)	67.8 (0.8)	29.3 (1.3)	2.0	806
PBE	87.4 (6.6)	26.3 (7.4)	61.6 (7.0)	22.1 (8.5)	7.3	852
TPSS	85.3 (8.7)	22.7 (11.0)	62.7 (5.9)	20.4 (10.2)	9.0	1350
B3LYP(ADMM)	97.2 (3.2)	40.0 (6.3)	75.9 (7.3)	37.1 (6.5)	5.8	1983
PBE0(ADMM)	94.0 (−)	33.7 (−)	68.6 (−)	30.6 (−)		2752

[a]Average timing $t(TiCp_2X)$ with X = Cl or anion in s of each single point calculation that includes Ti, running on 64 cores of a compute cluster with 2.3 GHz AMD-Opteron-CPUs and 128 GB RAM. The values in parentheses give the absolute deviation from the reference value, i.e., PBE0 for DZVP and PBE0(ADMM) for TZVP. RAD gives the average absolute deviation from the reference.

energy band gap could be underestimated. While the former one was found to be rather unimportant, the latter turned out to be relevant for the calculation of the optical absorbance spectrum.[130] The authors point out that self-interaction appears to be more relevant in positively charged systems generated by the removal of an electron and creation of a hole. In general, it is found that the excess electron can delocalize over cations or anions depending on the nature of the ions involved.[130]

Roy and Gill et al.[131,132] studied d-block metal ions (Ni^{2+}, Co^{2+}, and Cr^{3+}) in molten salts by a combined AIMD and experimental extended X-ray absorption fine structure (EXAFS) approach. They point out the importance of AIMD when studying such systems because the consideration of electronic interactions and spin polarization is necessary. They give a warning that the right prediction of the local dynamical coordination environment and chemical speciation of the complex solvent mixtures is necessary to allow high-quality predictions.[131,132]

Similarly, Salanne and co-workers used AIMD to study biredox ionic species in acetonitrile.[133] They used the GGA functional BLYP[127,128] in conjunction with the TZV2P basis set.[134] To describe the radical species properly, the scaled self-interaction correction[135,136] was applied. This work was later used to parametrize polarizable force fields because problems due to ad hoc developed force fields of radicals and the lack of polarization effects description for radical species can lead to inaccuracies in solvation and dynamics.[137]

To illustrate the difficulty of functional choice and computational time, we calculated the artificial gas phase exchange reaction (eq 2) of the chloride ligand of a titanocene

https://doi.org/10.1021/acs.jpcb.1c09092
J. Phys. Chem. B 2022, 126, 766−777

complex[138,139] with an anion from an IL ion pair as illustrated in Figure 4. The calculation of such processes is highly attractive for catalysts, and reaction design as quantitative predictions about the (reversible) modulation of the catalysts' redox potentials can be made. All four structures (titanocene complexes and ion pairs) for each IL in eq 2 have been optimized with the PBE0[129]/def2-SVP[140] level of theory with unrestricted DFT by the orca package.[141] Subsequently, the single point energy calculations were performed from the CP2K package.[142] The following functionals and basis sets were chosen: PBE0,[129] PBE,[129] revPBE,[143] BLYP,[127,128] B3LYP,[127,128] TPSS,[144] DZVP,[134] and TZVP.[134,145] The auxiliary density matrix method (ADMM) for the hybrid functionals was tested.[146] Pseudopotentials were chosen from ref 134. A value of 10^{-6} was used as target accuracy for the SCF convergence (EPS SCF 1.0×10^{-6}). A 200 Ry density CUTOFF criterion was employed with multigrids number 5 (NGRID 5 and REL CUTOFF 30) by using the smoothing for the electron density (NN10 SMOOTH) and its derivative (NN10).[147]

$$TiCp_2Cl + \text{cation}-\text{anion} \rightleftharpoons TiCp_2\text{anion} + \text{cation}-Cl \quad (2)$$

Table 1 summarizes the reaction energies of the exchange reaction (2), the average timing for the respective single point calculations, and the absolute deviations from the reference values. Additionally, we present RAD values which represent the averaged absolute deviation from the reference for a respective level of theory. Based on Table 1, an obvious anion effect is visible; that is, the reaction is on average by 60 kJ/mol energetically more favorable when $[OTf]^-$ is chosen than when $[NTf2]^-$ is the solvent anion. The cation effect is more subtle; when changing from $[C_4C_1Im]^+$ to $[pyrH4]^+$ the reaction becomes on average more favorable by about 28 kJ/mol and when changing from $[C_4C_1Im]^+$ to $[N_{H122}]^+$ by about 8 kJ/mol. Nevertheless, when changing the cation, the difference in the reaction energy is still greater than the deviation to the reference functional, i.e., above or within the RAD. We further see in Table 1 that different functionals perform differently for the reaction 2 (see RAD values). The consideration of the reaction only is of course a simplification because we did not treat transition states for which we expect larger differences to occur. However, we can observe a huge increase in computational time when hybrid functionals are being chosen. Without the ADMM approximation a factor of more than 40 has to be paid in computational costs. The comparison between revPBE and PBE0 (with ADMM) even yields a factor of 200 (5). When 100 ps with a time step of 0.5 fs is being targeted, 200000 steps need to be produced which shows again that a factor of 5 for each of these steps is difficult and a factor of 200 is unacceptable. Nevertheless, the use of a good electronic structure in such systems is important to obtain a proper description of these complicated systems. This simple consideration shows that the theoretical treatment of radicals in ionic liquids is far from being solved.

CONCLUSION

In this Perspective we discuss how theory can further approach complicated situations in ionic liquids (ILs). We showed at particular examples, namely reactions, chirality, and radicals in ILs, what progress was made and still has to be made in theoretical investigations to overcome the problems resulted from oversimplifications in models and methodologies. We chose these particular applications of IL research because they recently gained more importance, while exciting observations have also been made from purely academic research.

For reactions, one needs to consider that breaking and formation of bonds occur. This is solved by explicit *ab initio* molecular dynamics (AIMD) simulations, which treat the electronic structure on the fly. However, when applied to reactions, small system sizes and short simulation times become an obstacle to a realistic treatment. Solutions are given by simplified electronic structure methods, QM/MM as well as novel Monte Carlo techniques, or embedding methods that help to use more realistic time scales.

Chirality does not necessarily mean that reactions need to be considered, but again only a careful description of intermolecular forces allows the elucidation of the underlying intricate induction mechanisms. Identifying the chirality of the given molecule is often performed through spectroscopic methods, which provide a convenient connection between theory and experiments. To extract vibrational spectra from trajectories, time correlation function techniques are applied. To obtain satisfying spectra, the proper description of the intermolecular interactions and their influence on the bonding within the molecule is required, which again shows the advantages of describing the electronic structure explicitly. However, because of the immense computational demand of these calculations, it is necessary to implement new methodologies that allow for accurate results with faster calculations.

Our final example of radicals in ILs involves species with very complicated electronic structures. For such systems, only a handful of successful studies exists, in which force-field-based methods were employed. Furthermore, even in electronic structure calculations complications such as self-interaction error and time scale problems must be overcome. In some cases an elegant approach was applied, where a lower theoretical level was used to produce the trajectories, and the more accurate, higher level calculations were performed on top of the obtained structures. Alternatively, clusters of solute IL units can be treated by a high-level of quantum chemistry.

Thus, all the mentioned IL application examples have in common that the system size is large and complex, e.g., with many compounds, resulting in unknown and unexpected intermolecular interactions, while at the same time an explicit description of the electronic structure is in principle needed. For all of these advanced investigations that will dominate ionic liquid research in the next decades, theory will not be able to rely solely on standard force-field-based simulations. Again, many problems theoretical investigations will face in future will still be originated not only from system size or solvent effects but also in complex electronic structures. Polarizable force fields will often offer remedy, but they surely will not be sufficient in all cases.

AUTHOR INFORMATION

Corresponding Author

Barbara Kirchner − *Mulliken Center for Theoretical Chemistry, University of Bonn, D-53115 Bonn, Germany;* orcid.org/0000-0001-8843-7132; Email: kirchner@thch.uni-bonn.de

Authors

Jan Blasius − *Mulliken Center for Theoretical Chemistry, University of Bonn, D-53115 Bonn, Germany*

Vahideh Alizadeh − *Mulliken Center for Theoretical Chemistry, University of Bonn, D-53115 Bonn, Germany*

Andreas Gansäuer − *Kekulé-Institut für Organische Chemie und Biochemie, University of Bonn, D-53121 Bonn, Germany*

https://doi.org/10.1021/acs.jpcb.1c09092
J. Phys. Chem. B 2022, 126, 766−777

Oldamur Hollóczki − *Mulliken Center for Theoretical Chemistry, University of Bonn, D-53115 Bonn, Germany; Department of Physical Chemistry, Faculty of Science and Technology, University of Debrecen, H-4010 Debrecen, Hungary;* orcid.org/0000-0003-3105-7176

Complete contact information is available at: https://pubs.acs.org/10.1021/acs.jpcb.1c09092

Notes

The authors declare no competing financial interest.

Biographies

Barbara Kirchner holds a chair for theoretical chemistry at the Mulliken Center for Theoretical Chemistry in Bonn (Germany) where she is also currently head of the Department of Chemistry. Before that, she held the chair for Theoretical Chemistry at the University of Leipzig (Germany). She is a member of the transdisciplinary research areas "Building Blocks of Matter and Fundamental Interactions" and "Innovation and Technology for Sustainable Futures" at the University of Bonn. She is specialized in theoretical methods for liquids, for example ionic liquids and deep eutectic solvents. However, her research interests and impact reach far beyond the topic of ionic liquids; they cover a wide range of fields in theoretical, physical, (bio)organic, inorganic and sustainable chemistry, with a novel view on chemical problems. She investigates functional materials such as chemically active domains in liquids, bulk and interfacial liquid−liquid systems for extraction, and energy devices. Her research involves two larger software projects: Peacemaker and Travis. While the former program is gradually gaining more and more attention for predicting physical and chemical properties of liquids based on high level quantum chemical calculations, the latter allows a systematic characterization of molecular simulation trajectories and is used broadly in the international scientific community.

Jan Blasius is a Ph.D. student in the research group of Prof. Barbara Kirchner. He studied chemistry at the Rheinische Friedrich-Wilhelms-University of Bonn (Germany) and obtained his B.Sc. (2017) and M.Sc. degrees (2019) after work in the group of Barbara Kirchner. In his B.Sc. thesis he investigated a new theoretical approach for the prediction of mole fraction dependent acid dissociation. During his master studies he started to work in the field of molecular chirality and optical activity. In his M.Sc. thesis, he investigated and developed static and dynamic approaches for the calculation of vibrational circular dichroism spectra in the liquid state. He continues this work in his Ph.D. project and uses the developed methods to investigate chiral phenomena (e.g., chirality transfer) in the condensed phase.

Vahideh Alizadeh is pursuing her Ph.D. under the supervision of Prof. Barbara Kirchner at the University of Bonn (Germany). Her research focuses on molecular-level studies of interactions and reactions in deep eutectic solvents and ionic liquids by applying multiresolution computational methods such as AIMD, classical MD, and quantum chemistry methods. She is also one of Travis software developers. In her M.Sc., she investigated the electronic structure of lanthanide complexes and noncovalent interactions in organic compounds under the supervision of Prof. Mehdi D. Esrafili in Iran.

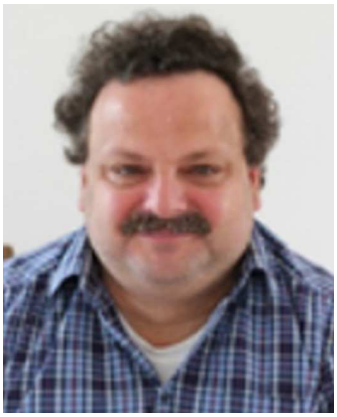

Andreas Gansäuer obtained his Ph.D. in the group of Prof. Reetz at the MPI für Kohlenforschung (Germany). After a postdoctoral position in the group of Prof. Trost at Stanford University (US), he completed his habilitation with Prof. Brückner. Since 2000 he is Professor of Organic Chemistry at the University of Bonn (Germany). His research interests include radical chemistry and catalysis. Both fields are ideally suited for mechanistic investigations in cooperation with theoretical and physical chemistry. These studies have led to the design of a number of novel catalytic radical reactions.

Oldamur Hollóczki received his Ph.D. in chemistry at the Budapest University of Technology and Economics (Hungary) in 2011. In 2012 he received the prestigious Alexander von Humboldt Fellowship, which allowed him to join the research group of Prof. Barbara Kirchner in Leipzig and later Bonn in Germany. From 2015 on, he was a leader of a junior research group at the University of Bonn (Germany), where he did his habilitation in 2021. Since 2021, he has a permanent position at the University of Debrecen (Hungary), where he is currently working on research in various fields, including organocatalysis, nanoplastics, and sustainable chemistry through quantum chemical calculations and classical and *ab initio* molecular dynamics simulations.

■ ACKNOWLEDGMENTS

The authors thank the DFG under the grant project number 406232243 for financial support and the University of Bonn for granting access to the Bonna cluster and the TRA matter for financial support. The authors also thank all the excellent researchers working on ionic liquids, especially those that did not enter this Perspective but nevertheless do not fail to impress us.

■ REFERENCES

(1) Pálvölgyi, Á. M.; Bitai, J.; Zeindlhofer, V.; Schröder, C.; Bica, K. Ion-Tagged Chiral Ligands for Asymmetric Transfer Hydrogenations in Aqueous Medium. *ACS Sustainable Chem. Eng.* **2019**, *7*, 3414−3423.
(2) Sang, S.; Unruh, T.; Demeshko, S.; Domenianni, L. I.; van Leest, N. P.; Marquetand, P.; Schneck, F.; Würtele, C.; de Zwart, F. J.; de Bruin, B.; et al. Photo-Initiated Cobalt-Catalyzed Radical Olefin Hydrogenation. *Chem.—Eur. J.* **2021**, *27*, 16978−16989.
(3) Hilche, T.; Reinsberg, P. H.; Klare, S.; Liedtke, T.; Schäfer, L.; Gansäuer, A. Design Platform for Sustainable Catalysis with Radicals: Electrochemical Activation of Cp2TiCl2 for Catalysis Unveiled. *Chem.—Eur. J.* **2021**, *27*, 4903−4912.
(4) Capdevila-Cortada, M.; Łodziana, Z.; López, N. Performance of DFT+U Approaches in the Study of Catalytic Materials. *ACS Catal.* **2016**, *6*, 8370−8379.
(5) Flieger, J.; Flieger, M. Ionic liquids toxicity—benefits and threats. *Int. J. Mol. Sci.* **2020**, *21*, 6267.
(6) Cho, C.-W.; Pham, T. P. T.; Zhao, Y.; Stolte, S.; Yun, Y.-S. Review of the toxic effects of ionic liquids. *Sci. Total Environ.* **2021**, *786*, 147309.
(7) Marion, S.; Vučemilović-Alagić, N.; Špadina, M.; Radenović, A.; Smith, A.-S. From Water Solutions to Ionic Liquids with Solid State Nanopores as a Perspective to Study Transport and Translocation Phenomena. *Small* **2021**, *17*, 2100777.
(8) Alizadeh, V.; Malberg, F.; Pádua, A. A. H.; Kirchner, B. Are there magic compositions in deep eutectic solvents? effects of composition and water content in choline chloride/ethylene glycol from ab initio molecular dynamics. *J. Phys. Chem. B* **2020**, *124*, 7433−7443.
(9) Doherty, B.; Zhong, X.; Acevedo, O. Virtual site OPLS force field for imidazolium-based ionic liquids. *J. Phys. Chem. B* **2018**, *122*, 2962−2974.
(10) Doherty, B.; Acevedo, O. OPLS force field for choline chloride-based deep eutectic solvents. *J. Phys. Chem. B* **2018**, *122*, 9982−9993.
(11) Zhong, X.; Velez, C.; Acevedo, O. Partial Charges Optimized by Genetic Algorithms for Deep Eutectic Solvent Simulations. *J. Chem. Theory Comput.* **2021**, *17*, 3078−3087.
(12) Neumann, J.; Golub, B.; Odebrecht, L.-M.; Ludwig, R.; Paschek, D. Revisiting imidazolium based ionic liquids: Effect of the conformation bias of the [NTf2] anion studied by molecular dynamics simulations. *J. Chem. Phys.* **2018**, *148*, 193828.
(13) Brehm, M.; Pulst, M.; Kressler, J.; Sebastiani, D. Triazolium-based ionic liquids: A novel class of cellulose solvents. *J. Phys. Chem. B* **2019**, *123*, 3994−4003.
(14) Gehrke, S.; Kirchner, B. Robustness of the hydrogen bond and ion pair dynamics in ionic liquids to different parameters from the reactive flux method. *J. Chem. Eng. Data* **2020**, *65*, 1146−1158.
(15) Alizadeh, V.; Geller, D.; Malberg, F.; Sánchez, P. B.; Padua, A.; Kirchner, B. Strong Microheterogeneity in Novel Deep Eutectic Solvents. *ChemPhysChem* **2019**, *20*, 1786−1792.
(16) Chaumont, A.; Engler, E.; Schurhammer, R. Is Charge Scaling Really Mandatory when Developing Fixed-Charge Atomistic Force Fields for Deep Eutectic Solvents? *J. Phys. Chem. B* **2020**, *124*, 7239−7250.
(17) Lewis, N. H. C.; Zhang, Y.; Dereka, B.; Carino, E. V.; Maginn, E. J.; Tokmakoff, A. Signatures of ion pairing and aggregation in the vibrational spectroscopy of super-concentrated aqueous lithium bistriflimide solutions. *J. Phys. Chem. C* **2020**, *124*, 3470−3481.
(18) Alizadeh, V.; Kirchner, B. Molecular level insight into the solvation of cellulose in deep eutectic solvents. *J. Chem. Phys.* **2021**, *155*, 084501.
(19) Gehrke, S.; Ray, P.; Stettner, T.; Balducci, A.; Kirchner, B. Water in Protic Ionic Liquid Electrolytes: From solvent separated ion pairs to water clusters. *ChemSusChem* **2021**, *14*, 3315−3324.
(20) Alfurayj, I.; Fraenza, C. C.; Zhang, Y.; Pandian, R.; Spittle, S.; Hansen, B.; Dean, W.; Gurkan, B.; Savinell, R.; Greenbaum, S.; et al. Solvation Dynamics of Wet Ethaline: Water is the Magic Component. *J. Phys. Chem. B* **2021**, *125*, 8888−8901.
(21) Zhang, Y.; Lewis, N. H. C.; Mars, J.; Wan, G.; Weadock, N. J.; Takacs, C. J.; Lukatskaya, M. R.; Steinrück, H.-G.; Toney, M. F.; Tokmakoff, A.; et al. Water-in-Salt LiTFSI Aqueous Electrolytes. 1. Liquid Structure from Combined Molecular Dynamics Simulation and Experimental Studies. *J. Phys. Chem. B* **2021**, *125*, 4501−4513.
(22) Livraghi, M.; Höllring, K.; Wick, C. R.; Smith, D. M.; Smith, A.-S. An Exact Algorithm to Detect the Percolation Transition in Molecular Dynamics Simulations of Cross-Linking Polymer Networks. *J. Chem. Theory Comput.* **2021**, *17*, 6449−6457.
(23) Schade, R.; Kenter, T.; Elgabarty, H.; Lass, M.; Schütt, O.; Lazzaro, A.; Pabst, H.; Mohr, S.; Hutter, J.; Kühne, T. D.; et al. Enabling Electronic Structure-Based Ab-Initio Molecular Dynamics Simulations with Hundreds of Millions of Atoms. arXiv preprint 16.04.2021, arXiv:2104.08245.
(24) Blasius, J.; Zaby, P.; Hollóczki, O.; Kirchner, B. Recognition in Chiral Ionic Liquids: The Achiral Cation Makes the Difference. *J. Org. Chem.* **2021**, DOI: 10.1021/acs.joc.1c00939.
(25) Esser, L.; Macchieraldo, R.; Elfgen, R.; Sieland, M.; Smarsly, B. M.; Kirchner, B. $TiCl_4$ Dissolved in Ionic Liquid Mixtures from Ab Initio Molecular Dynamics Simulations. *Molecules* **2021**, *26*, 79.
(26) Alizadeh, V.; Esser, L.; Kirchner, B. How is CO_2 absorbed into a deep eutectic solvent? *J. Chem. Phys.* **2021**, *154*, 094503.
(27) Fetisov, E. O.; Harwood, D. B.; Kuo, I.-F. W.; Warrag, S. E.; Kroon, M. C.; Peters, C. J.; Siepmann, J. I. First-principles molecular dynamics study of a deep eutectic solvent: Choline chloride/urea and its mixture with water. *J. Phys. Chem. B* **2018**, *122*, 1245−1254.
(28) Contreras, R.; Lodeiro, L.; Rozas-Castro, N.; Ormazábal-Toledo, R. On the role of water in the hydrogen bond network in DESs: an ab initio molecular dynamics and quantum mechanical study on the urea-betaine system. *Phys. Chem. Chem. Phys.* **2021**, *23*, 1994−2004.

(29) Zhang, Y.; Poe, D.; Heroux, L.; Squire, H.; Doherty, B. W.; Long, Z.; Dadmun, M.; Gurkan, B.; Tuckerman, M. E.; Maginn, E. J. Liquid structure and transport properties of the deep eutectic solvent ethaline. *J. Phys. Chem. B* **2020**, *124*, 5251−5264.
(30) Malik, A.; Dhattarwal, H. S.; Kashyap, H. K. Distinct Solvation Structures of CO_2 and SO2 in Reline and Ethaline Deep Eutectic Solvents Revealed by AIMD Simulations. *J. Phys. Chem. B* **2021**, *125*, 1852−1860.
(31) Wylie, L.; Seeger, Z. L.; Hancock, A. N.; Izgorodina, E. I. Increased stability of nitroxide radicals in ionic liquids: more than a viscosity effect. *Phys. Chem. Chem. Phys.* **2019**, *21*, 2882−2888.
(32) Wylie, L.; Oyaizu, K.; Karton, A.; Yoshizawa-Fujita, M.; Izgorodina, E. I. Toward improved performance of all-organic nitroxide radical batteries with ionic liquids: a theoretical perspective. *ACS Sustainable Chem. Eng.* **2019**, *7*, 5367−5375.
(33) Heid, E.; Hunt, P. A.; Schröder, C. Evaluating excited state atomic polarizabilities of chromophores. *Phys. Chem. Chem. Phys.* **2018**, *20*, 8554−8563.
(34) Seeger, Z. L.; Izgorodina, E. I. A Systematic Study of DFT Performance for Geometry Optimizations of Ionic Liquid Clusters. *J. Chem. Theory Comput.* **2020**, *16*, 6735−6753.
(35) Philippi, F.; Rauber, D.; Kuttich, B.; Kraus, T.; Kay, C. W. M.; Hempelmann, R.; Hunt, P. A.; Welton, T. Ether functionalisation, ion conformation and the optimization of macroscopic properties in ionic liquids. *Phys. Chem. Chem. Phys.* **2020**, *22*, 23038−23056.
(36) Philippi, F.; Pugh, D.; Rauber, D.; Welton, T.; Hunt, P. A. Conformational design concepts for anions in ionic liquids. *Chem. Sci.* **2020**, *11*, 6405−6422.
(37) Rowe, R.; Lovelock, K. R. J.; Hunt, P. A. Bi (III) halometallate ionic liquids: Interactions and speciation. *J. Chem. Phys.* **2021**, *155*, 014501.
(38) Perlt, E.; Ray, P.; Hansen, A.; Malberg, F.; Grimme, S.; Kirchner, B. Finding the best density functional approximation to describe interaction energies and structures of ionic liquids in molecular dynamics studies. *J. Chem. Phys.* **2018**, *148*, 193835.
(39) Rodríguez-Fernández, C. D.; Lago, E. L.; Schröder, C.; Varela, L. M. Non-additive electronic polarizabilities of ionic liquids: Charge delocalization effects. *J. Mol. Liq.* **2022**, *346*, 117099.
(40) Heid, E.; Fleck, M.; Chatterjee, P.; Schröder, C.; MacKerell, A. D., Jr. Toward prediction of electrostatic parameters for force fields that explicitly treat electronic polarization. *J. Chem. Theory Comput.* **2019**, *15*, 2460−2469.
(41) Low, K.; Tan, S. Y. S.; Izgorodina, E. I. An ab initio study of the structure and energetics of hydrogen bonding in ionic liquids. *Front. Chem.* **2019**, *7*, 208.
(42) Bodo, E.; Bonomo, M.; Mariani, A. Assessing the Structure of Protic Ionic Liquids Based on Triethylammonium and Organic Acid Anions. *J. Phys. Chem. B* **2021**, *125*, 2781−2792.
(43) Goloviznina, K.; Gong, Z.; Pádua, A. A. H. The CL &Pol polarizable force field for the simulation of ionic liquids and eutectic solvents. *Wiley Interdiscip. Rev. Comput. Mol. Sci.* **2021**, e1572.
(44) Goloviznina, K.; Canongia Lopes, J. N.; Costa Gomes, M.; Pádua, A. A. H. Transferable, Polarizable Force Field for Ionic Liquids. *J. Chem. Theory Comput.* **2019**, *15*, 5858−5871.
(45) Xu, L.; Izgorodina, E. I.; Coote, M. L. Ordered solvents and ionic liquids can be harnessed for electrostatic catalysis. *J. Am. Chem. Soc.* **2020**, *142*, 12826−12833.
(46) de Oliveira Cavalcante, A.; Chelli, R. Polarizability relaxation in water/ethanol mixtures. *J. Mol. Liq.* **2021**, *332*, 115839.
(47) Szabadi, A.; Elfgen, R.; Macchieraldo, R.; Kearns, F. L.; Woodcock, H. L.; Kirchner, B.; Schröder, C. Comparison between ab initio and polarizable molecular dynamics simulations of 1-butyl-3-methylimidazolium tetrafluoroborate and chloride in water. *J. Mol. Liq.* **2021**, *337*, 116521.
(48) Sharma, S.; Ivanov, A. S.; Margulis, C. J. A Brief Guide to the Structure of High-Temperature Molten Salts and Key Aspects Making Them Different from Their Low-Temperature Relatives, the Ionic Liquids. *J. Phys. Chem. B* **2021**, *125*, 6359−6372.
(49) Miao, L.; Song, Z.; Zhu, D.; Li, L.; Gan, L.; Liu, M. Ionic Liquids for Supercapacitive Energy Storage: A Mini-Review. *Energy Fuels* **2021**, *35*, 8443−8455.
(50) Stettner, T.; Balducci, A. Protic ionic liquids in energy storage devices: Past, present and future perspective. *Energy Storage Mater.* **2021**, *40*, 402−414.
(51) Liu, F.; Yu, J.; Qazi, A. B.; Zhang, L.; Liu, X. Metal-Based Ionic Liquids in Oxidative Desulfurization: A Critical Review. *Environ. Sci. Technol.* **2021**, *55*, 1419−1435.
(52) Scalfi, L.; Salanne, M.; Rotenberg, B. Molecular simulation of electrode-solution interfaces. *Annu. Rev. Phys. Chem.* **2021**, *72*, 189−212.
(53) Salanne, M. Ionic liquids for supercapacitor applications. *Top. Curr. Chem.* **2017**, *375*, 63.
(54) Dufils, T.; Jeanmairet, G.; Rotenberg, B.; Sprik, M.; Salanne, M. Simulating Electrochemical Systems by Combining the Finite Field Method with a Constant Potential Electrode. *Phys. Rev. Lett.* **2019**, *123*, 195501.
(55) Jonsson, E. Ionic liquids as electrolytes for energy storage applications-A modelling perspective. *Energy Storage Mater.* **2020**, *25*, 827−835.
(56) Groves, T. S.; Perez-Martinez, C. S.; Lhermerout, R.; Perkin, S. Surface Forces and Structure in a Water-in-Salt Electrolyte. *J. Phys. Chem. Lett.* **2021**, *12*, 1702−1707.
(57) Harper, J. B.; Kirchner, B.; Pavez, P.; Welton, T. Non-traditional solvent effects in organic reactions. *Phys. Chem. Chem. Phys.* **2021**, *23*, 26028−26029.
(58) Brzeczek-Szafran, A.; Wiecławik, J.; Barteczko, N.; Szelwicka, A.; Byrne, E.; Kolanowska, A.; Kwaśny, M. S.; Chrobok, A. Protic ionic liquids from di-or triamines: even cheaper Brønsted acidic catalysts. *Green Chem.* **2021**, *23*, 4421−4429.
(59) Hallett, J. P.; Welton, T. Room-Temperature Ionic Liquids: Solvents for Synthesis and Catalysis. 2. *Chem. Rev.* **2011**, *111*, 3508−3576.
(60) Tanner, E. E. L.; Hawker, R. R.; Yau, H. M.; Croft, A. K.; Harper, J. B. Probing the importance of ionic liquid structure: A general ionic liquid effect on an SN Ar process. *Org. Biomol. Chem.* **2013**, *11*, 7516−7521.
(61) Harper, J.; Kobrak, M. Understanding organic processes in ionic liquids: Achievements so far and challenges remaining. *Mini Rev. Org. Chem.* **2006**, *3*, 253−269.
(62) Harper, J. B.; Lynden-Bell, R. Macroscopic and microscopic properties of solutions of aromatic compounds in an ionic liquid. *Mol. Phys.* **2004**, *102*, 85−94.
(63) Yau, H. M.; Keaveney, S. T.; Butler, B. J.; Tanner, E. E.; Guerry, M. S.; George, S. R. D.; Dunn, M. H.; Croft, A. K.; Harper, J. B. Towards solvent-controlled reactivity in ionic liquids. *Pure Appl. Chem.* **2013**, *85*, 1979−1990.
(64) D'Anna, F.; Frenna, V.; Noto, R.; Pace, V.; Spinelli, D. Study of aromatic nucleophilic substitution with amines on nitrothiophenes in room-temperature ionic liquids: Are the different effects on the behavior of para-like and ortho-like isomers on going from conventional solvents to room-temperature ionic liquids related to solvation effects? *J. Org. Chem.* **2006**, *71*, 5144−5150.
(65) Marullo, S.; D'Anna, F.; Rizzo, C.; Billeci, F. Ionic liquid-s:"normal" solvents or nanostructured fluids? *Org. Biomol. Chem.* **2021**, *19*, 2076−2095.
(66) Chiappe, C.; Pieraccini, D. Ionic liquids: solvent properties and organic reactivity. *J. Phys. Org. Chem.* **2005**, *18*, 275−297.
(67) Wasserscheid, P.; Bösmann, A.; Bolm, C. Synthesis and properties of ionic liquids derived from the 'chiral pool'. *Chem. Commun.* **2002**, 200−201.
(68) Schulz, P. S.; Müller, N.; Bösmann, A.; Wasserscheid, P. Effective chirality transfer in ionic liquids through ion-pairing effects. *Angew. Chem., Int. Ed.* **2007**, *46*, 1293−1295.
(69) Bösmann, A.; Schulz, P. S.; Wasserscheid, P. Enhancing task specific ionic liquids' thermal stability by structural modification. *Monatsh. Chem.* **2007**, *138*, 1159−1161.

https://doi.org/10.1021/acs.jpcb.1c09092
J. Phys. Chem. B 2022, 126, 766−777

(70) Ding, J.; Armstrong, D. W. Chiral ionic liquids: synthesis and applications. *Chirality* **2005**, *17*, 281−292.
(71) Bica, K.; Gaertner, P. Applications of chiral ionic liquids. *Eur. J. Org. Chem.* **2008**, *2008*, 3235−3250.
(72) Ohno, H.; Fukumoto, K. Amino acid ionic liquids. *Acc. Chem. Res.* **2007**, *40*, 1122−1129.
(73) Strehmel, V. Radicals in ionic liquids. *ChemPhysChem* **2012**, *13*, 1649−1663.
(74) Wishart, J. F. *Ionic Liquids: Current State and Future Directions*; ACS: 2017; pp 251−272.
(75) Hayes, R.; Warr, G. G.; Atkin, R. Structure and Nanostructure in Ionic Liquids. *Chem. Rev.* **2015**, *115*, 6357−6426.
(76) Elfgen, R.; Holloczki, O.; Kirchner, B. A molecular level understanding of template effects in ionic liquids. *Acc. Chem. Res.* **2017**, *50*, 2949−2957.
(77) Allen, C.; Ghebreab, R.; Doherty, B.; Li, B.; Acevedo, O. Examining ionic liquid effects on mononuclear rearrangement of heterocycles using QM/MM simulations. *J. Phys. Chem. B* **2016**, *120*, 10786−10796.
(78) Velez, C.; Doherty, B.; Acevedo, O. Accurate Diels-Alder energies and Endo selectivity in ionic liquids using the OPLS-VSIL force field. *Int. J. Mol. Sci.* **2020**, *21*, 1190.
(79) Freire, M. G.; Neves, C. M. S. S.; Marrucho, I. M.; Coutinho, J. A. P.; Fernandes, A. M. Hydrolysis of Tetrafluoroborate and Hexafluorophosphate Counter Ions in Imidazolium-Based Ionic Liquids. *J. Phys. Chem. A* **2010**, *114*, 3744−3749.
(80) Firaha, D. S.; Kirchner, B. Tuning the carbon dioxide absorption in amino acid ionic liquids. *ChemSusChem* **2016**, *9*, 1591−1599.
(81) Bhargava, B.; Balasubramanian, S. Insights into the structure and dynamics of a room-temperature ionic liquid: ab initio molecular dynamics simulation studies of 1-n-butyl-3-methylimidazolium hexafluorophosphate ([bmim][PF6]) and the [bmim][PF6]- CO_2 mixture. *J. Phys. Chem. B* **2007**, *111*, 4477−4487.
(82) Goel, H.; Windom, Z. W.; Jackson, A. A.; Rai, N. Performance of density functionals for modeling vapor liquid equilibria of CO_2 and SO_2. *J. Comput. Chem.* **2018**, *39*, 397−406.
(83) Kirchner, B.; Seitsonen, A. P. Ionic Liquids from Car-Parrinello Simulations. 2. Structural Diffusion Leading to Large Anions in Chloraluminate Ionic Liquids. *Inorg. Chem.* **2007**, *46*, 2751−2754.
(84) Ballone, P.; Cortes-Huerto, R. Ab initio simulations of thermal decomposition and of electron transfer reactions in room temperature ionic liquids. *Faraday Discuss.* **2012**, *154*, 373−389.
(85) Firaha, D. S.; Hollóczki, O.; Kirchner, B. Computer-aided design of ionic liquids as CO_2 absorbents. *Angew. Chem., Int. Ed.* **2015**, *54*, 7805−7809.
(86) Firaha, D. S.; Hollóczki, O.; Kirchner, B. Computer-gestütztes Design ionischer Flüssigkeiten zur CO_2-Absorption. *Angew. Chem.* **2015**, *127*, 7916−7920.
(87) Firaha, D. S.; Kirchner, B. CO_2 absorption in the protic ionic liquid ethylammonium nitrate. *J. Chem. Eng. Data* **2014**, *59*, 3098−3104.
(88) Holloczki, O.; Firaha, D. S.; Friedrich, J.; Brehm, M.; Cybik, R.; Wild, M.; Stark, A.; Kirchner, B. Carbene formation in ionic liquids: spontaneous, induced, or prohibited? *J. Phys. Chem. B* **2013**, *117*, 5898−5907.
(89) Yamada, H. Comparison of solvation effects on CO_2 capture with aqueous amine solutions and amine-functionalized ionic liquids. *J. Phys. Chem. B* **2016**, *120*, 10563−10568.
(90) Luo, X. Y.; Lv, X. Y.; Shi, G. L.; Meng, Q.; Li, H. R.; Wang, C. M. Designing amino-based ionic liquids for improved carbon capture: One amine binds two CO_2. *AIChE J.* **2019**, *65*, 230−238.
(91) Shaikh, A. R.; Ashraf, M.; AlMayef, T.; Chawla, M.; Poater, A.; Cavallo, L. Amino acid ionic liquids as potential candidates for CO_2 capture: combined density functional theory and molecular dynamics simulations. *Chem. Phys. Lett.* **2020**, *745*, 137239.
(92) Ingenmey, J.; Gehrke, S.; Kirchner, B. How to harvest Grotthuss diffusion in protic ionic liquid electrolyte systems. *ChemSusChem* **2018**, *11*, 1900−1910.
(93) Le Donne, A.; Adenusi, H.; Porcelli, F.; Bodo, E. Structural features of cholinium based protic ionic liquids through molecular dynamics. *J. Phys. Chem. B* **2019**, *123*, 5568−5576.
(94) Hollóczki, O.; Wolff, A.; Pallmann, J.; Whiteside, R. E.; Hartley, J.; Grasser, M. A.; Nockemann, P.; Brunner, E.; Doert, T.; Ruck, M. Spontaneous Substitutions at Phosphorus Trihalides in Imidazolium Halide Ionic Liquids: Grotthuss Diffusion of Anions. *Chem.—Eur. J.* **2018**, *24*, 16323−16331.
(95) Hollóczki, O. Toward Anionic Structural Diffusion and Highly Conducting Ionic Liquid Electrolytes. *ACS Sustain. Chem. Eng.* **2019**, *7*, 2626−2633.
(96) Dreßler, C.; Kabbe, G.; Brehm, M.; Sebastiani, D. Exploring non-equilibrium molecular dynamics of mobile protons in the solid acid CsH2PO4 at the micrometer and microsecond scale. *J. Chem. Phys.* **2020**, *152*, 164110.
(97) Dreßler, C.; Kabbe, G.; Brehm, M.; Sebastiani, D. Dynamical matrix propagator scheme for large-scale proton dynamics simulations. *J. Chem. Phys.* **2020**, *152*, 114114.
(98) Urbach, C.; Jansen, K.; Shindler, A.; Wenger, U. HMC algorithm with multiple time scale integration and mass preconditioning. *Comput. Phys. Commun.* **2006**, *174*, 87−98.
(99) Bannwarth, C.; Caldeweyher, E.; Ehlert, S.; Hansen, A.; Pracht, P.; Seibert, J.; Spicher, S.; Grimme, S. Extended tight-binding quantum chemistry methods. *Wiley Interdiscip. Rev. Comput. Mol. Sci.* **2021**, *11*, e1493.
(100) Perlt, E.; Ray, P.; Hansen, A.; Malberg, F.; Grimme, S.; Kirchner, B. Finding the best density functional approximation to describe interaction energies and structures of ionic liquids in molecular dynamics studies. *J. Chem. Phys.* **2018**, *148*, 193835.
(101) Zentel, T.; Overbeck, V.; Michalik, D.; Kühn, O.; Ludwig, R. Hydrogen bonding in protic ionic liquids: structural correlations, vibrational spectroscopy, and rotational dynamics of liquid ethylammonium nitrate. *J. Phys. B: At. Mol. Opt. Phys.* **2018**, *51*, 034002.
(102) Karu, K.; Elhi, F.; Põhako-Esko, K.; Ivaništšev, V. Predicting Melting Points of Biofriendly Choline-Based Ionic Liquids with Molecular Dynamics. *Appl. Sci.* **2019**, *9*, 5367.
(103) Mosquera, M. A.; Jones, L. O.; Ratner, M. A.; Schatz, G. C. Quantum embedding for material chemistry based on domain separation and open subsystems. *Int. J. Quantum Chem.* **2020**, *120*, e26184.
(104) Oulevey, P.; Luber, S.; Varnholt, B.; Bürgi, T. Symmetry breaking in chiral ionic liquids evidenced by vibrational optical activity. *Angew. Chem., Int. Ed.* **2016**, *55*, 11787−11790.
(105) Oulevey, P.; Luber, S.; Varnholt, B.; Bürgi, T. Symmetriebruch in chiralen ionischen Flüssigkeiten: Nachweis durch vibratorisch-optische Aktivität. *Angew. Chem.* **2016**, *128*, 11962−11966.
(106) Ghidinelli, S.; Abbate, S.; Mazzeo, G.; Boiadjiev, S. E.; Lightner, D. A.; Longhi, G. Biliverdin chiral derivatives as chiroptical switches for pH and metal cation sensing. *Phys. Chem. Chem. Phys.* **2021**, *23*, 20138−20151.
(107) Koenis, M. A.; Nicu, V. P.; Visscher, L.; Kuehn, C.; Bremer, M.; Krier, M.; Untenecker, H.; Zhumaev, U.; Küstner, B.; Buma, W. J. Vibrational circular dichroism studies of exceptionally strong chirality inducers in liquid crystals. *Phys. Chem. Chem. Phys.* **2021**, *23*, 10021−10028.
(108) Weirich, L.; Merten, C. Induced VCD and conformational chirality in host-guest complexes of a chiral ammonium salt with crown ethers. *Phys. Chem. Chem. Phys.* **2021**, *23*, 18300−18307.
(109) Blasius, J.; Kirchner, B. Cluster-Weighting in Bulk Phase Vibrational Circular Dichroism. *J. Phys. Chem. B* **2020**, *124*, 7272−7283.
(110) Jähnigen, S.; Scherrer, A.; Vuilleumier, R.; Sebastiani, D. Chiral crystal packing induces enhancement of vibrational circular dichroism. *Angew. Chem., Int. Ed.* **2018**, *57*, 13344−13348.
(111) Jähnigen, S.; Scherrer, A.; Vuilleumier, R.; Sebastiani, D. VCD-Verstärkung durch chirale Packungseffekte in molekularen Kristallen. *Angew. Chem.* **2018**, *130*, 13528−13532.
(112) Le Barbu-Debus, K.; Bowles, J.; Jähnigen, S.; Clavaguéra, C.; Calvo, F.; Vuilleumier, R.; Zehnacker, A. Assessing cluster models of

https://doi.org/10.1021/acs.jpcb.1c09092
J. Phys. Chem. B 2022, 126, 766−777

solvation for the description of vibrational circular dichroism spectra: synergy between static and dynamic approaches. *Phys. Chem. Chem. Phys.* **2020**, *22*, 26047−26068.
(113) Kirchner, B.; Blasius, J.; Esser, L.; Reckien, W. Predicting Vibrational Spectroscopy for Flexible Molecules and Molecules with Non-Idle Environments. *Adv. Theory Simul.* **2021**, *4*, 2000223.
(114) Abbate, S.; Longhi, G.; Kwon, K.; Moscowitz, A. The use of cross-correlation functions in the analysis of circular dichroism spectra. *J. Chem. Phys.* **1998**, *108*, 50−62.
(115) Thomas, M.; Brehm, M.; Kirchner, B. Voronoi dipole moments for the simulation of bulk phase vibrational spectra. *Phys. Chem. Chem. Phys.* **2015**, *17*, 3207−3213.
(116) Thomas, M.; Kirchner, B. Classical magnetic dipole moments for the simulation of vibrational circular dichroism by ab initio molecular dynamics. *J. Phys. Chem. Lett.* **2016**, *7*, 509−513.
(117) Blasius, J.; Elfgen, R.; Hollóczki, O.; Kirchner, B. Glucose in dry and moist ionic liquid: vibrational circular dichroism, IR, and possible mechanisms. *Phys. Chem. Chem. Phys.* **2020**, *22*, 10726−10737.
(118) von Domaros, M.; Perlt, E.; Ingenmey, J.; Marchelli, G.; Kirchner, B. Peacemaker 2: Making clusters talk about binary mixtures and neat liquids. *SoftwareX* **2018**, *7*, 356−359.
(119) Koner, D.; Salehi, S. M.; Mondal, P.; Meuwly, M. Non-conventional force fields for applications in spectroscopy and chemical reaction dynamics. *J. Chem. Phys.* **2020**, *153*, 010901.
(120) André, F.; Hapiot, P.; Lagrost, C. Dimerization of ion radicals in ionic liquids. An example of favourable "Coulombic" solvation. *Phys. Chem. Chem. Phys.* **2010**, *12*, 7506−7512.
(121) Wylie, L.; Blesch, T.; Freeman, R.; Hatakeyama-Sato, K.; Oyaizu, K.; Yoshizawa-Fujita, M.; Izgorodina, E. I. Reversible Reduction of the TEMPO Radical: One Step Closer to an All-Organic Redox Flow Battery. *Chem. Eng.* **2020**, *8*, 17988−17996.
(122) Wylie, L.; Hakatayama-Sato, K.; Go, C.; Oyaizu, K.; Izgorodina, E. I. Electrochemical characterization and thermodynamic analysis of TEMPO derivatives in ionic liquids. *Phys. Chem. Chem. Phys.* **2021**, *23*, 10205−10217.
(123) Tan, S.; Barrera Acevedo, S.; Izgorodina, E. I. Generalized spin-ratio scaled MP2 method for accurate prediction of intermolecular interactions for neutral and ionic species. *J. Chem. Phys.* **2017**, *146*, 064108.
(124) Knudtzon, M. N.; Blank, D. A. Photodetachment and Electron Dynamics in 1-Butyl-1-methyl-pyrrolidinium Dicyanamide. *J. Phys. Chem. B* **2020**, *124*, 9144−9153.
(125) Leier, J.; Michenfelder, N. C.; Unterreiner, A.-N. Understanding the Photoexcitation of Room Temperature Ionic Liquids. *ChemistryOpen* **2021**, *10*, 72−82.
(126) Wang, Z.; Zhang, L.; Cukier, R. I.; Bu, Y. States and migration of an excess electron in a pyridinium-based, room-temperature ionic liquid: an ab initio molecular dynamics simulation exploration. *Phys. Chem. Chem. Phys.* **2010**, *12*, 1854−1861.
(127) Becke, A. D. Density-functional exchange-energy approximation with correct asymptotic behavior. *Phys. Rev. A* **1988**, *38*, 3098.
(128) Lee, C.; Yang, W.; Parr, R. G. Development of the Colle-Salvetti correlation-energy formula into a functional of the electron density. *Phys. Rev. B* **1988**, *37*, 785.
(129) Perdew, J. P.; Burke, K.; Ernzerhof, M. Generalized gradient approximation made simple. *Phys. Rev. Lett.* **1997**, *77*, 3865.
(130) Margulis, C. J.; Annapureddy, H. V. R.; De Biase, P. M.; Coker, D.; Kohanoff, J.; Del Pópolo, M. G. Dry excess electrons in room-temperature ionic liquids. *J. Am. Chem. Soc.* **2011**, *133*, 20186−20193.
(131) Roy, S.; Liu, Y.; Topsakal, M.; Dias, E.; Gakhar, R.; Phillips, W. C.; Wishart, J. F.; Leshchev, D.; Halstenberg, P.; Dai, S.; et al. A Holistic Approach for Elucidating Local Structure, Dynamics, and Speciation in Molten Salts with High Structural Disorder. *J. Am. Chem. Soc.* **2021**, *143*, 15298−15308.
(132) Gill, S. K.; Huang, J.; Mausz, J.; Gakhar, R.; Roy, S.; Vila, F.; Topsakal, M.; Phillips, W. C.; Layne, B.; Mahurin, S.; et al. Connections between the speciation and solubility of Ni (II) and Co (II) in molten ZnCl2. *J. Phys. Chem. B* **2020**, *124*, 1253−1258.
(133) Reeves, K. G.; Serva, A.; Jeanmairet, G.; Salanne, M. A first-principles investigation of the structural and electrochemical properties of biredox ionic species in acetonitrile. *Phys. Chem. Chem. Phys.* **2020**, *22*, 10561−10568.
(134) VandeVondele, J.; Hutter, J. Gaussian basis sets for accurate calculations on molecular systems in gas and condensed phases. *J. Chem. Phys.* **2007**, *127*, 114105.
(135) d'Avezac, M.; Calandra, M.; Mauri, F. Density functional theory description of hole-trapping in SiO_2: A self-interaction-corrected approach. *Phys. Rev. B* **2005**, *71*, 205210.
(136) Perdew, J. P.; Zunger, A. Self-interaction correction to density-functional approximations for many-electron systems. *Phys. Rev. B* **1981**, *23*, 5048.
(137) Berthin, R.; Serva, A.; Reeves, K. G.; Heid, E.; Schröder, C.; Salanne, M. Solvation of anthraquinone and TEMPO redox-active species in acetonitrile using a polarizable force field. *J. Chem. Phys.* **2021**, *155*, 074504.
(138) Gansäuer, A.; von Laufenberg, D.; Kube, C.; Dahmen, T.; Michelmann, A.; Behlendorf, M.; Sure, R.; Seddiqzai, M.; Grimme, S.; Sadasivam, D. V.; et al. Mechanistic study of the titanocene (III)-catalyzed radical arylation of epoxides. *Chem.−Eur. J.* **2015**, *21*, 280−289.
(139) Funk, P.; Richrath, R. B.; Bohle, F.; Grimme, S.; Gansäuer, A. Oxidation Under Reductive Conditions: From Benzylic Ethers to Acetals with Perfect Atom-Economy by Titanocene (III) Catalysis. *Angew. Chem., Int. Ed.* **2021**, *60*, 5482−5488.
(140) Weigend, F.; Ahlrichs, R. Balanced basis sets of split valence, triple zeta valence and quadruple zeta valence quality for H to Rn: Design and assessment of accuracy. *Phys. Chem. Chem. Phys.* **2005**, *7*, 3297−3305.
(141) Neese, F. The ORCA program system. *Wiley Interdiscip. Rev. Comput. Mol. Sci.* **2012**, *2*, 73−78.
(142) Hutter, J.; Iannuzzi, M.; Schiffmann, F.; VandeVondele, J. cp2k: atomistic simulations of condensed matter systems. *Wiley Interdiscip. Rev. Comput. Mol. Sci.* **2014**, *4*, 15−25.
(143) Perdew, J. P.; Ruzsinszky, A.; Csonka, G. I.; Vydrov, O. A.; Scuseria, G. E.; Constantin, L. A.; Zhou, X.; Burke, K. Restoring the density-gradient expansion for exchange in solids and surfaces. *Phys. Rev. Lett.* **2008**, *100*, 136406.
(144) Tao, J.; Perdew, J. P.; Staroverov, V. N.; Scuseria, G. E. Climbing the density functional ladder: Nonempirical meta-generalized gradient approximation designed for molecules and solids. *Phys. Rev. Lett.* **2003**, *91*, 146401.
(145) Ling, S.; Slater, B. Primary Basis Sets Optimised from Molecular Calculations. https://fossies.org/linux/cp2k/data/BASIS_MOLOPT_UCL (accessed: 2021-10-09).
(146) Guidon, M.; Hutter, J.; VandeVondele, J. Auxiliary density matrix methods for Hartree- Fock exchange calculations. *J. Chem. Theory Comput.* **2010**, *6*, 2348−2364.
(147) VandeVondele, J.; Krack, M.; Mohamed, F.; Parrinello, M.; Chassaing, T.; Hutter, J. Quickstep: Fast and accurate density functional calculations using a mixed Gaussian and plane waves approach. *Comput. Phys. Commun.* **2005**, *167*, 103−128.

https://doi.org/10.1021/acs.jpcb.1c09092
J. Phys. Chem. B 2022, 126, 766−777

H. Selective Chirality Transfer to the Bis(trifluoromethylsulfonyl)imide Anion of an Ionic Liquid

Jan Blasius* and Barbara Kirchner*

Received: 19 April 2023, Published online: 21 June 2023.

Reprinted (adapted) in appendix H with permission† from

J. Blasius and B. Kirchner, *Chem. Eur. J.* **2023**, e202301239.

doi:10.1002/chem.202301239.

For this article a Supporting Information is available free of charge at:
https://chemistry-europe.onlinelibrary.wiley.com/doi/abs/10.1002/chem.202301239.

Contributions to the manuscript

- Development of the concept
- Performance of all calculations
- Interpretation of the results
- Writing of the manuscript

*Mulliken Center for Theoretical Chemistry, Clausius Institute for Physical and Theoretical Chemistry, University of Bonn, Beringstr. 4–6, 53115 Bonn, Germany

10.1002/chem.202301239
WILEY-VCH

Selective Chirality Transfer to the Bis(trifluoromethylsulfonyl)imide Anion of an Ionic Liquid

Jan Blasius,[a] Barbara Kirchner*[a]

Chirality transfer from the chiral molecule (*R*)-1,2-propylene oxide to the achiral anion of the 1-ethyl-3-methylimidazolium bis(trifluoromethylsulfonyl)imide ionic liquid is observed. The chiral probe selectively affects only one part of the binary ionic liquid, i.e., it has been shown before experimentally and theoretically that the particular imidazolium cation can be affected by chirality transfer, but in the present system chirality is only transferred to the anion and not to both parts of the solvent (anion and cation). This observation is of high relevance because of its selectivity and because anion effects are usually much more important in ionic liquid research than cation effects. From *ab initio* molecular dynamics simulations, a conformational analysis and dissected vibrational circular dichroism spectra are obtained to study the chirality transfer. While in the neat ionic liquid two mirror imaged *trans* conformers of the anion occur almost equally, we observe an excess of one of these conformers in the presence of the chiral solute, causing optical activity of the anion. Although, the *cis* conformers are not tremendously affected by the chirality transfer, they gain in total population when (*R*)-1,2-propylene oxide is dissolved in the ionic liquid.

1. Introduction

Chirality is one of the most fundamental concepts in (bio)-chemistry, and accordingly there is an abundance of chiral substances, many of which are used in drug discovery, medical applications, separation processes or asymmetric catalysis. Among these substances, ionic liquids (ILs) are a particularly interesting class of solvents because they are formed from combinations of cations and anions. Being entirely composed of ions, ILs usually have cationic and anionic head groups together with attached side chains[1] and all parts of them can be functionalized[2] to serve a specific task. Often these task-specific effects are discussed in terms of components and in the majority of cases pronounced anion effects are observed, for example in the absorption of gases such as CO_2 in ILs.[3–5] Furthermore, the dominant role of the anion has recently been highlighted in battery and energy device electrolyte science[6–8] and even the reversion of the structural perturbation of DNA induced by fungicide through anions of an IL has been studied.[9]

[a] J. Blasius, Prof. Dr. B. Kirchner*
Mulliken Center for Theoretical Chemistry, Clausius-Institute for Physical and Theoretical Chemistry, University of Bonn, Beringstraße 4-6, D-53115 Bonn, Germany
E-mail: kirchner@thch.uni-bonn.de

Given the multitude of possible cation–anion combinations, many variations of ILs are possible and by introducing chiral units in one or both ions the subgroup of chiral ionic liquids (CILs) can be synthesized.[10,11] Prominent examples are for instance CILs that are based on ions from the chiral pool, e.g. amino acids.[12,13] Instead of employing permanently chiral ions to obtain CIL, it is also possible to design ILs based on achiral ions, which can, however, break their symmetry in a chiral environment. Bürgi and coworkers — who are experts in chirality transfer[14,15] — have recognized the importance of achiral ions early on and rightfully warned that "in the design of chiral ionic liquids for asymmetric synthesis [or other purposes], the structure of the achiral counter ion also has to be carefully considered."[16] This is certainly true for many organocatalytic and other reactions that haven been studied in ILs.[11,17–20] For other applications involving ILs, like for instance chiral separation or purification processes, one should be cautious as well.[11,21–23]

To highlight the importance of achiral ions in a chiral environment, Bürgi and coworkers used vibrational optical activity spectroscopy to show that the chiral anion of amino acid based CILs can induce chirality in the achiral 1-ethyl-3-methylimidazolium cation ($[C_2C_1Im]^+$).[16] In this particular case, the chirality transfer occurs by a symmetry breaking of the conformational distribution of the cation. On the other hand, our group investigated the structure of $[C_2C_1Im]^+$ in close proximity to chiral solutes by means of *ab initio* molecular dynamics (AIMD) simulations and calculated vibrational circular dichroism (VCD) spectra as well as by conformational analyses.[24,25] In particular, we observed that different forms of D-glucose dissolved in dry and moist 1-ethyl-3-methylimidazolium acetate ($[C_2C_1Im][OAc]$) can induce chirality in the achiral cation of the IL.[24] The chiral induction of the solute molecules onto the cation was evidenced by dissecting calculated VCD[26–33] spectra into the contributions of the individual ions and molecules. We observed a pronounced VCD activity of the cation with strong peaks above $1000\,cm^{-1}$. Thus, while in the above mentioned setup of Bürgi and coworkers a neat CIL was investigated, our setup contained chiral solute molecules dissolved in an achiral IL.

In a second study we dissolved a chiral solute (each (*R*)- and (*S*)-butan-2-ol) in the L-alaninate (i.e., (*S*)-alaninate) based CIL $[C_2C_1Im][L{-}ala]$, i.e. now the IL contains a chiral anion and we chose the achiral 1-ethyl-3-methylimidazolium as counterion.[24] We observed that the heterochiral system (i.e., (*R*)-butan-2-ol dissolved in $[C_2C_1Im][L{-}ala]$) is energetically more stabilized than the homochiral one (i.e., (*S*)-butan-2-ol dissolved in $[C_2C_1Im][L{-}ala]$). This energetic difference provides a clear distinction between the two systems. Interestingly, part of this stabilization originates

10.1002/chem.202301239
WILEY-VCH

from an asymmetrization of the cation which leads to more stable cation–solute encounter complexes (according to the three-point model[34]) in the heterochiral as compared to the homochiral system. This is also reflected by shorter cation–solute distances.

All of the above examples report chiral induction in achiral cations. However, as mentioned earlier, the anion usually has a much greater influence on the properties of an IL than the cation. Consequently, ILs that allow chiral induction effects in their achiral anions are of great interest for the design of e.g. separation processes or asymmetric catalysis.

2. Results and Discussion

To determine whether chirality transfer occurs at all, the calculation of VCD spectra and their decomposition into the contributions of the different species served as a promising approach before. Since VCD spectroscopy is the chiral version of infrared spectroscopy[26–33,35], it is very sensitive to the three-dimensional structure of molecules and aggregates. It is thus the perfect technique to investigate molecular conformations and conformational distributions. However, as calculated VCD spectra are very sensitive to conformational changes and intermolecular interactions,[25,36,37] they can suffer from an insufficient phase space sampling. To avoid such technical problems, we choose (*R*)-1,2-propylene oxide ((*R*)-PO) as chiral solute due to its very restricted conformational space. In addition, PO has been the subject of many VCD studies and is therefore well researched.[38–40] We simulated this molecule in the gas phase (labeled (*R*)-PO_{iso}) and in the achiral 1-ethyl-3-methylimidazolium bis(trifluoromethylsulfonyl) imide ($[C_2C_1Im][NTf_2]$) IL (labeled (*R*)-PO@IL) by means of AIMD simulations and employ an additional simulation of the neat IL for comparison (labeled IL).

AIMD simulations calculate the forces onto the atoms on the fly by solving the electronic structure in each instance. This allows to determine the electric ($\boldsymbol{\mu}$) and magnetic ($\mathbf{m}$) dipole moments in each time step and their cross-correlation[41] leads to the VCD spectrum $\Delta A(\omega)$ (Eq. 1) of the system:[42]

$$\Delta A(\omega) \propto \int_{-\infty}^{\infty} \left[\langle \dot{\boldsymbol{\mu}}(0) \cdot \dot{\mathbf{m}}(t) \rangle - \langle \dot{\mathbf{m}}(0) \cdot \dot{\boldsymbol{\mu}}(t) \rangle\right] e^{-i\omega t}\, \mathrm{d}t \quad (1)$$

with ω being the wavenumber and t is the time. Note that $\dot{\boldsymbol{\mu}}$ and $\dot{\mathbf{m}}$ are used because their correlation functions decay faster than those of $\boldsymbol{\mu}$ and $\mathbf{m}$, allowing the use of shorter simulation times.[35] In addition, although the calculated dipole moments certainly depend on the choice of reference point, especially for ionic systems, their general oscillations and thus their time derivatives are hardly affected by the chosen origin.[42] While Choi and Cho used classical definitions involving atomic partial charges to obtain the electric dipole moment,[43] we compute it by a radical Voronoi tessellation and subsequent integration of the electron density.[44] Similarly, we use for the magnetic dipole moment the classical definition for continuous current density distributions $\mathbf{j}(\mathbf{r})$:

$$\mathbf{m} = \frac{1}{2} \int_{\mathrm{Mol.}} \mathbf{r} \times \mathbf{j}(\mathbf{r})\, \mathrm{d}\mathbf{r} \quad (2)$$

In equation 2, $\mathbf{j}(\mathbf{r})$ is the electric current density and $\mathbf{r}$ the spatial coordinate. To obtain the current density, the following continuity equation is used:

$$\frac{\partial \rho(\mathbf{r})}{\partial t} + \nabla \cdot \mathbf{j}(\mathbf{r}) = 0 \quad (3)$$

The time derivative of the electron density $\rho(\mathbf{r})$ is obtained by finite differences of different simulation steps. As further condition the electric current density is chosen to be the product of the electron density and a conservative velocity field which avoids eddy currents:

$$\mathbf{j}(\mathbf{r}) = \rho(\mathbf{r})\mathbf{v}(\mathbf{r}) = -\rho(\mathbf{r})\nabla\alpha(\mathbf{r}) \quad (4)$$

This condition is necessary because in the continuity equation arbitrary eddy currents do not appear as changes of the electron density. Consequently, Eq. 3 alone does not uniquely determine the electric current density. Inserting Eq. 4 into the continuity equation and discretizing it by a finite difference approach allows to uniquely obtain the current density and subsequently the magnetic dipole moments. For analyzing the spectra and other structural features of the obtained trajectories we apply our trajectory analyzer TRAVIS.[45,46] The details of the calculations are presented in the supporting information.

In Figure 1 (top black spectrum) we show the validity of our approach by the simulated VCD spectrum of an isolated (*R*)-PO molecule in the gas phase. This spectrum compares excellent with experimental data[26,28] and previously calculated spectra from AIMD simulations[42] and quantum chemical calculations.[26,28,47] There is a pronounced

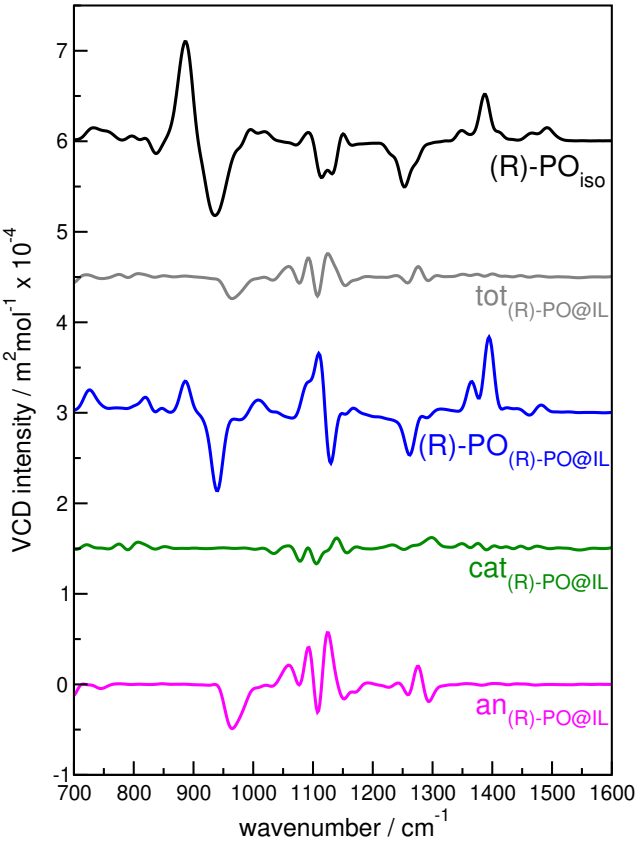

Figure 1. Calculated VCD spectra for the simulations (*R*)-PO_{iso} (black) and (*R*)-PO@IL. The total VCD spectrum of the (*R*)-PO@IL system is shown in grey, the individual contributions are shown for (*R*)-PO (blue), the $[C_1C_2Im]^+$ cation (green) and the $[NTf_2]^-$ anion (magenta). A large contribution from the anion to the spectrum is evidenced.

10.1002/chem.202301239
WILEY-VCH

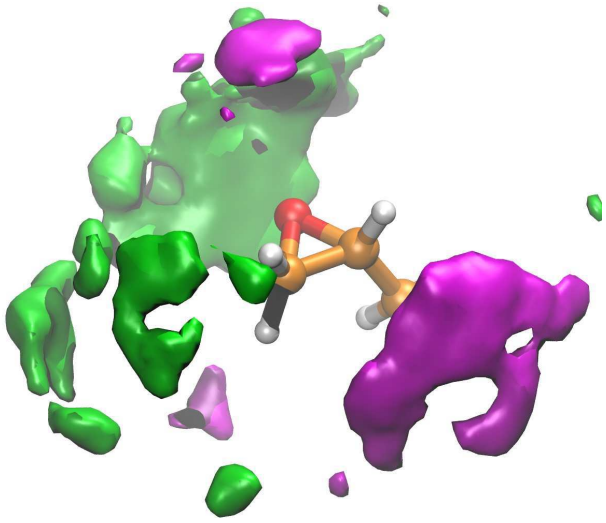

Figure 2. Spatial distribution functions for the system (*R*)-PO@IL with a maximum value of 76 %. The green surface contains all hydrogen atoms of the cation which are mostly located around the syn-side of the (*R*)-PO molecule. The magenta surface contains all oxygen and fluorine atoms of the anion which arrange around the anti-side of the (*R*)-PO molecule.

bisignate pattern between 850 cm^{-1} to 1000 cm^{-1}, a negative peak at around 1120 cm^{-1}, and a (−/+) signal between 1250 cm^{-1} to 1400 cm^{-1} in the gas phase. Compared to that, the total spectrum of the (*R*)-PO@IL system (grey spectrum in Figure 1) looks very different and is dominated by a (+/−/+/−/+) pattern between 1055 cm^{-1} to 1127 cm^{-1}. In addition, there is a negative peak at 960 cm^{-1} and a very small trisignate pattern at 1260 cm^{-1} to 1290 cm^{-1}. The pronounced difference of this spectrum compared to the one of (*R*)-PO_{iso} is a strong indication that (*R*)-PO is not the only species that contributes to the total spectrum of (*R*)-PO@IL.

Based on our computational approach, it is possible to consider the contributions from the individual molecules to the total spectrum of (*R*)-PO@IL, thus we show the contributions of (*R*)-PO (blue), the $[C_1C_2Im]^+$ cation (green), and the $[NTf_2]^-$ anion (magenta) in Figure 1. The spectrum of (*R*)-PO in (*R*)-PO@IL resembles the spectrum of the isolated (*R*)-PO molecule in (*R*)-PO_{iso}. However, the peaks are shifted by around 10 cm^{-1}, mostly to larger wavenumbers. Further changes of peak shapes and signs are observed at 840 cm^{-1} and between 1440 cm^{-1} to 1520 cm^{-1}. Moreover, the negative peak at around 1120 cm^{-1} changes to a (+/−) pattern when (*R*)-PO is dissolved in the IL. These changes are a strong indication for solvent effects and the presence of solute–IL interactions.

Turning to the individual contributions of the IL ions we observe two surprising results. First, contrary to our previous studies,[24,25] almost no contribution from the achiral cation to the total VCD spectrum of (*R*)-PO@IL is visible and only little perturbations in the region of 1060 cm^{-1} to 1140 cm^{-1} can be recognized. Second and very outstandingly, the anion shows a pronounced VCD activity and its spectrum contains many features that are similar to the ones observed in the total spectrum of (*R*)-PO@IL, i.e., the negative peak at 960 cm^{-1}, the (+/−/+/−/+) pattern between 1055 cm^{-1} to 1127 cm^{-1} and the trisignate pattern at 1260 cm^{-1} to 1290 cm^{-1}. This means that chirality is selectively transferred only to the anion and not to the cation.

Having determined that the anion is VCD active in (*R*)-PO@IL, we now try to unravel the (*R*)-PO–IL interactions in more detail. Upon inspection of the trajectory, we observe that the anions approach the (*R*)-PO molecule with their oxygen and fluorine atoms toward its stereo center $C^\star$, while the cations approach the oxygen atom of (*R*)-PO with their hydrogen atoms. In Figure 2 the spatial distribution functions of these distinct anion and cation atoms are shown. The green area clearly shows how the hydrogen atoms of the cation approach the oxygen atom of the (*R*)-PO molecule from the syn-side, i.e. the side of the methyl group, to form hydrogen bonds. The capability of the oxygen atom to accept hydrogen bonds was previously observed by Xu and coworkers in a study of PO dissolved in water.[38] Similarly, the magenta area shows that the fluorine and oxygen atoms of the anion approach the (*R*)-PO molecule at the hydrogen atom $H^\star$ attached to the stereo center $C^\star$, i.e., at the anti-side. Interestingly, Xu and coworkers were able to show that anti-conformations of PO@water clusters are energetically more stable than syn-conformations.[38] Consequently, chirality transfer in the water bending region was mainly observed for the anti-clusters. The authors assumed that the chirality transfer results from the explicit hydrogen bonding between water molecules and the chiral PO solute which fits well with the fact that in our case the anion experiences the symmetry breaking instead of the cation.[38]

To shed further light on the symmetry breaking of the $[NTf_2]^-$ anion, one first must understand the nature and more explicitly the conformations of the anion. The best description of the conformational space was provided by Canongia Lopes and coworkers.[48] Instead of analyzing the C−S−S−C pseudo dihedral — the S−S connection is interrupted by the sp^3-nitrogen atom —, they recommend to analyze the two proper dihedral angles consisting of the C−S−N−S chains. Canongia Lopes and coworkers discussed that, when these proper dihedral angles adopt values of either (90°, 90°) or (270°, 270°), this results in the *trans* conformer. On the other hand, when the C−S−N−S dihedral angles assume values of (90°, 230°) or (130°, 270°) the *cis* (or sometimes termed *gauche*) conformer is obtained. Altogether there are six possible combinations for these proper dihedrals, which result in two *trans* and four *cis* conformers of which each two *cis* conformers are identical. Thus, there are in total four conformations that remain, two *trans* and two *cis*. Importantly, within these conformers mirror images, i.e., enantiomeric conformers, are contained. An illustration of all possible dihedral rotations and conformers is shown in Figure 3.

To analyze the conformational distribution[49] of the $[NTf_2]^-$ anion, we show in Figure 4 combined distribution plots of the two proper C−S−N−S dihedral angles (◁C1–S1–N1–S2 versus ◁C2–S2–N1–S1) in the neat IL and in (*R*)-PO@IL. Additionally, we show the dihedral angle distribution of the $[NTf_2]^-$ anions in close proximity to (*R*)-PO together with ball-and-stick representations of the different conformers. The *trans* conformers (◁C−S−N−S = (90°, 90°) and (270°, 270°)) occur almost equally in the neat IL and show a higher population than the *cis* conformers. Turning to (*R*)-PO@IL, it is obvious that the occurrence of the *trans* conformers is not equal anymore, but there is an emphasize on the *trans* conformer t1 (◁C−S−N−S = (90°, 90°)) which can be confirmed if only the anions next to (*R*)-PO are observed (see Figure 4 lower left). Here it is clearly visible that anions anchored at the (*R*)-PO molecule preferably

10.1002/chem.202301239
WILEY-VCH

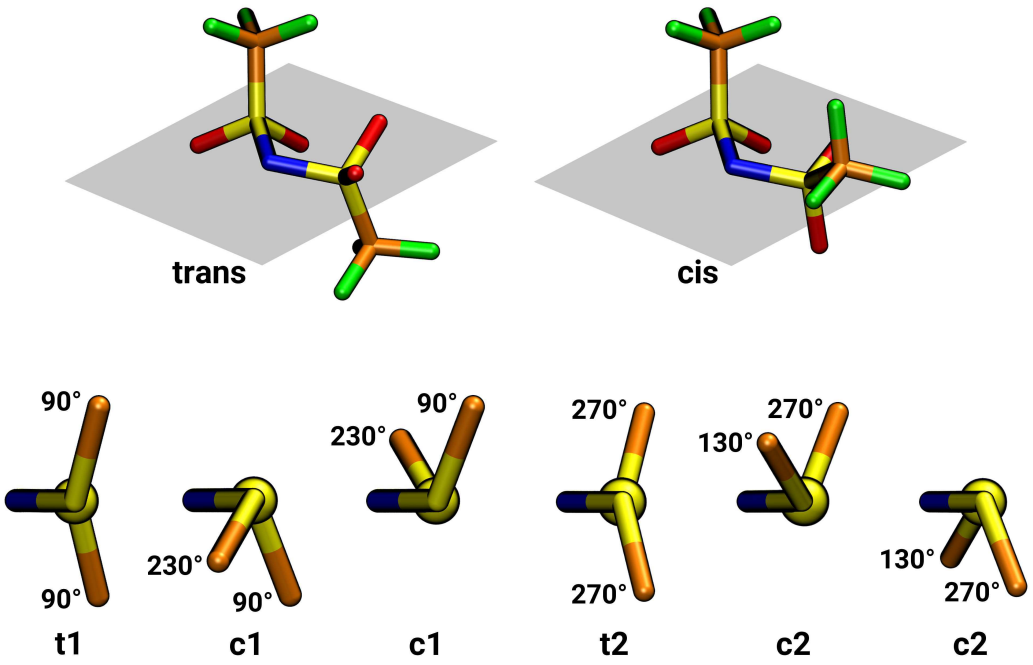

Figure 3. Top: Ball-and-stick images of the t2 *trans*- and c2 *cis*-conformers of $[NTf_2]^-$, the S−N−S plane is shown in grey. Bottom: Newman-like projections of all $[NTf_2]^-$ conformers showing the possible rotations of both C−S−N−S dihedrals. The color code for the atoms is: orange: carbon; blue: nitrogen; yellow: sulfur; red: oxygen; green: fluorine. Inspired by Canongia Lopes and coworkers.[48]

Table 1. Relative abundance in % of the four different bis(trifluoromethylsulfonyl)amide anion conformers in the neat IL and in (*R*)-PO@IL.

	t1	t2	c1	c2
IL	30.23	26.29	18.32	25.15
(*R*)-PO@IL	29.24	14.22	32.99	23.55

adopt the t1 over the mirrored t2 ($\sphericalangle$C−S−N−S = (270°, 270°)) conformation.

To put this qualitative discussion into quantitative numbers, we list in Table 1 the relative abundance of the four conformers which is obtained by integration of the corresponding peaks in Figure 4. From Table 1 we observe that approximately 57 % of the anions adopt a *trans* conformation in the neat IL while the remaining 43 % are present in *cis* conformation. This distribution changes upon addition of the chiral solute (*R*)-PO, i.e., 57 % of the anions in (*R*)-PO@IL adopt a *cis* conformation while only 43 % exist in a *trans* conformation. Already at this point the strong effect of the (*R*)-PO molecule is evident. If we now focus on the enantiomeric conformers, i.e. the mirror imaged conformers, we observe that the t1:t2 ratio of the *trans* conformers changes from a more equally distributed 1.2:1 ratio in the neat IL to an excess of t1 in (*R*)-PO@IL (2.1:1 ratio) which is the reason for the VCD activity of the anion. Interestingly, we observe a c1:c2 *cis* conformer ratio of 0.7:1 in the neat IL which changes to 1.4:1 in (*R*)-PO@IL. This enrichment of the c1 conformer may be an indication that the loss of t2 conformers follows a rearrangement to the c1 conformer.

3. Conclusion

To summarize, we observed a selective chirality transfer from (*R*)-1,2-propylene oxide to the achiral anion of the 1-ethyl-3-methylimidazolium bis(trifluoromethylsulfonyl) imide ($[C_2C_1Im][NTf_2]$) ionic liquid by means of *ab initio* molecular dynamics simulations. While it has been demonstrated before from experiment and theory that the 1-ethyl-3-methylimidazolium cation can be affected by chirality transfer, in the present system chirality is transferred only to the anion and not to both parts of the solvent, i.e., the cation and the anion. This observation is of high importance because of 1.) its selectivity and 2.) the fact that IL anion effects are much more important for chemical processes than cation effects, and previously chirality transfer has only been detected for IL cations. We observed this induced chirality by calculating and dissecting the vibrational circular dichorism spectrum of a simulated system containing (*R*)-1,2-propylene oxide dissolved in the mentioned IL. Considering the contributions from the different species, a large contribution of the anion to the total spectrum of the system was observed while only minor contributions were visible for the cation. Since it is known that (*R*)-1,2-propylene oxide transfers chiral information from its anti-side, it is clear that the anion of the IL is affected rather than the cation. This is the case because the cation approaches the (*R*)-1,2-propylene oxide from the syn-side to form hydrogen bonds with the oxygen atom. The anion on the other hand forms hydrogen bond like contacts with the hydrogen atom at the stereo center of (*R*)-1,2-propylene oxide and thus approaches the solute from the anti-side. Considering the complex conformational landscape of the anion, i.e., the four conformers of which each two are mirror images (i.e., enantiomeric conformers), we observe a symmetry breaking of the conformational distribution upon the addition of (*R*)-1,2-propylene oxide. We observe an excess of one *trans* conformer in the

10.1002/chem.202301239
WILEY-VCH

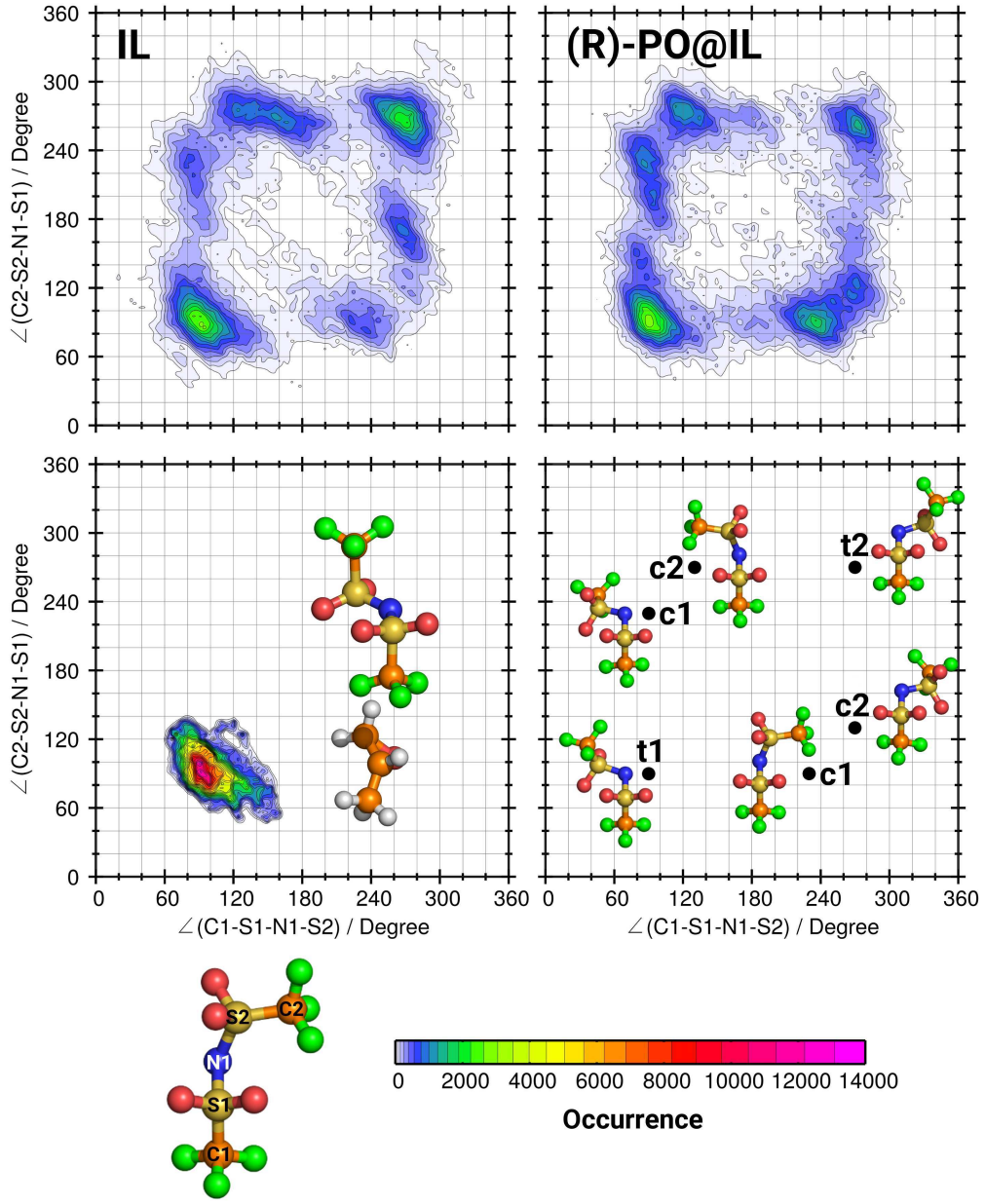

Figure 4. Conformational plots showing the populations of the $[NTf_2]^-$ anion in the systems IL and (*R*)-PO@IL. Plotted are the dihedral angles ◁C1–S1–N1–S2 versus ◁C2–S2–N1–S1. Above: Neat IL (left) and (*R*)-PO@IL (right). Bottom: Conformation of $[NTf_2]^-$ next to (*R*)-PO (left) as well as ball-and-stick representations of the different $[NTf_2]^-$ conformations (right). The color code for the atoms is: orange: carbon; blue: nitrogen; yellow: sulfur; red: oxygen; green: fluorine.

IL containing (*R*)-1,2-propylene oxide compared to the neat IL which results in observable optical activity of the anion. Such a molecular composition may affect the properties of ILs even more than when an achiral cation is asymmetrized. As a next step it will be interesting to investigate if and how ILs with permanently chiral cations can transfer chirality to achiral anions and which other achiral anions can be found that allow chiral transmission to them. The present results show not only that the type of ionic liquid has to be carefully considered because achiral ions can be influenced by chiral solutes or chiral counterparts, but more importantly, the chirality transfer can be directed or controlled by the right choice of chiral inducer molecule. This may have large implications for ionic liquids when they are applied in asymmetric processes such as catalysis or extraction.

Supporting Information

Additional references cited within the Supporting Information. [25,37,45,46,50–73]

Acknowledgements

This project (EOS 40007515) has received funding from the FWO and F.R.S.-FNRS under the Excellence of Science (EOS) programme.

Conflict of Interest

The authors declare no conflict of interest.

Keywords: Anion Effect • Chirality Transfer • Ionic Liquids • Molecular Dynamics • Vibrational Circular Dichroism

References

[1] F. Pabst, J. Gabriel, T. Blochowicz, *J. Phys. Chem. Lett.* **2019**, *10*, 2130–2134.
[2] H. Li, T. Niemann, R. Ludwig, R. Atkin, *J. Phys. Chem. Lett.* **2020**, *11*, 3905–3910.
[3] D. S. Firaha, O. Hollóczki, B. Kirchner, *Angew. Chem. Int. Ed.* **2015**, *54*, 7805–7809.
[4] J. F. Brennecke, B. E. Gurkan, *J. Phys. Chem. Lett.* **2010**, *1*, 3459–3464.
[5] W. Lin, M. Pan, Q. Xiao, H. Li, C. Wang, *J. Phys. Chem. Lett.* **2019**, *10*, 3346–3351.
[6] A. Balducci, *Ionic Liquids II* **2018**, 1–27.
[7] T. Rüther, A. I. Bhatt, A. S. Best, K. R. Harris, A. F. Hollenkamp, *Batter. Supercaps* **2020**, *3*, 793–827.
[8] F. Chen, M. Forsyth, *J. Phys. Chem. Lett.* **2019**, *10*, 7414–7420.
[9] S. Sarkar, P. Chandra Singh, *J. Phys. Chem. Lett.* **2020**, *11*, 10150–10156.
[10] P. Wasserscheid, A. Bösmann, C. Bolm, *Chem. Commun.* **2002**, 200–201.
[11] K. Bica, P. Gaertner, *Eur. J. Org. Chem.* **2008**, *2008*, 3235–3250.
[12] H. Ohno, K. Fukumoto, *Acc. Chem. Res.* **2007**, *40*, 1122–1129.
[13] X. Chen, X. Li, A. Hu, F. Wang, *Tetrahedron: Asymmetry* **2008**, *19*, 1–14.
[14] T. Achard, C. Tortoreto, A. I. Poblador-Bahamonde, L. Guenee, T. Bürgi, J. Lacour, *Angew. Chem. Int. Ed.* **2014**, *53*, 6140–6144.
[15] L. Riccardi, F. De Biasi, M. De Vivo, T. Bürgi, F. Rastrelli, G. Salassa, *ACS Nano* **2019**, *13*, 7127–7134.
[16] P. Oulevey, S. Luber, B. Varnholt, T. Bürgi, *Angew. Chem. Int. Ed.* **2016**, *55*, 11787–11790.
[17] M. Gruttadauria, S. Riela, C. Aprile, P. L. Meo, F. D'Anna, R. Noto, *Adv. Synth. Catal.* **2006**, *348*, 82–92.
[18] O. Acevedo, W. L. Jorgensen, J. D. Evanseck, *J. Chem. Theory Comput.* **2007**, *3*, 132–138.
[19] A. Cognigni, P. Gaertner, R. Zirbs, H. Peterlik, K. Prochazka, C. Schröder, K. Bica, *Phys. Chem. Chem. Phys.* **2016**, *18*, 13375–13384.
[20] A. Gilbert, R. S. Haines, J. B. Harper, *Org. Biomol. Chem.* **2020**, *18*, 5442–5452.
[21] M. C. Schopohl, C. Siering, O. Kataeva, S. R. Waldvogel, *Angew. Chem. Int. Ed.* **2003**, *42*, 2620–2623.
[22] A. Zehnacker, M. A. Suhm, *Angew. Chem. Int. Ed.* **2008**, *47*, 6970–6992.
[23] J. Flieger, J. Feder-Kubis, M. Tatarczak-Michalewska, *Int. J. Mol. Sci.* **2020**, *21*, 4253.
[24] J. Blasius, R. Elfgen, O. Hollóczki, B. Kirchner, *Phys. Chem. Chem. Phys.* **2020**, *22*, 10726–10737.
[25] J. Blasius, P. Zaby, O. Hollóczki, B. Kirchner, *J. Org. Chem.* **2021**, *87*, 1867–1873.
[26] R. W. Kawiecki, F. Devlin, P. Stephens, R. Amos, N. Handy, *Chem. Phys. Lett.* **1988**, *145*, 411–417.
[27] T. B. Freedman, X. Cao, R. K. Dukor, L. A. Nafie, *Chirality* **2003**, *15*, 743–758.
[28] C. Merten, J. Bloino, V. Barone, Y. Xu, *J. Phys. Chem. Lett.* **2013**, *4*, 3424–3428.
[29] T. Q. Teodoro, M. A. J. Koenis, R. Rüger, S. E. Galembeck, W. J. Buma, V. P. Nicu, L. Visscher, *J. Phys. Chem. A* **2018**, *122*, 9435–9445.
[30] S. Jähnigen, A. Zehnacker, R. Vuilleumier, *J. Phys. Chem. Lett.* **2021**, *12*, 7213–7220.
[31] D. Zhao, K. Liao, B. Hong, W. Li, S. Li, *Electron. Struct.* **2023**, *5*, 014001.
[32] K. Reiter, M. Kühn, F. Weigend, *J. Chem. Phys.* **2017**, *146*, 054102.
[33] M. Krupová, J. Kessler, P. Bouř, *ChemPlusChem* **2020**, *85*, 561–575.
[34] L. H. Easson, E. Stedman, *Biochem. J.* **1933**, *27*, 1257–1266.
[35] A. Scherrer, R. Vuilleumier, D. Sebastiani, *J. Chem. Phys.* **2016**, *145*, 084101.
[36] B. Kirchner, J. Blasius, L. Esser, W. Reckien, *Adv. Theory Simul.* **2021**, *4*, 2000223.
[37] B. Kirchner, J. Blasius, V. Alizadeh, A. Gansäuer, O. Hollóczki, *J. Phys. Chem. B* **2022**, *126*, 766–777.
[38] M. Losada, P. Nguyen, Y. Xu, *J. Phys. Chem. A* **2008**, *112*, 5621–5627.
[39] N. M. Kreienborg, J. Bloino, T. Osowski, C. H. Pollok, C. Merten, *Phys. Chem. Chem. Phys.* **2019**, *21*, 6582–6587.
[40] M. Fusè, G. Longhi, G. Mazzeo, S. Stranges, F. Leonelli, G. Aquila, E. Bodo, B. Brunetti, C. Bicchi, C. Cagliero, et al., *J. Phys. Chem. A* **2022**, *126*, 6719–6733.
[41] S. Abbate, G. Longhi, K. Kwon, A. Moscowitz, *J. Chem. Phys.* **1998**, *108*, 50–62.
[42] M. Thomas, B. Kirchner, *J. Phys. Chem. Lett.* **2016**, *7*, 509–513.
[43] J.-H. Choi, M. Cho, *J. Chem. Theory Comput.* **2011**, *7*, 4097–4103.
[44] M. Thomas, M. Brehm, B. Kirchner, *Phys. Chem. Chem. Phys.* **2015**, *17*, 3207–3213.
[45] M. Brehm, B. Kirchner, *J. Chem. Inf. Model.* **2011**, *51*, 2007–2023.
[46] M. Brehm, M. Thomas, S. Gehrke, B. Kirchner, *J. Chem. Phys.* **2020**, *152*, 164105.
[47] D. R. Galimberti, *J. Chem. Theory Comput.* **2022**, *18*, 6217–6230.
[48] J. N. Canongia Lopes, K. Shimizu, A. A. Pádua, Y. Umebayashi, S. Fukuda, K. Fujii, S.-i. Ishiguro, *J. Phys. Chem. B* **2008**, *112*, 1465–1472.
[49] F. Philippi, D. Pugh, D. Rauber, T. Welton, P. A. Hunt, *Chem. Sci.* **2020**, *11*, 6405–6422.
[50] R. L. Gardas, M. G. Freire, P. J. Carvalho, I. M. Marrucho, I. M. Fonseca, A. G. Ferreira, J. A. Coutinho, *J. Chem. Eng. Data* **2007**, *52*, 1881–1888.
[51] W. M. Haynes, *CRC Handbook of Chemistry and Physics*, CRC press: Boca Raton, Florida, **2014**.
[52] J. M. Martínez, L. Martínez, *J. Comput. Chem.* **2003**, *24*, 819–825.
[53] L. Martínez, R. Andrade, E. G. Birgin, J. M. Martínez, *J. Comput. Chem.* **2009**, *30*, 2157–2164.
[54] S. Plimpton, *J. Comput. Phys.* **1995**, *117*, 1–19.
[55] W. L. Jorgensen, D. S. Maxwell, J. Tirado-Rives, *J. Am. Chem. Soc.* **1996**, *118*, 11225–11236.
[56] J. N. Canongia Lopes, J. Deschamps, A. A. Pádua, *J. Phys. Chem. B* **2004**, *108*, 2038–2047.
[57] J. N. Canongia Lopes, A. A. Pádua, *J. Phys. Chem. B*

2004, *108*, 16893–16898.
[58] J. N. Canongia Lopes, A. A. Pádua, *J. Phys. Chem. B* **2006**, *110*, 19586–19592.
[59] CP2k developers group under the terms of the GNU General Public License; see http://www.cp2k.org.
[60] J. VandeVondele, M. Krack, F. Mohamed, M. Parrinello, T. Chassaing, J. Hutter, *Comput. Phys. Commun.* **2005**, *167*, 103–128.
[61] J. P. Perdew, A. Ruzsinszky, G. I. Csonka, O. A. Vydrov, G. E. Scuseria, L. A. Constantin, X. Zhou, K. Burke, *Phys. Rev. Lett.* **2008**, *100*, 136406.
[62] S. Goedecker, M. Teter, J. Hutter, *Phys. Rev. B* **1996**, *54*, 1703–1710.
[63] C. Hartwigsen, S. Gœdecker, J. Hutter, *Phys. Rev. B* **1998**, *58*, 3641–3662.
[64] M. Krack, *Theor. Chem. Acc.* **2005**, *114*, 145–152.
[65] J. VandeVondele, J. Hutter, *J. Chem. Phys.* **2007**, *127*, 114105.
[66] S. Grimme, J. Antony, S. Ehrlich, H. Krieg, *J. Chem. Phys.* **2010**, *132*, 154104.
[67] S. Grimme, S. Ehrlich, L. Goerigk, *J. Comput. Chem.* **2011**, *32*, 1456–1465.
[68] S. Nosé, *J. Chem. Phys.* **1984**, *81*, 511–519.
[69] W. G. Hoover, *Phys. Rev. A* **1985**, *31*, 1695–1697.
[70] http://plasma-gate.weizmann.ac.il/Grace/.
[71] http://www.gnuplot.info/.
[72] L. Schrödinger, W. DeLano, *PyMOL*. http://www.pymol.org/pymol.
[73] W. Humphrey, A. Dalke, K. Schulten, *J. Mol. Graphics* **1996**, *14*, 33–38.